MS109

Micromedia Limited

96
0
mm
10
20
30
40
50
60
70
80
90
100

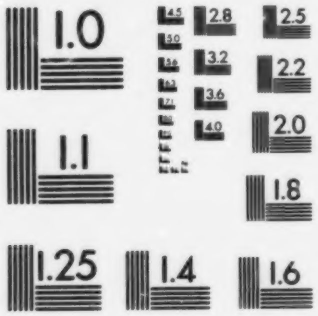
1.0
4.5
5.0
5.6
6.3
7.1
2.8
3.2
3.6
4.0
2.5
2.2
2.0
1.1
1.8
1.25
1.4
1.6

MICROCOPY RESOLUTION TEST CHART
NATIONAL BUREAU OF STANDARDS
STANDARD REFERENCE MATERIAL 1010a
(ANSI and ISO TEST CHART No. 2)

This statement was filmed with this document. If the pages of the document are less clear than this statement it is due to the poor photographic quality of the document.

NATIONAL MICROGRAPHICS ASSOCIATION

24x

Research & Technology Centre

[redacted]

REPORT NO.: 7-184-071-099/F CLASS: 4

TITLE: Evaluation of Heat Affected Zone and Weld Metal Toughness in Selected Steels - Phase 1. **Volume 1 of 2**

CLIENT: Department of Supply and Services

AUTHORS: S.R. Bala/S. Santyr

APPROVED: ________

Final Report Submitted to the Department of Supply and Services on completion of the 50/50 Cost Shared Program.

D.S.S. File No.: 23SQ.23440-4-9056
Serial No.: 0SQ84-00032

AMCA INTERNATIONAL LIMITED
Research and Technology Centre
August 1986

TITLE: EVALUATION OF HEAT AFFECTED ZONE AND WELD METAL TOUGHNESS IN SELECTED STEELS - PHASE 1.

FINAL REPORT

BY

S.R. Bala and S. Santyr

AMCA INTERNATIONAL LIMITED

RESEARCH AND TECHNOLOGY CENTRE

Work on this project was conducted under the auspices of the Canada Centre for Mineral and Energy Technology, Energy Mines and Resources, Canada.

350 pp

MICROMEDIA

D.S.S. FILE NUMBER:	23SQ.23440-4-9056
D.S.S. CONTRACT SERIAL NUMBER:	0SQ84-00032
CANMET PROJECT NUMBER:	4-9056
CANMET SCIENTIFIC AUTHORITY:	Dr. J. Bowker/Dr. J.E.M. Braid

TABLE OF CONTENTS

		Page
	Table of Contents	(i)
	Executive Summary	(iii)
	Acknowledgements	(v)
1.0	INTRODUCTION	1
	1.1 Background and Scope	2
	1.2 Objectives of the Present Work	6
2.0	EXPERIMENTAL PROCEDURE	8
	2.1 Materials	8
	2.1.1 Steels	8
	2.1.2 Consumables	8
	2.2 Weld Preparation	9
	2.3 Toughness Tests	10
	2.3.1 Charpy V-Notch Impact Testing	10
	2.3.2 Drop Weight Tests	11
	2.3.3 Crack Tip Opening Displacement (CTOD) Tests	12
	2.3.3.1 Test Procedure	12
	2.3.3.2 Metallography on Fractured CTOD Specimens	16
	2.3.3.3 Fractography and Fracture Initiation	17
	2.3.4 Gleeble Simulation	18
	2.3.4.1 Charpy V-Notch Impact Testing	19
	2.3.4.2 Instrumented Impact Testing	19
	2.4 Metallographic Examination	20
3.0	RESULTS AND OBSERVATIONS	21
	3.1 K-Joint Macrosections	21
	3.2 Microstructures	21
	3.3 Gleeble Simulation	24
	3.3.1 Charpy V-Notch Test Results	24
	3.3.2 Instrumented Impact Test Results	26
	3.3.3 Hardness Values of Gleeble Specimens	27
	3.3.4 Fractography of Gleeble Specimens	27
	3.4 Impact Energy Transition Curves for K-Joint Welds	28
	3.4.1 Algoma LT60 Steel	29
	3.4.2 A710 Gr. A Cl. 3 Steel	30
	3.4.3 MACS Steel	31
	3.5 Nil Ductility Transition Temperatures (NDT Temp.)	31
	3.6 CTOD Values	32
	3.6.1 Microstructures Near the Fatigue Precrack Front Along the Thickness	35
	3.6.2 Fractography of CTOD Specimens	37
	3.7 The Precipitates in the Coarse Grain HAZ as Analyzed by Extraction Carbon Replica and EDX Techniques	38

TABLE OF CONTENTS

(Continued)

Page

4.0 DISCUSSION 41
- 4.1 Gleeble Simulation 41
  - 4.1.1 Charpy V-Notch Test 41
  - 4.1.2 Instrumented Impact Test 42
- 4.2 CVN Impact Energy and Microstructure 42
  - 4.2.1 Algoma LT60 Steel 43
  - 4.2.2 A710 Gr. A Cl. 3 Steel 46
  - 4.2.3 Kawasaki MACS ACC and DQT Steels 48
- 4.3 CTOD Values and Microstucture 50
  - 4.3.1 Algoma LT60 Steel 52
  - 4.3.2 A710 Gr. A Cl. 3 Steel 54
  - 4.3.3 Kawasaki MACS Steel 54
  - 4.3.4 Microstructure, Fracture Initiation Sites, and the CTOD Values 55
  - 4.3.5 Fitness for Purpose Evaluation of the CG HAZ 56
  - 4.3.6 CVN-CTOD Correlations 59
- 4.4 NDT Temperatures 60
- 4.5 Relative HAZ Toughnesses in the Steels 60
  - 4.5.1 Gleeble CVN Tests 61
  - 4.5.2 K-Joint CVN Tests 61
  - 4.5.3 CTOD Values at -30°C 62
  - 4.5.4 NDT Transition Temperatures 62
  - 4.5.5 Summary of Steel Ranking 63

5.0 CONCLUSIONS 64

6.0 RECOMMENDATIONS FOR FUTURE WORK 66

7.0 REFERENCES 67

EXECUTIVE SUMMARY

Low carbon microalloyed steels now produced can give excellent toughness. However, from weld fabrication point of view, it has been found that the coarsening of grains in the heat affected zone (HAZ) adjacent to the fusion boundary, as well as the precipitation of carbonitrides of microalloying elements, can adversely affect the HAZ toughness in these steels. Post weld heat treatment, instead of improving HAZ toughness as in C-Mn steels, can cause further deterioration on account of increased precipitation hardening effect. To overcome some of these problems, Ti additions to form TiN particles which restrict grain growth in the HAZ, and Cu-Ni additions to lower C (and microalloy content) have been used in recent steel development. Thus, in this investigation the effect of heat input and postweld heat treatment on the toughness of coarse grain (CG) HAZ has been assessed in two steels, viz., Algoma LT60 (Nb-V) and A710 Gr. A Cl. 3 (Cu-Ni-Nb). The study employed full penetration welds in K-joints as well as Gleeble simulated HAZ. The CG HAZ toughness of these steels has been compared with that of the Ti-bearing Kawasaki MACS steel claimed to give good toughness at high heat input levels. In LT60 and A710 steels, the amount of CG HAZ present above 20% showed a dominating effect on the CTOD toughness, i.e., there was little change in the CTOD toughness with increase in CG above ≅20% CG HAZ.

The 40 J and the 0.2mm CTOD value transition temperatures of less than -50°C for MACS steel and less than -30°C for both the LT60 and A710 steels have been observed. These suggest that under certain combinations of heat input and heat treatment, the CG HAZ in all the three steels can meet the anticipated specification requirements of Canadian offshore and Arctic structural applications down to -30°C and only the CG HAZ in MACS steels can marginally meet this requirement down to -50°C.

ACKNOWLEDGEMENTS

The authors would like to thank L. Thompson, A. Hebert, F. Rauche, Z. Maksimovic, M. Chambers, L. Laurin, G. Williams and S. Bonfield for experimental assistance. The assistance of F. Haakman and D. Baker in preparing this report is also greatly appreciated.

Special thanks to J. Bowker, M. Letts, K.C. Wang and CANMET/PMRL for assistance and use of equipment for Gleeble simulations, instrumented impact and drop weight testing.

The work of G. Weatherly is also appreciated.

Sommaire Exécutif

Les aciers avec microalliage à base teneur de carbon maintenant disponible peuvent donné de bonne tenacité. Mais du point vue de la fabrication par soudure, il a été établi que le grossisement des grains dans la zone affecter par la chaleur (Z.A.C.) près de la bordure de fusion et, en plus la précipation des éléments de microalliages peuvent affecté d'une façon défavorable la tenacité de ces métaux dans cette Z.A.C.

Aulieu d'améliorer la tenacité dans la Z.A.C. pour les aciers C-Mn, le traitement thermique après soudage peut qu'accentué une dégradation causer par une augmentation de l'effect du durcicement de précipitation. Pour éviter ces problèmes, Ti est ajouté pour formé des particules de TiN qui restreindra le grossisement des grains dans la Z.A.C. et, l'addition de Cu-Ni pour réduire le C (et le contenue des microalliages) ont été utiliser dans le dévelopment de nouveaux métaux. Alors, dans cette enquête l'effect d'apport calorifique et le traitement thermique après soudage sur la tenacité des gros grains dans la Z.A.C. à été déterminer pour deux acier: Algoma LT60 (Nb-V) et A710 Gr A CL3 (Cu-Ni-Nb). Cette étude a employé la pleine pénétration des soudures de la forme-K et le format Gleeble pour assimiler Z.A.C. La tenacité des gros grains dans la Z.A.C. pour ces aciers on été comparé à l'acier Kawasaki Macs au Ti qui à la réputation d'avoir une bonne tenacité à des niveaux élever en apport calorifique.

Pour les aciers LT60 et A710, la quantité de gros grains au delà de 20% dans la Z.A.C. à pour effect de dominer la tenacité au déplacement de l'ouverture de pointe de la fissure (CTOD) et peu de changement fut noter avec une augmentation de gros grains au delà de 20%.

Des valeurs de Températures de Transition pour les CTOD de 40J et 0.2mm à moins de -50°C pour les acier MACS et de -30°C pour les aciers LT60 et A710 ont été observer. Ceci suggère que sous certaine combinaisons d'apport calorifique et de traitement thermique les gros grains dans Z.A.C. de ces trois aciers peuvent rencontré à la demande anticiper par le Canadian offshore, et pour les applications structurale de l'Arctique à des températures de -30°C. Seul les gros grains dans la Z.A.C. de acier MACS peu répondre á des demandes de -50°C.

1.0 INTRODUCTION

The environmental conditions, especially the ambient temperature, in the regions where the Canadian Offshore hydrocarbons are located, are unique and there is little past experience on suitability and adequacy of steels for structures in these environments. Design temperatures for structures exposed to ambient conditions could be in the order of -30° to -60°C. In order to meet these demands, steelmakers have relied largely on the use of microalloying elements to provide precipitation strengthening and grain refinement. In addition, steels are being improved by using thermal-mechanical treatments such as control rolled on-line accelerated cooling and quenching and tempering.

ASTM A710 Gr. A, Cl. 3, which is a precipitation hardened, low carbon, Cu-Ni-Cr-Mo-Nb steel, was designed initially for use in Arctic environments and is believed to have made significant in-roads in Navy ship applications.

The Algoma Steel Corporation has produced a special heat of steel with the aim of meeting Lloyds LT 60 specification requirements in thicknesses up to 75 mm. This steel is a modified version of CSA G40.21 Gr. 350 WT and is similar to BS 4360 Gr. 50 D which has been used extensively in North Sea applications.

Steel types ASTM A710 Gr. A, Cl. 3 and Lloyds LT 60 (from Algoma Steel Corp. Ltd.) are two potential steels for use in Arctic and Offshore applications, both of which could be produced in Canada.

1.1 BACKGROUND AND SCOPE

The formability and weldability of the above two steels with respect to low temperature applications have been examined in an earlier investigation (Ref. 1). In addition, both the weld and heat affected zone properties play an important role in design of welded fabrications. The present report focuses on the heat affected zone toughness aspect, with weld metal to be addressed in a subsequent program.

In weld heat-affected zones (HAZ), microalloying elements can significantly affect properties through their effects on austenite grain size, transformation characteristics and precipitation strengthening. (Ref. 2-44) Microalloying elements taken into solution during the high temperature portion of the weld thermal cycle, are available to reprecipitate during cooling. Precipitation serves to tie up free nitrogen from the matrix as well as providing inhibitors to grain growth and dislocation mobility. The time and temperature required for reprecipitation generally become available in higher heat input, multipass and stress-relieved welds (Ref. 2,8,9).

The importance of the effect of precipitation characteristics on toughness properties led to the inclusion in the present study of an analysis of a selected number of specimens for a) the nature and size distribution of any fine scale precipitation and b) the nature of the decomposition products of austenite, particularly with respect to the formation of the MA phase or carbides during cooling.

In Nb-V steels, the microstructure in the supercritical region of the HAZ typically consists of low temperature transformation products. This microstructure is predominantly bainitic, often with primary ferrite sideplates (Widmanstatten) at prior austenite grain boundaries of the CG (coarse grain) HAZ.

The bainitic structure[37, 45, 46] referred to in this study is similar to upper bainite which forms at higher temperatures and consists of elongated carbide aggregates aligned parallel to the major axis of the ferrite laths and present in regions between the laths. The ferrite laths are arranged in sheaves separated by low angle boundaries. In addition to the carbide aggregates, the regions between the ferrite laths may also have martensite and retained austenite particles of different shapes. Each "sheaf" separated by high angle boundaries forms a packet (bainitic colony). Each grain in the CG HAZ, as outlined by the prior austenite grain boundary, constitutes several of these packets as shown in the typical micrograph in Figure 1.

Such microstructures are generally thought to give poor cleavage resistance, particularly when bainite "packet size" (distance between high angle boundaries within a prior austenite grain) is large. This packet size which is the effective grain size for cleavage, increases as prior austenite grain size increases, and many believe that the CG HAZ is the region most likely to have poor toughness (Ref. 2, 5, 32). This presumed low toughness in the CG HAZ has led to increased efforts to sample as large a proportion of CG HAZ as possible.

In most steels low HAZ toughness can be found at very low and high heat input levels. However, the effect of heat input on HAZ toughness depends on the steel composition. At high heat inputs microalloyed steels show a deterioration in toughness, the magnitude of which increases with an increase in the level of microalloying. This toughness deterioration is attributed to the precipitation of Nb and V rich precipitates and the coarse austenite grain size associated with the increase in heat input (Ref. 34 and 38).

The interstitial nitrogen in the base metal can affect subcritical HAZ embrittlement. The AlN particles present in the base metal can be taken into solution in the grain coarsened HAZ and become available in the HAZ to influence cleavage resistance either through dynamic strain aging or solid solution effects. The root regions of an as-welded joint usually will have the lowest toughness due to dynamic strain aging (Ref. 34). One of the ways to improve the root toughness is by backgouging.

Other regions of the HAZ in some steels display lower cleavage resistance and these regions cannot be overlooked when assessing results (Ref. 2, 34). In particular, the subcritical and the intercritically reheated CG HAZ regions found in multipass welds are thought to have reduced toughness. The structures present in a weld HAZ can be altered greatly when a second bead is laid over the first one as in multipass welds.

The reheated HAZ will have improved toughness in some regions, generally in those which become refined, and deterioration in others such as in coarse grained supercritical regions reheated to intercritical temperatures. In order to assess the multi-structure properties of a joint such as might be found in service, tests must be carried out on real weld specimens to assess the true HAZ toughness properties. A simulated thermal cycle can be used to produce a single cycle CG HAZ specimen in order to determine properties for this region only.

A survey of the literature shows that there have been a number of studies performed to characterize HAZ toughness properties and their relationship to microstructure (Ref.4, 22, 23, 47-51). However, understanding of the structure/property relationships remains limited to specific steel compositions.

1.2 OBJECTIVES OF THE PRESENT WORK

In light of the increased concern and limited data available for HAZ toughness of microalloyed steels, two such steels, viz., CSA G40.21 Gr. 350 WT (Algoma-Lloyds LT60 steel) and ASTM A710 Gr. A Cl. 3 steel have been examined in the present study. Also, a third steel, viz., Japanese EH36 grade steel produced by the multi-accelerated cooling system (MACS steels) which has been claimed to give excellent HAZ toughness at high heat input levels[52, 53] has also been included in this program for comparison purposes.

The objectives of the program were as follows:

A. To evaluate and compare the CVN and instrumented impact toughness of a relatively homogeneous CG HAZ obtained by Gleeble simulations at various heat inputs.

B. To evaluate the toughness of CG HAZ in K welds at selected heat inputs, and in as-welded and postweld heat treated conditions, as well as to assess the suitability of these steels for structural applications for Canadian offshore and Arctic oil and gas development. The criteria used in assessing the suitability of the steels was their fracture toughness, viz., CVN transition temperature, CTOD values at -30°C, and NDT temperature.

C. To develop correlations between the CTOD toughness and the proportions of the CG HAZ.

D. To compare the toughness of the CG HAZ in both the Gleeble simulated and the real welds, in the as-welded and the stress-relieved conditions.

E. To develop a correlation between CTOD and CVN toughnesses.

F. To assess the behaviour of selected K-joint welds in wide plate tests.

2.0 EXPERIMENTAL PROCEDURE

2.1 MATERIALS

2.1.1 Steels

Heat affected zone toughness properties have been determined for the following three steels:

1)	A710 Gr. A, Cl 3	50 mm (Kawasaki Steel Corp.)
2)	Lloyds LT 60	63 mm (Algoma Steel Corp.)
3)	EH 36 (multi-accelerated cooled: MACS ACC)	50 mm (Kawasaki Steel Corp.)
	for use in "as-welded"condition only	
	EH 36 (direct quench and temper: MACS DQT)	50 mm (Kawasaki Steel Corp.)
	for use in "stress-relieved"condition only	

Chemical compositions and mechanical properties of the three steels are listed in Tables 1 and 2 respectively.

2.1.2 Consumables

Welding consumables were chosen to have composition and toughness properties compatible with the base materials. These are:

ARMCO W-19 (3.2 mm) with Lincoln 880 flux. (37J @ -110°C AW, 50J @ -110°C SR)

OERLIKON SD2-3Ni (4.0 mm) with Lincoln 880 flux.

2.2 WELD PREPARATION

For each steel/heat input combination four full-thickness plates, 1.2m in length, were submerged-arc welded using a Miller CP/CC 1500P machine (see Appendix B, Figures B1 and B2).

The operating conditions, selected after a series of optimization trials for each heat input, are given in Table 3A. K-joint preparations (both nose and flat edge) were machined prior to welding to ensure good fit up as well as the straightest possible HAZ. Similarly, angle and sidewall distance of the electrode were carefully controlled. The first side of each weld was completely welded under high restraint in order to minimize distortion which was controlled to 1° maximum. Plates were backgouged and lightly ground, then the second side was completely welded. Welding was not alternated from side to side in the root in order to avoid misaligning the straight HAZ. Each plate contained the length of the weld parallel to the rolling direction. The matrix of steel-heat input combinations for the welds made is given in Table 3B.

Two of the welded plates for each heat input were stress relieved at 620°C for two hours and furnace cooled. Thus, in all, 12 steel-heat input-post weld heat treatment combinations (test conditions) were examined.

Blanks for CTOD, CVN and NDT test specimens were flame cut from the welds. As well, one macrosection was taken from each welded plate in order to assess weld quality and HAZ straightness and microstructure.

2.3 TOUGHNESS TESTS

2.3.1 Charpy V-notch Impact Testing

The blanks for the preparation of CG HAZ Charpy specimens were extracted from the subsurface and the root location of each weld. The subsurface blanks were removed from just below the nail head (approximately 3 mm to 5 mm below the surface) of the final weld beads in side one, such that a straight HAZ could be obtained. The root blanks were obtained from the T/2 location of the plates (first bead from the second side). Each blank was etched to reveal the fusion boundary and the HAZ. The lines were drawn along the CG HAZ corresponding to the straight portion of the K-groove weld. These blanks were used in the preparation of CVN specimens.

For each test condition, at least 15 standard Charpy specimens for the CG HAZ (in the root or the subsurface region), 10 x 10mm in cross section and 55mm long, were machined with the length of the specimen perpendicular to the welding direction. The Charpy specimens were re-etched and notched in the side of the specimen which was normal to the surface of the plate, such that the root of the notch coincided with the CG HAZ.The impact tests were carried out in a range of temperatures to obtain the full transition curves.

For one test condition, the impact energy transition curves were also determined both for the weld metal and the refined structure of the HAZ (subsurface location).

A limited amount of metallography was performed on the tested CVN specimen to resolve the scatter observed in the CVN data. One half of the tested specimen was sectioned at the center of the face containing the notch, perpendicular to the notch. Also some of the specimens were sectioned along the notch root. In both cases, the sectioned surface was mounted, polished, and etched to examine the root of the notch location in the HAZ, the microstructure along the root, and the fracture path.

2.3.2 Drop Weight Tests

The drop weight test is another standard and economical test developed for assessing toughness characteristics of structural steels under dynamic loading conditions. ASTM Standard E208 (Ref. 54) establishes specimen sizes and procedures to determine the nil ductility transition (NDT) temperature -- the maximum temperature where a standard drop weight specimen breaks when tested according to the provisions of this method.

In this study, NDT temperatures for the CG HAZs were established for each test condition. The specimen blanks were removed from the subsurface location just below the nail head (approx. 3mm to 5mm below the plate surface) on side one of the weldment, such that a fairly straight CG HAZ could be obtained. For each test condition, eight P2 type specimens (130 x 50 x 19mm in size) were prepared from the etched blanks such that the notching of the crack starter weld coincided with the CG HAZ of the test weld, and the surface of the specimen where the crack starter weld was deposited was parallel to the plate surface.

The drop weight tests were carried out as per ASTM E208-81 at CANMET/PMRL. The test was repeated at the break - no break temperatures. All of the tested specimens were etched to observe the location of the starting crack and the fracture.

A limited number of specimens tested at the break - no break temperatures were sectioned for metallography. The metallography was performed to examine the exact location of the starting crack, as well as the fracture path in the HAZ. Metallography was also performed on some specimens which showed anomaly in the test results.

2.3.3 Crack Tip Opening Displacement (CTOD) Tests

2.3.3.1 Test Procedure

The CTOD test was used to measure the fracture initiation characteristics of the CG HAZ under static loading conditions. Essentially, full thickness specimens of preferred geometry (B x 2B in section) and with the welding direction transverse to the length of the specimen were used to test the coarse grain region of the HAZ. The thickness was reduced by milling approximately 3mm from each surface of the plate. This accomplished two things: (a) it removed most of the "nail head" of the final beads, and (b) it allowed the CG HAZ to be square with the surface which, due to distortion, would not otherwise have been square.

For LT 60 steel, the final thickness was 57mm, whereas for A710 Gr. A Cl. 3 and MACS steels, the final machined thickness was 44.5mm. Initially, the surface corresponding to the plate surface in each CTOD specimen was milled fully. Subsequently, to reduce the machining time, only the weldment location was reduced in thickness (≅ 3mm on each surface of the plate) by milling a total of 2B wide region symmetrically about the straight portion of the CG HAZ of the K-weld. The specimen dimensions are shown in Figure 2.

A through-thickness notch was made in the HAZ such that the root of the notch would sample the maximum amount of coarse grain in the HAZ. One of the as-welded specimens was fatigue precracked as per BS 5762 (Ref. 55) and tested. The fractured specimen showed irregular fatigue precrack growth and the test was invalid because of non-uniformity of the precrack. The non-uniform growth of the fatigue crack is known to be due to the presence of residual stresses. It has been recommended by The Welding Institute (U.K.) that the notch ligament, in the as welded specimen, be locally compressed, plastically to a total depth of 1% of the total thickness. (Ref. 56, 57, 58). Following this recommendation, a few 57mm thick (B) specimens were locally compressed using 25mm diameter indentations from both sides of the ligament. The 25mm diameter indentor was used, due to load capacity limitations. The notch ligament was locally compressed plastically to a total of 1% of the thickness using three equally-spaced indentations. The first indentation was placed at the notch root. The last indentation was placed about 6mm away from the bottom surface. When precracked, these specimens showed bowl-shaped fatigue precrack fronts indicating that the local compressing strain was higher than actually needed. Later, the notch ligaments in all of the as-welded specimens were locally compressed from both sides to a total plastic compression of 0.35 to 0.45% of the thickness B. For 57mm thick specimens, three equally-spaced 25mm diameter indentations were used, whereas for 44.5 mm thick specimens, only two equally-spaced 25 mm diameter indentations were used.

The as-welded CTOD specimens with their notch ligament locally compressed and the stress-relieved specimens (without local compression of the notch ligaments) were fatigue precracked to obtain a total a/W ratio of 0.45 to 0.55. For the initial 1mm of the fatigue precracking, maximum load was calculated using $K_f \leq 0.6\ \sigma_y\ B^{\frac{1}{2}}$. For the final 3mm of fatigue cracking, the maximum load was reduced in accordance with $K_f \leq 0.4\ \sigma_y\ B^{\frac{1}{2}}$. The R ratio was in the range of 0 to 0.1.

The CTOD tests were performed to BS 5762-79 (Ref. 55) using the Pegasus 635 kN servohydraulic material test system. A test speed of 0.04 mm/s was used. The knife edges, 3mm in thickness, were glued to the specimen with a Loctite Superbonder 430 adhesive. Using a CTOD gauge mounted on the specimen (knife edge) to monitor the displacement, a total travel displacement of ≅4mm could be measured. Initially, at least five specimens were tested at both -30° and -60°C, with the aim of obtaining at least three that had been notched and fatigue precracked such that the crack tip resides in the coarse grain region of the HAZ. The test temperature of -60°C was found to be too low, and hence, later tests were carried out at -50° instead. At least four specimens per heat input were tested at each of those temperatures. The tests were terminated when the specimen failed (unstable crack growth) sometime after an initial pop-in. The specimens were broken open at the end of the test, and the crack lengths measured.

2.3.3.2 Metallography on Fractured CTOD Specimens

Initially one-half of the fractured CTOD specimen was sectioned across the fatigue precrack (FC) as shown in Figure 3c, polished and etched to reveal the microstructure. The proportion of various microstructures along the fatigue precrack on the etched surface was determined quantitatively using a vernier. The major microstructures categorized were the coarse grain HAZ, fine grain HAZ, weld metal, the remainder to include the rest. These "other" structures included the subcritical, intercritical, refined and the base material structures.

After the initial examination, the fractured CTOD specimen was also sectioned across the fracture path about 1mm below the fatigue precrack front, polished, and etched. Again, the microstructure along the fracture path line on the etched surface was determined quantitatively using a vernier.

2.3.3.3 Fractography and Fracture Initiation

One-half of the fractured CTOD specimen was used for metallography and the other half was used for fractographic analysis. For the latter, the fracture surface was viewed through a low magnification binocular stereoscope. The fracture initiation location was identified by the point of convergence of the tear ridges. Sometimes more than one initiation location was observed. These locations were marked with a felt pen (on the fatigue precrack surface) and these along with the adjacent regions on the fracture surface were then examined in the SEM. The black mark acted as a reference point. The fracture initiation site was located microscopically as the converging point for the river lines.

Initially, for LT 60 steel, the fracture surfaces were sectioned longitudinally across the mid-thickness of the specimens to show the locations of fatigue precrack tip and the "crack path." Later, some of the fractured surfaces were also sectioned longitudinally across the fracture initiaion locations, polished, and etched. Pictures were taken at suitable magnifications to show the locations of the fatigue precrack tip and the fracture initiation site.

2.3.4 Gleeble Simulation

Three heat inputs were chosen for thermal simulations. These were carried out using the Gleeble 1500 equipment at CANMET/PMRL.

Thermal cycles for the three heat inputs (1.6, 3.5 and 5.4 kJ/mm) were determined experimentally. Bead on plate welds were made on two inch thick plate preheated to 100°C, using the operating conditions shown in Table 3. Cooling curves were recorded as mV vs time on a Sargent Welch X:Y strip chart recorder connected through an Omega - CJ cold junction compensator to a harpoon type Pt, Pt/13% Rh, thermocouple. The thermocouple was manually plunged into the weld pool directly behind the arc and the thermal cycle monitored until the temperature fell below 100°C.

Experimental thermal cycle data was programmed into the Gleeble and the bars,10mm x 10mm x 80mm in size, were individually cycled to the appropriate heat input simulation. Critical thermal data is given in Table 4.

For each heat input/steel combination, 15 bars were left in the "as-cycled" condition. The remaining 15 bars were stress relieved at 620°C for 2 hours and furnace cooled.

2.3.4.1 Charpy V-Notch Impact Testing

Some of the specimens for each heat input, both in the as-welded and stress-relieved conditions, were used for CVN impact tests as per ASTM A370. Transition curves were developed up to a maximum temperature of 25°C. Although this did not allow determination of upper shelf energies in all cases, it was considered adequate for the type of service conditions that this work is focused on.

Prior to Gleeble cycling, a line was scribed on the surface of each specimen upon which the optical pyrometer was centered. The Charpy V-notch was located directly over this line to ensure that coarse grain HAZ material was sampled.

2.3.4.2 Instrumented Impact Testing

The remaining specimens for each heat input were used for precracked instrumented impact tests. Testing was carried out using the facilities at CANMET/PMRL.

Both load and energy vs time traces were obtained automatically during testing.

Higher test temperatures were required to obtain useful data, as precracked Charpy tests can show transition temperatures of 20°-30°C higher than CVN transition temperatures. For this reason, impact data was obtained up to a maximum temperature of 50°C.

A 0.6mm thick slot was cut to a depth of 1mm. Once again this was located along the line scribed prior to Gleeble cycling. Subsequently a fatigue crack was grown to a depth of 5mm so that a/W was approximately .5 for each specimen.

2.4. METALLOGRAPHIC EXAMINATION

Extensive metallographic examination was carried out on representative Gleeble and K-joint weld specimens for each test condition.

Grain size, microstructure and hardness were examined so that results could be more fully explained. Precipitation characteristics of some specimens were also examined (see Appendix A). Some of the specimens were examined in a scanning electron microscope.

3.0 RESULTS AND OBSERVATIONS

3.1 K-JOINT MACROSECTIONS

Photomacrographs of transverse sections of each weld are shown in Appendix B (Figures B-3 through B-14). In most welds, the coarse grain HAZ (straight portion of the fusion boundary) region is fairly straight.

In some cases, lack of straightness in the HAZ is seen. This seems to depend on the amount of material removed during backgouging. This can offset the root or in some cases the entire second side of the weld. As well, the angular distortion which occurs during welding of the first side can cause lack of straightness in the coarse grained HAZ.

3.2 MICROSTRUCTURES

Microstructural analysis was carried out both in the capping pass to sample unreheated HAZ, as well as in the root to sample multipass effects. The schematic in Figure 4 shows the effect of multiple passes on underlying regions. The five main regions of interest are also indicated in Figure 4, these being; coarse grain supercritical (>50µm), fine grain supercritical (20-50µm), intercritical, subcritical and intercritically reheated supercritical. Photomicrographs of the base material microstructure and of intercritically reheated supercritical regions of the HAZ (as-welded condition) for each of the three steels are shown in Figures 5 through 11. The prior austenite grain sizes measured in the CG region of the HAZ are given in Table 5.

Other than the minor differences in prior austenite grain sizes as shown in Table 5, the microstructures of coarse grain regions of HAZ (at a magnification of 500X) of A710 and LT 60 are quite similar. Both have predominantly bainitic structures, and frequently Widmanstatten ferrite nucleated at prior austenite grain boundaries was also observed. Although the bainitic structures in the HAZ of both steels have ferrite with carbon rich second phase, in each case, the carbon is present in a different form.

(a) In A710 most of the carbon is retained in the form of "MA" phase at ferrite boundaries, which decomposes to carbides upon stress relief. It has been suggested that this phase can act as an initiation site for cleavage, (Ref. 52), however, there is no substantial experimental evidence to support this.

(b) In LT 60, the carbon is present as lamellar iron rich carbides. Upon stress relief, as well as at higher heat inputs, carbon is precipitated as coarse (Fe, Cr, Mn) mixed carbides and as fine (Nb, V) carbo-nitrides.

The MACS steels are Ti containing steels and as such, the prior austenite grain size is much smaller than the Nb, V steels due to grain boundary pinning by Ti rich nitrides.

The structure also is noticeably different in that it contains polygonal ferrite as well as ferrite laths with second phase. Carbide precipitation is favoured over MA formation and the second phase in ferrite consists of "feathery" iron rich plates of carbide. The grain boundaries are much less well defined in this steel and carbides form more randomly, i.e., they are not as clearly aligned as in the other steels.

The intercritically reheated supercritical regions of the HAZ at the fusion boundary also contained coarse grain regions. The grain boundaries of these coarse grains are "decorated". (Refer to Figures 6 to 11).

The "decorated" boundaries when examined in a scanning electron microscope showed small pearlite colonies in the "decorated" regions. A typical pearlite colony observed in the "decorated" region is shown in Figure 12.

For all three steels, the combined effects of microalloying elements and the low carbon content on transformation characteristics are such that martensite and grain boundary ferrite do not form in the range of heat input levels used in this program.

Figures 13 through 21 show the microstructures of CG and FG supercritical regions in the Gleeble simulated specimens. Except for the grain size, there is no significant difference in the microstructures of the supercritical CG HAZ of K-joint welds and the respective Gleeble simulated specimens at a magnification of X500.

3.3 GLEEBLE SIMULATION

3.3.1 Charpy V-notch Test Results

Individual Charpy V-notch transition curves are shown in Appendix C (Figures C-1 through C-18). These include curves for three heat inputs in both the as-welded and stress-relieved conditions for each of the three steels.

Figures 22 through 27 show the effects of heat input on the CVN impact energy values for each of the three steels. Although there is considerable scatter in results, smooth lines are drawn close to the average CVN values, and these plots show the following:

(a) There is a little effect of heat input on the transition curves for the "as-welded" Gleeble specimens of LT60 steel. On stress-relieving, the impact energy decreases over the respective as-welded condition for the same steel (Refer to Figures 22 and 23). However, this decrease is small.

(b) The impact energy transition temperatures increase with increasing heat input for both the as-welded and stress-relieved Gleeble specimens of A710 Gr. A Cl. 3 steel. Stress-relieving considerably deteriorates the impact energy transition temperatures of the respective as-welded Gleeble specimens as shown in Figures 24 and 25.

(c) The impact energy transition temperatures are lowest at 3.5 kJ/mm heat input and highest at 1.6 kJ/mm heat input for the as-welded and stress-relieved conditions of the Gleeble specimens for MACS steels, and stress-relieving seems to marginally increase the transition temperature at all the heat inputs.

Figures 28 through 33 show a comparison of the CVN impact energy values for the three steels at each of the three heat input levels. In each case, the impact energy transition temperature increases in the as-welded and the stress-relieved condition in the following order of the steels: MACS, A710 Gr. A Cl. 3, and LT60 steels.

3.3.2 Instrumented Impact Test Results

Table C-8 (Appendix C) lists the results of the instrumented impact test. Fracture toughness values (K_{1d}) were calculated directly from the instrumented impact data. These are shown graphically in Appendix C (Figures C-19 through C-36) for individual steel/heat input combinations.

Figures 34 through 39 show the effects of heat input on the precracked specimen K_{1d} values for each of the three steels.

Keeping the scatter in mind, it is hard to discern any consistent effect of heat input on the K_{1d} values or transition temperature for any of the steels. Stress-relieving, in general leads to deterioration in the K_{1d} values. As a matter of fact, in the stress-relieved condition, LT60 and A710 steels do not show any increase in K_{1d} value over the temperature range tested. Overall, these results are similar to the CVN impact energy results. However, the K_{1d} transition curves fall to the right of the corresponding CVN impact energy transition curves i.e., the ductile-brittle transition temperatures obtained from the instrumented impact tests are higher than those from the CVN impact tests.

Figures 40 through 45 show a comparison of the K_{1d} values for all three steels at each of the three heat input levels.

In the as-welded condition, the relative ranking of those steels is the same as from CVN tests, viz., MACS steel has the best CG HAZ toughness and the LT60 CG HAZ is the least tough. In the stress-relieved condition, the differences are minor, and one could infer that MACS steel is somewhat better than the other two.

3.3.3 Hardness Values of Gleeble Specimens

The average hardness values found in the coarse grain supercritical region of Gleeble specimens are given in Table 6. The hardness generally decreases with an increase in heat input for the as-welded condition. The change in hardness due to stress-relieving, does not show any general trend of increase or decrease.

3.3.4 Fractography of Gleeble Specimens

Some of the tested Gleeble specimens representative of each steel/heat input combination, were examined in the SEM to assess cleavage characteristics. Figures 46 through 48 show the cleavage facet appearance for the three steels. It was thought that facet size might correspond to "packet" size. The typical cleavage facet size was in fact smaller than the average prior austenite grain size, and as such, could represent "packet" size.

3.4 IMPACT ENERGY TRANSITION CURVES FOR K-JOINT WELDS

The CVN impact energy transition plots obtained for the CG HAZs are given for all test conditions Figures 49 to 60. The CVN data is given in Appendix C (C1 - C7). Smooth curves are drawn through the lowest impact energy values in these plots. The microstructural location at the root of the notch, and fracture initiation and propagation, obtained from limited metallography of the tested CVN specimens, are marked in these Figures. Also, Figures 61 to 69 show the microstructures at the root of some of the notches, with most of these located in the CG HAZ. For specimens in which there was no CG HAZ present along the root of the notch, the data points have been omitted.

The CVN impact energy transition curves obtained for the as-welded subsurface specimen from LT 60 steel weldments produced at 3.5 kJ/mm heat input, with the notch in the CG HAZ, weld metal, and the "intercritical + normalized" (refined) regions, respectively, are given in Figure 70.

A large scatter in the CVN data is observed. (Refer to Figures 49 to 60). The metallography carried out at the notch root location partly explains some of the scatter observed. The notch roots contained different amounts of CG HAZ. The fusion boundary that is less than ideally straight and a host of microstructures present along the fusion boundary make it difficult to place the notch so as to sample only the CG HAZ. It was commonly found that the grain coarsened HAZ close to the fusion boundary gave the minimum CVN impact energy. Hence, smooth transition curves were drawn through the minimum CVN impact energy values, and may be more representative of the CG HAZ. In addition, transition curves were drawn for the average values. The following comparisons are based upon average CVN plots, noting that comparisons based on minimum CVN plots would not be much different.

3.4.1 Algoma LT60 Steel

(a) In the as-welded condition, the CVN impact toughness of the root region is generally thought to be lower than that for the subsurface region. This is observed to be the case at 3.5 kJ/mm. However, at 5.4 kJ/mm, at least in the lower shelf and transition regions, the HAZ at root has better toughness. As far as the effect of heat input is concerned, at the subsurface location, better HAZ toughness is obtained at 3.5 kJ/mm than at 5.4 kJ/mm. At root location, the toughnesses are similar at the two heat inputs.

(b) In the stress-relieved condition, the CVN transition temperatures for the subsurface at 3.5 kJ/mm heat input and for the root at 5.4 kJ/mm are lower than those for the root and surface respectively. The transition temperatures of the CG HAZ for the subsurface locations are comparable at both the heat inputs, while at the root location, these temperatures are lower for the 5.4 kJ/mm heat input than for the 3.5 kJ/mm heat input.

(c) The CVN transition temperatures of the CG HAZ obtained at 3.5 kJ/mm heat input deteriorated on stress-relieving except at the root region at temperatures above -35°C, where the absorbed energies were higher. At 5.4 kJ/mm heat input, stress-relieving improved the CVN transition temperatures of the HAZ.

(d) The CVN transition temperatures of the weld metal seem to be lower than those of the CG HAZ. The limited number of data points for the refined region also show that its transition temperatures are lower than those for the CG HAZ (Refer to Figures 49 and 70).

3.4.2 A710 Gr. A Cl. 3 Steel

(a) In the as-welded condition, there is no consistent trend in the changes in transition temperatures with location or heat input. Thus, transition temperatures are lower for the root location at 1.6 kJ/mm and 3.5 kJ/mm, whereas at 5.4 kJ/mm, the subsurface location has lower transition temperatures. With increasing heat input, the transition curves for the root location move to higher temperatures. In comparison, at the subsurface location, they move to lower temperatures (improved toughness).

(b) On stress-relieving, the transition temperatures of the CG HAZ in the root and subsurface regions were similar at each heat input level. The 5.4 kJ/mm transition curves were the left most (best toughness) and those for 3.5 kJ/mm were the right most, with those for 1.6 kJ/mm falling in-between.

(c) At heat inputs of 1.6 and 3.5 kJ/mm, stress-relieving increased the CVN transition temperatures of the as-welded CG HAZ at both locations tested. However, at 5.4 kJ/mm heat input, stress-relieving did not seem to have any effect on the transition temperatures of the subsurface region, but decreased the temperatures in the root region of the as-welded CG HAZ.

3.4.3 MACS Steel

(a) In both the as-welded and stress-relieved cases, the CVN transition temperatures of the CG HAZ in the subsurface regions were lower than those for the root region.

(b) Stress-relieving improved the transition temperatures of the CG HAZ at both subsurface and root locations.

3.5 NIL DUCTILITY TRANSITION TEMPERATURES (NDT TEMP.)

The drop weight test data is given in Tables 7 to 12 for all the test conditions. The locations of the starting crack and the crack path, as observed from metallography, are also given in these Tables. Figures 71 to 76 show the specimen batches tested.

Most of the cracks are located in the CG HAZ. The microstructures observed in some of the specimens tested at the nil ductility transition temperatures (NDT temp.) are shown in Figures 77 to 83. The nil ductility transition temperature was established as the maximum temperature at which at least one specimen breaks, with the starting crack and crack path in the coarse grain heat-affected zone. Thus, from the drop weight test data, the NDT temperatures established within 5°C for the CG HAZ (subsurface location) are given in Table 13.

The NDT temperatures of the CG HAZ increased with the heat input in both the as-welded and the stress-relieved conditions for the LT60 and A710 Gr. A Cl. 3 steels. Also, the NDT temperatures of the CG HAZ always improved with the stress-relief heat treatment over the as-welded condition. There is little difference in the NDT temperatures of the HAZ between the three steels in the as-welded condition at 5.4 kJ/mm heat input.

3.6 CTOD VALUES

The CTOD values were calculated from the load displacement plots using the expression given in BS 5762, i.e.,

$$\delta_c,\ \delta_u,\ \text{or}\ \delta_m = \frac{K^2(1-\nu^2)}{2\sigma_y E} + \frac{0.4(W-a)\ Vp}{0.4W + 0.6a + Z}$$

where, $K = \frac{YP}{BW^{\frac{1}{2}}}$ and P and Vp are the force and plastic component of clip gauge opening displacement respectively, which correspond to the relevant values of V_c, V_u, or V_m (refer to Figure 84);

δ_c = crack opening displacement at either (a) unstable fracture or (b) onset of arrested brittle crack or pop-in. This term only applies where there is no evidence in either (a) or (b) to suggest that slow crack growth has occurred;

δ_m = crack opening displacement at first attainment of maximum force plateau;

δ_u = crack opening displacement at either (a) unstable fracture or (b) onset of arrested brittle crack or pop-in. This term only applies where there is evidence of either (a) or (b) to suggest that slow crack growth has occurred;

Y = a compliance function corresponding to crack length/test piece width ratios (a/W);

ν = Poisson's ratio assumed to be 0.3;

E = Young's modulus assumed to be 207×10^3 MPa (30×10^6 psi)

Z = thickness of the knife edges (3mm);

σ_y = yield strength.

Appropriate yield strength values (σ_y) obtained at the test temperatures are desirable for use in the calculation of CTOD values (δ). However, due to the number of structures present along the fatigue precrack front, and the difficulty in establishing the yield strength values of the CG HAZ at the test temperatures, only the yield strength values of the base material available from the mill reports were used in the calculation of the δ values. The σ_y values of 386, 582, 431, and 439 MPa were used in the calculations for Algoma LT 60, A710 Gr. A Cl. 3, MACS

(ACC), and MACS (DQT) steels, respectively. It should be noted that one could use the hardness values of the CG HAZ to calculate the yield strength values. However, when there are several structures involved, this approach would also be an approximation.

The CTOD values obtained and the test temperatures are given in Tables 14 to 25. Only two CTOD values are invalid due to non-uniform fatigue precrack fronts. There are pop-ins in about 15 specimens, however only five of them are worth noting since the failure loads in the latter, are greater than the pop-in loads. These specimens are marked in the Tables.

It is quite evident from the difficulty in placing the fatigue precrack front in the CG HAZ, the number of tests performed and the large range of CTOD values obtained at a test temperature, that the CTOD values are influenced by the amounts of different microstructures present. The HAZ of MACS steel welded at 5.4 kJ/mm heat input and A710 steel welded at 1.6 kJ/mm heat input showed higher CTOD values than those of the other heat input/steel combinations. However, the effect of heat input and the stress-relief heat treatment do not become apparent until the microstructural analysis is performed.

3.6.1 Microstructures Near the Fatigue Precrack Front Along the Thickness

The microstructures such as CG HAZ, FG HAZ, weld metal, and the other structures present along the fatigue precrack and the fracture path near the fatigue precrack front are shown for some of the specimens in Figures 85 to 91. The amounts of each microstructure type (mentioned above), present along the thickness in the fatigue precrack and the fracture path near the fatigue precrack front, are given in Tables 26 to 37.

The maximum amounts of CG HAZ obtained along the fatigue precrack are approximately 68% (70% if the fusion boundary is considered as CG HAZ), 68%, 45%, and 50% for the LT60, A710, MAC (ACC) and MACS (DQT) steels, respectively.

Table 5 gives the approximate size of the grains in the grain coarsened HAZ. This table shows that the grain size increases with heat input in LT60 and A710 steels. The grain size of the CG HAZ in MACS steel is the lowest and in LT60 steel is the highest for the same heat input level used.

The brittle fracture initiation sites identified macroscopically are marked in Figures 85 to 91, and the microstructures present at the fracture initiation sites are given in Tables 26 to 37. The microstructures present at the fracture initiation sites for some of the specimens are shown in Figures 92 to 100. Also, some of the fracture surfaces sectioned longitudinally at mid-thickness as well as through fracture initiation sites, show the locations of the fatigue crack and the fracture path in the HAZ. These are shown in Figures 101 to 109. The following observations are possible:

(a) The brittle fracture initiation sites were always identifiable on the fracture surface.

(b) Brittle fracture initiation always occurred in the central 1/3 of the thickness B.

(c) In some specimens, where multiple fracture initiations occurred, the initiation sites were mostly (≅90%) in the central half of the thickness B. The microstructure at the fracture initiation sites depended on the proportions of the microstructures present at or near the fatigue precrack front along the thickness; i.e. if there is a higher amount of a particular microstructure present, then there is a greater chance of finding an initiation site in that structure.

(d) Approximately 75% of the specimens examined had at least one of the fracture initiation sites in the CG HAZ corresponding to fracture path along the thickness. Also, 75% of the specimens showed that at least one of the fracture initation sites positioned along the thickness, corresponded to the CG HAZ in the fatigue precrack. At least 66% of specimens had at least one of the fracture initiation sites in the CG HAZ, at the same location along the thickness, corresponding to both the fatigue precrack and the fracture path.

3.6.2 Fractography of CTOD Specimens

Figures 110 to 117 show the fracture surfaces of some of the CTOD specimens. Figure 110 shows the irregular shape of the fatigue precrack front in an "as-welded" specimen which was precracked without local compression of the notch ligament. The bowl-shaped fatigue crack front can be seen in Figure 112, which was obtained when the notch ligament of the specimen, in the as-welded condition, was locally compressed to a plastic strain of ≅1% of the thickness B. Uniform fatigue precrack fronts were seen when the notch ligaments of specimens in the as-welded condition were locally compressed to a plastic strain of 0.35 to 0.45% of the thickness as shown in Figures 113 to 115. Uniform fatigue precrack fronts were also obtained in all of the specimens which were in the stress-relieved condition as shown in Figures 111, 116(b), 117(a), and 117(d).

It should be noted that some of the specimens showed notable brittle crack growth within the fatigue precrack. These are shown in Figure 114. Figure 118 shows the scanning electron micrograph of the region shown in Figure 114.

The fracture initiation sites, identified using a scanning electron microscope as the source of diverging river patterns, are shown in Figures 119 to 127 for some of the specimens. It can be observed that in a few cases, the fracture initiation occurred at an inclusion present in the base material (Figures 123 to 125). However, in many cases, the initiation seems to be occurring at the ductile tear ridges, inclusion sites, or the facet boundaries of the CG HAZ.

The EDX analysis of the inclusion present at the initiation site in specimen 6A3 is shown in Figure 128. This inclusion contained Mn, Al, Ti, Ce, Ca, and Fe.

3.7 THE PRECIPITATES IN THE COARSE GRAIN HAZ AS ANALYZED BY EXTRACTION CARBON REPLICA AND EDX TECHNIQUES

The following gives the summary of the work performed on the CG HAZ for the three steels. (Refer to Appendix A).

(a) LT60 Steel
Parent Plate - Contained Hexagonal AlN and finer (Nb, V) carbides (7nm)

CG HAZ (As-welded)

1.6 kJ/mm heat input - Lamellar Fe-rich carbides plus a few undissolved AlN particles.

3.5 kJ/mm heat input - Same as above - Fe-rich carbides at grain boundary (GB).

5.4 kJ/mm heat input - Coarse carbides at ferrite GB.
- Fine scale precipitation of presumably - (Nb, V) (C, N).

CG HAZ (Stress-relieved)

1.6 - 5.4 kJ/mm heat input - Variety of particle morphologies.

- Coarse spheroidal or lath shaped carbides, randomly distributed, predominantly Fe based with smaller amounts of Cr and Mn.
- Small particles distributed throughout - (Nb, V) (C, N), (approx. 11nm)
- Hexagonal AlN.

Discussion

The fine scale precipitation which is observed at high heat input (HI) in the as-welded condition may have occurred during the cooling cycle.

The stress-relief (SR) heat treatment might have caused further precipitation and coarsening of (Nb, V) rich precipitates.

(b) A710 Gr. A Cl. 3 Steel

Parent Plate - Consists of Fe, Cr rich carbides 0.1μm in size and fine distribution of 8-50nm size Nb (C, N) and Cu precipitates.

CG HAZ (As-welded)

1.6 kJ/mm heat input - Replicas are featureless. Some scattered Ti and Nb cuboidal particles, no carbides. In a low C steel, most of the C is retained in MA phase at ferrite boundaries in the bainitic structure.

5.4 kJ/mm heat input - Essentially no change.

CG HAZ (Stress-relieved)

1.6 - 5.4 kJ/mm heat	- Precipitation of arrays of coarse carbides outlining ferrite grains.
	- Very fine precipitates -- probably Cu or Nb (C, N).

Discussion

Complete dissolution of (Fe, Cr) (C, N) during weld thermal cycle in the CG HAZ. Sometimes these precipitate out on cooling cycle. No precipitation could be observed.

(c) Kawasaki MACS Steel

CG HAZ (As-welded)

5.4 kJ/mm heat input	- Devoid of any precipitates up to a distance of 50 μm from fusion boundary - a few coarse Ti-rich cuboids and Nb rich precipitates.
	- Fe-rich ill defined feathery plates which were formed during cooling cycle.

CG HAZ (Stress-relieved)

5.4 kJ/mm heat input	- Contained coarse, fine, and very fine particles.
	- Coarse particles - Fe-rich carbides.
	- Fine spherical particles (0.1 μm) - Fe-rich carbides or FeS.
	- Very fine particles - Nb-rich particles.

Discussion

Ti-rich nitrides survive during welding cycle. Nb taken into solution precipitates out on SR.

4.0 DISCUSSION

4.1 GLEEBLE SIMULATION

4.1.1 Charpy V-Notch Impact Test

In general, the CVN transition curves indicated relatively poor toughness for heat affected zones for all test conditions, in relation to the CVN results from the K-joint welds.

This was anticipated since Gleeble simulated specimens have a relatively large region (≅5mm width) containing only single cycle, coarse grain structure. The lower number of grain boundaries may cause grain boundary carbides to be larger and may enhance cleavage initiation, while the larger grain size may enhance cleavage propagation. In the real weld, in contrast, the coarse grain region is narrower, the absolute grain size is finer, and there is a multiplicity of microstructures next to the fusion boundary. As well, there is a large variation in yield strength across the weld zone, that is, the weld metal, HAZ and base plate each have their own properties.

For these reasons, impact tests on Gleeble specimens are likely to yield worse results than the same tests carried out on multipass, multimicrostructure specimens, as is observed in Table 38.

The effects of heat input and postweld heat treatment on CVN impact energies of Gleeble specimens, are discussed in a subsequent section along with results from the K-joint welds.

4.1.2 Instrumented Impact Test

The instrumented impact test uses a notched, precracked impact specimen. Since the fatigue precrack length may vary slightly from specimen to specimen, the energy vs temperature curve will not necessarily yield reproducible results. For this reason, the crack length measured after testing and yield stress (σ_y) determined during the test, are used to calculate a K_{1d} (dynamic fracture toughness) parameter.

This parameter can only be compared qualitatively with the Charpy V-notch impact results. Trends between the two tests are similar as shown in Figures 22 to 33 and 34 to 39. As in the Gleeble Charpy V-notch results, stress relieving the samples consistently reduced the toughness.

4.2 CVN IMPACT ENERGY AND MICROSTRUCTURE

As shown in Table 39, the proportions of various microstructures present at the root of the notch in CVN specimens vary at the subsurface and the root locations of the K-joint weldments. Also, different microstructures were present along the fracture path of the CVN specimens tested. In CVN tests the microstructures at the notch root as well as along the fracture path influence the CVN energy absorbed values. Therefore, if the proportions of the CG

HAZ present at the notch root and along the fracture path are such that they do not have a dominant effect on the CVN toughness, then whatever comparisons of the CVN toughness with different combinations of heat input, heat treatment, and steel are attempted would be invalid as far as the CG HAZ toughness is concerned. However, from a practical point of view, such a comparison is informative.

Comparing the CVN transition curves obtained for the CG HAZ, the weld metal and the refined regions of the HAZ in LT60 steel (refer to Figures 49 and 70), it is debatable whether the CG HAZ has a dominant effect in yielding lower CVN toughness. Again, one should consider the fact that the so called CG HAZ may have contained as low as or lower than 50% CG in the CVN specimens and should be cautious in drawing any conclusions as to the dominant effect of CG HAZ on the CVN toughness.

4.2.1 Algoma LT60 Steel

The Charpy data for Gleeble and K-weld specimens can be summarized as follows to show the effects of heat input and stress relief:

40J average transition temperatures (°C)

	1.6 kJ/mm		3.5 kJ/mm				5.4 kJ/mm			
	AW	SR	AW		SR		AW		SR	
Gleeble	+15	+9	+3		+17		+7		+10	
			Root	SS	Root	SS	Root	SS	Root	SS
K-Joint			-46	-59	-37	-42	-48	-34	-66	-42

Effect of Heat Input on 40J average transition temp.

Gleeble - AW	3.5 kJ/mm > 5.4 > 1.6 (+3 to +15°C)
K-Joint - AW Root	3.5 ≅ 5.4 kJ/mm
AW SS	3.5 > 5.4 (-59 vs. -34°C)
Gleeble - SR	1.6 = 5.4 > 3.5 (10 to 17°C)
K-Joint - SR Root	5.4 > 3.5 (-66 vs. -37°C)
SR SS	5.4 = 3.5 kJ/mm

Effect of Stress-Relief on 40J average transition temp.

3.5 kJ/mm root → deterioration

3.5 kJ/mm SS → deterioration

5.4 kJ/mm root → improvement

5.4 kJ/mm root → improvement

Gleeble → deterioration at both heat inputs

It is clear that there is no uniform trend regarding the effects of heat input or stress relief on the notch toughness. As far as the Gleeble results are concerned, in the as-welded condition, the 40J transition temperatures are in the range of +3 to +15°C, which in light of the scatter in results, suggests no significant effect of heat input. Stress-relieving seems to consistently cause deterioration although the shift in transition temperature is no more than 6°C. (Refer to Figure 129.)

Before rationalizing the K-joint results, it should be noted that:

(i) the root region CG HAZ may not necessarily be inferior in toughness since the first side root bead which is subjected to greater dilution and strain aging had been removed by backgouging and grinding, and the first root bead from the second side is subjected to a lower level of welding strain.

(ii) due to somewhat larger grain size and fine precipitates observed at the 5.4 kJ/mm heat input, the toughness in the as-welded condition is expected to be worse at 5.4 kJ/mm than at 3.5 kJ/mm.

That indeed is the case for as-welded Gleeble and the subsurface location. Since the root location is subjected to subsequent thermal cycles, it can be considered as partially stress-relieved. At 5.4 kJ/mm, this thermal cycling at the root, or furnace stress-relieving could lead to tempering of the microstructure and coarsening and aging of precipitates. This, in turn, leads to lower hardness (265 to 220 HV_{10}) and the observed improved toughness in the as-welded root and at both subsurface and root locations as a result of stress-relieving. (Refer to Figures 129 and 130.)

The as-welded CG HAZ at 3.5 kJ/mm did not show any precipitates; in effect it was in an underaged condition. The as-welded root location and both root and subsurface locations upon stress-relieving, may therefore be subjected to precipitation hardening (260 to 270 HV_{10}), and hence the observed deterioration in toughness.

4.2.2 A710 Gr. A Cl. 3 Steel

The 40J average transition temperatures, and the effects of heat input and postweld heat treatments can be summarized as follows:

40J average transition temperatures (°C)

	1.6 kJ/mm				3.5 kJ/mm				5.4 kJ/mm			
	AW		SR		AW		SR		AW		SR	
Gleeble	-36		+5		-24		+11		-11		+8	
	Root	SS	Root	SS	Root	SS	Root	SS	Root	SS	Root	SS
K-Joint	-90	-70	-60	-52	-78	-70	-40	-40	-46	-86	-84	-84

Effect of Heat Input on 40J transition temperature

Gleeble -	AW	1.6 > 3.5 > 5.4 (-36 to -11°C)
K-Joint -	AW Root	1.6 > 3.5 > 5.4 (-80, -78, -46°C)
	AW SS	5.4 > 3.5 = 1.6 (-86, -70, -70°C)
Gleeble -	SR	1.6 = 3.5 = 5.4 (+5 to 11°C)
K-Joint -	SR Root	5.4 > 1.6 > 3.5 (-84, -60, -40°C)
	SR SS	5.4 > 1.6 > 3.5 (-84, -52, -40°C)

From the results of the Gleeble specimens, it is observed that as the heat input increases from 1.6 kJ/mm to 5.4 kJ/mm, the 40J average transition temperature for this CG HAZ also increases (from -36°C to -11°C). Refer to Figure 131. Since there was no evidence of any fine scale precipitation reported by Weatherly, at any of these heat inputs and Cu precipitation could not be detected because of the Cu peak present from the substrate holding the specimen, it is difficult to say if precipitation could be responsible for this decrease in toughness. Hardness values give no indication as, overall, there is a decrease in hardness from HV_{10} 290 to 270 over this heat input range. Microstructurally, an increase in grain size and bainite packet size is observed with increase in heat input, and that is expected to increase the transition temperatures. The role of second phases (MA, carbides etc.) is difficult to assess based on the limited metallography.

On stress-relieving, the Gleeble specimens show a deterioration in toughness and the prior weld heat input does not have any significant effect on the transition temperature obtained (+5 to +11°C). The deterioration in toughness is consistent with observations noted before, viz., precipitation of an array of coarse carbides outlining the ferrite grains, fine precipitation (≅2-3nm) of Cu or Nb

(CN) and the changes in hardness on stress relieving (increase at 5.4 kJ/mm, and small decrease at 1.6 and 3.5 kJ/mm).

The CVN results from K-joint, however do not follow as uniform a pattern as noted above. In the as-welded condition, the CVN's at the root location follow the above trend, but at the subsurface location, the heat input effect is minimal (refer to Figure 132). Upon stress-relieving, the expected deterioration is observed, at least qualitatively, at 1.6 and 3.5 kJ/mm heat input. However, at 5.4 kJ/mm, the transition temperature is less than -80°C. There is no obvious explanation for this exception, except the possibility that the notch sampled other microstructures present in larger proportion, which masked the effect of the coarse grain region.

4.2.3 Kawasaki MACS ACC and DQT Steels

The 40J average transition temperature data (°C) for this steel is summarized below:

	1.6 kJ/mm		3.5 kJ/mm		5.4 kJ/mm			
	AW	SR	AW	SR	AW		SR	
Gleeble	-50	-42	-78	-62	-70		-50	
					Root	SS	Root	SS
K-Joint					-63	-80	-85	-101

Both the ACC and DQT steels have essentially the same chemical compositions; the only difference being their heat treatment after the final rolling and therefore, the AW and SR results may be compared as being for the same steel, at least to first approximation.

The Gleeble specimens indicate that in the as-welded condition, the best toughness is obtained at 3.5 kJ/mm. Since no fine scale precipitation was observed even at 5.4 kJ/mm, and the grain size at 1.6 kJ/mm was somewhat finer than at 3.5 kJ/mm, the best toughness at 3.5 kJ/mm must be due to the particular type, size, and distribution of the second phase present.

On stress-relieving, there is an increase in the transition temperature which ranges from about -10° to -20°C, and this is most probably related to the very fine precipitation (probably Nb rich carbides) observed by Weatherly (Appendix A). The lowest transition temperature is again at 3.5 kJ/mm heat input, as was the case for the as-welded condition. It should also be noted that of the three steels, the Kawasaki DQT steel has the best CG HAZ toughness as indicated by Gleeble specimens in the stress-relieved condition, and most likely, its low Nb content is an important factor in that.

Unlike the Gleeble results, the CG HAZ in the real weldment showed an improvement in the transition temperature when stress-relieved, and once again, it may be attributed to the likelihood of the notch sampling microstructures other than the coarse grain region which instead of deteriorating, improve upon stress relief.

4.3 CTOD VALUES AND MICROSTRUCTURES

The microstructure in the HAZ, close to the fusion boundary in the straight portion of the K-weld, is not uniform. Hence, even if the through thickness fatigue precrack is located in the HAZ next to a perfectly straight fusion boundary of the K-weld, the microstructure would not be 100% CG HAZ. Thus, while performing a through thickness CTOD test for the CG HAZ in a multipass K-weld, one cannot expect 100% of the fatigue precrack front to be in CG HAZ. Also, if the fusion boundary is not straight which is the case in practice, the fatigue precrack front can sample only a portion of the maximum possible CG HAZ. Along with the CG HAZ, one would expect to see FG HAZ, refined structures and weld metal. There is the other difficulty in obtaining the fatigue precrack front at the exact plane, where the notch axis and notch tip are located, due to the effect of microstructure on the "wandering" of the fatigue precrack front. Strictly speaking, to establish the CTOD values representative of the CG HAZ, one would require a large number of data points and a statistical analysis in which the effects of various microstructures present on the CTOD values can be evaluated. However, such an analysis is not possible in the present study because of the limited number of data points available.

In this study, the intention was to determine the CTOD values for the CG HAZ and hence every effort was made to sample a large proportion of the CG HAZ along the fatigue precrack front. Unlike the CVN impact energy, the CTOD values give fracture initiation characteristics under static loading conditions and hence brittle fracture initiation becomes important. Most of the specimens tested show the brittle fracture initiation sites in the CG HAZ. Also, as the CVN impact energy suggests and the literature indicates (Ref. 2, 34) the CG HAZ has the lowest toughness in the HAZ. In view of this, the CTOD values obtained were plotted against the amount of CG HAZ present near the fatigue precrack front along the thickness. These are shown in Figures 133 to 138. For certain heat inputs, LT60 and A710 Gr A Cl 3 steels showed a steep drop in the CTOD values as the CG HAZ increased from 0 to ~ 20%. However, for MACS steel such an observation is not possible because of the lack of data points between 0 and 20% of CG HAZ. Above 20% to 40% CG HAZ, the CTOD value seems to remain constant, showing the predominant effect of CG HAZ. The amount of CG HAZ above which the CTOD value remains constant, varies with the dominance of other microstructures present and the steels. For each set of 4 to 6 specimens at a given test temperature, the CTOD values were averaged for those specimens that had shown ≥ 20% coarse grain region along the fatigue precrack front, and these are given in Table 40 for each steel. These average values may not be representative of the CG HAZ since the proportion of CG HAZ covers a wide range and there are only a limited number of data points available.

4.3.1 Algoma LT 60 Steel

Unlike the CVN impact energy results, CTOD values showed improvement in values as a result of stress relief heat treatment or increase in heat input. (Refer to data in Table 38 to 40 and Figures 133, 136 and 139). This may be due to the fact that even though the CG HAZ is the dominating factor above 20% CG HAZ, the absolute value of the CTOD is still determined by the overall microstructures present. It should be noted that the CTOD test establishes the initiation toughness under static loading conditions, unlike the CVN test. The CTOD values were obtained at two temperatures and hence, with respect to the CTOD value transition curves, their exact locations on the curves cannot be established. Most of all, considering the ideal microstructures obtained in the Gleeble simulation, the change in the 27J and 40J CVN impact energy transition temperatures observed due to the change in heat input or stress-relieving is not that significant. At this point, the effect of local compression of the notch ligament should not be overlooked. When the notch ligament was plastically compressed to 1% of the thickness in order to relieve the residual stresses, a bowl shaped fatigue precrack front was obtained, indicating that there is an effect of local compression on the properties. If the residual stress is of yield strength magnitude, then the notch ligament needs to be locally compressed only to the yield load level. Thus, local compression of the notch ligament to 0.35 to 0.45% of the thickness would seem to have a deleterious effect on the CTOD values being measured. However, this effect may be very small.

The refined structure is known to give higher toughness in the HAZ. Also, the weld metal and the base material may have higher CTOD toughness than the CG HAZ. Thus, depending on the weldment microstructures sampled by the fatigue precrack, the CTOD values would vary. It is likely that the whole host of microstructures present at the fatigue precrack front may be responsible in yielding the higher CTOD values at 5.4 kJ/mm as compared to 3.5 kJ/mm heat input, and on stress-relieving as compared to the as-welded condition. It should be recalled that CVN's from the K-joint also gave mixed results regarding the effect of heat input, and post weld heat treatment on transition temperature, unlike the

Gleeble specimens where for the CG simulated HAZ, stress relieving consistently leads to a deterioration in toughness.

4.3.2 A710 Gr A Cl 3 Steel

The average CTOD values given in Table 39 and plotted in Figure 140 can be deceptive since each data point may represent a different amount of coarse grain region at the fatigue crack tip. The CTOD values plotted against the % CG HAZ in Figures 134 & 137 give a better picture of the effect of increase in heat input and stress-relief heat treatment on the CTOD values. Even with a limited number of data points and a large scatter, the plot shows an decrease in CTOD values as the heat input increases. Also, the effect of stress-relief heat treatment is to decrease the CTOD values over the as-welded condition. This is completely consistent with the Gleeble simulation results, and with those of K-joint CVN's except at 5.4 kJ/mm.

4.3.3 Kawasaki MACS Steel

Both the ACC and DQT steels showed consistently higher CTOD values with large range compared to LT60 and A710 Gr A Cl 3 steels. Even with the large range, CG HAZ in ACC as-welded steel seems to give slightly higher CTOD values than those of DQT stress-relieved steel. (Refer to Figures 135 to 138). The higher toughness observed in the CG HAZ of ACC steel than that of DQT steel is consistent with the results of Gleeble simulated specimens.

4.3.4 Microstructure, Fracture Initiation Sites and the CTOD Values

1. Table 5 gives the approximate size of the grains in the grain coarsened HAZ. Generally, as the grain size increases, the toughness decreases. For any given heat input/steel combinations, there is a range of grain size existing in the CG HAZ. In the CTOD tests, in addition to sampling different microstructures, the fatigue crack also samples different grain sizes in the CG HAZ. Thus the sampling of a range of grain sizes may be responsible for of the differences observed in the CTOD values.

2. Tables 26 to 37 also list the microstructure present along the thickness in the fracture path at or near the initiation site. There is some difference in the proportions of various microstructures present along the fatigue precrack and the fracture path. The proportions of various microstructures including the CG HAZ present along the thickness in the fracture path at or near the initiation site or present along the fatigue precrack front are unable to explain the variations in the CTOD values calculated.

3. Brittle fracture initiation occurred 100% of the time in the central 1/3 of the thickness B. This shows that the higher constraint levels present at the central 1/3 of the thickness B are responsible for the fracture initiation. In the central 1/3 of the thickness B, irrespective of the proportions of various microstructures present, the majority of the CTOD specimens have one initiation site in the CG HAZ. Even though the structure in and around the initiation site could affect the CTOD values, plotting the CTOD values vs. % CG HAZ present in the central 1/3 of the thickness B (in the fatigue precrack), did not alter the relative position of CTOD vs % CG HAZ plots shown in Figures 133 to 138.

4.3.5 Fitness for Purpose Evaluation of the CG HAZ

Using the CTOD design curve approach, allowable defect sizes ($\bar{a}_{max}$)can be calculated from the CTOD values obtained, using the following equations: (Ref. 59, 60, 61).

$$\bar{a}_{max} = \frac{\delta E}{2\pi\ \sigma_y\ (\sigma_{app}/\sigma_y)^2} \quad \text{for } \frac{\sigma_{app}}{\sigma_y} \le 0.5$$

and $$\bar{a}_{max} = \frac{\delta E}{2\pi\ \sigma_y\ (\sigma_{app}/\sigma_y - 0.25)^2} \quad \text{for } \frac{\sigma_{app}}{\sigma_y} \ge 0.5$$

Here, σ_y is the yield stress, E is the Young's modulus of elasticity and σ_{app} is the total stress at the defect location (without the defect present) and is given by:

$\sigma_{app} = (\sigma_{design\ stress} \times \text{stress conc. factor}) + \text{residual stress (from welding)}$

For the three steels, the allowable defect sizes in the CG HAZ were calculated from the CTOD values given in Table 40 for HAZ's containing more than 20% CG. In these calculations the maximum residual stress in the as-welded condition is of the magnitude of σ_y and is considered to be zero in the stress-relieved condition. In addition, the stress concentration factor is assumed to be one and the design stress to be 0.6 of σ_y (parent material). Strictly, one should use the tensile properties of the CG HAZ in the CTOD value or the defect size calculations. One could estimate the yield strength of the CG HAZ by its hardness. However, this would only give an approximate yield strength value for the CG HAZ. Also, due to the presence of other microstructures at the fatigue precrack front, calculations of the CTOD values using any estimated yield strength value would be only an approximation. The tensile properties of the CG HAZ were not determined and hence the properties of the base material were used (refer to Table 2). Based upon HAZ hardness values in Table 6, this approach would overestimate the defect size in LT60 steel compared to the other two steels.

Even though the average CTOD values given in Table 40 and hence the allowable defect sizes, do not reveal the true property of the CG HAZ, for practical purposes, these values are adequate for classifying the steels and determining the effect of stress relief heat treatment.

Considering the 5.4 kJ/mm heat input, in the as-welded condition the allowable defect sizes for CG HAZ ($\geq$ 20%) in LT60, A710 and MACS (ACC) steels were estimated to be 15, 9 and 53mm. The allowable defect sizes in these steels could be improved to 81, 57 and 172mm, respectively, by reducing the residual stresses to zero due to stress relief heat treatment. This shows that even though stress-relieving deteriorates the 27J and 40J CVN transition temperature of the CG HAZ due to Nb, V (CN) and/or Cu precipitation, it will have a beneficial effect on reducing the residual stresses, hence, improving the allowable defect sizes of the CG HAZ over the as-welded condition. Once again, comparing the allowable defect sizes in the CG HAZ, the three steels: MACS (ACC, DQT), Algoma LT60, and A710 Gr A Cl 3 are rated in that order.

Using an approach similar to the CTOD design curve approach, the allowable crack size was calculated, from the K_{1D} values, assuming a nominal stress of $.6\sigma y$. The allowable crack size as a function of temperature is shown in Figures 141 through

146 for the three steels at each of the three heat inputs in both the as-welded and stress-relieved conditions. At -30°C, the allowable crack (defect) sizes, keeping in mind the limitation due to use of base material yield strength, decrease in the following order of steels: Lloyds LT60, MACS, and A710 for all combinations of heat input/heat treatment simulated in this study. Defect sizes calculated from both CTOD and K_{1d} values suggest that A710 steel is poor in tolerating defects compared to LT60 and MACS steels. Also, defect size calculations suggest that CTOD or K_{1d} toughness alone may not reveal the suitability of the material for a particular service application.

4.3.6 CVN-CTOD Correlations

In Figures 147 to 150, the CTOD values for the CG HAZ in all the steels at -30° and -50°C were plotted against the 27J and 40J transition temperatures for both as-welded and stress-relieved conditions.(Ref. 62) The CTOD values decreased, except at -30°C in the as-welded condition, with the increase in 27J and 40J transition temperatures. At -30°C, in the as-welded condition, the CTOD value remained constant with increase in transition temperature. Also, at -30°C, a slight improvement in CTOD values due to stress-relief heat treatment could be noticed over the whole CVN transition temperature range. The limited number of data points makes it impossible to derive any reliable empirical correlation.

4.4 NDT TEMPERATURES

Referring to Table 38, the NDT temperatures of the CG HAZ did not compare closely with the 27J transition temperatures. Also, the NDT temperatures of the CG HAZ always improved with the stress-relief heat treatment over the as-welded condition which is again contrary to the Gleeble results. One may expect such a discrepancy because (a) the specimens were removed from the subsurface of the plates and fracture initiation occurs from the subsurface location and runs into the thickness, unlike the CVN impact tests where the notch was in the thickness side; (b) it is a dynamic initiation test wherein the structure on the surface along the line where the crack starter slot was placed becomes important; and (c) the root radii of the notch and the crack in the crack starter bead are different from those of the CVN specimens. (Refer to Figures 77 to 83). The NDT temperatures are still useful in determining the crack arrest characteristics of the CG HAZ.

4.5 RELATIVE HAZ TOUGHNESSES IN THE STEELS

From the previous observations and discussions, it is clear that different tests employed lead to different rankings of the steels. That is not entirely unexpected because of the differing nature of the tests; static versus dynamic initiation, root radii, 100% CG region versus mixed microstructures, etc. All the same, based on the tests employed, the following rankings can be established.

4.5.1 Gleeble CVN Tests (100% CG region, 40J transition temperature)

In the as-welded condition, the MACS steels has consistently the lowest transition temperature (-50 to -74°C) at all heat inputs, and the LT60 steel fared the worst (+3 to +15°C). The A710 steel was in-between (-11 to -36°C). On stress-relieving, the MACS steel retained its superiority (-42 to -101°C), whereas LT60 and A710 steels suffered deterioration (+9 to +17°C, and +5 to +11°C, respectively) such that there is not much to choose between them.

4.5.2 K-Joint CVN Tests (Mixed Microstructures in HAZ, 40J transition temperature)

At 5.4 kJ/mm heat input and in as-welded condition, the MACS steel seems to have the best toughness (-50°C, -80°C), and the LT60 steel is most inferior (-45°, -34°C), although in light of the scatter, it should be pointed out that these differences may be minor. On stress-relieving, the LT60 HAZ results remain the most inferior (-66°, -42°C) compared to the other two steels (-74 to -101°C).

At the lower heat input, viz., 3.5 kJ/mm, the A710 steel has a lower transition temperature (-70 to -78°C) than the LT60 steel (-48 to -59°C), but in the stress-relieved condition, they both suffer deterioration and have about the same transition temperature (-37 to -42°C).

4.5.3 CTOD Values at -30°C (Mixed microstructure HAZ)

At 5.4 kJ/mm heat input and as-welded condition, the HAZ in MACS steel has excellent CTOD value (.943 max.), whereas LT60 and A710 HAZ CTOD values are comparable although the former is marginally better (.238mm versus .213mm). On stress-relieving, all three have similar CTOD values (.354 to .39mm).

At 3.5 kJ/mm where MACS steel was not tested, the LT60 steel HAZ has a marginally superior CTOD value than A710 steel HAZ, both in the as-welded and stress-relieved condition (.129 versus .101 and .334 versus .147mm).

4.5.4 NDT Transition Temperature (Mixed Microstructure HAZ)

All the NDT transition temperatures determined are in the range -45 to -75°C, and for any particular test condition, the differences in the NDT transition temperature for the HAZ's in the three steels do not exceed 10°C, which may not be very significant.

All the same, the results indicate that the HAZ in A710 steel had the lowest NDT transition temperatures in both as-welded and stress-relieved condition when compared to the other steels. The MACS steel surprisingly had the highest NDT temperature at 5.4 kJ/mm. See Table 38.

4.5.5 Summary of Steel Ranking

Ignoring minor exceptions, it is clear that overall the MACS (ACC) and (DQT) steel had the best heat affected zone toughness over the heat input range examined. In terms of its chemistry, this superiority can be attributed to Ti treatment and its low Nb content which respectively leads to HAZ grain growth restriction next to the fusion boundary and limits the extent of precipitation at high heat inputs or during the stress relief treatment.

The HAZ in A710 steel definitely has superior toughness at low heat inputs. The differing performances in various tests suggests that upon stress relief, initiation resistance is improved (CTOD and NDT temperature) but propagation resistance suffers (CVN value).

The HAZ Lloyds LT60 steel performs similarly at all heat input levels used. However, CTOD data indicates that it may actually have better initiation fracture toughness at higher heat inputs. Stress-relieving seems to help initiation resistance (CTOD and NDT temperature) but the propagation resistance is little affected.

5.0 CONCLUSIONS

1. The Ti-treated, MACS steels show better HAZ toughness properties than the Cb-V normalized or the Cu-Ni-Cr-Mo-Nb precipitation hardened steels.

2. The Ti-treated MACS steels perform better at high heat inputs but still quite well at lower heat inputs.

3. A710 Gr. A, Cl. 3 appears to perform best at lower heat inputs.

4. For certain heat inputs, LT60 and A710 Gr. A Cl. 3 steels show a steep drop in the CTOD toughness as the amount of CG HAZ increases from 0 to ≅20% and above 20 to 40% CG HAZ the CTOD toughness seems to remain constant. There is a dominating effect of CG HAZ on the CTOD toughness when present in amounts ≥20% and this amount would vary according to steel grades.

5. The beneficial effects of stress relief heat treatment on the toughness of CG HAZ are debatable for A710 Gr. A, Cl. 3. It appears that stress-relief heat treatment improves cleavage initiation resistance but deteriorates

propagation resistance (i.e. under high strain rate, or impact loading).

6. Lloyds LT 60 appears to perform relatively consistently at all heat inputs tested, however, based on CTOD test results it may show improvements at higher heat inputs.

7. Stress-relief heat treatment appears to be beneficial in improving cleavage initiation resistance for LT 60 but has little effect on propagation resistance, although some improvement is seen for higher heat inputs.

8. Under certain conditions of heat input/heat treatment combinations, the average CVN and CTOD toughness of the CG HAZ were >40J and $\geq$0.2mm, respectively, at -30°C for LT60 and A710 steels and at -50°C for MACS steel. This suggests that for the Canadian offshore and Arctic structures where higher toughness is required at ambient temperatures in the range -30° to -50°C, the LT60 and A710 steels may marginally meet the anticipated minimum specified toughness at -30°C and the MACS steels may meet the same at -50°C.

6.0 RECOMMENDATIONS FOR FUTURE WORK

It is stated that the intercritical and the subcritical regions of the HAZ may have poor toughness. Also, the structure and the toughness of the decorated regions of the reheated CG regions of HAZ are different than those of the as-welded CG HAZ. Thus to understand the structure-toughness relationships fully, the following needs to be investigated:

(a) Microstructural examination, CVN and CTOD toughness evaluation for the intercritical and subcritical regions of the straight portion of the HAZ in K-groove weldments for the steels under investigation.

(b) Gleeble simulation of the intercritical and the reheated regions of the HAZ. The microstructural examination and the CVN toughness determination of the Gleeble simulated specimens.

7.0 REFERENCES

1. Bala, S.R. and Pond, S., "Weldability and Formability of Two Candidate Steels for Offshore Structures and Arctic Vessels", DSS Contract OSQ82-00212, 1983.

2. Pisarski, H.G. and Pargeter, R.J., "Fracture Toughness of HAZ's in Steels For Offshore Platforms". Metal Construction, July 1984, p. 412.

3. Bowker, J.T., Glover, A.G., and Lazor, R.B., "The Structure and Toughness of the Weld Heat-Affected Zone of a C-Mn-V Steel". PMRL Report MRP/PMRL 83-56 (OP-J).

4. Cuddy, L.J., Lally, J.S., and Porter L.F., "Improvement of Toughness In the HAZ High-Heat Input Welds in Ship Steels". Conference Proceedings of International Conference on Technology and Applications of HSLA Steels, Oct.3-6, 1983, Philadelphia ASM Publication, p. 697.

5. McCutcheon, D.B., McGrath, J.T., Godden, M.J., Ruddle, G.E., and Embury, J.D., "The Effect of Microalloy Additions on the HAZ Notch Toughness of a C-Mn-Mo Line Pipe Steel". Conference Proceedings of International Conference on Technology and Applications of HSLA Steels, Oct. 3-6, 1983, Philadelphia ASM Publication, p. 881.

6. Nishio, K., Tashima, K., Katoh, M., and Mukae, S., "Effect of Ti and N on Notch Toughness of Synthetic Weld HAZ". Trans of JWS Vol. 15, No. 2, Oct. 1984, p. 120.

7. Fujita, H., and Kamiya, O., "Study on J_{ic} Fracture Toughness in the Weld HAZ of a Structure Steel". Trans of JWS, Vol. 14, No. 2, Oct. 1983, p. 2.

8. Entrekin, C.H. Jr., "Effect of Stress Relief on Microalloyed Weld Metal Impact Properties". The Welding Journal, August 1983, p. 197-S.

9. Suzuki, S., and Weatherly, G.C., "Grain Coarsening and Precipitate Behaviour in Simulated HAZ of Ti-Nb Bearing Steels". Paper presented at CANMET/CSIRA Conference on "Inclusions and Residuals in Steels: Effects on Fabrication and Service Behaviour". March 5, 1985, Ottawa.

10. Kangas, P, and Sorsa I, "Effect of Multi-run Welding on the Deformation and Fracture Toughness of Restraint Welded Joint", Acta Univ. Oul, C 26, 1983, Metallurg. 4.

11. Thaulow, C, Paauw, A.J., Gunleiksrud, A, and Naess, O., "Heat Affected Zone Toughness of a Low Carbon Microalloyed Steel". Metal Construction, February 1985, p. 94R.

12. Hulka K, and Heisterkamp. F, "Physical Metallurgy Properties and Weldability of Pipeline Steels with Various Niobium Contents", Conference proceeding of International Conference on Technology and Applications of HSLA Steels, Oct. 3-6, 1983.

13. Cuddy, L, and Raley J. " Austenite Grain Coarsening in Microalloyed Steels". Metallurgical Transactions A, Vol 14A, October 1983.

14. Lazor, R.D., McDonald R.D. and Glover A.G., "Properties of Welds in Thick Section Nb-containing Steels." Welding in Energy Related Projects, Welding Institute of Canada Publication, 1983.

15. Baumgardt, H, deBoer, H and Musgen, B., "High Strength Steels for Offshore Technology" Metal Construction, January 1984, p. 15.

16. Houghton, D., Weatherly, G., and Embury, J., "Microchemistry of Carbonitrides in the HAZ of HSLA Steels". Advances in the physical metallurgy and applications of steels. International Conference Sept 21-24, 1981.

17. McCutcheon, D.B., McGrath, J.T., Godden, M.J., Ruddle,G.E., Weatherly, G. and Houghton, D.C., "Improvement of Submerged Arc Weld Heat Affected Zone Toughness by Titanium Additions to Linepipe Steels". MiCon 82: Optimization of processing properties and service performance through microstructural control. ASTM STP 792. 1982, p 227.

18. Nakao, U., Oshige, H., and Noi, S., "Distributions of Microstructure and Toughness in HAZ of Multipass Welded High Strength Steel". The Fourth International Symposium of the JWS, November 1982.

19. Kirkwood, P., "Welding of Niobium Containing Microalloyed Steels". International Conference "Niobium 81", Nov. 9-12, 1981.

20. Sage, A.M., "A Review of the Physical Metallurgy of High Strength, Low Alloy Line Pipe and Pipe Fitting Steels". International Conference on Steels for Line Pipe and Pipeline Fittings, London, Oct 21-23, 1981.

21. Gladman, T., and Dewsnap, R.F., "The Effects of Alloying Additions on the Properties of Controlled-Rolled V-Nb Steels". International Conference on Steels for Line Pipe and Pipeline Fittings, London, Oct 21-23, 1981.

22. Cochrane, R.C., and Morrison, W.B., "Transformation Characteristics of Some Line Pipe Steels Containing Nb,V and Mo and Their Relationship to Processing and Microstructure". International Conference on Steels for Line Pipe and Pipeline Fittings, London, Oct. 21-23, 1981.

23. Cochrane,R.C., and Keville, B.R., "Influence of Inclusion Morphology on Microstructure and Toughness of Submerged Arc Weldments".International Conference on STeels for Line Pipe and Pipeline Fittings, London, Oct. 21-23, 1981.

24. Woodhead, J.H., "Some Effects of Cooling Rate on Structure and Properties of Vanadium and Niobium Structural Steels". International Conference on STeels for Line Pipe and Pipeline Fittings, London, Oct. 21-23, 1981.

25. Brown, C.M., and McCutcheon, D.B., "A V-Mo-Nb Steel for Arctic Pipelines". International Conference on Steels for Line Pipe and Pipeline Fittings, London, Oct. 21-23, 1981.

26. Heisterkamp, F., Bergmann, B., Stuart H and Chaussy, L, "Developments in Niobium Steels for Line Pipe Applications". International Conference on Steels for Line Pipe and Pipeline Fittings, London, Oct. 21-23, 1981.

27. Crooks, M, Garrett-Reed, A., Vandersande, J., and Owen, W. "Precipitation and Recrystallization in some Vanadium and Vanadium-Niobium Microalloyed Steels. Metallurgical Transactions A, Vol. 12A, December 1981.

28. Gittos, M.F., and Dolby, R.E., "Predicting the HAZ Toughness of C and C-Mn Steels - Welding at 2 kJ/mm" TWI Research Bulletin. Vol 9, 1979. No. 4.

29. Yoshino, Y., and Stout, R.D., "Effect of Microalloys on the Notch Toughness of Line Pipe Seam Welds". Welding Research Supplement - The Welding Journal, March 1979, Pg. 59-s.

30. Graville, B., and Rothwell, A.B., " Effect of Niobium on HAZ Toughness Using the Instrumented Charpy Test". Metal Construction, October 1977, P. 455.

31. Hannerz, N.E. "Effect of Cb on HAZ Ductility in Constructional HT Steels". The Welding Journal, May 1975, p. 162-s.

32. Dolby, R.E., "Factors Controlling Weld Toughness - The Present Position", Part 1 - HAZ WI Research Report 11/1976/M, May 1976.

33. Cane, M. and Dolby, R.E., "Metallurgical Factors Controlling the HAZ Fracture Toughness of Submerged Arc Welded C-Mn Steels". WI Research Report.

34. Dolby, R.E., "HAZ Toughness of Structural and Pressure Vessel Steels - Improvement and Prediction", The Welding Journal, 1979, No. 8, p. 225-s to 238-s.

35. Davey, T.G., "The Effect of Welding Parameter Charges on the Heat-Affected Zone Microstructure and Toughness of Single Pass Welds in 25mm Thick C-Mn Steels". Welding Institute, U.K., Research Report, 1981, Aug., 156/1981, for Research Members Only.

36. Pisarski, H.G., and Pargeter, R.J., "Fracture Toughness of Weld Heat-Affected Zones in Steels Used in Constructing Offshore Platforms", A paper presented at WIC/ISC International Conference "Welding in Energy Related Projects", Toronto, Canada, Sept. 20-21, 1983.

37. Rothwell, A.B., Glover, A.G., McGrath, J.T. and Weatherly, G.C., "Heat-Affected Zone Toughness in High Strength Pipeline Steels", Proceedings of the 5th Bolton Landing Conference "Weldments-Physical Metallurgy and Failure Phenomena", Aug. 1978, pp. 257-269.

38. Hannerz, N.E., "Heat-Affected Zone Toughness of Steel as Influenced by Copper", Acta Univ. Oul. C26, 1983, Metallog. 4, 1983, University of Oulu, Printing Centre Oulu. The Third Scandinavian Symposium in Materials Science, June 20-21, 1983, University of Oulu, Oulu Finland.

39. Gondoh, H., Sato, M., Kanya, K., Miyasaka, A., and Yosuda, I., "Behaviour of Nitrogen, Nitrides and Carbides in Weld Heat-Affected Zone", Presented at the 101st, ISIJ Meeting, April 1981, Lecture No. S291.

40. Godden, M.J. and Boyd, J.D., "Characterization of Microstructures in Weld Heat Affected Zones by Electron Microscopy", Microstructures Science, 1981, Vol. 9, p. 343-354.

41. Bain, .E.C, and Paxton, H.W., "Alloying Elements in Steel", ASM, 1966, p. 279.

42. Ackert, R.J., McLean, M.K., and Ray, J.D., "LT 60 Plate for Arctic Application", Presented at the 23rd Annual CIM Conference of Metallurgists, August 19-22, 1984, Quebec City, Quebec.

43. Nishio, K., Tashima, K., Katoh, M., and Mukae, S., "Effects of Ti and N on Notch Toughness of Synthetic Weld Heat-Affected Zone", Trans. Jap. Weld. Soc. 1984, Vol 15, No. 2, pp. 40 - 48.

44. Signes, E.G., and Baker, J.C., "Effect of Columbium and Vanadium on the Weldability of HSLA Steels", The Welding Journal, 1979, Vol 58, No. 6, pp. 179-s to 187-s.

45. Samuels, L.E. "Optical Microscopy of Carbon Steels", ASM, Metals Park, Ohio, 44073, 1980. pp. 28-34.

46. Krauss, G. "Principles of Heat Treatment of Steel", ASM, Metals Park, Ohio, 44073, 1980. pp. 75-80.

47. Kasugai, T. and Inagaki, M., "Microstructures and Their Morphologies in Weld Zone". Fourth International Symposium of the JWS, November 1982.

48. Tweed J and Knott J.F., "Microstructure Toughness Relationships in a C-Mn Weld Metal". Proceedings of the 4th E.C.F. Conference, P. 127.

49. Pickering, F.B., "The Optimization of Microstructures in Steel and Their Relationship to Mechanical Properties". Hardenability Concepts with Applications to Steel Symposium held Oct 24-26, 1977.

50. Shehata, M.T., and Boyd, J.D. "Quantitative Correlations Between Toughness and Microstructure for Commercial Line Pipe Steel". International Conference on Advances in the Physical Metallurgy and Applications of Steels. Liverpool, Sept. 21-24, 1981.

51. Dolby, R.E., "Advances in the Welding Metallurgy of Steel". International Conference on Advances in the Physical Metallurgy and Applications of Steels. Liverpool, Sept, 21-24, 1981.

52. Ikawa, H., Oshige, H. and Tanoue, T., "Effect of Martensite - Austenite Consistuent on HAZ Toughness of a High Strength Steel". Transaction of JWS, Vol. 11, No. 2, Oct. 1980.

53. Naylor, J.P. and Blondeau, R., "The Respective Roles of the Packet Size and The Lath Width on Toughness". Metallurgical Transaction A, Vol. 7A, June 1976.

54. ASTM E208 - 81, 1983 Annual Book of ASTM Standards, Section 3, Metals Test Methods and Analytical Procedures, Vol. 03.01 Metals - Mechanical Testing; Elevated and Low Temperature Tests.

55. BS 5762 - 1979 "Methods for Crack Opening Displacement (COD) Testing", British Standards Institution.

56. Towers, O.L., and Robinson, P., "Procedures for Fatigue Cracking Fracture Toughness Testpieces, with Particular Reference to Weldments", The Welding Insititute Research Bulletin, 1982, Vol. 23, No. 4, pp. 112-120.

57. Towers, O.L. and Dawes, M.G., "Welding Institute Research on the Fatigue Pre-cracking of Fracture Toughness Specimens", Presented at ASTM Symposium on "User's Experience with Elastic-plastic Fracture Toughness Test Methods", held in Louisville, Kentucky, U.S.A., April 20-22, 1983.

58. "The Use (and Abuse) of CTOD", Metal Construction, 1982, Vol. 14, No. 5, pp. 272-277.

59. Harrison, J.D. et al. "The COD Approach and Its Applications to Welded Structures". Philadephia ASTM STP668, 1979.

60. Kamath, M.S., "The COD Design Curve: An Assessment of Validity Using Wide Plate Tests". International J. Press. Vessels and Piping, 9 (2), 1981, 79-105.

61. Smith, I.J. et al. "A Defect Assessment Method Using Finite Elements and the CTOD Design Curve, for Use in the Design of Offshore Welded Structures". Paper 21, 2nd Internatioanl Conference on Offshore Welded Structures, London, November 1982.

62. Dolby, R.E. "Charpy V and COD Correlations Between Test Data for Ferritic Weld Metals", Metal Construction, 1981, Vol. 13, No. 1, pp. 43-51.

TABLE 1

CHEMICAL COMPOSITION OF FOUR EXPERIMENTAL STEELS (in Wt%)

Element	Algoma LT 60	A710 Gr.A, Cl.3.	MACS (ACC)	MACS (DQT)
C	.12	.05	.07	.07
Mn	1.39	.62	1.32	1.47
Si	.28	.30	.26	.24
Cr	.17	.72	.01	.01
Mo	.03	.18	.001	.001
Ni	.15	.88	.02	.16
Cu	.15	1.05	.01	.16
V	.053	---	.003	.004
Nb	.041	.041	.017	.016
Al	.027	.040	.034	.023
Ti	---	.002	.020	.020
P	.017	.011	.006	.008
S	.011	.004	.002	.002
O	.0035	.0017	.0025	.0017
N	.0063	.0037	.0031	.0025

TABLE 2

MECHANICAL PROPERTIES OF FOUR EXPERIMENTAL STEELS

	YS (MPa)	UTS (MPa)	Elongation (% in 50mm)	Notch Toughness (CVNL)
Algoma LT 60	386	516	30	211J @ -60°C
A710 Gr. A, Cl. 3	581	669	29	182J @ -60°C
MACS (ACC)	431	516	34	295J @ -60°C
MACS (DQT)	439	525	36	248J @ -60°C

TABLE 3A

WELDING PARAMETERS

	HEAT INPUT		
	1.6 kJ/mm	3.5 kJ/mm	5.4 kJ/mm
Preheat	100°C	100°C	100°C
Interpass	110°C	110°C	110°C
Groove geometry	45°K-joint	45°K-joint	45°K-joint
Nose	3.2 mm	4.8 mm	4.8 mm
Root gap	None	None	None
Electrical Stickout	31.8 mm	31.8 mm	31.8 mm
Voltage (DCRP)	32V	32V	34V
Current	500A	500A	650A
Travel Speed	10.2 mm/s	4.7 mm/s	4.1 mm/s
Electrode Diam.	3.2 mm	3.2 mm	4.0 mm
Electrode Angle	90°	90°	90°
Electrode Dist. from Sidewall	1.6 mm	1.6 mm	3.2 mm
Backgouge			
Voltage	60V	60V	60V
Current	500A	500A	500A
Travel Speed	12.7 mm/s	12.7 mm/s	12/7 mm/s
Plate Angle	2°	2°	2°
Dist. from side wall at top	3.2 mm	3.2 mm	3.2 mm

TABLE 3B

WELDING CONDITIONS USED FOR K-JOINT WELDS

	HEAT INPUT EXAMINED		
Steel	1.6 kJ/mm	3.5 kJ/mm	5.4 kJ/mm
LT60	No	Yes	Yes
A710	Yes	Yes	Yes
MACS EH36	No	No	Yes

TABLE 4

GLEEBLE SIMULATION

THERMAL CYCLE PARAMETERS

Heat Input, kJ/mm (100°C preheat)	Peak Temperature, °C	Time Above 1000°C s	T800/500, s
1.6	1350	5.5	20
3.5	1350	10	35
5.4	1350	11	51

TABLE 5

PRIOR AUSTENITE GRAIN SIZE
(Straight Line Intercept Method)

	Gleeble			K-Joint		
	1.6 kJ/mm	3.5 kJ/mm	5.4 kJ/mm	1.6 kJ/mm	3.5 kJ/mm	5.4 kJ/mm
Lloyds LT 60	90.1 μm (122 max)	107.5 μm (190 max)	125.0 μm (233 max)	---	70 - 165 μm	90 - 160 μm
A710 Gr.A,Cl 3	99.3 μm (171 max)	118.5 μm (180 max)	129.8 μm (207 max)	51 - 70 μm	60 - 81 μm	60 - 110 μm
MACS (ACC)	87.2 μm (145 max)	100.5 μm (158 max)	105 μm (180 max)	---	---	50 - 78 μm
MACS (DQT)	85.8 μm	88.6 μm	92.7 μm	---	---	46 - 80 μm

TABLE 6

AVERAGE HARDNESS FOUND IN COARSE GRAIN SUPERCRITICAL REGION OF GLEEBLE SPECIMENS

	HEAT INPUT		
	1.6 kJ/mm	3.5 kJ/mm	5.4 kJ/mm
	Average Hardness (HV_{10})		
Lloyds LT 60			
(AW)	279	260	265
(SR)	240	270	220
A710			
(AW)	290	285	270
(SR)	280	280	290
MACS			
(AW)	235	230	190
(SR)	215	240	275

TABLE 7

DROP WEIGHT TEST RESULTS FOR CG HAZ IN LT 60 STEEL WELDED WITH 3.5 kJ/mm HEAT INPUT

AS WELDED (1A)

TEMP. °C	BREAK	STARTING CRACK OR CRACK PATH LOCATION
-30	NB	
-50	NB	
-55	NB	
	NB	
	NB	
-60	B	CG HAZ
	B	
-70	B	

STRESS-RELIEVED (1S)

TEMP. °C	BREAK	STARTING CRACK OR CRACK PATH LOCATION
-30	NB	
-50	NB	
-60	NB	
-65	NB	
	NB	
	B	O + FG + CG HAZ
-70	NB	
	B	

NB - No Break
B - Break
CG - Coarse Grain HAZ
FG - Fine Grain HAZ
O - All The Other Structures

TABLE 8

DROP WEIGHT TEST RESULTS FOR THE CG HAZ IN LT60 STEEL WELDED WITH 5.4 kJ/mm HEAT INPUT

AS WELDED (2A)

TEMP. °C	BREAK	STARTING CRACK OR CRACK PATH LOCATION
-40	NB	
	NB	
-45	B	CG HAZ
	B	
-50	B	

STRESS-RELIEVED (2S)

TEMP. °C	BREAK	STARTING CRACK OR CRACK PATH LOCATION
-50	NB	
-55	NB	
-60	NB	
	B	CG HAZ
-65	B	
	B	
-70	B	

NB - No Break
B - Break

TABLE 9

DROP WEIGHT TEST RESULTS FOR THE CG HAZ IN A710 Gr A, Cl 3 STEEL WELDED WITH 5.4 kJ/mm HEAT INPUT

AS WELDED (3A)

TEMP.°C	BREAK	STARTING CRACK OR CRACK PATH LOCATION
-45	NB	
-50	NB	CG HAZ
	NB	
	B	CG HAZ + FB + WM
-55	NB	WM
	B	CG HAZ
-60	B	CG HAZ
	B	

STRESS-RELIEVED (3S)

TEMP.°C	BREAK	STARTING CRACK OR CRACK PATH LOCATION
-50	NB	
-60	NB	CG HAZ
	NB	
-65	NB	WM
	B	CG HAZ
	B	
-70	NB	CG HAZ (?)
	NB	

NB - No Break
B - Break
CG - Coarse Grain HAZ
FG - Fine Grain HAZ
WM - Weld Metal

TABLE 10

DROP WEIGHT TEST RESULTS FOR THE CG HAZ IN A710 Gr. A, Cl 3 STEEL WELDED WITH 3.5 kJ/mm HEAT INPUT

AS WELDED (4A)

TEMP. °C	BREAK	STARTING CRACK OR CRACK PATH LOCATION
-55	NB	WM
	NB	CG HAZ
-60	NB	CG HAZ
	B	O + FG + CG HAZ
	B	
-65	B	O + FG + CG HAZ
	B	

STRESS-RELIEVED (4S)

TEMP. °C	BREAK	STARTING CRACK OR CRACK PATH LOCATION
-70	NB	CG HAZ
	NB	
-75	B	O + FB + CG HAZ
	B	O + FG + CG HAZ
-80	B	

NB - No Break
B - Break

TABLE 11

DROP WEIGHT TEST RESULTS FOR THE CG HAZ IN A710 Gr.A, Cl 3 STEEL WELDED WITH 1.6 kJ/mm HEAT INPUT

AS WELDED (5A)

TEMP. °C	BREAK	STARTING CRACK OR CRACK PATH LOCATION
-50	NB	
-55	NB	CG HAZ
	NB	
-60	NB	WM
	B	CG HAZ
	B	

STRESS-RELIEVED (5S)

-50	NB	
-60	NB	
-70	NB	FG + CG HAZ
	NB	
-75	NB	WM
	B	CG HAZ
-80	B	
	B	

NB - No Break
B - Break

TABLE 12

DROP WEIGHT TEST RESULTS FOR THE CG HAZ IN MACS ACC AND DQT STEELS WELDED WITH 5.4 kJ/mm HEAT INPUT

AS WELDED (ACC, 6A)

TEMP. °C	BREAK	STARTING CRACK OR CRACK PATH LOCATION
-40	NB	CG HAZ
	NB	
-45	B	FB + CG
-50	B	
-55	B	CG HAZ
-60	B	

STRESS-RELIEVED (6S)

-50	NB	
	NB	
-55	NB	WM
	NB	WM
	B	CG HAZ
-60	B	CG HAZ
	B	
	B	

NB - No Break
B - Break

TABLE 13

NIL DUCTILITY TRANSITION TEMPERATURE FOR THE CG HAZ

Batch No.	Condition	Steel	Heat Input kJ/mm	NDT Temperature °C
1A	AW	LT 60	3.5	-60
1S	SR			-65
2A	AW	LT 60	5.4	-45
2S	SR			-60
3A	AW	A710 Gr.A,Cl 3	5.4	-50
3S	SR			-65
4A	AW	A710 Gr.A,Cl 3	3.5	-60
4S	SR			-75
5A	AW	A710 Gr.A,Cl 3	1.6	-60
5S	SR			-75
6A	AW	MACS (ACC)	5.4	-45
6S	SR	MACS (DQT)	5.4	-55

AW - As-welded
SR - Stress-relieved

TABLE 14
The CTOD Values for the As-Welded CG HAZ for LT60 Steel Welded with 3.5 kJ/mm Heat Input

Specimen Number	Test Temp. °C	a(av) ** mm	B mm	W mm	Y	σ_y MPa	V_p mm	P_{max} 10^3 N	δ_c^* δm (δu) mm
1A 1	-60	66.10	57.0	114.0	13.97	386	1.2192	196	(0.382)[a]
1A 2	-30	64.65	57.0	114.0	13.33	386	2.9058	234.89	(0.807)
1A 3	-60	65.17	57.0	114.0	13.57	386	0.0381	120.93	0.050*c
1A 4	-30	63.74	57.0	114.0	12.95	386	0.2286	169.3	(0.127)
1A 5	-60	58.27	57.0	114.0	11.00	386	0.638	230.2	(0.269)[b]
1A 6	-60	63.45	56.84	114.0	12.86	386	0	90.076	0.021*c
1A 7	-30	66.00	57.32	114.2	13.87	386	2.3520	206.8	(0.639)
1A 8	-30	62.51	56.91	114.1	12.46	386	4.8108	236.87	(1.287)
1A 9	-30	64.89	57.0	113.8	13.47	386	0.3905	180.15	(0.178)
1A 10	-30	64.75	57.1	114.1	13.38	386	0.36195	178.49	(0.169)
1A 11	-30	64.88	57.4	114.3	13.38	386	0.0333 1.8193	115.092 153.456	(0.043)c (0.457)
1A 12	-60	62.37	57.3	114.3	12.37	386	0.4567	185.148	(0.192)

z = 3mm $\nu = 0.3$ $E = 207 \times 10^3$ MPa

$** = a(av) = \frac{a_2 + a_3 + a_4}{3}$

a,b = invalid results because of non-uniform fatigue precrack front.

c = pop-in occurred.

TABLE 15
The CTOD Values for the Stress-Relieved CG HAZ for LT60 Steel Welded with 3.5 kJ/mm Heat Input

Specimen Number.	Test Temp. °C	a(av) ** mm	B mm	W mm	Y	σ_y MPa	V_p mm	P_{max} 10^3 N	δ_c^* δm (δu) mm
1S 1	-60	59.52	57.0	114.0	11.40	386	0.4572	216.02	(0.212)
1S 2	-60	59.79	57.0	114.0	11.52	386	0.0095	127.61	0.036*
1S 3	-60	61.96	57.0	114.0	12.30	386	0.3530	196	(0.175)
1S 4	-30	61.03	57.4	114.2	11.87	386	0.6756	196	(0.251)
1S 5	-30	60.21	57.3	114.0	11.64	386	3.8862	252.71	(1.118)
1S 6	-30	60.99	57.12	113.84	11.96	386	1.3145	205.17	(0.419)
1S 7	-60	60.65	57.21	113.84	11.83	386	0.0286	153.46	0.058*
1S 8	-30	60.89	57.13	113.9	11.91	386	4.4577	233.53	(1.229)
1S 9	-30	66.79	57.6	113.92	14.28	386	1.1144	172.64	(0.329)
1S 10	-60	62.69	57.0	114.1	12.50	386	0.1048	182.65	(0.105)
1S 11	-30	59.87	57.4	114.3	11.48	386	(1.7907)	218.508	(0.556)
1S 12	-30	62.47	57.3	114.3	12.42	386	(1.0573)	185.148	(0.335)
1S 13	-60	60.15	57.3	114.3	11.56	386	(0.2286)	195.156	(0.136)
1S 14	-60	61.45	57.4	114.3	12.04	386	(0.0095)	112.590	(0.030)

$z = 3\text{mm}$ $\nu = 0.3$ $E = 207 \times 10^3$ MPa

$** = a(av) = \frac{a_2 + a_3 + a_4}{3}$ a = pop-ins

TABLE 16

The CTOD Values for the As-Welded CG HAZ for LT60 Steel Welded with 5.4 kJ/mm Heat Input

Specimen Number	Test Temp. °C	a(av) ** mm	B mm	W mm	Y	σ_y MPa	V_p mm	P_{max} 10^3 N	δ_c^* δm (δu) mm
2A 1	-30	63.99	57.0	114.3	13.00	386	(0.105)	149.28	(0.082)
2A 2	-30	62.02	57.2	114.0	12.30	386	(0.734)	200.16	(0.271)
2A 3	-30	62.67	57.2	114.3	12.46	386	(0.810)	197.66	(0.286)
2A 4	-30	63.21	57.0	114.2	12.73	386	0.0381*	116.76	0.043*
2A 5	-30	62.93	57.2	114.2	12.59	386	0.0190*	109.25	0.033*[a]
2A 6	-30	63.85	57.0	114.0	13.00	386	(0.324)	178.48	(0.158)
2A 7	-50	64.47	57.2	114.2	13.23	386	0.019*	156.79	0.070*
2A 8	-50	64.74	57.0	114.2	13.33	386	0.0286*	122.60	0.047*
2A 9	-50	62.50	57.0	114.3	12.42	386	0.000*	107.59	0.027*
2A 10	-50	63.70	57.0	114.3	12.86	386	(0.0572)	139.28	(0.063)

$z = 3\text{mm}$ $\nu = 0.3$ $E = 207 \times 10^3$ MPa

$** = a(av) = \frac{a_2 + a_3 + a_4}{3}$

a = pop-in occurred

TABLE 17

The CTOD Values for the Stress-Relieved CG HAZ for LT60 Steel Welded with 5.4 kJ/mm Heat Input

Specimen Number	Test Temp. °C	a(av) ** mm	B mm	W mm	Y	σ_y MPa	V_p mm	P_{max} 10^3 N	δ_c^* δm (δu) mm
2S 1	-30	60.63	57.3	114.2	11.75	386	(0.638)	194.32	(0.240)
2S 2	-30	60.20	57.2	114.1	11.64	386	(0.667)	197.66	(0.251)
2S 3	-30	63.07	57.2	114.2	12.64	386	(3.143)	207.66	(0.848)
2S 4	-30	61.55	57.2	114.3	12.04	386	(0.714)	183.48	(0.250)
2S 5	-30	61.85	57.0	114.3	12.16	386	(0.438)	180.14	(0.181)
2S 6	-50	60.77	57.0	114.3	11.79	386	(0.763)	195.99	(0.274)
2S 7	-50	61.87	57.2	114.3	12.16	386	0.0095*	114.26	0.032*
2S 8	-50	61.04	57.1	114.0	11.91	386	(0.057)	173.47	(0.080)
2S 9	-50	60.53	57.1	114.0	11.75	386	0.0095*	123.43	0.035*

$z = 3\text{mm}$ $\nu = 0.3$ $E = 207 \times 10^3$ MPa

$$** = a(av) = \frac{a_2 + a_3 + a_4}{3}$$

TABLE 18
The CTOD Values for the As-Welded CG HAZ for A710 Gr A Cl 3 Steel Welded with 5.4 kJ/mm Heat Input

Specimen Number	Test Temp. °C	a(av) ** mm	B mm	W mm	Y	σ_y MPa	V_p mm	P_{max} 10^3 N	δ_c^* δm (δu) mm
3A 1	-30	48.85	44.5	88.9	12.55	582	(0.3048)	152.622	(0.151)
3A 2	-30	49.92	44.5	88.6	13.14	582	(0.5429)	151.788	(0.209)
3A 3	-30	54.02	44.5	88.8	15.50	582	(0.2381)	110.088	(0.109)
3A 4	-30	49.19	44.4	89.0	12.68	582	0.02858*	135.108	0.070*
3A 5	-30	48.98	44.6	88.8	12.64	582	(0.276)	152.622	(0.144)
3A 6	-30	49.71	44.5	88.8	13.00	582	(2.1908)	165.132	(0.600)
3A 7	-50	49.93	44.5	88.9	13.09	582	(0.04763)	98.412	(0.046)
3A 8	-50	49.65	44.4	88.8	12.95	582	(0.05715)	102.999	(0.052)
3A 9	-50	50.37	44.5	88.7	13.38	582	(0.09525)	111.756	(0.069)
3A 10	-50	49.70	44.5	89.0	12.91	582	(1.12395)	164.298	(0.355)

$z = 3\text{mm}$ $\nu = 0.3$ $E = 207 \times 10^3$ MPa

$$** = a(av) = \frac{a_2 + a_3 + a_4}{3}$$

TABLE 19

The CTOD Values for the Stress-Relieved CG HAZ for A710 Gr A Cl 3 Steel Welded with 5.4 kJ/mm Heat Input

Specimen Number	Test Temp. °C	a(av) ** mm	B mm	W mm	Y	σ_y MPa	V_p mm	P_{max} 10^3 N	δ_c^* δm (δu) mm
3S 1	-30	46.80	44.5	89.0	11.56	582	(2.0193)	171.804	(0.596)
3S 2	-30	49.32	44.5	88.8	12.77	582	(0.7430)	136.776	(0.238)
3S 3	-30	47.88	44.5	88.9	12.04	582	(0.400)	150.120	(0.168)
3S 4	-30	48.48	44.6	88.9	12.33	582	(0.0762)	115.926	(0.062)
3S 5	-30	48.10	44.0	88.8	12.20	582	(0.0381)	87.153	(0.034)
3S 6	-30	47.59	44.5	88.9	11.91	582	3.867	158.877	1.029
3S 7	-50	48.18	44.5	88.9	12.20	582	0.02858*	100.914	0.0395*
3S 8	-50	52.25	44.5	88.9	14.39	582	(0.10478)	106.752	(0.073)
3S 9	-50	48.21	44.6	88.8	12.25	582	0.01905*	93.825	0.033*
3S 10	-50	46.62	44.5	88.5	11.60	582	(0.06668)	127.602	(0.064)

$z = 3\text{mm}$ $\nu = 0.3$ $E = 207 \times 10^3$ MPa

$** = a(av) = \frac{a_2 + a_3 + a_4}{3}$

TABLE 20

The CTOD Values for the As-Welded CG HAZ for A710 Gr A Cl 3 Steel Welded with 3.5 kJ/mm Heat Input

Specimen Number	Test Temp. °C	a(av) ** mm	B mm	W mm	Y	σ_y MPa	V_p mm	P_{max} 10^3 N	δ_c^* δm (δu) mm
4A 1	-30	48.56	44.5	88.9	12.37	582	(0.21336)	143.448	(0.119)
4A 2	-30	48.87	44.5	88.9	12.55	582	(0.04763)	105.084	(0.049)
4A 3	-30	48.39	44.5	88.9	12.30	582	(0.3905)	160.962	(0.178)
4A 4	-30	48.94	44.5	88.9	12.55	582	(0.14288)	130.938	(0.092)
4A 5	-30	49.24	44.5	88.9	12.73	582	(0.2858)	150.120	(0.145)
4A 6	-30	49.42	44.5	88.9	12.82	582	(0.0381)	97.995	(0.043)
4A 7	-50	48.82	44.5	88.9	12.50	582	(0.4191)	160.128	(0.185)
4A 8	-50	49.05	44.5	88.9	12.64	582	(0.7049)	165.966	(0.260)
4A 9	-50	49.16	44.5	88.9	12.68	582	(0.1334)	133.023	(0.092)
4A 10	-50	49.45	44.5	88.9	12.82	582	0.00953*	82.149	0.026*

$z = 3$mm　　$\nu = 0.3$　　$E = 207 \times 10^3$ MPa

$** = a(av) = \frac{a_2 + a_3 + a_4}{3}$

TABLE 21
The CTOD Values for the Stress-Relieved CG HAZ for A710 Gr A Cl 3 Steel Welded with 3.5 kJ/mm Heat Input

Specimen Number	Test Temp. °C	a(av) ** mm	B mm	W mm	Y	σ_y MPa	V_p mm	P_{max} 10^3 N	δ_c^* δm (δu) mm
4S 1	-30	53.32	44.5	88.9	15.10	582	(0.7525)	123.015	(0.226)
4S 2	-30	49.27	44.5	88.9	12.91	582	(0.7239)	151.371	(0.251)
4S 3	-30	48.09	44.5	88.9	12.16	582	(0.0381)	105.501	(0.044)
4S 4	-30	48.75	44.5	88.9	12.46	582	(0.2000)	143.448	(0.116)
4S 5	-30	48.53	44.5	88.9	12.37	582	(0.05715)	115.098	(0.051)
4S 6	-30	49.24	44.5	88.9	12.73	582	(0.06668)	110.505	(0.058)
4S 7	-50	50.66	44.5	88.9	13.47	582	0.0000*	77.145	0.023*
4S 8	-50	49.64	44.5	88.9	12.91	582	(0.3715)	141.780	(0.157)
4S 9	-50	48.38	44.5	88.9	12.30	582	0.00334*	94.242	0.030*
4S 10	-50	48.03	44.5	88.9	12.12	582	(0.13335)	134.274	(0.089)

$z = 3mm$ $\nu = 0.3$ $E = 207 \times 10^3$ MPa

$** = a(av) = \frac{a_2 + a_3 + a_4}{3}$

TABLE 22
The CTOD Values for the As-Welded CG HAZ for A710 Gr A Cl 3 Steel Welded with 1.6 kJ/mm Heat Input

Specimen Number	Test Temp. °C	a(av) ** mm	B mm	W mm	Y	σ_y MPa	V_p mm	P_{max} 10^3 N	δ_c^* δm (δu) mm
5A 1	-30	50.50	44.6	89.0	13.33	582	(0.1334)	122.598	(0.087)
5A 2	-30	49.01	44.6	89.0	12.59	582	(0.9335)	170.136	(0.318)
5A 3	-30	50.50	44.6	89.0	13.33	582	(0.3143)	144.282	(0.149)
5A 4	-30	50.63	44.6	89.0	13.42	582	(0.7049)	155.124	(0.249)
5A 5	-30	49.71	44.6	89.0	12.95	582	1.2573	165.132	0.386
5A 6	-30	49.89	44.6	89.0	13.04	582	(0.89535)	164.715	(0.303)
5A 7	-50	49.24	44.6	89.0	12.68	582	(0.96203)	170.136	(0.324)
5A 8	-50	49.85	44.6	89.0	13.00	582	(0.5334)	159.294	(0.214)
5A 9	-50	49.89	44.6	89.0	13.04	582	(0.4001)	152.205	(0.175)
5A 10	-50	49.07	44.6	89.0	12.59	582	(0.37148)	156.792	(0.170)
5A 11	-50	51.01	44.6	89.0	13.62	582	(0.69533)	154.290	(0.247)

$z = 3$mm $\nu = 0.3$ $E = 207 \times 10^3$ MPa

$** = a(av) = \frac{a_2 + a_3 + a_4}{3}$

TABLE 23
The CTOD Values for the Stress-Relieved CG HAZ for A710 Gr A Cl 3 Steel Welded with 1.6 kJ/mm Heat Input

Specimen Number	Test Temp. °C	a(av) ** mm	B mm	W mm	Y	σ_y MPa	V_p mm	P_{max} 10^3 N	δ_c^* δm (δu) mm
5S 1	-30	49.44	44.6	89.0	12.82	582	(2.2479)	136.776	(0.587)
5S 2	-30	48.88	44.6	89.0	12.50	582	(0.0574)	145.533	(0.557)
5S 3	-30	48.65	44.6	89.0	12.42	582	(1.3621)	134.274	(0.384)
5S 4	-30	48.22	44.6	89.0	12.20	582	(5.1435)	155.958	(1.318)
5S 5	-30	48.80	44.6	89.0	12.46	582	(4.6482)	148.452	(1.173)
5S 6	-50	48.06	44.6	89.0	12.12	582	(0.9239)	135.942	(0.281)
5S 7	-30	50.10	44.6	89.0	13.09	582	(1.2383)	132.606	(0.344)
5S 8	-50	50.19	44.6	89.0	13.19	582	(0.3905)	119.679	(0.140)
5S 9	-50	48.32	44.6	89.0	12.20	582	(0.3524)	129.270	(0.137)
5S 10	-50	50.23	44.6	89.0	13.19	582	(2.8575)	140.946	(0.719)

$z = 3$mm $\nu = 0.3$ $E = 207 \times 10^3$ MPa

$** = a(av) = \frac{a_2 + a_3 + a_4}{3}$

TABLE 24

The CTOD Values for the As-Welded CG HAZ for MACS (ACC) Steel Welded with 5.4 kJ/mm Heat Input

Specimen Number	Test Temp. °C	a(av) ** mm	B mm	W mm	Y	σ_y MPa	V_p mm	P_{max} 10^3 N	δ_c^* δm (δu) mm
6A 1	-30	48.29	44.5	88.9	12.25	431	(3.1623)	147.618	(0.855)
6A 2	-30	48.49	44.5	88.9	12.33	431	(4.3625)	145.950	(1.136)
6A 3	-30	49.70	44.5	88.9	12.95	431	(4.1243)	146.784	(1.051)
6A 4	-30	49.92	44.5	89.9	13.09	431	(4.6292)	145.116	(1.158)
6A 5	-30	49.33	44.5	89.9	12.77	431	(2.2670)	136.359	(0.614)
6A 6	-50	48.28	44.5	88.9	12.25	431	(0.2858)	120.096	(0.132)
6A 7	-30	50.04	44.5	88.9	13.14	431	(4.1148)	145.116	(1.038)
6A 8	-50	48.99	44.5	88.9	12.59	431	(1.1240)	130.104	(0.342)
6A 9	-50	49.73	44.5	88.9	12.95	431	(0.2000)	120.930	(0.117)
6A 10	-50	48.54	44.5	88.9	12.37	431	(0.0667)	97.578	(0.058)
6A 11	-50	48.90	44.5	88.9	12.55	431	(0.8573)	135.942	(0.286)

$z = 3\text{mm}$ $\nu = 0.3$ $E = 207 \times 10^3$ MPa

$** = a(av) = \frac{a_2 + a_3 + a_4}{3}$

TABLE 25
The CTOD Values for the Stress-Relieved CG HAZ for MACS (DQT) Steel Welded with 5.4 kJ/mm Heat Input

Specimen Number	Test Temp. °C	a(av) ** mm	B mm	W mm	Y	σ_y MPa	V_p mm	P_{max} 10^3 N	δ_c^* δm (δu) mm
6S 1	-30	48.44	44.5	89.0	12.30	439	(2.1526)	126.768	(0.585)
6S 2	-30	48.18	44.5	88.89	12.20	439	(5.5817)	142.614	(1.434)[a]
6S 3	-30	48.22	44.45	88.86	12.25	439	(1.7717)	121.764	(0.490)
6S 4	-30	48.32	44.5	89.0	12.25	439	(3.6290)	135.108	(0.952)
6S 5	-30	49.42	44.46	89.0	12.77	439	(0.9906)	111.756	(0.288)
6S 6	-30	49.46	44.5	88.97	12.82	439	(4.3053)	129.270	(1.075)[b]
6S 7	-50	48.12	44.4	88.9	12.16	439	(0.2191)	115.092	(0.109)
6S 8	-50	49.22	44.5	89.0	12.68	439	(2.9909)	132.606	(0.779)
6S 9	-50	51.07	44.5	89.0	13.67	439	(2.7242)	118.428	(0.671)
6S 10	-50	49.41	44.5	88.9	12.82	439	(2.9432)	128.436	(0.759)
6S 11	-50	44.76	43.8	87.1	11.11	439	(0.7811)	126.768	(0.264)

$z = 3\text{mm}$ $\nu = 0.3$ $E = 207 \times 10^3$ MPa

$** = a(av) = \frac{a_2 + a_3 + a_4}{3}$

a,b tests were stopped after the maximum travel limit reached in the clip gauge.

Table 26: Microstructures of the Fatigue Crack and the Fracture Path, Measured Along the Thickness B, Near the Fatigue Precrack Front for LT 60 Steel Welded with 3.5 kJ/mm Heat Input (As-Welded)

Sp. No.	Test Temp. °C	δ* (δu) (δm) mm	Location in B	Microstructure, %										Fracture Initiation (mm)	
				Fatigue Crack (FC)					Fracture Path (FP)						
				CG HAZ C	FG HAZ F	Other O	Weld W	Fus.B. B	C	F	O	W	B	FC	FP
1A-2	-30	(0.807)	Full B			100									
			Mid 1/3 B			100									
1A-4	-30	(0.127)	Full B	31	9	60	0								
			Mid 1/3 B	26	5	68									
1A-7	-30	(0.639)	Full B			100									
			Mid 1/3 B			100									
1A-8	-30	(1.287)	Full B			100									
			Mid 1/3 B			100									
1A-9	-30	(0.178)	Full B	65	18	14	3								
			Mid 1/3 B	53	26	16	5								
1A-10	-30	(0.169)	Full B	46	23	21	10								
			Mid 1/3 B	32	10	26	32								
1A-1	-60	(0.382)	Full B	37		63									
			Mid 1/3 B	16		84									
1A-3	-60	0.050*	Full B	59	14	23	4								
			Mid 1/3 B	74	16		11								
1A-5	-60	(0.269)	Full B	45	18	37									
			Mid 1/3 B	74	26										
1A-6	-60	0.021*	Full B	49	19	32									
			Mid 1/3 B	63	16	21									
1A-11	-30	0.043*	Full B	30	5	61	4		25	16	56	3		C(37)	C(37)
		(0.457)	Mid 1/3 B	5	16	79			16	11	73				
1A-12	-60	(0.192)	Full B			100					91	9		O(27)	O(27)
			Mid 1/3 B			100					100				
			Full B												
			Mid 1/3 B												

Table 27: Microstructures of the Fatigue Crack and the Fracture Path, Measured Along the Thickness B, Near the Fatigue Precrack Front for LT 60 Steel Welded with 3.5 kJ/mm Heat Input (Stress-Relieved)

Sp. No.	Test Temp. °C	δ^* (δu) (δm) mm	Location in B	Microstructure, %										Fracture Initiation (mm)	
				Fatigue Crack (FC)					Fracture Path (FP)						
				CG HAZ C	FG HAZ F	Other O	Weld W	Fus.B. B	C	F	O	W	B	FC	FP
1S-4	-30	(0.251)	Full B	25	12	67	5								
			Mid 1/3 B	11	26	63									
1S-5	-30	(1.118)	Full B			100									
			Mid 1/3 B			100									
1S-6	-30	(0.419)	Full B	35	19	12	33								
			Mid 1/3 B	16	11	5	68								
1S-8	-30	(1.229)	Full B	14	9	77									
			Mid 1/3 B	21		79									
1S-9	-30	(0.329)	Full B	50	10	28	12								
			Mid 1/3 B	37	5	21	37								
1S-11	-30	(0.556)	Full B	4	10	39	47		5	5	40	49		C(28),W(13)	W(28,13)
			Mid 1/3 B	5	32	21	42		11	11	26	53			
1S-12	-30	(0.335)	Full B	32	11	9	49		39	32	23	7		C(33),W(13)	C(33,13)
			Mid 1/3 B	37	21		42		47	21	16	16			
1S-1	-60	(0.212)	Full B	11	19	53	17								
			Mid 1/3 B	21	10	66	3								
1S-2	-60	0.036*	Full B	7	4	3	86								
			Mid 1/3 B	10	11	11	68								
1S-3	-60	(0.175)	Full B	21	5	14	60								
			Mid 1/3 B	5	5	21	69								
1S-7	-60	0.058*	Full B	7		93									
			Mid 1/3 B	21		79									
1S-10	-60	(0.105)	Full B	5			95								
			Mid 1/3 B				100								
1S-13	-60	(0.136)	Full B	16	5	44	35		19	11	56	14		C(31)	C(31)
			Mid 1/3 B	21	5	42	32		32	16	32	21			

(Cont'd) Table 27: Microstructures of the Fatigue Crack and the Fracture Path, Measured Along the Thickness B, Near the Fatigue Precrack Front for LT 60 Steel Welded with 3.5 kJ/mm Heat Input (Stress-Relieved)

Sp. No.	Test Temp. °C	δ* (δu) (δm) mm	Location in B	Microstructure, %										Fracture Initiation (mm)	
				Fatigue Crack (FC)					Fracture Path (FP)						
				CG HAZ C	FG HAZ F	Other O	Weld W	Fus.B. B	C	F	O	W	B	FC	FP
1S-14	-60	0.030*	Full B	19	9	46	26		14	9	58	19		C(12,32)	C(12),F(32)
			Mid 1/3 B	5	10	58	26		10	5	68	16			
			Full B												
			Mid 1/3 B												
			Full B												
			Mid 1/3 B												
			Full B												
			Mid 1/3 B												
			Full B												
			Mid 1/3 B												
			Full B												
			Mid 1/3 B												
			Full B												
			Mid 1/3 B												
			Full B												
			Mid 1/3 B												
			Full B												
			Mid 1/3 B												
			Full B												
			Mid 1/3 B												
			Full B												
			Mid 1/3 B												
			Full B												
			Mid 1/3 B												

Table 28: Microstructures of the Fatigue Crack and the Fracture Path, Measured Along the Thickness B, Near the Fatigue Precrack Front for LT 60 Steel Welded with 5.4 kJ/mm Heat Input (As-Welded)

Sp. No.	Test Temp. °C	δ* (δu) (δm) mm	Location in B	Microstructure, %										Fracture Initiation (mm)	
				Fatigue Crack (FC)					Fracture Path (FP)						
				CG HAZ C	FG HAZ F	Other O	Weld W	Fus.B. B	C	F	O	W	B	FC	FP
2A-1	-30	(0.082)	Full B	19	12	53	16		21	10	56	12		W(39),O(28)	C(39),O(28)
			Mid 1/3 B	5	5	53	37		42	5	53				
2A-2	-30	(0.271)	Full B	35	7	26	19	12^a	23	9	38	30		C(35),B(25)	W(35),F(25)
			Mid 1/3 B	32	5	16	47		10	11	26	53			
2A-3	-30	(0.286)	Full B	37		23	35	5^a	46	10	33	11		W(28),O(23)	C(28)
			Mid 1/3 B	16		26	58		53	5	32	10		C(18)	O(34,39)
2A-4	-30	0.043*	Full B	11	5	63	21		14	12	68	5		W(29),B(22)	C(29),F(22)
			Mid 1/3 B	16		26	58		37	37	26			O(19)	O(19)
2A-5	-30	0.033*	Full B						16	26	54	4			C(29)
			Mid 1/3 B						37	32	31				
2A-6	-30	(0.158)	Full B	37		28	35		42	12	32	14		C(41)	W(41),C(30)
			Mid 1/3 B	11			89		68	5	6	21		W(30,22)	O(22)
2A-7	-50	0.070*	Full B						38	32	28	2			C(34,27)
			Mid 1/3 B						53	26	21				F(31)
2A-8	-50	0.047*	Full B	46	7	7	30	11^a	49	26	25			C(39,17)	C(39,29)
			Mid 1/3 B	11	5		84		68	16	16			W(29)	F(17)
2A-9	-50	0.027*	Full B	35	5	60			32	5	63			C(30)	C(30)
			Mid 1/3 B	74		26			68	5	27				
2A-10	-50	(0.063)	Full B	35	5	53		7	33	12	55			B(36),O(26)	C(26,36)
			Mid 1/3 B	26	16	42		16	47	16	37				
			Full B												
			Mid 1/3 B												
			Full B												
			Mid 1/3 B												
			Full B												
			Mid 1/3 B												

a = scratches due to grinding

Table 29: Microstructures of the Fatigue Crack and the Fracture Path, Measured Along the Thickness B, Near the Fatigue Precrack Front for LT 60 Steel Welded with 5.4 kJ/mm Heat Input (Stress-Relieved)

Sp. No.	Test Temp. °C	δ* (δu) (δm) mm	Location in B	Microstructure, %										Fracture Initiation (mm)	
				Fatigue Crack (FC)					Fracture Path (FP)						
				CG HAZ C	FG HAZ F	Other O	Weld W	Fus.B. B	C	F	O	W	B	FC	FP
2S-1	-30	(0.240)	Full B	57		6	23		18	49	8	25		C(37,21)	F(37),C(21)
			Mid 1/3 B	21		11	68		10	11	5	74			
2S-2	-30	(0.251)	Full B	5		28	67		18	12	45	25		C(23)	F(23)
			Mid 1/3 B	11		16	73		47	32	5	16			
2S-3	-30	(0.548)	Full B	53	3	9	21	14	11	37	49	3		C(34)	C(34)
			Mid 1/3 B	5	5	16	42	32	32	5	63				
2S-4	-30	(0.250)	Full B	32	9	14	7	38	25	32	33	10		O(31),C(12)	F(31),C(12)
			Mid 1/3 B	21	5	16	37	21	37	21	11	31			
2S-5	-30	(0.181)	Full B	11	5	18	30	37	28	11	42	19		W(45,26)	W(45),O(34)
			Mid 1/3 B						47	16	32	5		O(34),C(17)	C(26,17)
2S-6	-50	(0.274)	Full B	42	14	25	19		42	14	25	19		C(33,20)	C(33,20)
			Mid 1/3 B	58	5	16	21		58	5	16	21			
2S-7	-50	0.032*	Full B	21	23	9	47		21	23	9	47		C(42,31)	C(42,31)
			Mid 1/3 B	5			95		5			95			
2S-8	-50	(0.080)	Full B	47	5	12	18	18	14	30	23	33		B(25)	C(25)
			Mid 1/3 B	16		11	53	21	16	26		58			
2S-9	-50	0.035*	Full B	25	12	18	45		25	12	18	45		C(32,27)	C(32,27)
			Mid 1/3 B	42	16	10	32		42	16	10	32			
			Full B												
			Mid 1/3 B												
			Full B												
			Mid 1/3 B												
			Full B												
			Mid 1/3 B												
			Full B												
			Mid 1/3 B												

Table 30: Microstructures of the Fatigue Crack and the Fracture Path, Measured Along the Thickness B, Near the Fatigue Precrack Front for A710 Gr. A Cl. 3 Steel Welded with 5.4 kJ/mm Heat Input (As-Welded)

Sp. No.	Test Temp. °C	δ* (δu) (δm) mm	Location in B	Microstructure, %										Fracture Initiation (mm)	
				Fatigue Crack (FC)					Fracture Path (FP)						
				CG HAZ C	FG HAZ F	Other O	Weld W	Fus.B. B	C	F	O	W	B	FC	FP
3A-1	-30	(0.151)	Full B	32	30	4	34		32	30	4	34		C(16)	C(16)
			Mid 1/3 B	43	14		43		43	14		43			
3A-2	-30	(0.209)	Full B	32	32	16	20		52	32	2	14		C(23,16)	C(23,16)
			Mid 1/3 B	36	36	28			71	15		14			
3A-3	-30	(0.109)	Full B	50	7		43		41	14	2	43		C(25,12)	W(25),C(12)
			Mid 1/3 B	64			36		22	21		57			
3A-4	-30	0.070*	Full B	55	4	9	32		32	11	7	50		W(31),C(18)	W(31),C(18)
			Mid 1/3 B												
3A-5	-30	(0.144)	Full B	41	23	7	29		41	23	7	29		C(21,16)	C(21,16)
			Mid 1/3 B	64	21		14		64	21		14			
3A-6	-30	(0.600)	Full B	27	18	41	14		27	14	7	52		O(22),C(17)	O(22),C(17)
			Mid 1/3 B	29	14		57		57	21	22				
3A-7	-50	(0.046)	Full B	43	30		27		43	30		27		C(23,12)	C(23,12)
			Mid 1/3 B	64	7		29		64	7		29			
3A-8	-50	(0.052)	Full B	50	16	7	27		50	16	7	27		C(31,29,23)	C(31,29,23)
			Mid 1/3 B	57	43				57	43					
3A-9	-50	(0.069)	Full B	16			84		16			84		B(19)	B(19)
			Mid 1/3 B	50			50		50			50			
3A-10	-50	(0.355)	Full B	20	14	39	27		20	14	39	27		O(26,16)	O(26,16)
			Mid 1/3 B			100					100				
			Full B												
			Mid 1/3 B												
			Full B												
			Mid 1/3 B												
			Full B												
			Mid 1/3 B												

Table 31: Microstructures of the Fatigue Crack and the Fracture Path, Measured Along the Thickness B, Near the Fatigue Precrack Front for A710 Gr. A Cl. 3 Steel Welded with 5.4 kJ/mm Heat Input (Stress-Relieved)

Sp. No.	Test Temp. °C	δ* (δu) (δm) mm	Location in B	Microstructure, %										Fracture Initiation (mm)	
				Fatigue Crack (FC)					Fracture Path (FP)						
				CG HAZ C	FG HAZ F	Other O	Weld W	Fus.B. B	C	F	O	W	B	FC	FP
3S-1	-30	(0.596)	Full B	32	16	48	4		25	22	33	20		C(21),F(13) O(27)	C(21,13,27)
			Mid 1/3 B	50	29	21			79	21					
3S-2	-30	(0.238)	Full B	25			75		29		36			B(28),C(14)	W(28,14)
			Mid 1/3 B				100		21		79				
3S-3	-30	(0.168)	Full B	52	25	18	5		52	25	18	5		C(21)	C(21)
			Mid 1/3 B	57	29	14			57	29	14				
3S-4	-30	(0.062)	Full B	57	23	11	9		57	23	11	9		C(25)	C(25)
			Mid 1/3 B	71	21		7		71	21		7			
3S-5	-30	(0.034)	Full B	52	16	23	9		52	16	23	9		C(22,17)	C(22,17)
			Mid 1/3 B	72	14	14			72	14	14				
3S-6	-30	1.029	Full B	21	2	70	7		21	2	70	7		O(30,20,15)	O(30,20,15)
			Mid 1/3 B			100					100				
3S-7	-50	0.039*	Full B	68	20	5	7		68	20	5	7		C(38),B(22)	C(38),B(22)
			Mid 1/3 B	86	7		7		86	7		7			
3S-8	-50	(0.073)	Full B	64	20	7	9		64	20	7	9		C(28)	C(28)
			Mid 1/3 B	93	7				93	7					
3S-9	-50	0.033*	Full B	46	20	32	2		48	25	27			C(26,25,22)	C(26,25,22)
			Mid 1/3 B	85	7	7			64	29	7				
3S-10	-50	(0.064)	Full B	30	20	39	11		59	9	27	5		F(23),C(19)	C(23,19)
			Mid 1/3 B	36	28	36			57	22	21				
			Full B												
			Mid 1/3 B												
			Full B												
			Mid 1/3 B												
			Full B												
			Mid 1/3 B												

Table 32: Microstructures of the Fatigue Crack and the Fracture Path, Measured Along the Thickness B, Near the Fatigue Precrack Front for A710 Gr. A Cl. 3 Steel Welded with 3.5 kJ/mm Heat Input (As-Welded)

Sp. No.	Test Temp. °C	δ* (δu) (δm) mm	Location in B	Microstructure, %										Fracture Initiation (mm)	
				Fatigue Crack (FC)					Fracture Path (FP)						
				CG HAZ C	FG HAZ F	Other O	Weld W	Fus.B. B	C	F	O	W	B	FC	FP
4A-1	-30	(0.119)	Full B	14	4	70	11		93	2	5			C(27)	C(27)
			Mid 1/3 B	21		43	36		79	7	14				
4A-2	-30	(0.049)	Full B	21		18	61		75		11	14		C(29)	C(29)
			Mid 1/3 B	14			86		71			29			
4A-3	-30	(0.178)	Full B	48			48		79	5	2	14		W(21)	W(21)
			Mid 1/3 B	21			79		57			43			
4A-4	-30	(0.092)	Full B	52		30	18		77	2	18	2		C(32),W(18)	C(32,18)
			Mid 1/3 B	43			57		93			7			
4A-5	-30	(0.145)	Full B	43		27	30		77	2	5	16		C(13),B(22)	C(13),B(22)
			Mid 1/3 B	21		29	50		57			43			
4A-6	-30	(0.043)	Full B	43	7	36	14		59	7	18	16		C(18,6)	C(18,16)
			Mid 1/3 B	64			36		50		50				
4A-7	-50	(0.185)	Full B	25			75		27			73		W(19)	W(19)
			Mid 1/3 B				100					100			
4A-8	-50	(0.260)	Full B	34	5	50	11		34	5	50	11		B(19),O(28)	B(19),O(28)
			Mid 1/3 B	36		29	35		21	7	43	29			
4A-9	-50	(0.092)	Full B	45		39	16		68	5	16	11		B(22)	B(22)
			Mid 1/3 B	50		14	36		36		36	28			
4A-10	-50	0.026*	Full B	53		11	36		61	2	25	11		C(27,25)	O(27),B(25)
			Mid 1/3 B	36			64		50		14	36			
			Full B												
			Mid 1/3 B												
			Full B												
			Mid 1/3 B												
			Full B												
			Mid 1/3 B												

Table 33: Microstructures of the Fatigue Crack and the Fracture Path, Measured Along the Thickness B, Near the Fatigue Precrack Front for A710 Gr. A Cl. 3 Steel Welded with 3.5 kJ/mm Heat Input (Stress-Relieved)

Sp. No.	Test Temp. °C	δ* (δu) (δm) mm	Location in B	Microstructure, %										Fracture Initiation (mm)	
				Fatigue Crack (FC)					Fracture Path (FP)						
				CG HAZ C	FG HAZ F	Other O	Weld W	Fus.B. B	C	F	O	W	B	FC	FP
4S-1	-30	(0.226)	Full B	50	4	34	11		57	5	23	16		B(17)	B(17)
			Mid 1/3 B	57		7	36		50			50			
4S-2	-30	(0.251)	Full B	64	2	20	14		64	14	20	2		C(23),B(15)	C(23,15)
			Mid 1/3 B	64	7	7	22		43	7	43	7			
4S-3	-30	(0.044)	Full B	18		73	9		55	14	32			B(20)	B(20)
			Mid 1/3 B	36		36	28		93	7					
4S-4	-30	(0.116)	Full B	16			84		50	2	4	43		W(27,21)	W(27,21)
			Mid 1/3 B	21			79		14	7		79			
4S-5	-30	(0.051)	Full B	46		16	38		75	9		16		W(22)	C(22)
			Mid 1/3 B	29		7	64		71			29			
4S-6	-30	(0.058)	Full B	41	4	21	34		64	23	9	4		B(28),C(25)	C(28,25)
			Mid 1/3 B	57	7	29	7		64	21	14				
4S-7	-50	0.023*	Full B	41			59		73	7	6	14		C(22)	C(22)
			Mid 1/3 B	79			21		100						
4S-8	-50	(0.157)	Full B	50		27	23		45	7	32	16			
			Mid 1/3 B	43		36	21		21	14	50	14			
4S-9	-50	0.030*	Full B	9			91		36	4	2	57		W(18)	W(18)
			Mid 1/3 B				100		50			50			
4S-10	-50	(0.089)	Full B	34	7	32	27		66	9	18	7		B(31),C(16)	C(31,16)
			Mid 1/3 B	50	7		43		79	7	7	7			
			Full B												
			Mid 1/3 B												
			Full B												
			Mid 1/3 B												
			Full B												
			Mid 1/3 B												

Table 34: Microstructures of the Fatigue Crack and the Fracture Path, Measured Along the Thickness B, Near the Fatigue Precrack Front for A710 Gr. A Cl. 3 Steel Welded with 1.6 kJ/mm Heat Input (As-Welded)

Sp. No.	Test Temp. °C	δ* (δu) (δm) mm	Location in B	Microstructure, %										Fracture Initiation (mm)	
				Fatigue Crack (FC)					Fracture Path (FP)						
				CG HAZ C	FG HAZ F	Other O	Weld W	Fus.B. B	C	F	O	W	B	FC	FP
5A-1	-30	(0.087)	Full B	50	9	39	2		66	14	11	9		C(22)	C(22)
			Mid 1/3 B	50	14	36			50	7	29	14			
5A-2	-30	(0.318)	Full B	39	2	23	36		46	2	16	36		O(23,20)	O(23,20)
			Mid 1/3 B	21		43	36		21		50	29			
5A-3	-30	(0.149)	Full B	43		57			73	4	20	2		C(22)	C(22)
			Mid 1/3 B	29		71			64	7	29				
5A-4	-30	(0.249)	Full B	41		50	9		55	2	39	4		O(23)	C(23)
			Mid 1/3 B	29		71			64		36				
5A-5	-30	(0.386)	Full B	43		14	43							W(31),O(22)	W(31),O(22)
			Mid 1/3 B	36		43	21								
5A-6	-30	(0.303)	Full B	27			73		41	4	9	45		W(25,16)	C(25,16)
			Mid 1/3 B				100		21		21	57			
5A-7	-50	(0.324)	Full B	41		7	52		52			48		W(26) C(22,19)	W(26) C(22,19)
			Mid 1/3 B	21			79		21			79			
5A-8	-50	(0.214)	Full B	20		16	64		46	5	4	45		B(25),W(20)	C(25),B(20)
			Mid 1/3 B	21			79		36						
5A-9	-50	(0.175)	Full B	25		27	48		55		16	30		W(32),O(20)	C(32),O(20)
			Mid 1/3 B	7		57	36		7		50	43			
5A-10	-50	(0.170)	Full B	43	2	30	20	4	70	14	2	14		C(22,16)	C(22,16)
			Mid 1/3 B	21	7	29	29	14	57	7		36			
5A-11	-50	(0.247)	Full B	30		45	20	5	39	2		59		O(20)	W(20)
			Mid 1/3 B	29		57		14	7			93			
			Full B												
			Mid 1/3 B												
			Full B												
			Mid 1/3 B												

Table 35: Microstructures of the Fatigue Crack and the Fracture Path, Measured Along the Thickness B, Near the Fatigue Precrack Front for A710 Gr. A Cl. 3 Steel Welded with 1.6 kJ/mm Heat Input (Stress-Relieved)

Sp. No.	Test Temp. °C	δ* (δu) (δm) mm	Location in B	Microstructure, %										Fracture Initiation (mm)	
				Fatigue Crack (FC)					Fracture Path (FP)						
				CG HAZ C	FG HAZ F	Other O	Weld W	Fus.B. B	C	F	O	W	B	FC	FP
5S-1	-30	(0.587)	Full B	27		52	21		41		59			O(28,22)	O(28,22)
			Mid 1/3 B	7		93					100				
5S-2	-30	(0.557)	Full B	9		61	30		7		55	39		W(25)	W(25)
			Mid 1/3 B	7		22	71		14		79	7			
5S-3	-30	(0.384)	Full B	21		25	54		48		25	27		B(32),C(17)	C(32),O(17)
			Mid 1/3 B	14		79	7		14		79	7			
5S-4	-30	(1.318)	Full B	7		52	41		36		36	25		W(29),B(8)	B(29,8)
			Mid 1/3 B	7		86	7		7		93				
5S-5	-30	(1.173)	Full B	14		61	25		20		61	18		O(28,25) C (16)	O(28,25) C(16)
			Mid 1/3 B	14		86			14		86				
5S-6	-50	(0.281)	Full B	36		23	41		41	2	32	25		C(26),W(15)	O(26),B(15)
			Mid 1/3 B	14		72	14		29	7	57	7			
5S-7	-30	(0.344)	Full B	16	2	46	32	4	45		25	30		F(21)	F(21)
			Mid 1/3 B		7	43	36	14	36		28	36			
5S-8	-50	(0.140)	Full B	23		9	55	14	41			59		W(26),B(17)	W(26),B(17)
			Mid 1/3 B				79	21				100			
5S-9	-50	(0.137)	Full B	23		25	52		34		25	41		W(19)	W(19)
			Mid 1/3 B	7		21	72				28	72			
5S-10	-50	(0.719)	Full B	14		82	4		5	4	90			O(22)	O(22)
			Mid 1/3 B	7		93			9		100				
			Full B												
			Mid 1/3 B												
			Full B												
			Mid 1/3 B												
			Full B												
			Mid 1/3 B												

Table 36: Microstructures of the Fatigue Crack and the Fracture Path, Measured Along the Thickness B, Near the Fatigue Precrack Front for MACS (ACC) Steel Welded with 5.4 kJ/mm Heat Input (As-Welded)

Sp. No.	Test Temp. °C	δ* .(δu) (δm) mm	Location in B	Microstructure, %										Fracture Initiation (mm)	
				Fatigue Crack (FC)					Fracture Path (FP)						
				CG HAZ C	FG HAZ F	Other O	Weld W	Fus.B. B	C	F	O	W	B	FC	FP
6A-1	-30	(0.855)	Full B	36		14	50		34	16	30	20		B(22)	C(22)
			Mid 1/3 B	57			43		50	21	29				
6A-2	-30	(1.136)	Full B	18		16	66		41	14	27	18		C(21)	F(21)
			Mid 1/3 B	21		7	72		21	14	21	43			
6A-3	-30	(1.051)	Full B	39	7	34	20		27	23	32	18		C(21)	C(21)
			Mid 1/3 B	57	14	29			28	36	36				
6A-4	-30	(1.158)	Full B	43	11	25	21		30	9	41	20		C(26)	F(26)
			Mid 1/3 B	43	14	43			36	7	57				
6A-5	-30	(0.614)	Full B	30	11	30	27		48	9	27	16		C(20)	C(20)
			Mid 1/3 B	43	7	14	36		64	7	7	22			
6A-6	-50	(0.132)	Full B	41	11	30	18		43	20	27	9		C(20)	C(20)
			Mid 1/3 B	71	14	14			36	28	36				
6A-7	-30	(1.038)	Full B	34	28	20	22		27	11	43	18		C(20),F(32)	C(20),0(32)
			Mid 1/3 B	43	14	29			14	22	64				
6A-8	-50	(0.342)	Full B	27	16	30	27		36	16	43	5		W(24)	C(24)
			Mid 1/3 B	29	14	28	29		64	29	7				
6A-9	-50	(0.117)	Full B	45	11	27	16		23	23	29	25		C(20)	C(20)
			Mid 1/3 B	64	14	22			36	28	36				
6A-10	-50	(0.058)	Full B	36	25	25	14		23	41	36			C(19)	C(19)
			Mid 1/3 B	36	28	36			50	14	36				
6A-11	-50	(0.286)	Full B	34	18	18	30		34	23	9	23		B(21)	C(21)
			Mid 1/3 B	22	28	7	43		43	21	36				
			Full B												
			Mid 1/3 B												
			Full B												
			Mid 1/3 B												

Table 37: Microstructures of the Fatigue Crack and the Fracture Path, Measured Along the Thickness B, Near the Fatigue Precrack Front for MACS (DQT) Steel Welded with 5.4 kJ/mm Heat Input (Stress-Relieved)

Sp. No.	Test Temp. °C	δ* (δu) (δm) mm	Location in B	Microstructure, %										Fracture Initiation (mm)	
				Fatigue Crack (FC)					Fracture Path (FP)						
				CG HAZ C	FG HAZ F	Other O	Weld W	Fus.B. B	C	F	O	W	B	FC	FP
6S-1	-30	(0.585)	Full B	34	16	36	14		34	27	30	9		C(22)	C(22)
			Mid 1/3 B	28	22	50			57	29	14				
6S-2	-30	(1.434)	Full B	41	7	45	7		27	27	30	16		C(22)	F(22)
			Mid 1/3 B	36	7	57			14	43	43				
6S-3	-30	(0.490)	Full B	50	2	32	16		27	11	57	5		B(28)	C(28)
			Mid 1/3 B	43		29	28		50	14	36				
6S-4	-30	(0.952)	Full B	39	11	27	22		18	52	18	11		F(20)	F(20)
			Mid 1/3 B	86	14				7	57	36				
6S-5	-30	(0.288)	Full B	23	5		73		32	25	27	16		B(22)	O(22)
			Mid 1/3 B	22	14		64		22	36	21	21			
6S-6	-30	(1.075)	Full B	25	7	36	32		30	11	45	14		C(32),B(16)	C(32,16)
			Mid 1/3 B	43		7	50		36		64				
6S-7	-50	(0.109)	Full B	34	11	18	36		43	14	11	32		W(25),C(8)	W(25),C(8)
			Mid 1/3 B	14	7		79		64	14	22				
6S-8	-50	(0.779)	Full B	9			91		27	2		71		W(23)	W(23)
			Mid 1/3 B				100					100			
6S-9	-50	(0.671)	Full B	32	4	9	55		30	14	18	39		B(26),C(15)	C(26),F(15)
			Mid 1/3 B	43	7	14	36		14	29	43	14			
6S-10	-50	(0.759)	Full B	4		34	61		27	14	25	34		W(26,17)	C(26,17)
			Mid 1/3 B				100		50	7		43			
6S-11	-50	(0.264)	Full B	14		11	75		45	23	9	23		W(34,16)	F(34),C(16)
			Mid 1/3 B	7			93		57	29	14				
			Full B												
			Mid 1/3 B												
			Full B												
			Mid 1/3 B												

TABLE 38

IMPACT ENERGY VALUES AND THE NDT TEMPERATURES

SP. NO.	HI kJ/mm	NDT TEMP. °C	TRANS. TEMP. °C					
			CG HAZ				GLEEBLE	
			27J	40J	27J	40J	27J	40J
			Average		Minimum		Average	
1AR			-52	-46	-33	-23	-4	+3
1AS		-60	-62	-59	-62	-59		
1SR	3.5		-38	-37	-29	-23	+4	+17
1SS		-65	-43	-42	-35	-31		
2AR			-62	-48	-25	-20	+4	+7
2AS		-45	-37	-34	-25	-20		
2SR	5.4		-71	-66	-63	-56	+6	+10
2SS		-60	-48	-42	-36	-30		
3AR			-52	-46	-37	-31	-18	-11
3AS	5.4	-50	-89	-86	-89	-86		
3SR			-86	-84	-86	-84	+7	+8
3SS		-65	-86	-84	-84	-82		
4AR			-84	-78	-82	-77	-29	-24
4AS	3.5	-60	-84	-70	-75	-72		
4SR			-41	-40	+1.5	+10	+6	+11
4SS		-75	-44	-40	-35	-34		
5AR			-102	-90	-93	-88	-43	-36
5AS	1.6	-60	-80	-70	-68	-62		
5SR			-64	-60	-60	-60	+4	+5
5SS		-75	-56	-52	-52	-40		
6AR			-64	-63	-50	-50	-72	-70
6AS	5.4	-45	-80	-80	-80	-80		
6SR			-90	-85	-77	-74	-55	-50
6SS		-55	-102	-101	-102	-101		

TABLE 39

MICROSTRUCTURE PRESENT AT THE ROOT OF THE NOTCH IN CVN SPECIMENS

SP. NO	Microstructure, %			
	CG HAZ	FG HAZ	Refined	WM
1AS (4)	50		50	
1AR (7)	80	5	15	
1SS (-80)	56		44	
1SR (11)	75	25		
2AS (17)	65	5	30	
2AR (-80)	75	25		
2SS (16)	45	25	30	
2SR (-80)	65		35	
3AS (18)	75	25		
3AR (18)	90	10		
3SS (11)	75	25		
3SR (11)	80	20		
4AS (-90)	55			45
(-100)	55			45
4AR (18)	75			25
4SS (17)	75	15		10
4SR (19)	95	5		
5AS (-90)	60	40		
5AR (-90)	100			
5SS (9)	35	35	25	5
(-110)	50			50
5SR (-80)	100			
(-80)	30			70
6AS (-90)	60	10	30	
6AR (8)	45	25	30	
6SS(-110)	60	15	25	
6SR (2)	60	25	15	

TABLE 40

THE CTOD VALUES AND THE AMOUNT OF CG HAZ

SP. NO	TEST TEMP. °C	(Fatigue crack) CG HAZ %	CTOD VALUES, mm	
			Average	Minimum
1A	-30	20 - 66	0.129 (4)	0.043*
	-60	20 - 60	0.036 (2)	0.021
1S	-30	20 - 50	0.334 (4)	0.251
	-60	10 - 20	0.138 (4)	0.030
2A	-30	20 - 38	0.238 (3)	0.158
	-50	20 - 50	0.052 (4)	0.027
2S	-30	20 - 70	0.380 (4)	0.240
	-50	20 - 65	0.105 (4)	0.032
3A	-30	20 - 55	0.213 (6)	0.070
	-50	20 - 50	0.151 (3)	0.046
3S	-30	20 - 46	0.354 (6)	0.034
	-50	20 - 68	0.052 (4)	0.033
4A	-30	20 - 52	0.101 (4)	0.043
	-50	20 - 53	0.141 (4)	0.026
4S	-30	20 - 64	0.147 (4)	0.044
	-50	20 - 50	0.090 (3)	0.023
5A	-30	20 - 50	0.249 (6)	0.087
	-50	20 - 43	0.221 (5)	0.170
5S	-30	20 - 27	0.486 (2)	0.384
	-50	20 - 36	0.186 (3)	0.137
6A	-30	20 - 43	0.943 (5)	0.614
	-50	20 - 45	0.187 (5)	0.058
6S	-30	20 - 50	0.804 (6)	0.288
	-50	20 - 34	0.390 (2)	0.109

TABLE 41

THE ALLOWABLE DEFECT SIZES FOR THE CG HAZ (≥20%) ESTIMATED FROM THE CTOD VALUES GIVEN IN TABLE 40

SP. NO.	TEST TEMPERATURE °C	Allowable Defect Size, mm	
		Average	Minimum
1A	-30	8.2	2.7
	-60	2.3	1.3
1S	-30	81.2	61.0
	-60	33.5	7.3
2A	-30	15.1	10.0
	-50	3.3	1.7
2S	-30	92.3	58.3
	-50	25.5	7.8
3A	-30	9.0	2.9
	-50	6.3	1.9
3S	-30	57.4	5.5
	-50	8.4	5.3
4A	-30	4.2	1.8
	-50	5.9	1.1
4S	-30	23.8	7.1
	-50	14.6	3.7
5A	-30	10.5	3.6
	-50	9.3	7.1
5S	-30	78.7	62.2
	-50	30.1	22.2
6A	-30	53.4	34.8
	-50	10.6	3.3
6S	-30	172.1	61.6
	-50	83.5	23.3

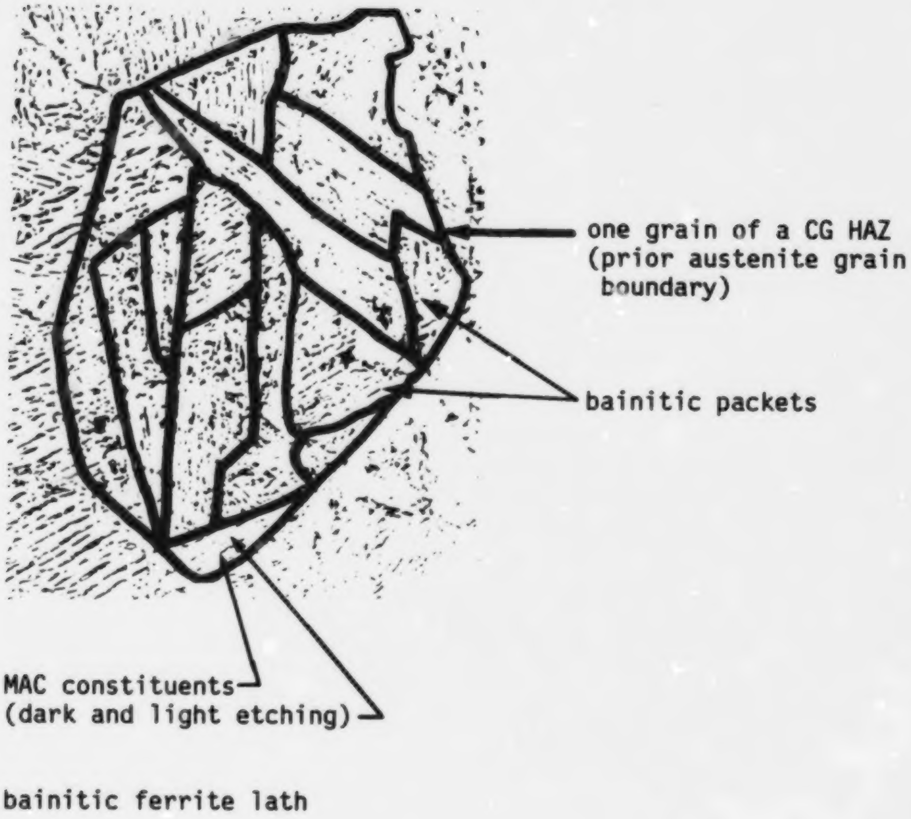
one grain of a CG HAZ (prior austenite grain boundary)
bainitic packets
MAC constituents (dark and light etching)
bainitic ferrite lath

Figure 1: Grain of a CG HAZ and the Bainitic Structure

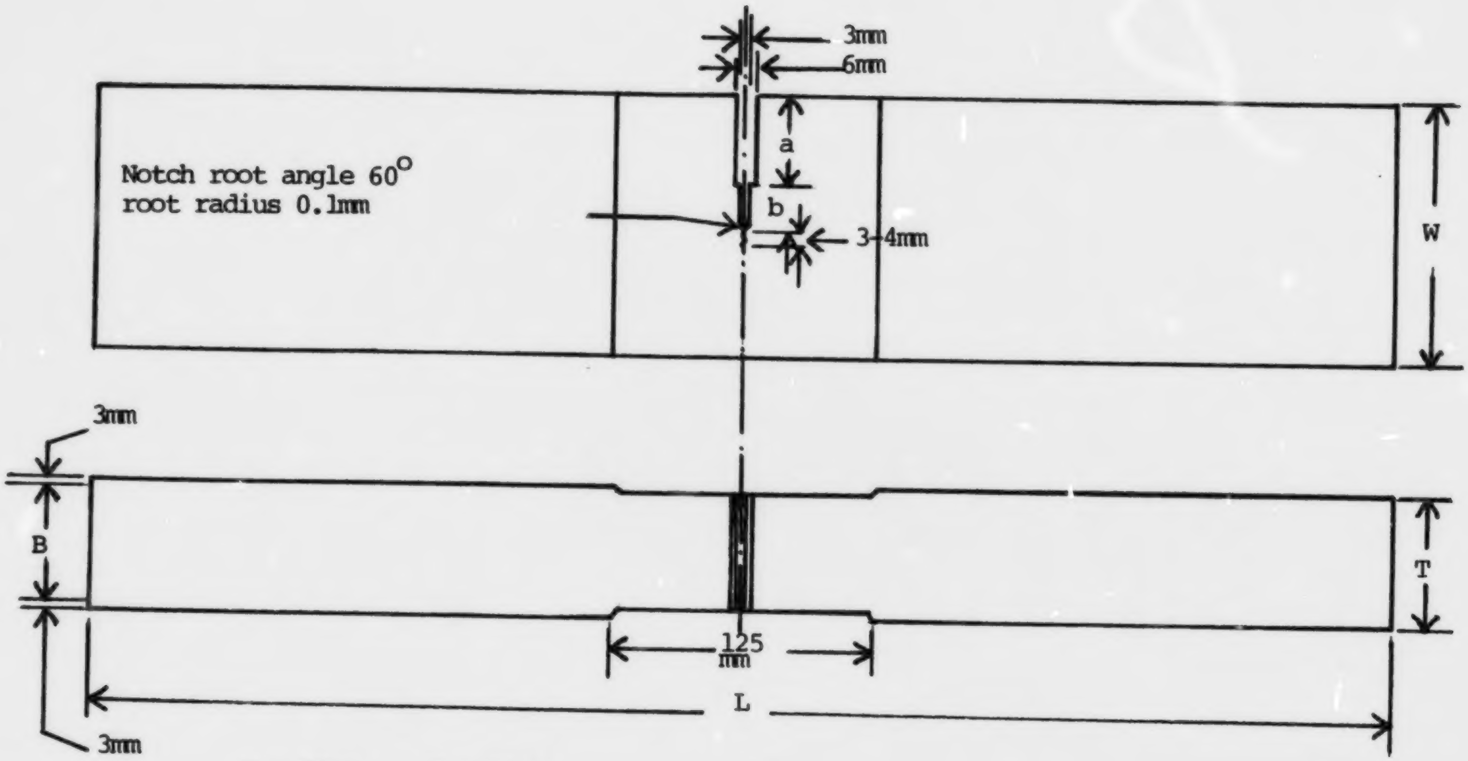
3mm
6mm
a
b
3-4mm
Notch root angle 60°
root radius 0.1mm
W
3mm
B
T
125 mm
L
3mm

	T = 63mm	T = 50mm
W =	114mm	89mm
B =	57mm	44.5mm
L =	570mm	445mm
a =	38mm	25mm
b =	16mm	16mm

Figure 2 : Dimensions of the CTOD specimens

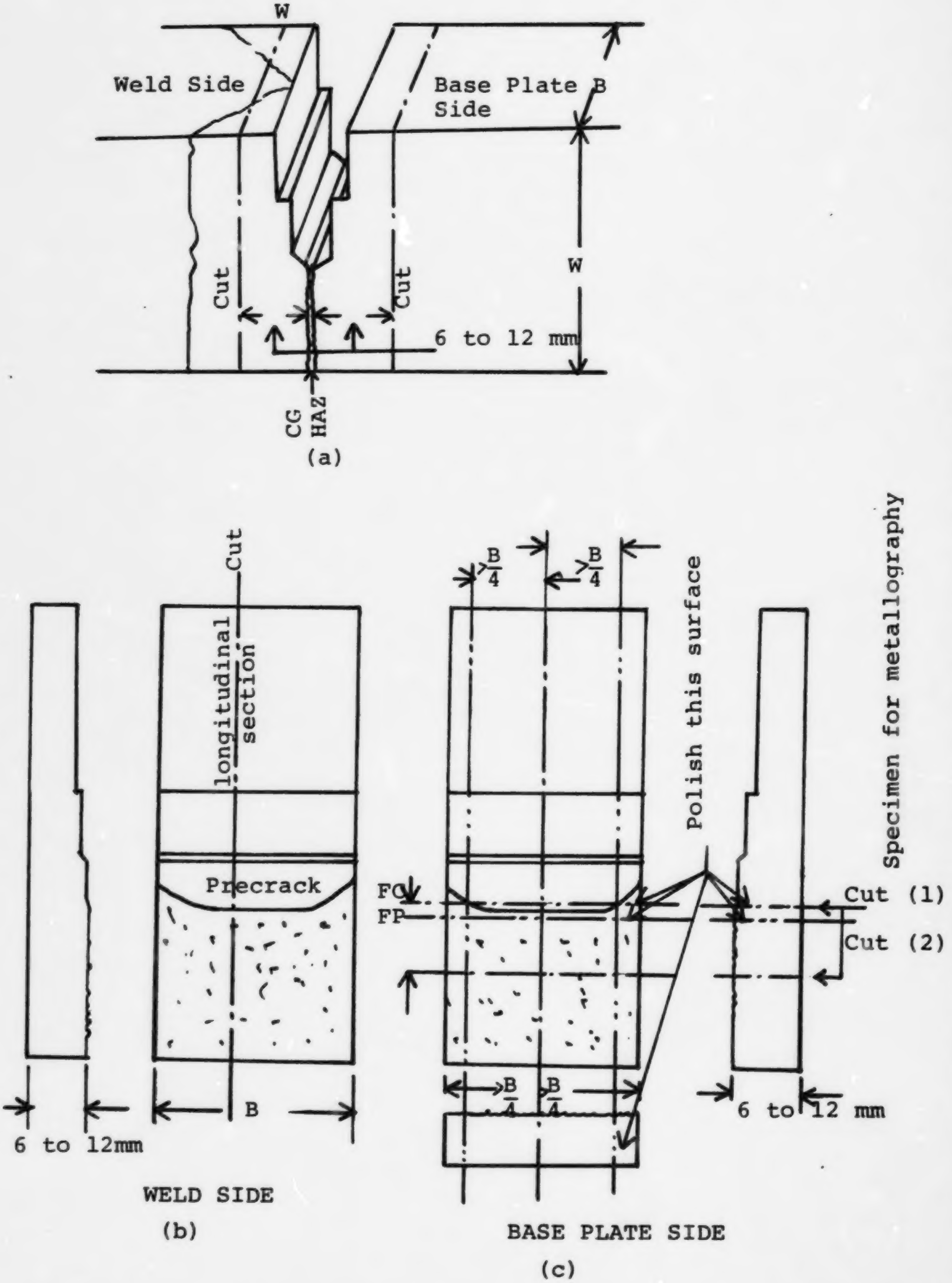

W
Weld Side
Base Plate Side
B
W
Cut
Cut
6 to 12 mm
CG
HAZ
(a)
Cut
longitudinal section
Precrack
6 to 12mm
B
WELD SIDE
(b)
>B/4
>B/4
Polish this surface
Specimen for metallography
FC
FP
Cut (1)
Cut (2)
B/4
B/4
6 to 12 mm
BASE PLATE SIDE
(c)

FIGURE 3: Sectioning of the (a) CTOD specimen for metallography (b) longitudinal section through fracture initiation and (c) transverse section in the fatigue crack (FC) and the fracture path (FP) near the fatigue front.

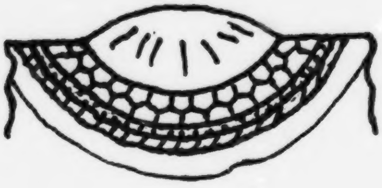

a) SINGLE BEAD

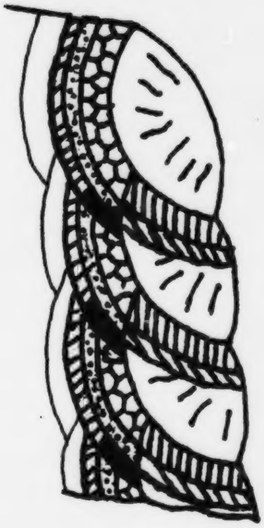

b) MULTIPASS BEAD

HEAT AFFECTED ZONE

▦ - coarse grained supercritical

⁙ - fine grained supercritical

▨ - intercritical

☐ - subcritical

■ - intercritically reheated supercritical

WELD METAL

⌇ - coarse columnar

▥ - recrystallized coarse

▧ - recrystallized fine

FIGURE 4: Schematic Representation of Weld Metal/Heat Affected Zone Microstructures

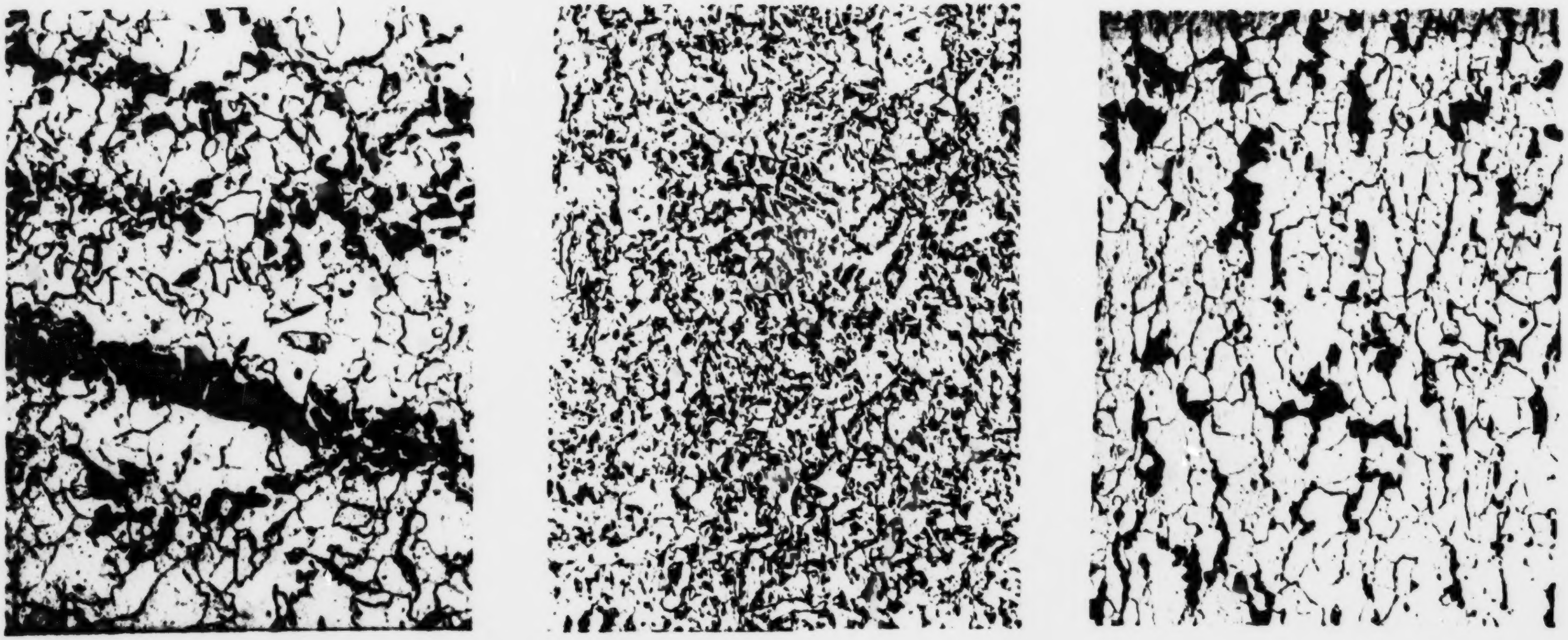
(a) (b) (c)

FIGURE 5: Microstructures of base plates a) Lloyds LT 60, Neg. 8010, Mag. 500 x; b) A710 Gr. A, Cl. 3, Neg. 8023, Mag. 500 x; c) MACS (ACC), Neg. 8211, Mag. 500 x.

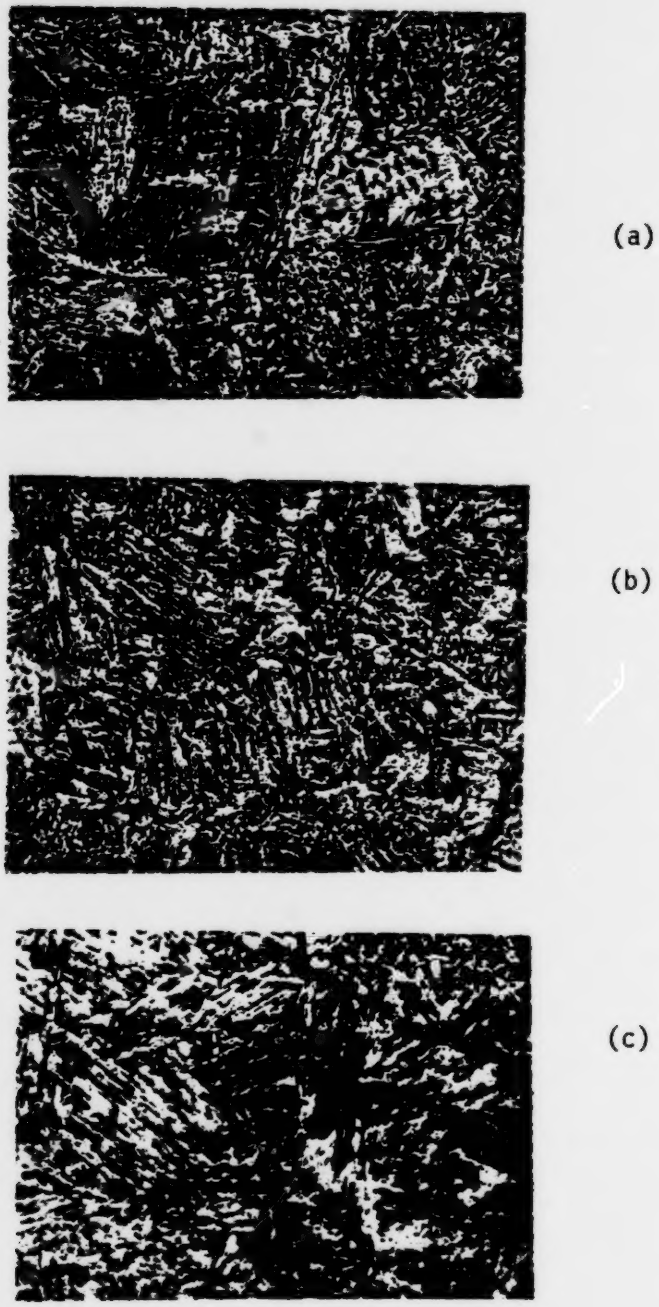

FIGURE 6: HAZ microstructure of Lloyds LT 60 welded at 3.5 kJ/mm.
a) coarse grained supercritical, Neg. 7958, Mag. 500 x.
b) fine grained supercritical Neg. 7959, Mag. 500 x.
c) intercritically reheated, supercritical, Neg. 8007, Mag. 500 x.

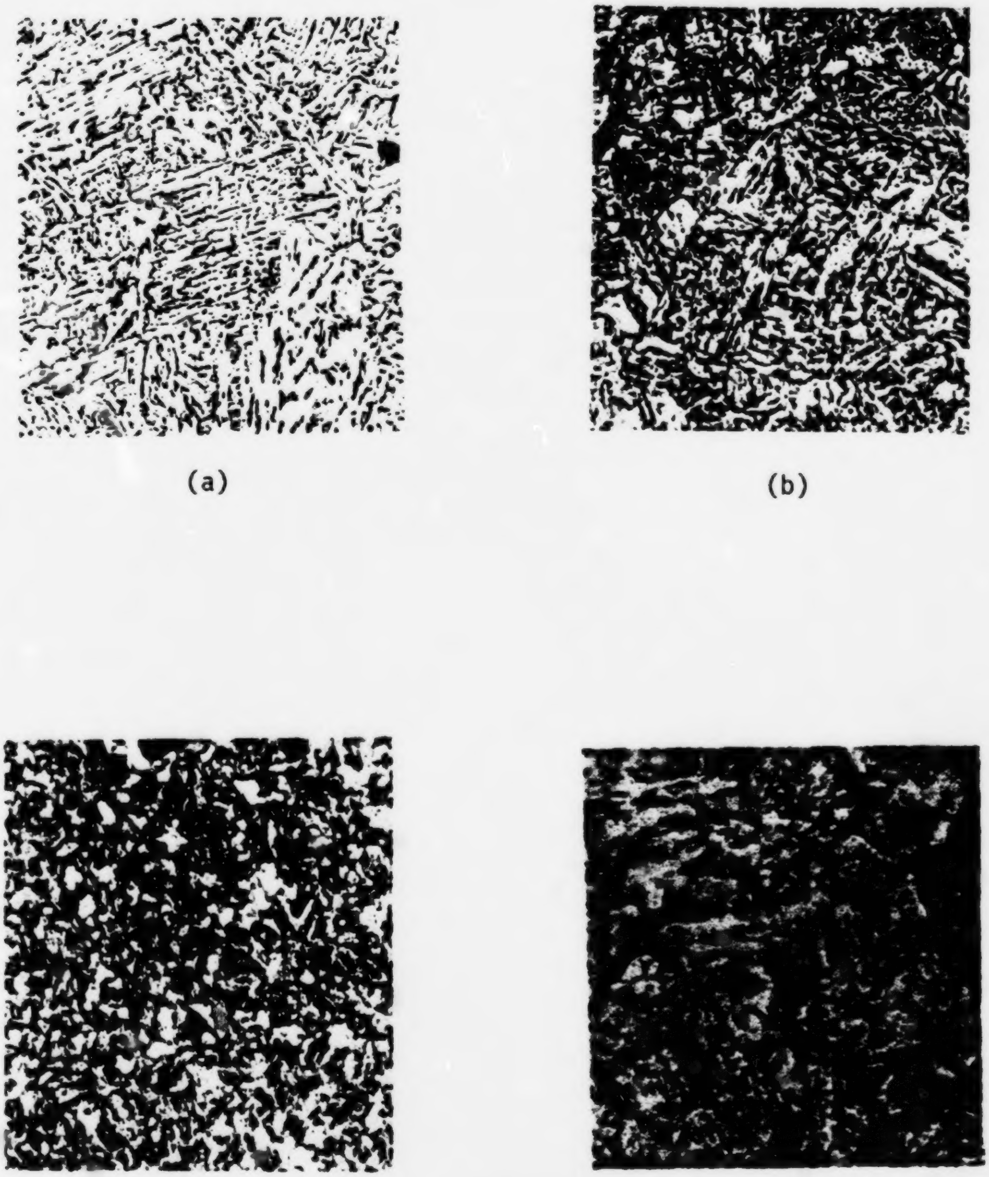

(a) (b)

(c) (d)

FIGURE 7: HAZ microstructure of Lloyds LT 60 welded at 5.4 kJ/mm.
a) coarse grained supercritical, Neg. 8436, Mag. 500 x.
b) fined grained supercritical, Neg. 7955, Mag. 500 x.
c) intercritical, Neg. 8019, Mag. 500 x.
d) intercritically reheated, supercritical, Neg. 8011, Mag. 500 x.

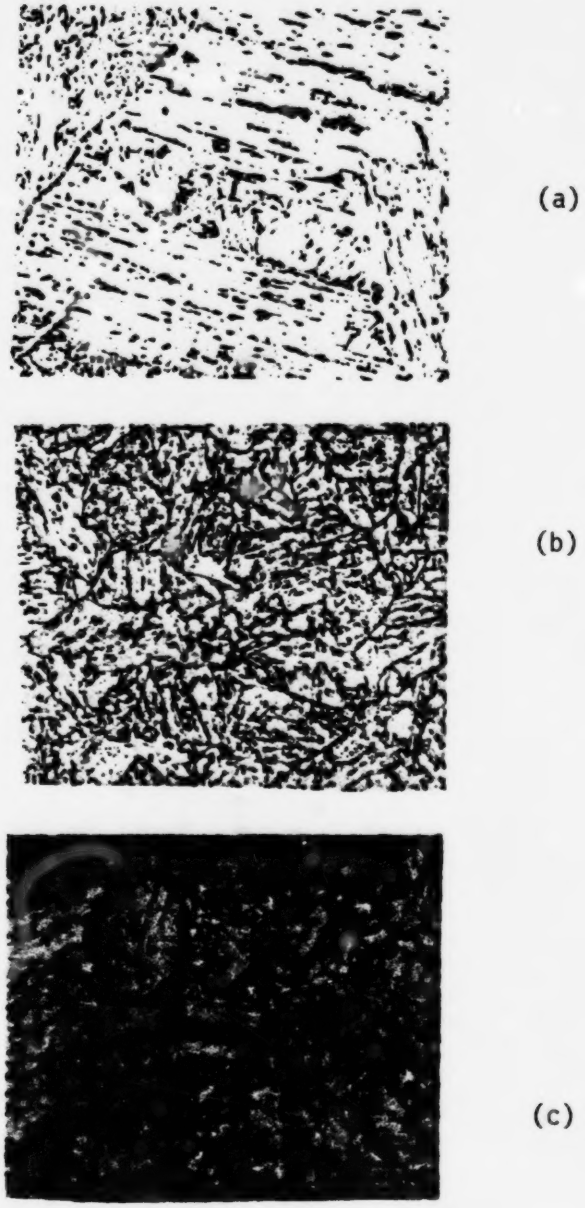

FIGURE 8 : HAZ microstructure of A710, Gr. A, Cl. 3 welded at 1.6 kJ/mm.

a) coarse grained supercritical, Neg. 8165, Mag. 500 x.
b) fine grained supercritical, Neg. 8166, Mag. 500 x.
c) intercritically reheated, supercritical, Neg. 8169, Mag. 500 x.

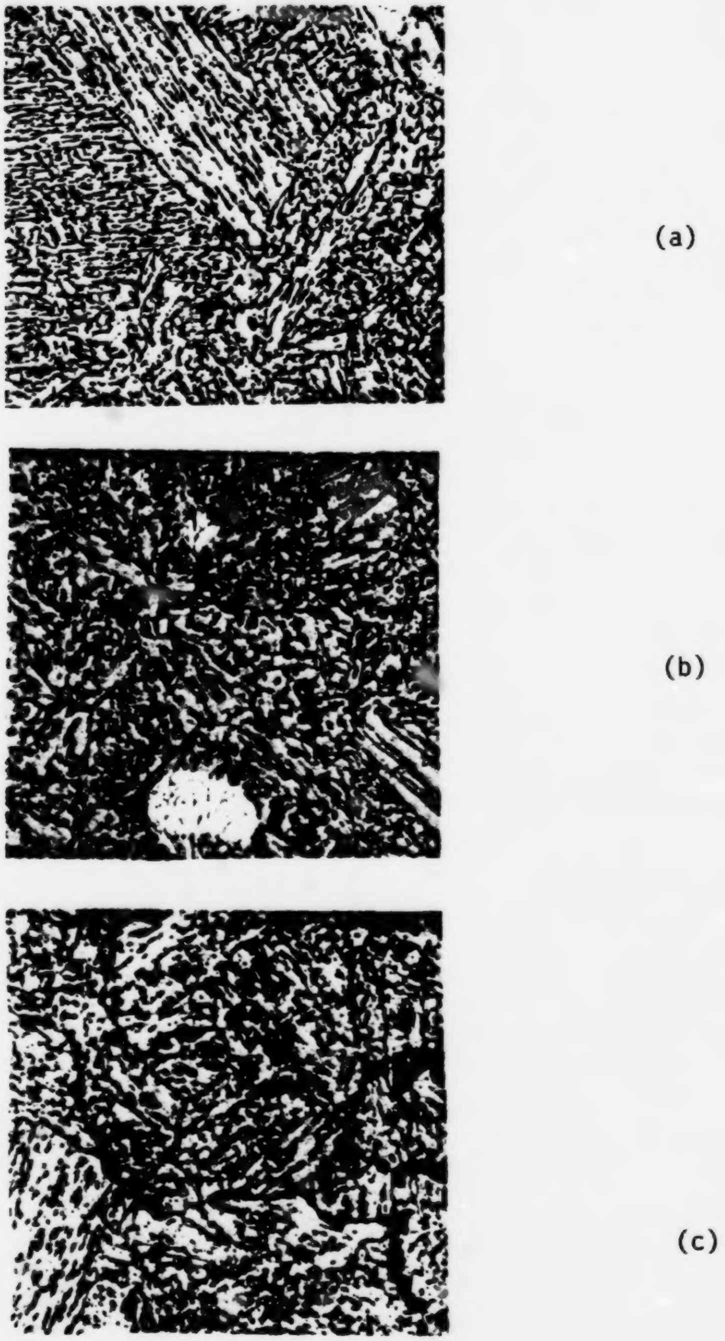

FIGURE 9: HAZ microstructure of A710, Gr. A, Cl. 3 welded at 3.5 kJ/mm.

a) coarse grained supercritical, Neg. 8170, Mag. 500 x.
b) fine grained supercritical, Neg. 8171, Mag. 500 x.
c) intercritically reheated, supercritical, Neg. 8174, Mag. 500 x.

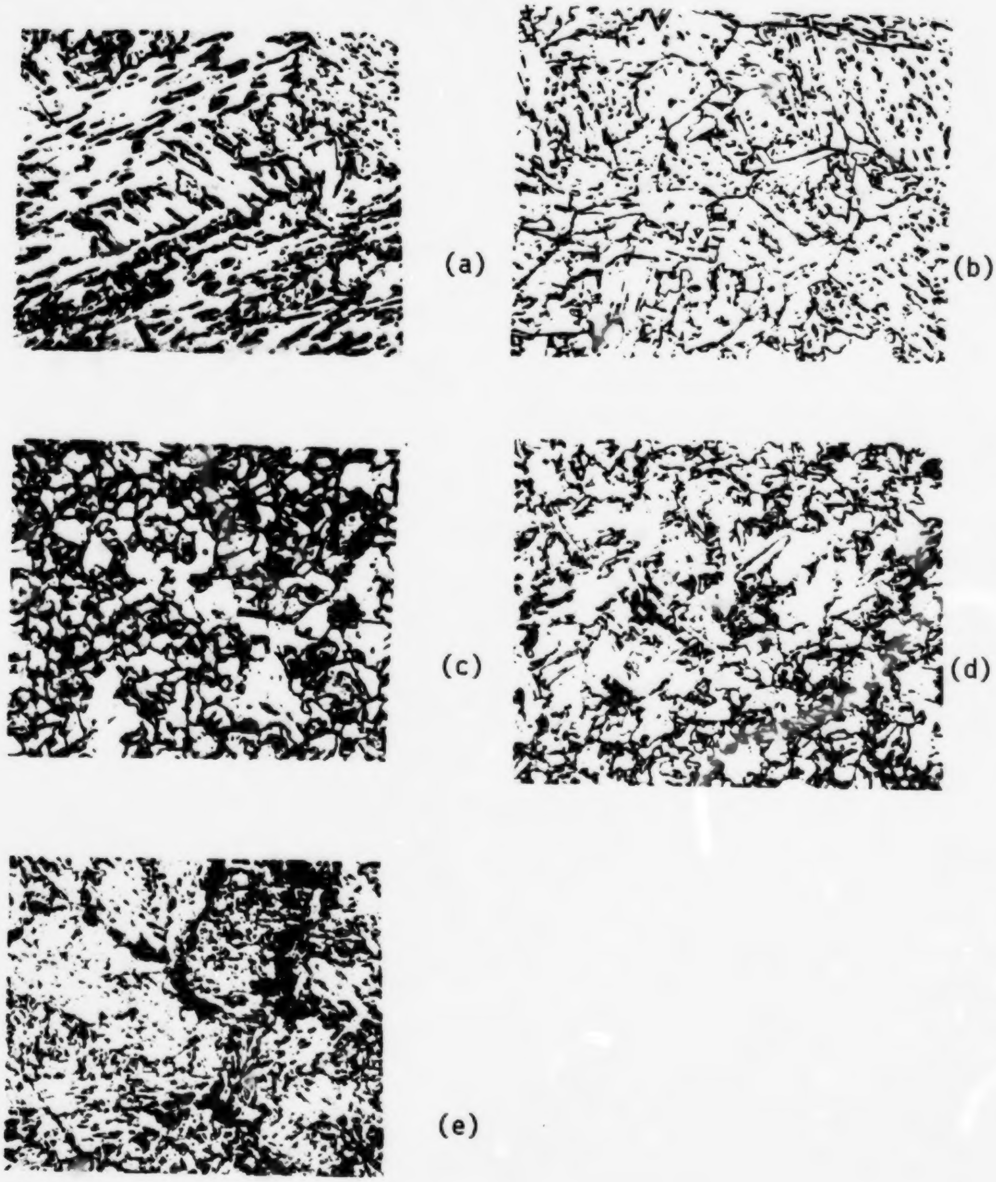

FIGURE 10 : HAZ microstructure of A710 Gr. A, Cl. 3 welded at 5.4 kJ/mm.

a) coarse grained supercritical, Neg. 8691, Mag. 500 x.
b) fine grained supercritical, Neg. 8692, Mag. 500 x.
c) intercritical, Neg. 8693, Mag. 500 x.
d) subcritical, Neg. 8694, Mag. 500 x.
e) intercritically reheated, supercritical, Neg. 8022; Mag. 500 x.

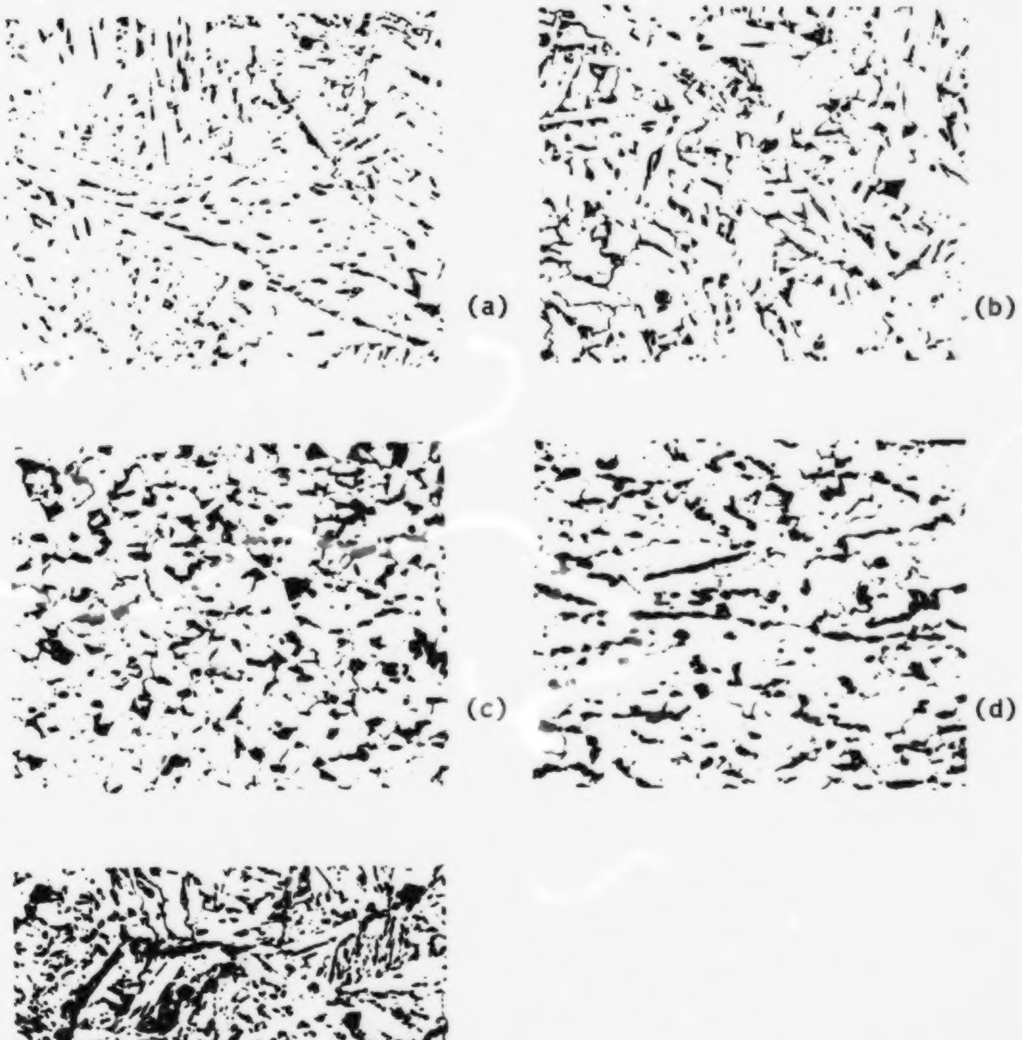

FIGURE 11: HAZ microstructure of EH 36 (ACC) welded at 5.4 kJ/mm and MACS (DQT) welded at 5.4 kJ/mm and stress-relieved.

a) MACS (ACC) coarse grained supercritical, Neg. 8381, Mag. 500 x.
b) MACS (ACC) fine grained supercritical, Neg. 8382, Mag. 500 x.
c) MACS (ACC) intercritical, Neg. 8213, Mag.500 x.
d) MACS (ACC) subcritical, Neg. 8214, Mag. 500 x.
e) MACS (ACC) intercritical reheated, supercritical, Neg. 8215, Mag. 500 x.

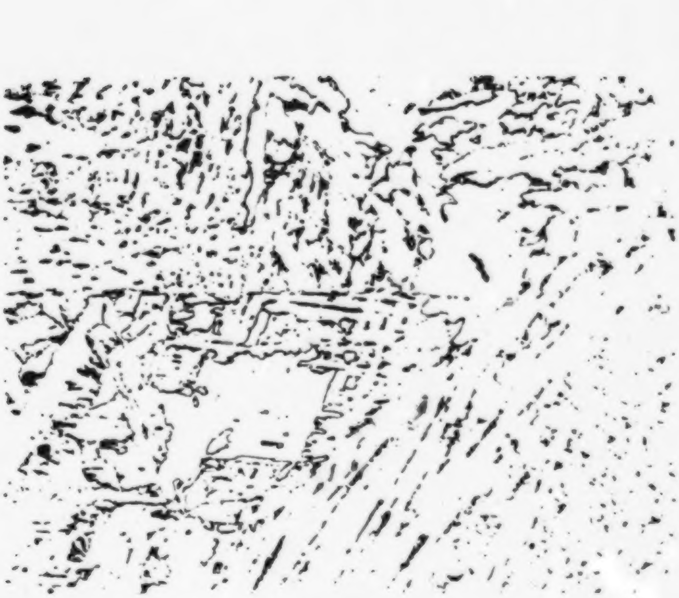

(f)

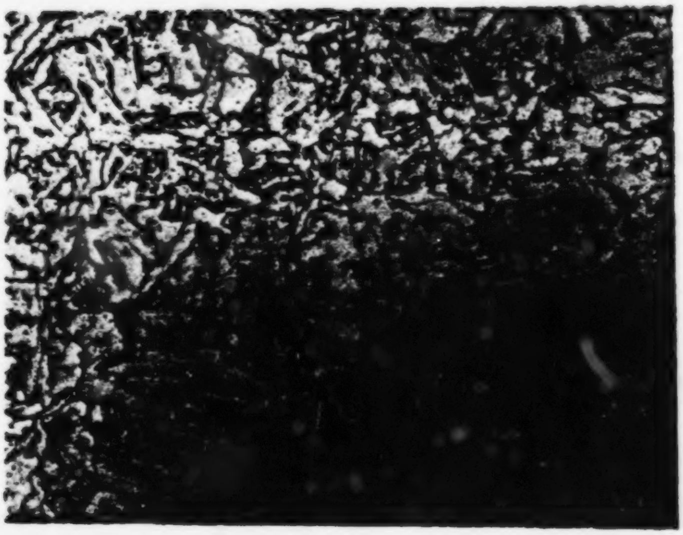

(g)

FIGURE 11: Continued.
f) MACS (DQT) coarse grained supercritical, Neg. 8383, Mag. 500 x.
g) MACS (DQT) fine grained supercritical, Neg. 8384, Mag. 500 x.

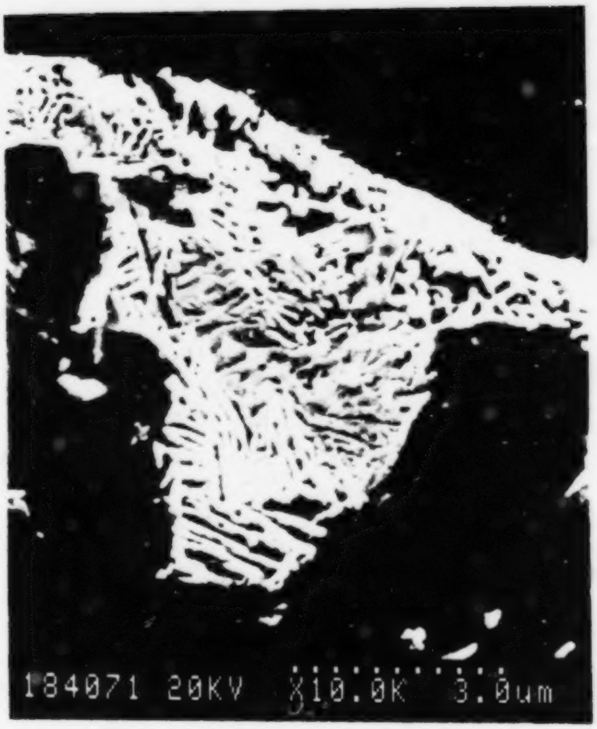
184071 20KV X10.0K 3.0um

Figure 12: Scanning electron micrograph of the decorated region. Neg. No. SEM 36.

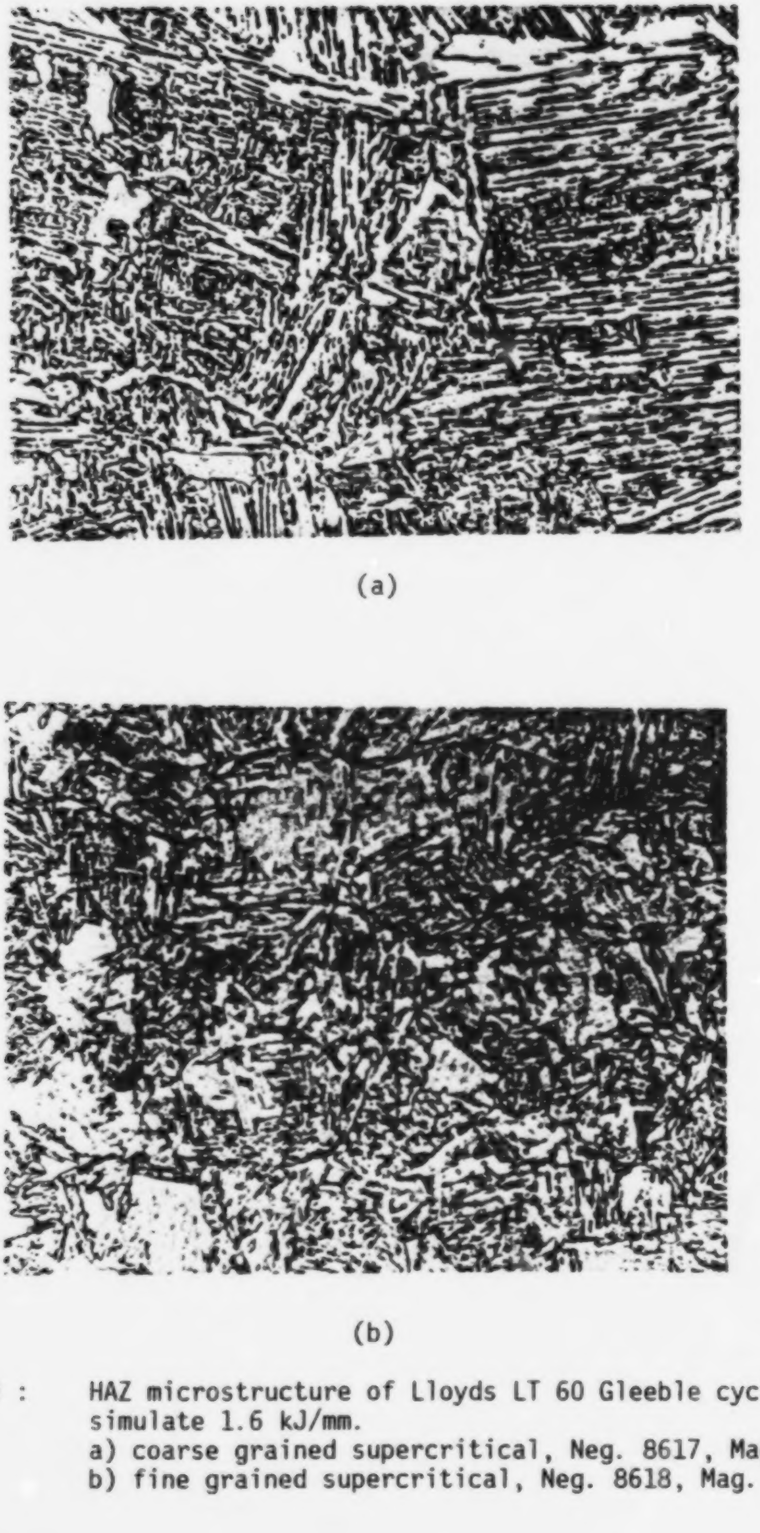

FIGURE 13 : HAZ microstructure of Lloyds LT 60 Gleeble cycled to simulate 1.6 kJ/mm.
a) coarse grained supercritical, Neg. 8617, Mag. 500 x.
b) fine grained supercritical, Neg. 8618, Mag. 500 x.

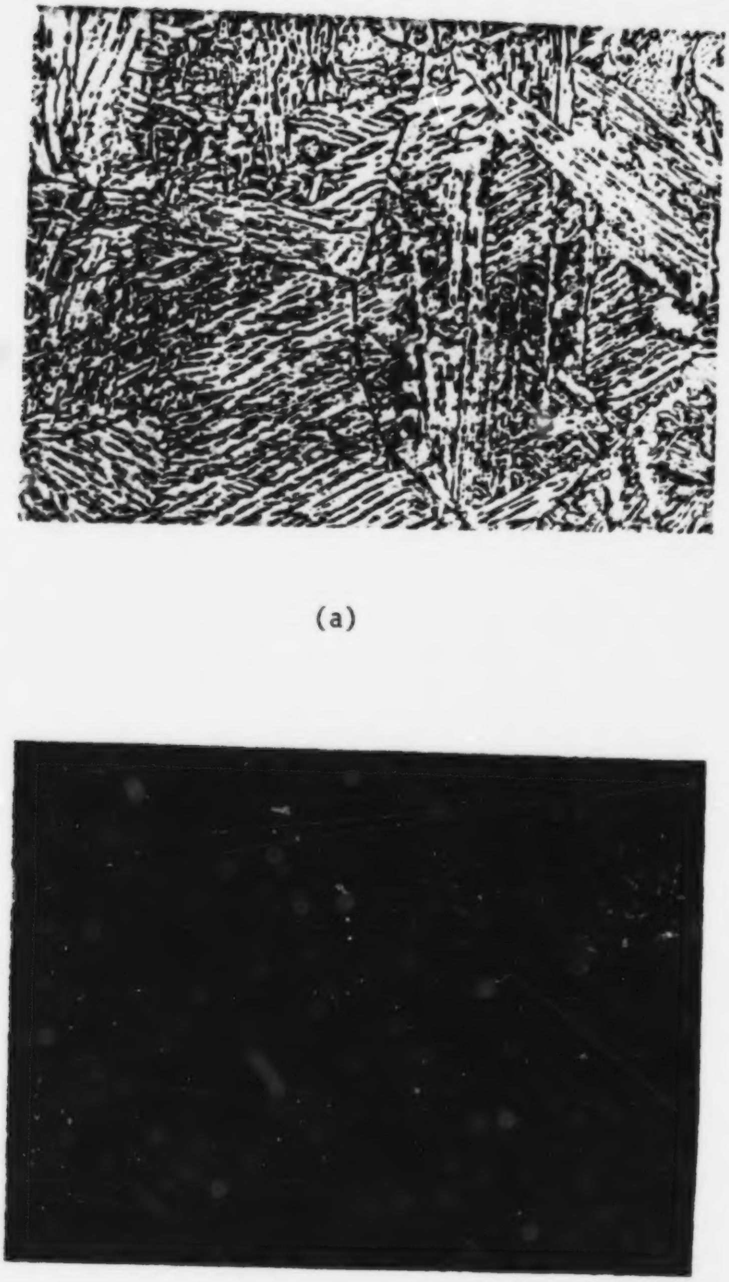

(a)

(b)

FIGURE 14 : HAZ microstructure of Lloyds LT 60, Gleeble cycled to simulate 3.5 kJ/mm.
a) coarse grained supercritical, Neg. 7942, Mag. 500 x.
b) fine grained supercritical, Neg. 8628, Mag. 500 x.

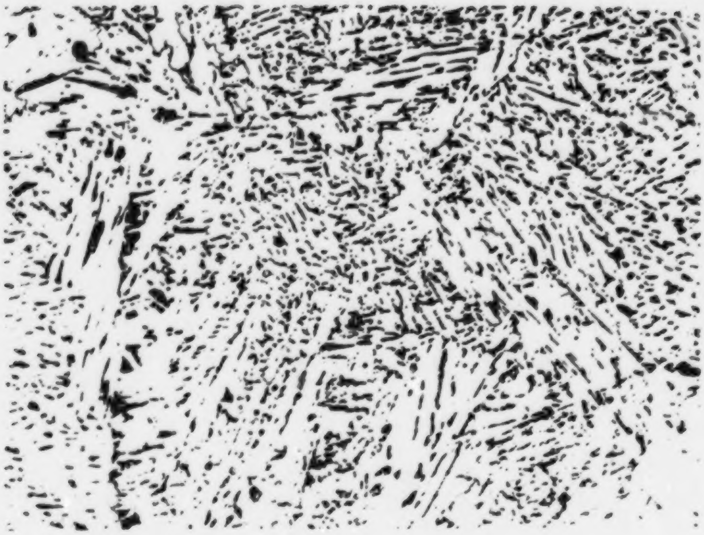

(a)

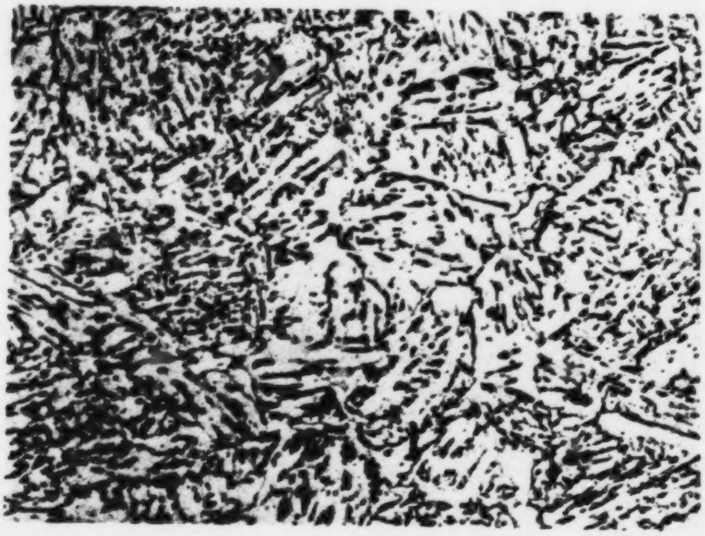

(b)

FIGURE 15: HAZ microstructure of Lloyds LT 60, Gleeble cycled to simulate 5.4 kJ/mm.
a) coarse grained supercritical, Neg. 8625, Mag. 500 x.
b) fine grained supercritical, Neg. 8626, Mag. 500 x.

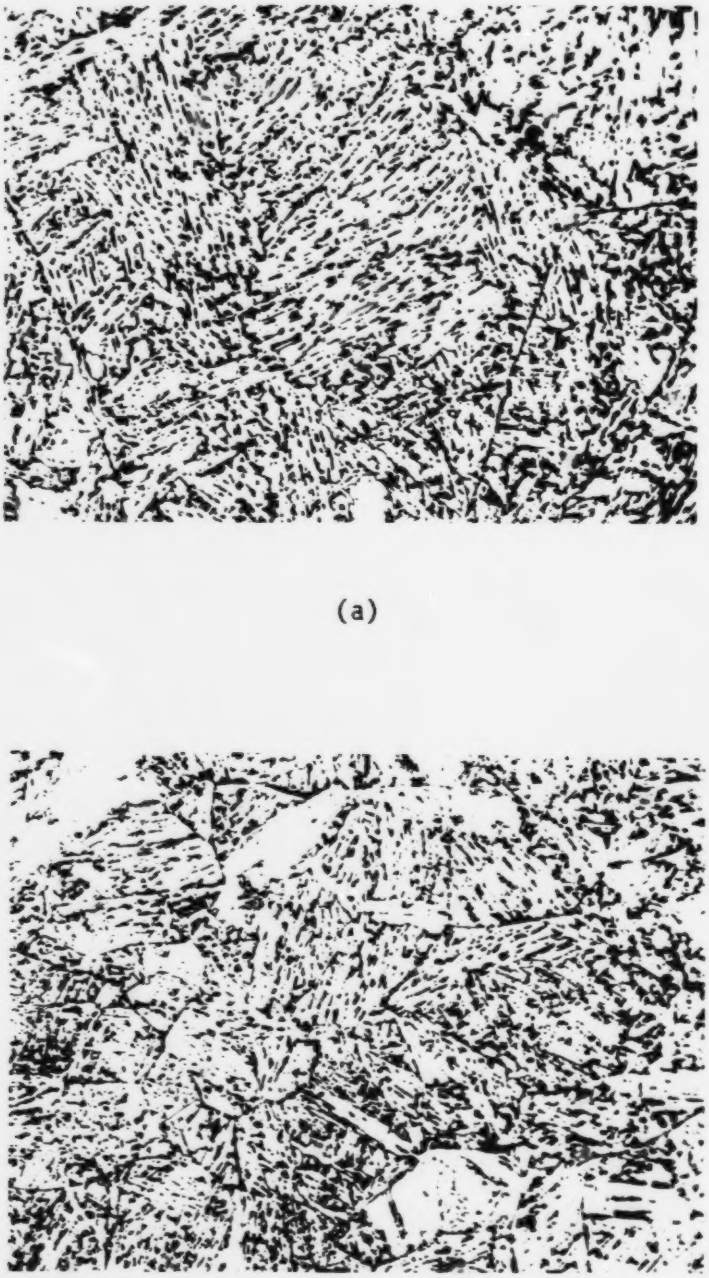

(a)

(b)

FIGURE 16: HAZ microstructure of A710, Gr. A, Cl. 3, Gleeble cycled to simulate 1.6 kJ/mm.
a) coarse grained supercritical, Neg. 8686, Mag. 500 x.
b) fine grained supercritical, Neg. 8685, Mag. 500 x.

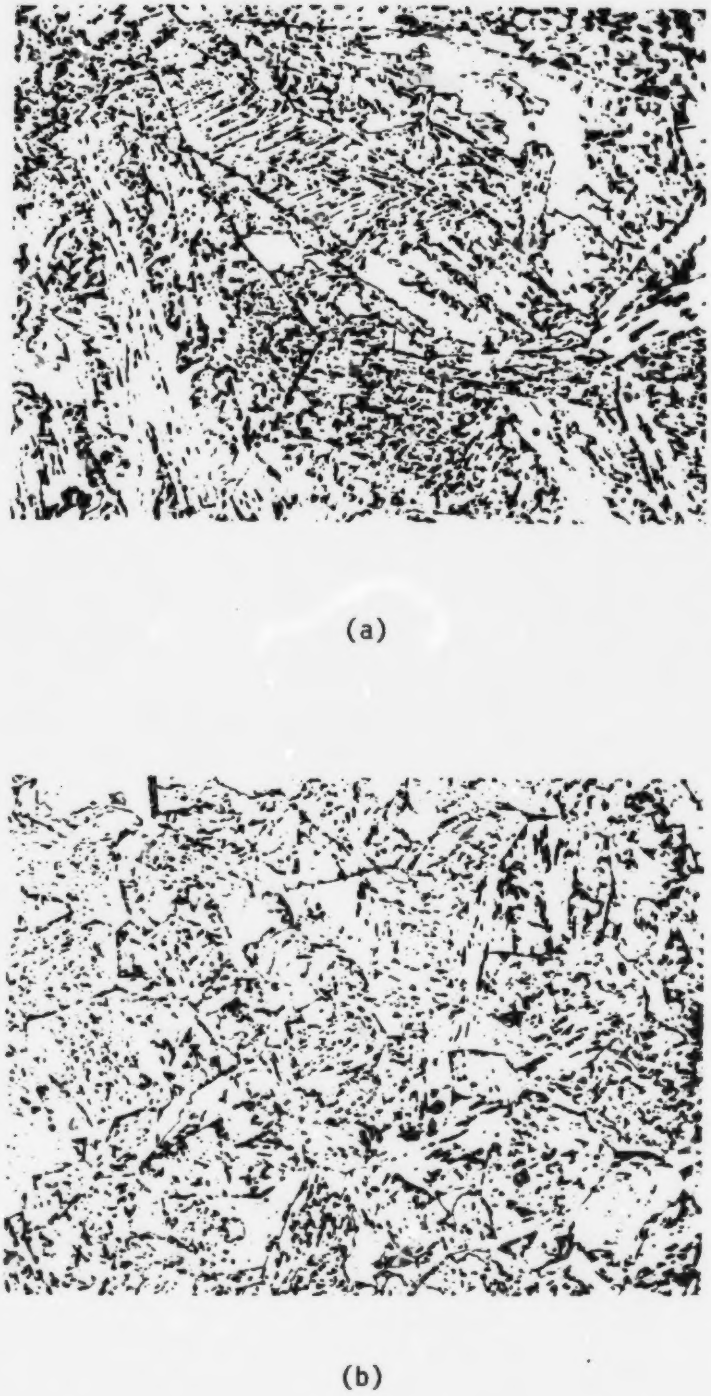

FIGURE 17 : HAZ microstructure of A710, Gr. A, Cl. 3, Gleeble cycled to simulate 3.5 kJ/mm.
a) coarse grained supercritical, Neg. 8687, Mag. 500 x.
b) fine grained supercritical, Neg. 8688, Mag. 500 x.

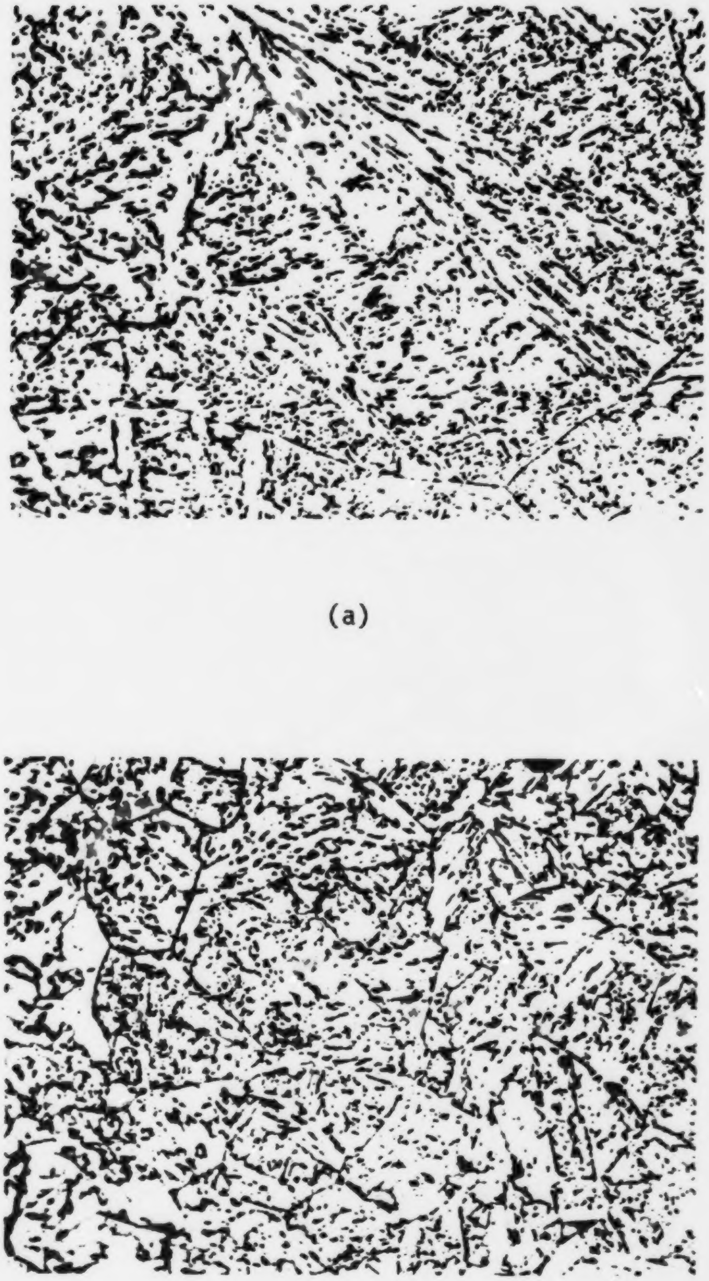

(a)

(b)

FIGURE 18: HAZ microstructure of A710, Gr. A, Cl. 3, Gleeble cycled to simulate 5.4 kJ/mm.
a) coarse grained supercritical, Neg. 8689, Mag. 500 x.
b) fine grained supercritical, Neg. 8690, Mag. 500 x.

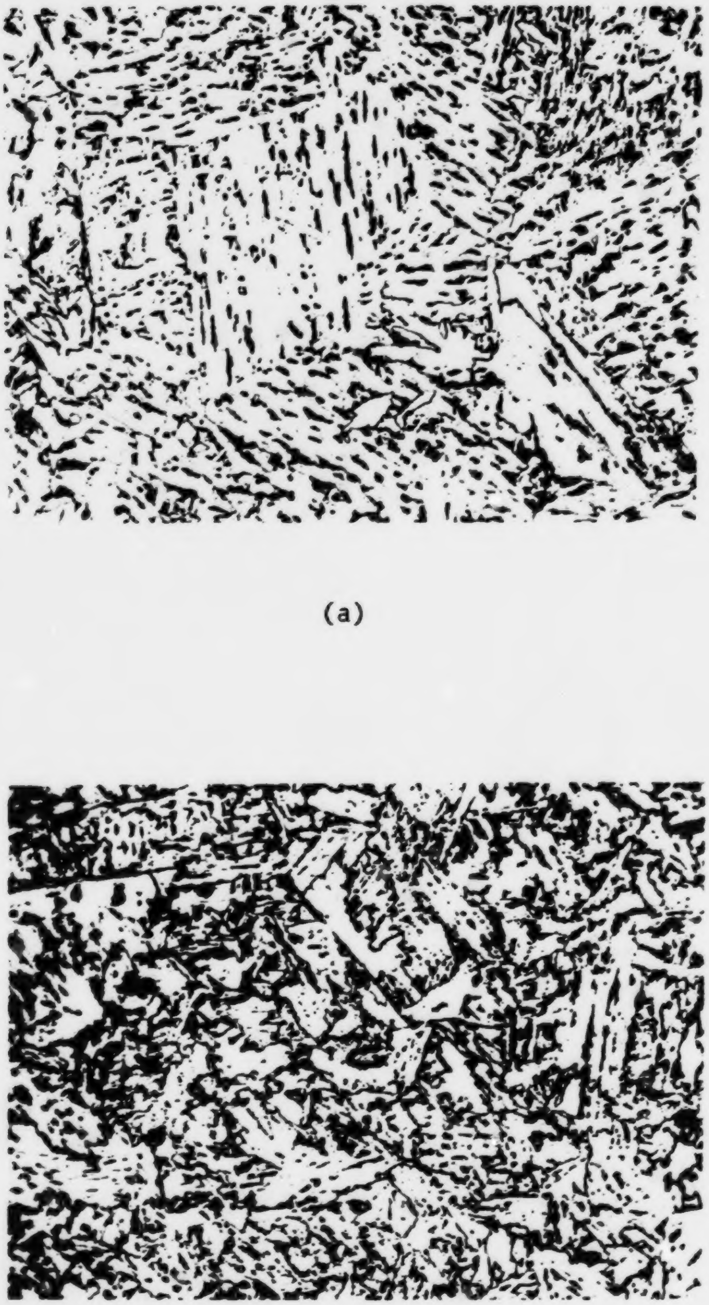

(a)

(b)

FIGURE 19: HAZ microstructure of MACS (ACC), Gleeble cycled to simulate 1.6 kJ/mm.
a) coarse grained supercritical, Neg. 8497, Mag. 500 x.
b) fine grained supercritical, Neg. 8695, Mag. 500 x.

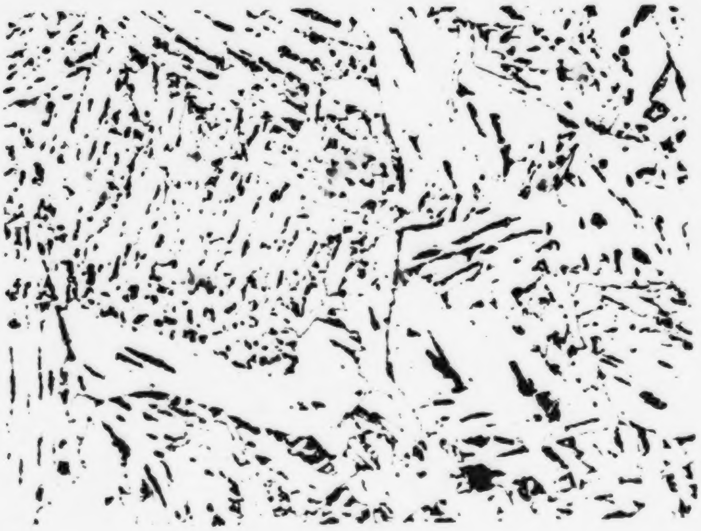

(a)

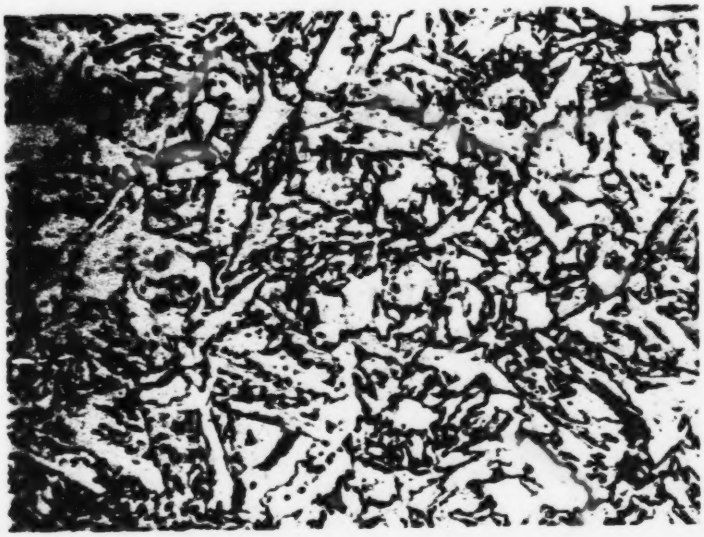

(b)

FIGURE 20 : HAZ microstructure of MACS (ACC) Gleeble cycled to simulate 3.5 kJ/mm.
a) coarse grained supercritical, Neg. 8499; Mag. 500 x.
b) fine grained supercritical, Neg. 8696, Mag. 500 x.

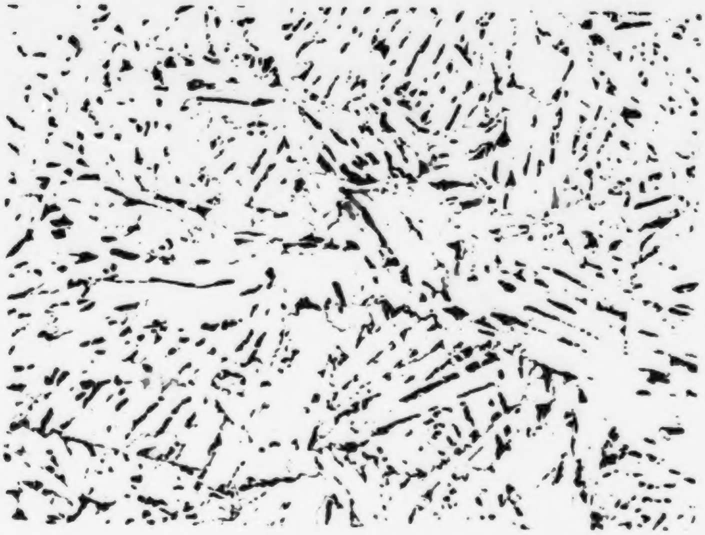

(a)

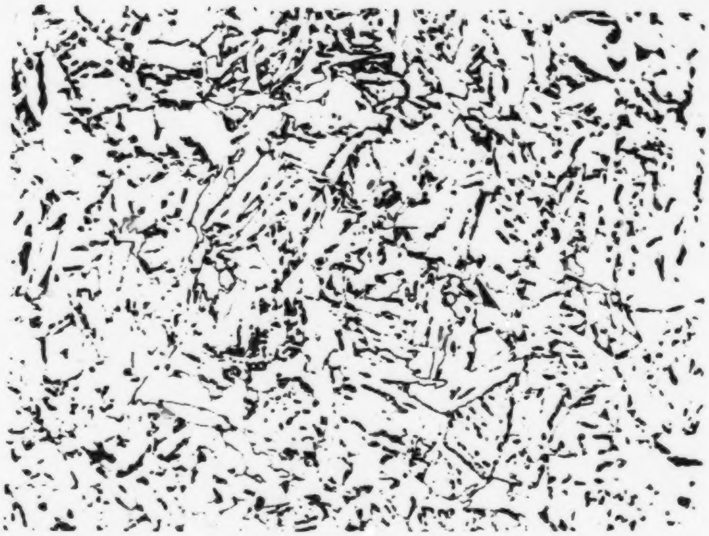

(b)

FIGURE 21 : HAZ microstructure of MACS (ACC), Gleeble cycled to simulate 5.4 kJ/mm.
a) coarse grained supercritical, Neg. 8629, Mag. 500 x.
b) fine grained supercritical, Neg. 8630, Mag. 500 x.

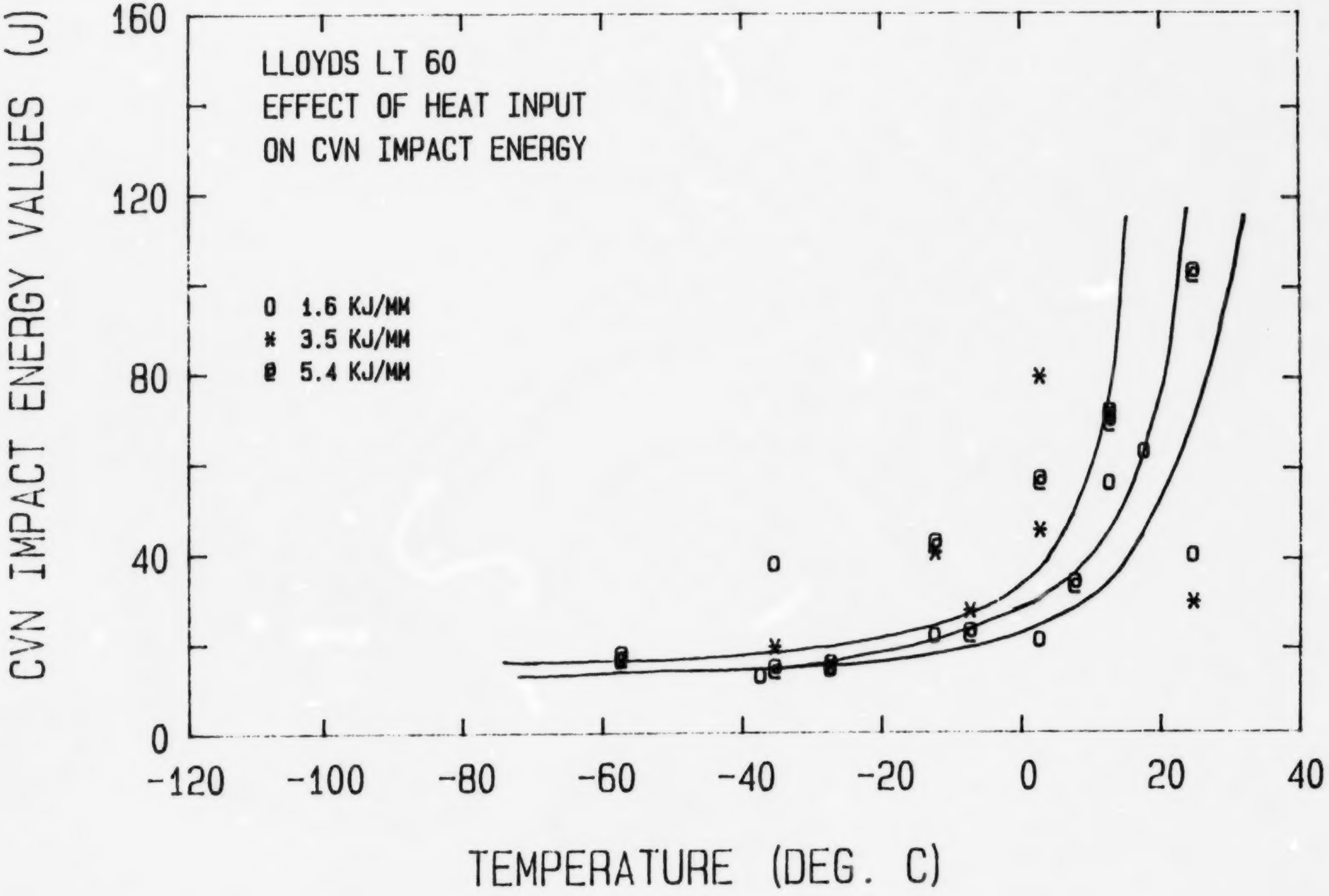

FIGURE 22 : Lloyds LT 60 - effect of heat input on CVN impact energy in "as-welded" Gleeble specimens.

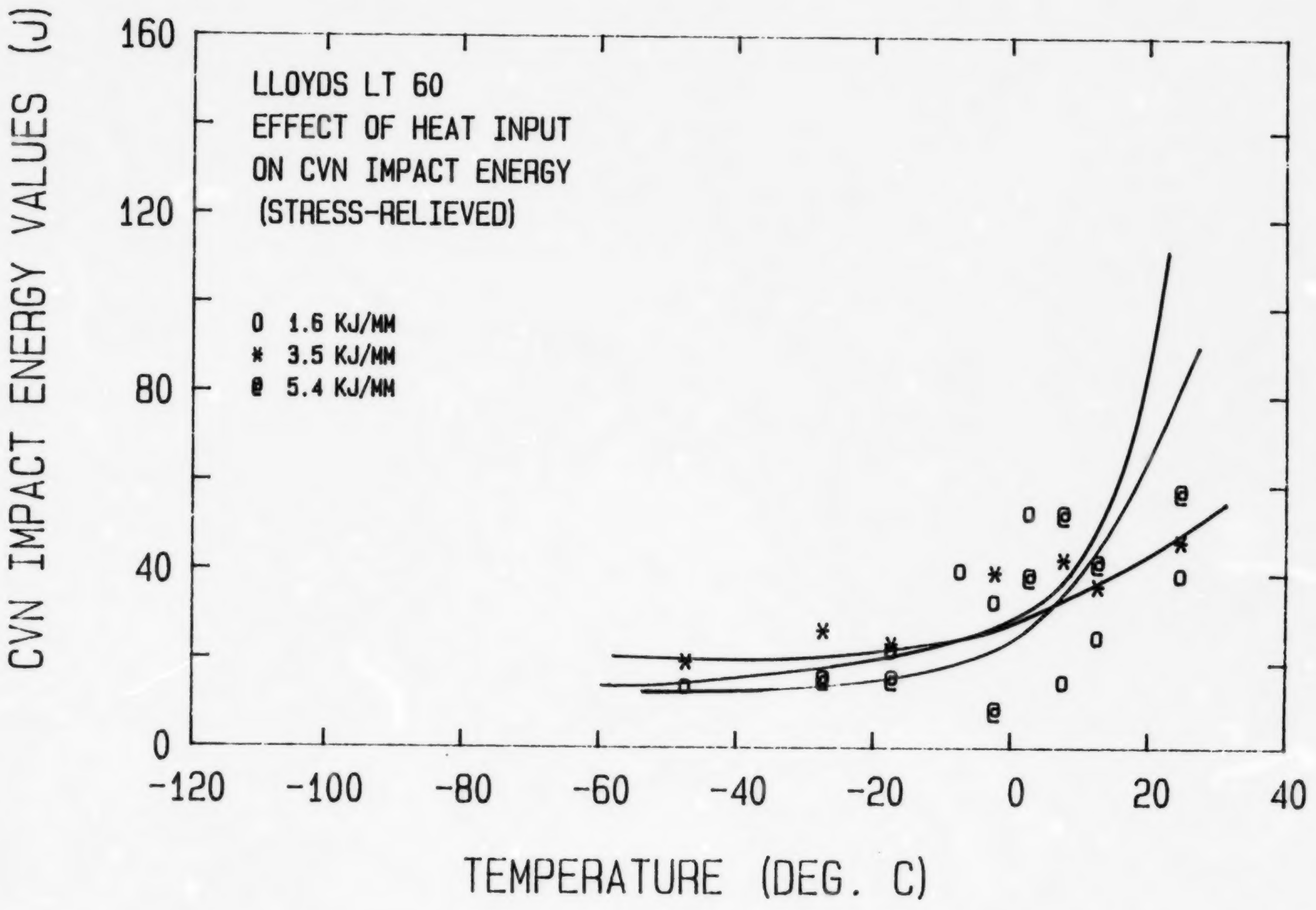

FIGURE 23 : Lloyds LT 60 - effect of heat input on CVN impact energy in "stress-relieved" Gleeble specimens.

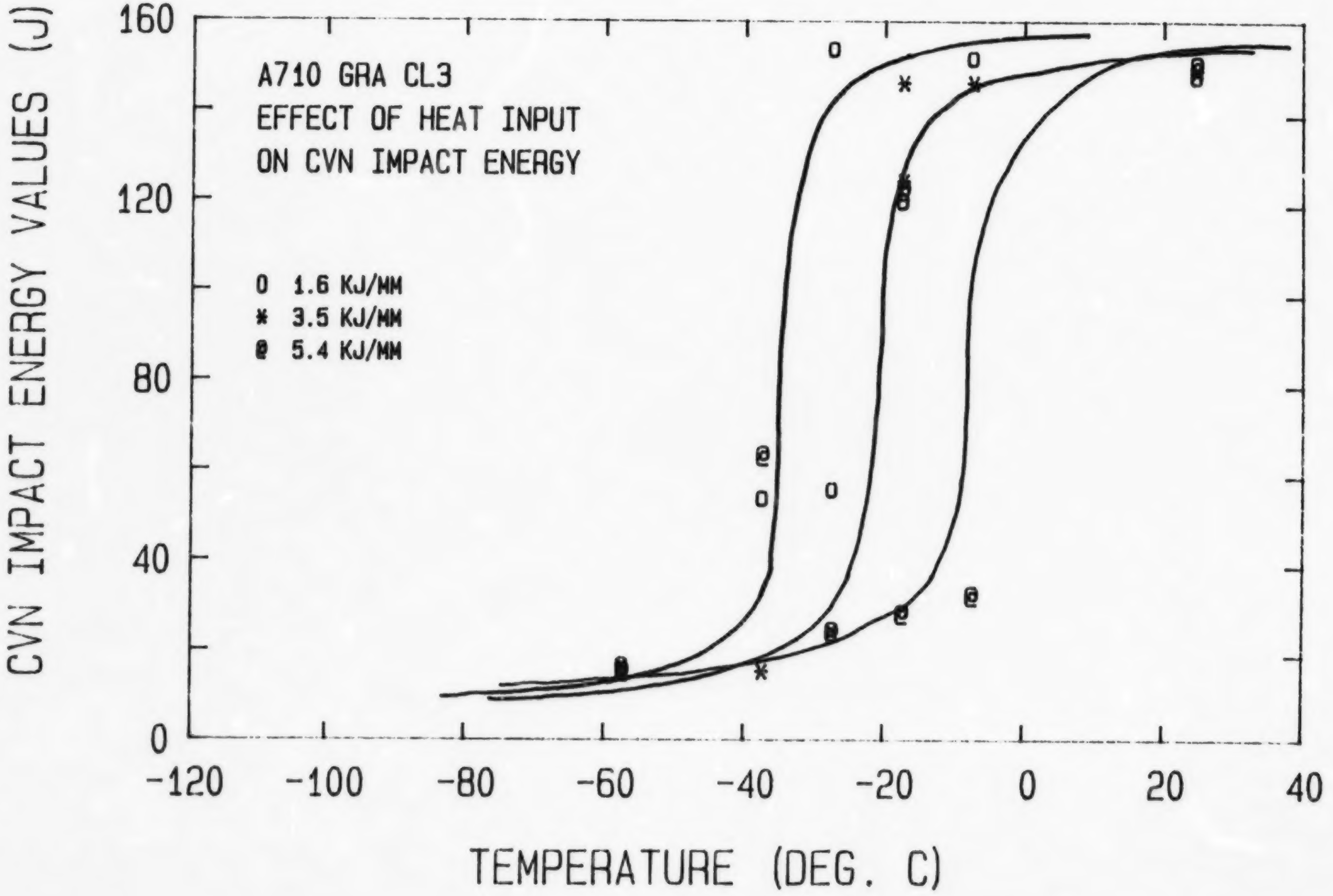

FIGURE 24 : A710, Gr. A, Cl.3 - effect of heat input on CVN impact energy in "as-welded" Gleeble specimens.

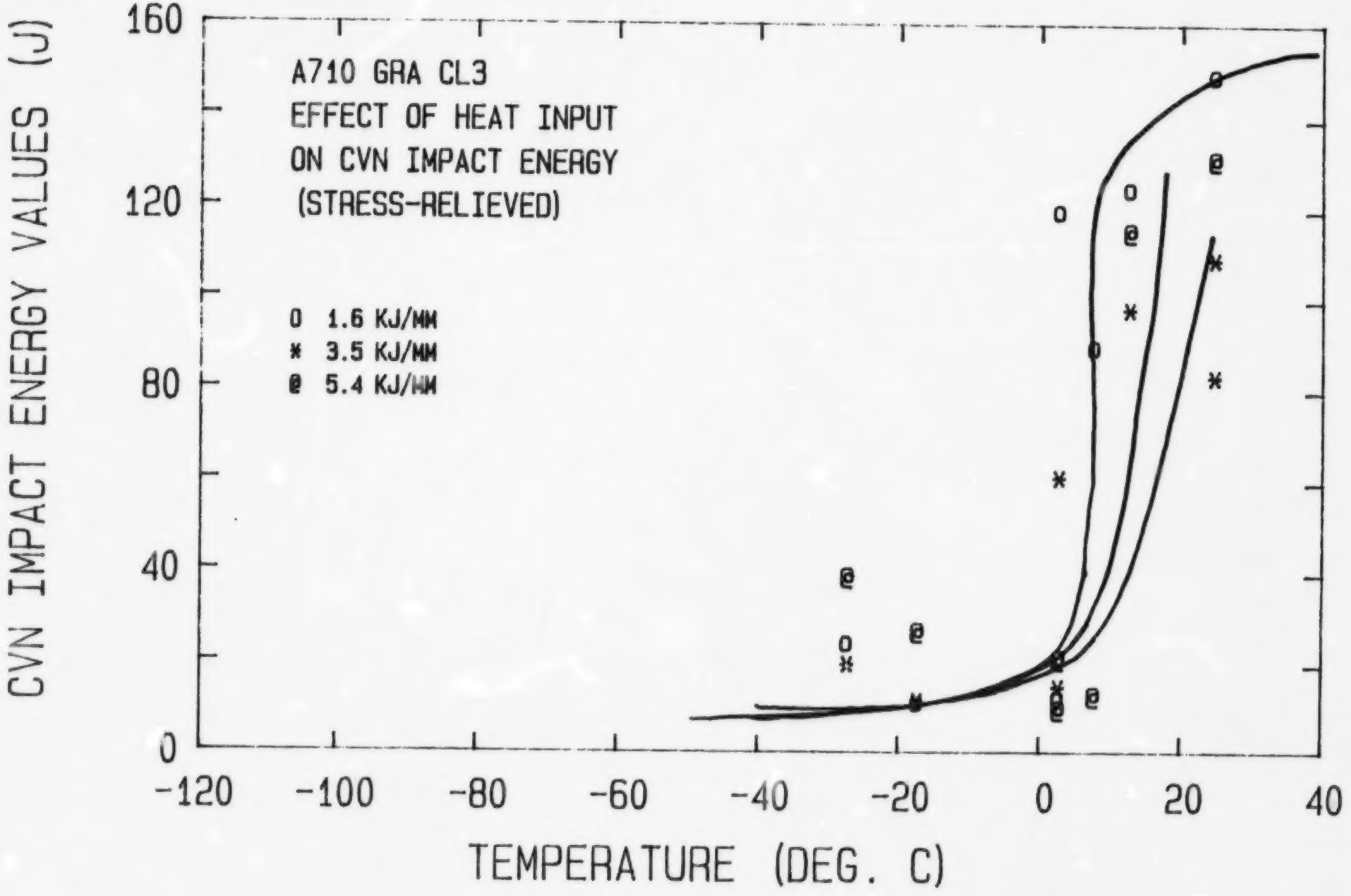

FIGURE 25 : A710, Gr. A, Cl. 3 - effect of heat input on CVN impact energy in "stress-relieved" Gleeble specimens.

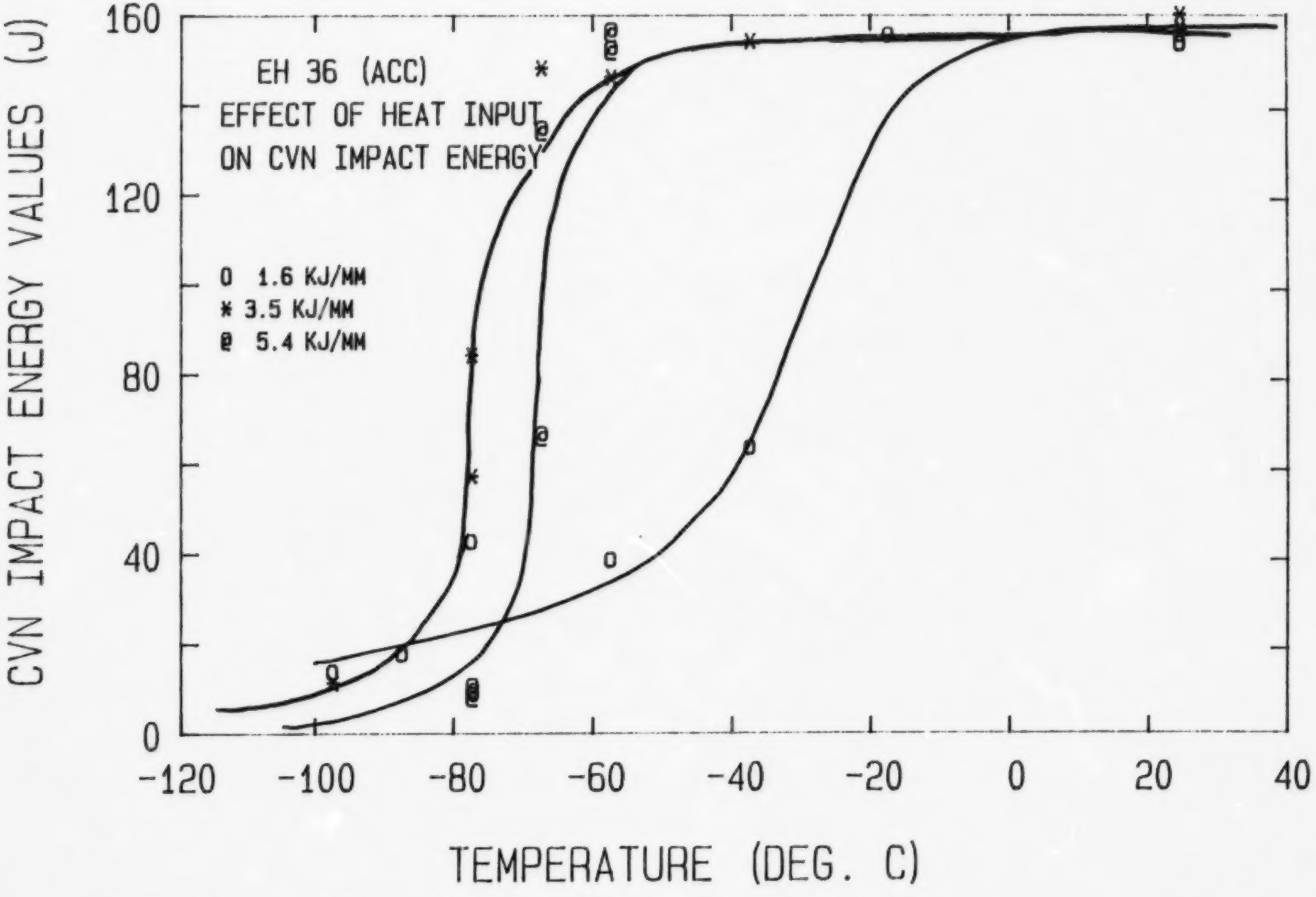

FIGURE 26 : MACS (ACC) - effect of heat input on CVN impact energy in "as-welded" Gleeble specimens.

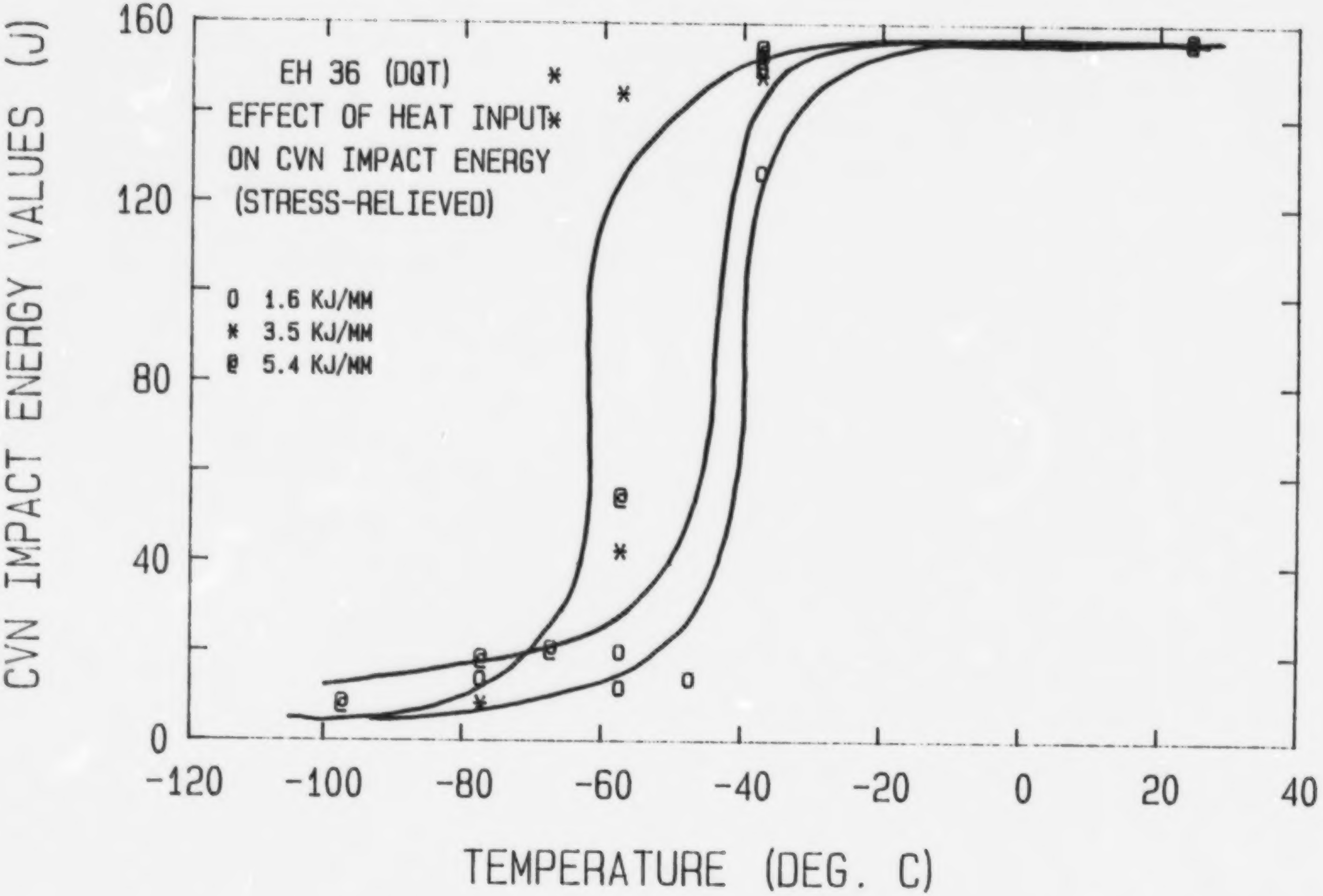

FIGURE 27: MACS (DQT) - effect of heat input on CVN impact energy in "stress-relieved" Gleeble specimens.

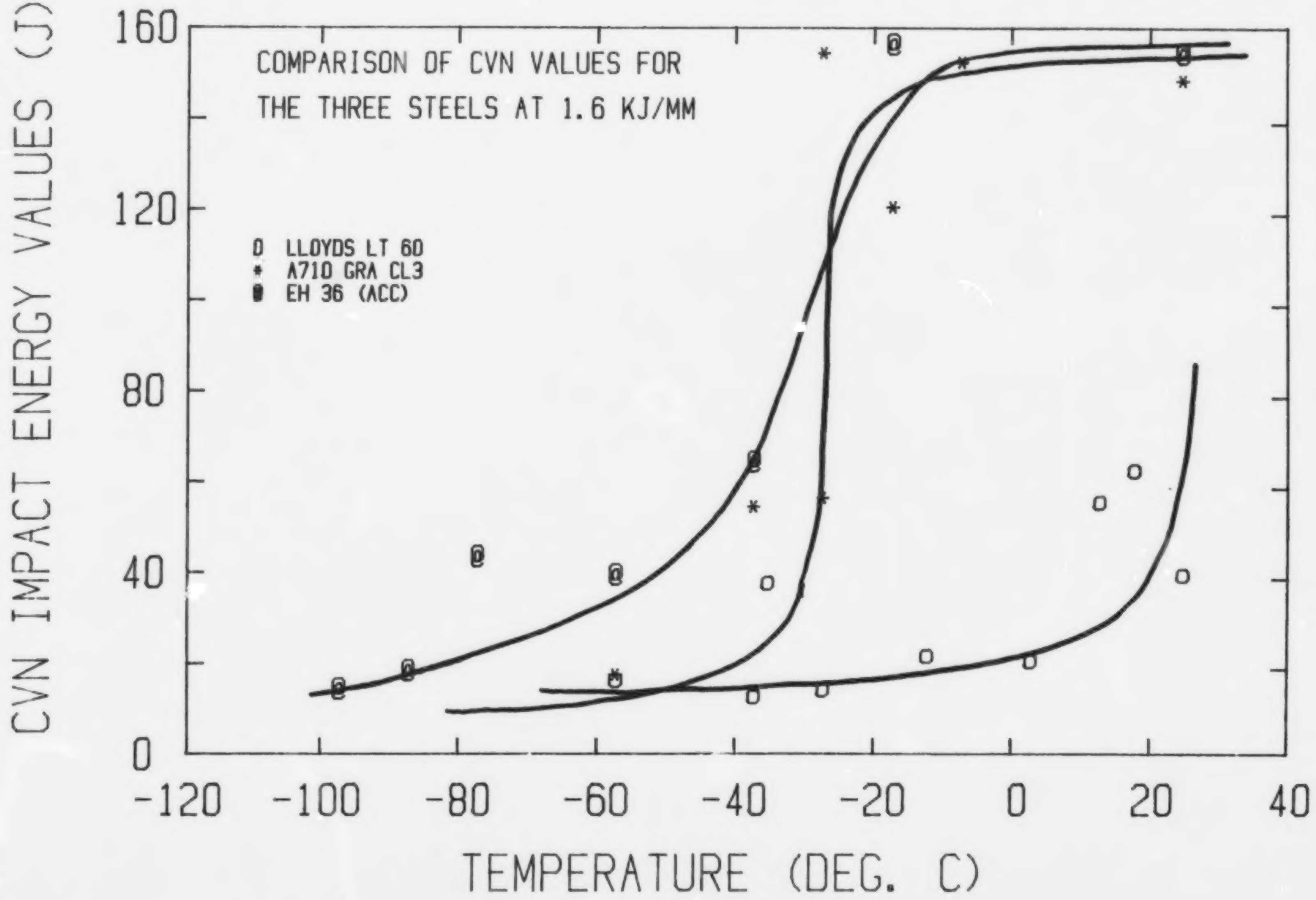

FIGURE 28 : Comparison of Gleeble specimens CVN energy for the three steels at 1.6 kJ/mm in the "as-welded" condition.

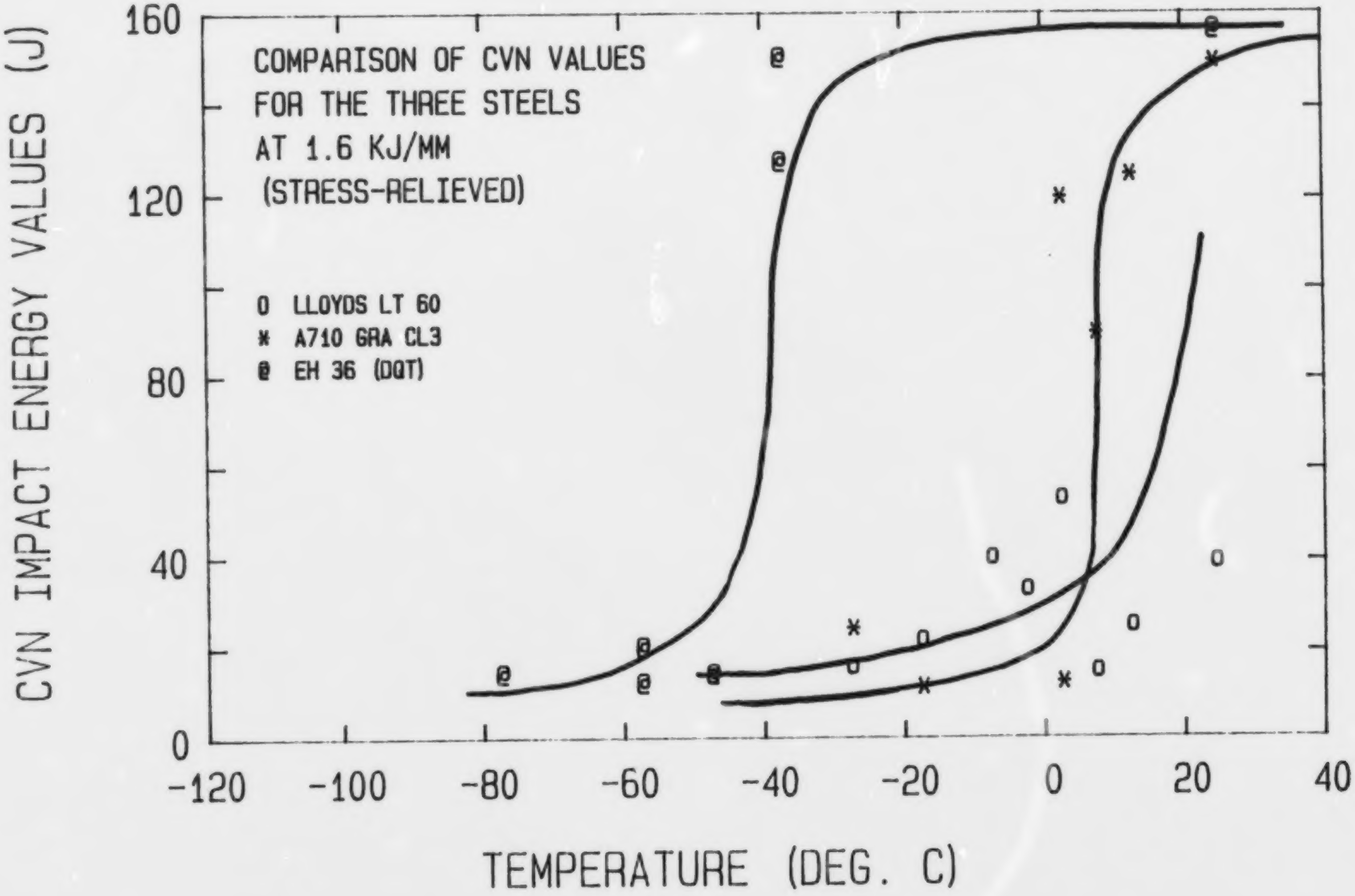

FIGURE 29: Comparison of Gleeble specimers CVN energy for the three steels at 1.6 kJ/mm in the "stress-relieved" condition.

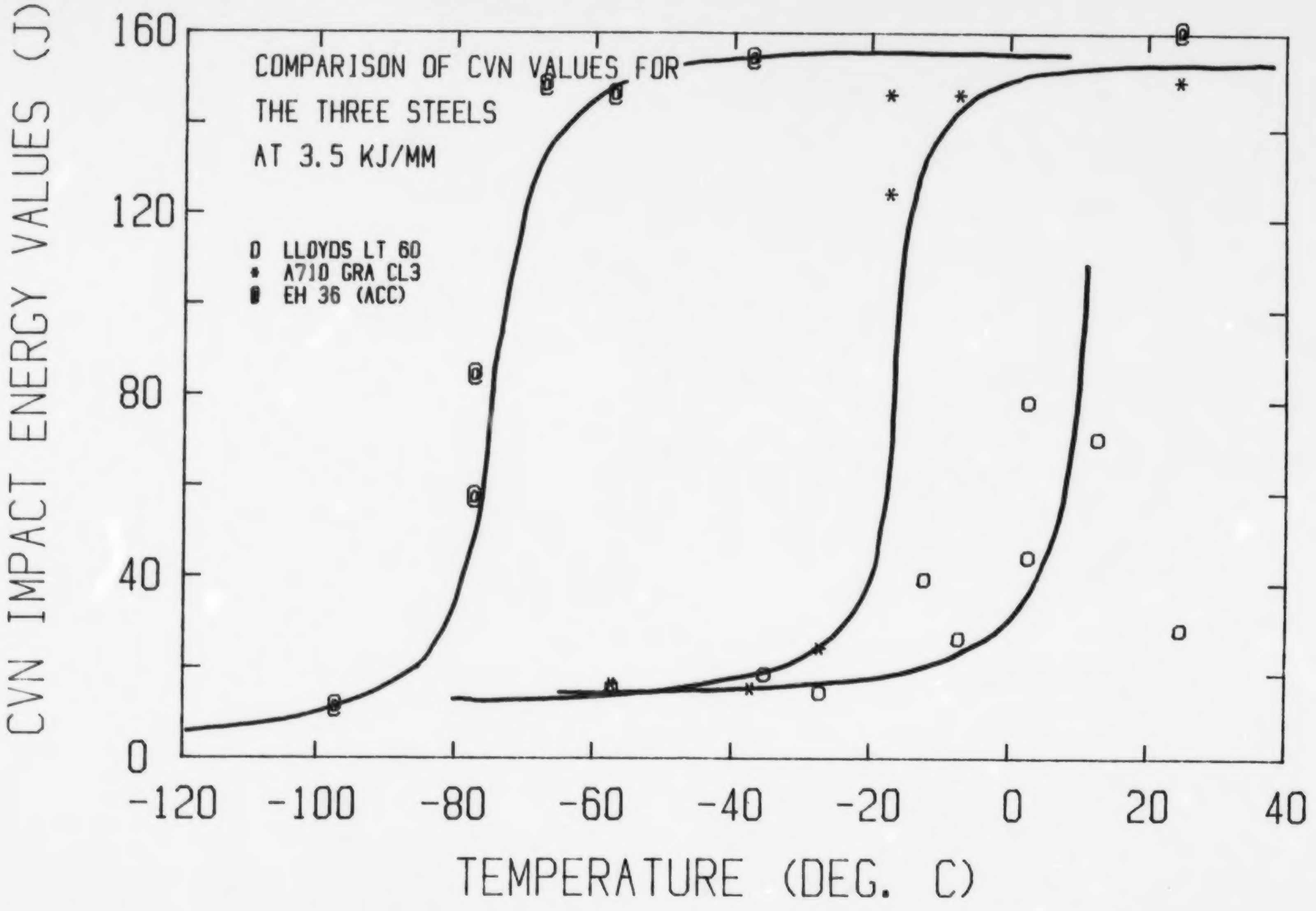

FIGURE 30 : Comparison of Gleeble specimens CVN energy for the three steels at 3.5 kJ/mm in the "as-welded" condition.

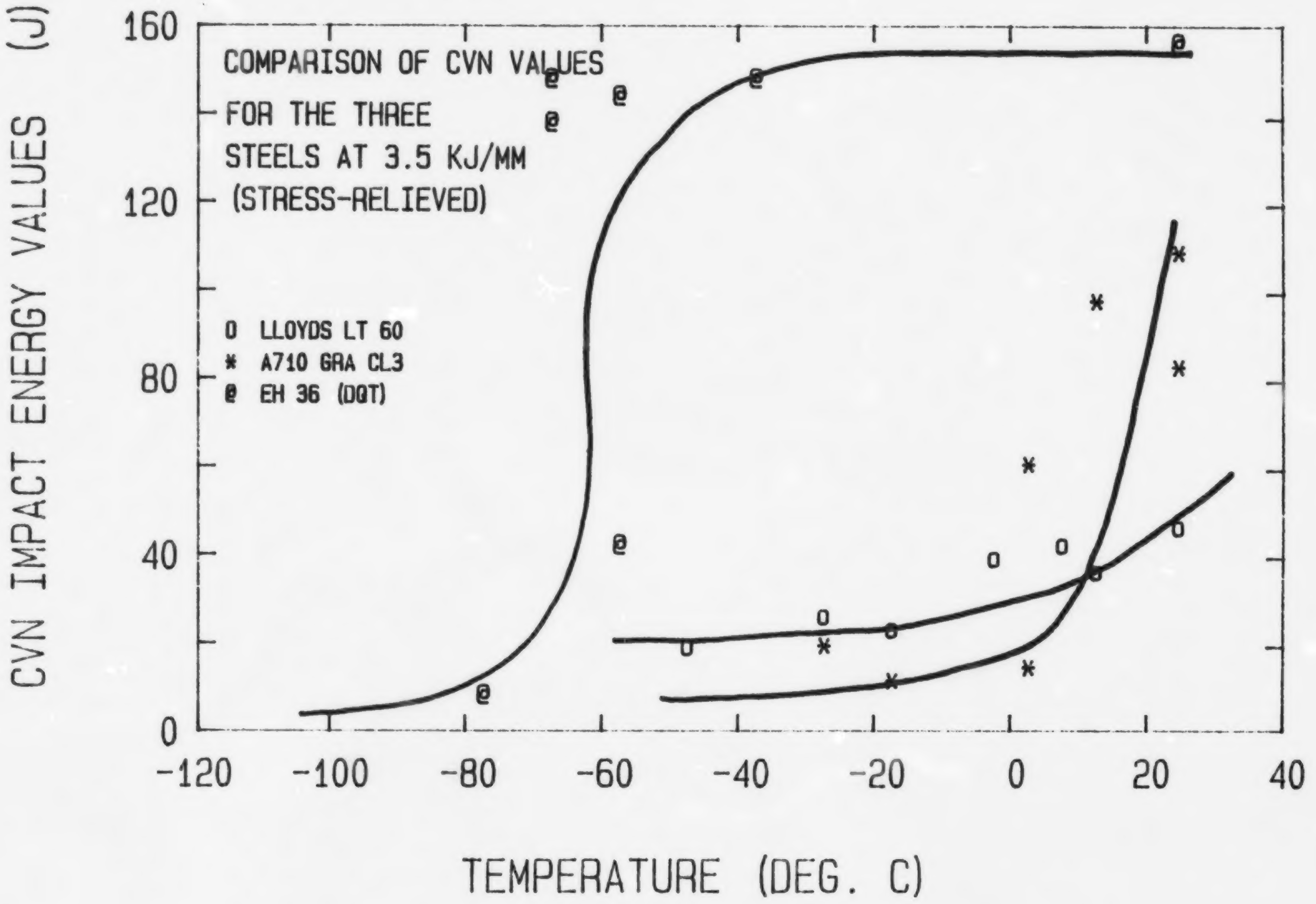

FIGURE 31 : Comparison of Gleeble specimens CVN energy for the three steels at 3.5 kJ/mm in the "stress-relieved" condition.

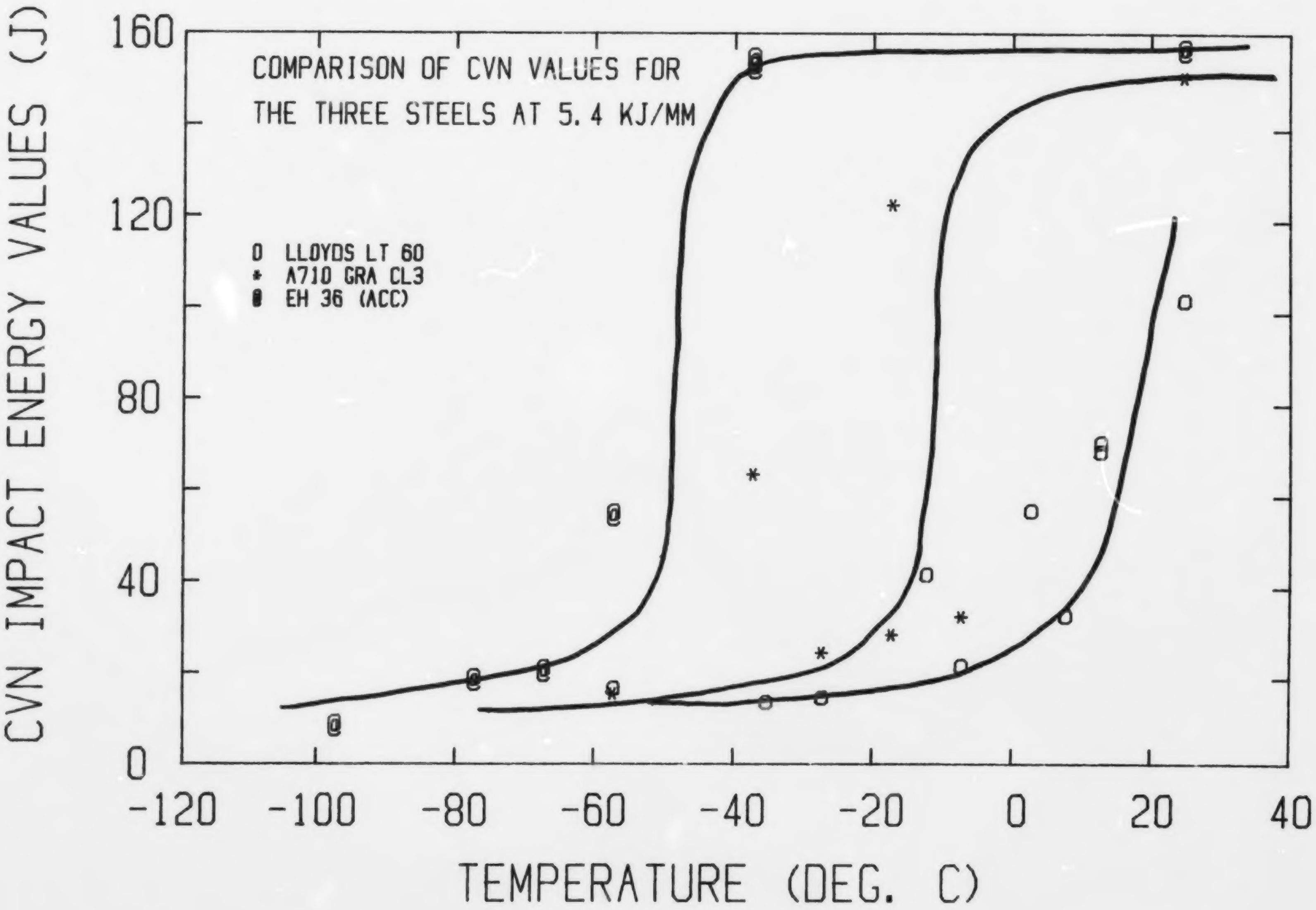

FIGURE 32 : Comparison of Gleeble specimen CVN energy for the three steels at 5.4 kJ/mm in the "as-welded" condition.

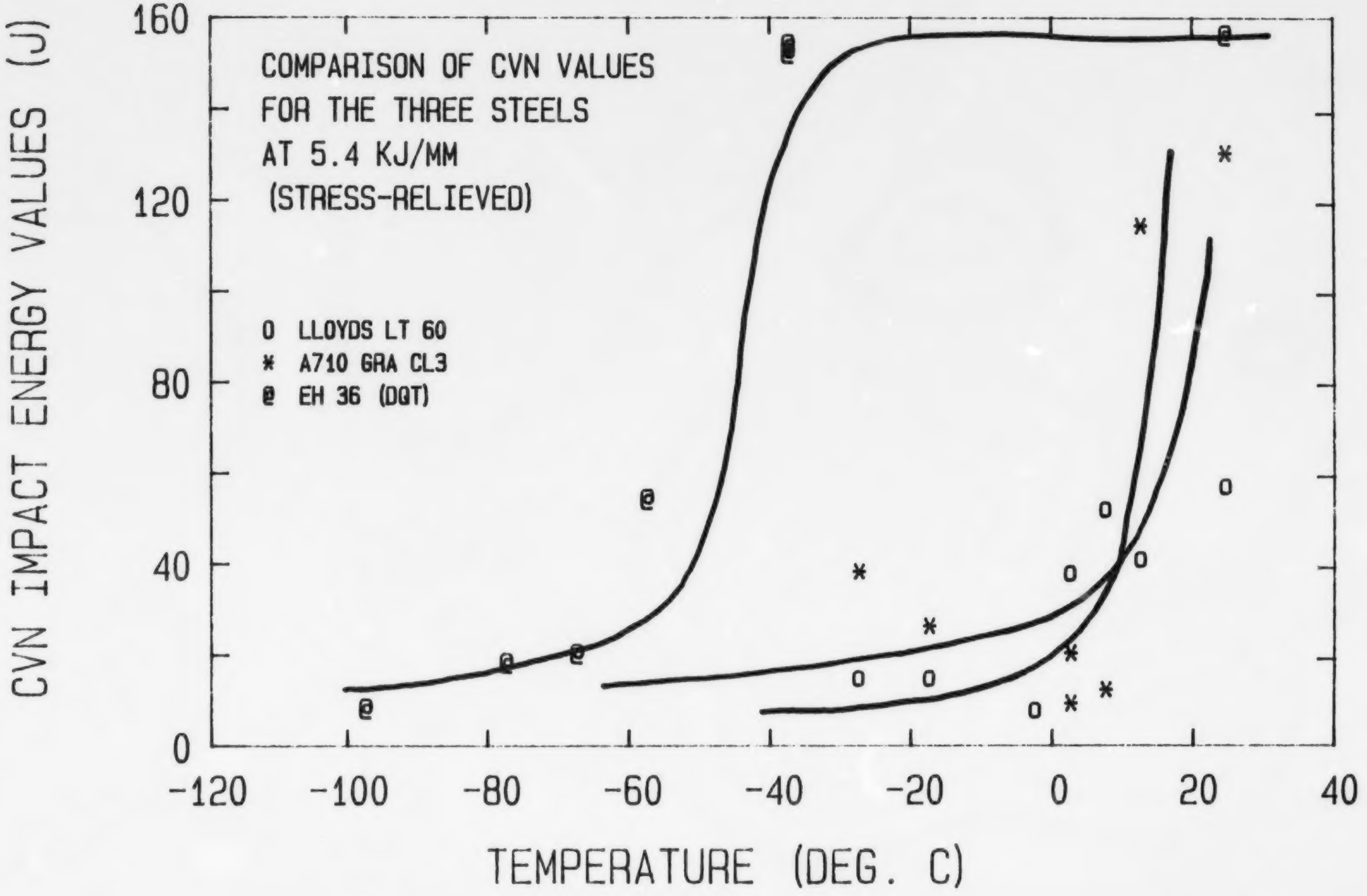

FIGURE 33 : Comparison of Gleeble specimens CVN energy for the three steels at 5.4 kJ/mm in the "stress-relieved" condition.

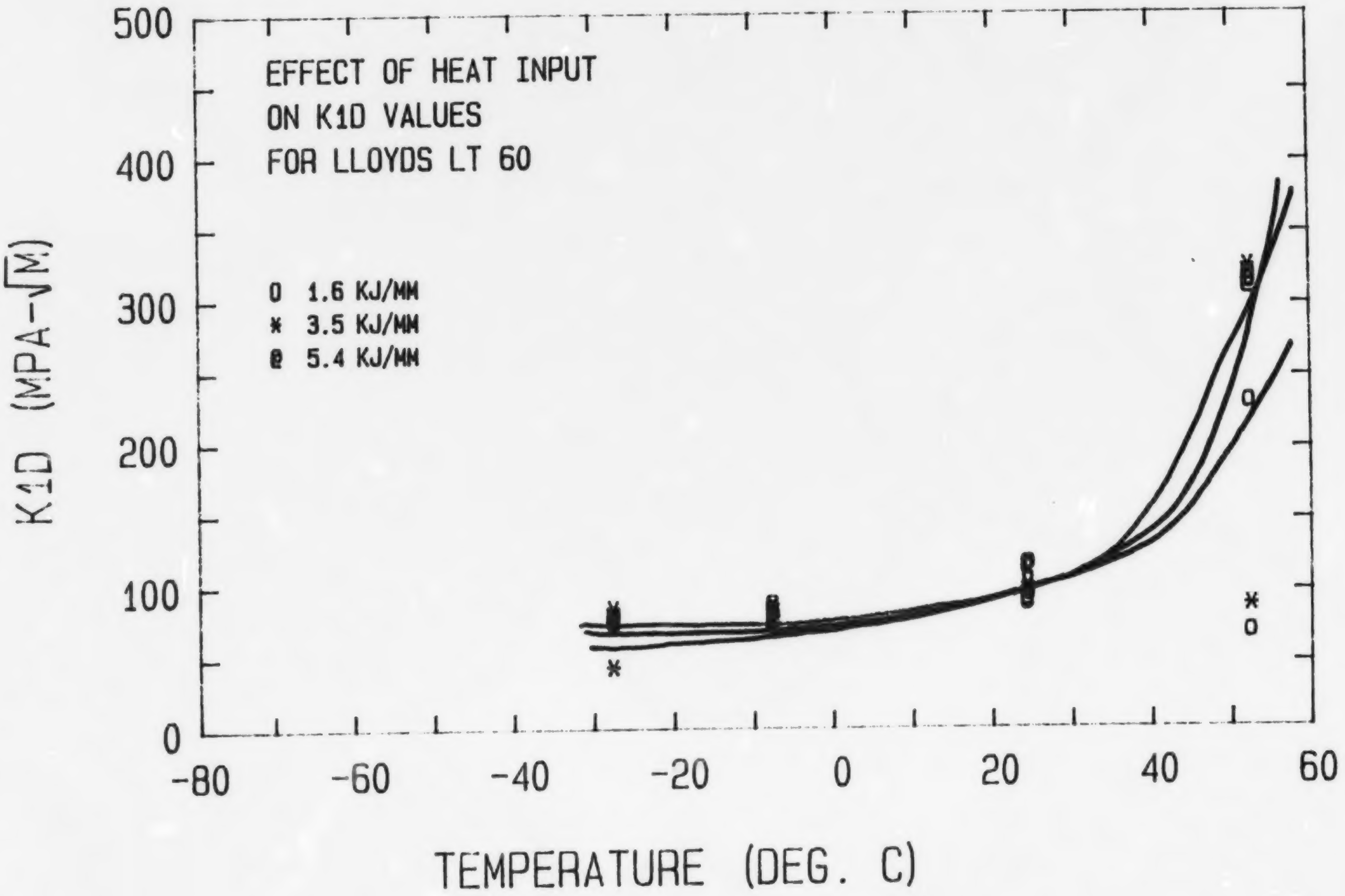

FIGURE 34 : Lloyds LT 60 - Effect of heat input on K1d instrumented impact toughness values in "as-welded" Gleeble specimens.

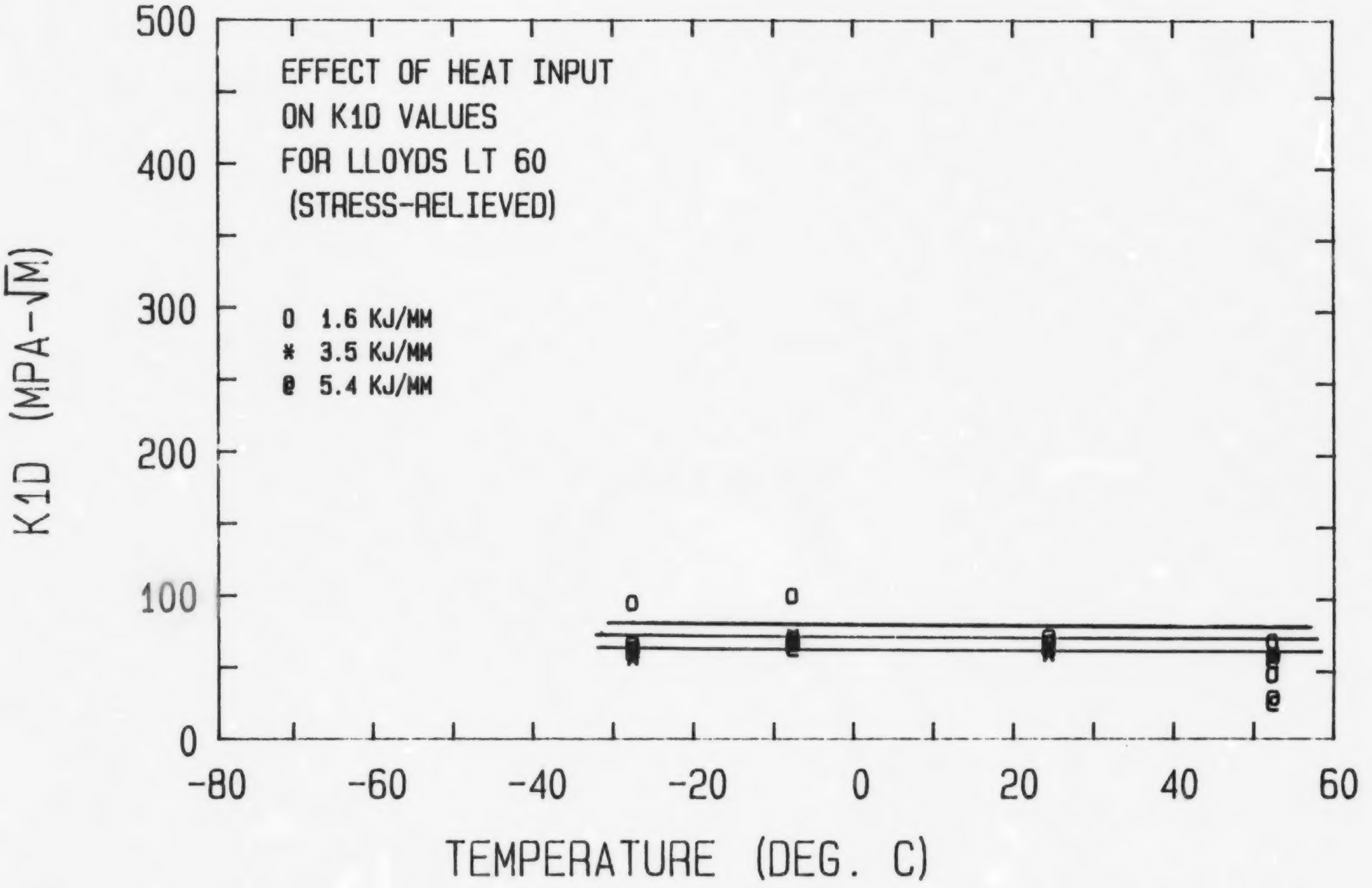

FIGURE 35 : Lloyds LT 60 - Effect of heat input on K_{1d} instrumented impact toughness values in "stress-relieved" specimens.

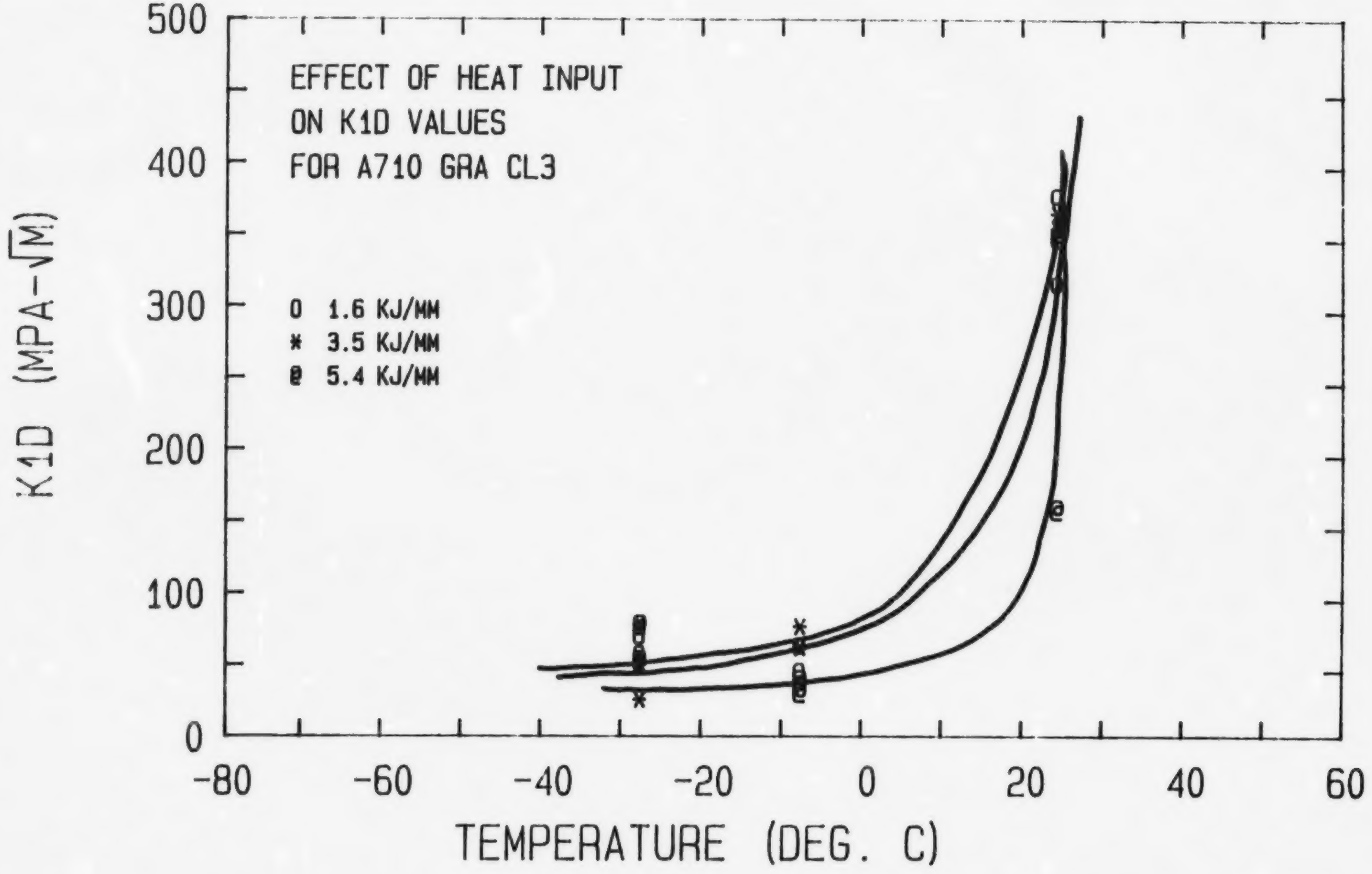

FIGURE 36 : A710, Gr . A, Cl. 3, - Effect of heat input on K_{1d} instrumented impact toughness values in "as-welded" specimens.

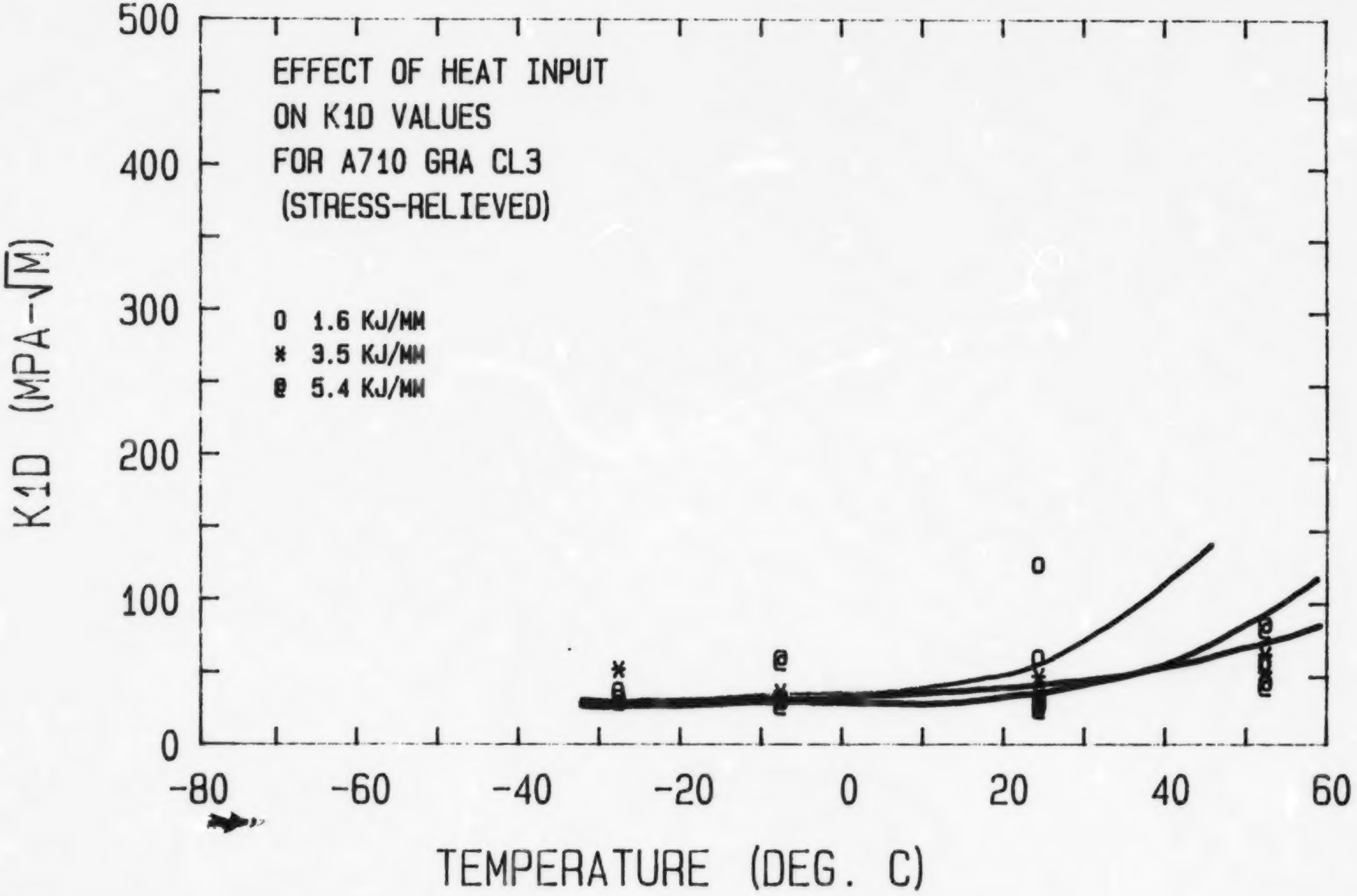

FIGURE 37 : A710, Gr. A., Cl. 3, - Effect of heat input on K_{1d} instrumented impact toughness values in "stress-relieved" specimens.

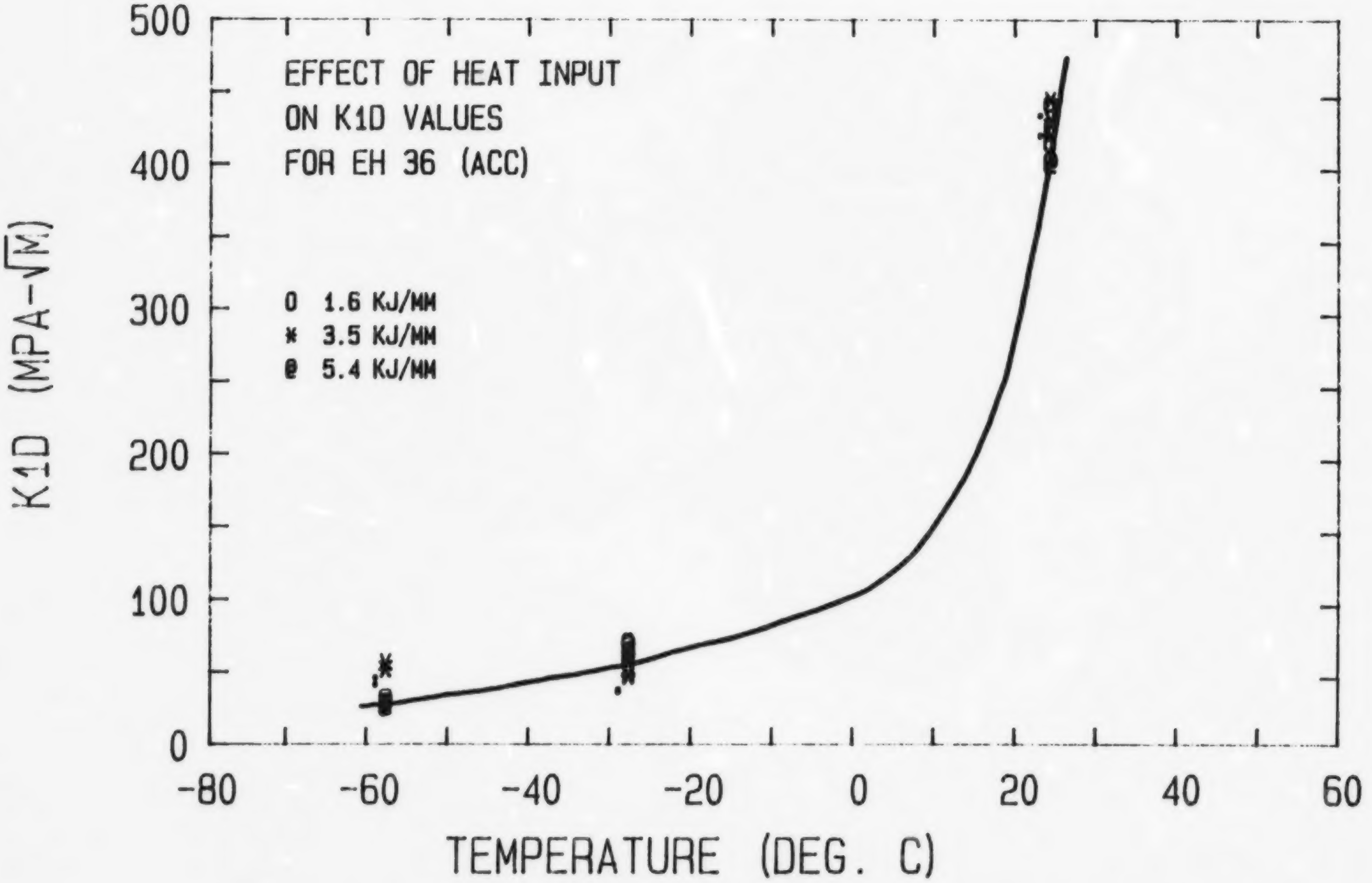

FIGURE 38 : MACS (ACC) - Effect of heat input on K_{1d} instrumented impact toughness values in "as-welded" specimens.

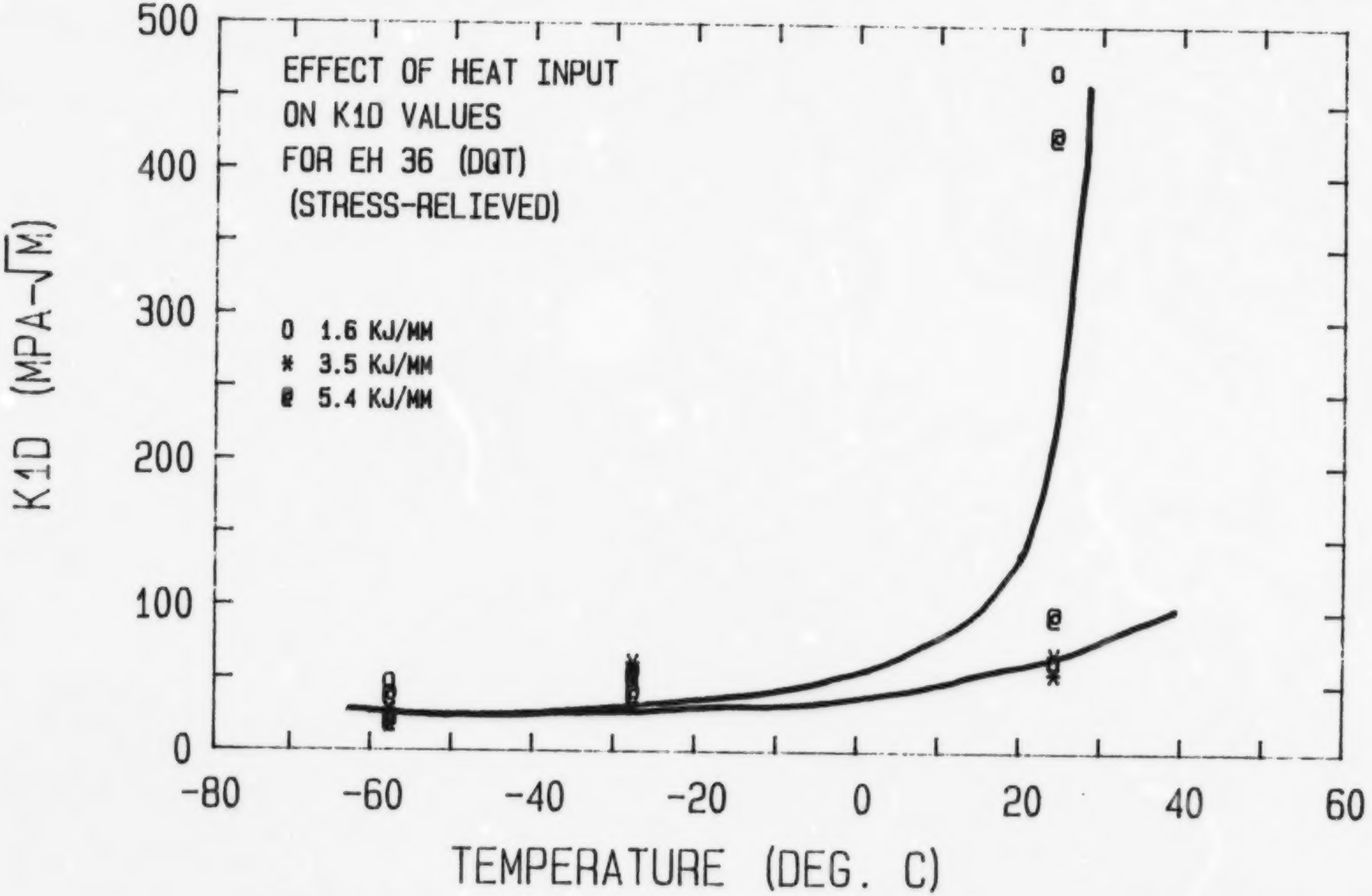

FIGURE 39 : MACS (DQT) - Effect of heat input on K_{1d} instrumented impact toughness values in "stress-relieved" specimens.

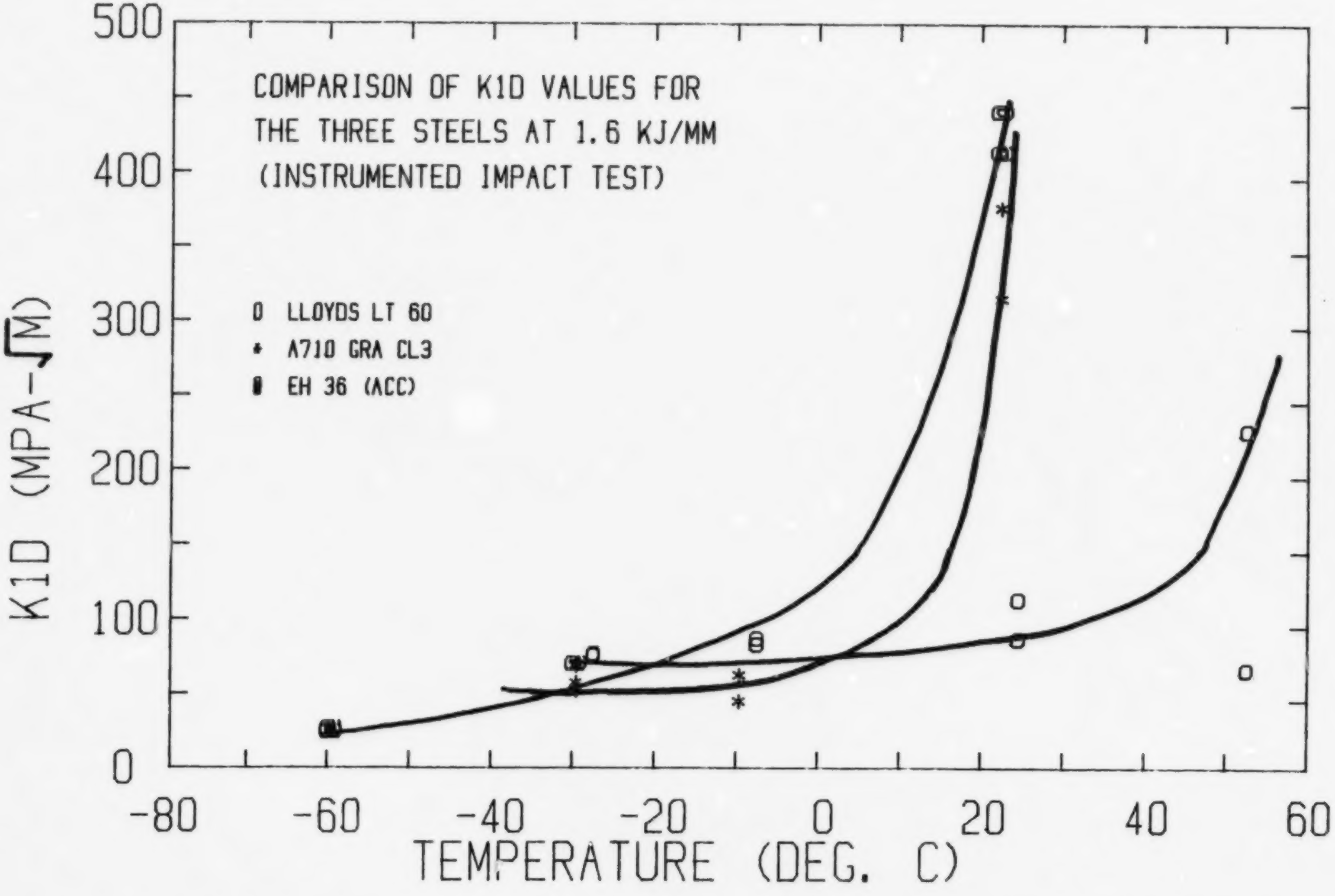

FIGURE 40 : Comparison of Gleeble specimen K_{1d} values for the three steels at 1.6 kJ/mm in the "as-welded" condition.

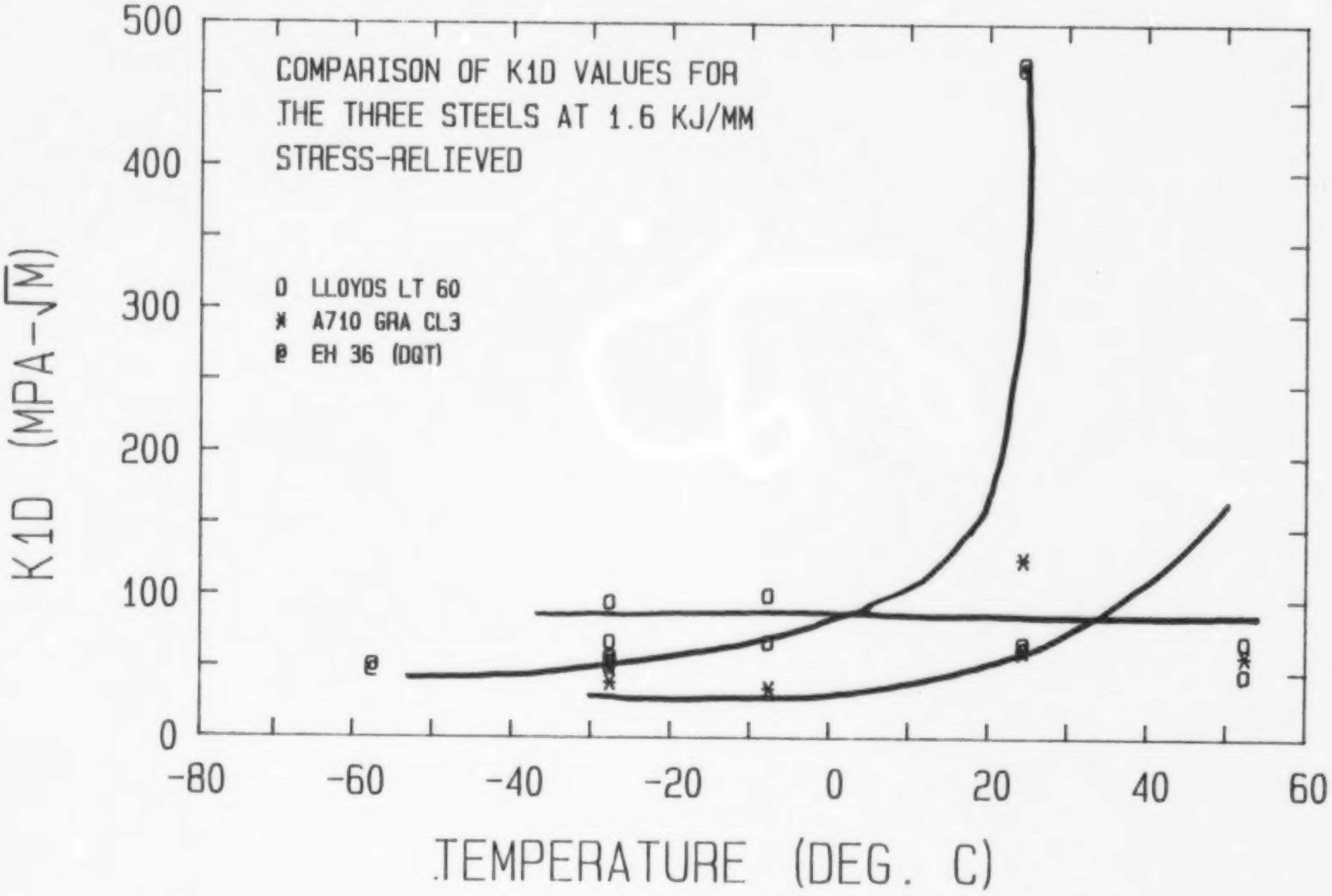

FIGURE 41 : Comparison of Gleeble specimen K_{1d} values for the three steels at 1.6 kJ/mm in the "stress-relieved" condition.

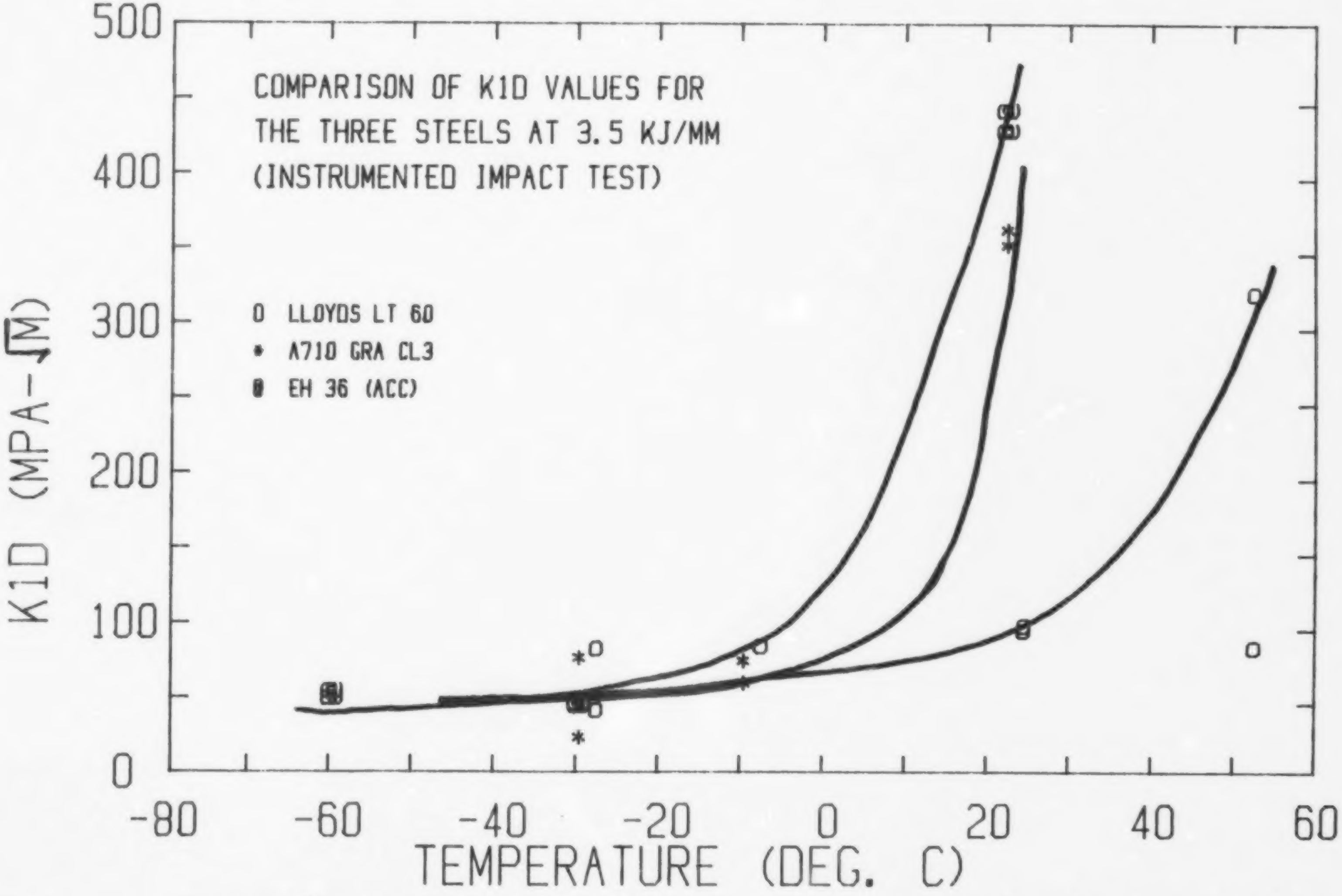

FIGURE 42 : Comparison of Gleeble specimen K_{1d} values for the three steels at 3.5 kJ/mm in the "as-welded" condition.

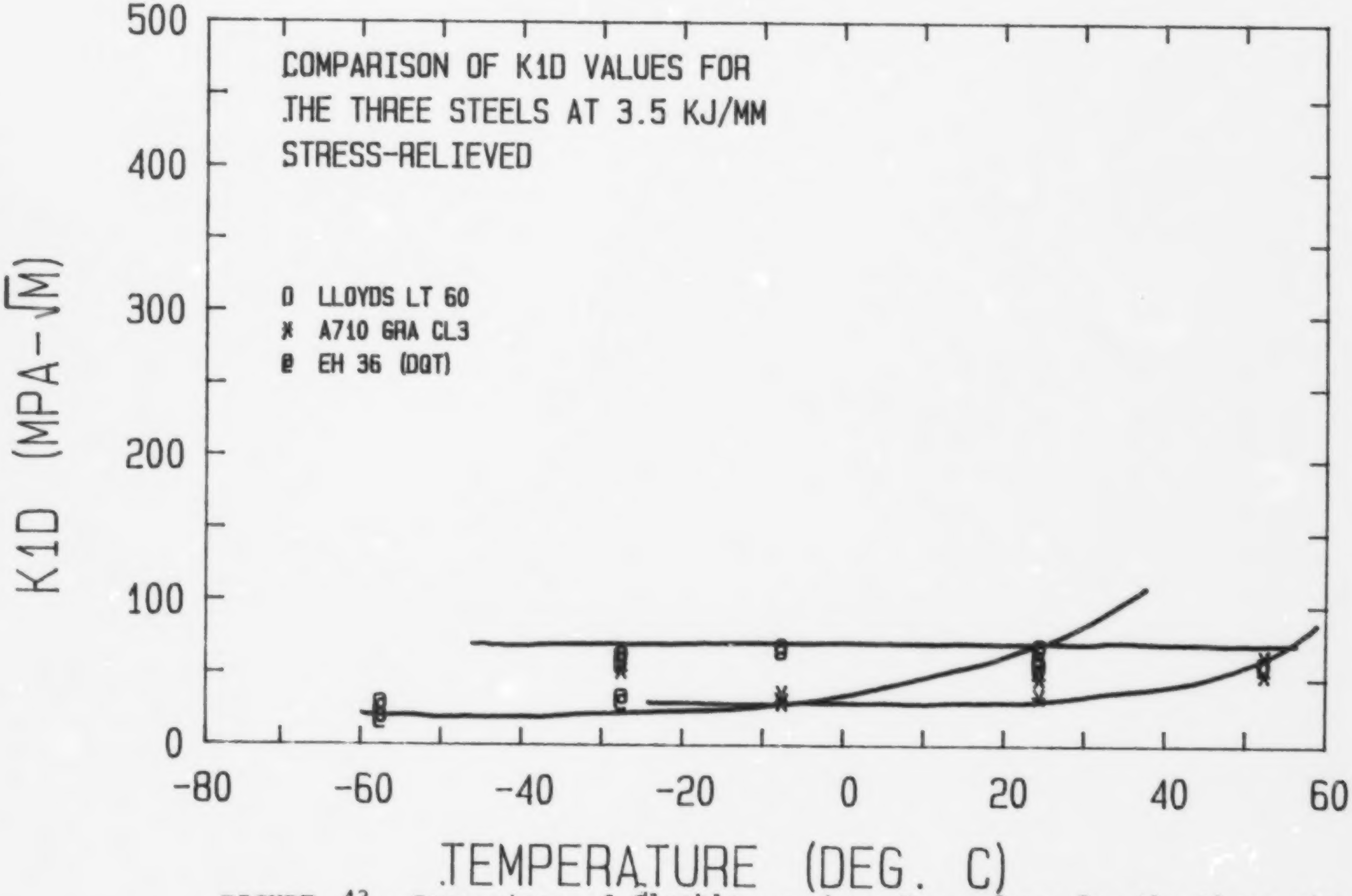

FIGURE 43 : Comparison of Gleeble specimen K_{1d} values for the three steels at 3.5 kJ/mm in the "stress-relieved" condition.

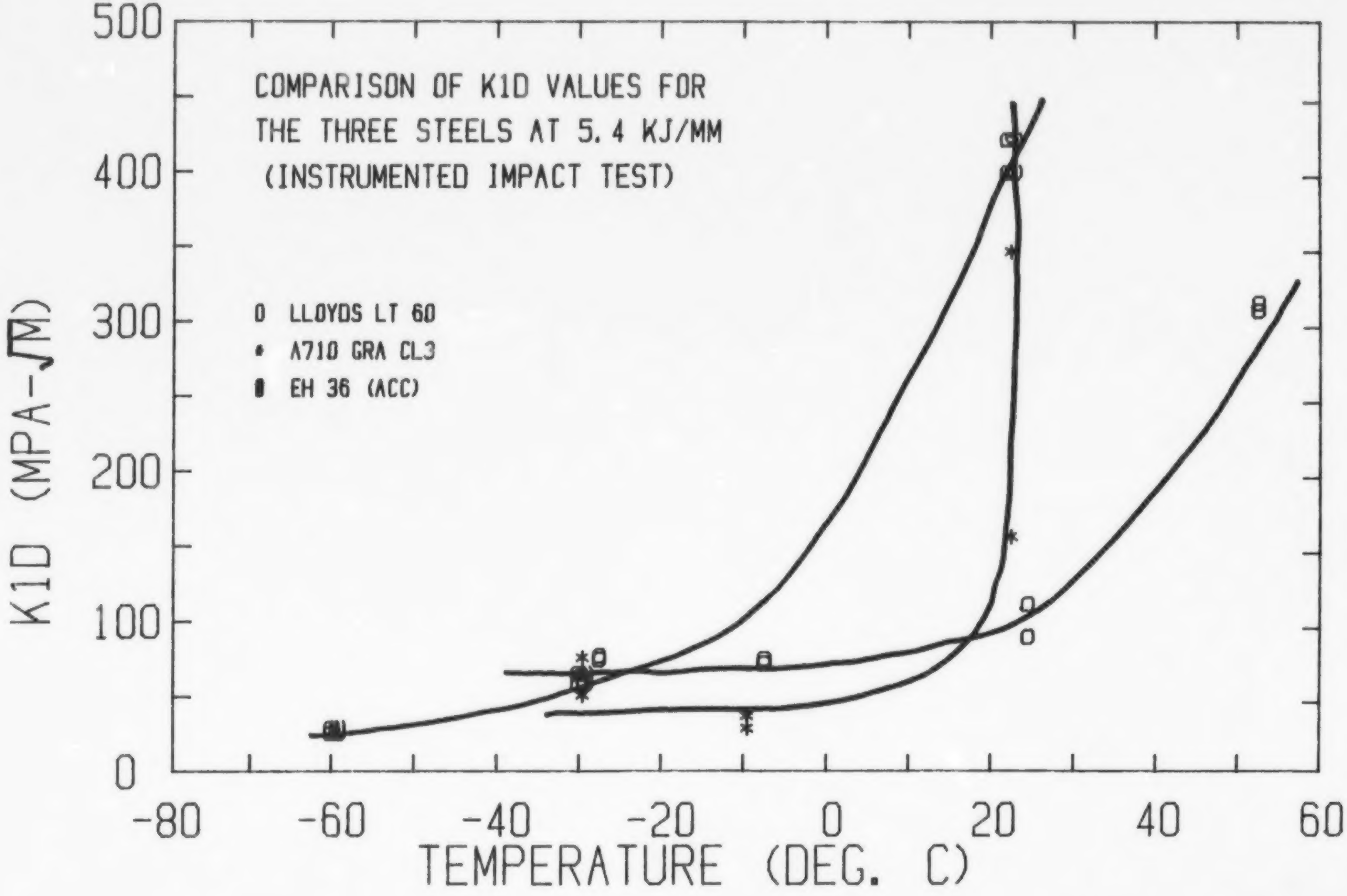

FIGURE 44 : Comparison of Gleeble specimen K_{1d} values for the three steels at 5.4 kJ/mm in the "as-welded" condition.

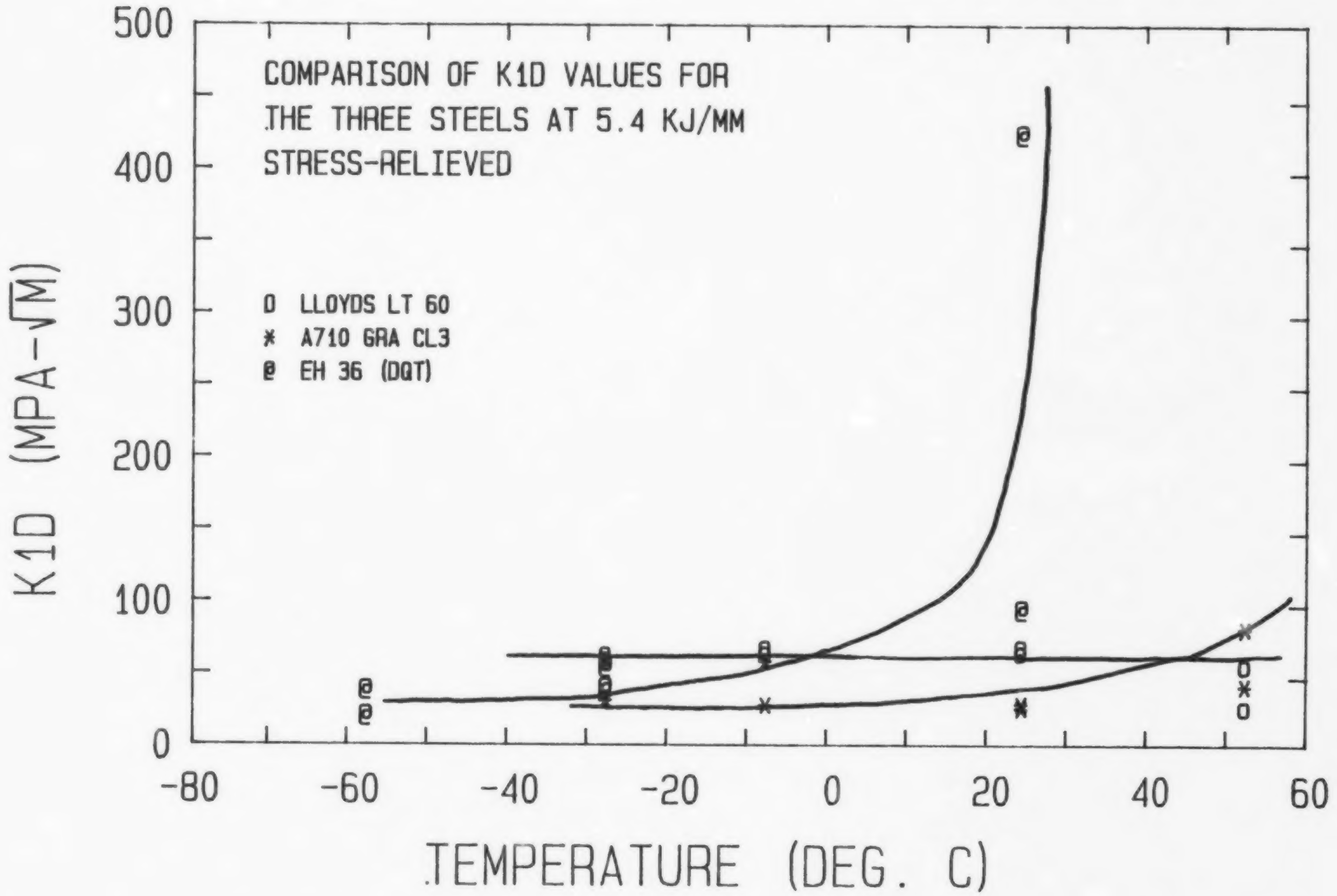

FIGURE 45 : Comparison of Gleeble specimen K_{1d} values for the three steels at 5.4 kJ/mm in the "stress-relieved" condition.

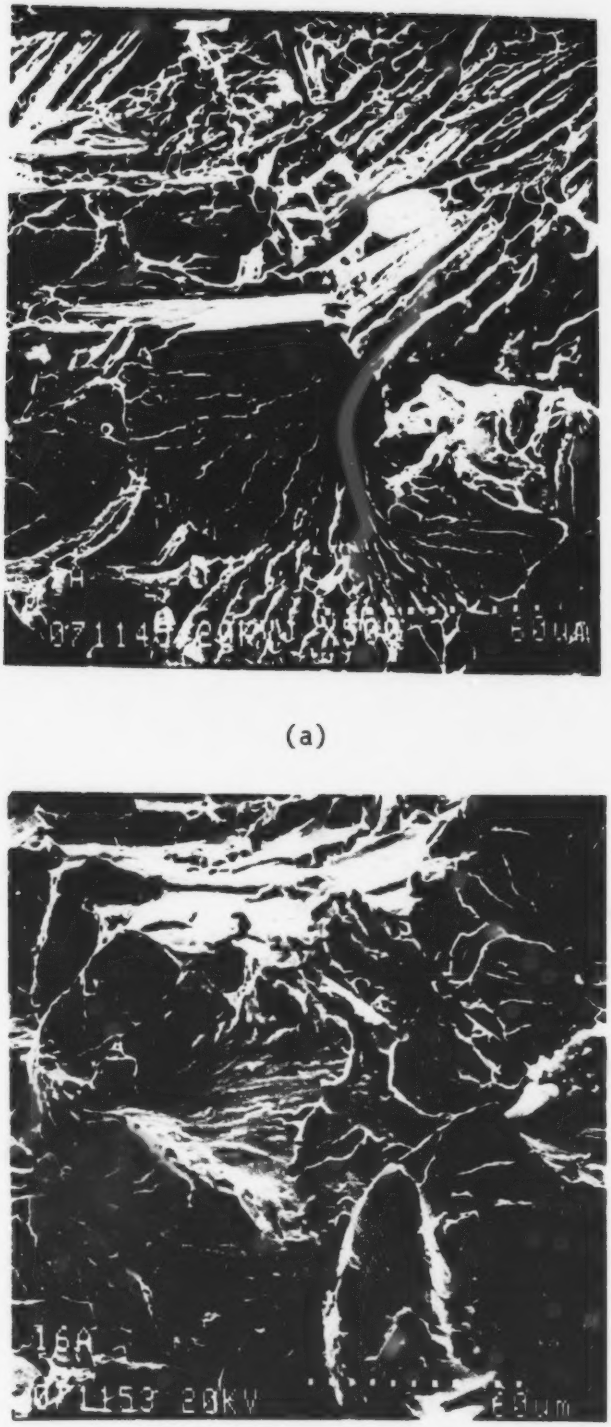
H
071145 20KV X500
60UM
16A
071153 20KV
60um

(a)

(b)

FIGURE 46 : SEM photograph showing typical cleavage facets found in Lloyds LT 60, Gleeble cycled, CVN impact specimens.
a) 1.6 kJ/mm, Neg. 145, Mag. 500 x.
b) 3.5 kJ/mm, Neg. 153, Mag. 500 x.

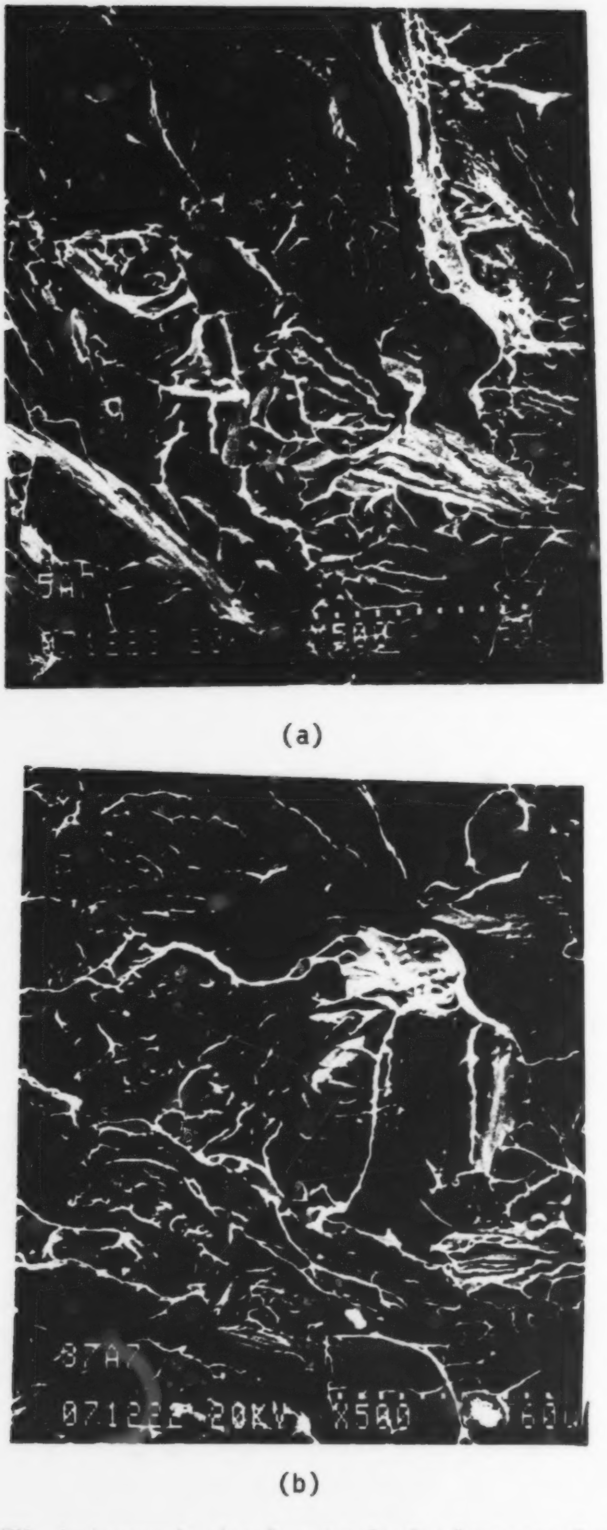
5H
X500
87A7
071222 20KV X500

(a)

(b)

FIGURE 47: SEM photograph showing typical cleavage facets found in A710 Gr. A, Cl. 3, Gleeble cycled CVN impact specimens.
a) 1.6 kJ/mm, Neg. 223, Mag. 500 x.
b) 5.4 kJ/mm, Neg. 222, Mag. 500 x.

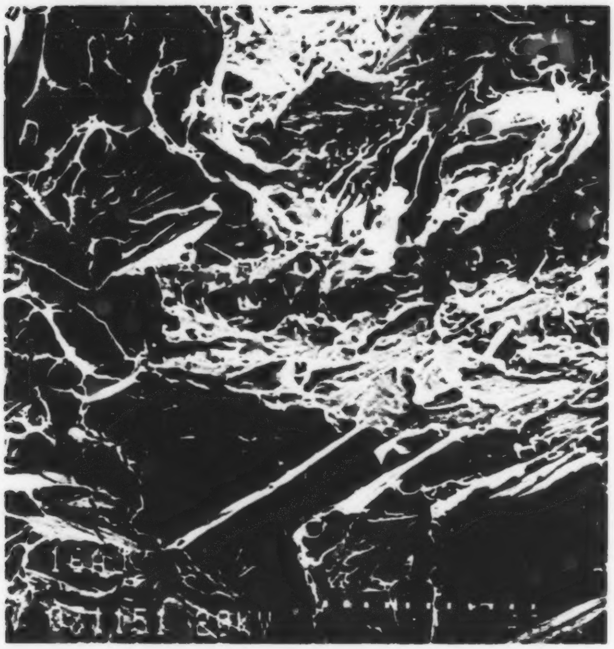

(a)

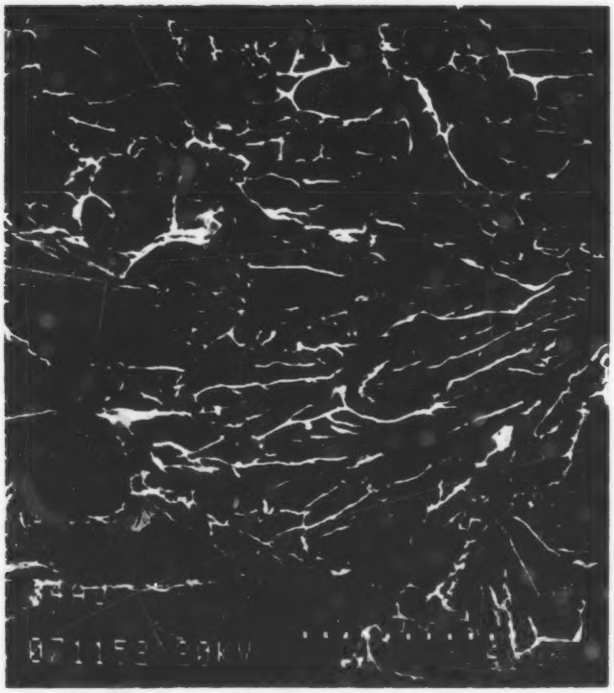

(b)

FIGURE 48: SEM photograph showing typical cleavage facets found in EH 36 (ACC), Gleeble cycled, CVN impact specimens.
a) 1.6 kJ/mm, Neg. 151, Mag. 500 x.
b) 5.4 kJ/mm, Neg. 152, Mag. 500 x.

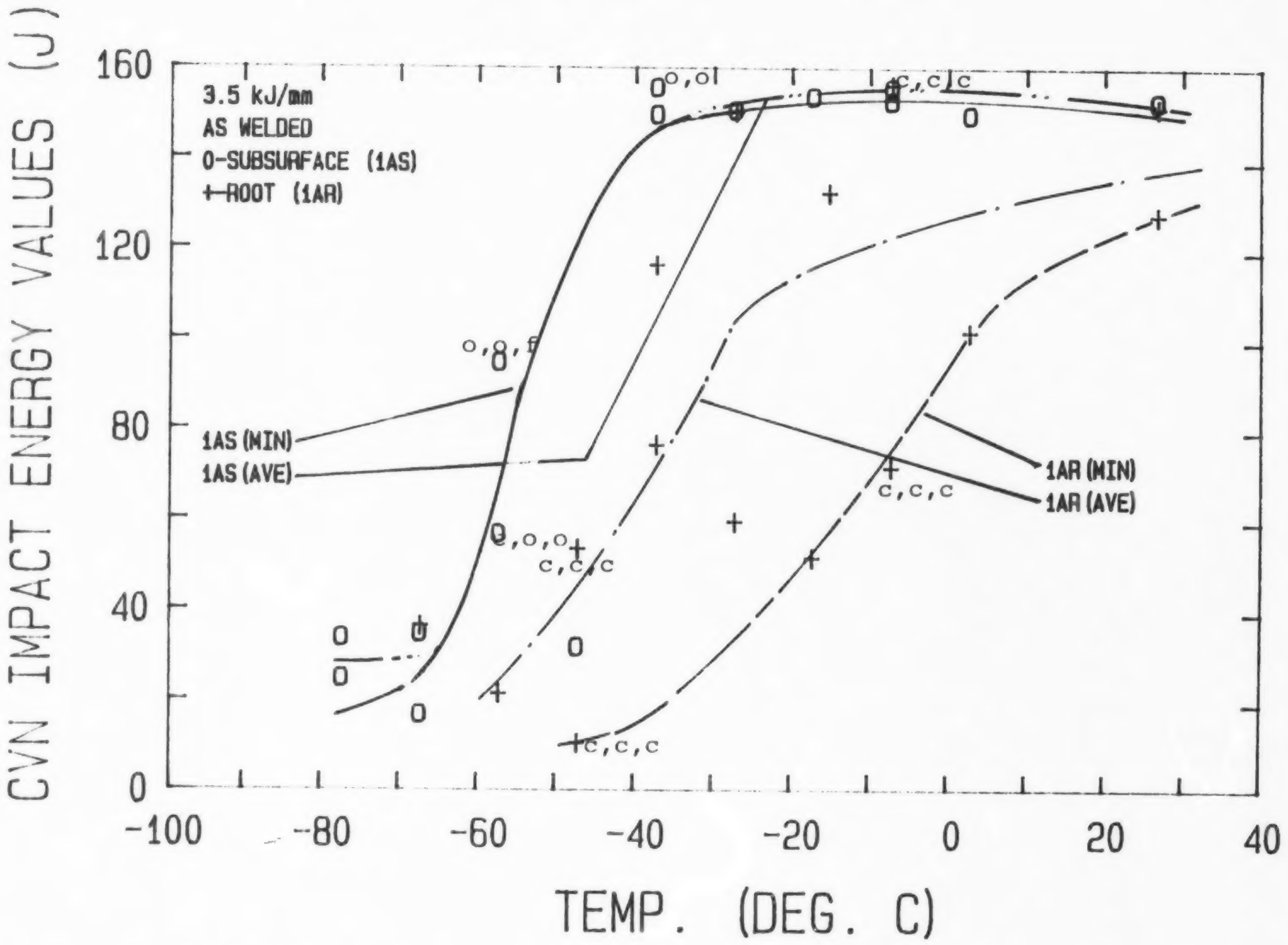

FIGURE 49: CVN impact energy transition curves for the "as-welded" CG HAZ in LT 60 steel welded with 3.5 kJ/mm heat input. Notch root and fracture path locations: c = CG HAZ, f = fine grain HAZ, W = weld metal, b = fusion boundary and o = all the other structures.

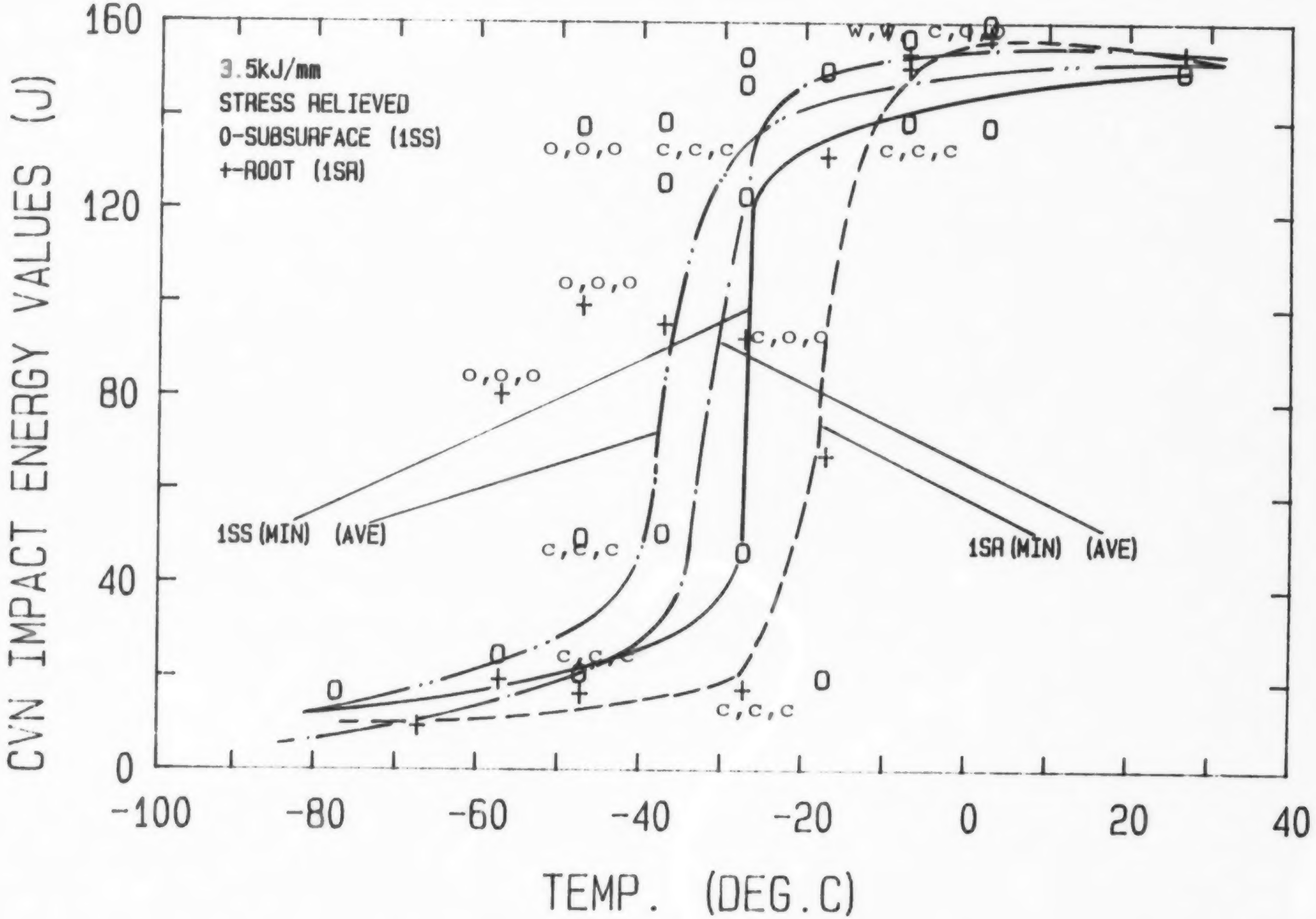

FIGURE 50: CVN impact energy transition curves for the "stress-relieved" CG HAZ in LT 60 steel welded with 3.5 kJ/mm heat input.

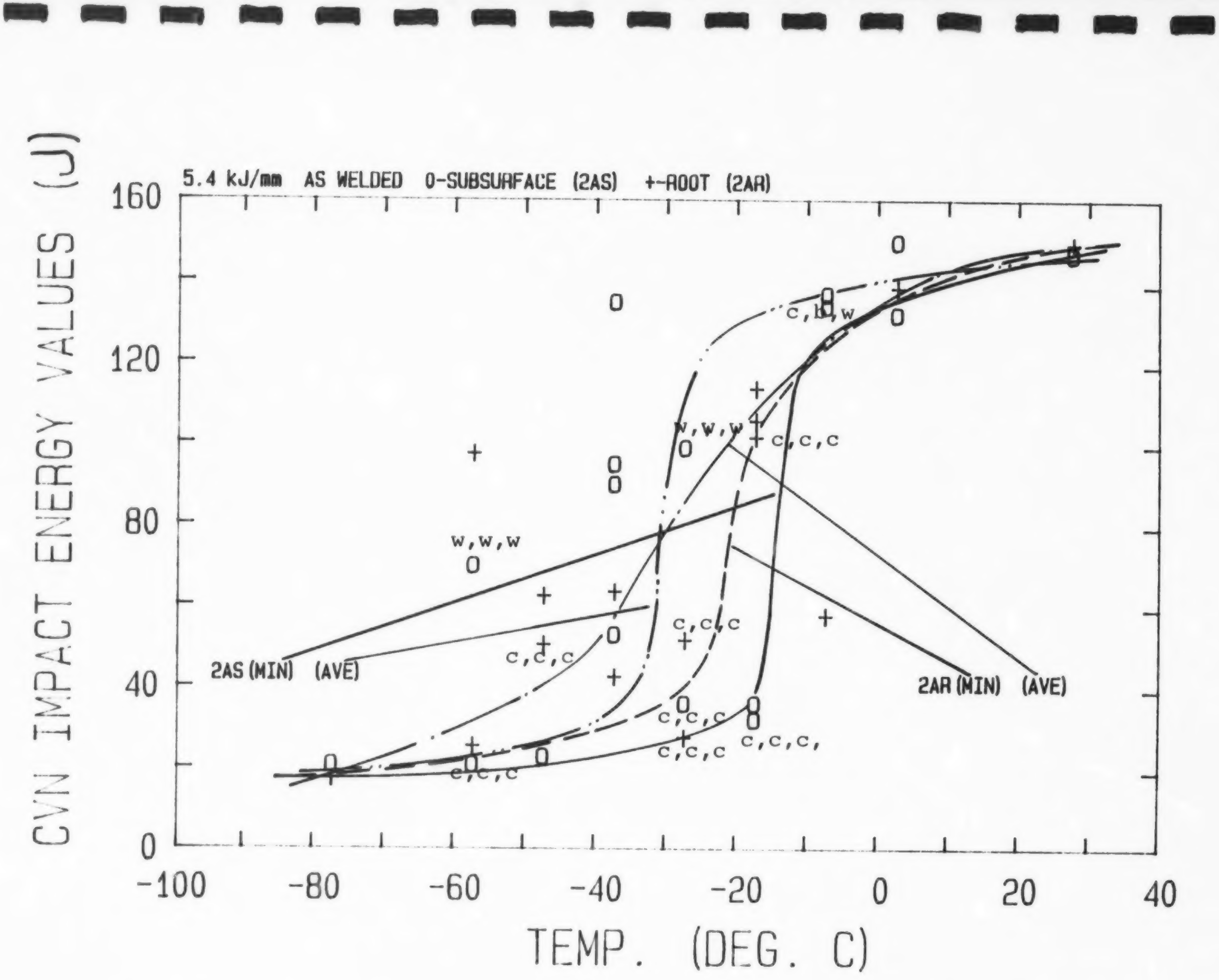

FIGURE 51: CVN impact energy transition curves for the "as-welded" CG HAZ in LT 60 steel welded with 5.4 kJ/mm heat input.

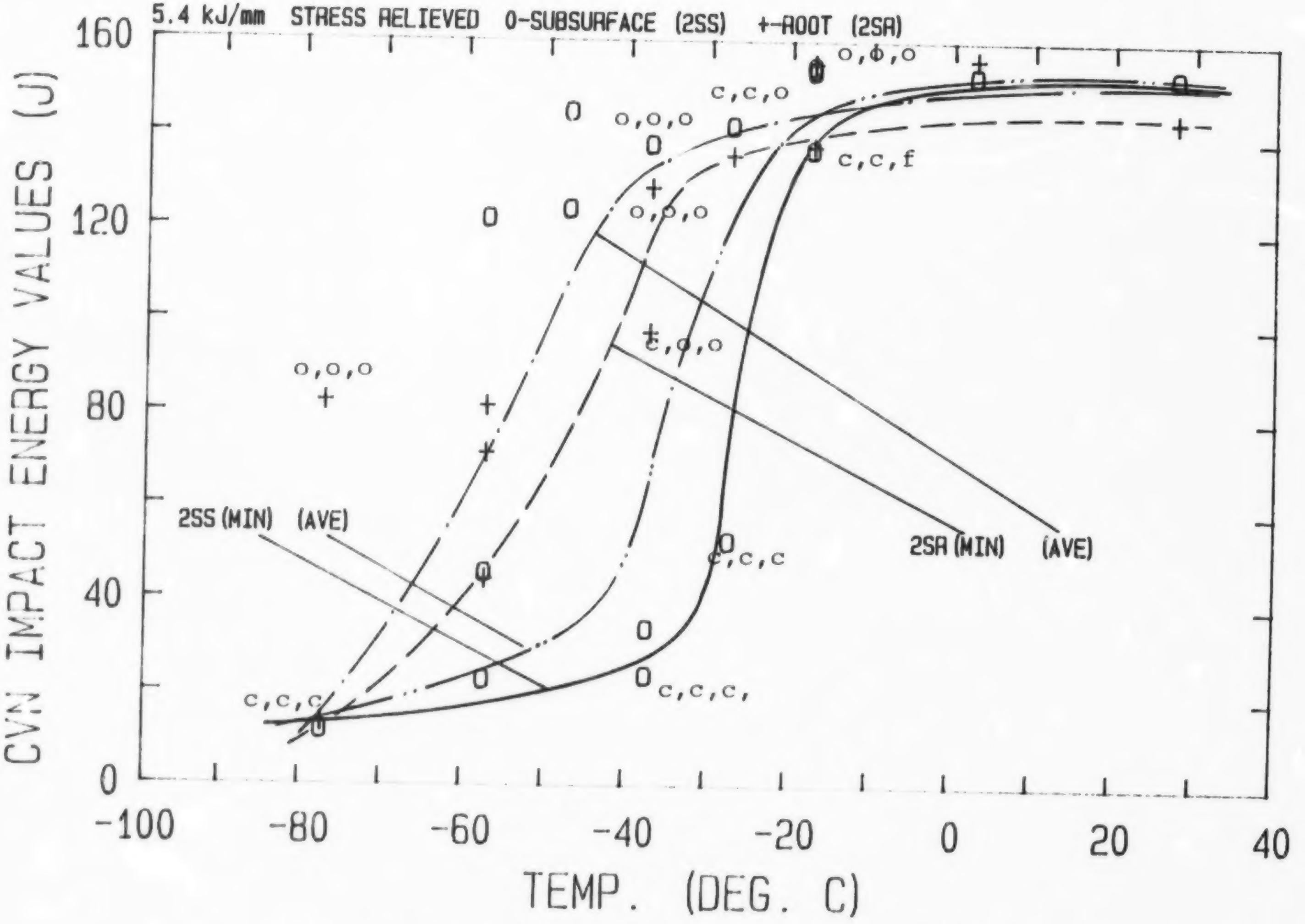

FIGURE 52: CVN impact energy transition curves for the "stress-relieved" CG HAZ in LT 60 steel welded with 5.4 kJ/mm heat input.

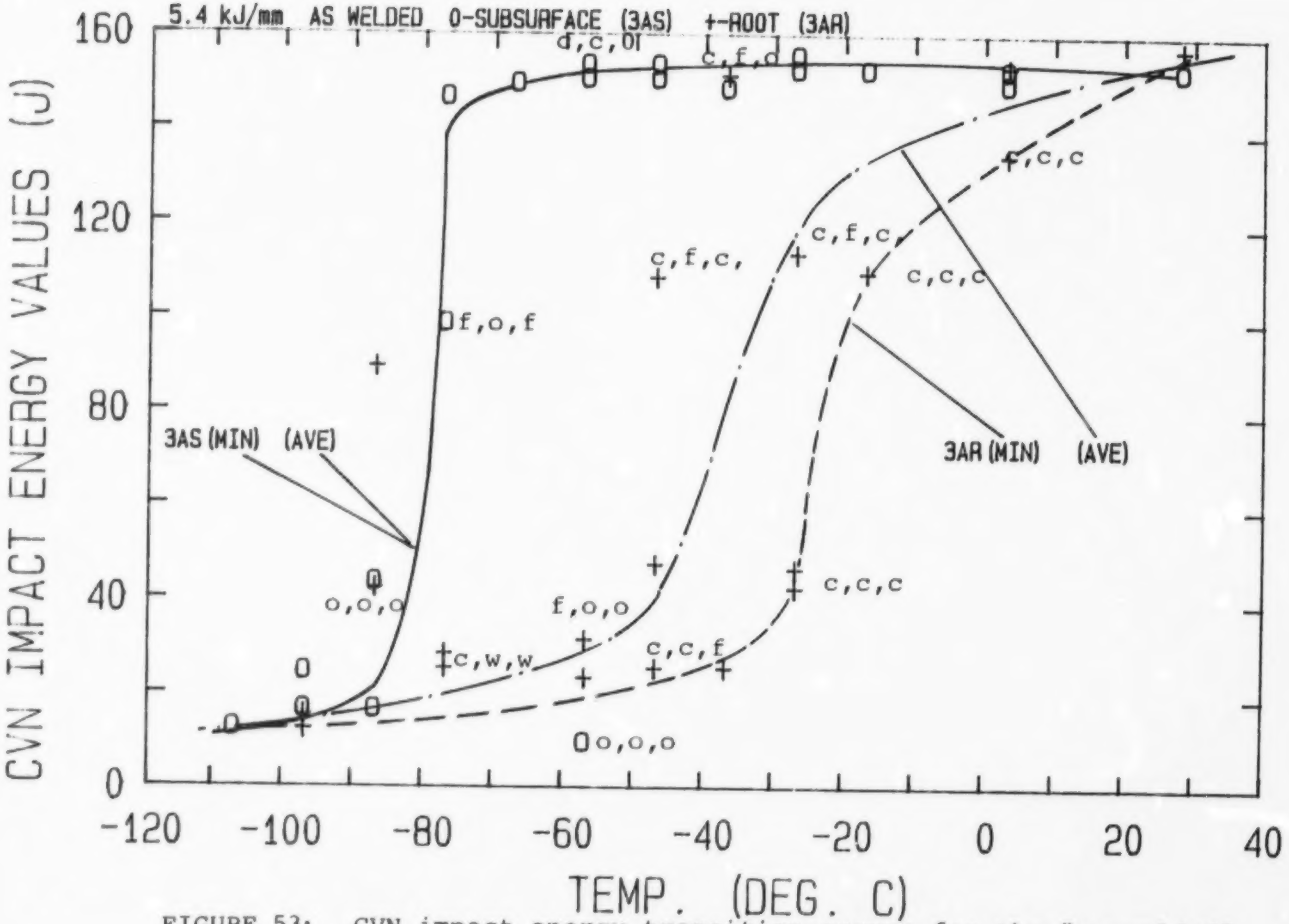

FIGURE 53: CVN impact energy transition curves for the "as-welded" CG HAZ in A710, Gr. A, Cl. 3 steel welded with 5.4 kJ/mm heat input.

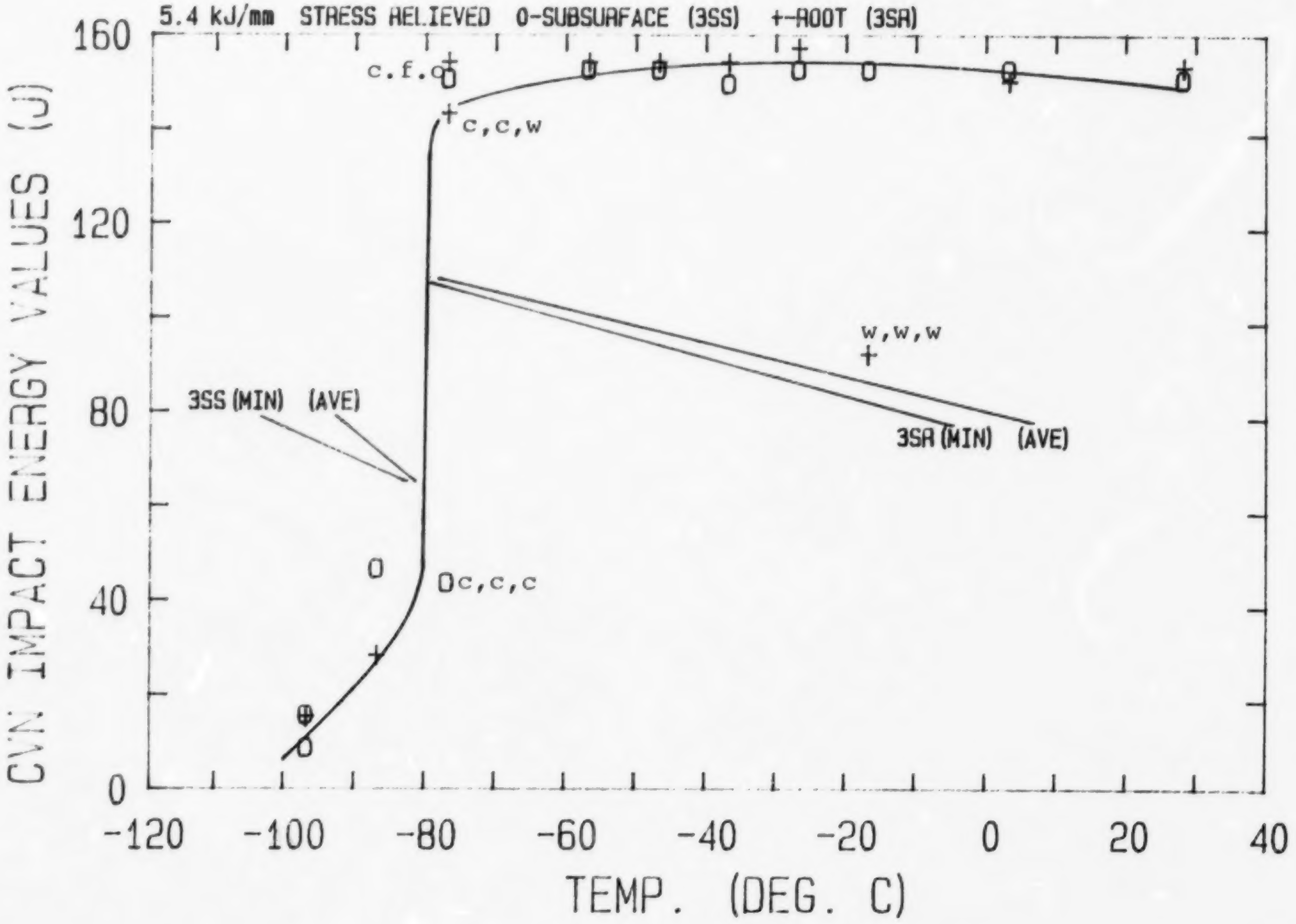

FIGURE 54: CVN impact energy transition curves for the "stress-relieved" CG HAZ in A710, Gr. A, Cl. 3 steel welded with 5.4 kJ/mm heat input.

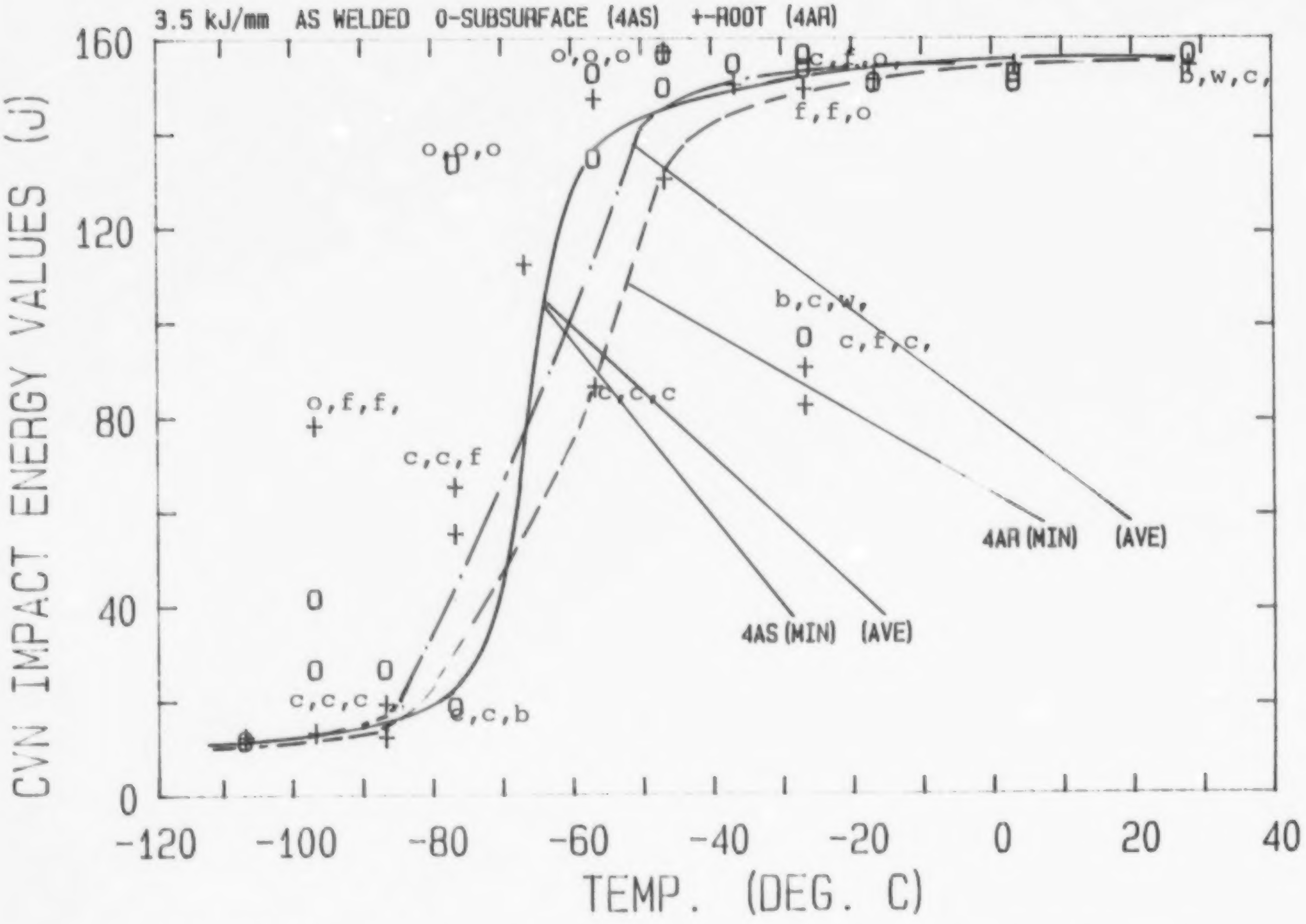

FIGURE 55: CVN impact energy transition curves for the "as-welded" CG HAZ in A710, Gr. A, Cl. 3 steel welded with 3.5 kJ/mm heat input.

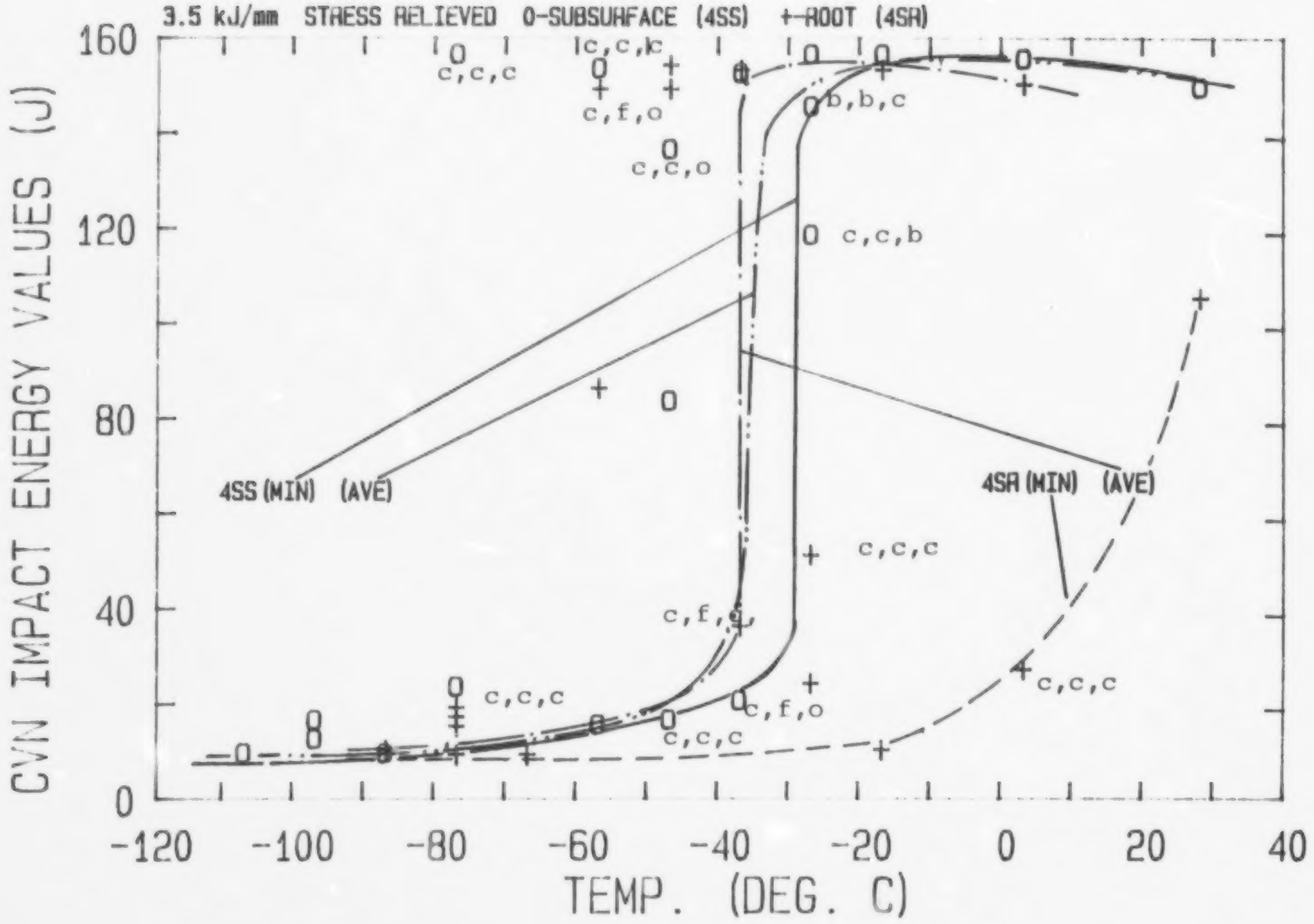

FIGURE 56: CVN impact energy transition curves for the "stress-relieved" CG HAZ in A710, Gr. A, Cl. 3 steel welded with 3.5 kJ/mm heat input.

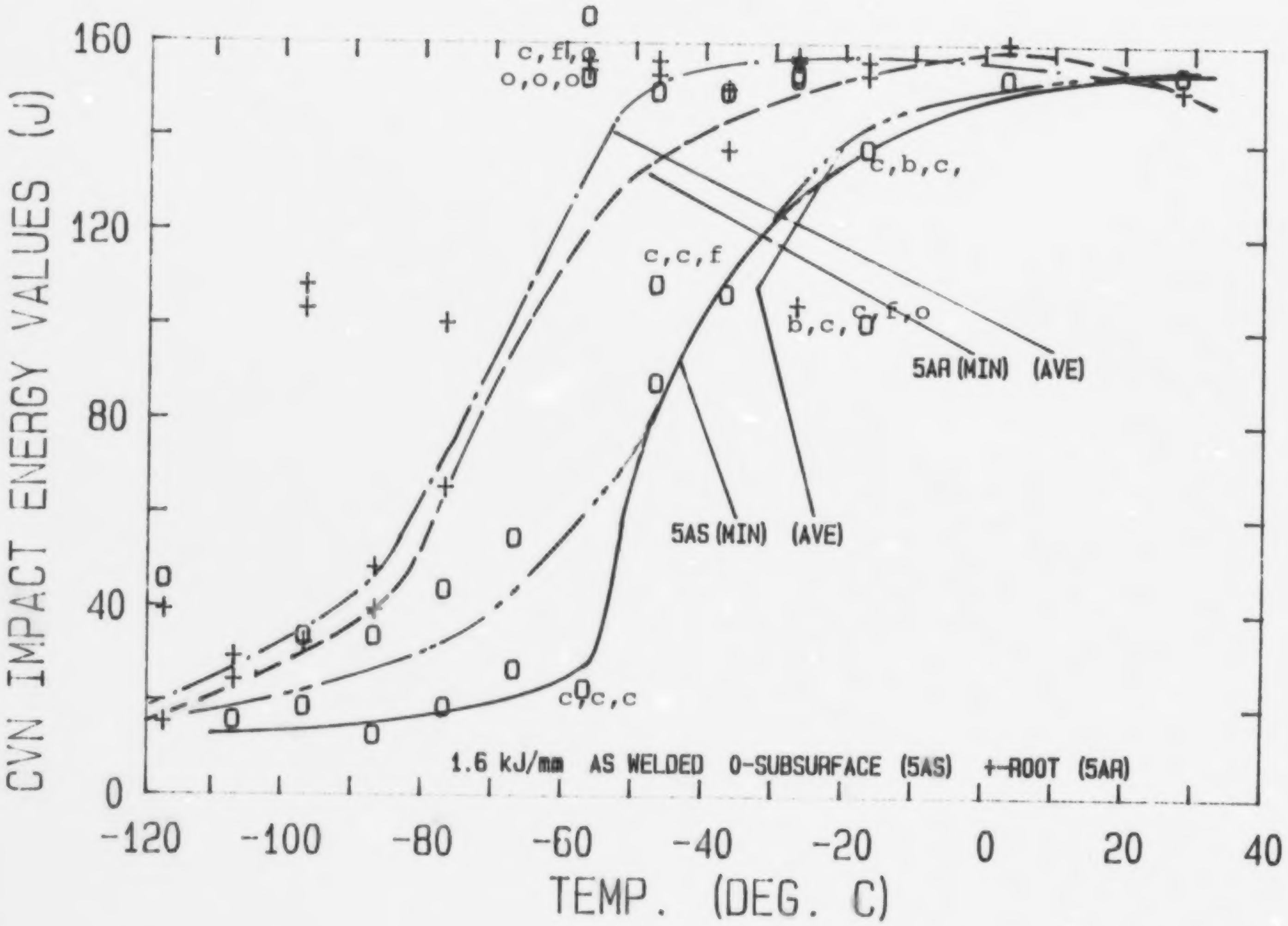

FIGURE 57: CVN impact energy transition curves for the "as-welded" CG HAZ in A710, Gr. A., Cl. 3 steel welded with 1.6 kJ/mm heat input.

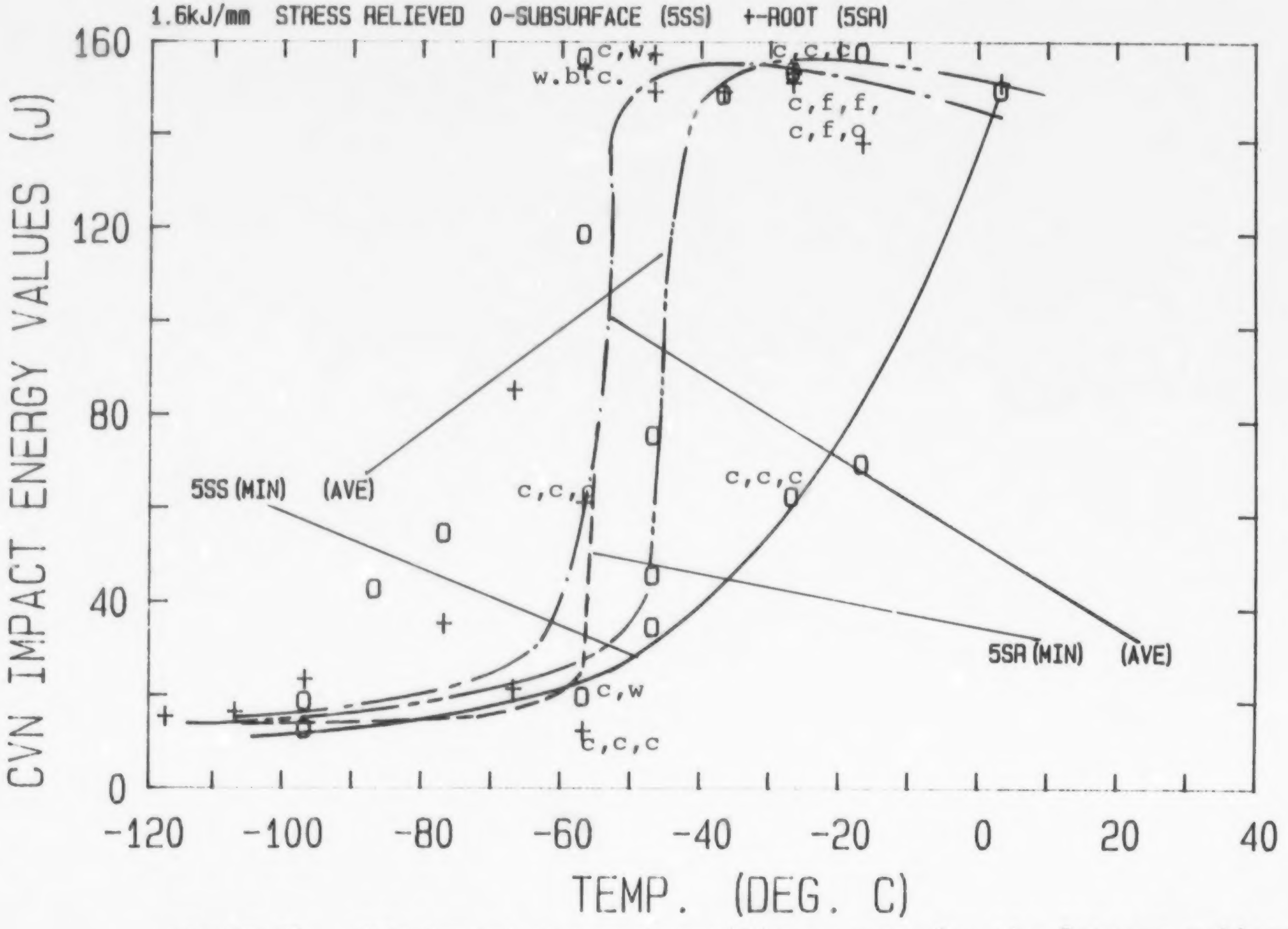

FIGURE 58: CVN impact energy transition curves for the "stress-relieved" CG HAZ in A710, Gr. A, Cl. 3 steel welded with 1.6 kJ/mm heat input.

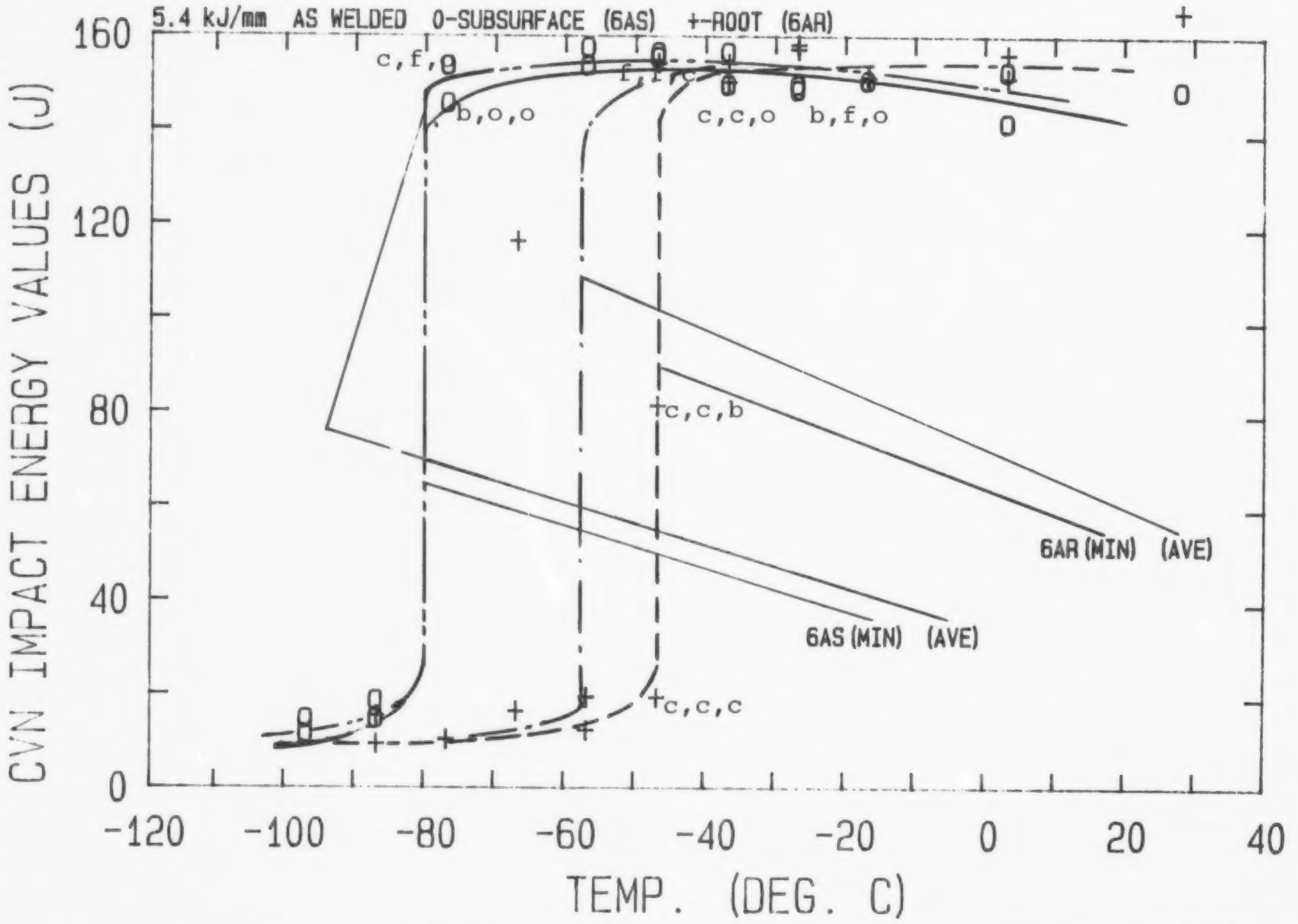

FIGURE 59: CVN impact energy transition curves for the "as-welded" CG HAZ in MACS (ACC) steel welded with 5.4 kJ/mm heat input.

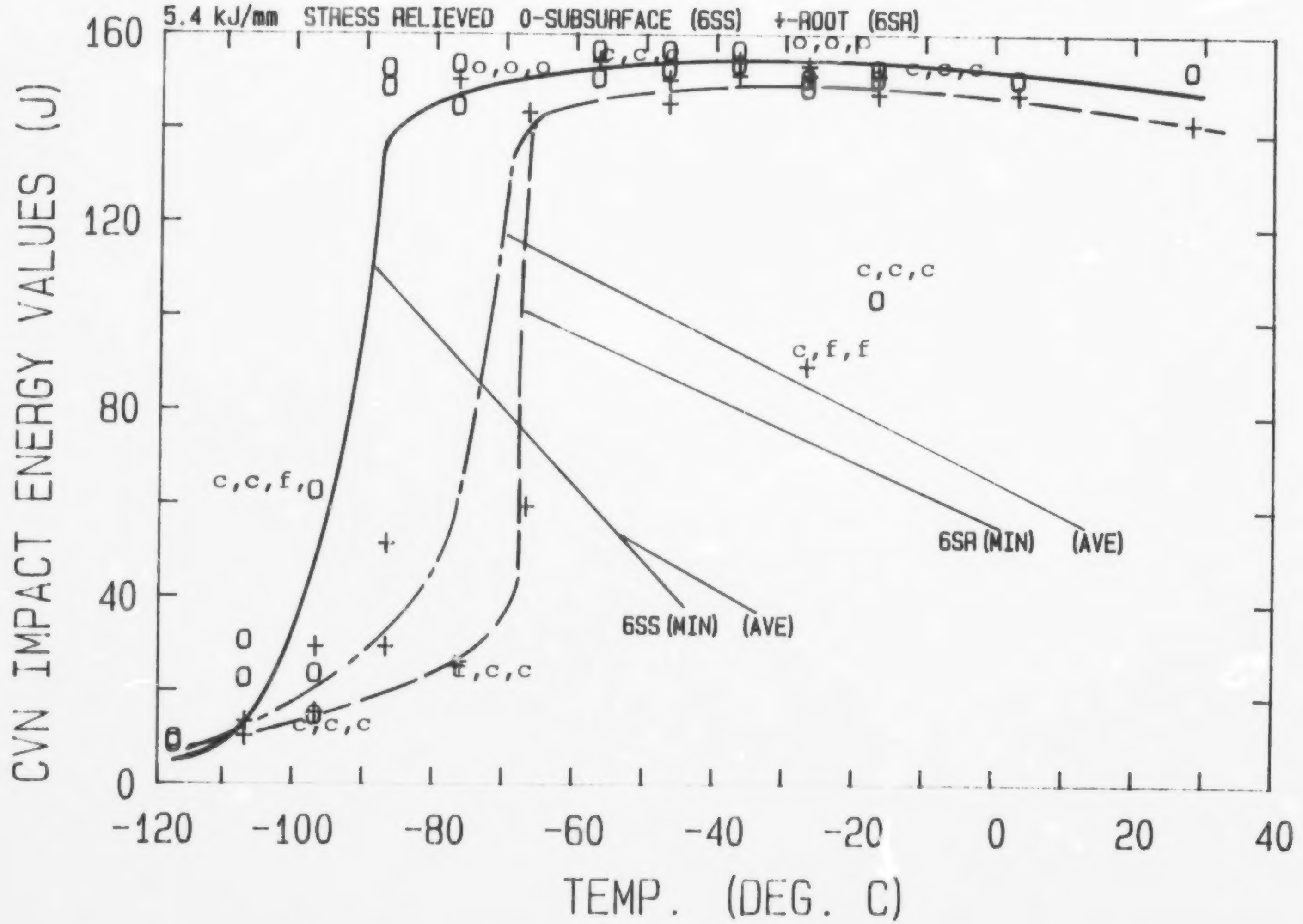

FIGURE 60: CVN impact energy transition curves for the "stress-relieved" CG HAZ in MACS (DOT) steel welded with 5.4 kJ/mm heat input.

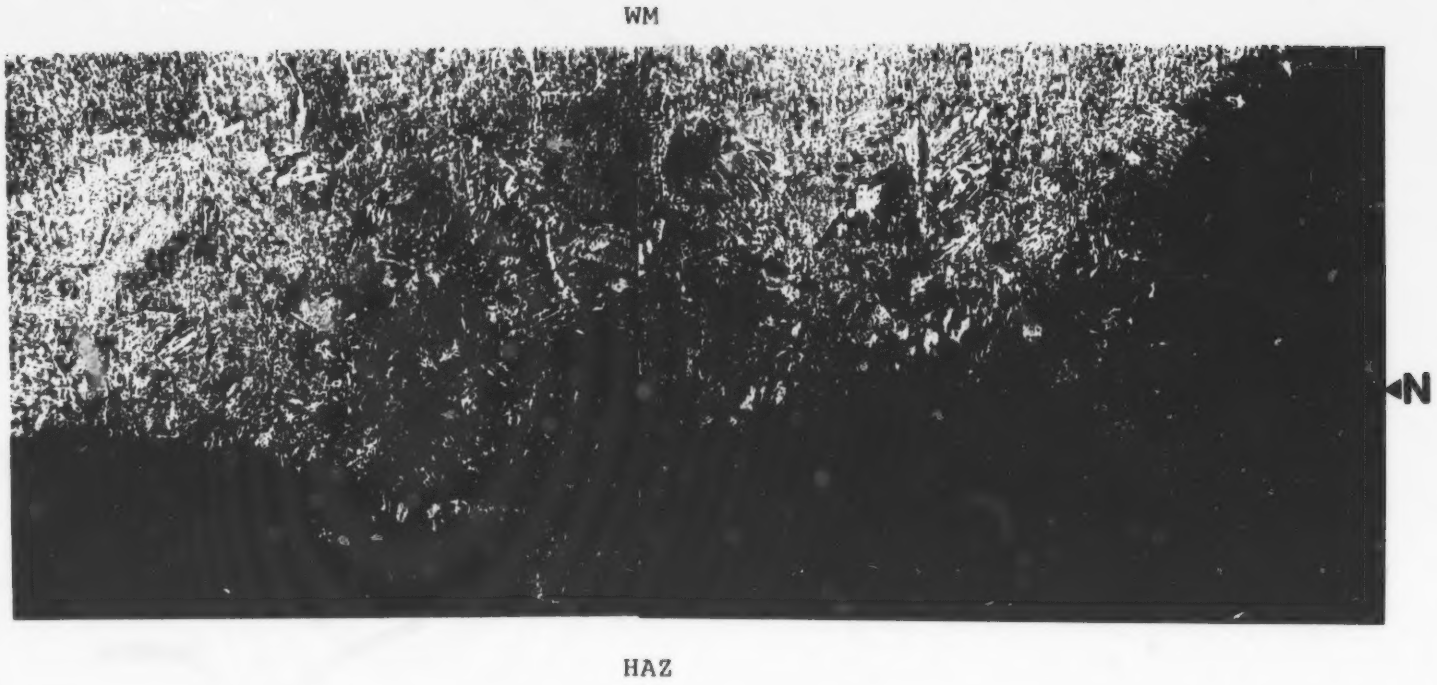

FIGURE 61: The microstructure at the root of the notch location in CVN specimen 1AR tested at -10°C (66J), Neg. 7994 and 7995, Mag. 100 x. (WM - weld metal, HAZ - heat affected zone and N - notch root).

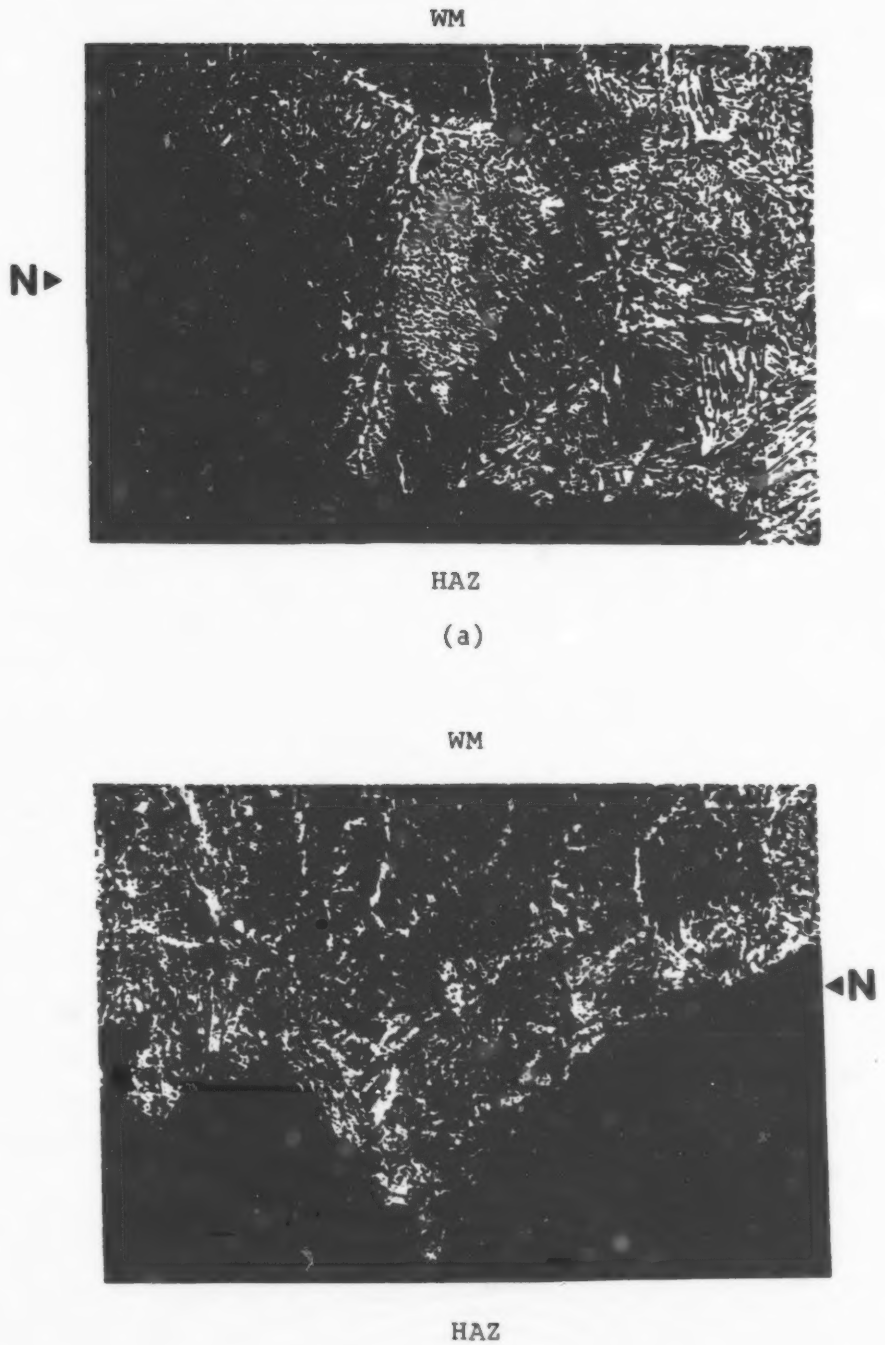

FIGURE 62: The microstructure at the root of the notch location in CVN specimens (a) 1AR tested at -50°C (7J), Neg. 8330, Mag. 200 x; and (b) 1SR tested at -30°C (12J), Neg. 8328, Mag. 200 x.

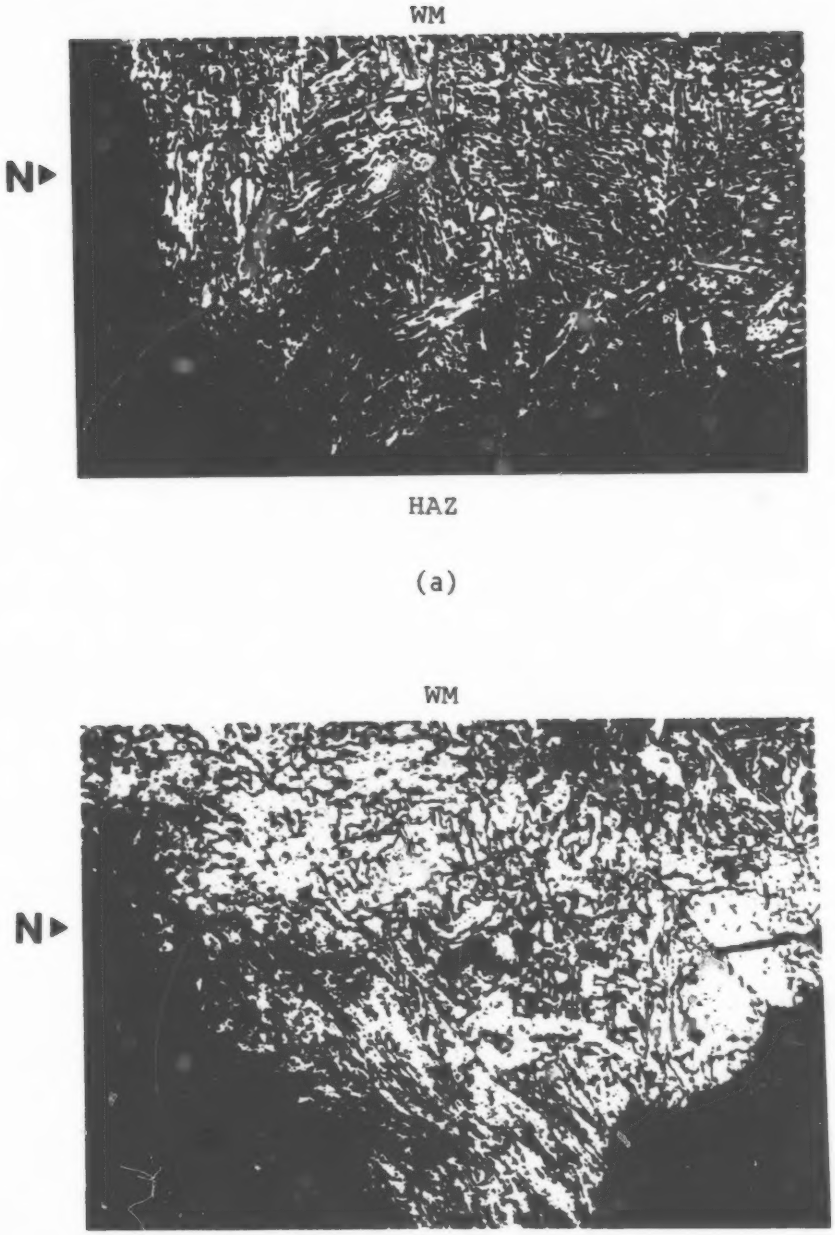

FIGURE 63: The microstructure at the root of the notch location in CVN specimens (a) 2AR tested at -30°C (22J), Neg. 8326, Mag. 200 x; and (b) 2SS tested at -30°C (48J), Neg. 8331, Mag. 200 x.

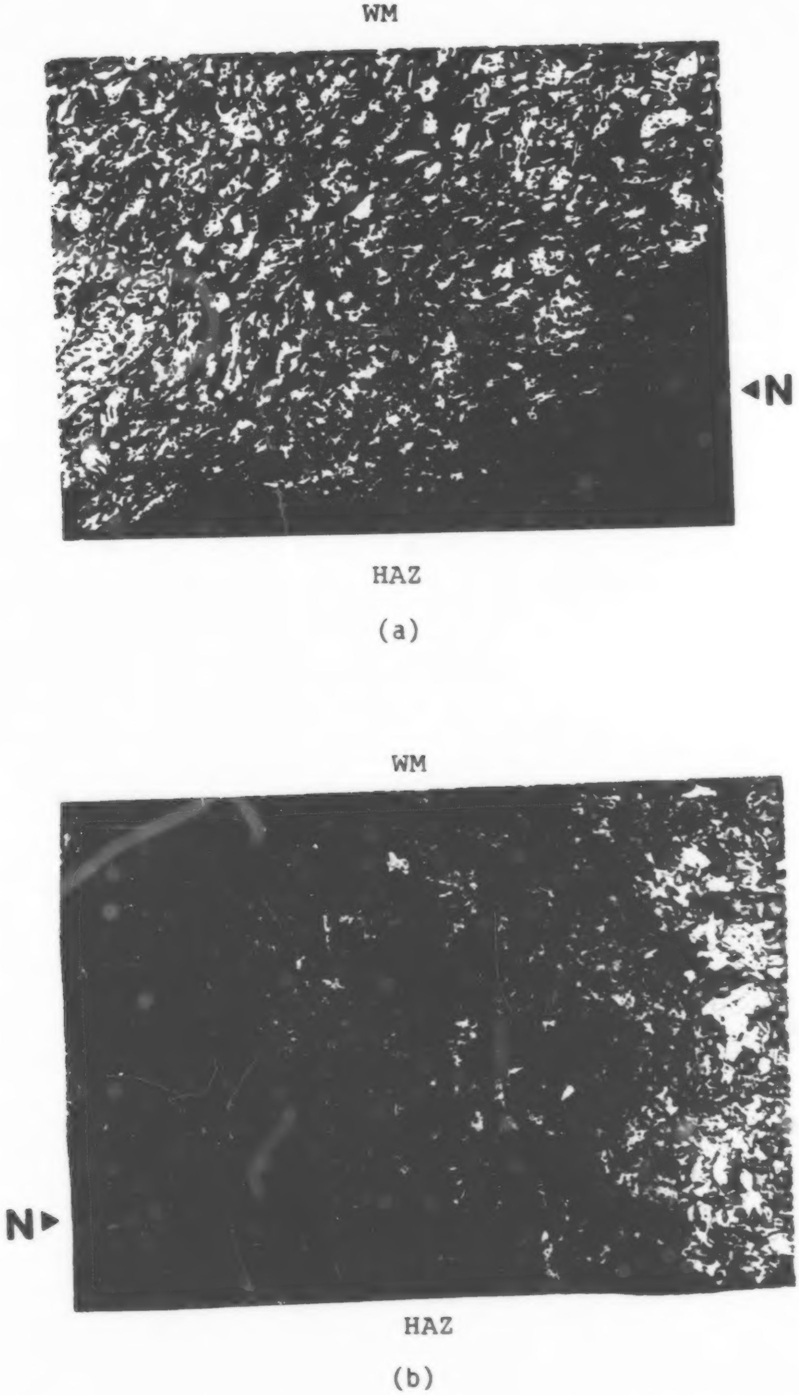

FIGURE 64: The microstructure at the root of the notch location in CVN specimens (a) 3AS tested at -60°C (149J), Neg. 8418, Mag. 200 x; and (b) 3AR tested at -30°C (37J), Neg. 8413, Mag. 200 x.

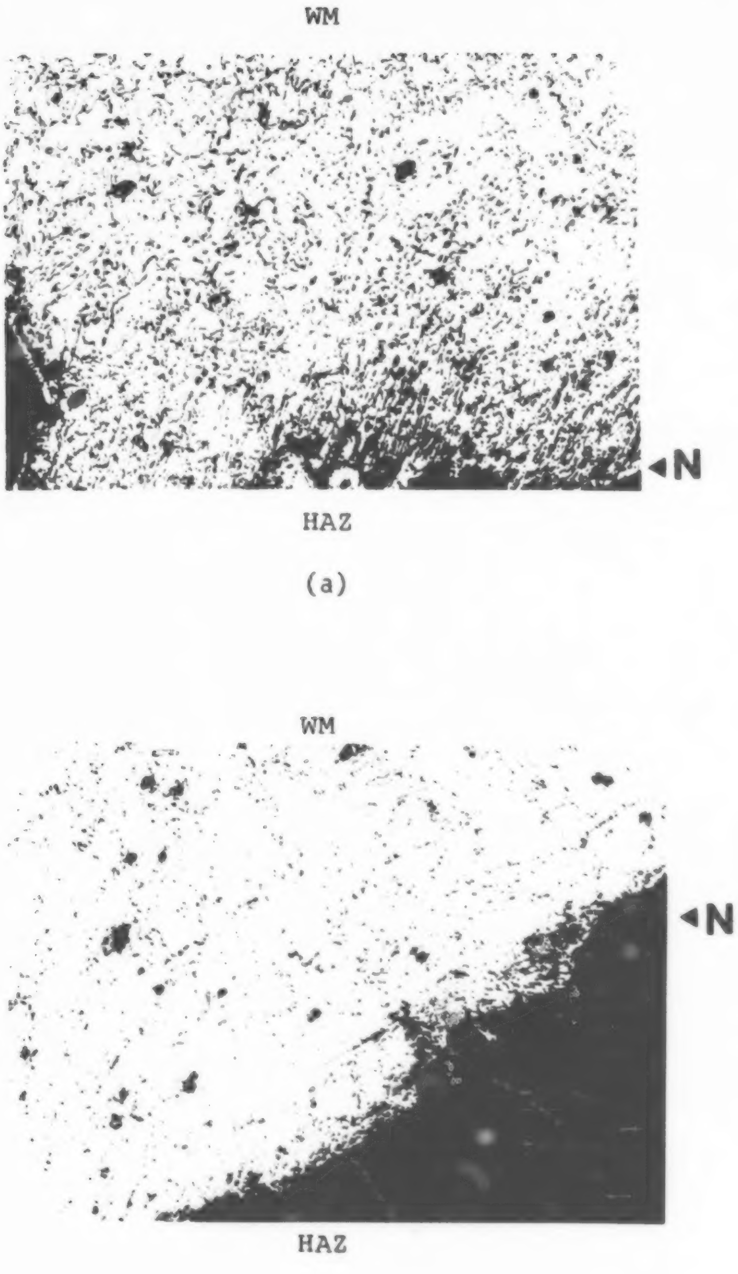

(a)

(b)

FIGURE 65: The microstructure at the root of the notch location in CVN specimens (a) 3SR tested at -30°C (138J), Neg. 8410, Mag. 200 x; and (b) 3SS tested at -80°C (39J), Neg. 8428, Mag. 200 x.

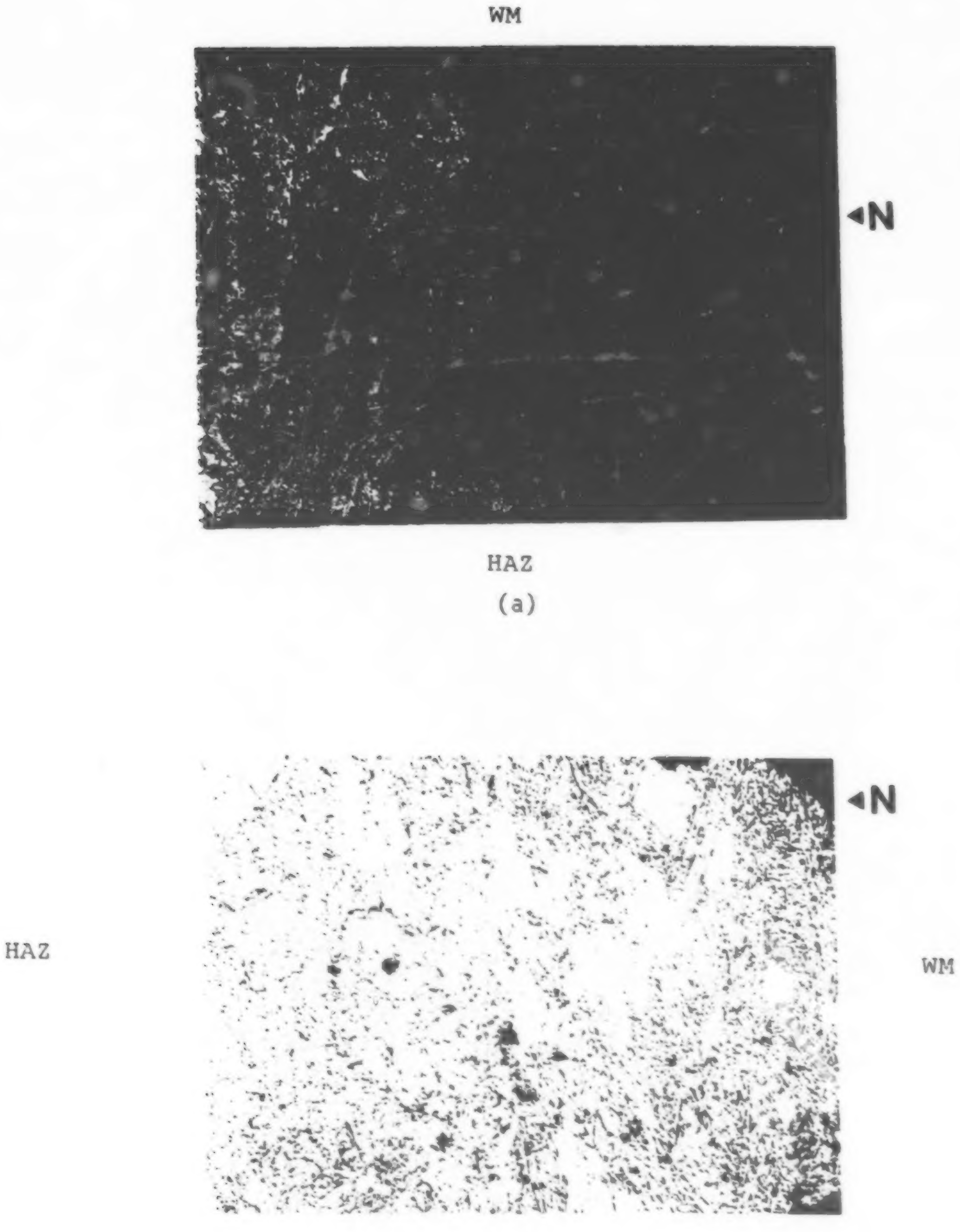

(a)

(b)

FIGURE 66: The microstructure at the root of the notch location in CVN specimens (a) 4AS tested at -80 °C (14J), Neg. 8433, Mag. 200 x; and (b) 4AR tested at -30°C (85J), Neg. 8417, Mag. 200 x.

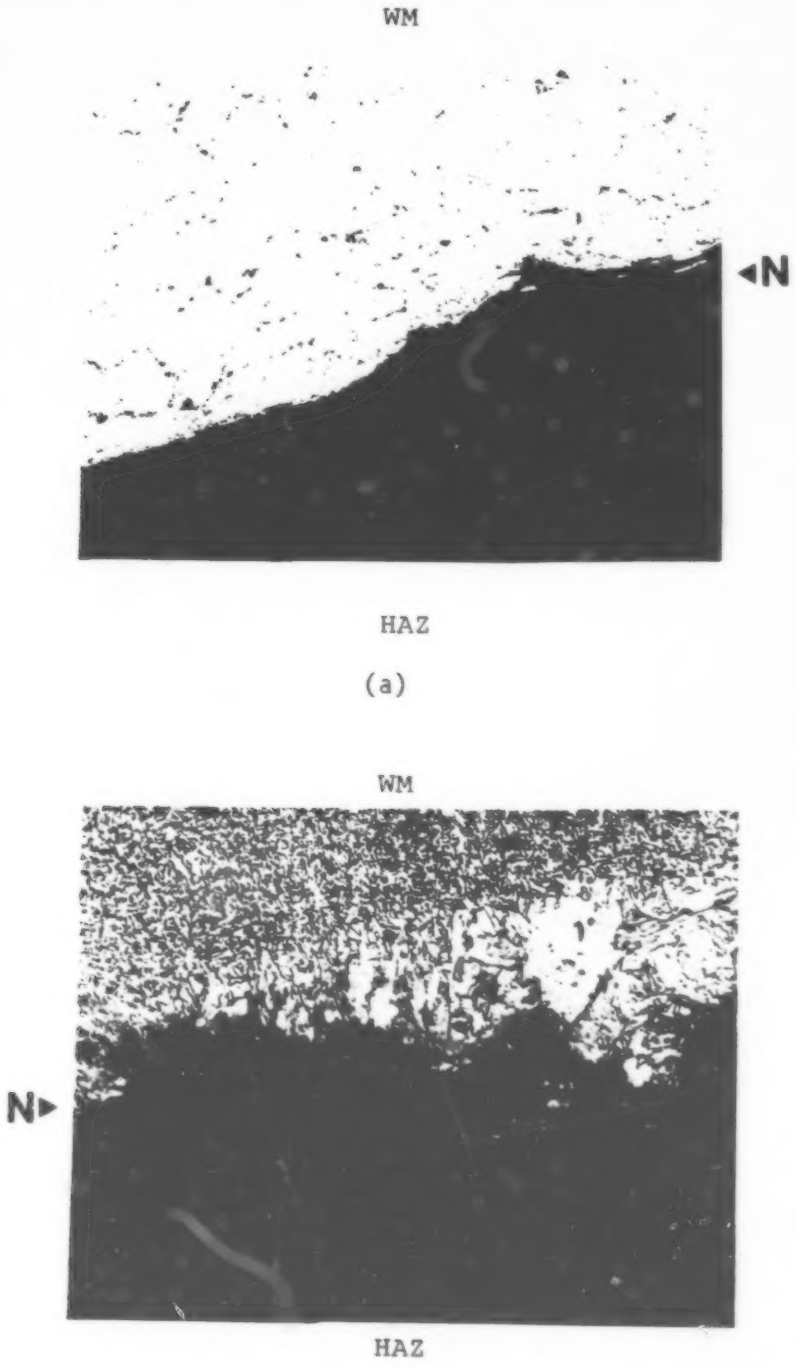

(a)

(b)

FIGURE 67: The microstructure at the root of the notch location in CVN specimens (a) 4SR tested at -60°C (81J), Neg. 8415, Mag. 200 x; and (b) 4SS tested at -50°C (12J), Neg. 8414, Mag. 200 x.

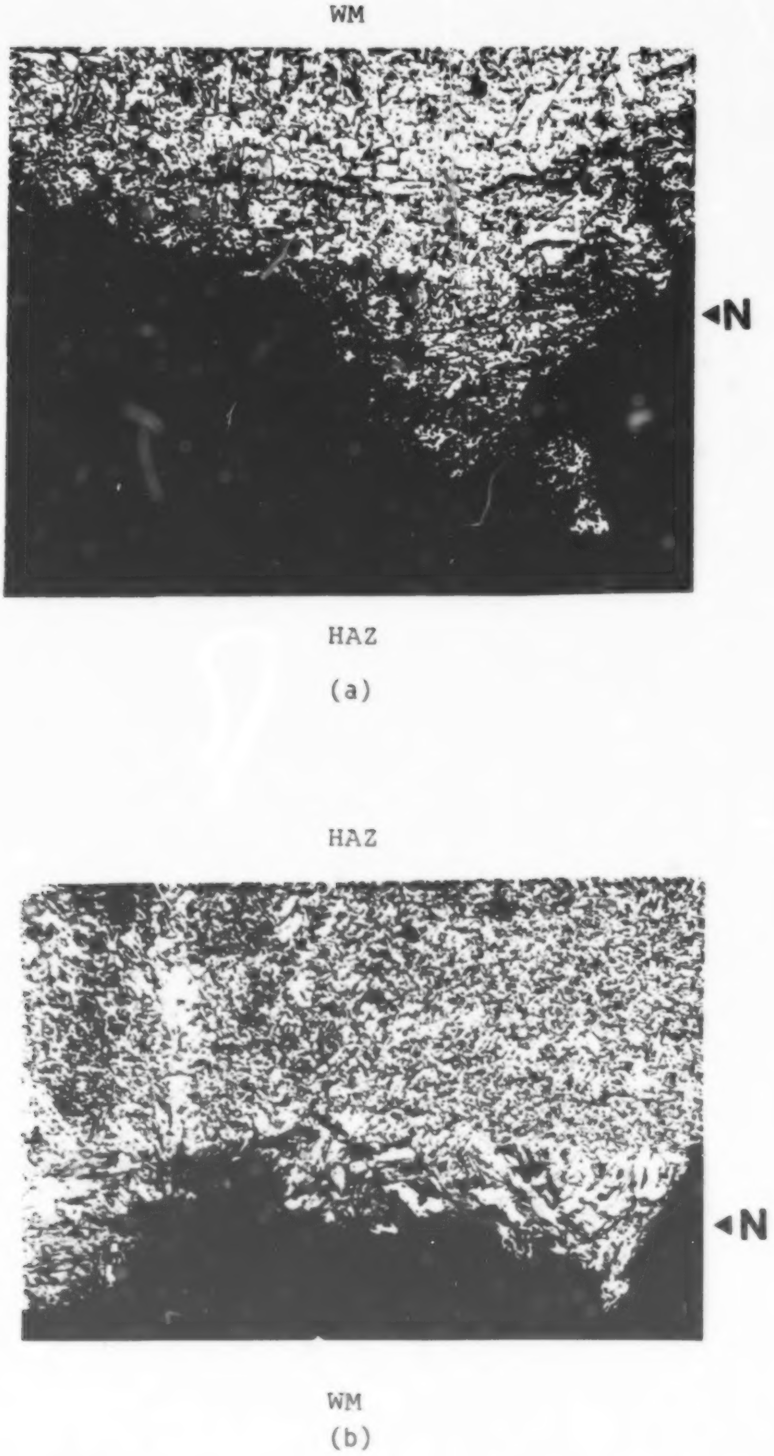

FIGURE 68: The microstructure at the root of the notch location in CVN specimens (a) 5AS tested at -60°C (18J), Neg. 8427, Mag. 200 x; and (b) 5SR tested at -60°C (7J), Neg. 8423, Mag. 200 x.

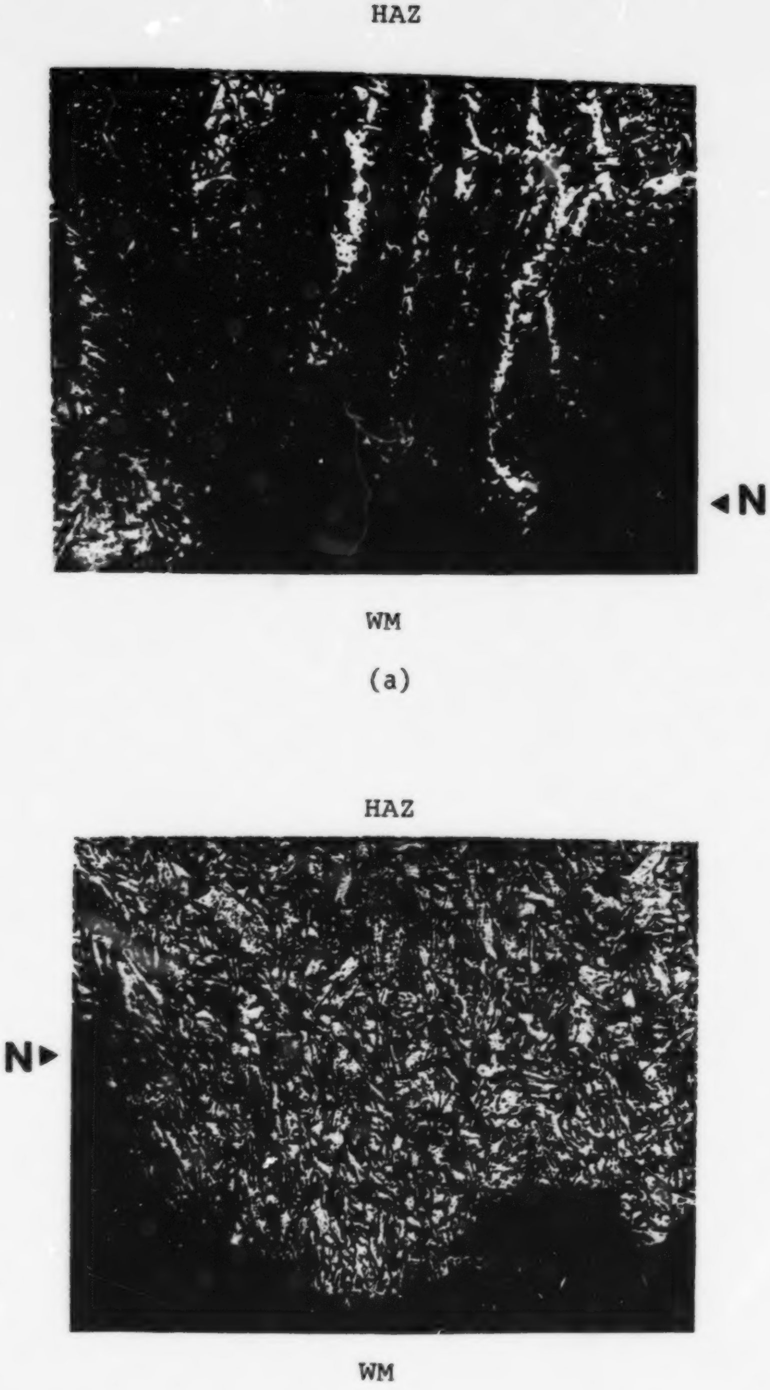

(a)

(b)

FIGURE 69: The microstructure at the root of the notch location in CVN specimens (a) 6AR tested at -50°C (14J), Neg. 8489, Mag. 200 x; and (b) 6SS tested at -100 °C (10J), Neg. 8432, Mag. 200 x.

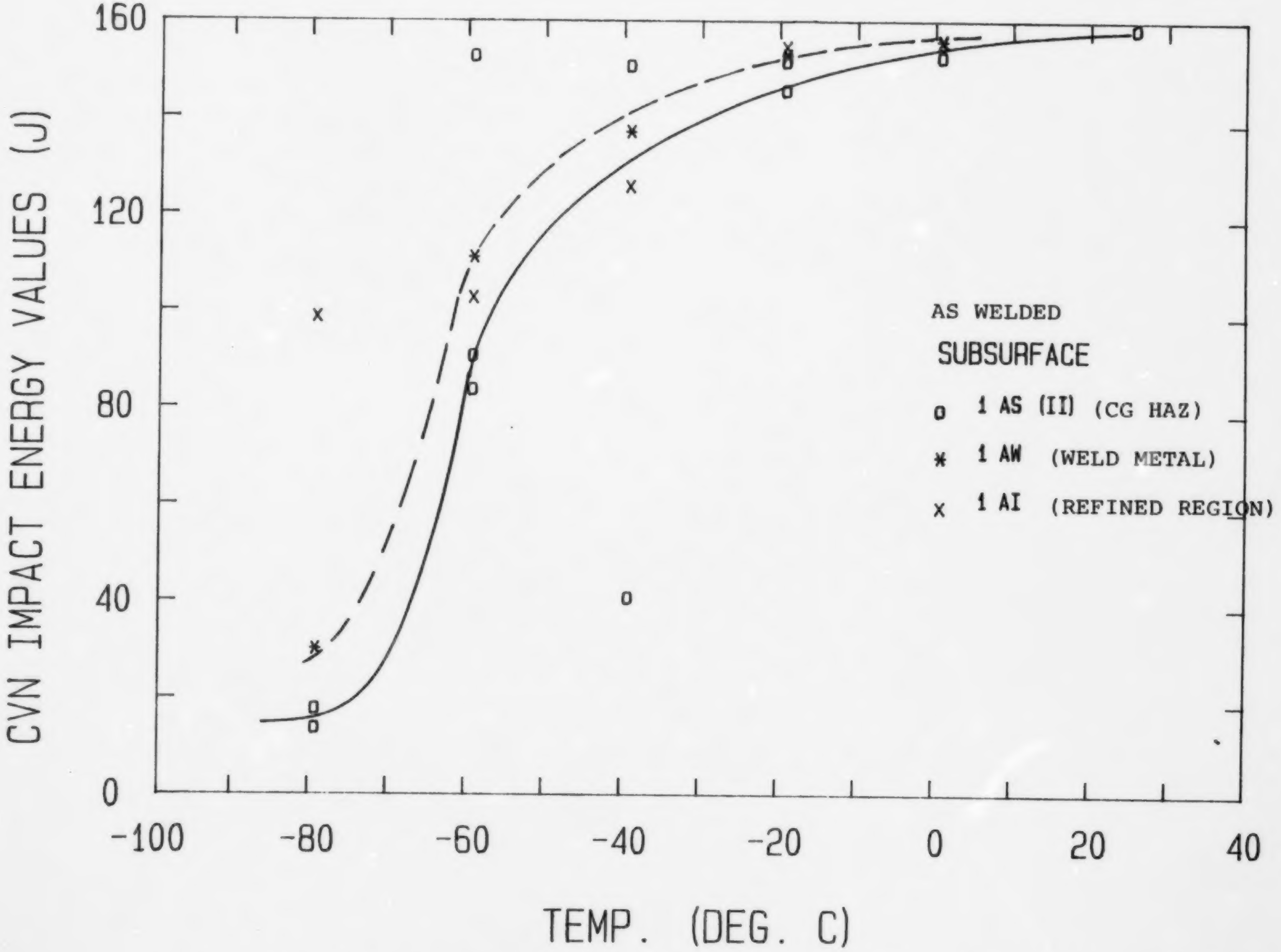

FIGURE 70 : CVN impact energy transition curves for the CG HAZ, Weld Metal and the refined HAZ in LT 60 steel (as-welded condition), welded with 3.5 kJ/mm heat input.

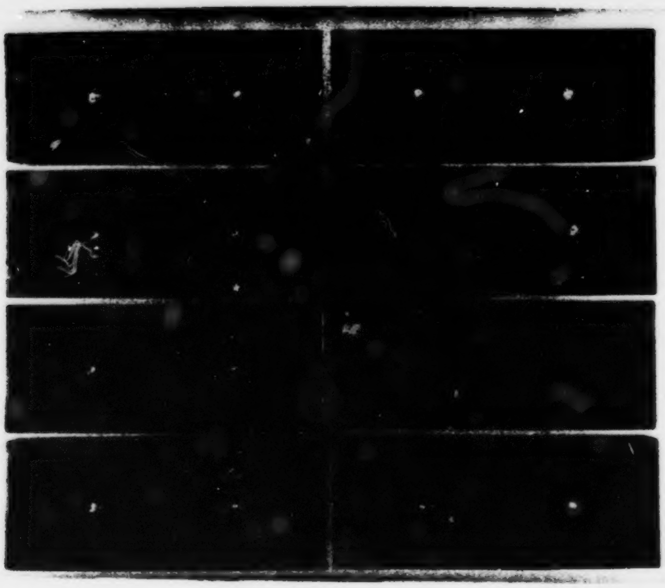

(a)

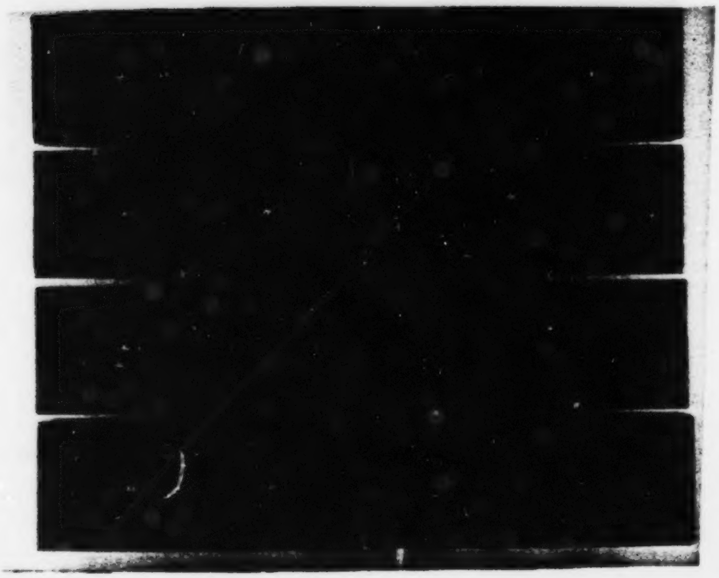

(b)

FIGURE 71: The drop weight test specimens for the CG HAZ in Algoma LT60 steel welded with 3.5 kJ/mm heat input (a) as-welded (1A), Neg. 7891; and (b) stress-relieved (1S) conditions, Neg. 7892.

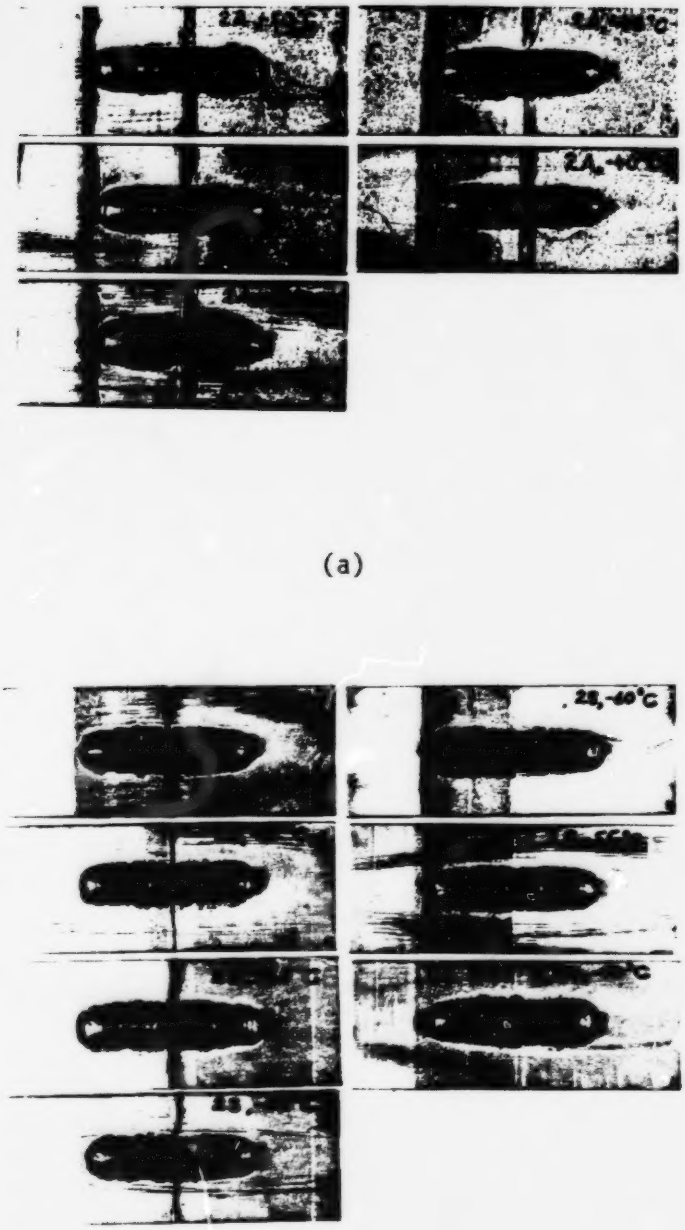

(a)

(b)

FIGURE 72: The drop weight test specimens for the CG HAZ in Algoma LT60 steel welded with 5.4 kJ/mm heat input (a) as-welded (2A) Neg. 52-E-4; and (b) stress-relieved (2S) conditions, Neg. 52-E-1.

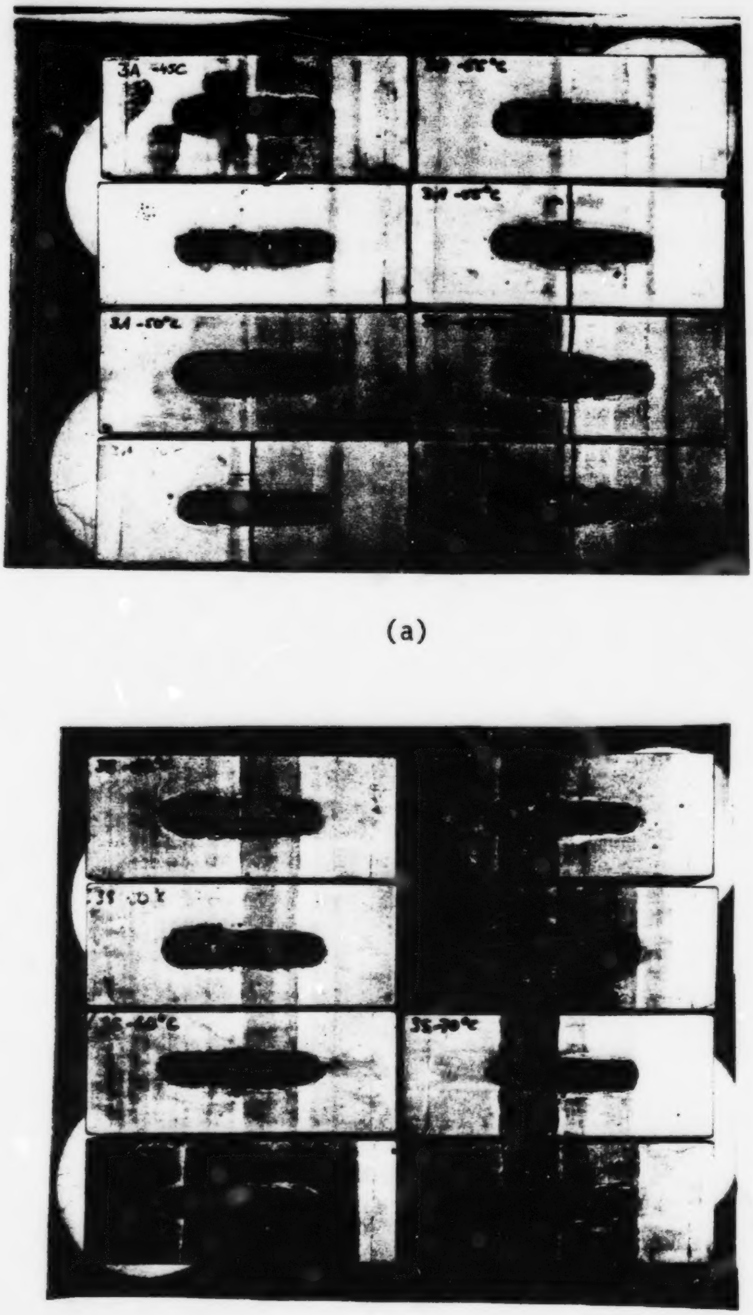
3A -45C
3A -50°C
3S -60°C
3S -30°C

(a)

(b)

FIGURE 73: The drop weight test specimens for the CG HAZ in A710 Gr. A, Cl. 3 steel welded with 5.4 kJ/mm heat input (a) as-welded (3A), Neg. 8206; and (b) stress-relieved (3S) conditions, Neg. 8207.

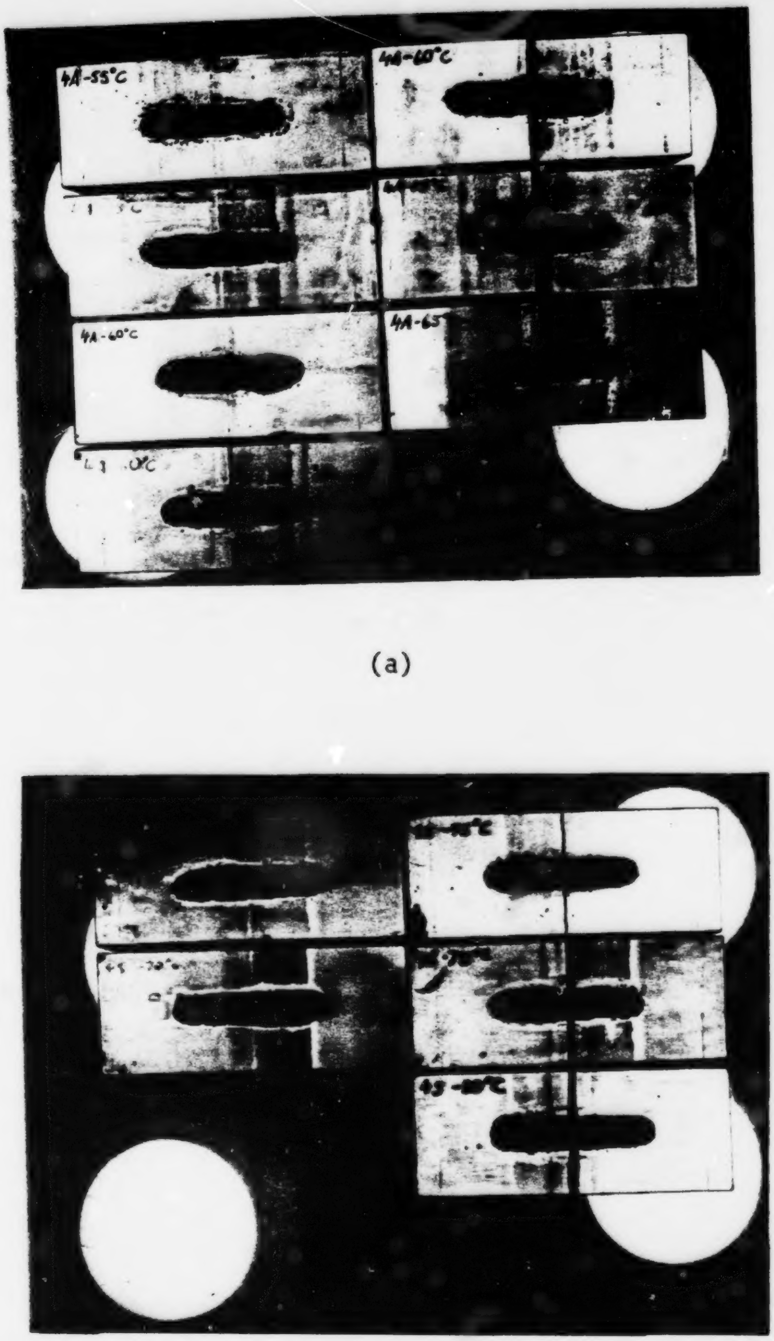
4A-55°C
4A-60°C
4A-60°C
4A-65
4S-20°C

(a)

(b)

FIGURE 74: The drop weight test specimens for the CG HAZ in A710 Gr. A, Cl. 3 steel welded with 3.5 kJ/mm heat input (a) as-welded (4A), Neg. 8208; and (b) stress-relieved (4S) conditions, Neg. 8209.

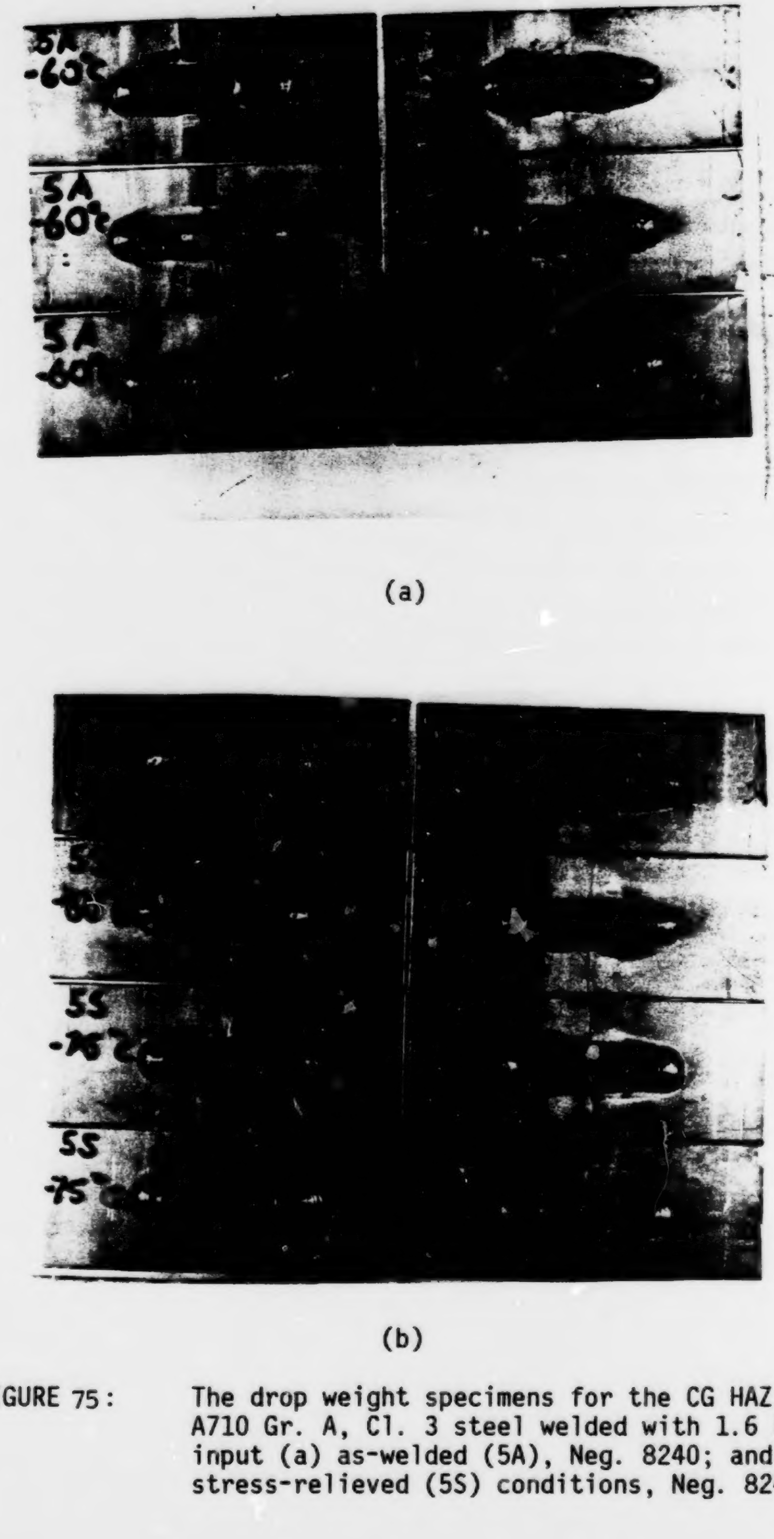
5A
-60°C
5A
-60°C
5A
-60°C
5S
-60°C
5S
-75°C
5S
-75°C

(a)

(b)

FIGURE 75: The drop weight specimens for the CG HAZ in A710 Gr. A, Cl. 3 steel welded with 1.6 kJ/mm heat input (a) as-welded (5A), Neg. 8240; and (b) stress-relieved (5S) conditions, Neg. 8241.

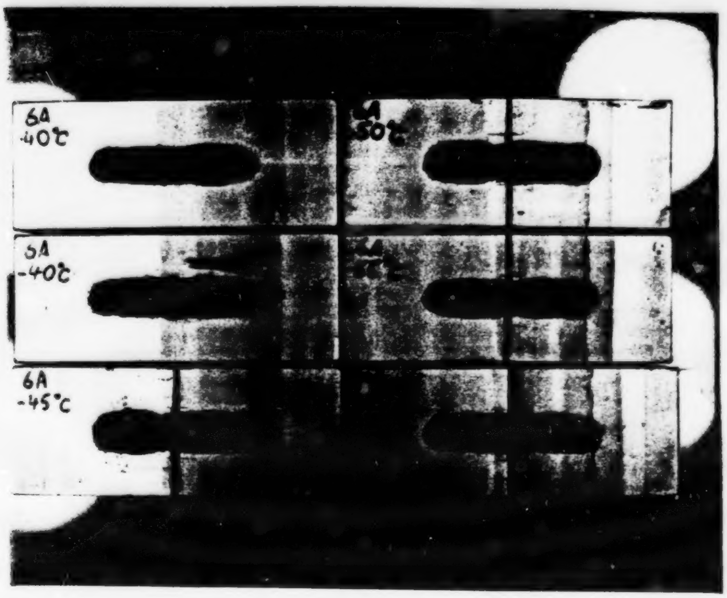
6A
40°C
6A
50°C
6A
-40°C
6A
-45°C

(a)

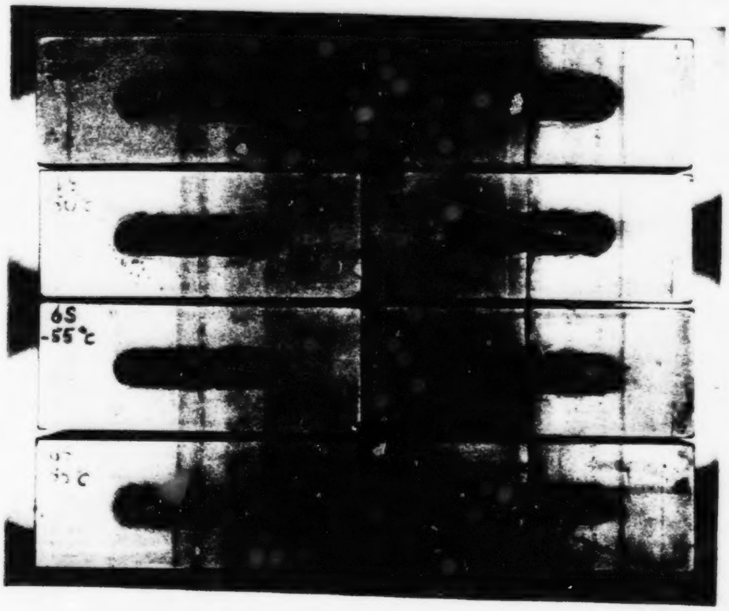

(b)

FIGURE 76. The drop weight specimens for the CG HAZ in Kawasaki MACS steel welded with 5.4 kJ/mm heat input (a) as welded (ACC, 6A), Neg. 8257; and (b) stress-relieved (DQT, 6S) conditions, Neg. 8258.

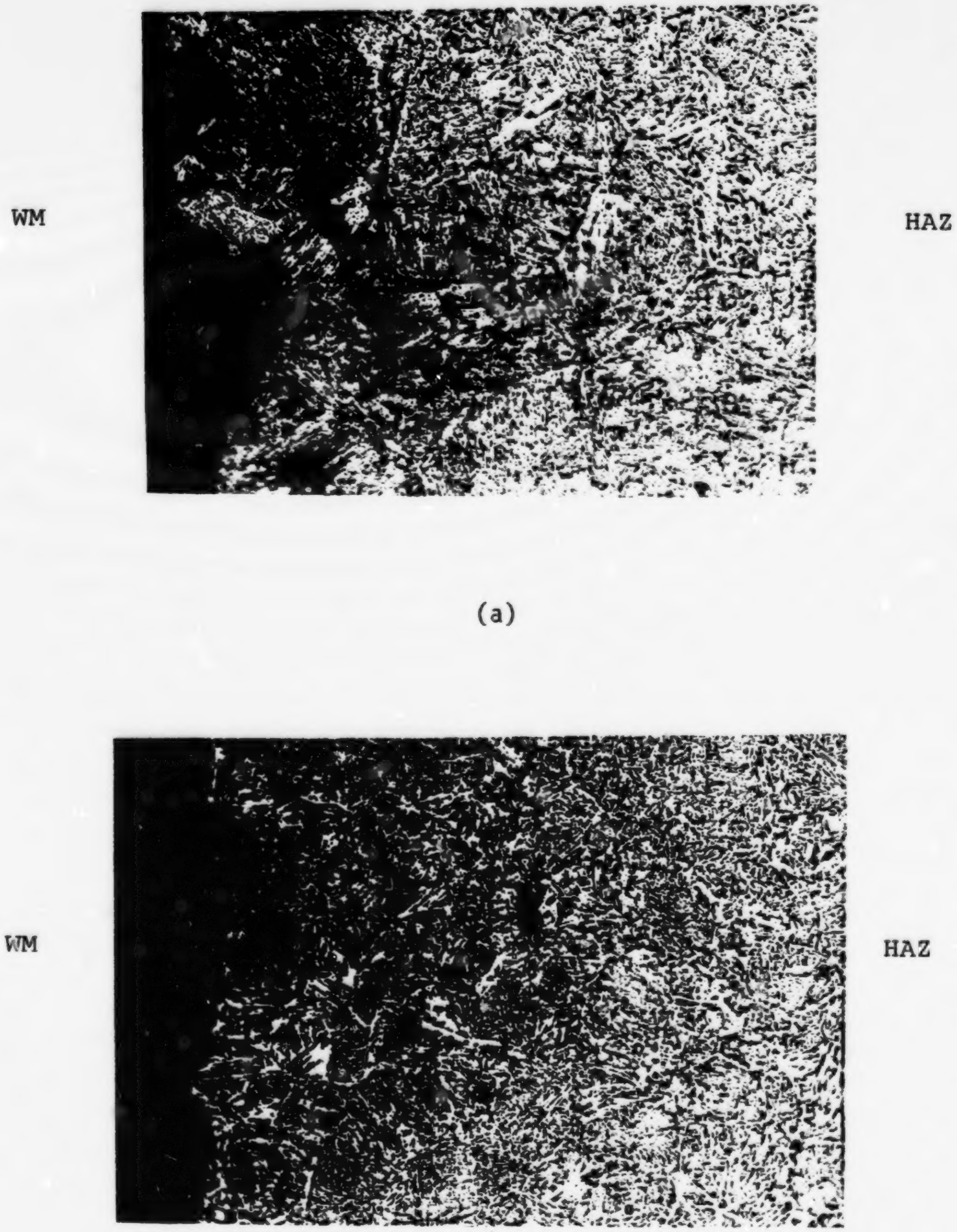

(a)

(b)

FIGURE 77: The location of the crack in the broken drop weight specimen showing the CG HAZ in (a) 1A specimen tested at -60°C. Neg. 7898, Mag. 200 x; and (b) 1S specimen tested at -65°C, Neg. 7897, Mag. 200 x.

WM

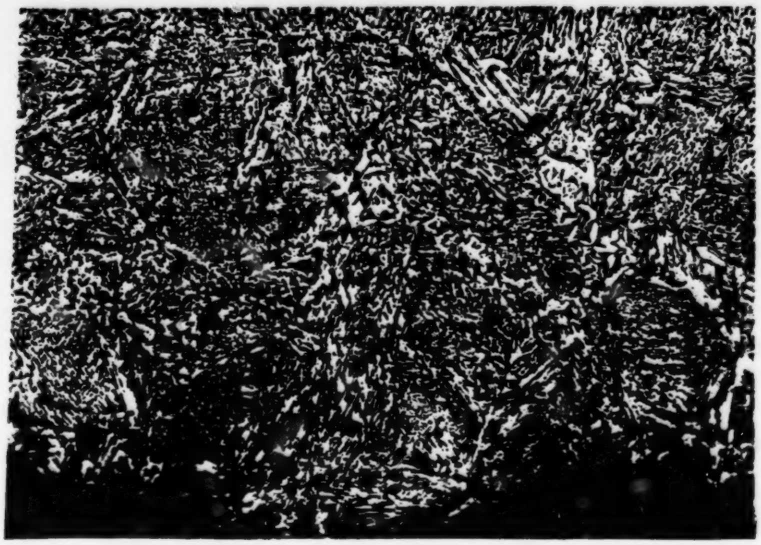

HAZ

(a)

WM

HAZ

(b)

FIGURE 78: The location of the crack in the broken drop weight specimen showing the CG HAZ in (a) 2A specimen tested at -45 °C, Neg. 8288, Mag. 200 x; and (b) 2S specimen tested at -60°C, Neg. 8287, Mag. 200 x.

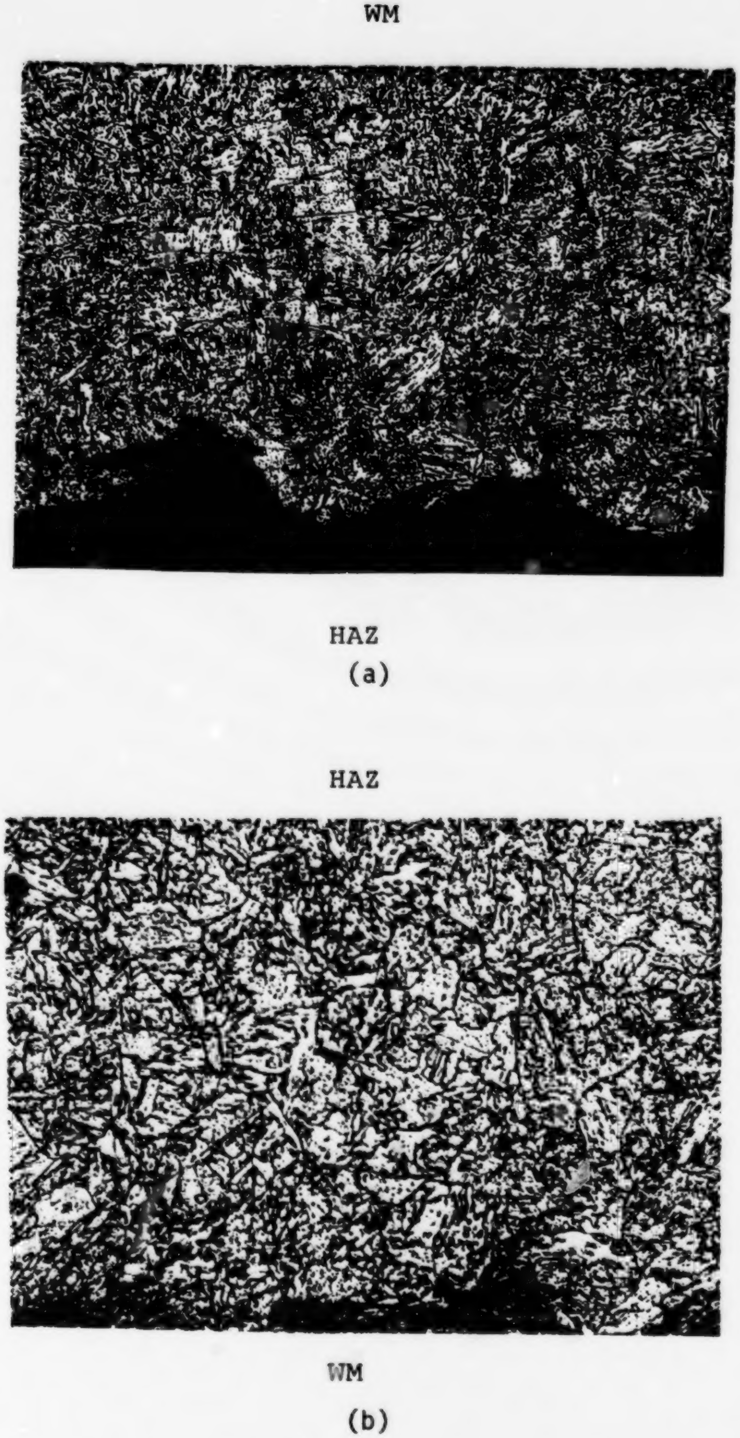

FIGURE 79: The location of the crack in the broken drop weight specimen showing the CG HAZ in (a) 3A specimen tested at -50°C, Neg. 8280, Mag. 200 x; and (b) 3S specimen tested at -65°C, Neg. 8283, Mag. 200 x.)

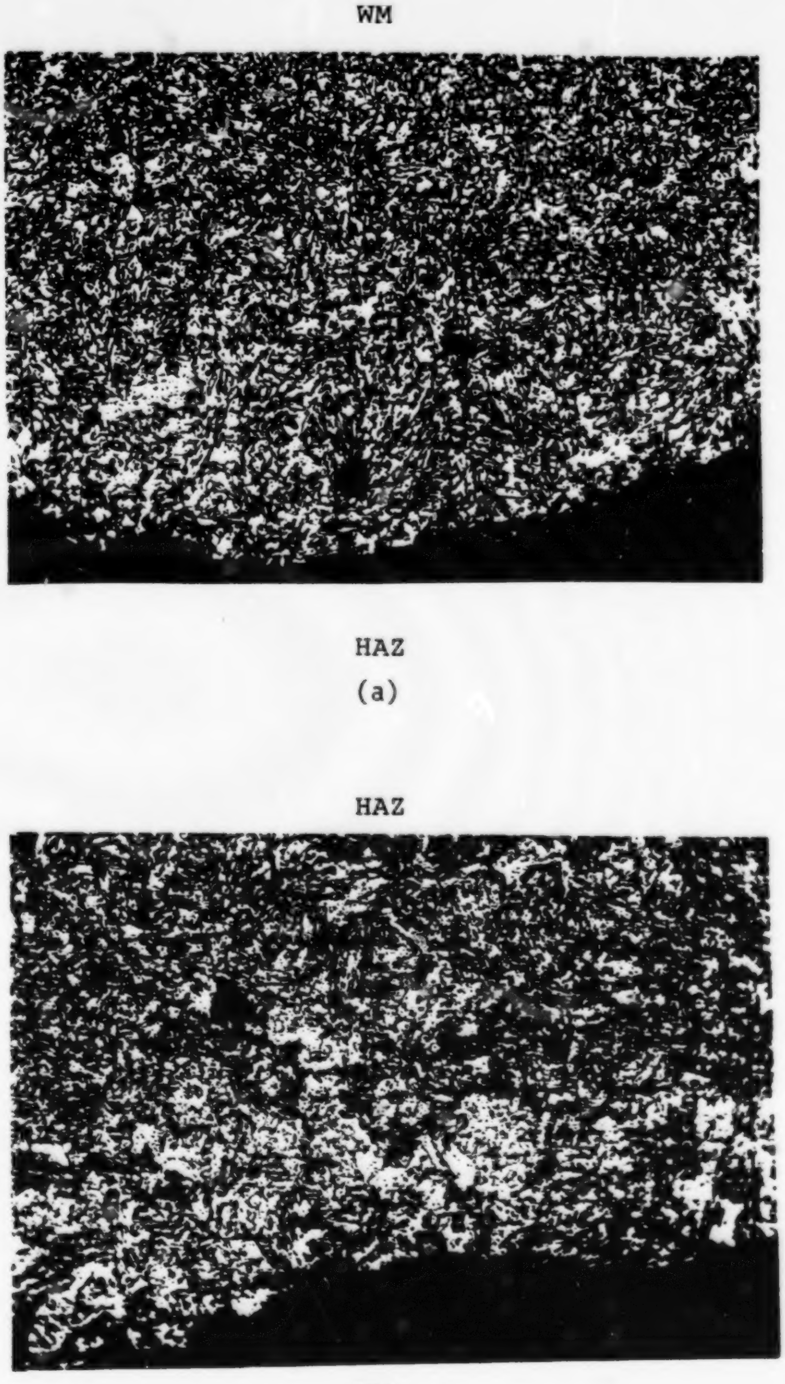

(a)

(b)

FIGURE 8Q: The location of the crack in the broken drop weight specimen showing (a) the refined HAZ structure in 4A tested at -65°C, Neg. 8284, Mag. 200 x; and (b) the CG HAZ structure in 4A tested at -60°C, Neg. 8285, Mag. 200 x.

WM

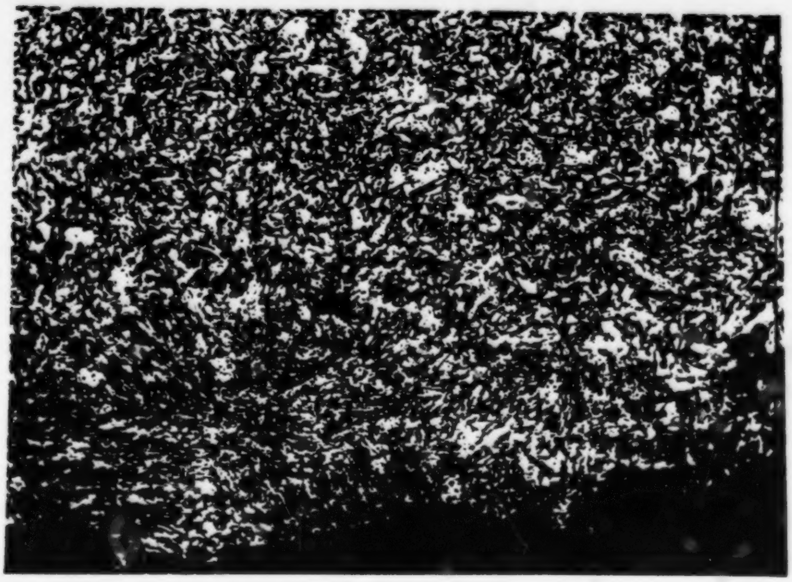

HAZ

FIGURE 81: The location of the crack in the broken drop weight specimen showing the refined HAZ in 4S tested at -75°C, Neg. 8286, Mag. 200 x.

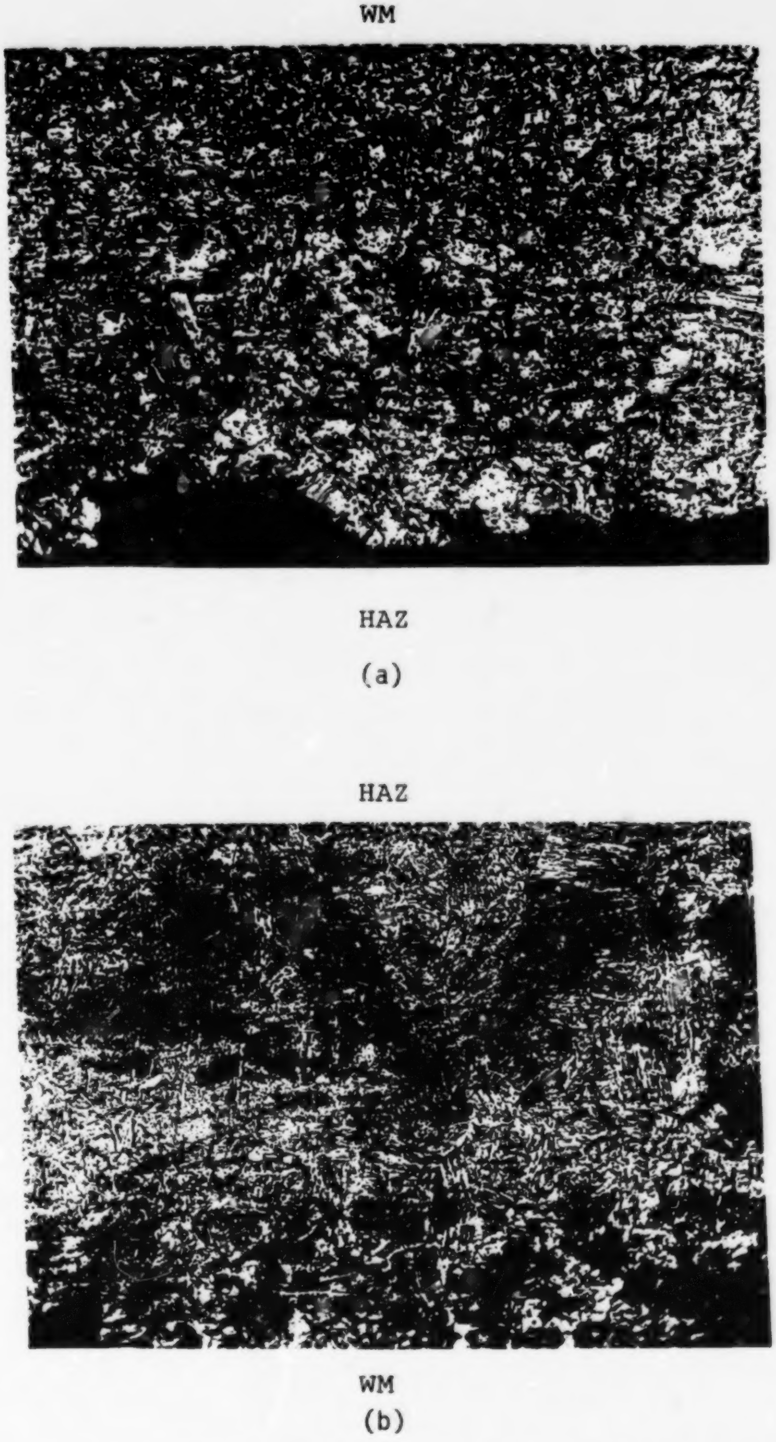

FIGURE 82 The location of the crack in the broken drop weight specimen showing the CG HAZ in (a) 5A tested at -60°C, Neg. 8336, Mag. 200 x; and (b) 5S tested at -75°C, Neg. 8332, Mag. 200 x.

HAZ

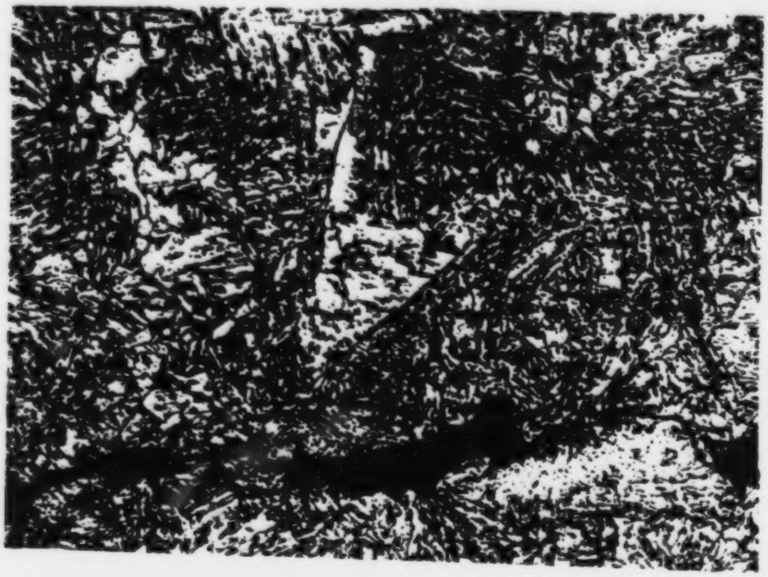

WM

(a)

HAZ

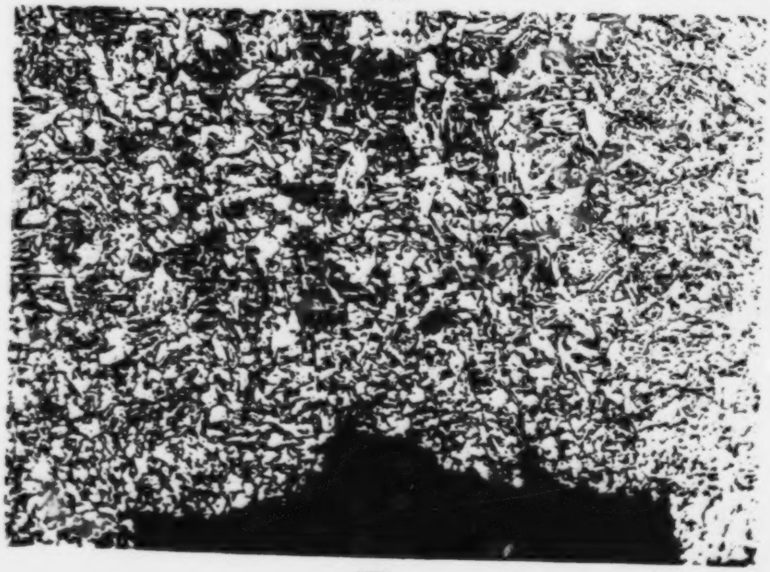

WM

(b)

FIGURE 83: The location of the crack in the broken drop weight specimen showing (a) the refined region in 6A tested at -45°C, Neg. 8334, Mag. 200 x; and (b) the CG HAZ in 6S tested at -60°C, Neg. 8333, Mag. 200 x.

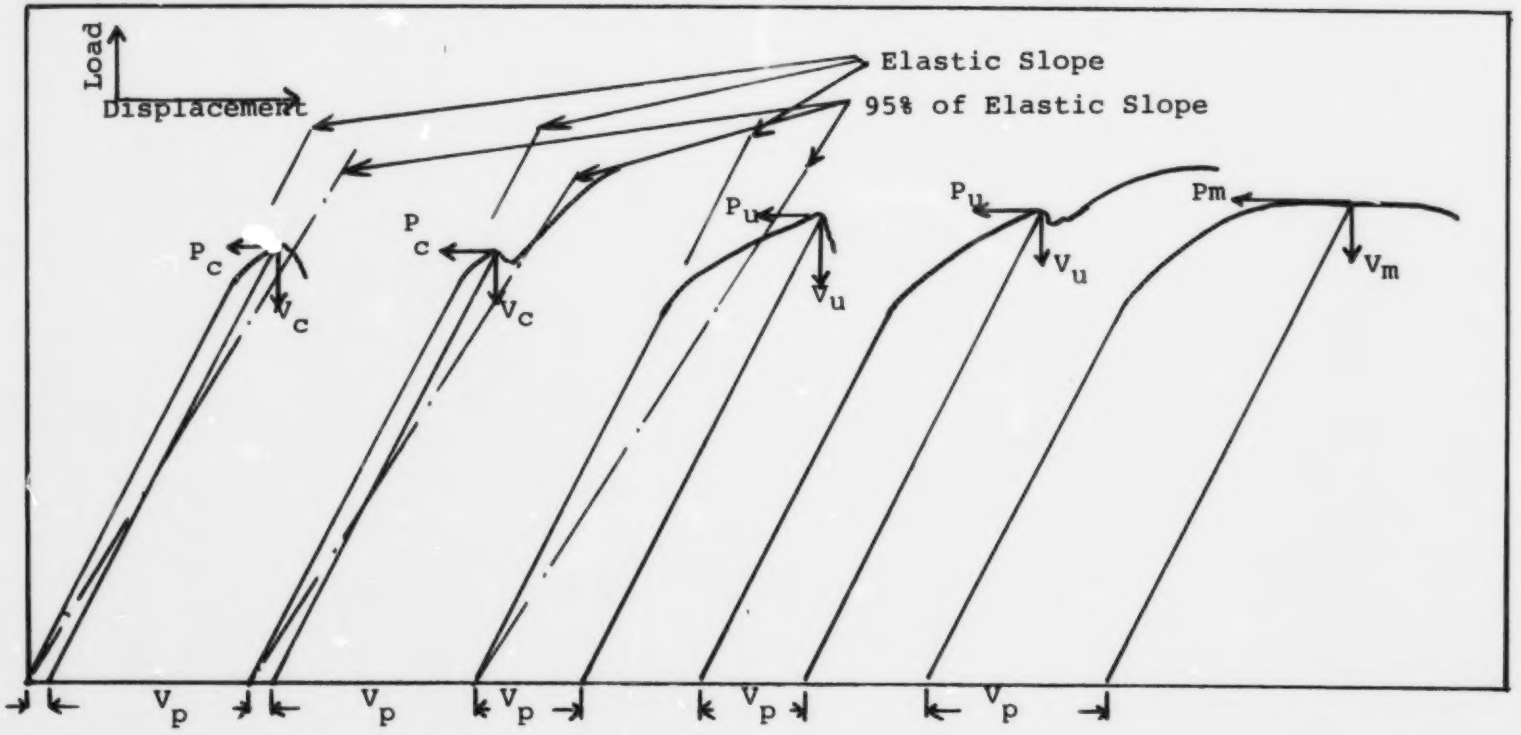
Load
Displacement
Elastic Slope
95% of Elastic Slope
P_c
V_c
P_c
V_c
P_u
V_u
P_u
V_u
Pm
V_m
V_p
V_p
V_p
V_p
V_p

FIGURE 84: Load - clip gauge displacement curves.

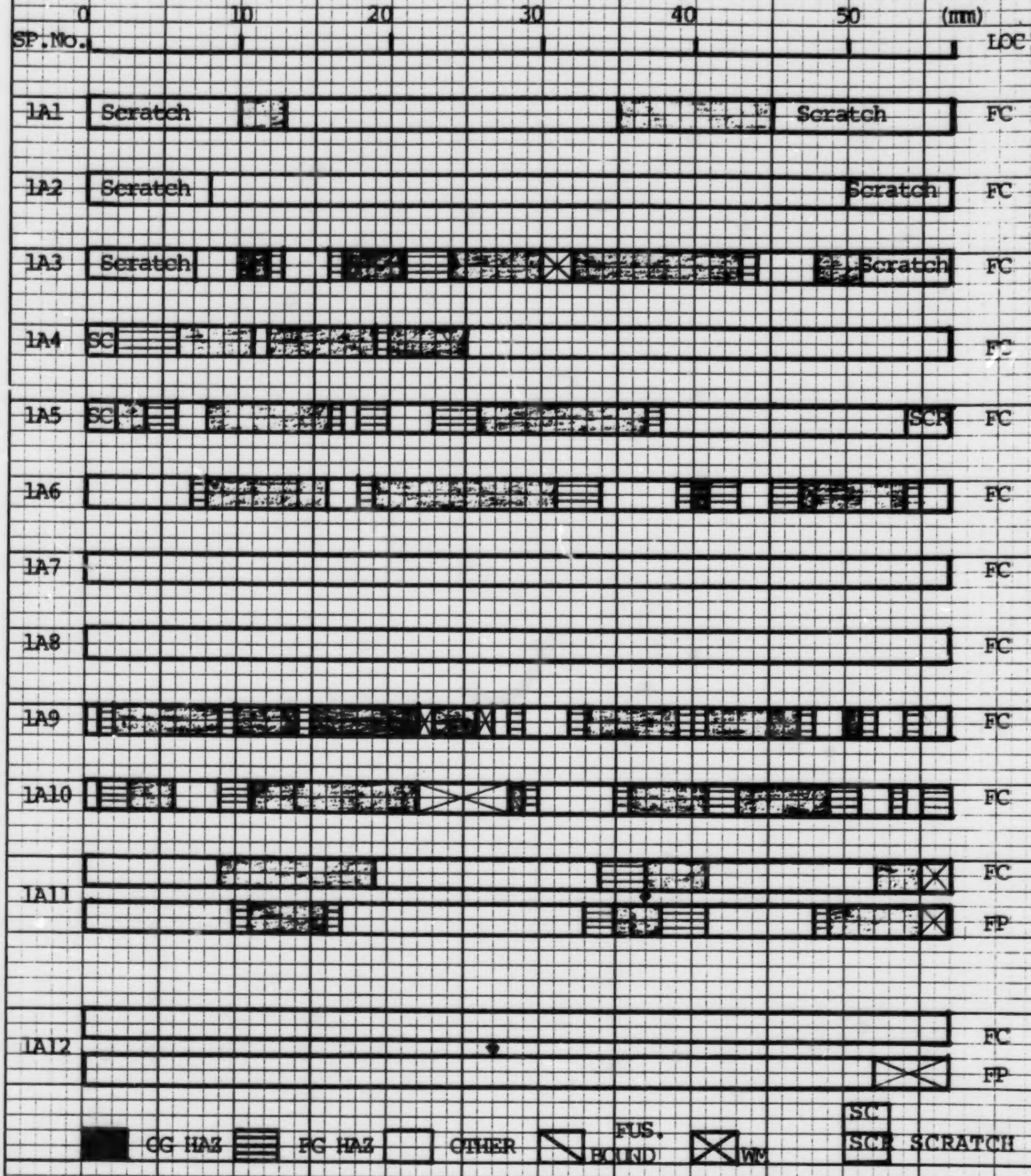

Figure 85 :The microstructure and the position of the fracture initiation site (♦), along the thickness, in the fatigue crack (FC) as well as the fracture path (FP) of the 1A series CTOD specimens (LT60 Steel, 31.5 kJ/mm, as welded)

K•E 46 0780 KEUFFEL & ESSER CO. MADE IN U.S.A.

1S

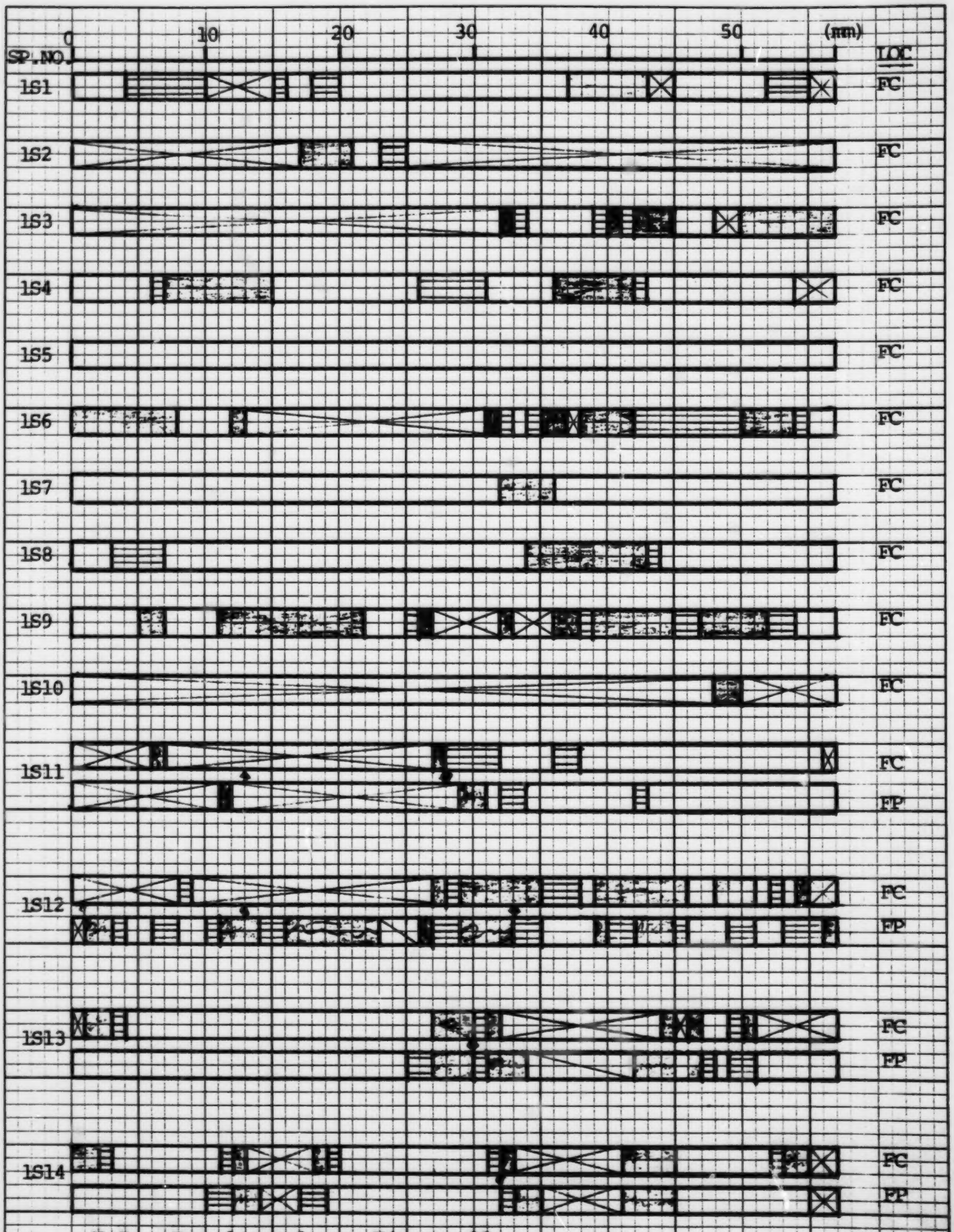

N.B. For legend see Figure 39.

Figure 86 : The microstructure and the position of the fracture initiation site (◆), along the thickness, in the fatigue crack (FC) as well as the fracture path (FP) of the 1S series CTOD specimens (LT60 Steel, 3.5 kJ/mm, stress-relieved)

K+E 10 X 10 TO THE INCH • 7 X 10 INCHES KEUFFEL & ESSER CO. MADE IN U.S.A. 46 0780

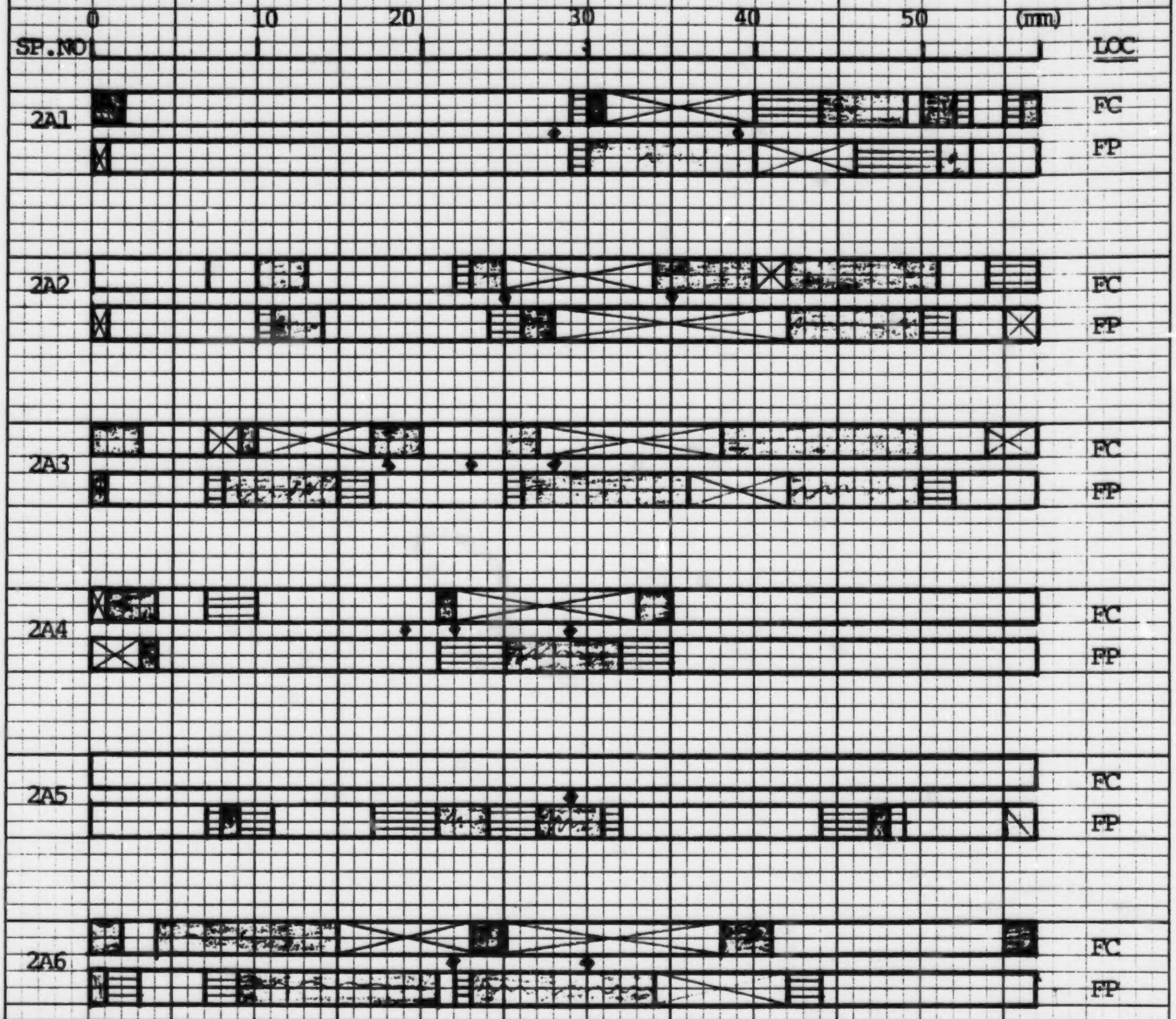

N.B. For legend see Figure 39.

Figure 87: The microstructure and the position of the fracture initiation site (♦), along the thickness, in the fatigue crack (FC) as well as the fracture path (FP) of the 2A series CTOD specimens (LT60 Steel, 5.4 kJ/mm, as welded)

K+E 10 X 10 TO THE INCH • 7 X 10 INCHES KEUFFEL & ESSER CO. MADE IN U.S.A. 46 0780

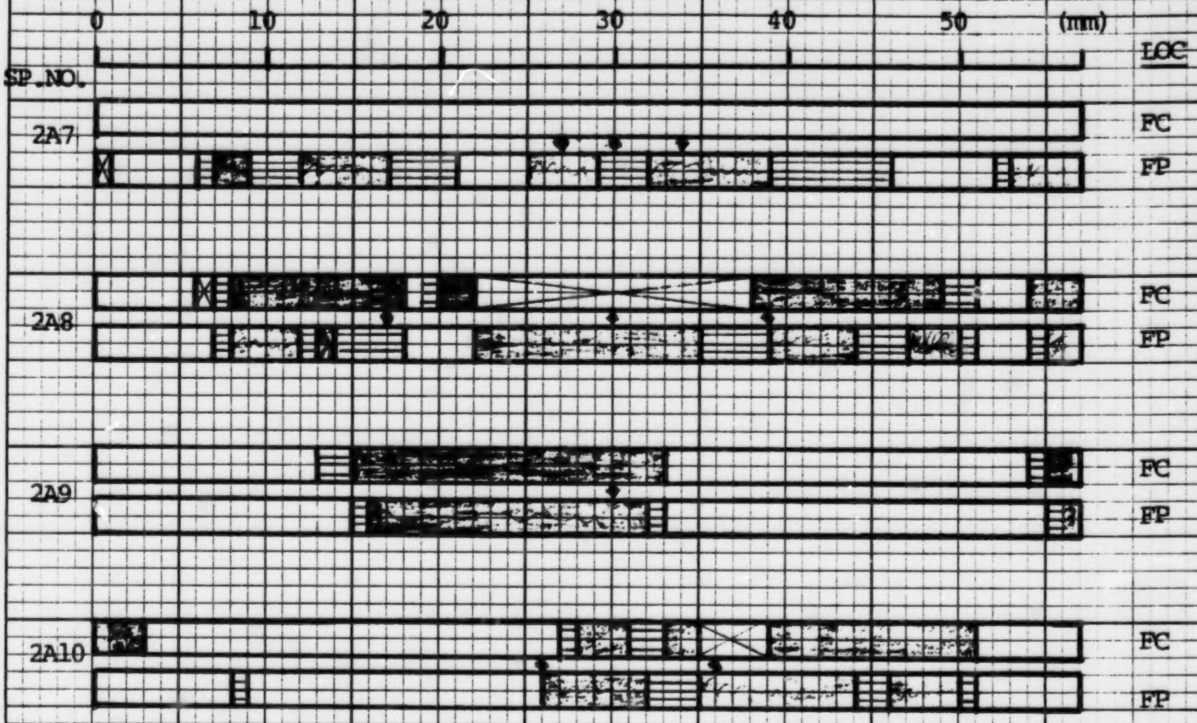

Figure 87 Continuation

46 0780
K·E KEUFFEL & ESSER CO. MADE IN U.S.A.

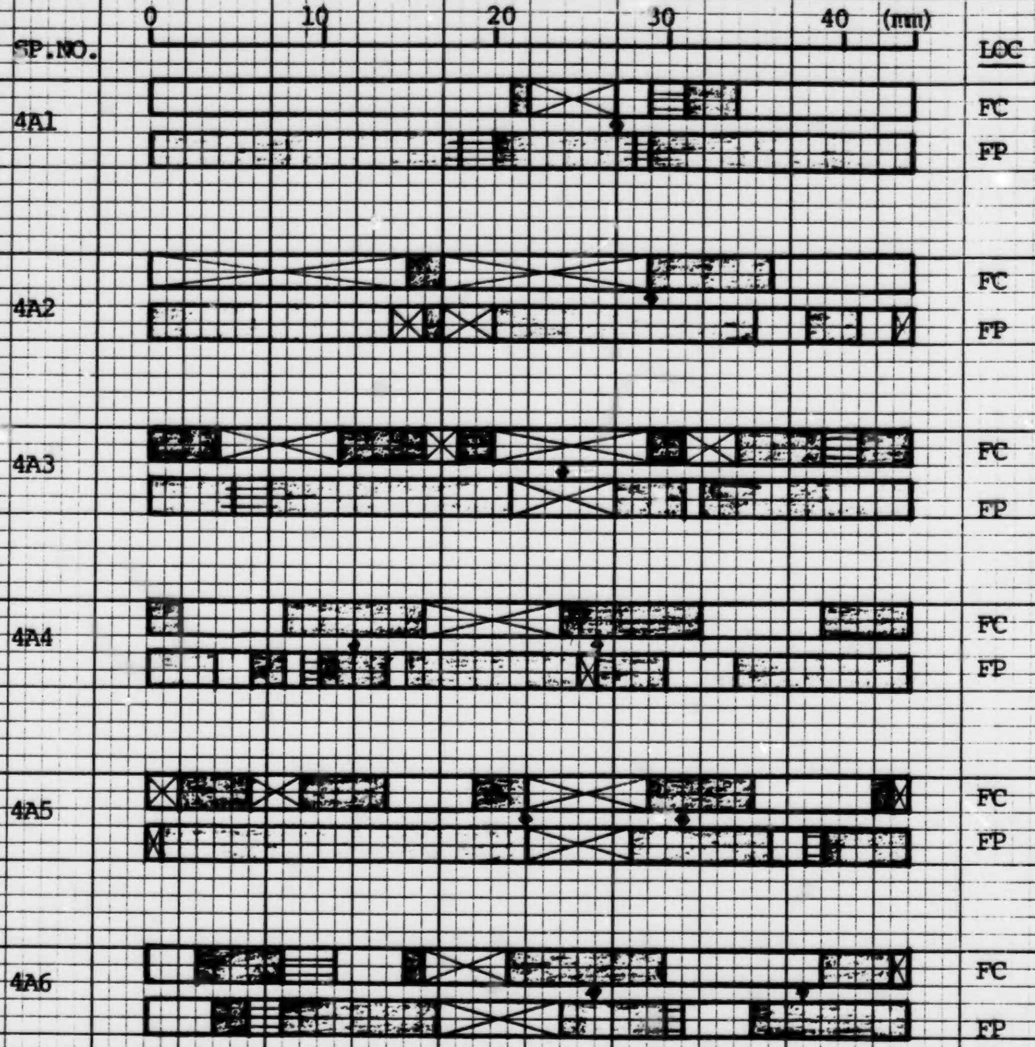
0
10
20
30
40
(mm)
SP.NO.
LOC
4A1
FC
FP
4A2
FC
FP
4A3
FC
FP
4A4
FC
FP
4A5
FC
FP
4A6
FC
FP

N.B. For legend see Figure 39.

Figure 88: The microstructure and the position of the fracture initiation site (♦), along the thickness, in the fatigue crack (FC) as well as the fracture path (FP) of the 4A series CTOD specimens (A710 Gr A Cl 3 Steel, 3,5 kJ/mm, as welded)

K·E 10 X 10 TO THE INCH • 7 X 10 INCHES KEUFFEL & ESSER CO. MADE IN U.S.A. 46 0780

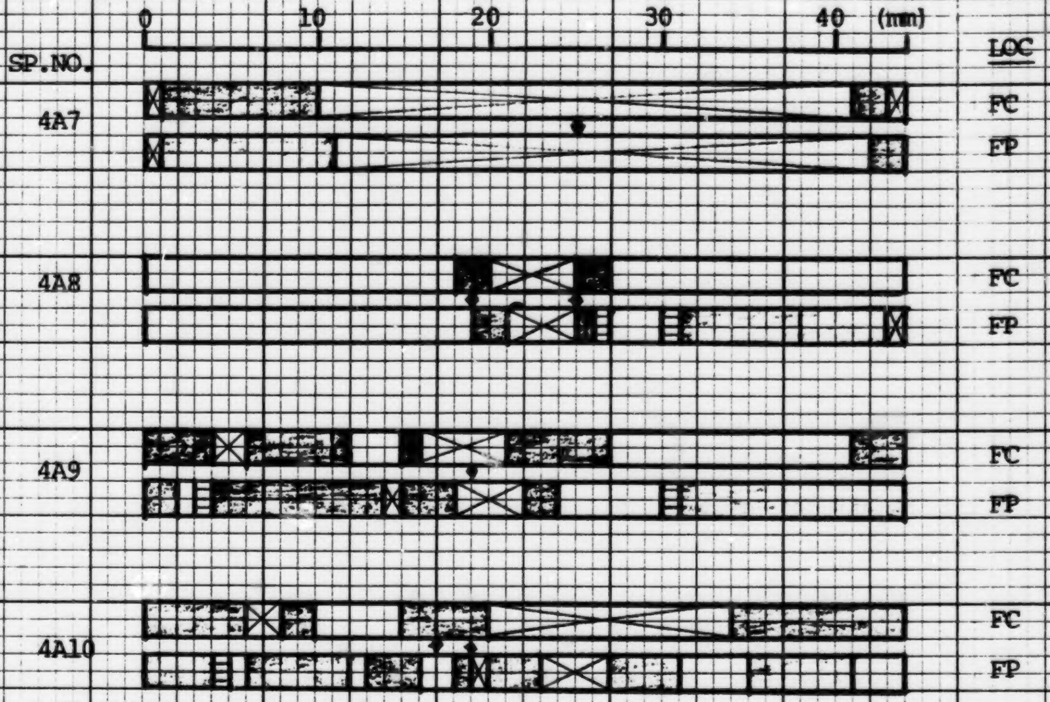

Figure 88 ~~continuation.~~

46 0780
K+E 10 X 10 TO THE INCH 7 X 10 INCHES
KEUFFEL & ESSER CO. MADE IN U.S.A.

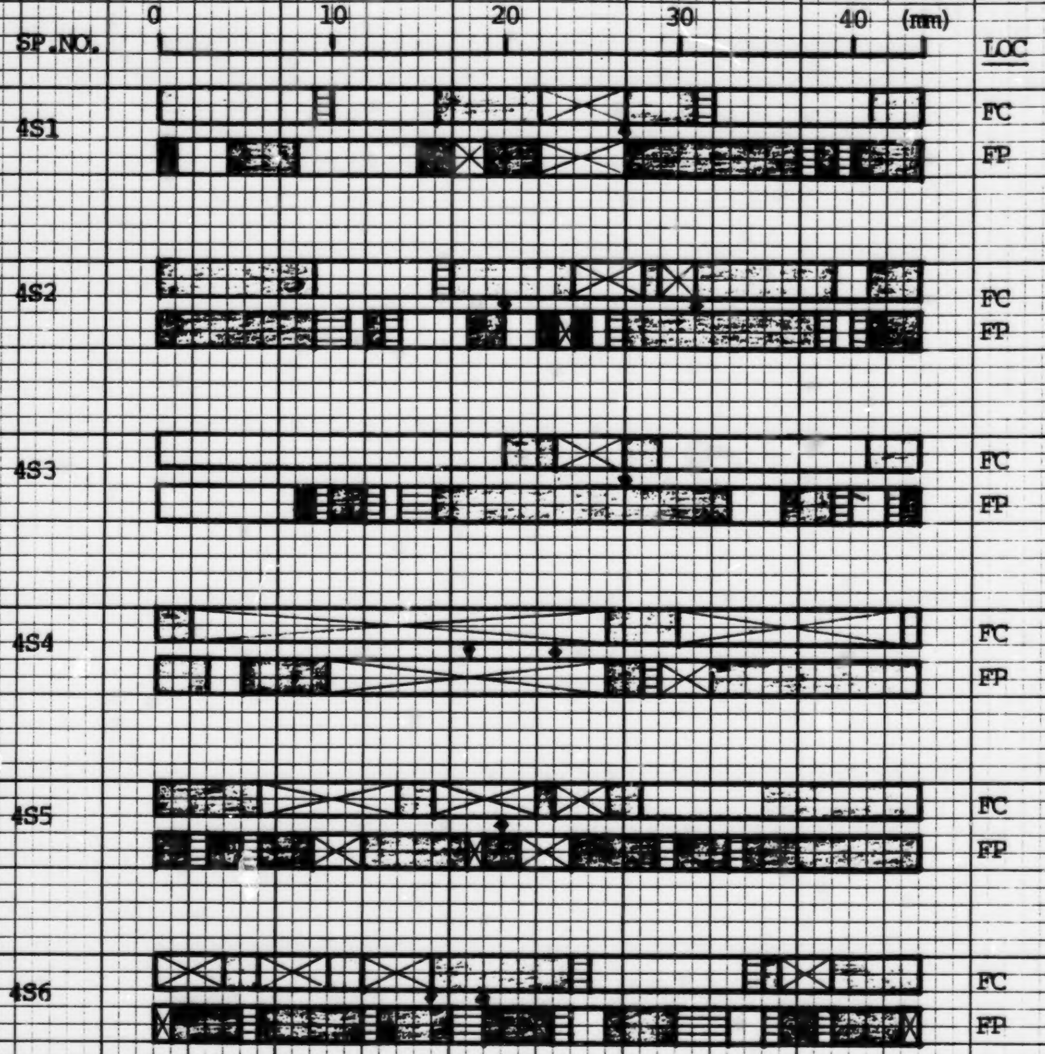
0
10
20
30
40
(mm)
SP.NO.
LOC
4S1
4S2
4S3
4S4
4S5
4S6
FC
FP

N.B. For legend see Figure 39.

Figure 89: The microstructure and the position of the fracture initiation site (♦), along the thickness, in the fatigue crack (FC) as well as the fracture path (FP) of the 4S series CTOD specimens (A710 Gr A Cl 3 Steel, 3.5 kJ/mm, stress relieved)

46 0780
KEUFFEL & ESSER CO. MADE IN U.S.A.

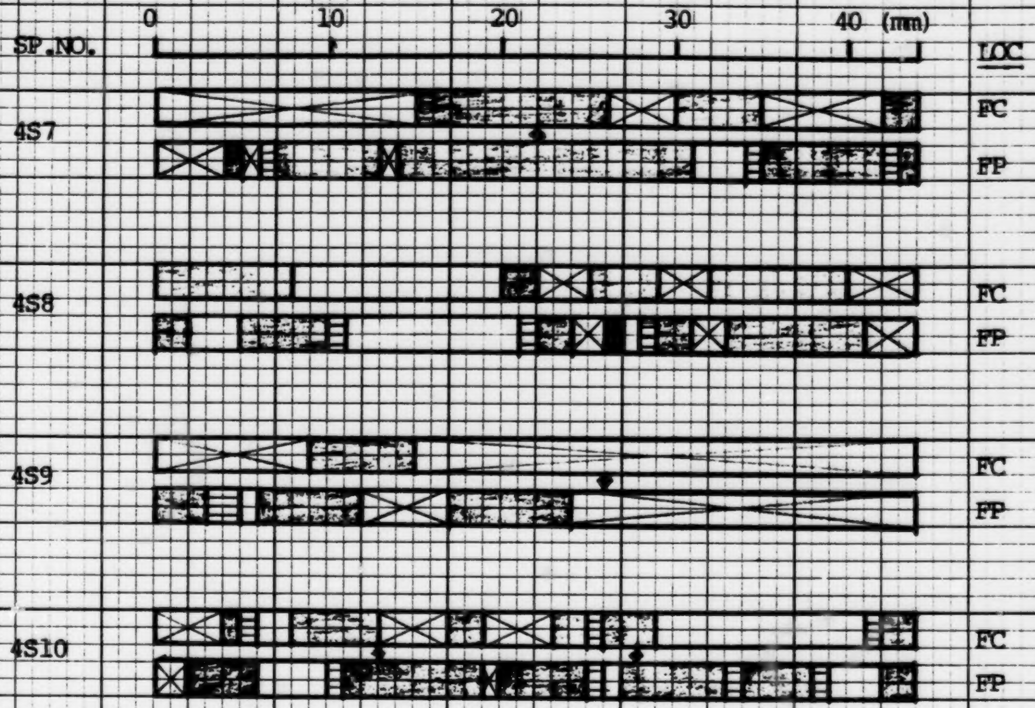

Figure 89 continuation.

K+E 10 X 10 TO THE INCH • 7 X 10 INCHES
KEUFFEL & ESSER CO. MADE IN U.S.A.
46 0780

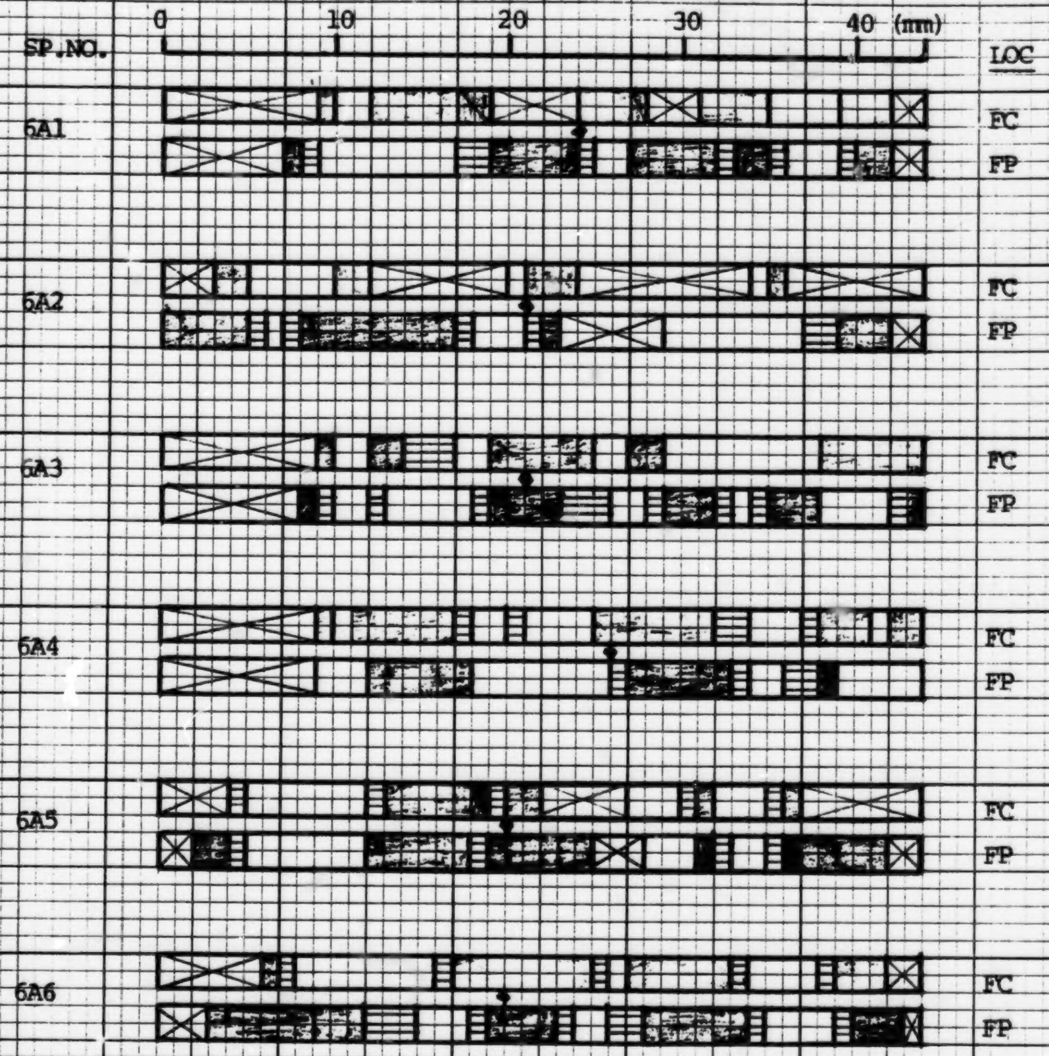
SP.NO.
0
10
20
30
40 (mm)
LOC
6A1
6A2
6A3
6A4
6A5
6A6
FC
FP

N.B. For legend see Figure 39.

Figure 90 : The microstructure and the position of the fracture initiation site (♦), along the thickness, in the fatigue crack (FC) as well as the fracture path (FP) of the 6A series specimens (MACS-ACC Steel, 5.4 kJ/mm, as welded)

KEUFFEL & ESSER CO. MADE IN U.S.A.

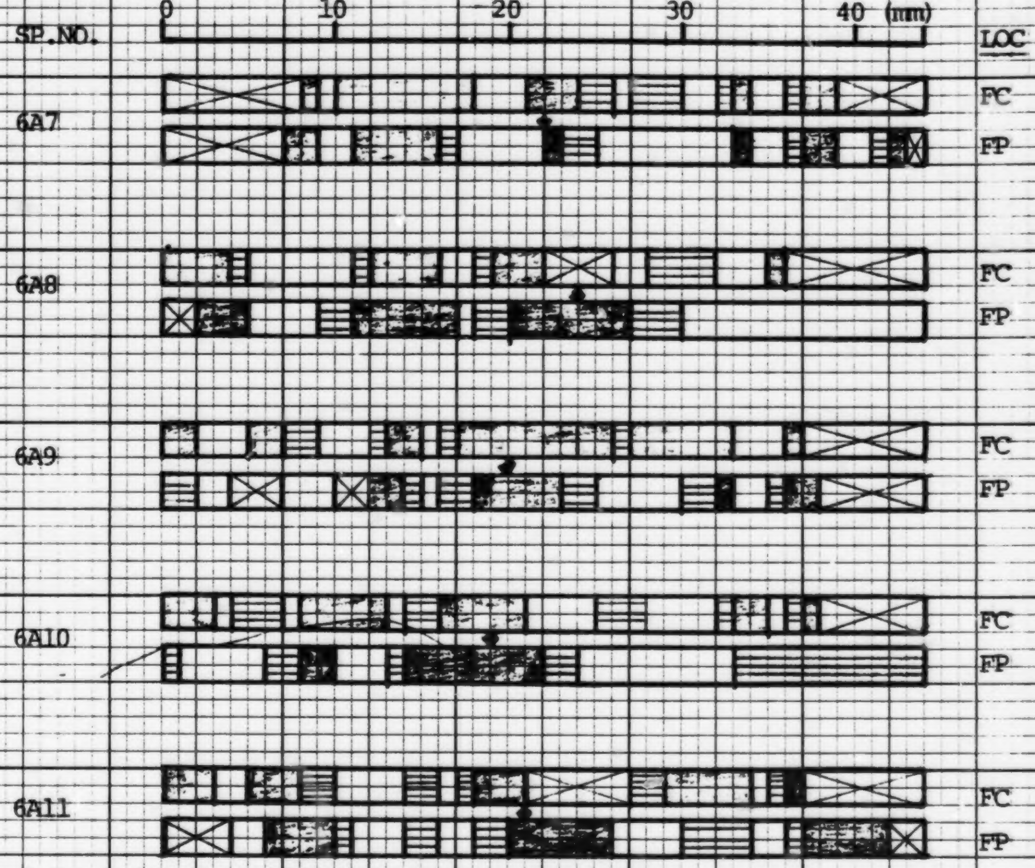
SP.NO.
0
10
20
30
40 (mm)
LOC
6A7
FC
FP
6A8
FC
FP
6A9
FC
FP
6A10
FC
FP
6A11
FC
FP

Figure 90 continuation.

10 X 10 TO THE INCH • 7 X 10 INCHES
KEUFFEL & ESSER CO. MADE IN U.S.A.
46 0780

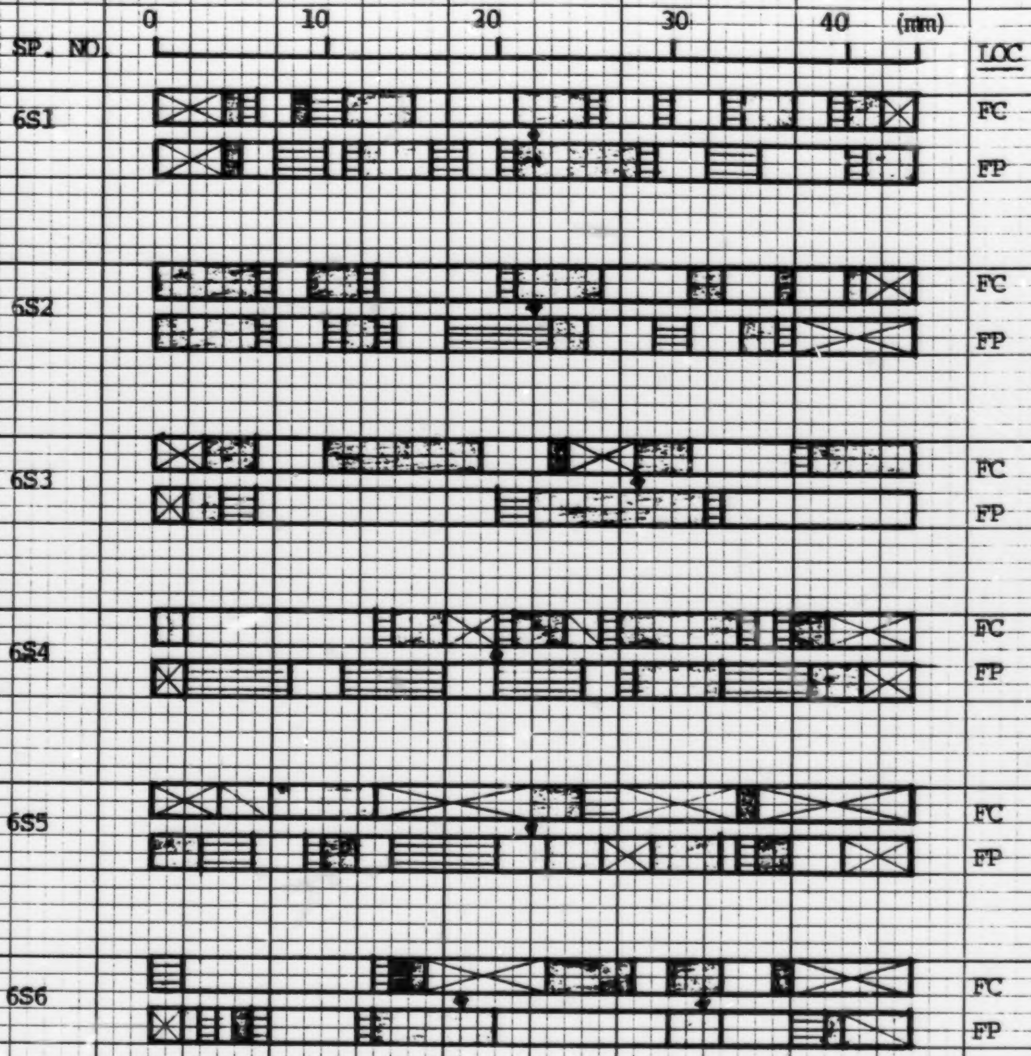
0
10
20
30
40
(mm)
SP. NO.
LOC
6S1
6S2
6S3
6S4
6S5
6S6
FC
FP

N.B. For legend see Figure 39.

Figure 91 : The microstructure and the position of the fracture initiation site (♦), along the thickness, in the fatigue crack (FC) as well as the fracture path (FP) of the 6S series CTOD specimens (MACS-DOT Steel, 5.4 kJ/mm, stress relieved)

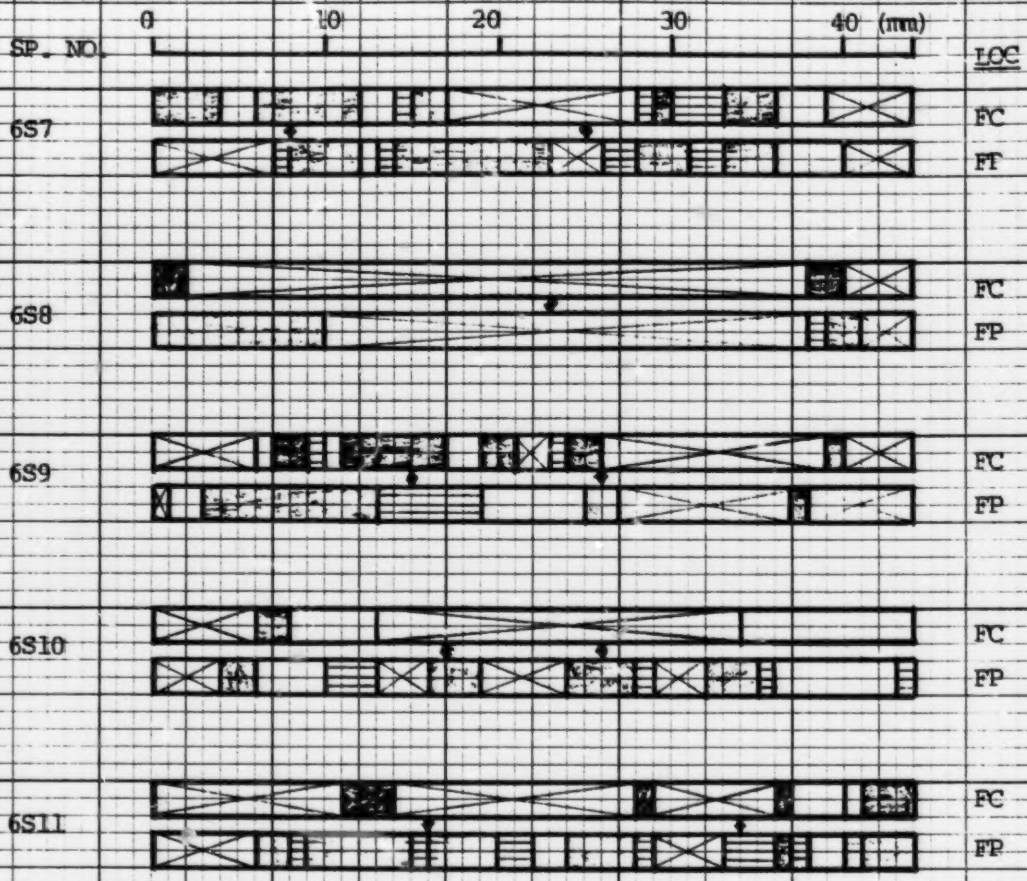

Figure 91continuation.

46 0780
K•E TO THE INCH• INCHES
KEUFFEL & ESSER CO. MADE IN U.S.A.

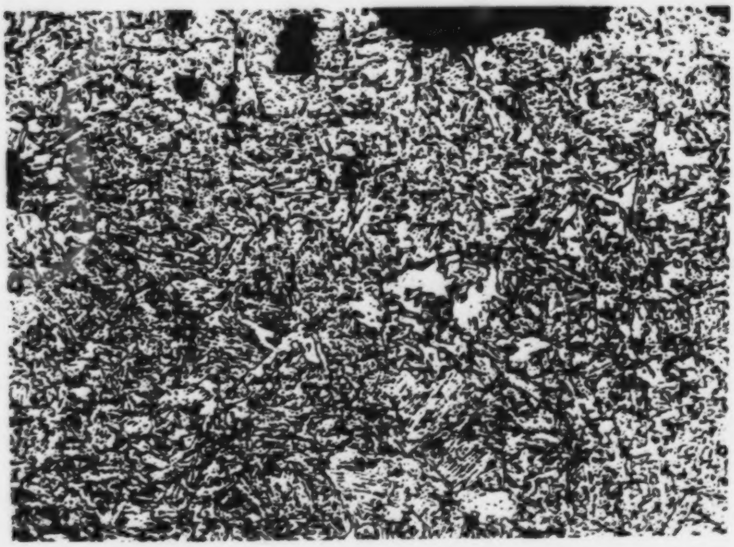

(a)

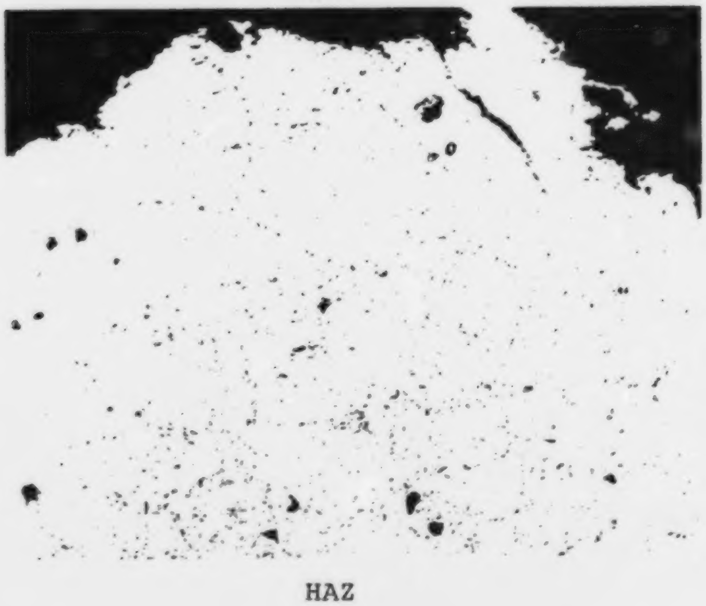

(b)

FIGURE 92: The region of CG HAZ in the fatigue precrack, (perpendicular to the plane of paper) near the precrack front of the CTOD specimens (a) 1A9, Neg. 8293, Mag. 200 x; and (b) 1A10, Neg. 8340, Mag. 200 x.

WM

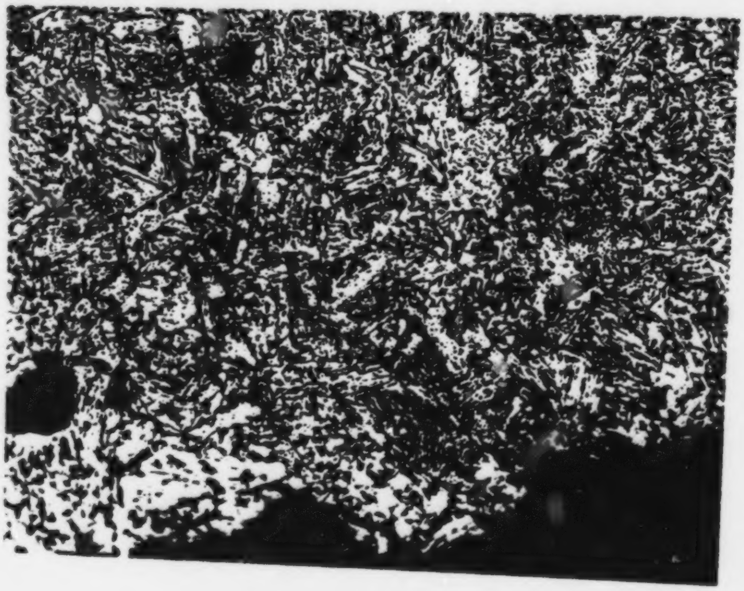

HAZ

FIGURE 93: The region of CG HAZ in the fatigue precrack, (perpendicular to the plane of paper), near the precrack front of the CTOD specimen 1S9, Neg. 8292, Mag. 200 x.

HAZ

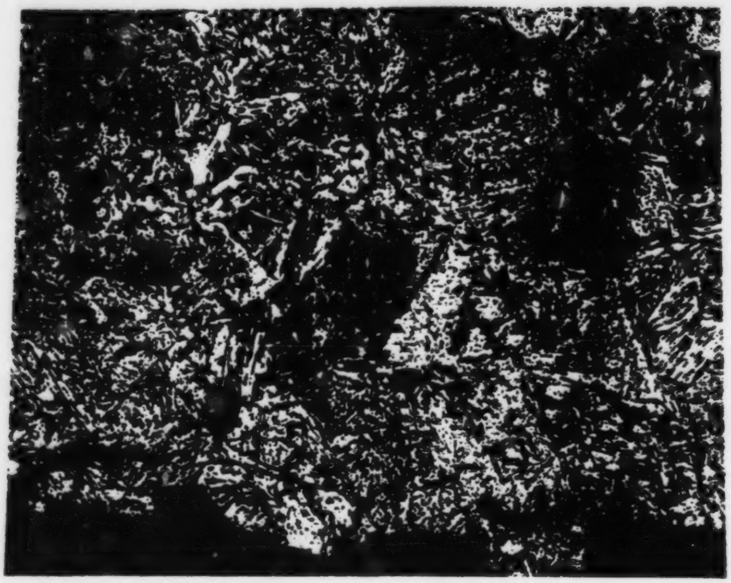

WM

(a)

HAZ

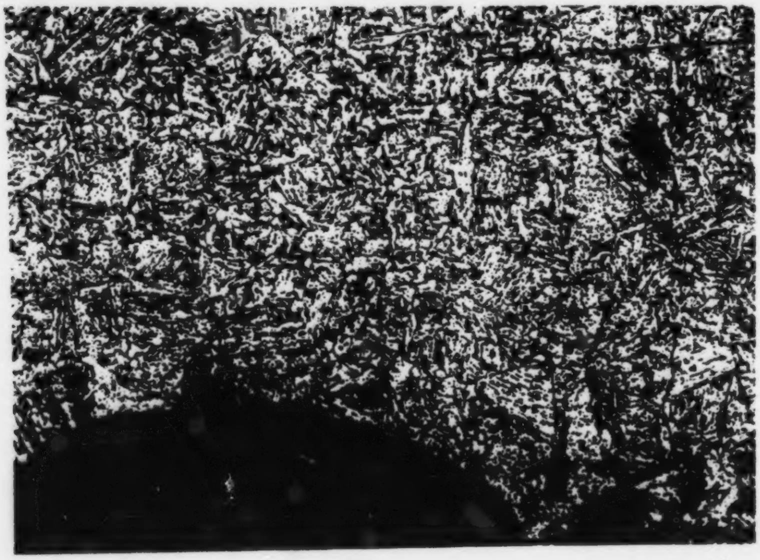

WM

(b)

FIGURE 94: The CG HAZ microstructure in the fracture path, 1 mm below the fatigue precrack front at the same location along the thickness of the CTOD specimen where the brittle fracture initiation site is located in (a) 2A3, Neg. 8300, Mag. 200 x; and (b) 2S4, Neg. 8296, Mag. 200 x.

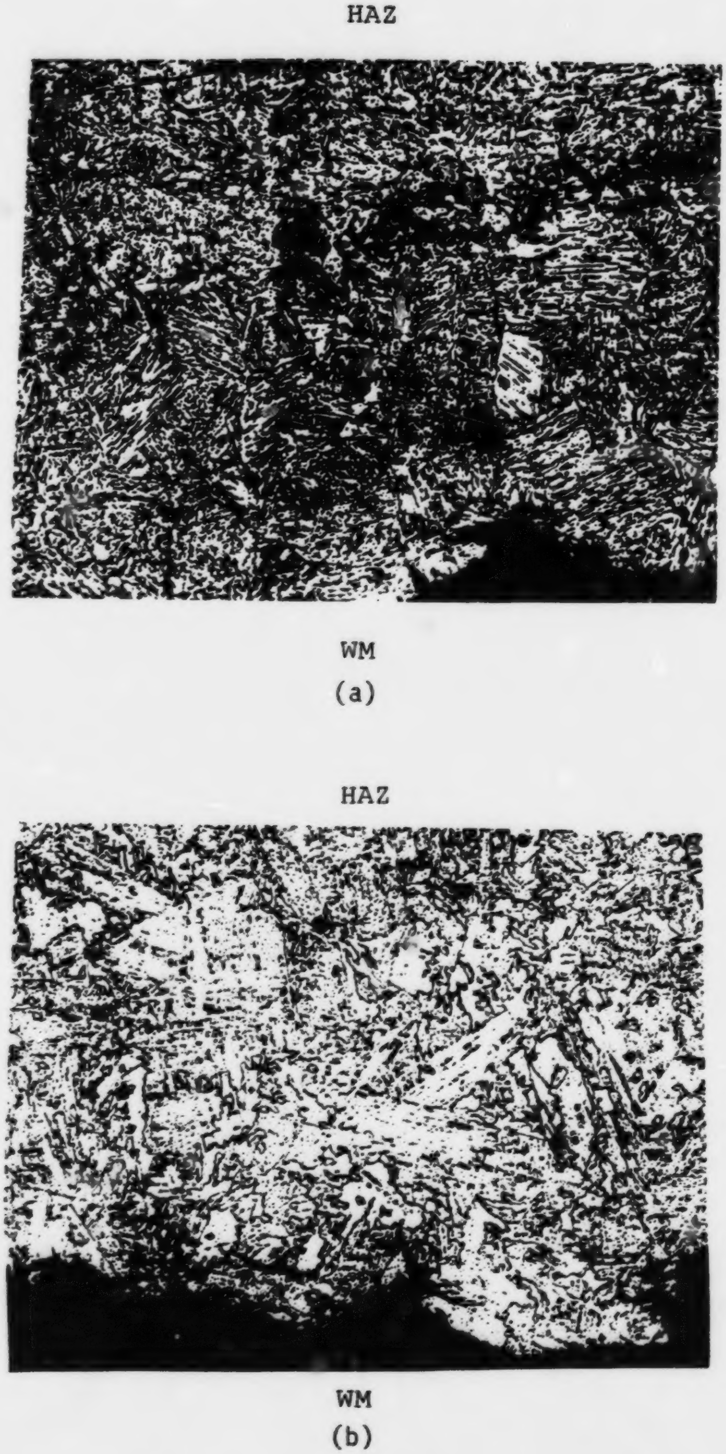

FIGURE 95: The CG HAZ microstructure in the fracture path, 1 mm below the fatigue precrack front at the same location along the thickness of the CTOD specimen where the brittle fracture initiation site is located in (a) 2A8, Neg. 8298, Mag. 200 x; and (b) 2S6, Neg. 8353, Mag. 200 x.

HAZ

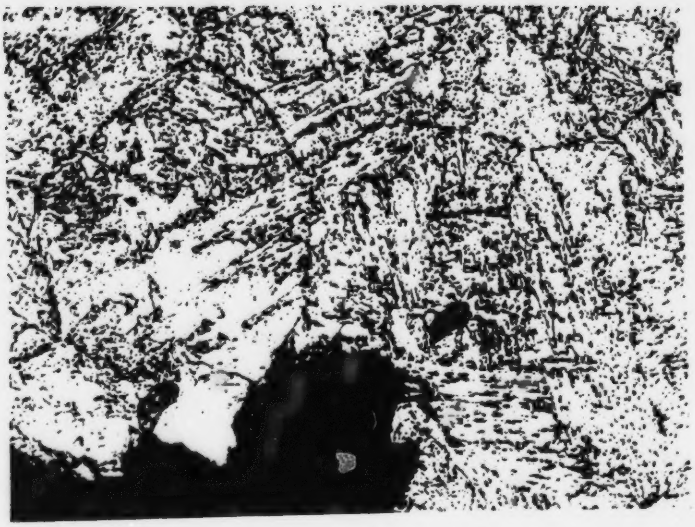

WM

(a)

HAZ

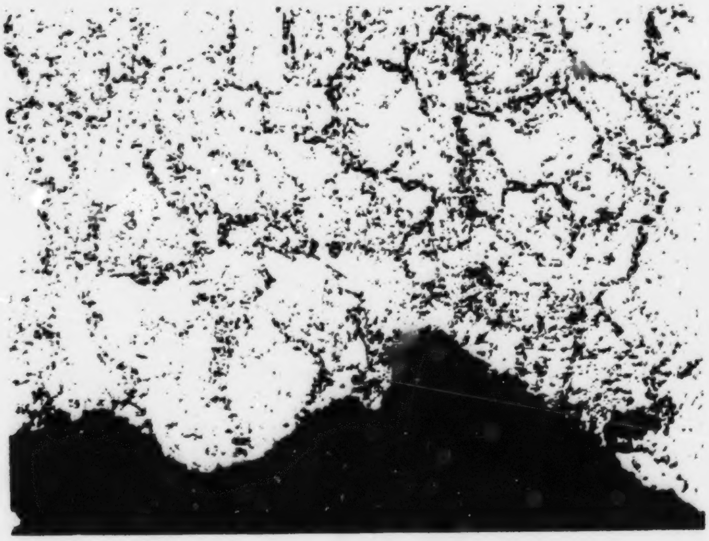

WM

(b)

FIGURE 96: The CG HAZ microstructure in the fracture path, 1 mm below the fatigue precrack (perpendicular to the plane of paper) front at the same location along the thickness of the CTOD specimen where the brittle fracture initiation site is located in (a) 3A7, Neg. 8542, Mag. 200 x; and (b) 3S7, Neg. 8701, Mag. 200 x.

HAZ

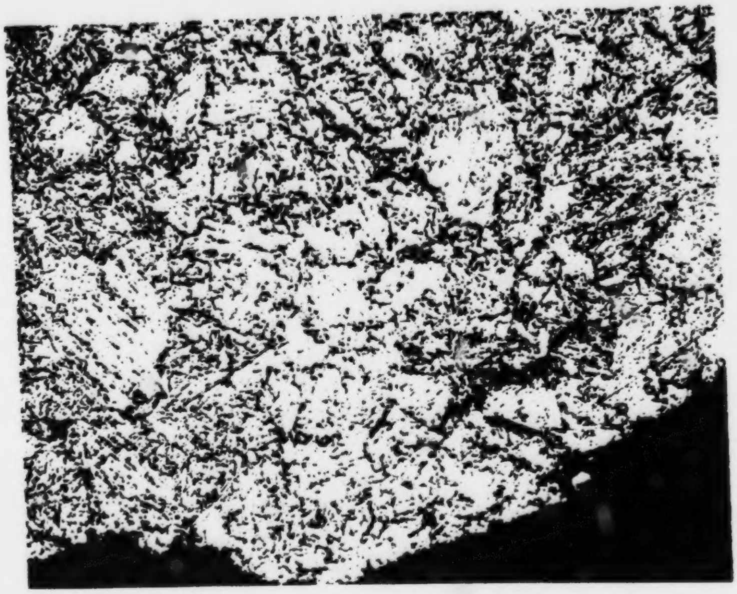

WM

FIGURE 97: The CG HAZ microstructure in the fracture path, 1 mm below the fatigue precrack (perpendicular to the plane of paper) front at the same location along the thickness of the CTOD specimen where the brittle fracture initiation site is located in 3A2, Neg. 8337, Mag. 200 x.

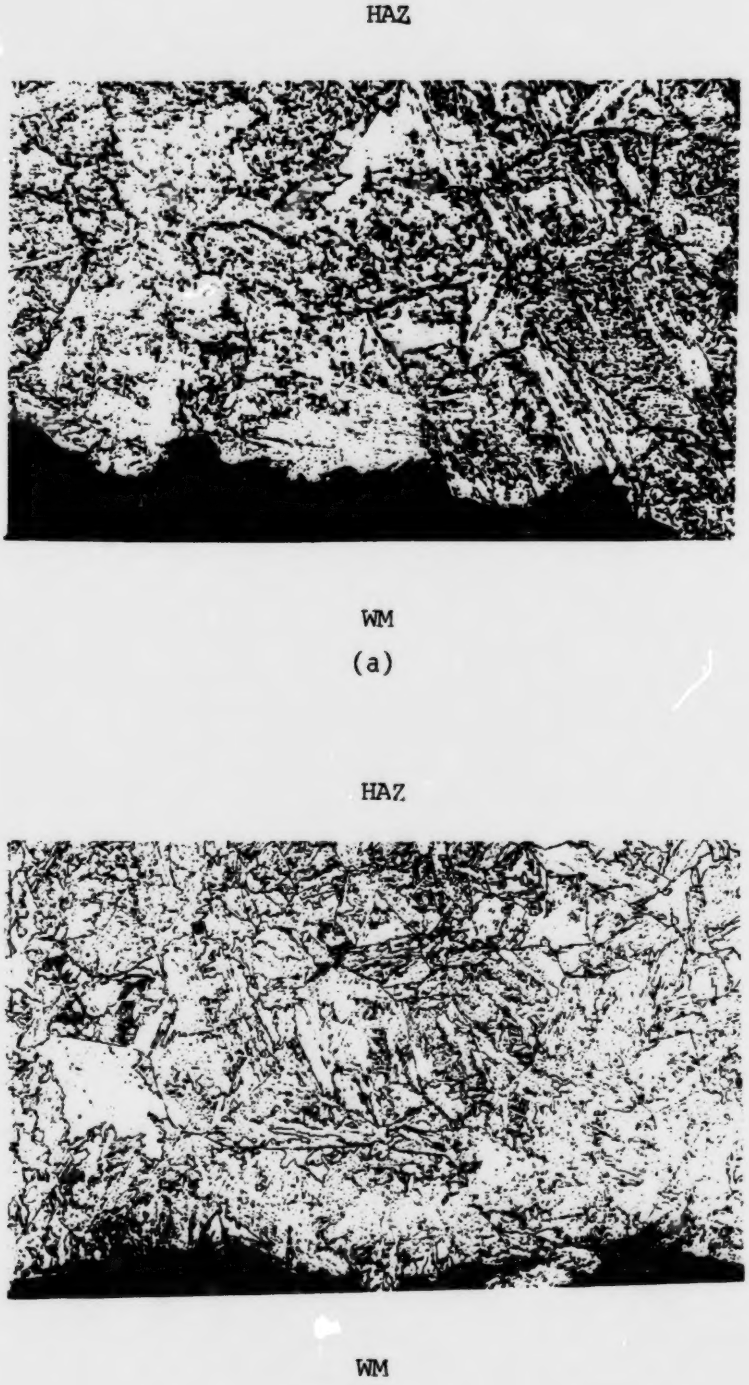

(b)

FIGURE 98: The CG HAZ microstructure in the fracture path, 1 mm below the fatigue precrack (perpendicular to the plane of paper) front at the same location along the thickness of the CTOD specimen where the brittle fracture initiation site is located in (a) 4A5, Neg. 8551, Mag. 200 x; and (b) 4S10, Neg. 8549, Mag. 200 x.

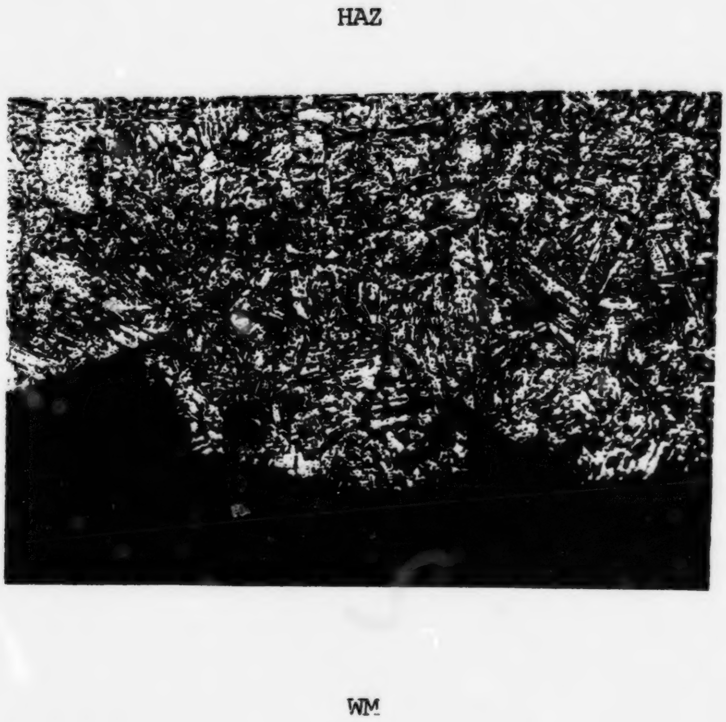

FIGURE 99: The CG HAZ microstructure in the fracture path, 1 mm below the fatigue precrack (perpendicular to the plane of paper) front at the same location along the thickness of the CTOD specimen where the brittle fracture initiation site is located in 5A4, Neg. 8547, Mag. 200 x.

HAZ

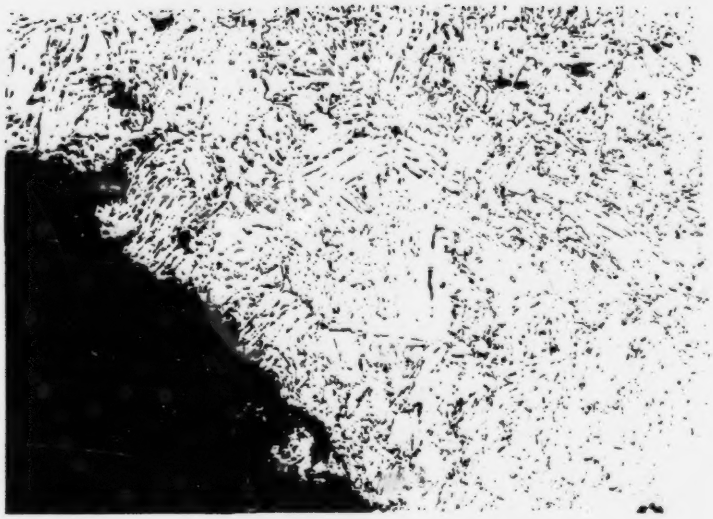

WM

(a)

HAZ

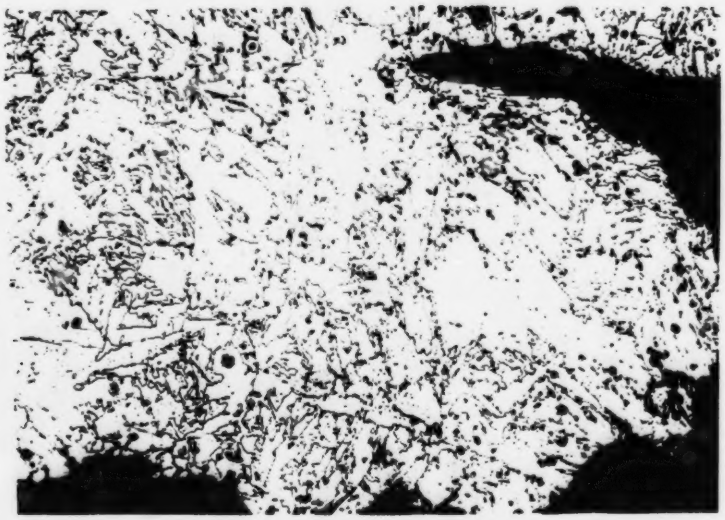

WM

(b)

FIGURE 100: The CG HAZ microstructure in the fracture path, 1 mm below the fatigue precrack (perpendicular to the plane of paper) front at the same location along the thickness of the CTOD specimen where the brittle fracture initiation site is located in (a) 6A2, Neg. 8604, Mag. 200 x; and (b) 6S7, Neg. 8602, Mag. 200 x.

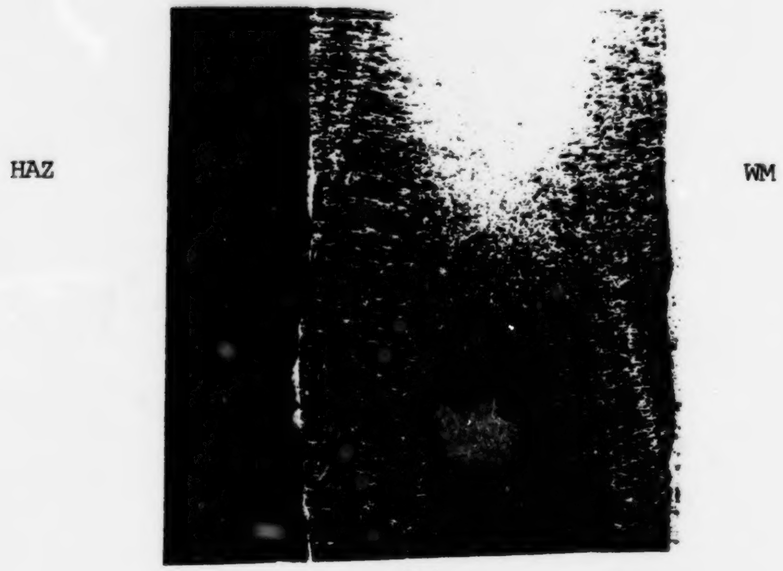

(a)

(b)

FIGURE 101: The longitudinal section showing the location of the tip of fatigue precrack (arrow mark) and the fracture path at the mid thickness (B/2) of the CTOD specimen 1A6, (a) Neg. 8350, Mag. 5 x; and (b) Neg. 8355, Mag. 200 x.

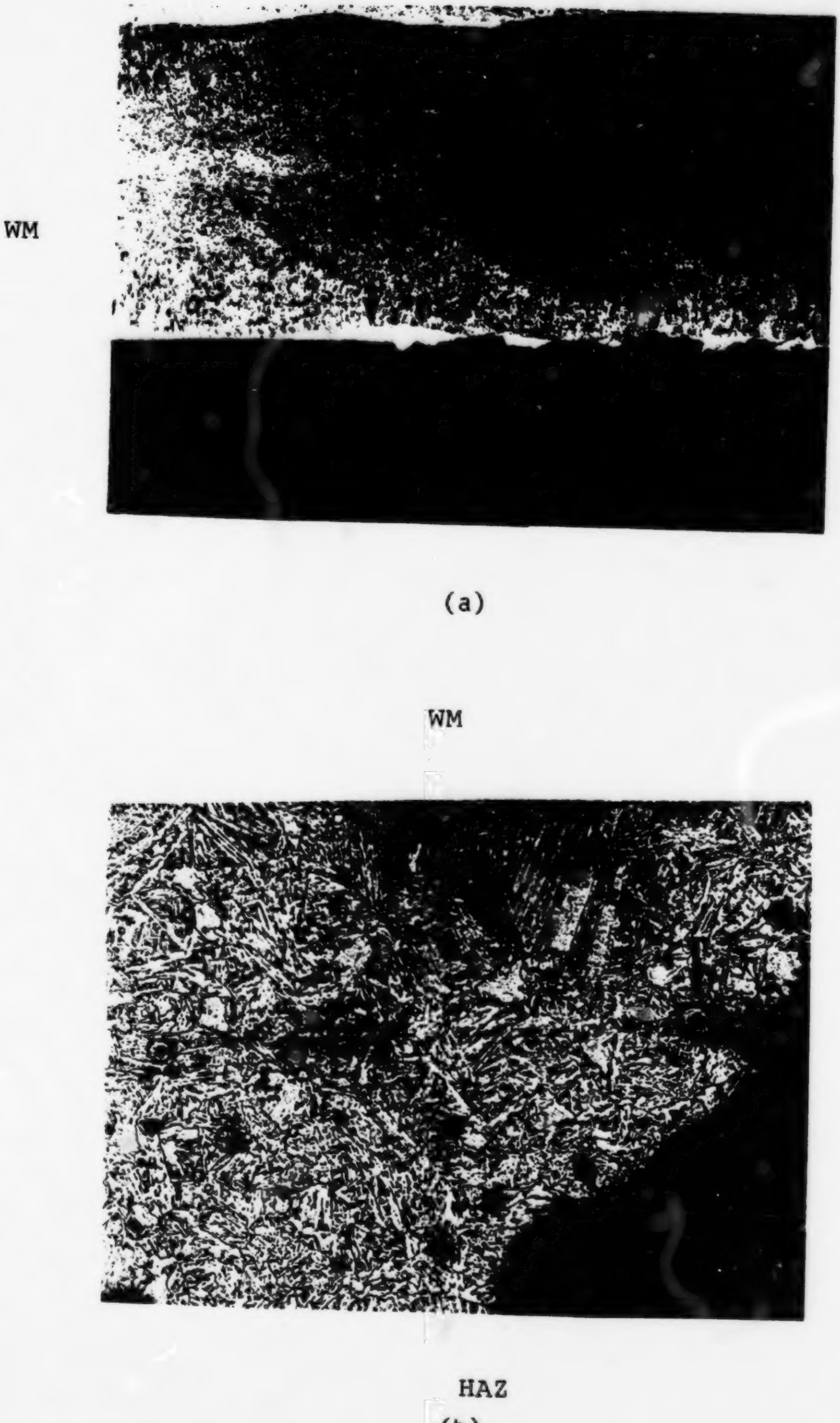

(a)

(b)

FIGURE 102: The longitudinal section showing the location of the tip of fatigue precrack (arrow mark) and the fracture path at mid thickness (B/2) of the CTOD specimen 1A9, (a) Neg. 7978, Mag. 5 x; and (b) Neg. 8356, Mag. 200 x.

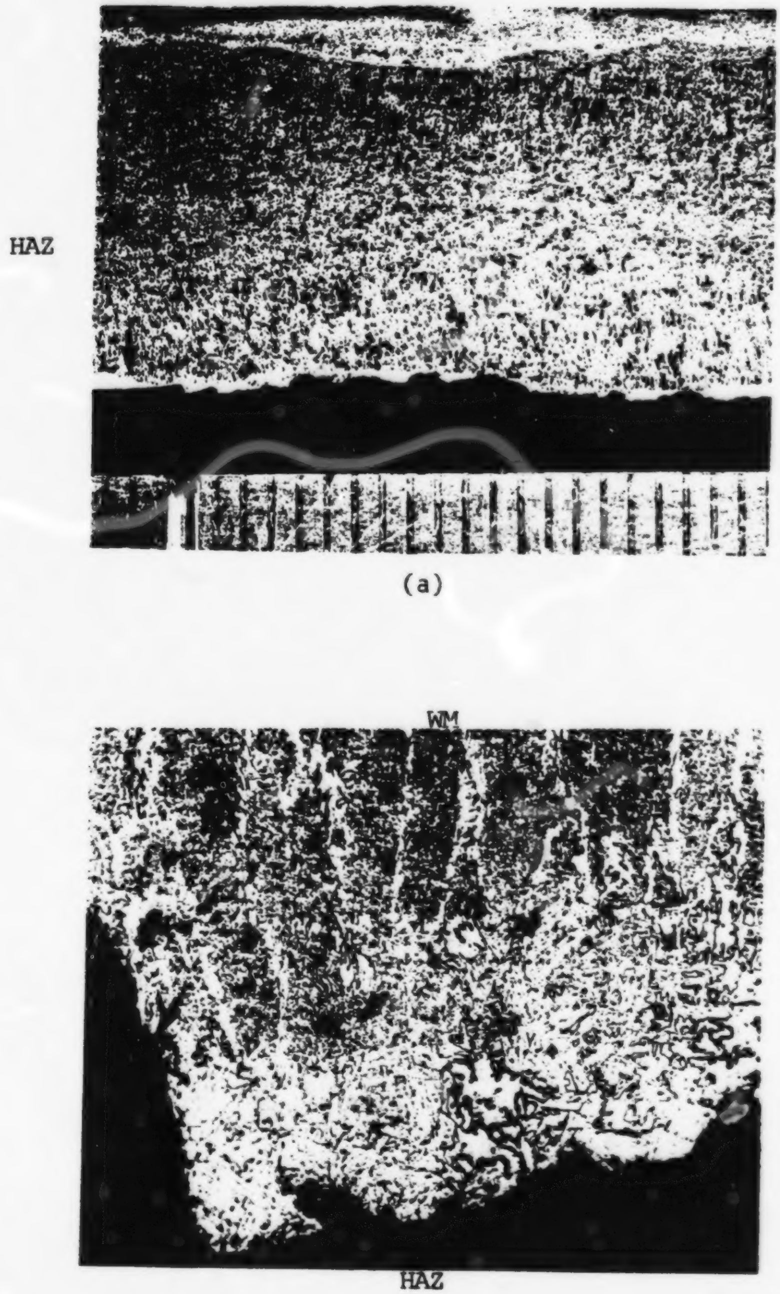

(a)

(b)

FIGURE 103: The longitudinal section showing the location of the tip of fatigue precrack (arrow mark) and the fracture path at the mid thickness (B/2) of the CTOD specimen 1S9, (a) Neg. 7985, Mag. 5 x; and (b) Neg. 8357, Mag. 200 x.

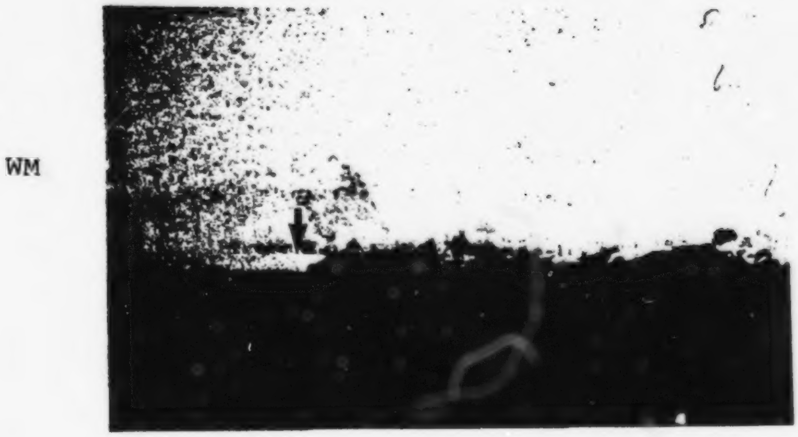

(a)

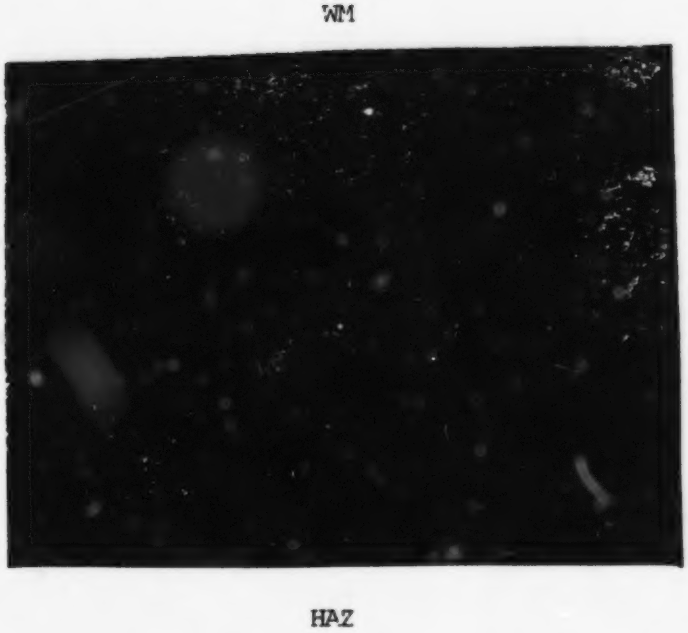

(b)

FIGURE 104: The longitudinal section showing the location of the tip of fatigue precrack (arrow mark) and the fracture path at the fracture initiation site of the CTOD specimen 3A2, (a) Neg. 8544, Mag. 5 x; and (b) Neg. 8536, Mag. 200 x.

WM

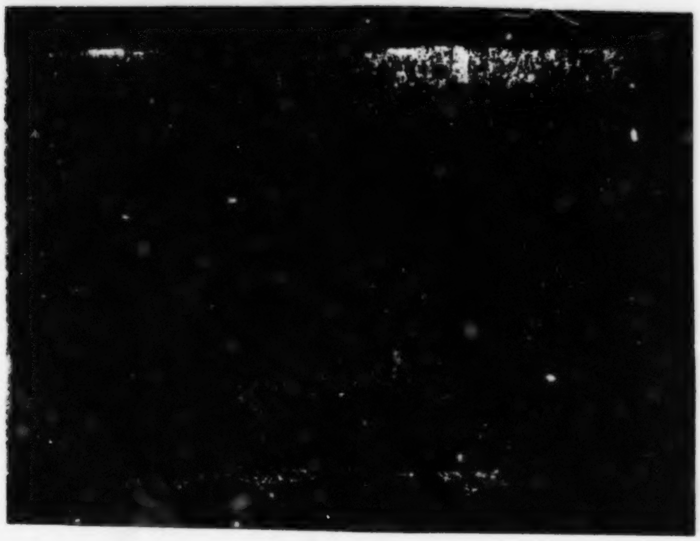

(a)

WM

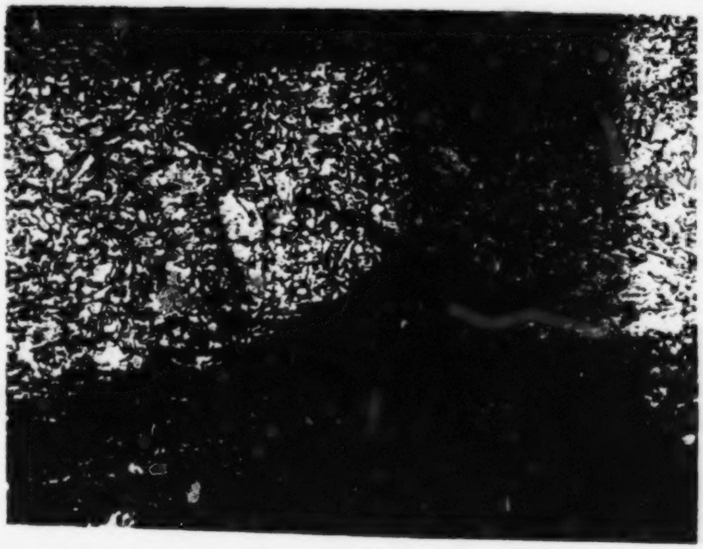

HAZ

(b)

FIGURE 105: The longitudinal section showing the location of the tip of fatigue precrack (arrow mark) and the fracture path at the fracture initiation site of the CTOD specimen 3S9 (a) Neg. 8543, Mag. 5 x;, and (b) Neg. 8535, Mag. 200 x.

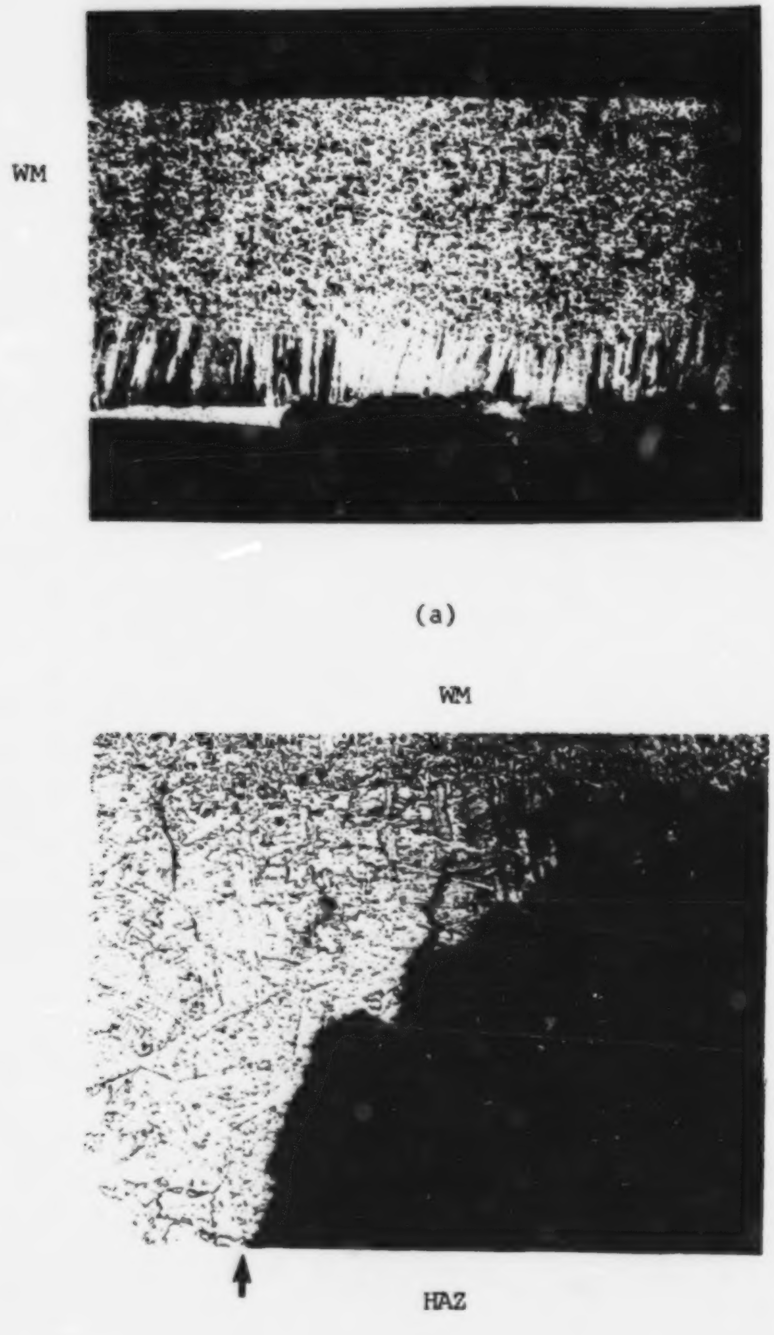

(a)

(b)

FIGURE 106: The longitudinal section showing the location of the tip of fatigue precrack (arrow mark) and the fracture path at the fracture initiation site of the CTOD specimen 4S1, Neg. 8542, Mag. 5 x; and (b) Neg. 8534, Mag. 200 x.

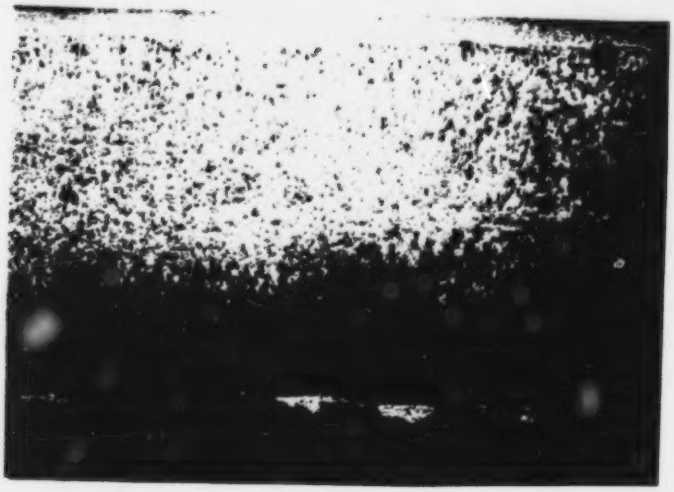

(a)

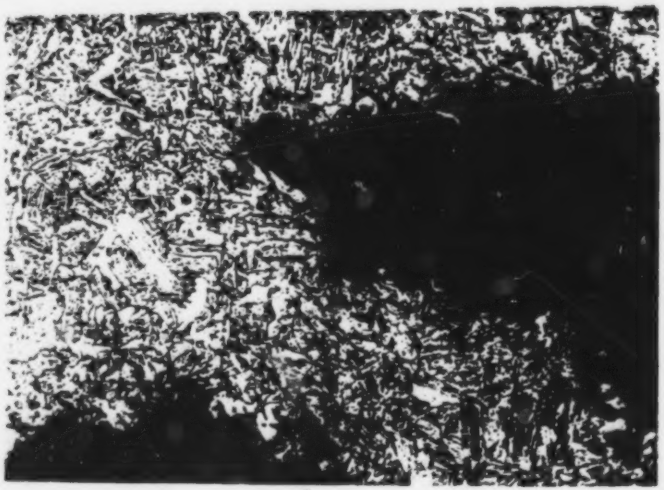

(b)

FIGURE 107: The longitudinal section showing the location of the tip of fatigue precrack (arrow mark) and the fracture path at the fracture initiation site of the CTOD specimen 5A4, (a) Neg. 8546, Mag. 5 x; and (b) Neg. 8538, Mag. 200 x.

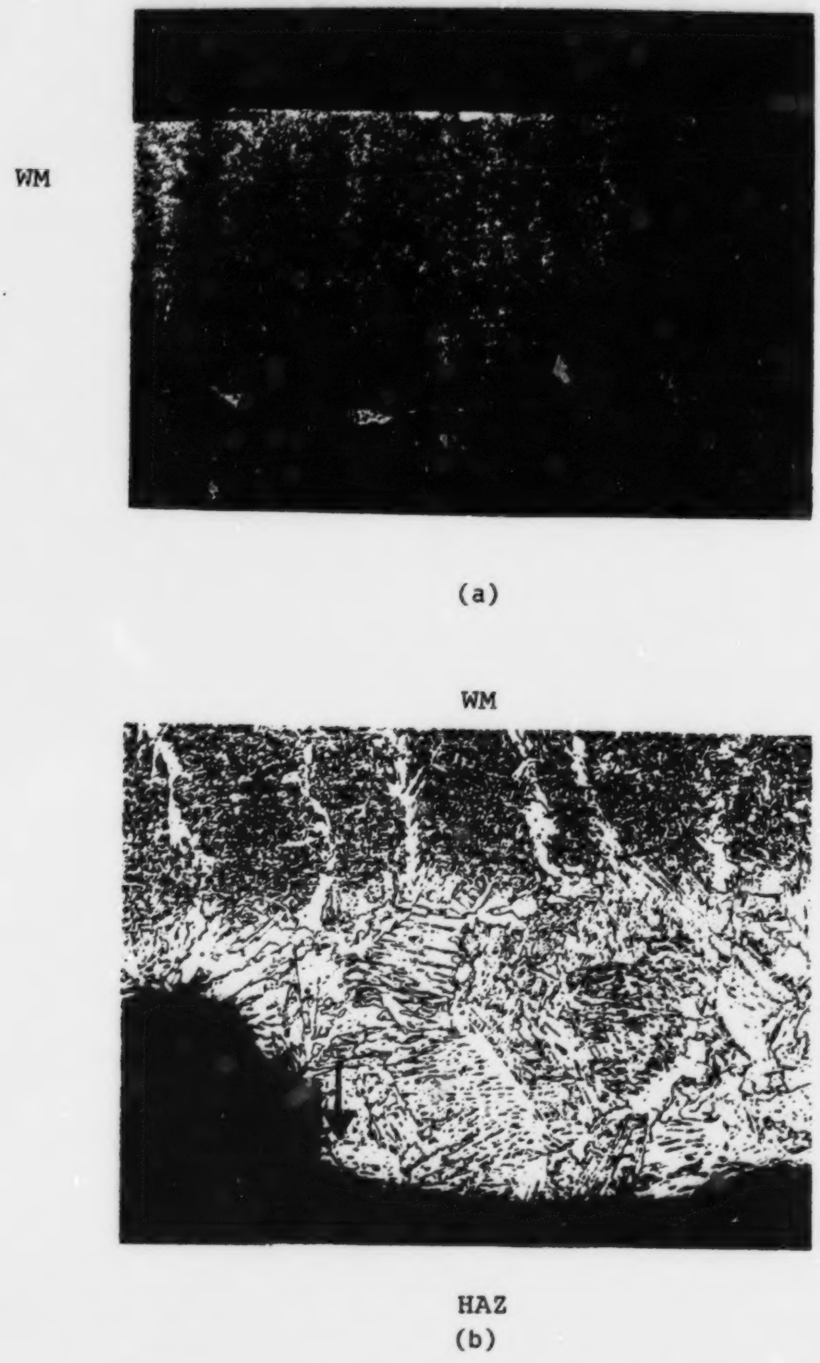

FIGURE 108: The longitudinal section showing the location of the tip of fatigue precrack (arrow mark) and the fracture path at the fracture initiation site of the CTOD specimen 6A9, (a) Neg. 8632, Mag. 5 x; and (b) Neg. 8613, Mag. 200 x.

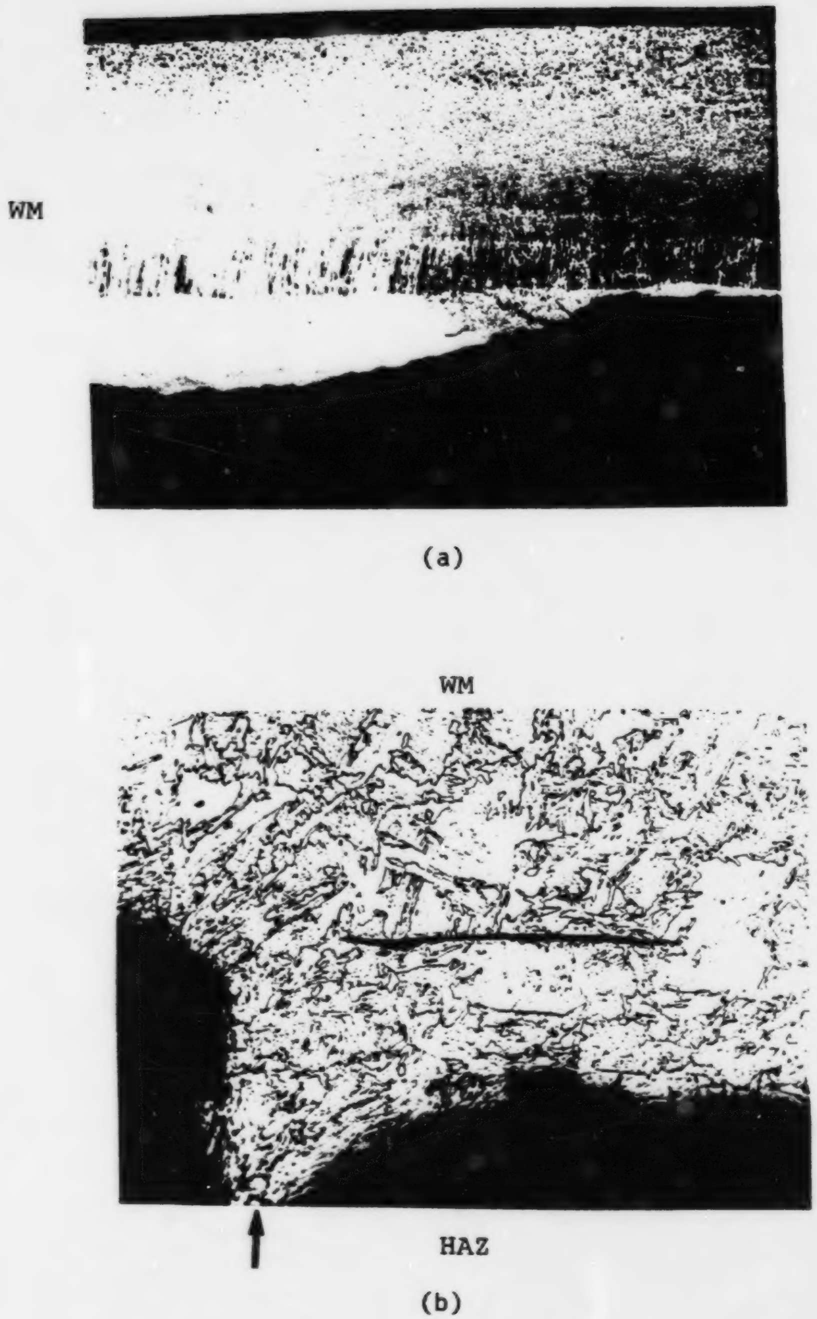

FIGURE 109: The longitudinal section showing the location of the tip of fatigue precrack (arrow mark) and the fracture path at the fracture initiation site of the CTOD specimen 6S9, (a) Neg. 8634, Mag. 5 x; and (b) Neg. 8616, Mag. 200 x.

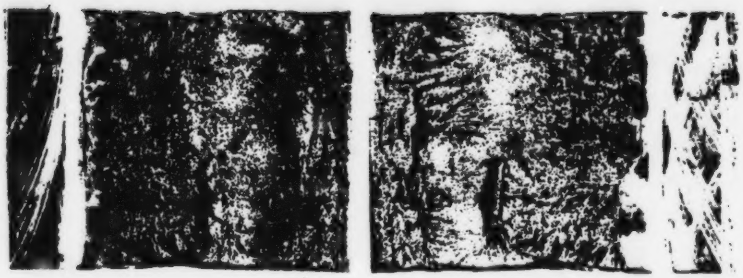

FIGURE 110: Fatigue precrack in the as-welded CTOD specimen 1A5, no pre-compression of the notch ligament, showing irregular precrack front, Neg. 51-C-2.

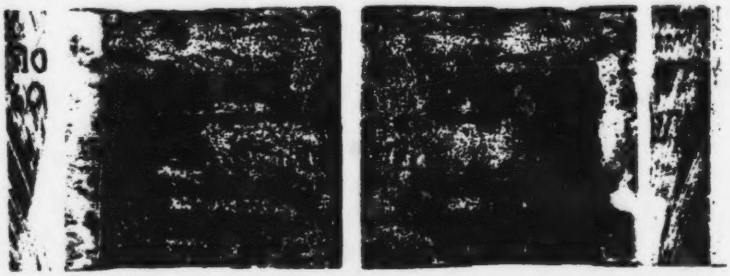

FIGURE 111: Fatigue precrack in the stress-relieved CTOD specimen 1S10, no pre-compression of the notch ligament, showing uniform precrack front, Neg. 51-C-6.

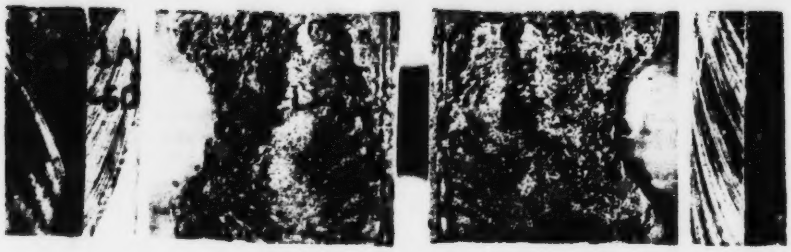

FIGURE 112: Fatigue precrack in the as-welded CTOD specimen 1A1, notch ligament pre-compressed to give total indentation depth of 1% of thickness, showing bowl shaped precrack front, Neg. 7924.

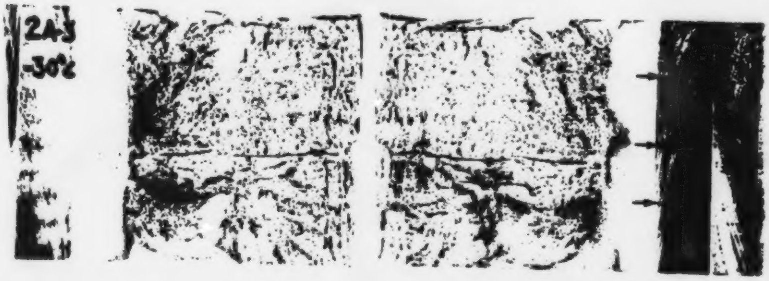

FIGURE 113: Fatigue precrack in the as-welded CTOD specimen 2A3, notch ligament pre-compressed to give total indentation depth of 0.35 - 0.40% of thickness, showing uniform precrack front and the fracture initiation sites (lines marked) along the thickness, Neg. 52-A-3.

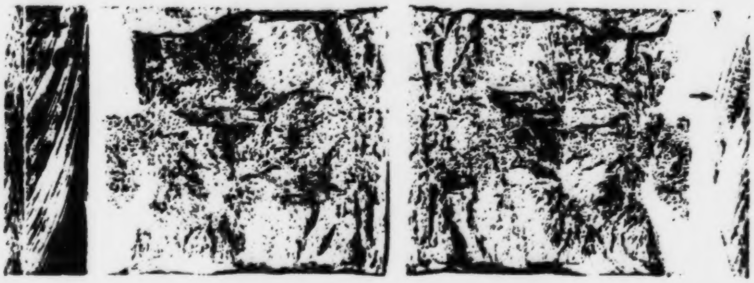

FIGURE 114: Fatigue precrack in the as-welded CTOD specimen 2A9 showing the brittle fracture region (BF) in the fatigue crack and the fracture initiation location (lines marked) along the thickness, Neg. 52-B-3.

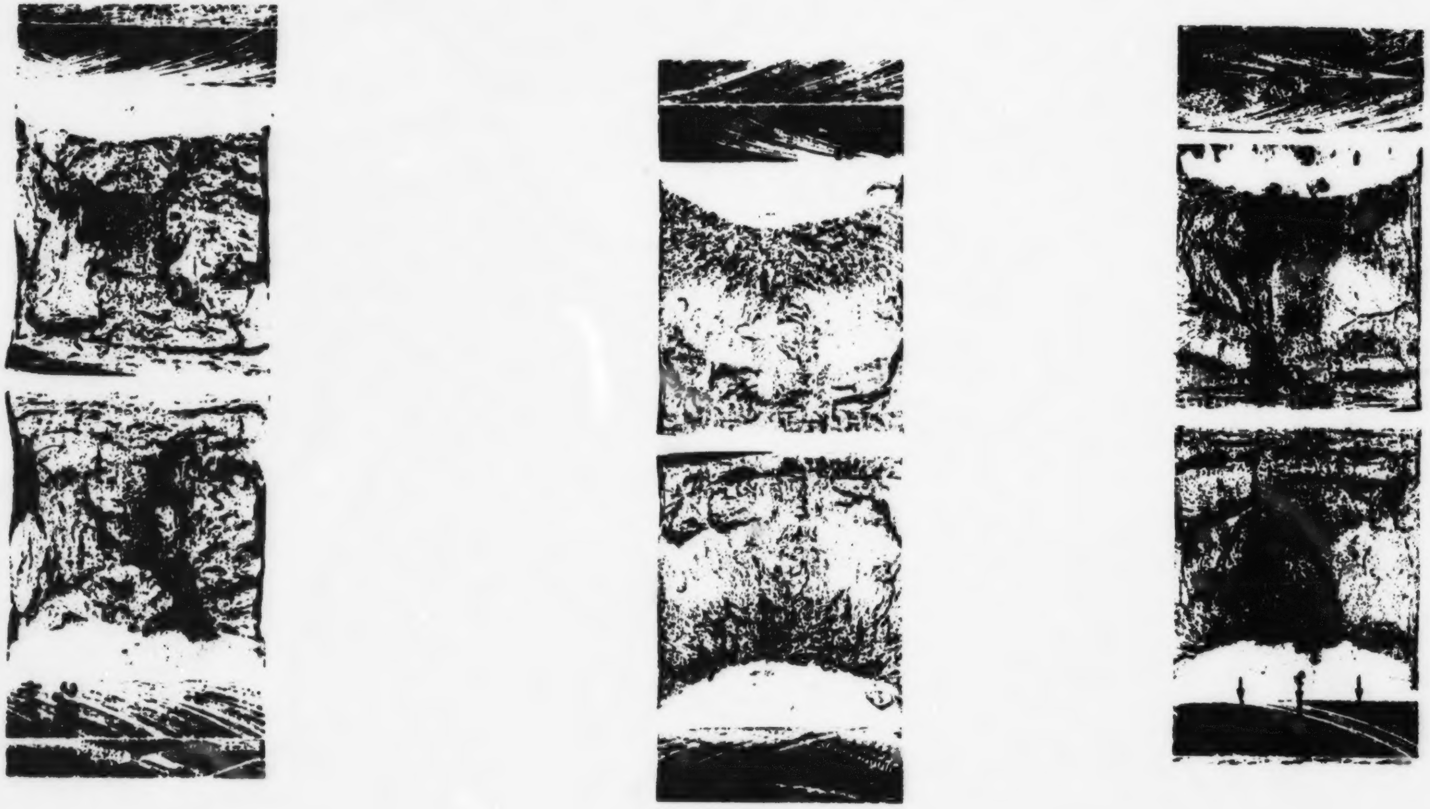

(a) (b) (c)

FIGURE 115: Fracture surfaces showing the locations of the fracture initiations (lines marked) in the CTOD specimens (a) 2A4, (b) 2A7 and (c) 2A8, Neg. 52-A-4, 52-B-1, 52-B-2.

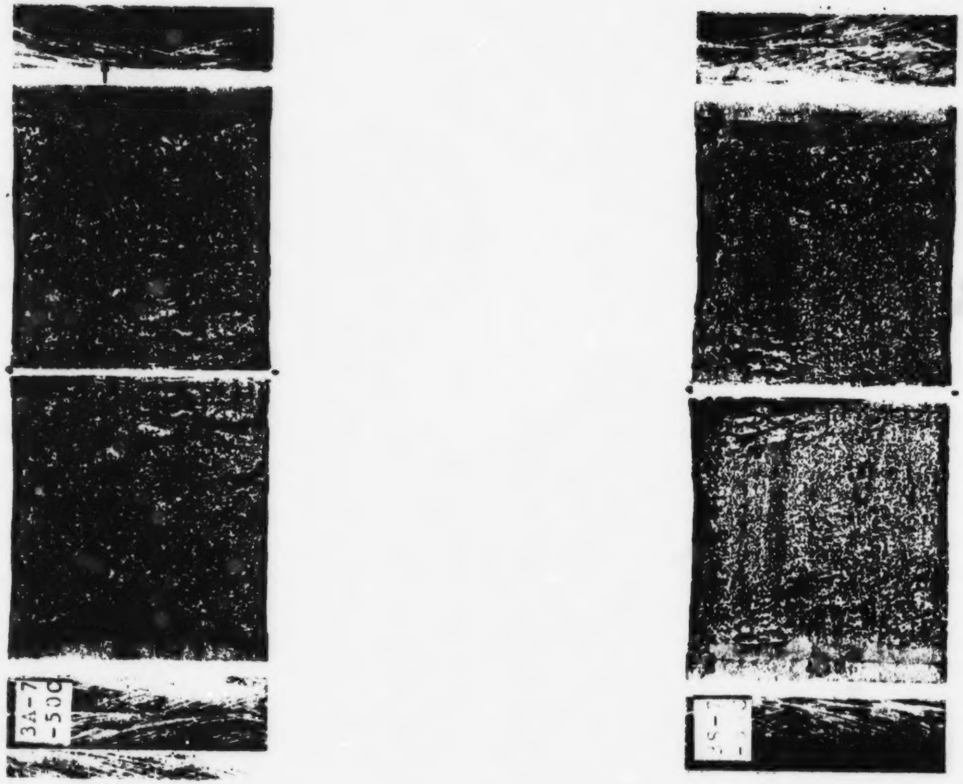

(a) (b)

FIGURE 116: Fracture surfaces showing the locations of the fracture (lines marked) initiations in the CTOD specimens (a) 3A7 and (b) 3S7, Neg. 58-C-3 and 58-A-4.

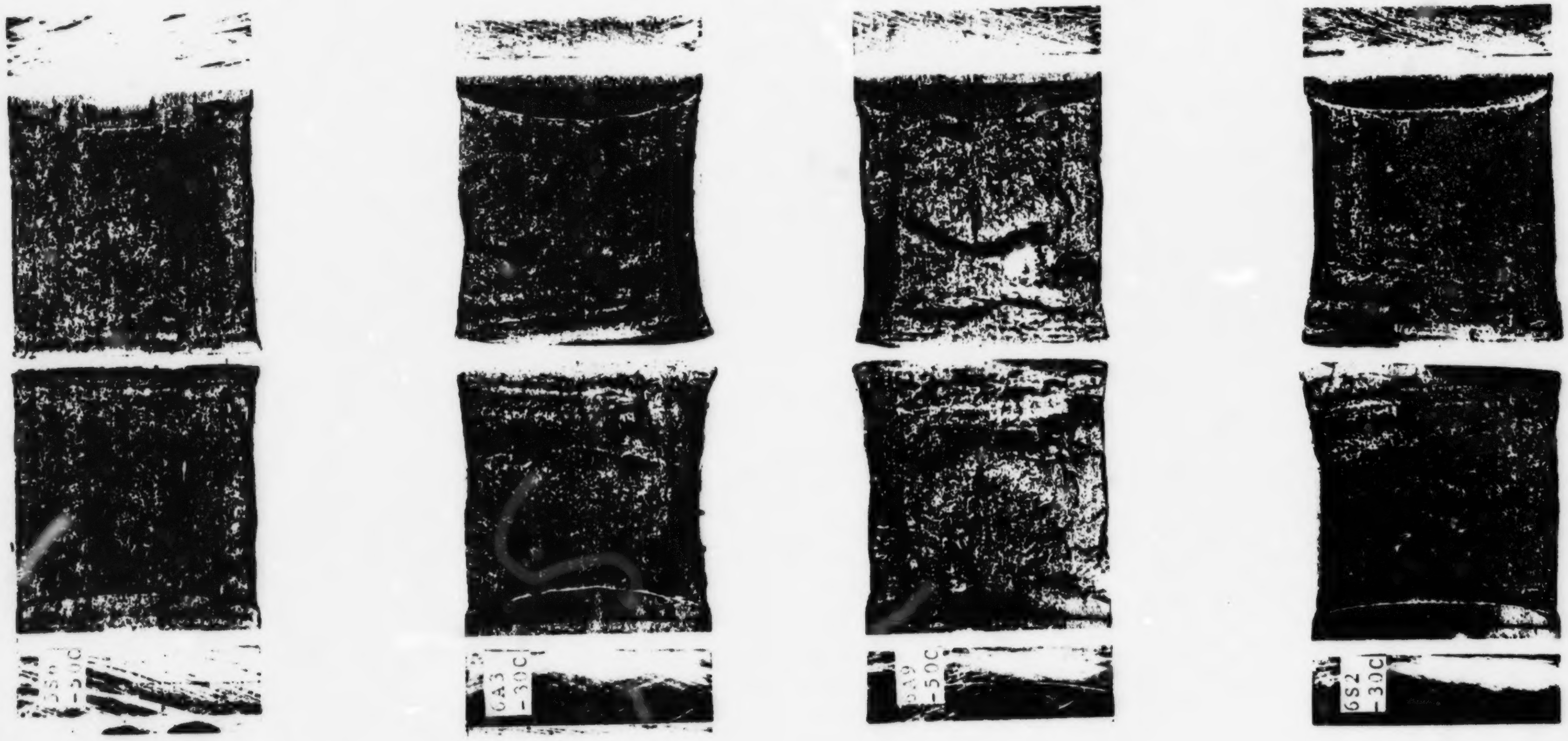

(a) (b) (c) (d)

FIGURE 117: Fracture surfaces showing the locations of the fracture initiations (lines marked) along the thickness of the CTOD specimens (a) 5S6, (b) 6A3, (c) 6A9 and (d) 6S2; Neg. 61-E-6, 67-A-6, 67-B-6, and 67-C-4.

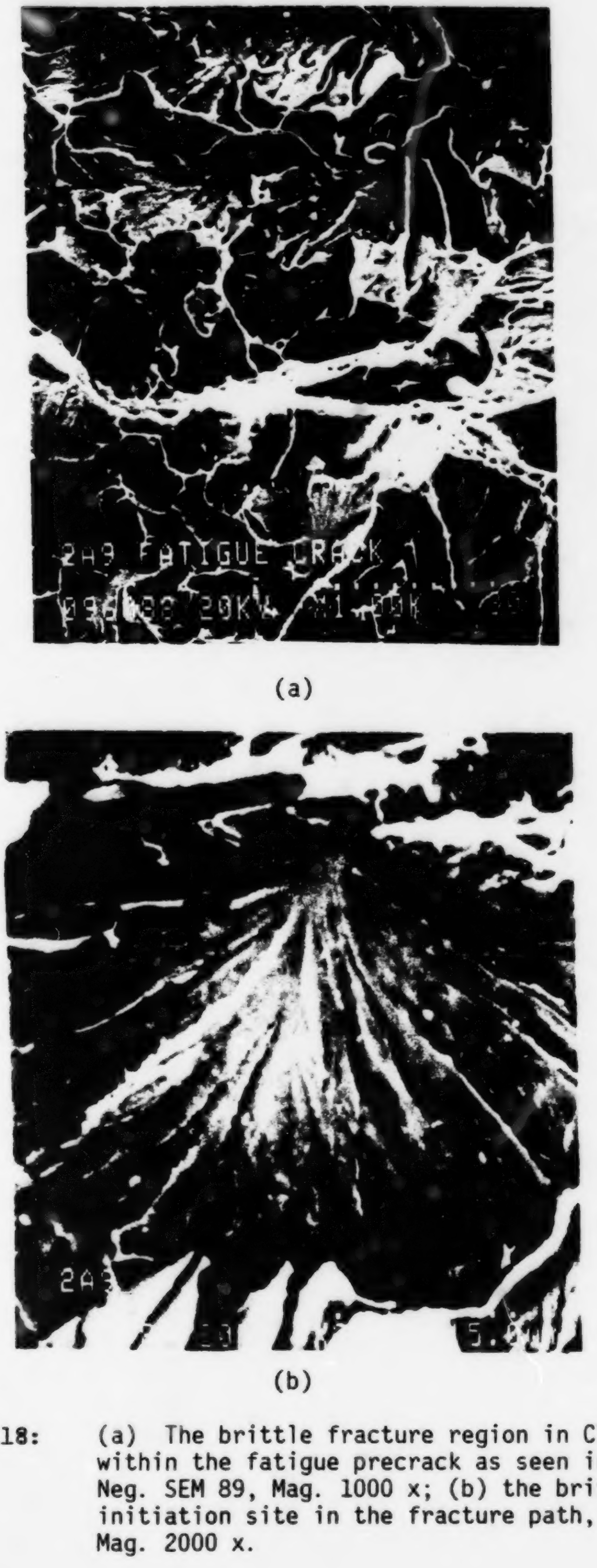
2A9 FATIGUE CRACK
20KV
2A9

(a)

(b)

FIGURE 118: (a) The brittle fracture region in CTOD specimen 2A9 within the fatigue precrack as seen in Figure 68, Neg. SEM 89, Mag. 1000 x; (b) the brittle fracture initiation site in the fracture path, Neg. SEM 90, Mag. 2000 x.

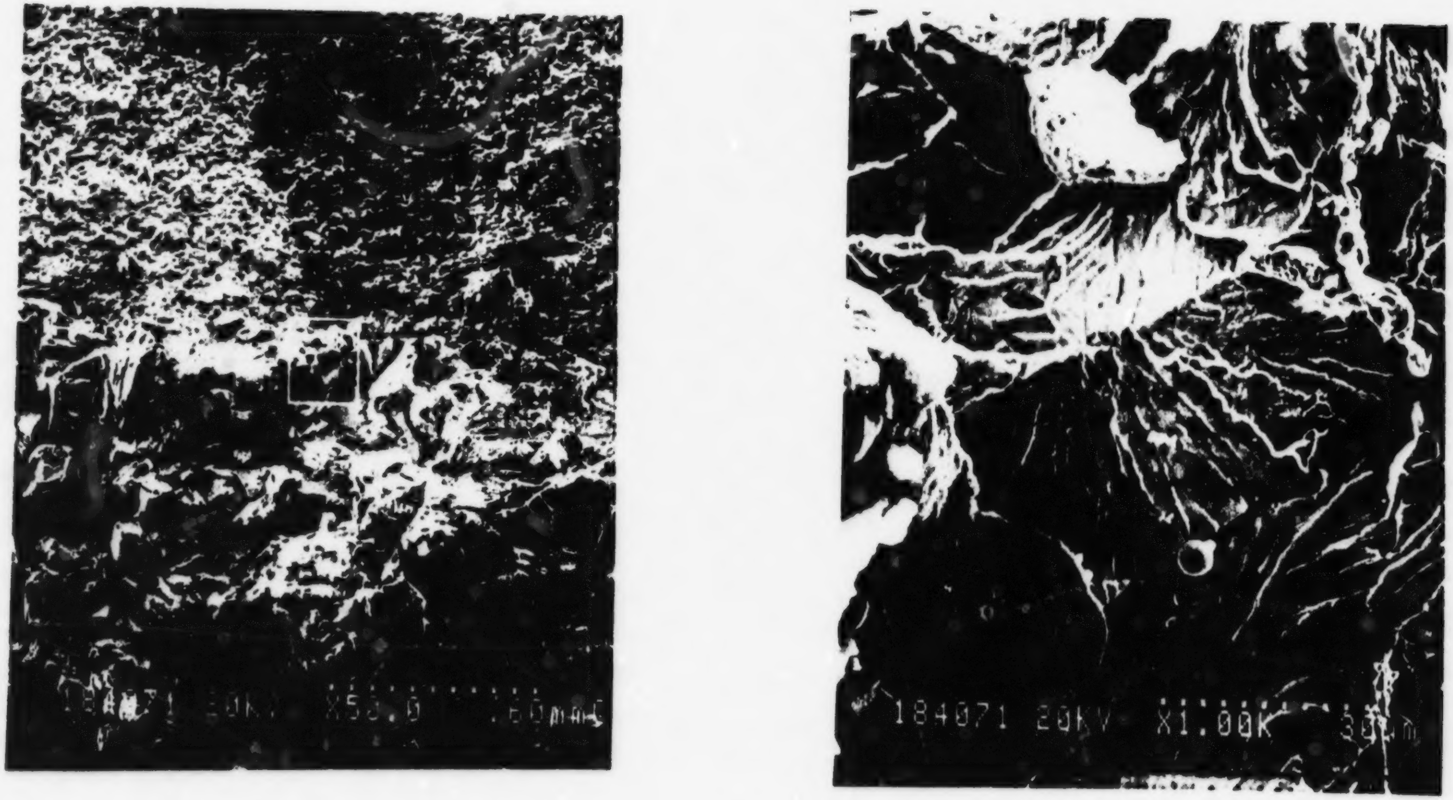
X50.0
184071 20KV X1.00K 30µm

(a) (b)

FIGURE 119: The brittle fracture initiation site in relation to the fatigue precrack front in CTOD specimen 2A4, (a) Neg. SEM 12, Mag. 50 x; and (b) the fracture initiation site. Neg. SEM 10, Mag. 1000 x.

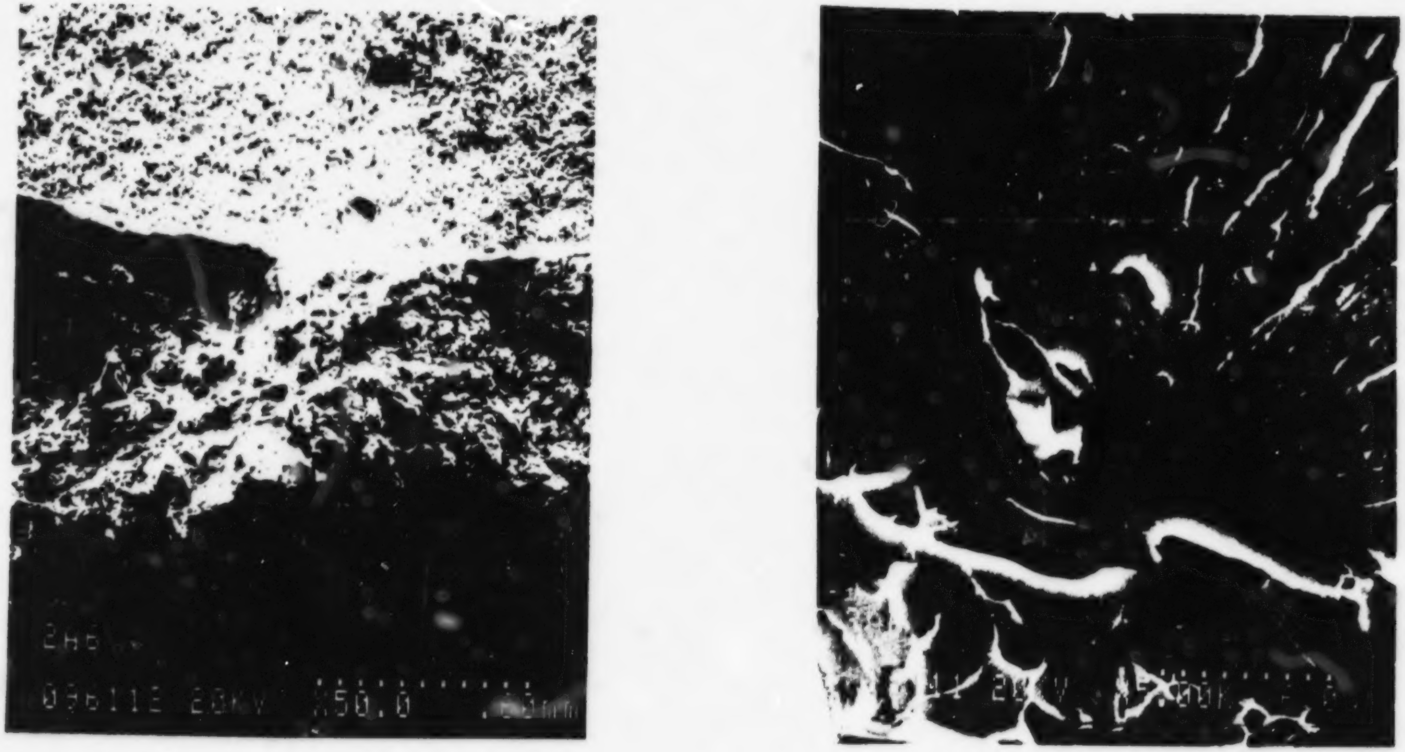

(a)

(b)

FIGURE 120: The brittle fracture initiation site in relation to the fatigue precrack front in CTOD specimen 2A6, Neg. SEM 112, Mag. 50 x; and (b) the fracture initiation site showing some porosity (microvoid coalescence), Neg. SEM 111, Mag. 5000 x.

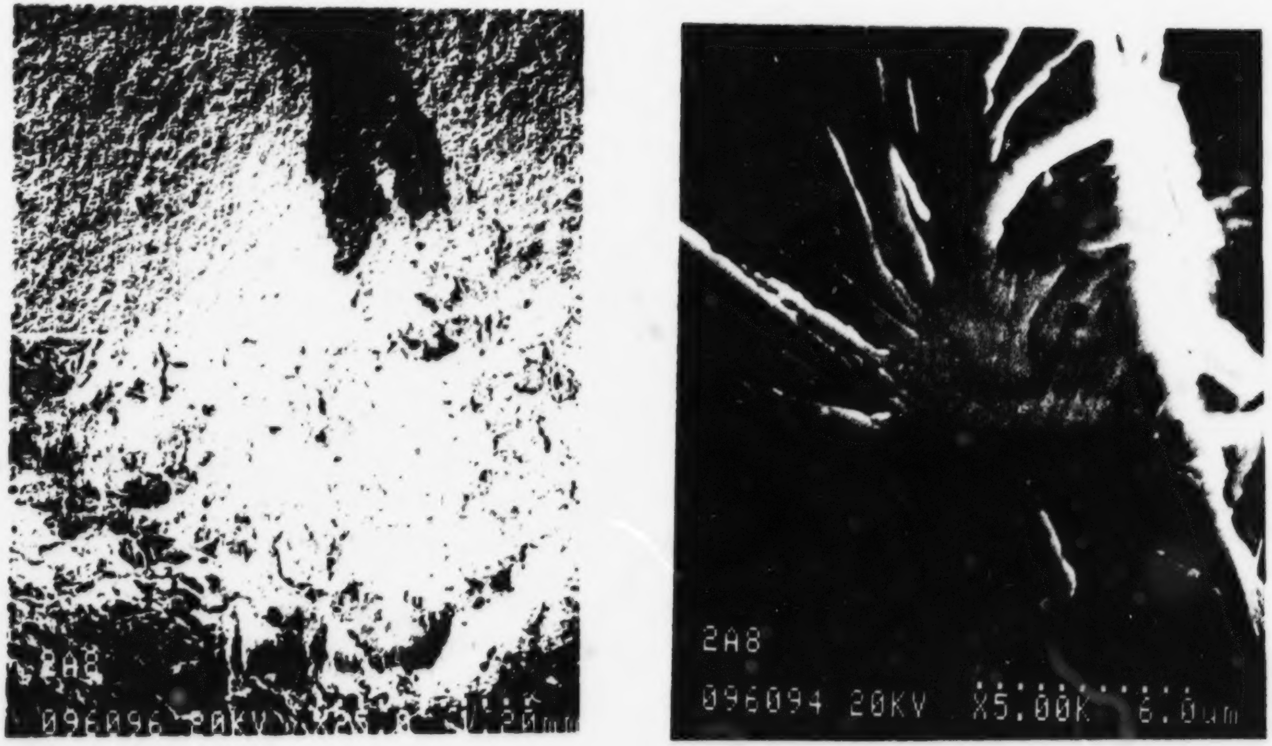
2A8
2A8
096094 20KV X5.00K 6.0um

(a) (b)

FIGURE 121: The brittle fracture initiation site in relation to the fatigue precrack front in CTOD specimen 2A8, (a) Neg. SEM 96, Mag. 25 x; and (b) the fracture initiation site (refer to Figure 115) showing some inclusions, Neg. SEM 94, Mag. 5000 x.

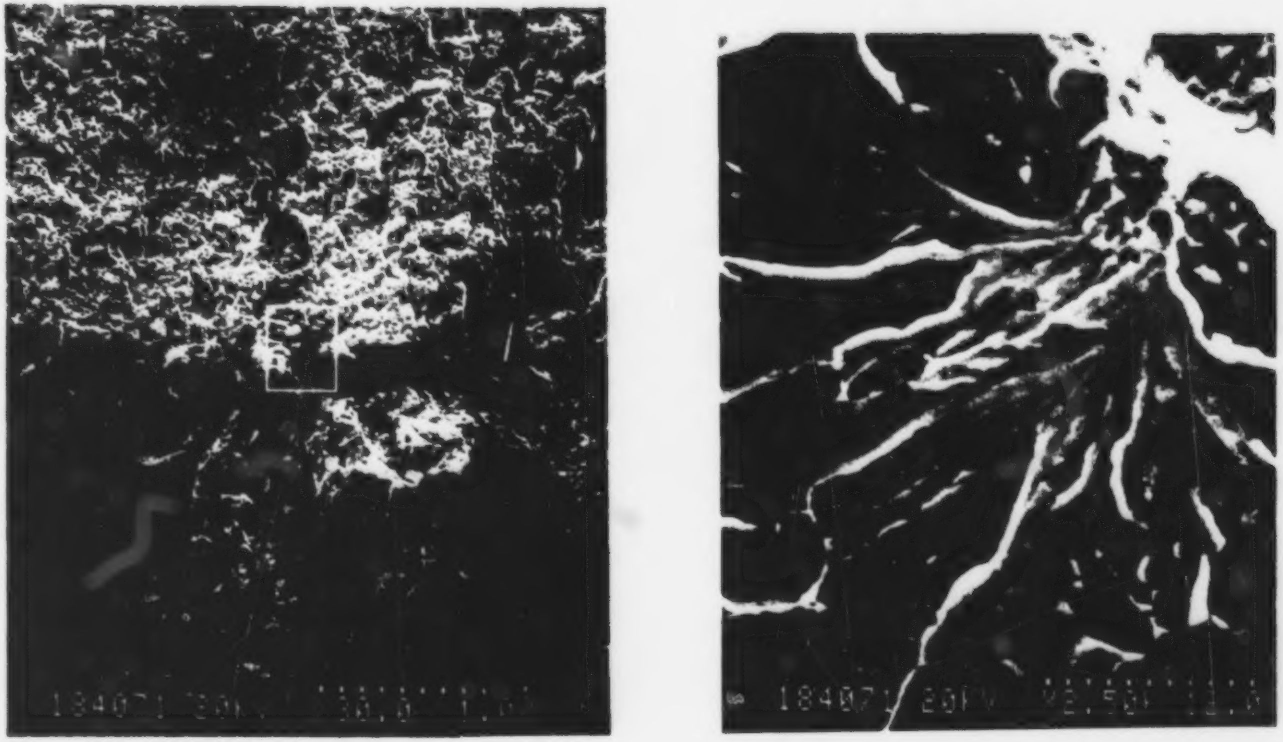

(a)

(b)

FIGURE 122: (a) The brittle fracture initiation site in relation to the fatigue precrack front, in CTOD specimen 3A7, Neg. SEM 21, Mag. 30 x; and (b) the fracture initiation site (refer to Figure 116), Neg. SEM 20, Mag. 2500 x.

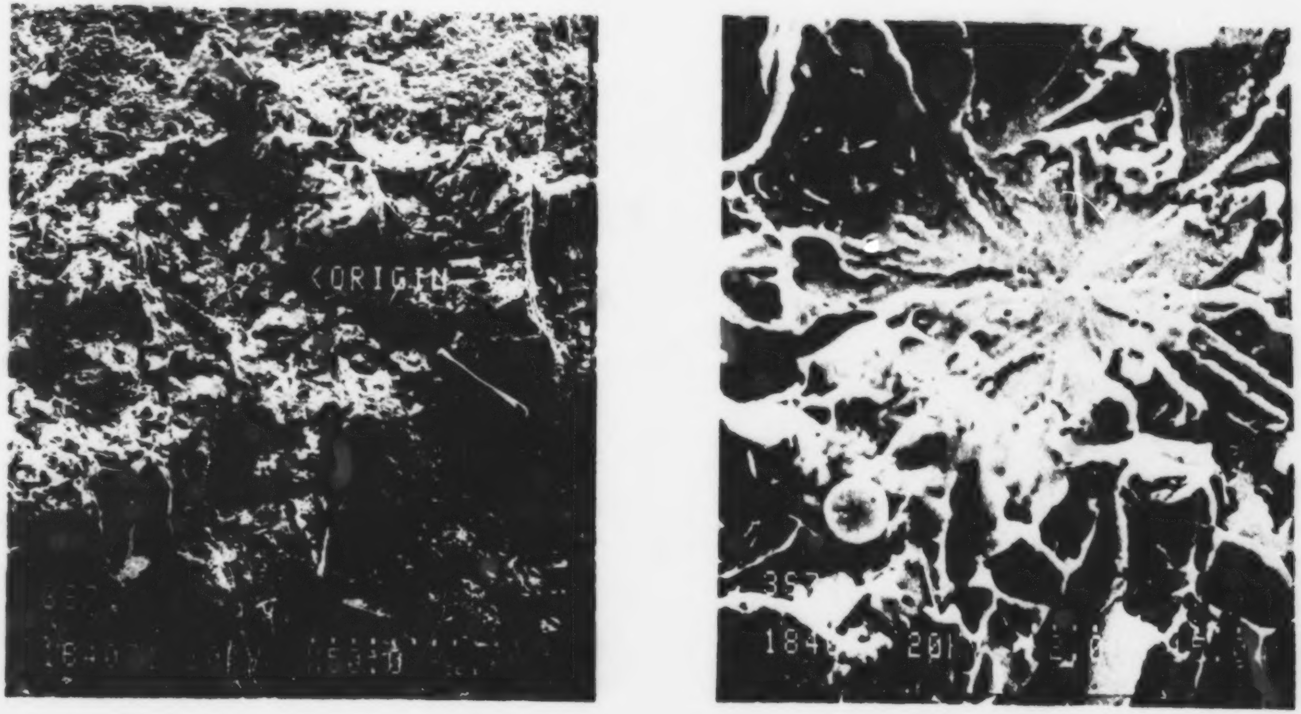

(a)

(b)

FIGURE 123: (a) The brittle fracture initiation site in relation to the fatigue precrack front in CTOD specimen 3S7, Neg. SEM 26, Mag. 50 x; and (b) the fracture initiation site (refer to Figure 116) showing some porosity , Neg. SEM 19, Mag. 2000 x.

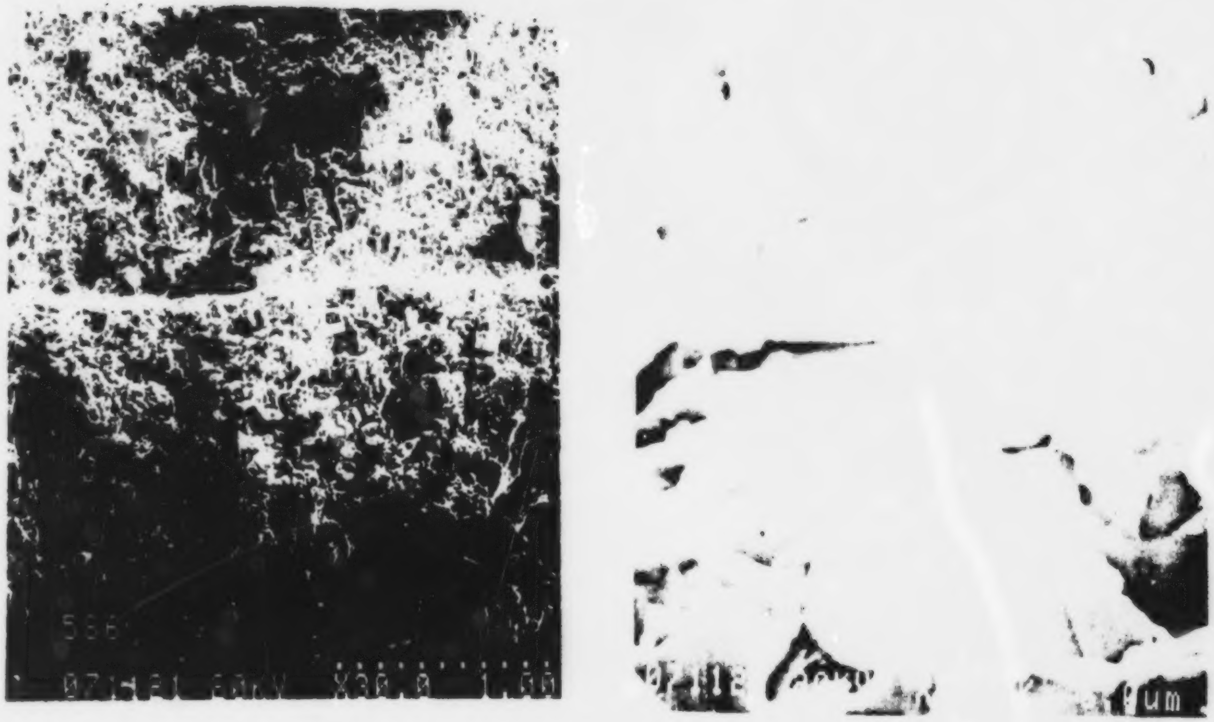

(a) (b)

FIGURE 124: (a) The brittle fracture initiation site in relation to the fatigue precrack front in CTOD specimen 5S6, Neg. SEM 121, Mag. 30 x; and (b) the fracture initiation site (refer to Figure 117), Neg. SEM 120, Mag. 5000 x.

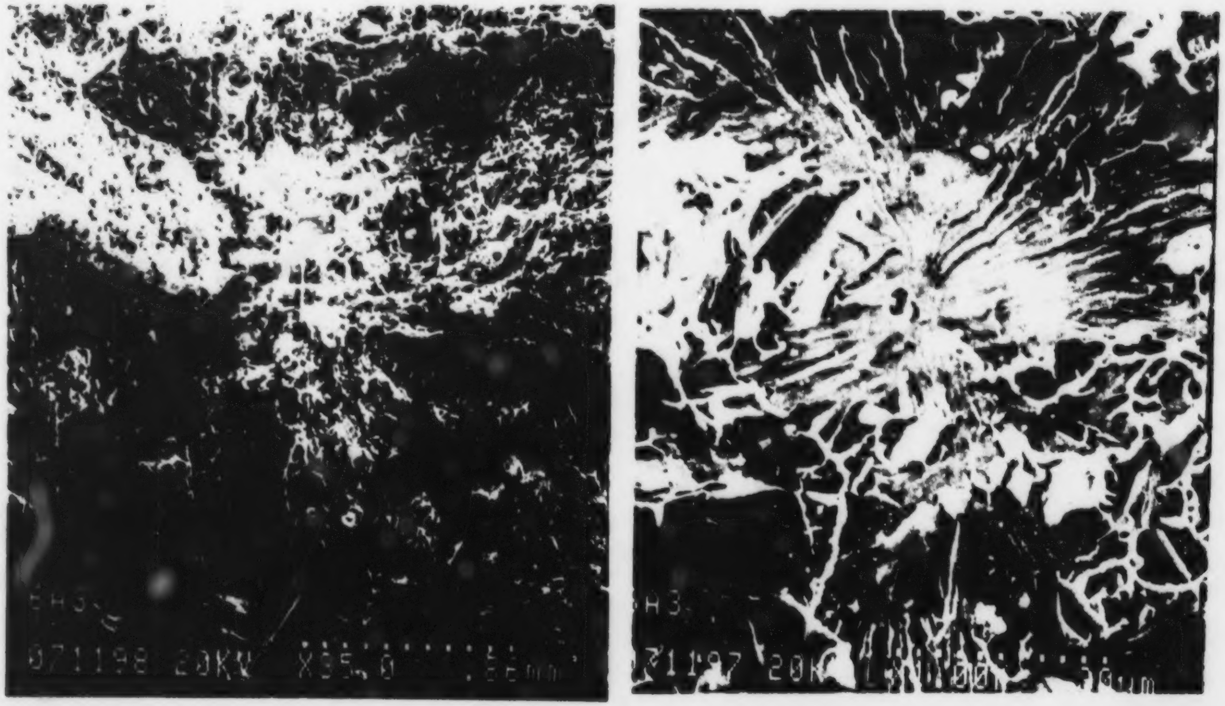
6H3
071198 20KV X35.0
H3
71197 20K

(a) (b)

FIGURE 125: (a) The brittle fracture initiation site in relation to the fatigue precrack front in CTOD specimen 6A3, Neg. SEM 198, Mag. 35 x; and (b) the fracture initiation site (refer to Figure 117) showing an inclusion, Neg. SEM 197, Mag. 1000 x.

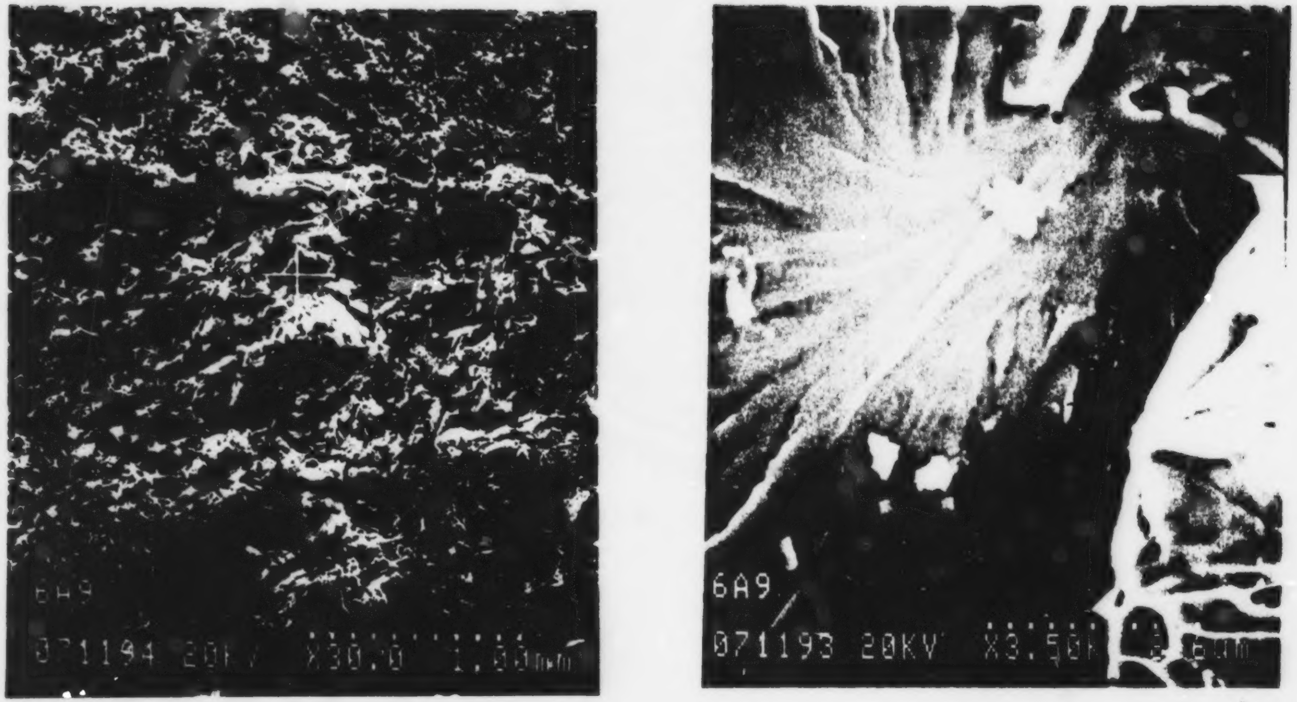
6A9
071194 20KV X30.0 1.00mm
6A9
071193 20KV X3.50K

(a) (b)

FIGURE 126: (a) The brittle fracture initiation site in relation to the fatigue precrack front in CTOD specimen 6A9, Neg. SEM 194, Mag. 30 x; and (b) the fracture initiation site (refer to Figure 117) showing an inclusion, Neg. SEM 193, Mag. 3500 x.

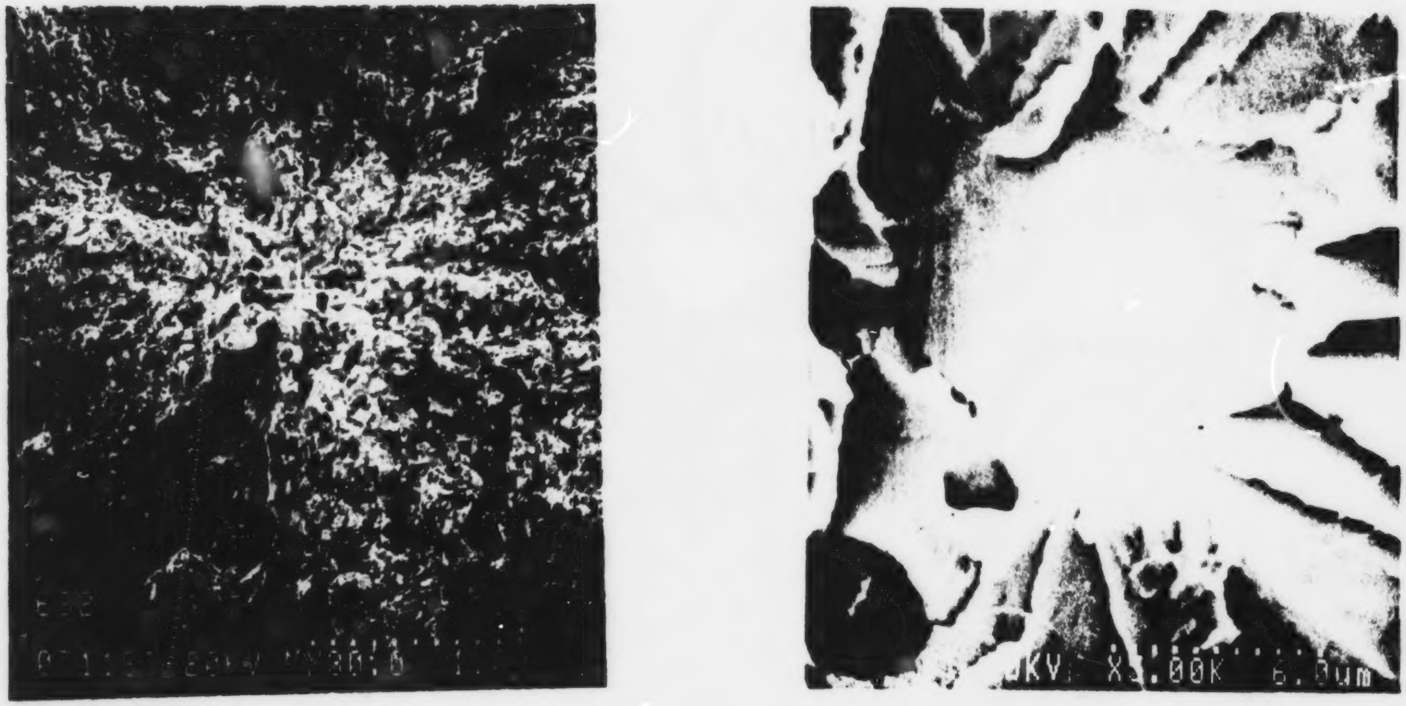

(a) (b)

FIGURE 127: (a) The brittle fracture initiation site in relation to the fatigue precrack front in CTOD specimen 6S2, Neg. SEM 183, Mag. 30 x; and (b) the fracture initiation site (refer to Figure 117) showing the cleavage facet as the origin, Neg. SEM 181, Mag. 5000 x.

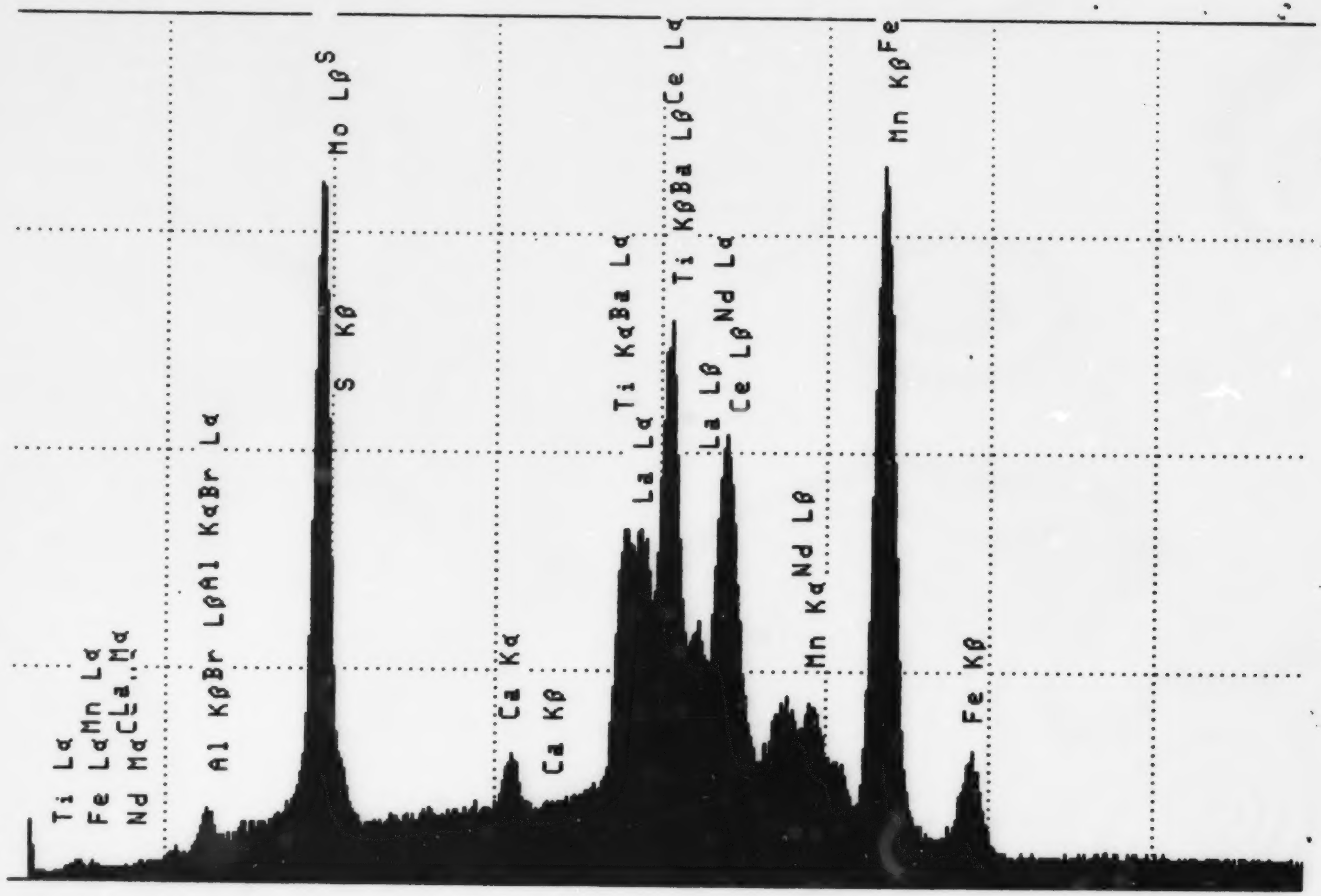

FIGURE 128: The SEM X-ray spectrum of the inclusion at the fracture initiation site in the CTOD specimen 6A3.

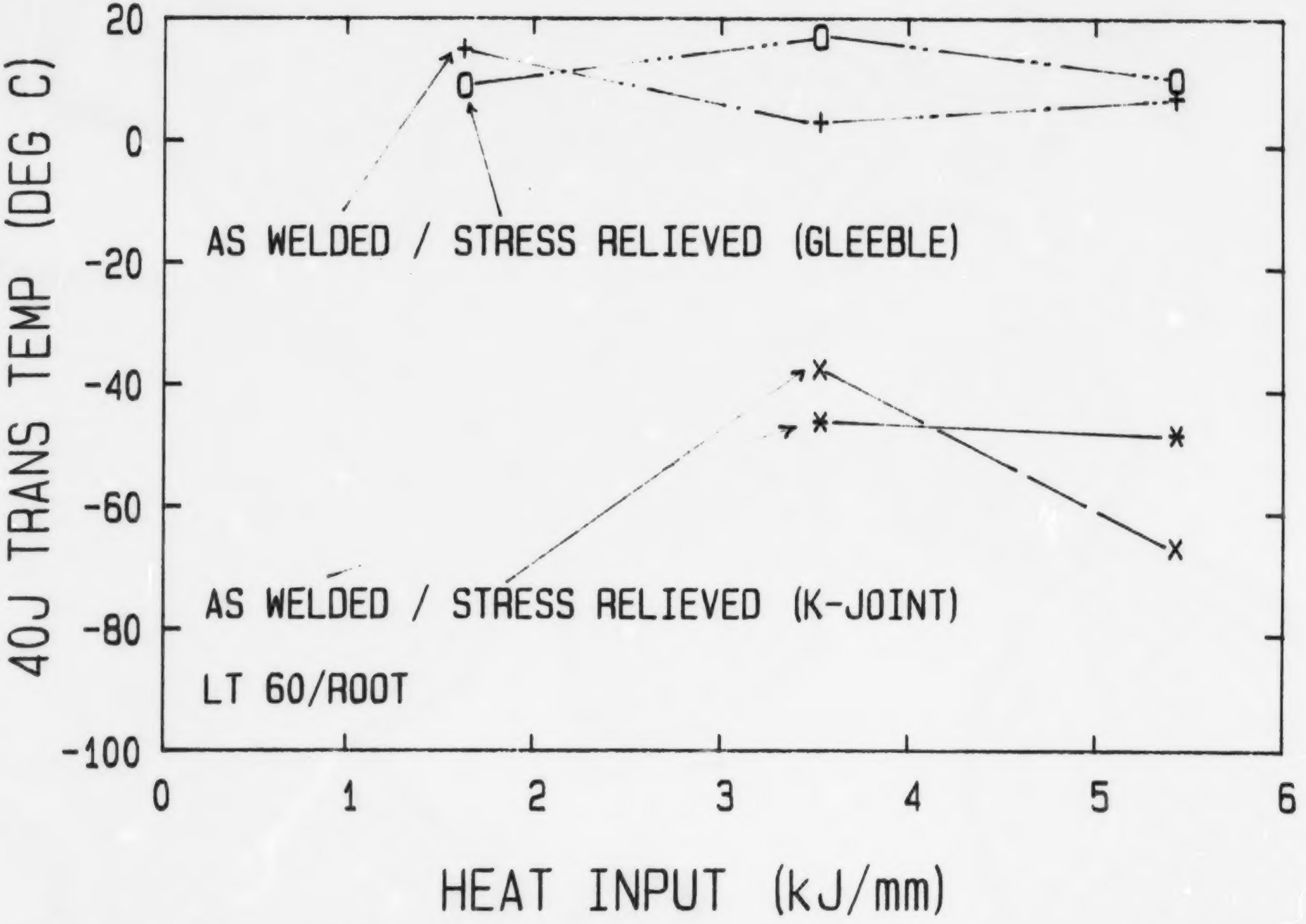

FIGURE 129: 40J transition temperature (average values) vs. heat input plots for HAZ in LT60 steel (root region in K-joint + Gleeble).

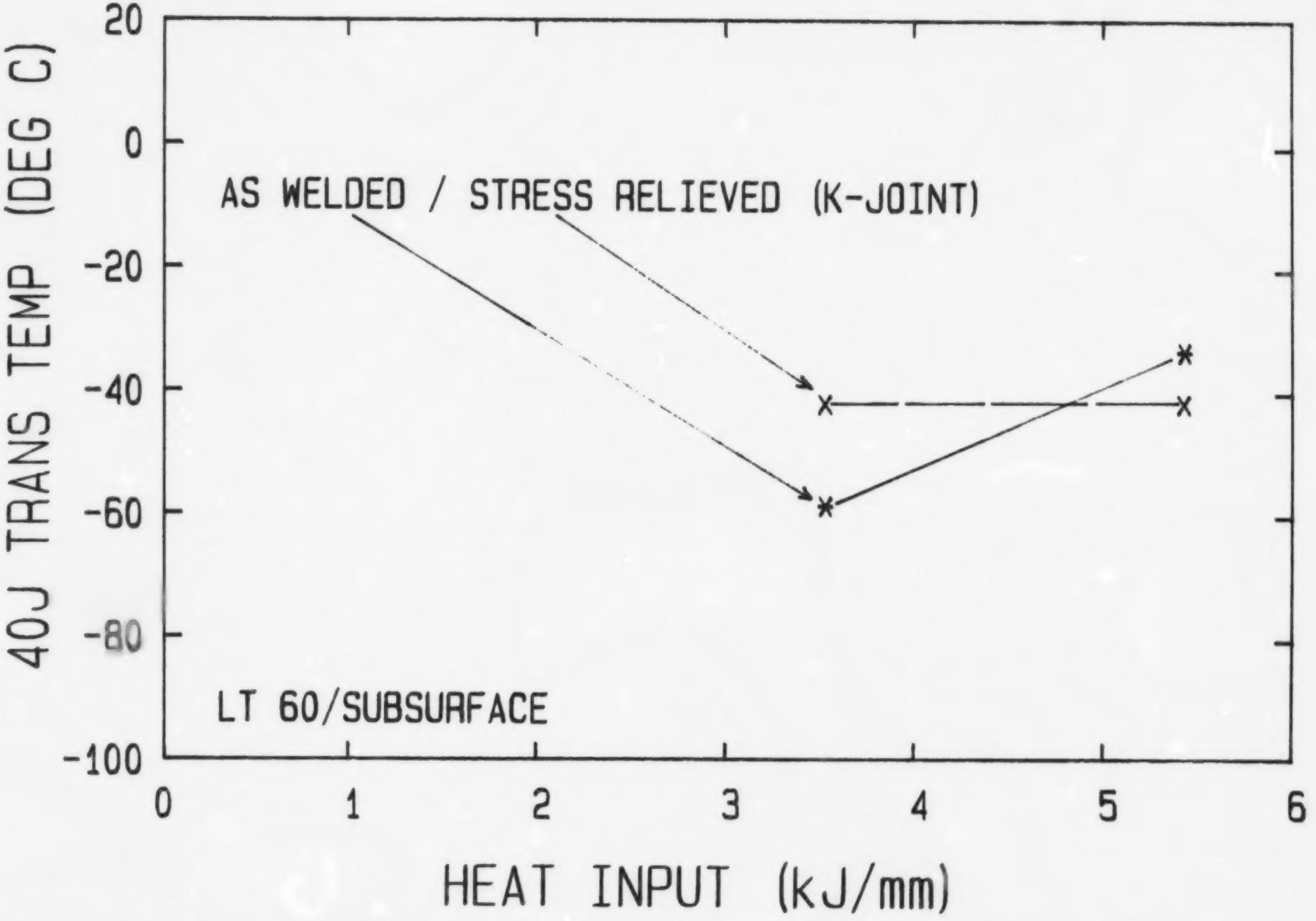

FIGURE 130: 40J transition temperature (average values) vs. heat input plots for HAZ in LT60 steel (subsurface region in K-joint).

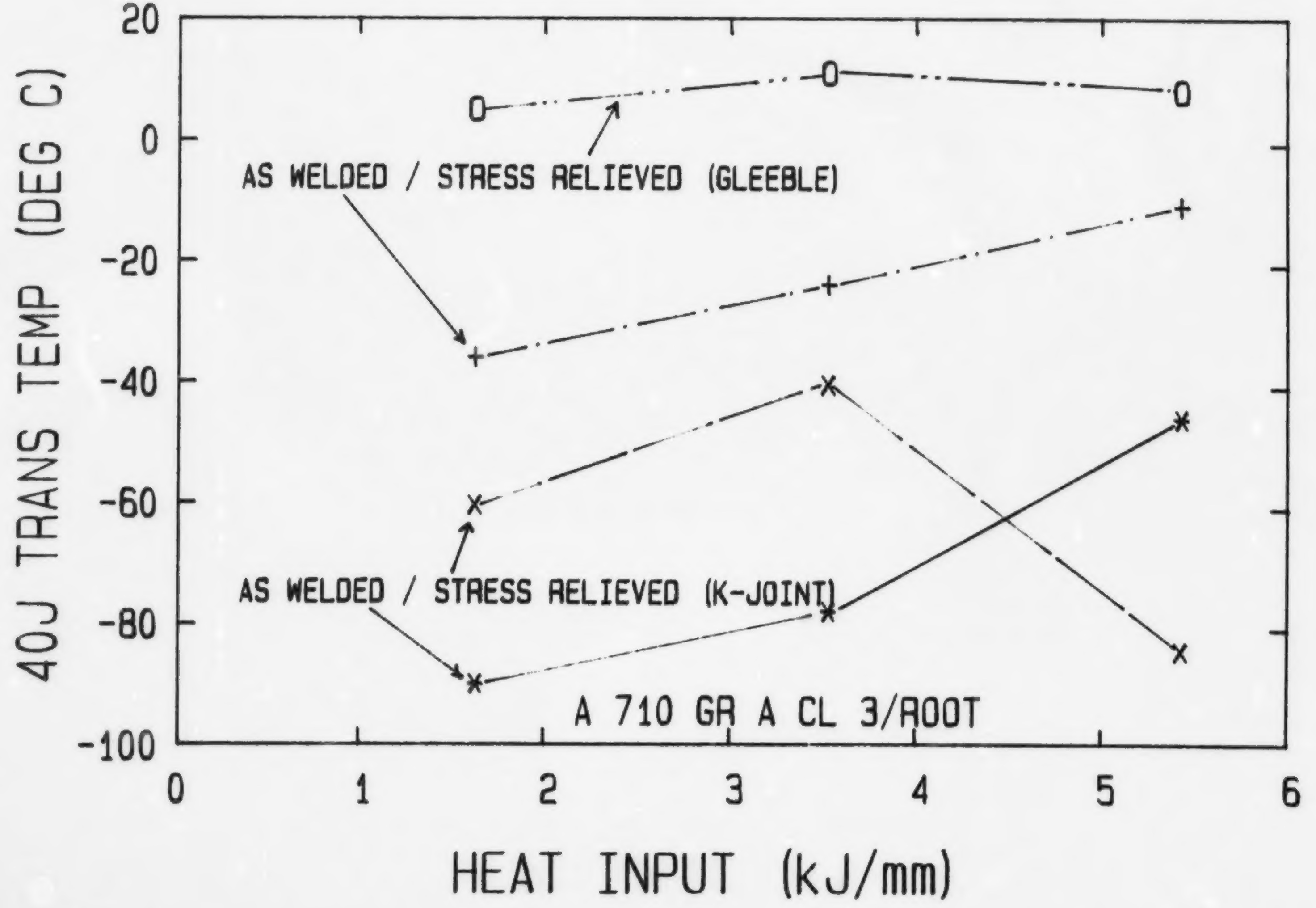

FIGURE 131: 40J transition temperature (average values) vs. heat input plots for HAZ in A710 Gr. A Cl. 3 steel (root region in K-joint + Gleeble).

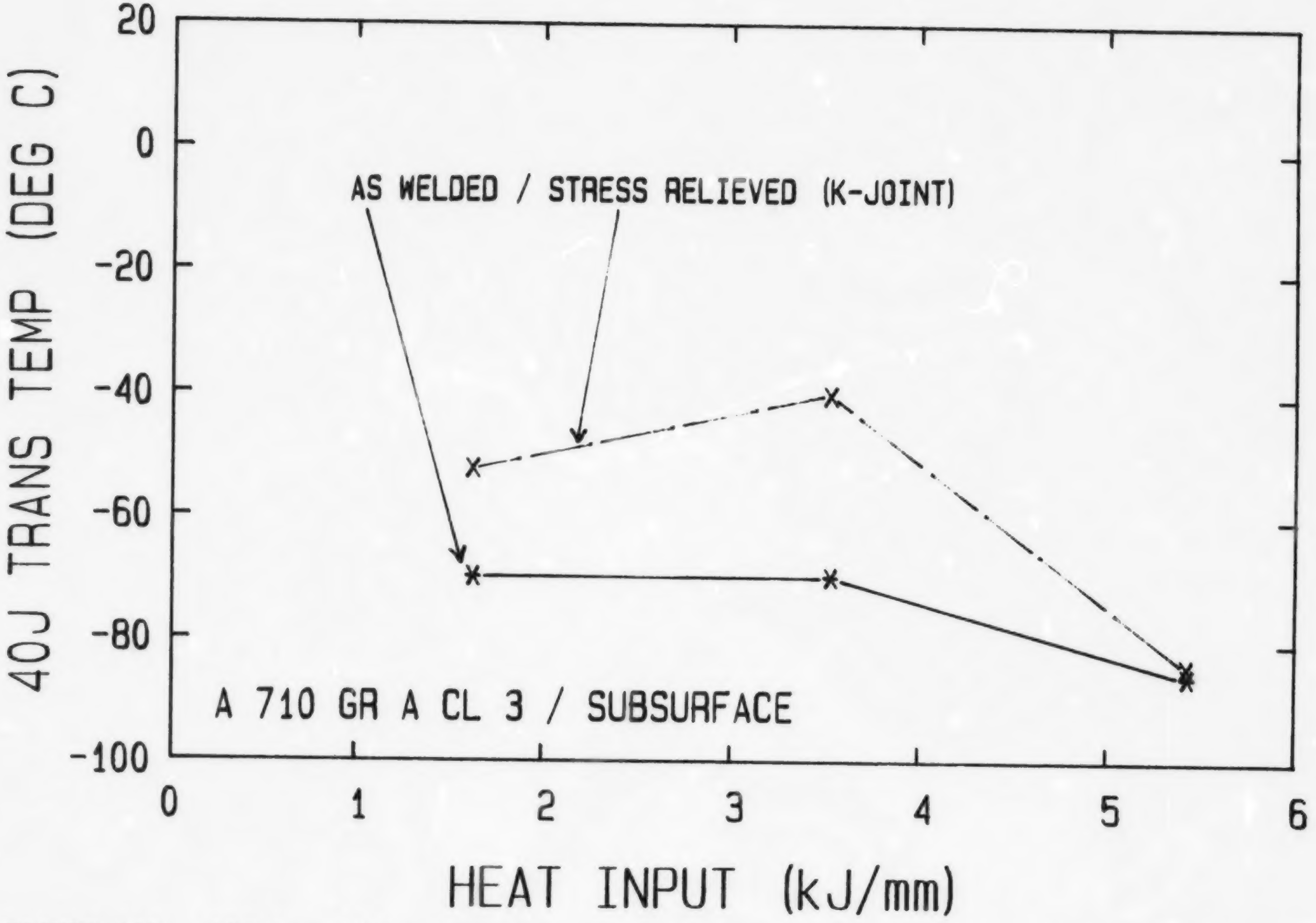

FIGURE 132: 40J transition temperature (average values) vs. heat input plots for HAZ in A710 Gr. A Cl. 3 steel (subsurface region).

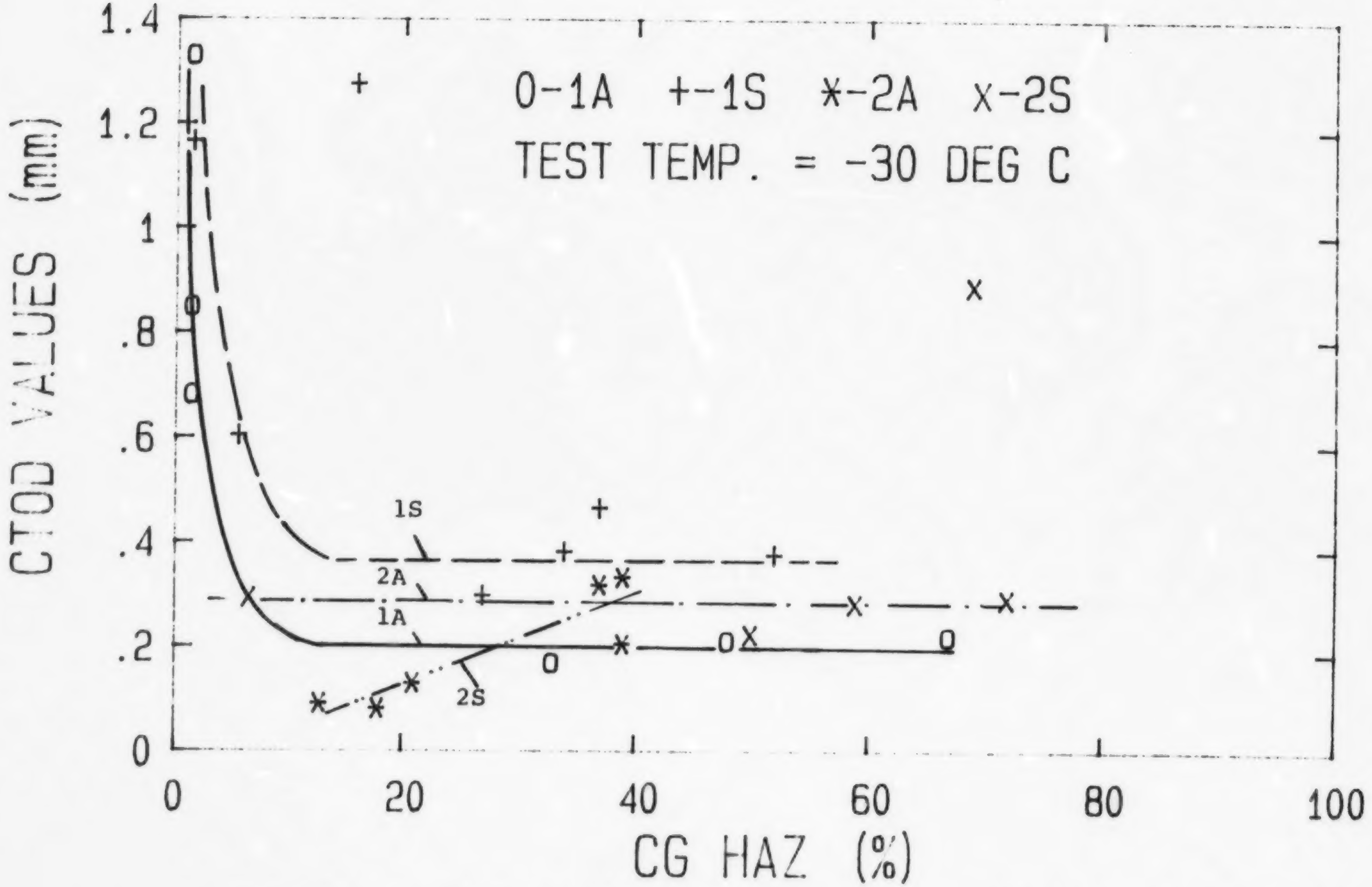

FIGURE 133: Relationship between CTOD values at -30°C and % CG HAZ in the fatigue precrack (near the precrack front) measured along the thickness B for LT 60 steel.

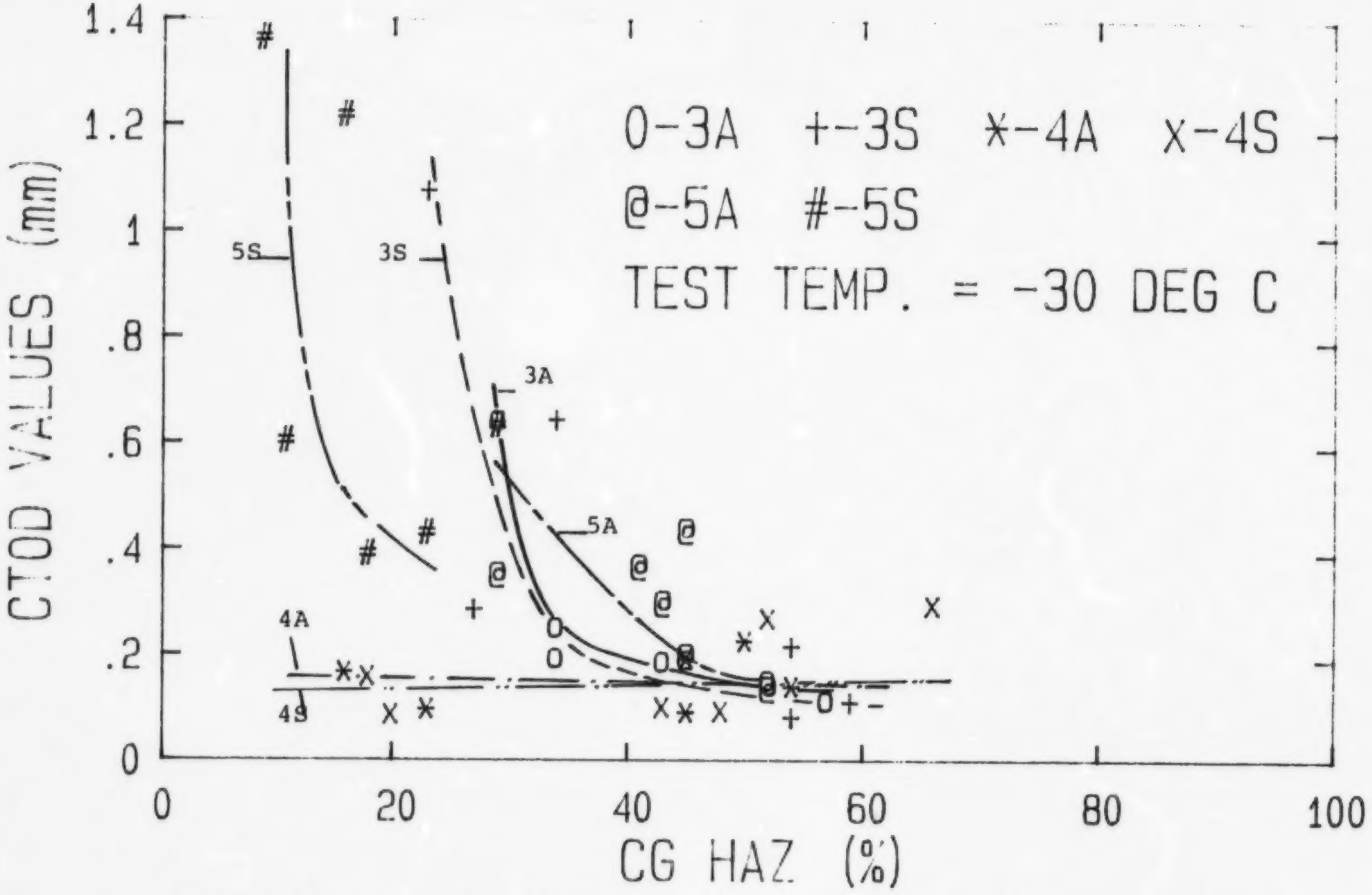

FIGURE 134: Relationship between CTOD values at -30°C and % CG HAZ in the fatigue precrack (near the precrack front) measured along the thickness B for A710 Gr. A, Cl. 3 steel.

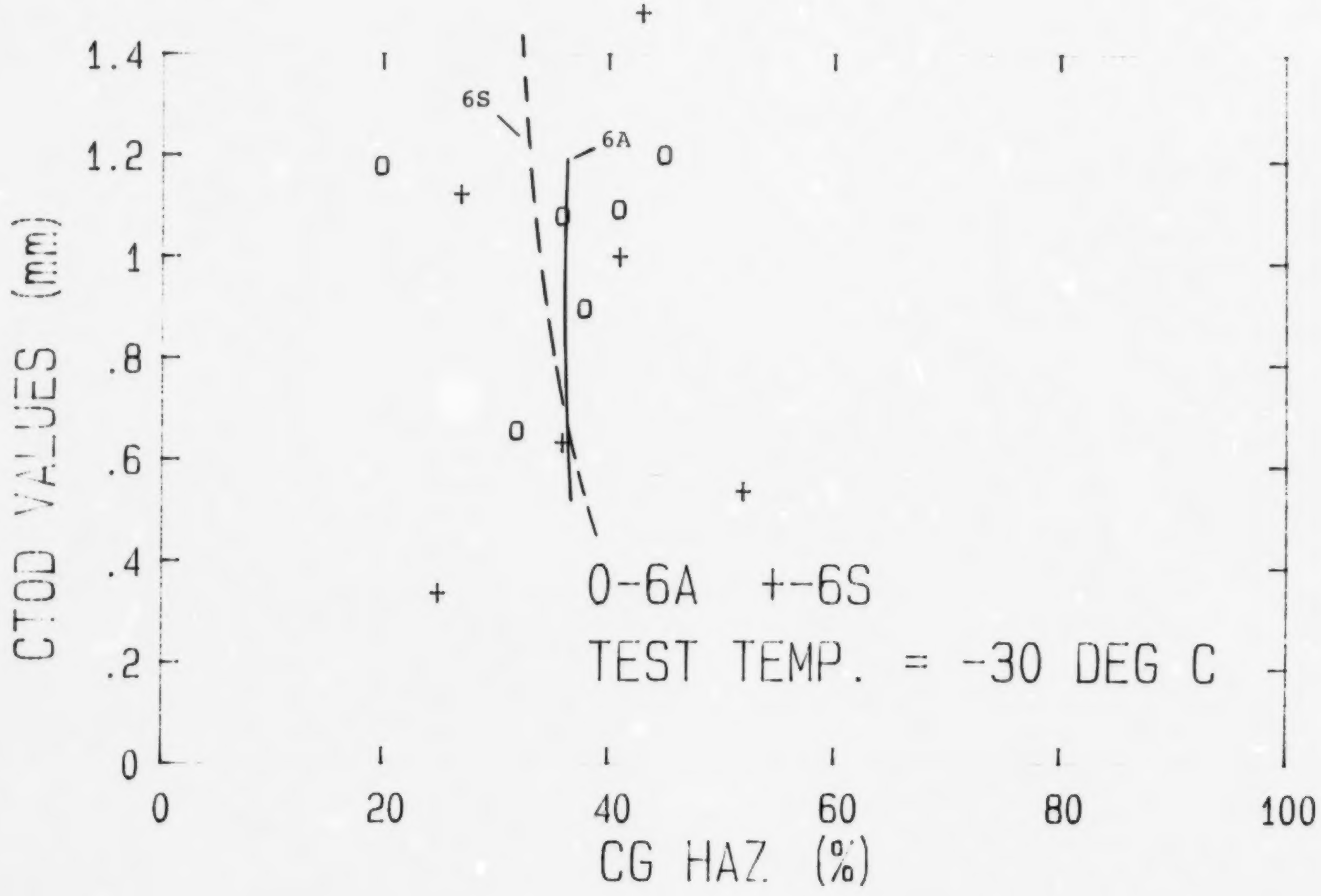

FIGURE 135: Relationship between CTOD values at -30°C and % CG HAZ in the fatigue precrack (near the precrack front) measured along the thickness B for MACS (ACC, DQT) steels.

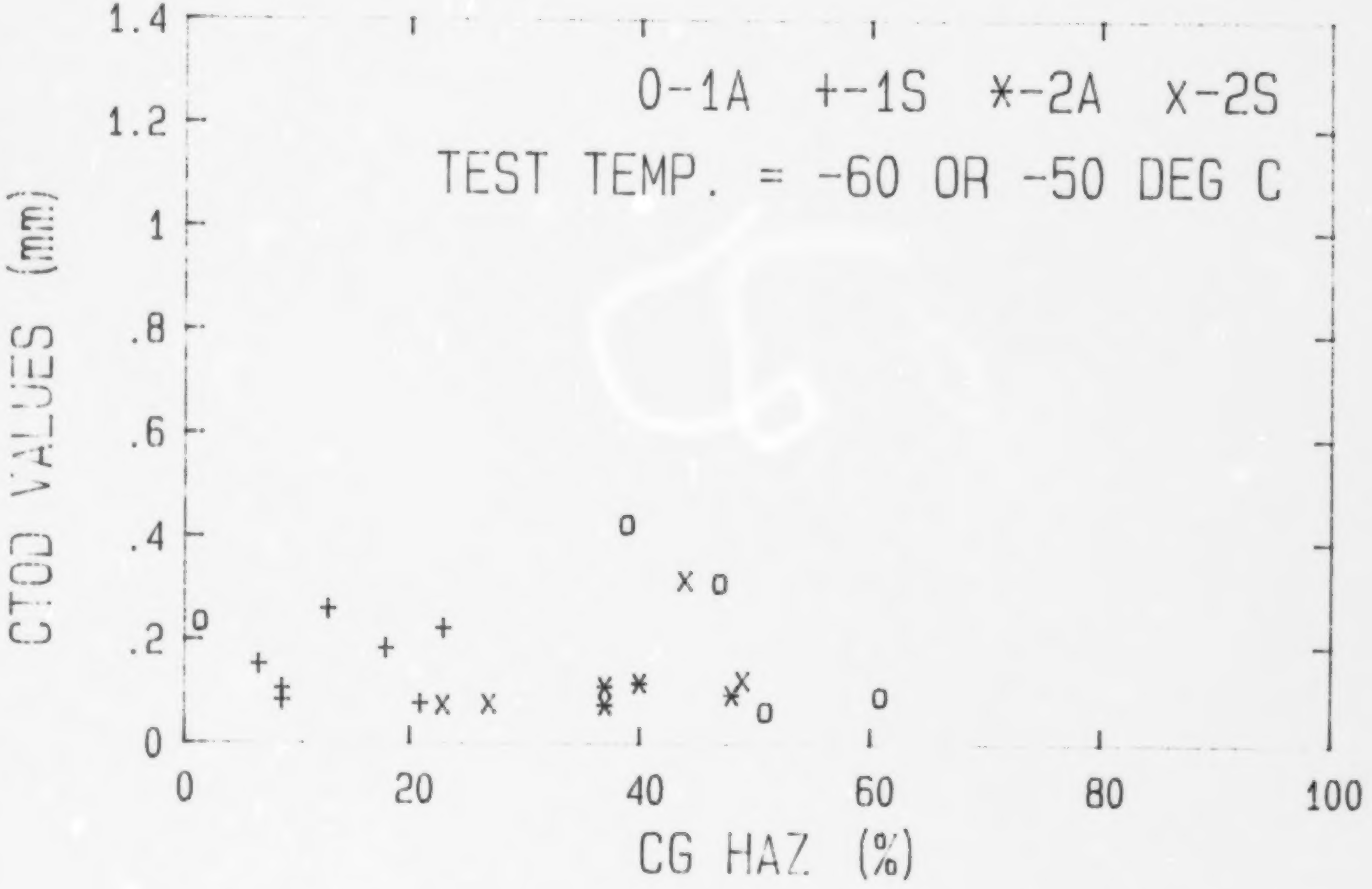

FIGURE 136: Relationship between CTOD values at -50°C and % CG HAZ in the fatigue precrack (near the precrack front) measured along the thickness B for LT 60 steel.

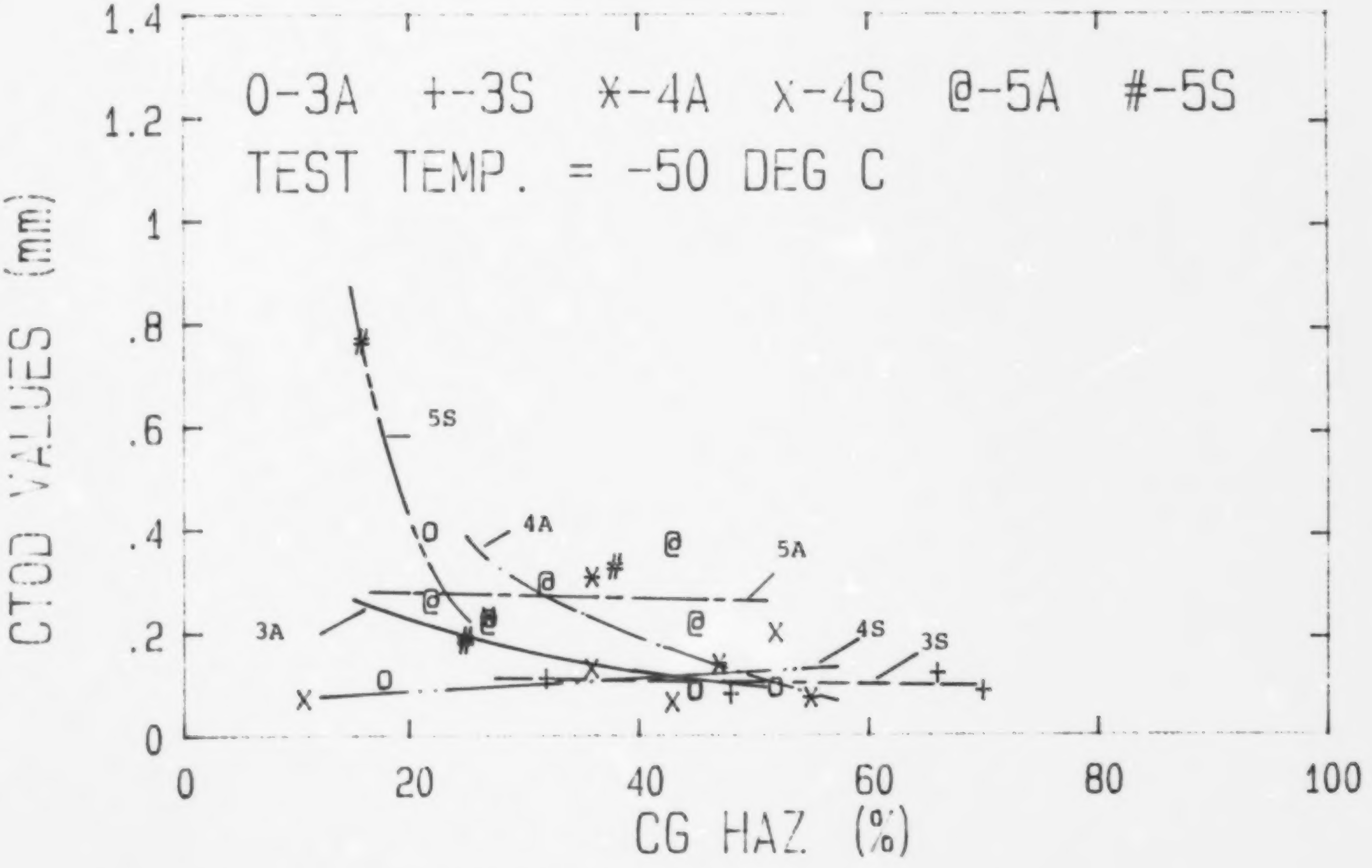

FIGURE 137: Relationship between CTOD values at -50°C and % CG HAZ in the fatigue precrack (near the precrack front) measured along the thickness B for A710, Gr. A, Cl. 3 steel.

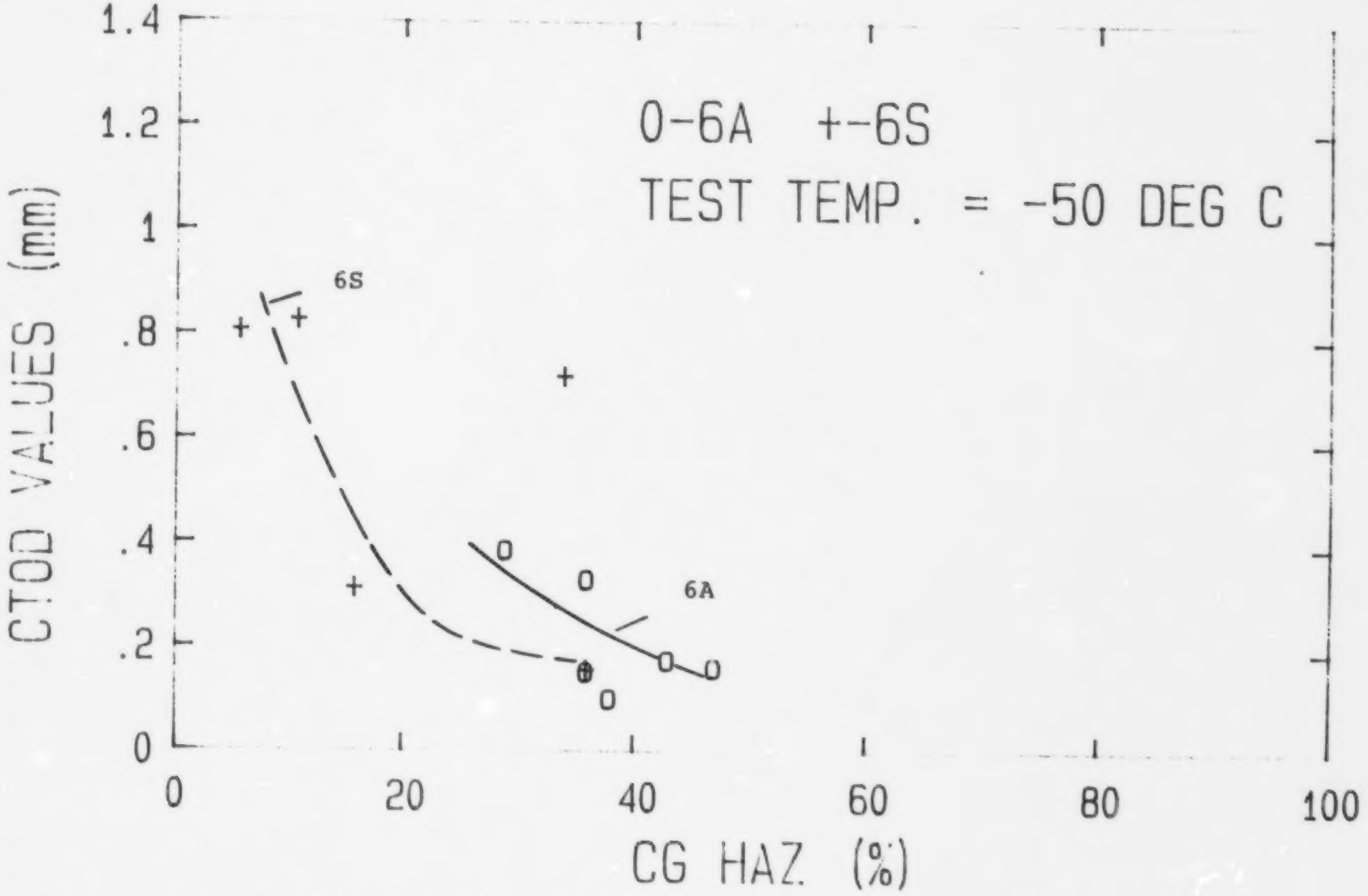

FIGURE 138: Relationship between CTOD values at $-50^{o}C$ and % CG HAZ in the fatigue precrack (near the precrack front) measured along the thickness B for MACS (ACC,DQT) steels.

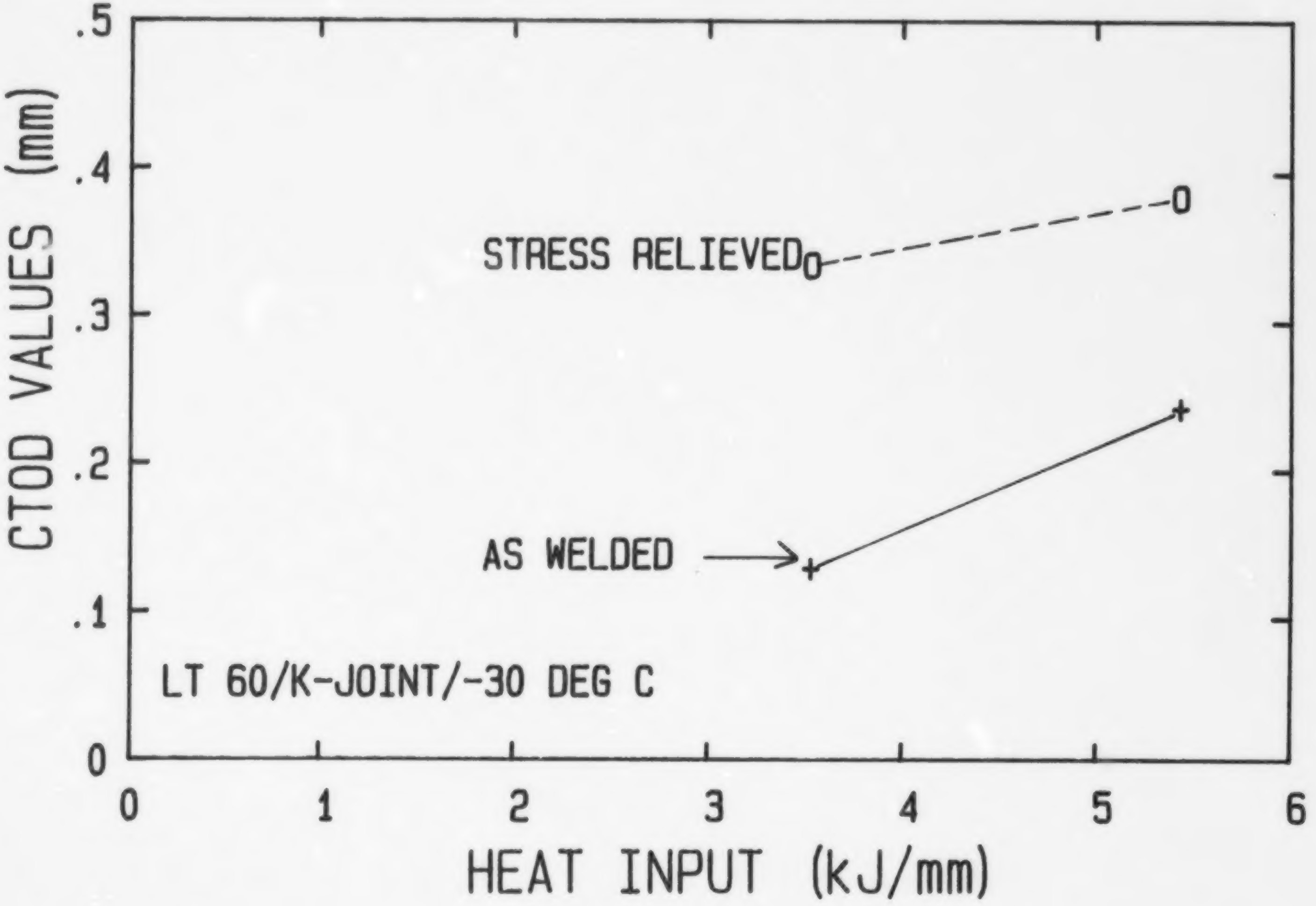

FIGURE 139 : CTOD values at -30^{o}C (average) vs heat input plots for HAZ in LT60 steel (K-joint).

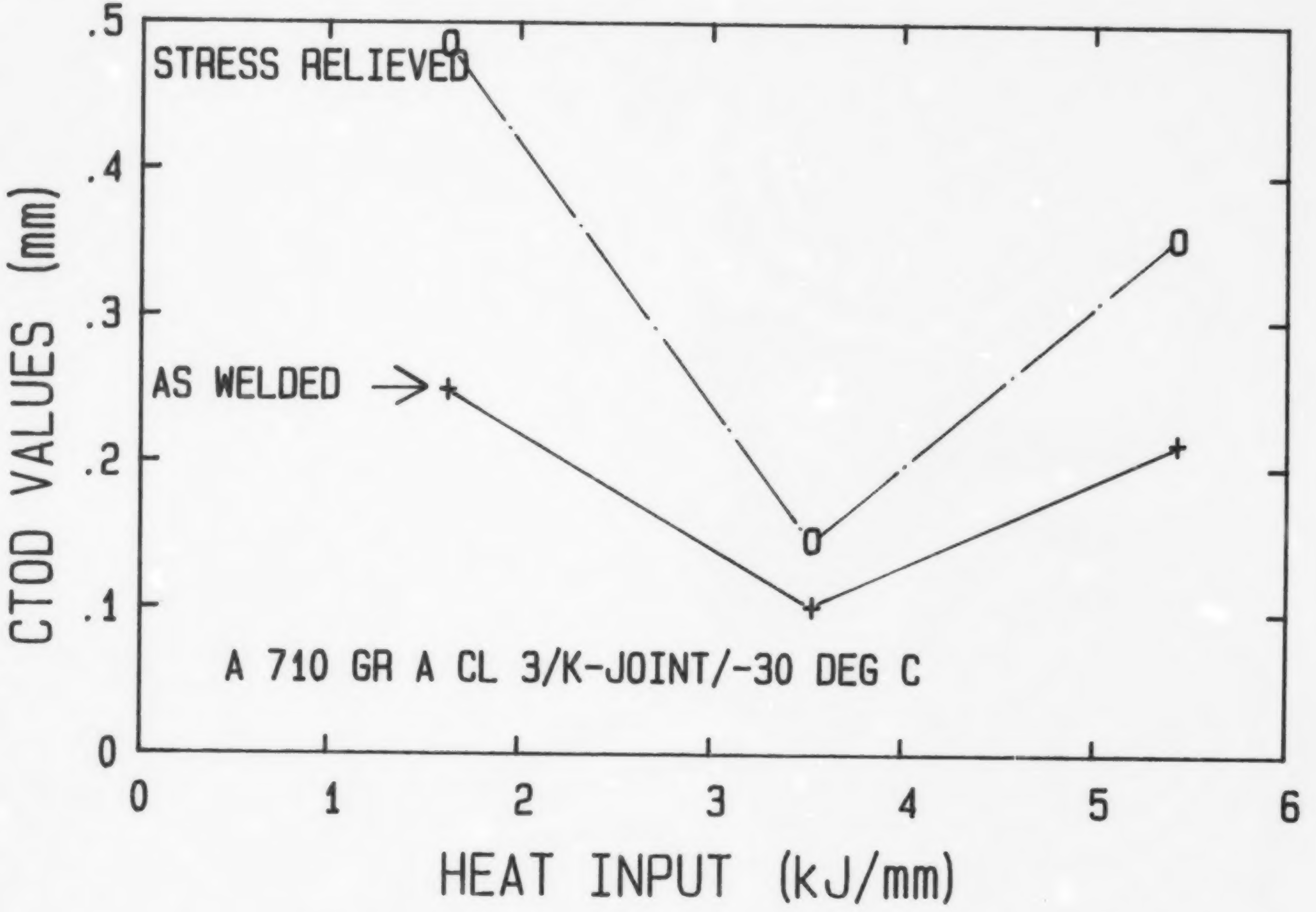

FIGURE 140 : CTOD values at -30°C (average) vs heat input plots for the HAZ in A710, Gr. A, Cl 3 steel (K-joint).

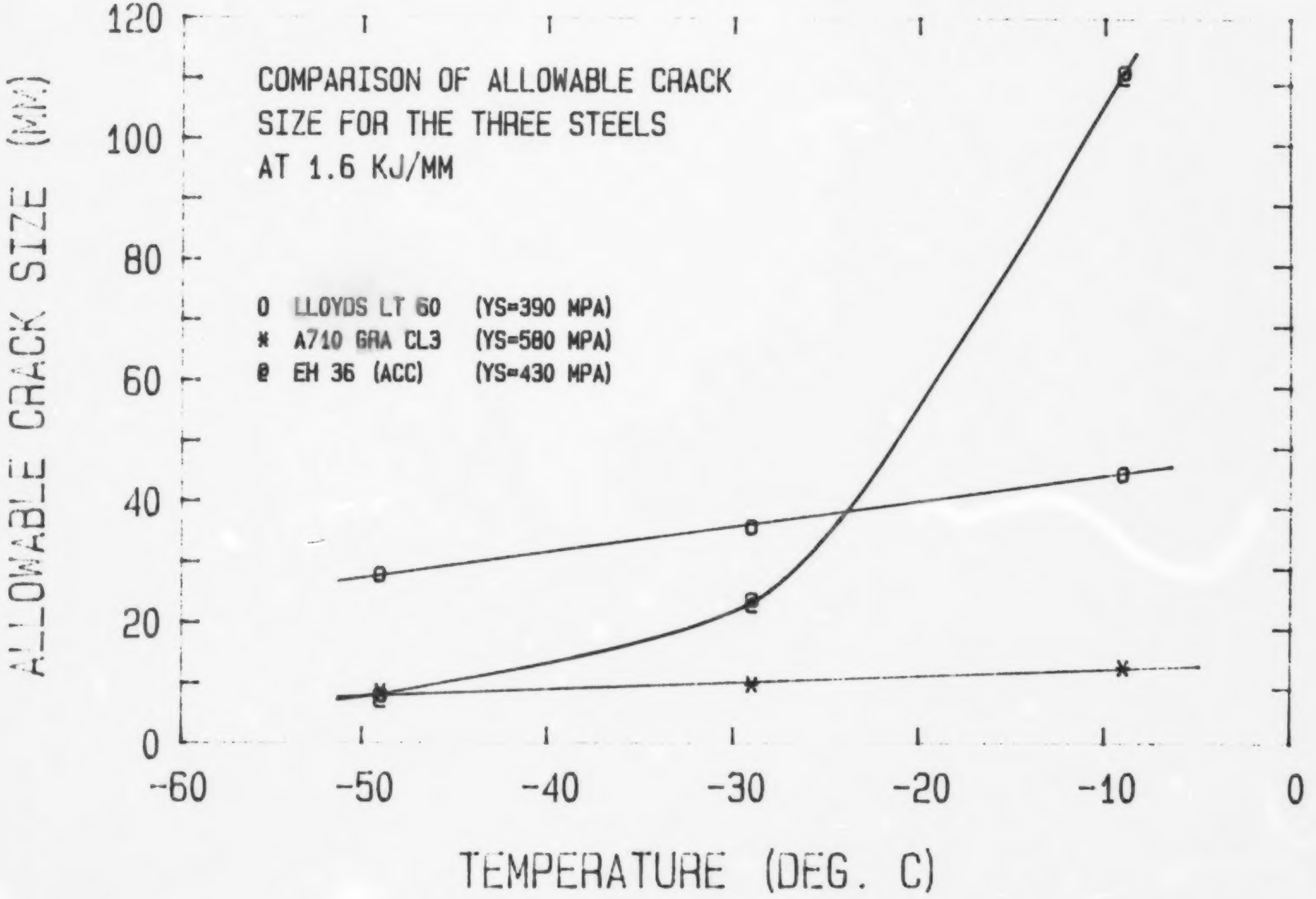

FIGURE 141 : Comparison of allowable crack sizes calculated from K_{1d} values, for the three steels at 1.6 kJ/mm in the "as-welded" condition.

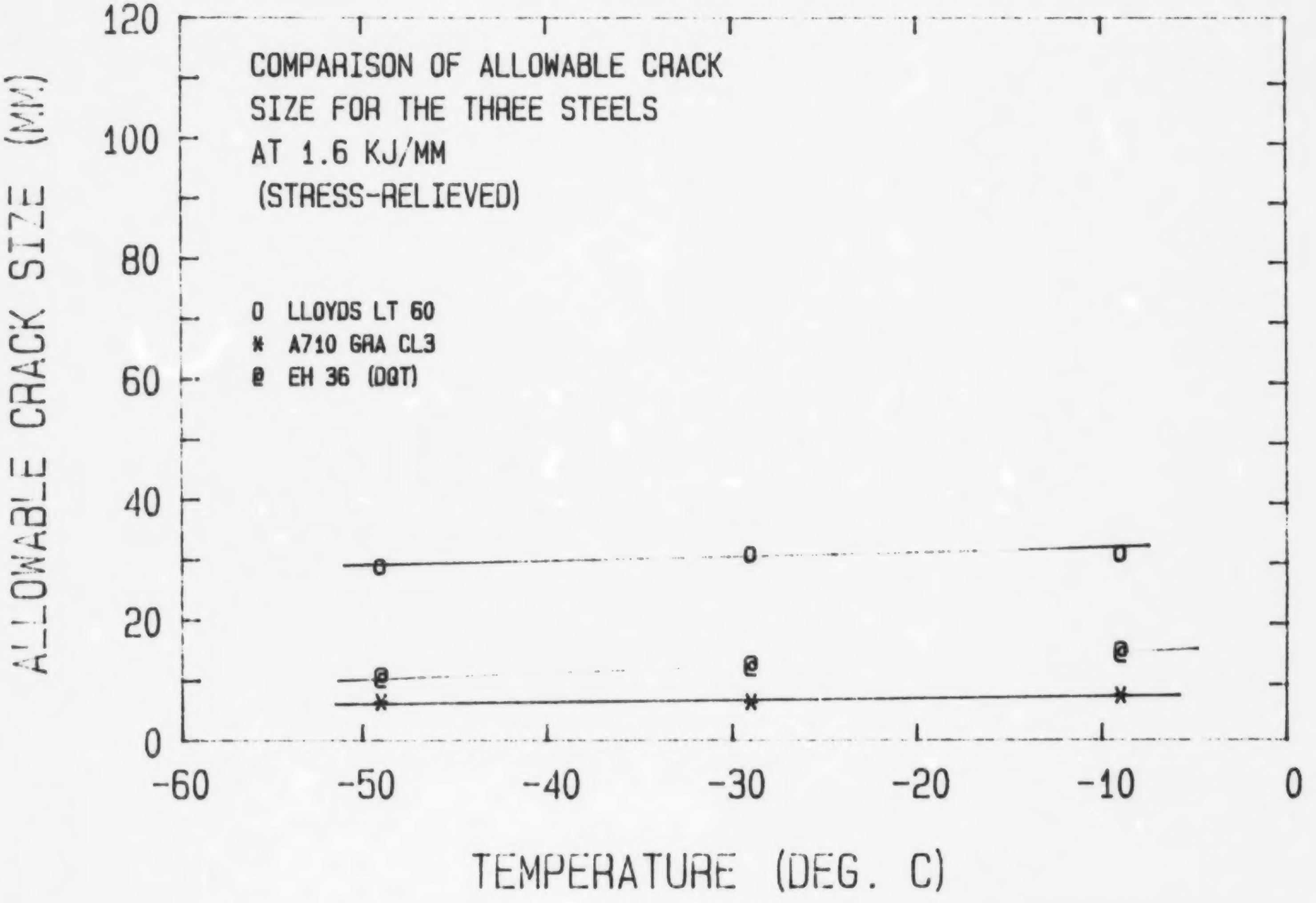

FIGURE 142 : Comparison of allowable crack sizes calculated from K_{Id} values, for the three steels at 1.6 kJ/mm in the "stress-relieved" condition.

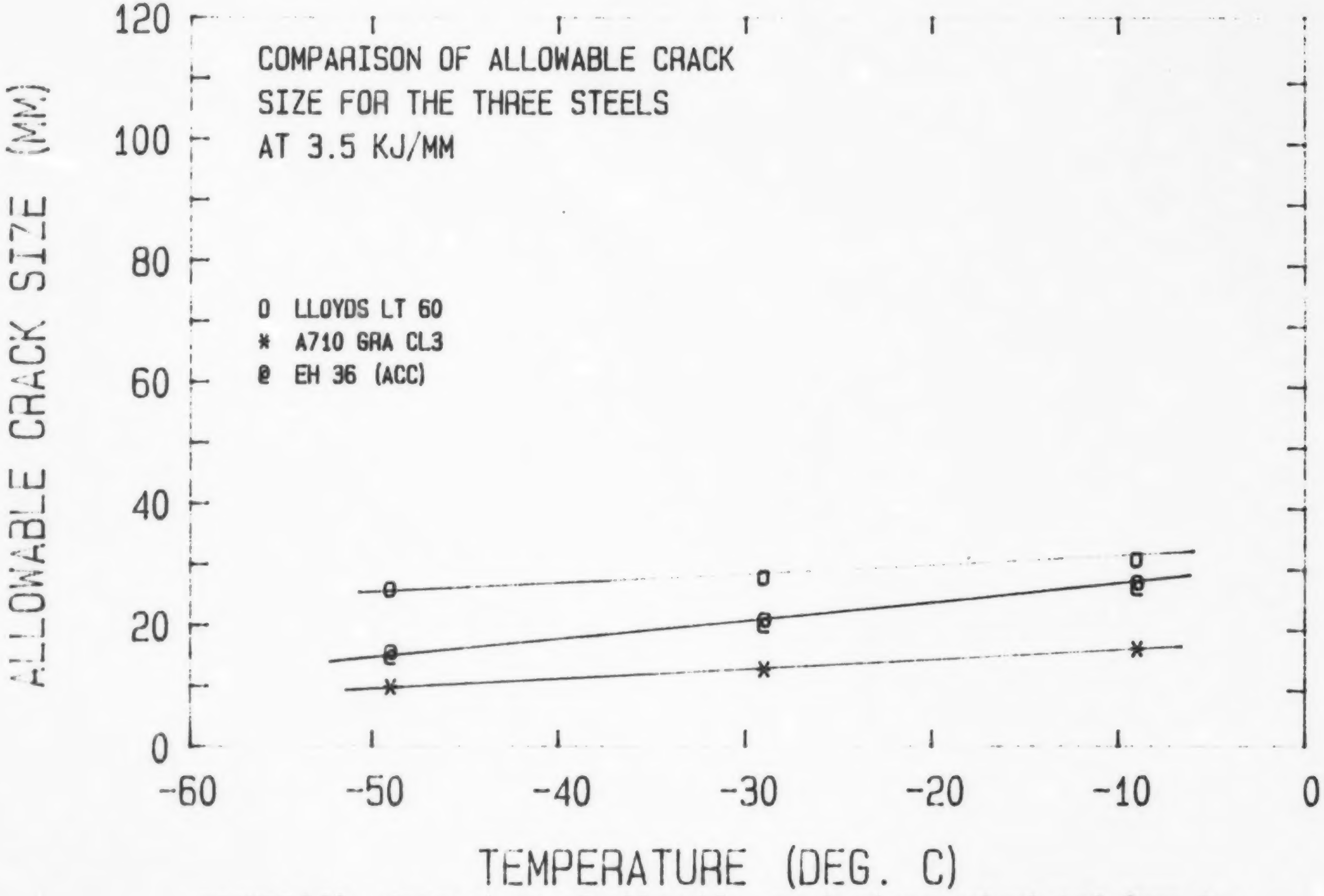

FIGURE 143 : Comparison of allowable crack sizes calculated from K_{1d} values, for the three steels at 3.5 kJ/mm in the "as-welded" condition.

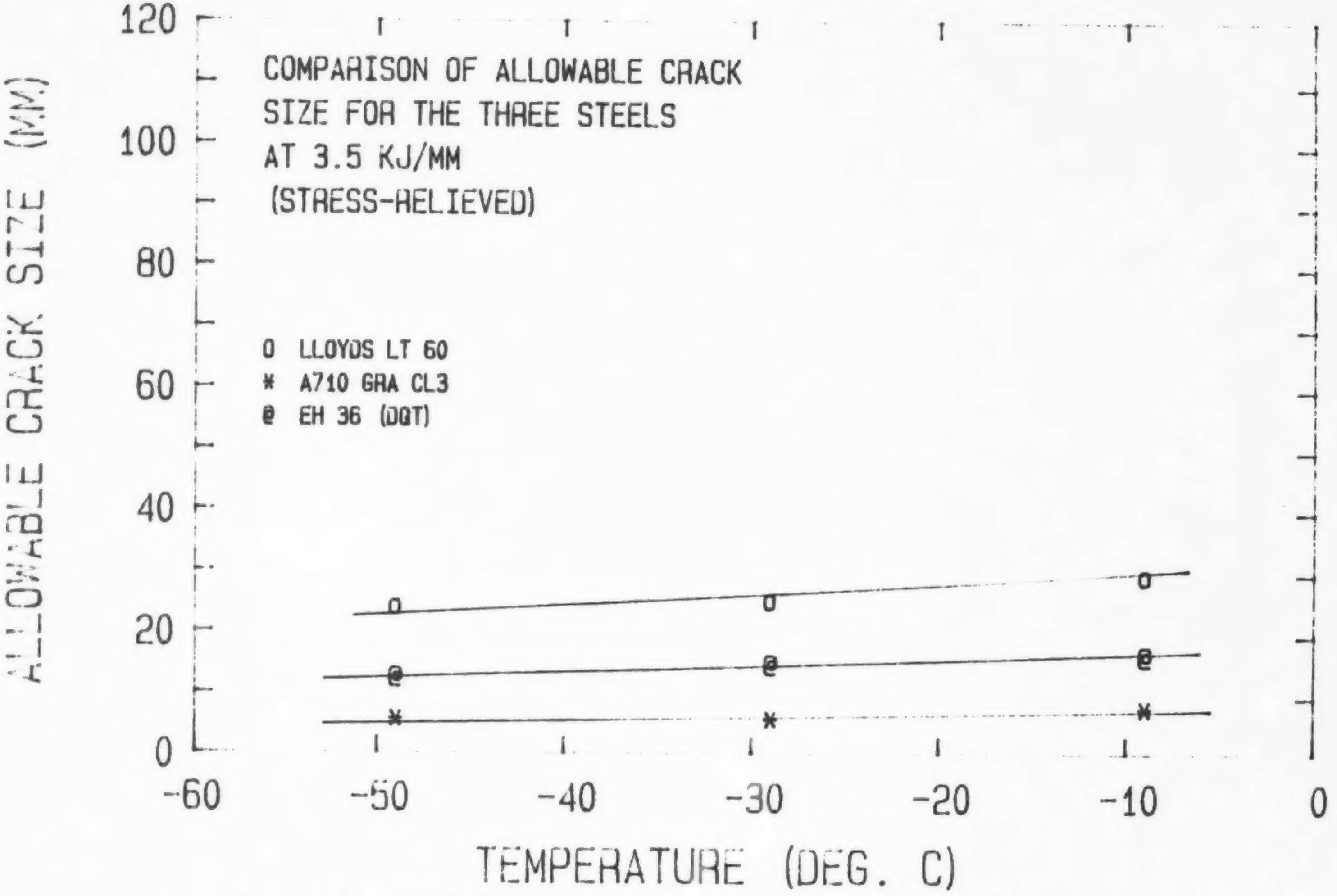

FIGURE 144 : Comparison of allowable crack sizes calculated from K_{1d} values, for the three steels at 3.5 kJ/mm in the "stress-relieved" condition.

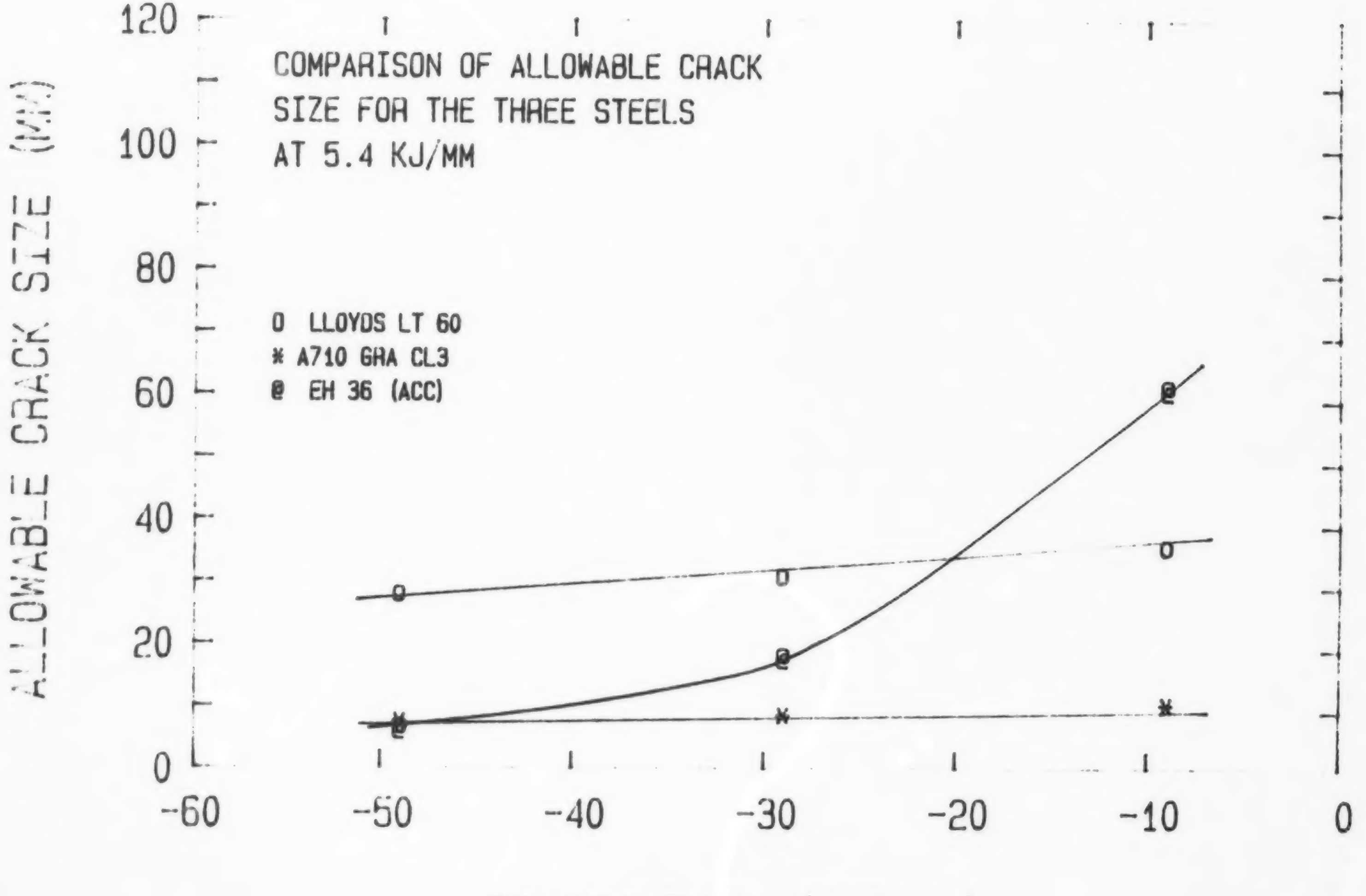

FIGURE 145: Comparison of allowable crack sizes calculated from K_{Id} values, for the three steels at 5.4 kJ/mm in the "as-welded" condition.

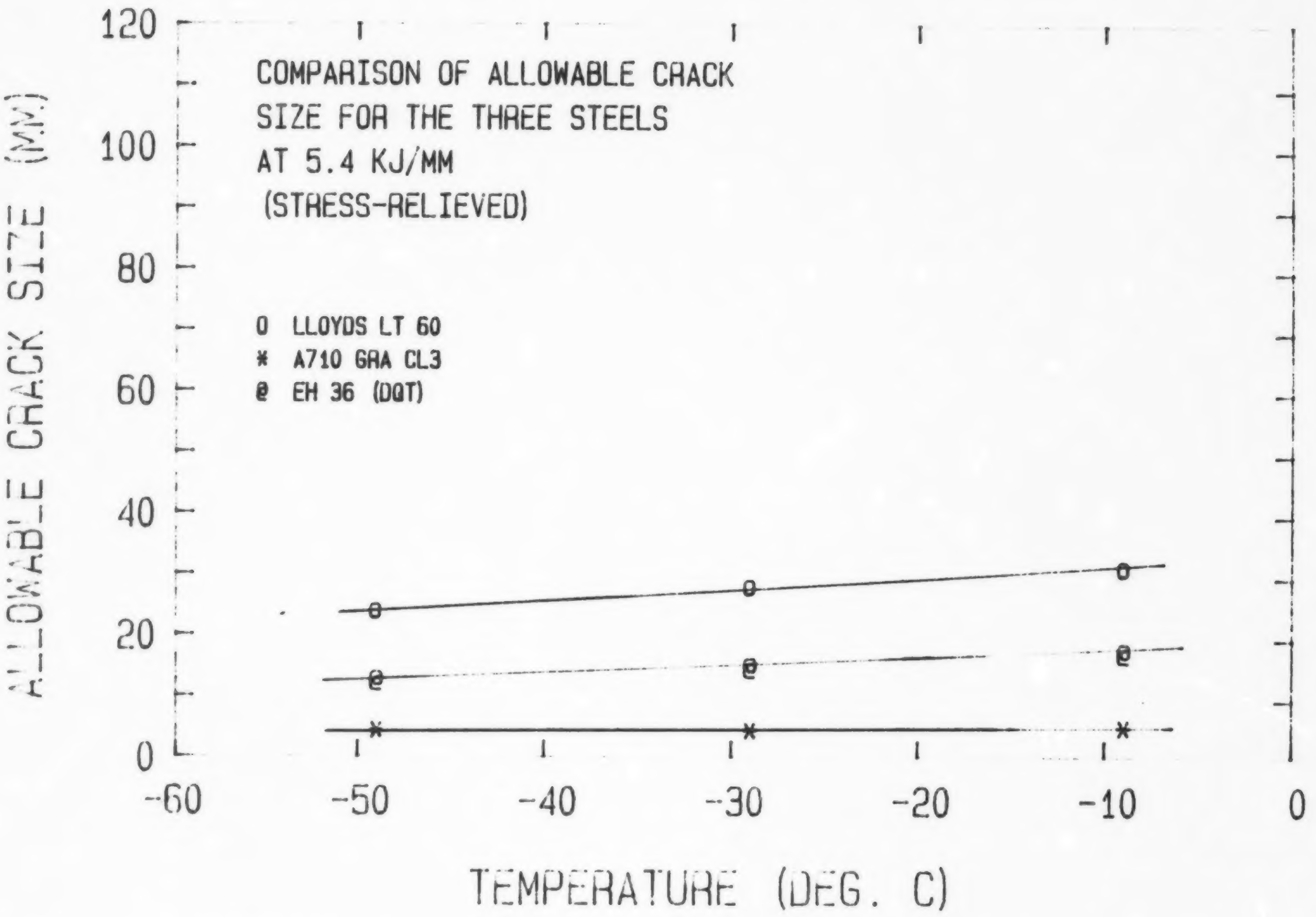

FIGURE 146 : Comparison of allowable crack sizes calculated from K_{1d} values, for the three steels at 5.4 kJ/mm in the "stress-relieved" condition.

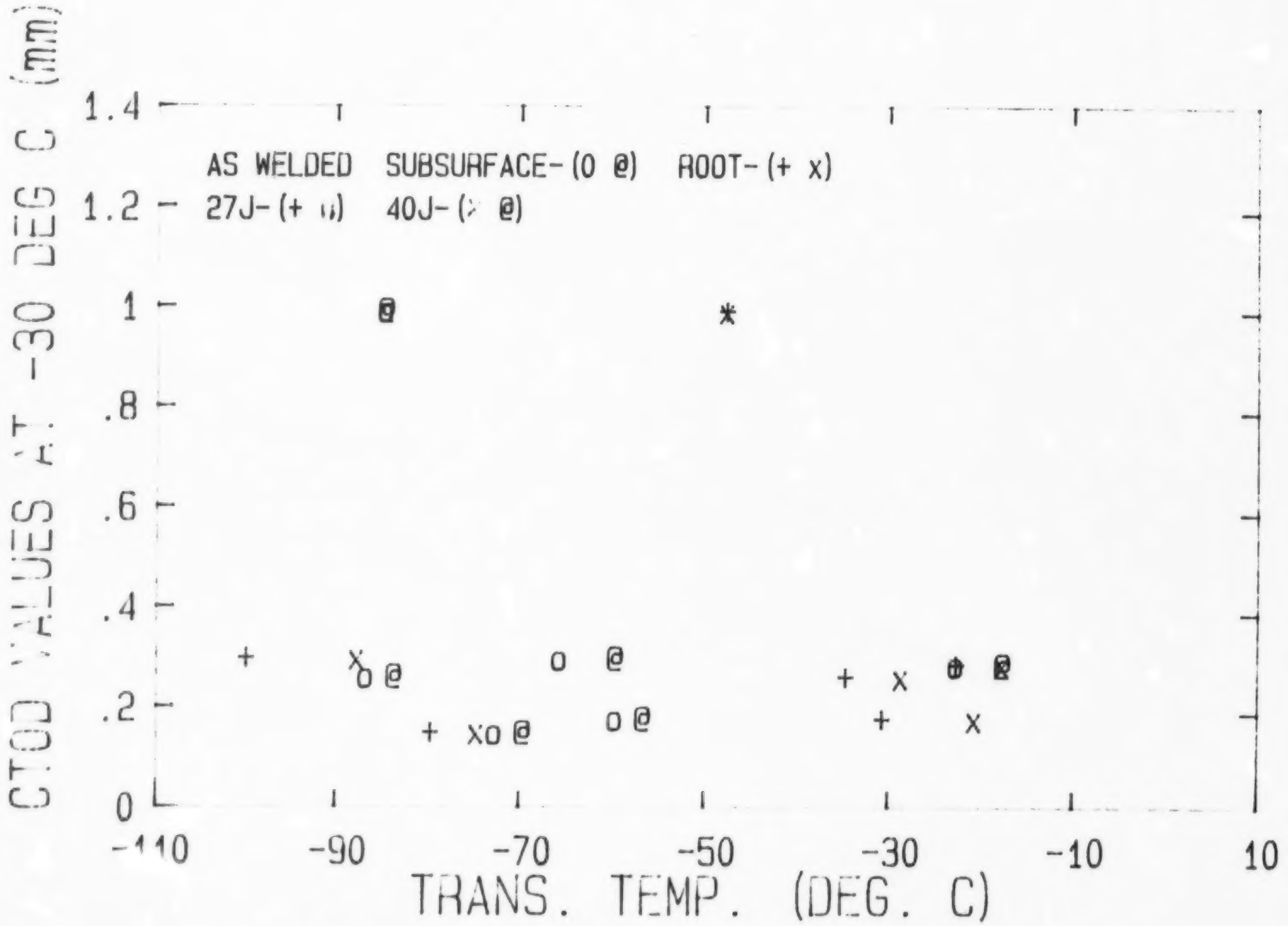

FIGURE 147: Relationship between CTOD values at -30^{o}C and the 27J or 40J transition temperatures for the CG HAZ in all the steels (as welded condition).

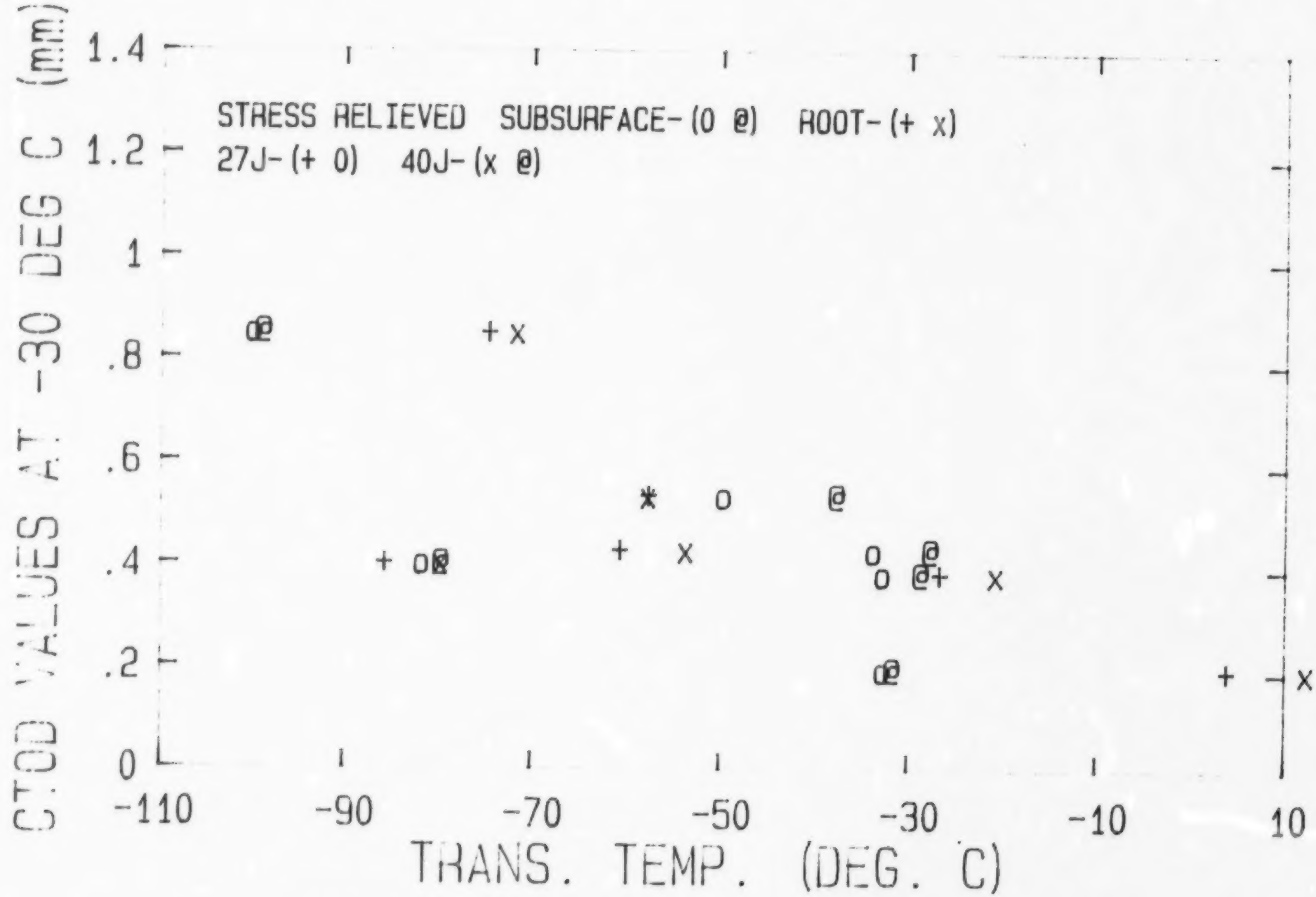

FIGURE 148: Relationship between CTOD values at -30°C and the 27J or 40J transition temperatures for the CG HAZ in all the steels (stress-relieved condition).

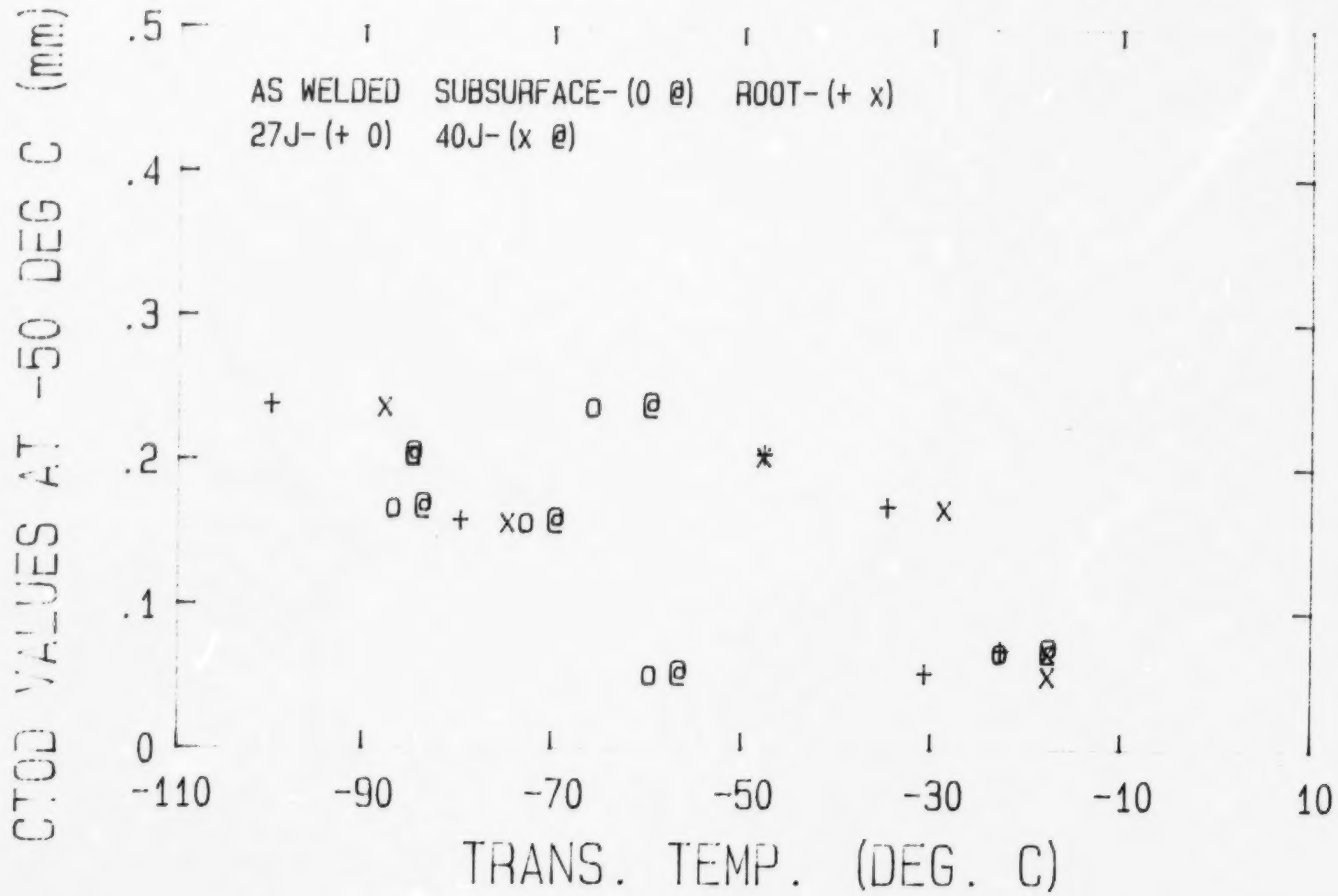

FIGURE 149 : Relationship between CTOD values at -50°C and the 27J or 40J transition temperatures for the CG HAZ in all the steels (as-welded condition).

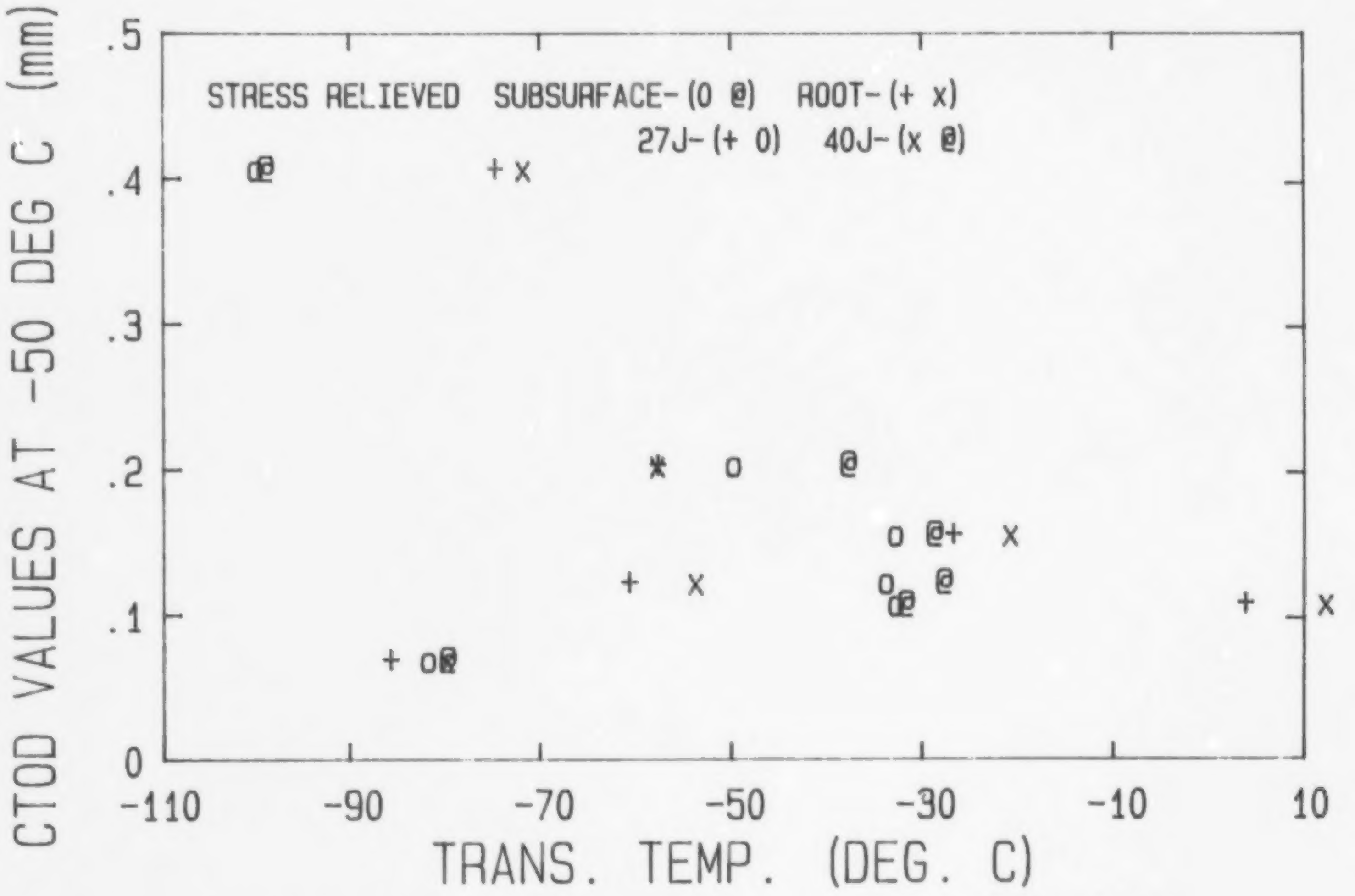

FIGURE 150: Relationship between CTOD values at -50°C and the 27J or 40J transition temperatures for the CG HAZ in all the steels. (stress-relieved condition)

APPENDIX "A"

Microstructural Characterization of HAZ Structures in a Series of HSLA Steels

A report for M. Lalit, AMCA by G.C. Weatherly, Department of Metallurgy and Materials Science, University of Toronto, Toronto.

1. Introduction

A series of steels (as described in the main body of the report) were provided for examination. These steels are identified in the Table below; the ones marked by an asterisk were used in this study.

Steel	LT60		A 710		Kawasaki (MACS)	
Heat Treatment	AW	SR	AW	SR	AW	SR
Heat input						
1.6KJ/mm	*		*	*		
3.5KJ/mm	*					
5.5KJ/mm	*	*	*	*	*	*

Samples were provided both in the form of mounted and polished specimens taken from the fusion line of multipass welds and Gleeble simulation samples corresponding to the heat inputs noted above. All the samples were examined using the extraction carbon replica technique and EDX/analysis. For the multipass welds, these replicas were taken from an area of the sample that encompassed the fusion line boundary in a region of the weld that corresponded to a single pass zone. The approximate location of the fusion line was identified by the technique developed at Toronto whereby the weld-metal can be characterized by the presence of nearly spherical, ∿ 1μm sized, inclusions. Where necessary the characteristic microstructures from the weldments could be compared to those of the Gleeble samples, where there is no uncertainty as to the thermal cycle experienced by the alloy.

The structures of the coarse-grained HAZ adjacent to the fusion line were studied to identify (a) the nature and size distribution of any fine-scale precipitation, (b) the nature of the decomposition products of austenite, particularly with respect to the formation of the M-A phase or carbides during cooling. The results for each steel are presented and discussed separately.

2.(a) A710 (parent plate)

This steel is a low C, Nb and Cu-containing grade which, prior to welding was in the quenched and aged condition. Its composition is 0.05C, 0.62Mn, 0.72Cr, 0.88Ni, 1.05Cu, 0.041Nb and 0.01N. The microstructure of the parent plate of this steel is shown in Figure 1. It consists of a series of Fe, Cr rich carbides, ∿ 0.1μm in diameter, with a much finer dispersion of particles, 8-50 nm in diameter. The majority of these fine particles analyzed as Nb(C,N), but some gave no peak other than Cu and are presumably Cu precipitates. (Note that all the samples were mounted on Cu grids. Fluorescense of the grid material always gave a Cu signal in the x-ray spectrum from all the particles.)

.../2

(b) A710 (as welded, Gleeble)

1.6KJ mm^{-1}

The method used to identify the fusion line boundary is illustrated in Figure 2, where the weld metal inclusionsterminate at a fairly well defined line in the micrograph. Once this line was identified, areas adjacent to it in the coarse-grained HAZ could be explored. The replicas from this region were essentially featureless. A few isolated faceted cuboidal particles were found (see Figure 3a), which contained both Ti and Nb (Figure 3b), but no carbides could be extracted. On stress-relief heat treatment, carbide precipitation was quite evident (see below), so we conclude that for this low C steel, most of the carbon is retained in the form of the MA phase at ferrite boundaries in the bainitic structure of the CGHAZ.

5.5KJ mm^{-1}

The microstructure of the CGHAZ after this heat input was very similar to that seen after the lower heat input, at the magnification level of the TEM Fewer Ti-Nb bearing cuboidal particles were found than in the lower heat input weldment, but apart from this qualitative observation there appeared to be no other significant differences.

(c) A710 (stress relief heat treatment, welded and Gleeble samples)

1.6KJ mm^{-1}

The stress relief heat treatment applied to all the samples was 2 hours at 620°C. This treatment produced two significant microstructural changes (a) precipitation of arrays of carbides outlining the ferrite grains (Figure 4) and (b) very fine precipitation (Figure 5). The particle size of the fine precipitation was ∿ 2-3 nm; no x-ray spectra could be obtained from these particles, but they probably are either Cu or Nb(C, N).

5.5KJ mm^{-1}

The microstructures of the stress-relief heat treated samples after the higher heat input welding were again similar to those observed in the lower heat input specimens. Coarse carbides precipitated at ferrite grain boundaries and a very fine precipitation within the grains were observed (Figure 6).

(d) Discussion

The behaviour of this steel can be explained by noting that its relatively low C and microalloying contents would lead to complete dissolution of any Nb or (Fe, Cr)-based carbo-nitrides during the weld thermal cycle in the coarse-grained HAZ. Figure 7 shows the results of unpublished calculations of Suzuki and Weatherly*, where the dissolution time of NbC particles is plotted as a function of particle size at 1150, 1250°and 1350°C. The maximum size of NbC particles in A710 was ∿ 50 nm. Particles of this size dissolve in ∿ 0.2 secs at 1350°C and ∿ 2 secs at 1250°C, so that a zone essentially devoid of any precipitation would be found next to the fusion line for both heat inputs. The observation of occasional Ti-containing particles in this steel (presumably associated with trace impurities of Ti) can be explained by the much lower solu-

---

*S. Suzuki and G.C. Weatherly "Particle Dissolution and Precipitation during the Weld Thermal Cycle in Nb and Ti-bearing HSLA Steels", to be published.

.../3

bility of (Ti, Nb)N particles which would not dissolve duing the weld thermal cycle.

In certain situations reprecipitation might be expected during the cooling cycle of those elements that have dissolved during the heating leg of the thermal cycle. Whether reprecipitation occurs or not will depend on the total alloying content in the alloy and the heat input. A higher alloying content in the alloy and greater heat input would favour precipitation. For A710, even at a heat input of 5.5KJ mm^{-1}, no precipitation could be detected in the CGHAZ next to the fusion line.

As noted above the extent of the denuded zone (i.e. the zone devoid of any precipitates) will depend on the peak temperature reached in the HAZ. The presence of trace amounts of Ti made any direct estimate of the size of the precipitate free zone difficult as all areas contained a very low density of (Ti, Nb) particles. However, a comparison of Figures 1 and 3a demonstrates that the majority of the particles in the parent plate have dissolved in the CGHAZ.

Stress relief heat treatment has brought about the expected changes in the microstructure of the steel i.e. precipitation of coarse carbides at ferrite lath boundaries and a much finer distribution of NbC and Cu throughout the grain. This fine-scale distribution of precipitates would strengthen the lattice.

3. Kawasaki (MACS)

This steel contained 0.09C, 0.78Ni, 0.017 Nb, 0.01Ti, 0.034Al and 0.003N. It was examined only after the highest heat inputs (5.5KJ/mm), both in the as-welded state and after Gleeble thermal simulation. The effect of a stress relief heat treatment was also studied.

(a) As-welded

The same technique described earlier was employed to identify the fusion line boundary. The CGHAZ immediately next to the fusion line was devoid of any precipitates, but at a distance of ∿ 50µm a few coarse Ti-rich cuboids were observed (Figure 8). The density of these cuboids increased as the distance from the fusion line boundary increased (Figure 9). In addition to Ti these cuboids contained Nb (see Figure 9(b)), in agreement with previous observations (1,2) in Nb-Ti grades of HSLA steels.

Carbides were observed in the replicas as rather ill-defined feathery plates. An example is shown in Figure 8. X-ray microanalysis demonstrated that these carbides are Fe-rich (Figure 10) and must be formed during the cooling cycle as the austenite decomposes. (Note that the greater C content of this steel in comparison to that of A710 would favour carbide precipitation rather than MA formation during the cooling cycle.)

(b) Stress relief heat treatment

The microstructure after the stress relief heat treatment is shown in Figures 11 and 12. A distribution of coarse, fine and very fine particles were observed, together with the occasional cuboidal particles observed after welding. The coarse particles were Fe-rich carbides with a similar composition to that shown in Figure 10. The fine spherical particles (∿ 0.1µm in size) proved to be

.../4

either Fe-rich carbides or FeS (see Figs 11(b) and (c)). The very fine particles (Figure 12) could not be reliably analyzed because of contamination problems but they are probably Nb-rich carbides.

(c) Discussion

The composition of this steel was similar to one that we have recently studied extensively at Toronto(3). The results of the present investigation bear out the conclusions of that broader study. The Ti and N contents of the steel are approximately balanced, so that at the highest temperatures experienced during the weld thermal cycle only Ti-rich nitrides survive to provide the pinning effect for grain growth control. Small amounts of Nb are dissolved in these nitrides. Again no fine-scale precipitation is found after welding at this heat input, but on stress-relief heat treatment the Nb taken into solution during the weld thermal cycle can reprecipitate in the form of the fine precipitates shown in Figure 12.

4. LT60

The chemical composition of this steel was reported to be 0.12C, 1.29 Mn, 0.26 Si, 0.15 Cr, 0.05 Mo, 0.15 Ni, 0.25 Cu, 0.07 V, 0.04 Nb, 0.03 Al, 0.006N. Of the three steels studied here LT60 contained the highest levels of both the interstitial elements C and N and the microalloying elements V and Nb. The microstructure of the parent plate (Figure 13) contained a mixed distribution of hexagonal platelets of AlN and finer (Nb, V) carbides. The latter particles had an average size of 7 nm and on the extraction replicas were often directly associated with the AlN particles. X-ray analysis gave indications of both species (Figure 13b).

(a) As welded, Gleeble

1.6KJ/mm

After this treatment, the CGHAZ contained only lamellar carbides (Figure 14) which were again Fe-rich, plus a few coarse undissolved AlN particles (Figure 15).

3.5KJ/mm

The microstructures after this treatment appeared to be very similar to those observed at the lower heat input. Lamellar Fe-rich carbides were found at the ferrite boundaries (Figure 16).

5.5KJ/mm

At this heat input fine scale precipitation was observed in addition to the coarse carbides at ferrite grain boundaries. This fine scale precipitation was observed both in the weld metal and the HAZ (Figure 17), and is shown at higher magnification in Figure 18 which comes from a Gleeble simulated sample. The average size of the small precipitates after this treatment was ∿ 5 nm. These particles again contained both Nb and V and are probably (Nb, V)(C,N).

(b) After stress-relief heat treatment

(1.6 and 5.5KJ/mm)

The microstructures of these two conditions after the stress relief heat treatment were very similar. A variety of particle morphologies and sizes were observed. At low magnification, relatively coarse spheroidal or lath shaped carbides were randomly distributed throughout the microstructure (Figure 19a);

.../5

They contained predominantly Fe, with lesser amounts of Cr and Mn. (Figure 19b). The V peak visible in the spectrum of Figure 19b comes from the small particles which were distributed throughout the replica, and may be seen more clearly in Figure 20a. The hexagonal shaped particle in this micrograph is AlN: the smaller particles are (Nb, V)(C, N), having an average size of ∿ 11nm. The x-ray spectrum (Figure 20b) shows the peaks associated with these different species.

(c) Discussion

The most interesting result in this alloy was the observation of fine scale precipitation both in the CGHAZ of weldments and Gleeble simulated samples after a heat input of 5.5KJ/mm, while none was observed for the two lower heat inputs. As we have shown earlier Nb(C,N) particles (and for that matter (Nb,V)(C,N) particles) of the size range encountered in this alloy would be expected to dissolve during the weld thermal cycle. The presence of precipitation can only be explained if these precipitates nucleate and grow during the cooling leg of the thermal cycle. The relatively slow cooling rates associated with the 5.5KJ/mm heat input weldments, and the higher microalloying content of this steel (in comparison to the A710 or Kawasaki compositions), offers a possible explanation as to why precipitation was observed only in this steel. Stress relief heat treatment causes further precipitation and coarsening of these (Nb,V) rich precipitates as well as copious precipitation of coarser Fe-rich carbides.

References

1. D.C. Houghton, G.C. Weatherly and J.D. Embury, "Recent Advances in the Physical Metallurgy of Steels", University of Liverpool, p.135, Metals Society, London (1982).
2. S. Suzuki and G.C. Weatherly, CANMET/CSIRA Conference, Ottawa, March 1985, to be published.
3. S. Suzuki, M.A.Sc. thesis, University of Toronto (1985).

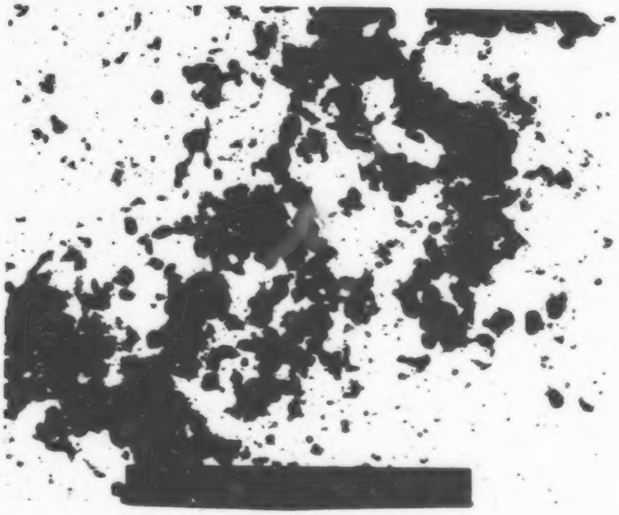

Figure 1. A710, parent plate microstructure, showing a bimodal distribution of Fe-rich carbides and fine precipitates, 8-50 nm in diameter, believed to be Nb(C,N) or Cu particles. (x20,000)

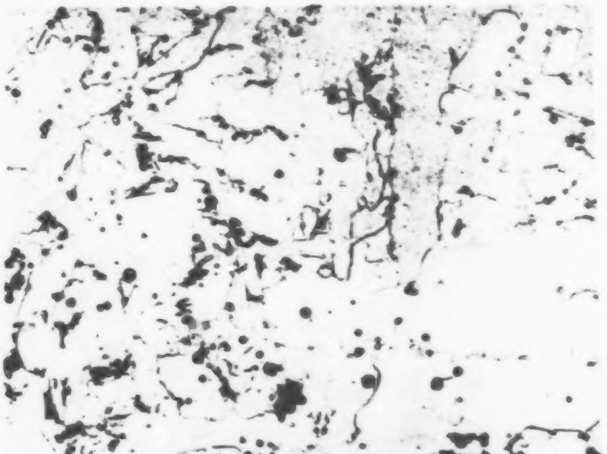

Figure 2. A710, 1.6KJ mm^{-1} sample as welded, single pass region. The fusion line boundary is identified as the line where the weld metal inclusions are no longer visible. (x3,500)

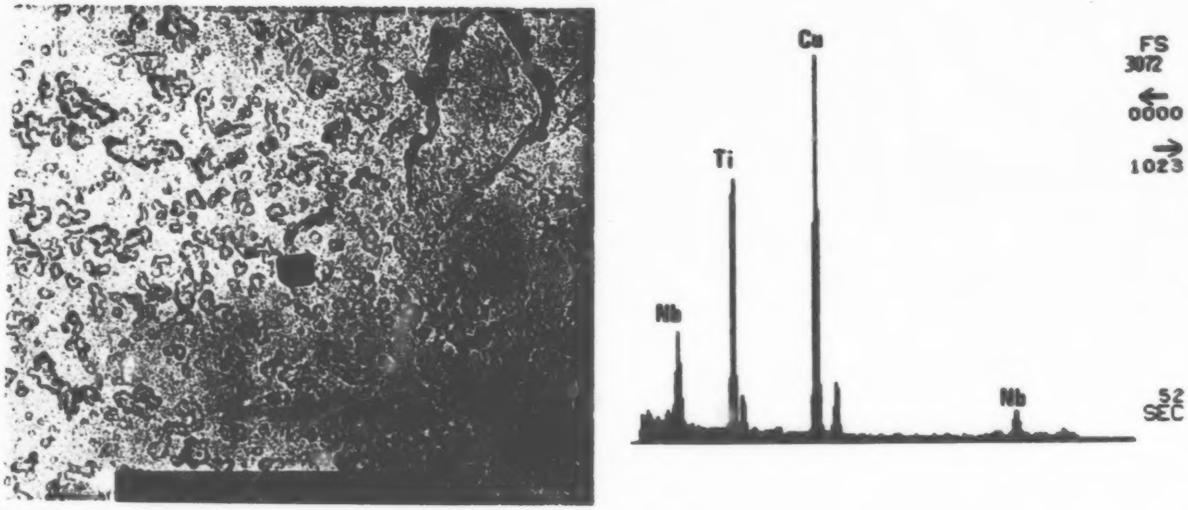
Cu
Ti
Nb
Nb
FS
3072
←
0000
→
1023
52
SEC

Figure 3(a). A710, 1.6KJ/mm Gleeble sample, showing faceted cuboidal particle (x60,000). (b) X-ray analysis from particle showing Ti and Nb peaks.

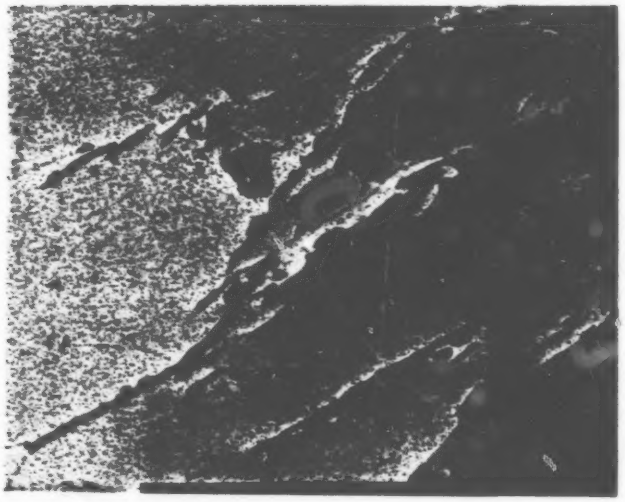

Figure 4. A710, 1.6KJ/mm thermal simulation followed by stress relief heat treatment, showing arrays of carbides outlining ferrite grain boundaries. (x9,000)

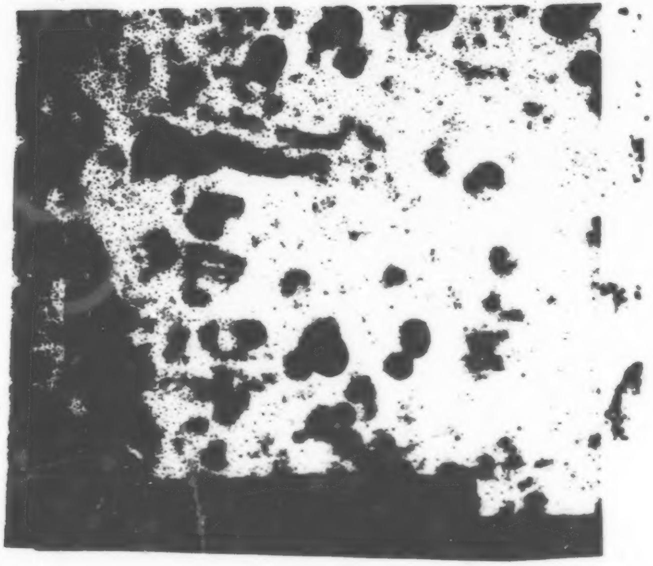

Figure 5. As Figure 4, showing fine scale precipitation.(x90,000)

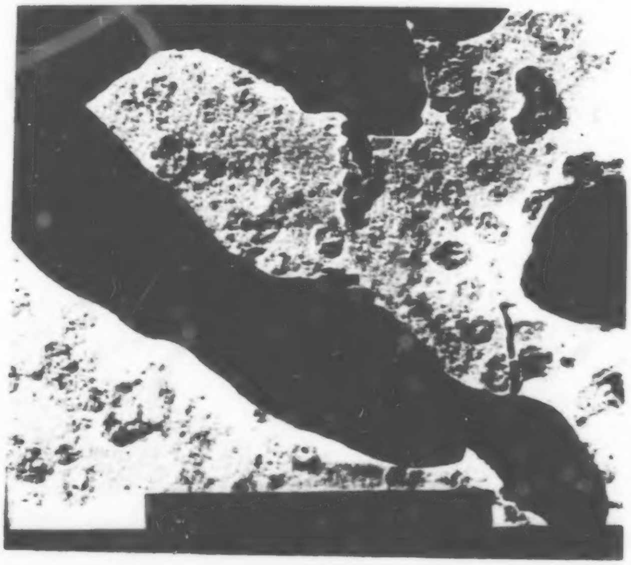

Figure 6. As Figure 4, for Gleeble sample given thermal simulation corresponding to 5.5KJ/mm heat input, showing coarse carbides and fine precipitates. (150,000)

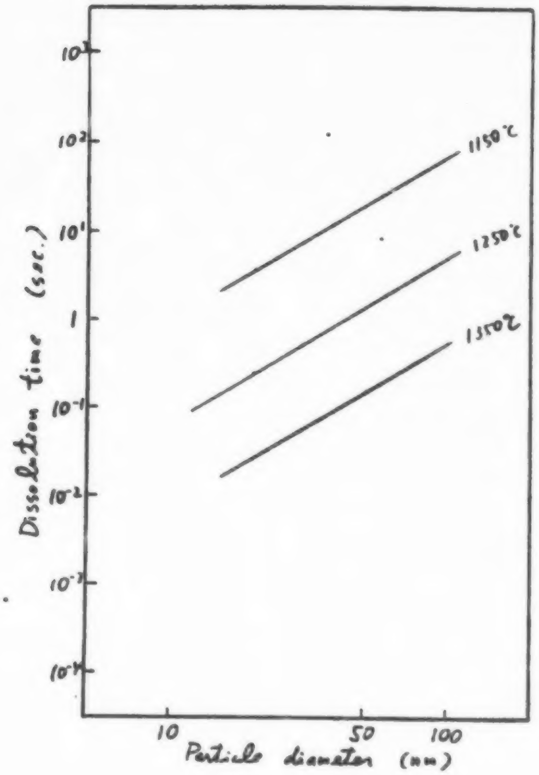

Figure 7. Dissolution time for NbC particles as a function of particle diameter and temperature (1150, 1250 and 1350°C) in a steel containing 0.05 w/o Nb, 0.05 w/o C.

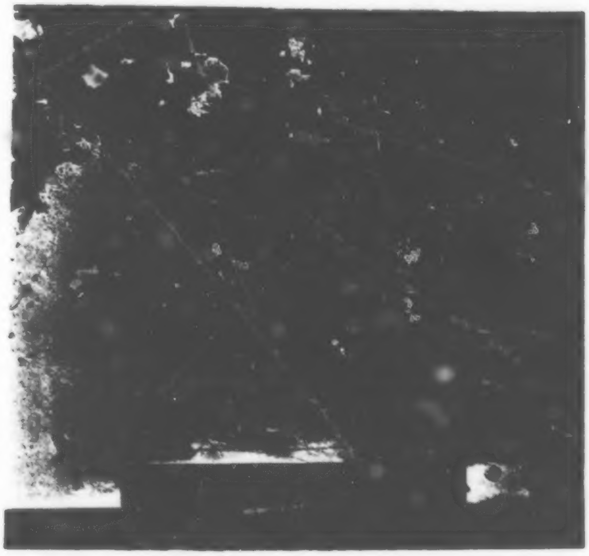

Figure 8. Kawasaki Steel (MACS), 5.5KJ/mm, weld sample; Ti-rich cuboids close to the fusion line boundary. (x15,000)

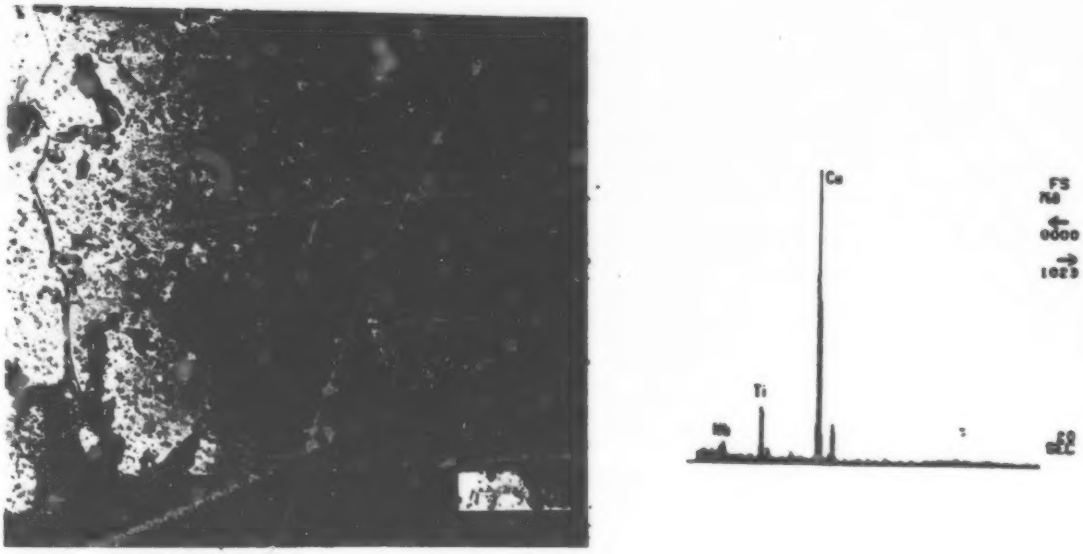
Cu
Ti
Nb
FS
768
←
0000
→
1023
20
SEC

Figure 9(a). As Figure 8, ∿ 400μm from fusion boundary showing cuboidal particles. (x15,000)
(b) X-ray analysis from cuboid showing Nb and Ti peaks.

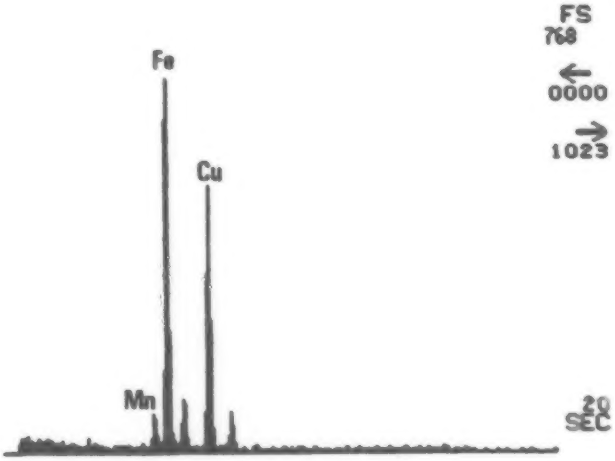

Figure 10. X-ray microanalysis of feathery plates seen in Figure 8 showing Fe and Mn peaks.

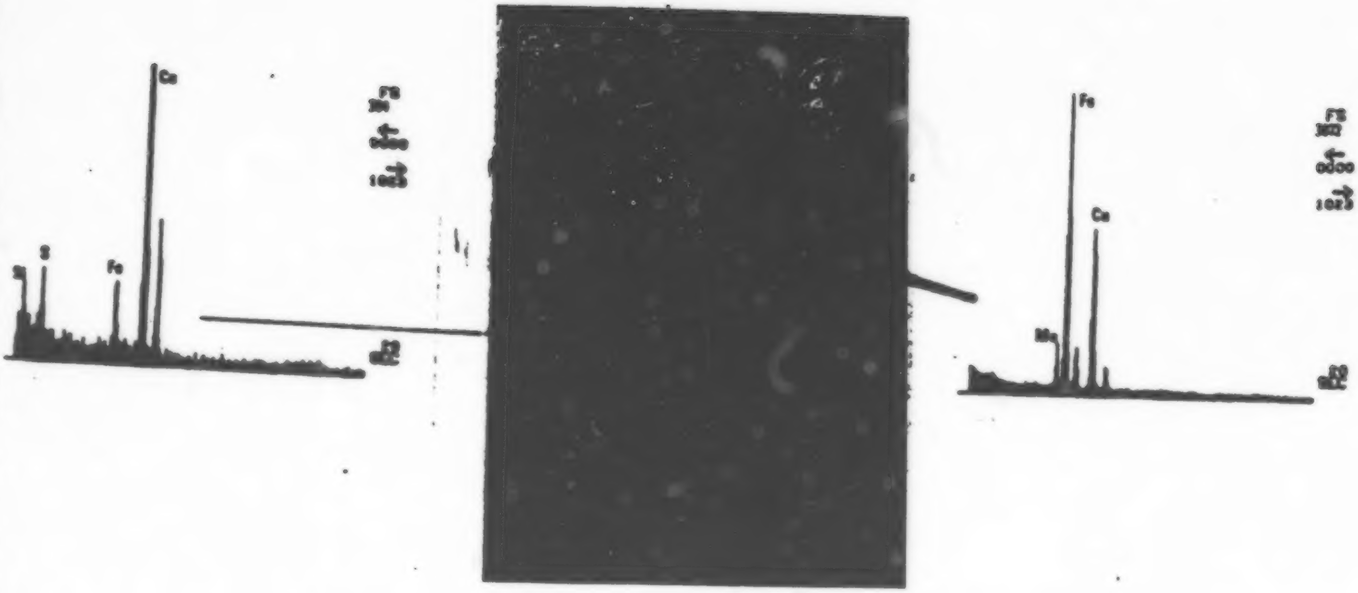

Figure 11(a). Kawasaki steel, 5.5KJ/mm, Gleeble simulated specimen showing distribution of ∽ 0.1μm sized spherical particles. (x150,000)
(b) microanalysis of particle in Figure 11a showing Fe and Mn peaks.
(c) microanalysis of a second particle in Figure 11a showing Fe and S peaks.

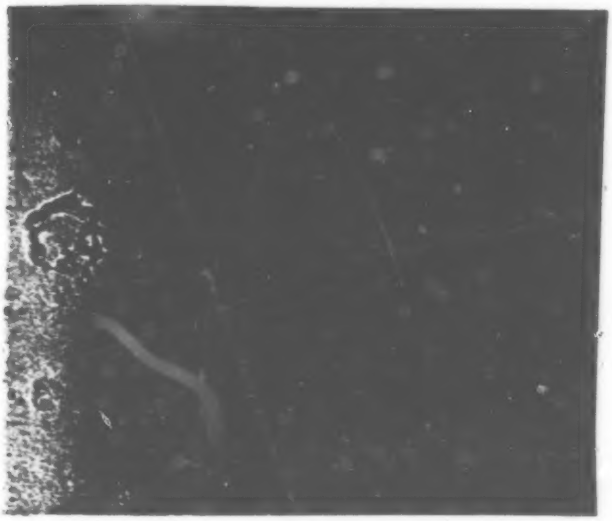

Figure 12. As Figure 11, showing distribution of very small precipitates. (x150,000)

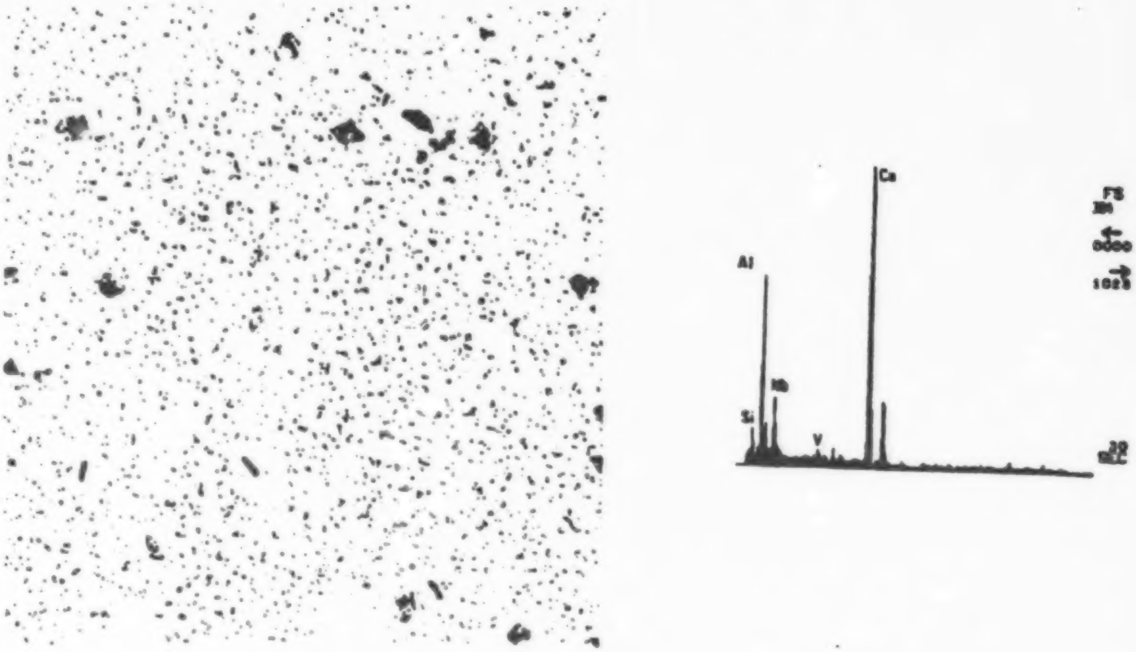

Figure 13(a). LT60, parent plate microstructure, showing a distribution of hexagonal platelets of AlN and (Nb,V) rich carbo-nitrides. (x11,000) (b) X-ray microanalysis of particles seen in Figure 13(a) showing Al, Nb and V peaks.

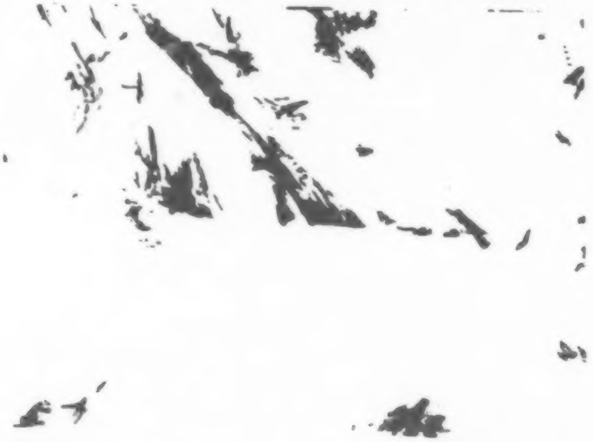

Figure 14. LT60KJ/mm, as welded showing carbides at ferrite boundaries. (x10,000)

Figure 15. As Figure 14, showing undissolved AlN particles. (x30,000)

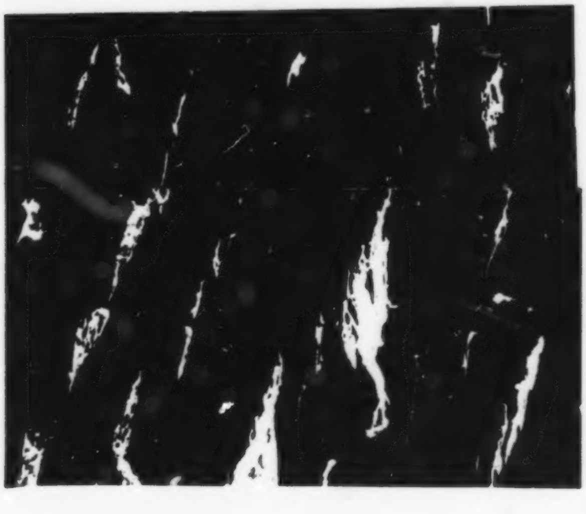

Figure 16. LT60, 3.5KJ/mm, Gleeble simulation sample, showing lamellar carbides. (x5,000)

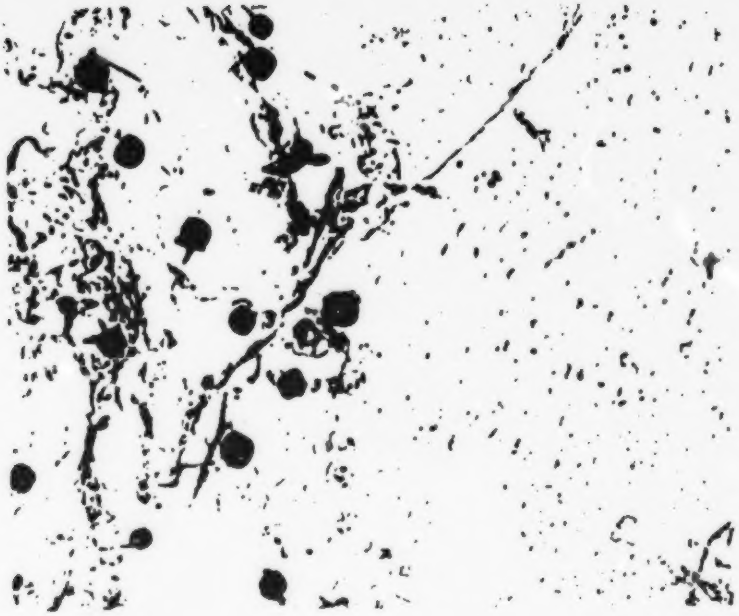

Figure 17. LT60, 5.5KJ/mm, as welded showing fusion line boundary with weld metal inclusions and fine precipitation. (x27,000)

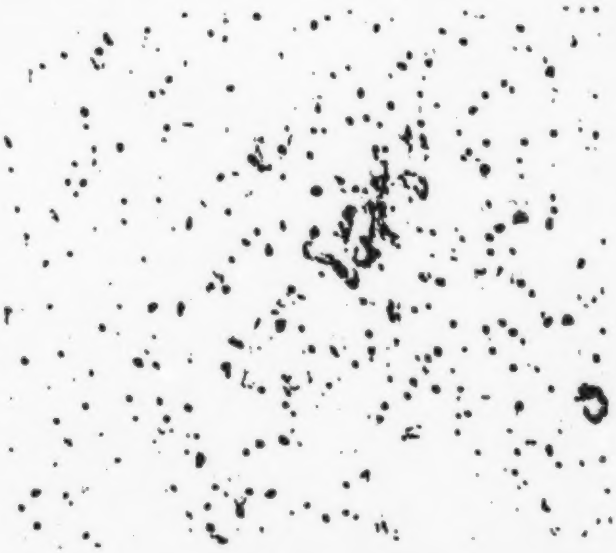

Figure 18. LT60, 5.5KJ/mm, Gleeble simulation showing precipitation. (x87,000)

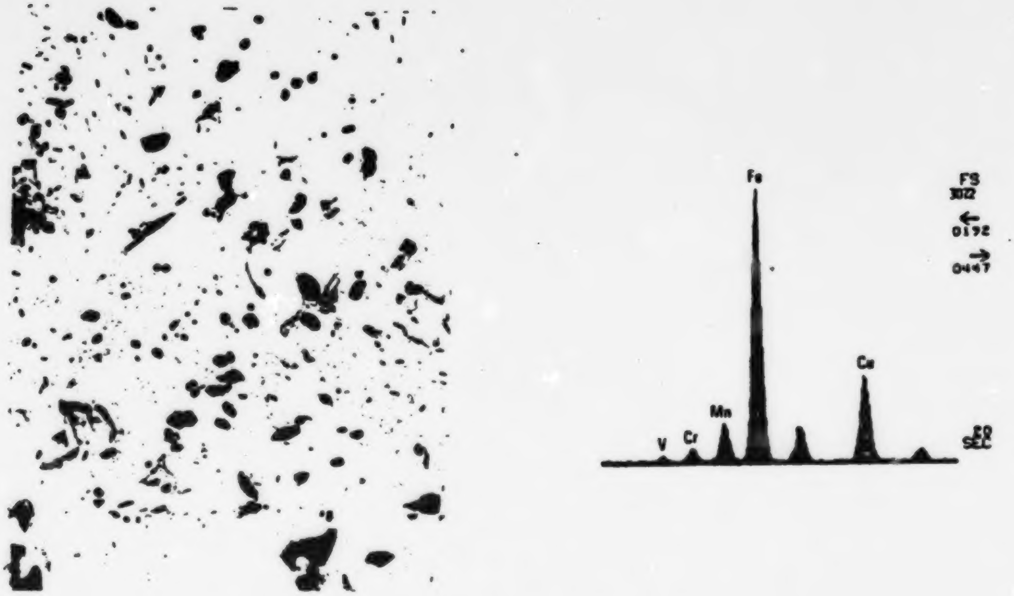
Fe
FS
0192
0447
Cu
Mn
Cr
V
SEC

Figure 19(a). LT60, 5.5KJ/mm after stress relief heat treatment showing spheroidal and lath shaped coarse carbides. (x5,000)
(b) X-ray analysis of particles seen in Figure 19(a) showing Fe, Cr and Mn peaks.

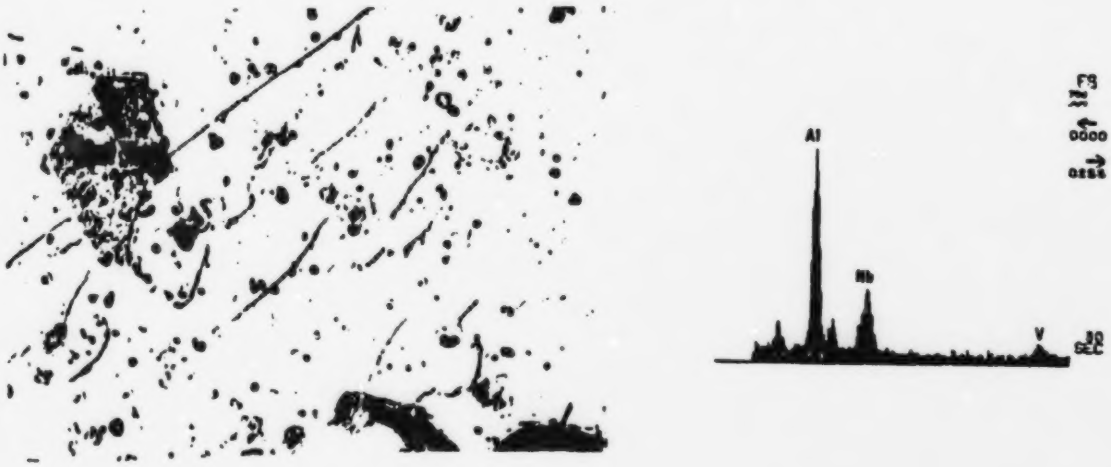
Al
Nb
V
FS
0000
SEC

Figure 20(a). As above, showing AlN particle and fine scale precipitation. (x87,000)
(b) X-ray analysis of AlN particle showing Al, Nb and V peaks.

APPENDIX "B"

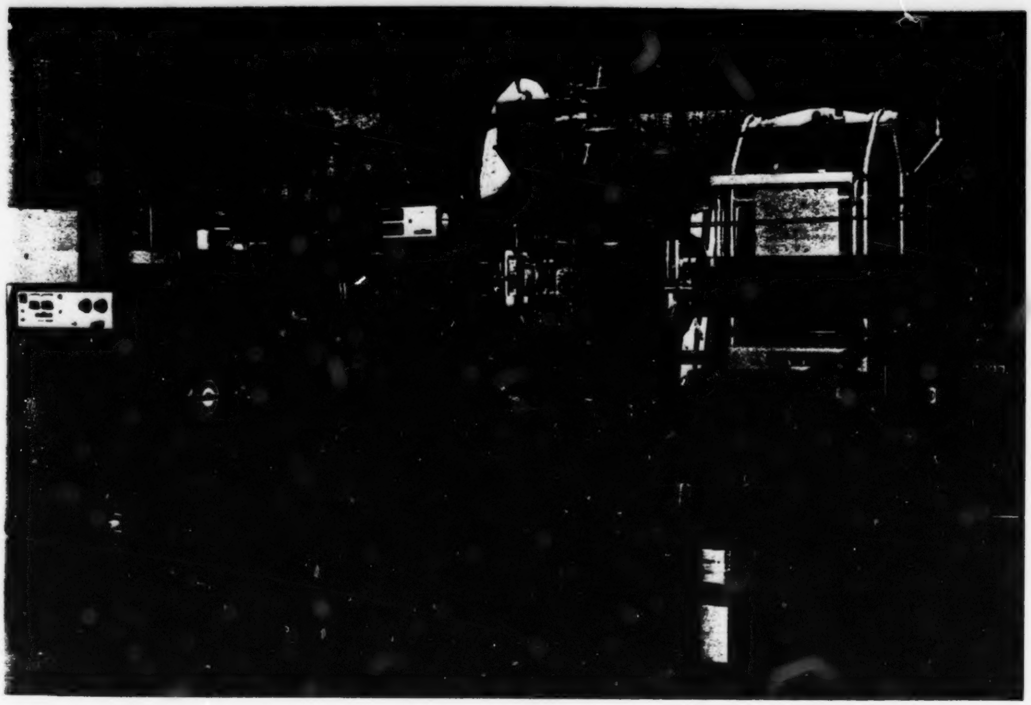

FIGURE B1: Miller CP/CC 1500 P machine with jig and 1.2m plate in place for welding.

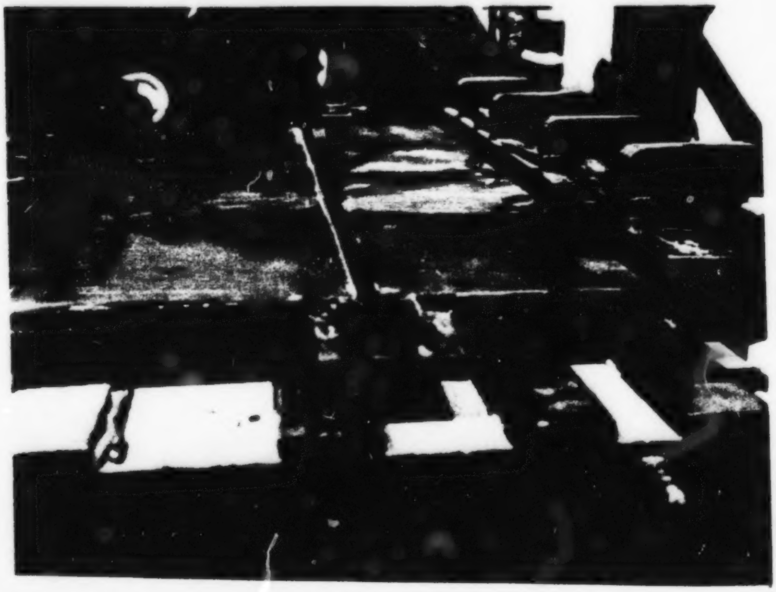

FIGURE B2: Close-up showing plate restrained in jig with electrode distance from the sidewall measured.

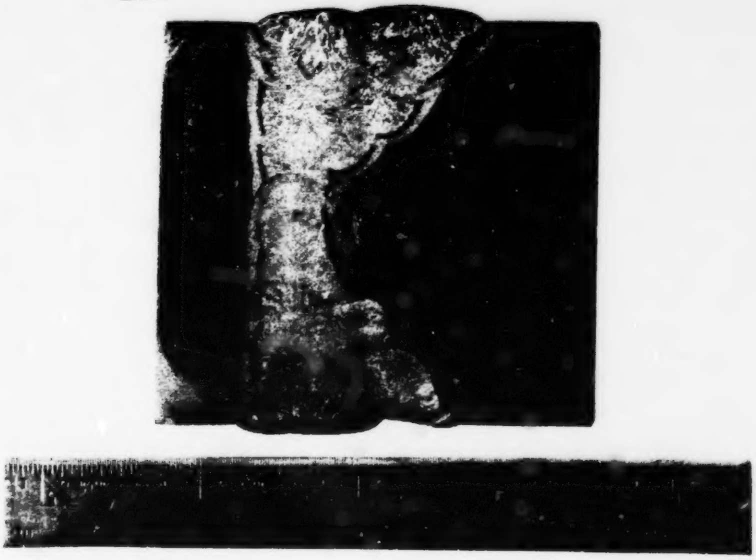

FIGURE B3: K-joint macrosection for Condition 1A - LT 60; 3.5 kJ/mm; as-welded.

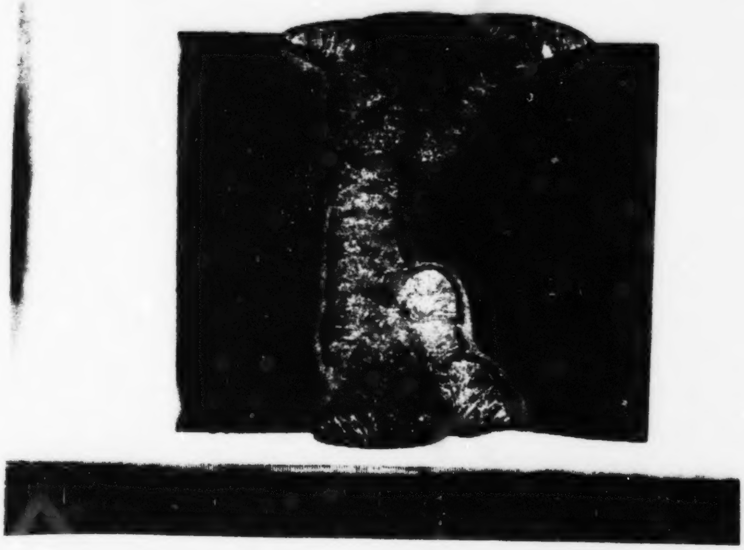

FIGURE B4: K-joint macrosection for condition 1S - LT 60; 3.5 kJ/mm; stress-relieved.

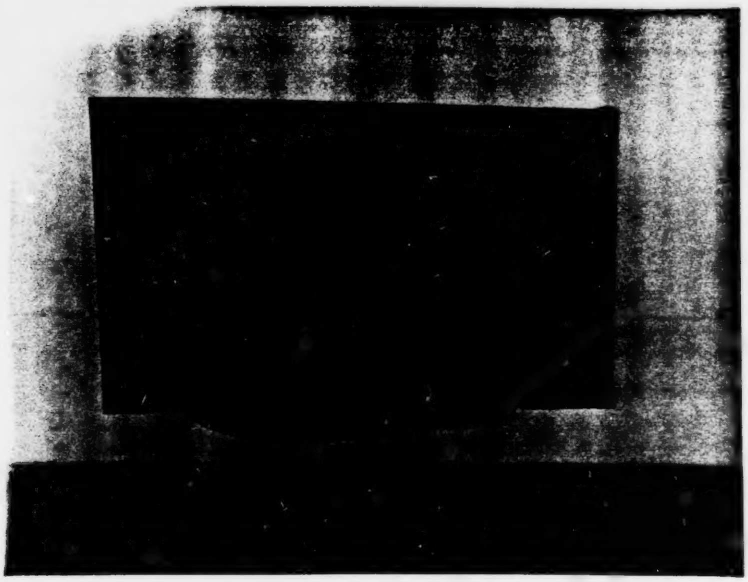

FIGURE B5: K-joint macrosection for Condition 2A - LT 60; 5.4 kJ/mm; as-welded.

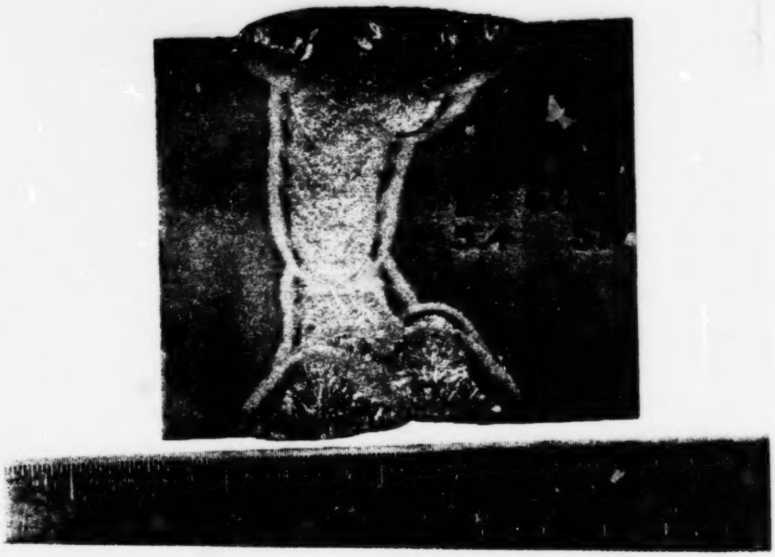

FIGURE B6: K-joint macrosection for Condition 2S - LT 60; 5.4 kJ/mm; stress-relieved.

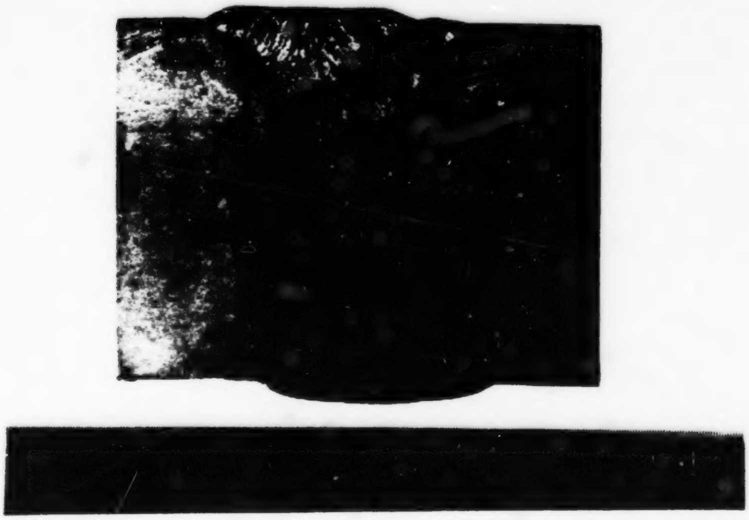

FIGURE B7: K-joint macrosection for Condition 3A - A710 Gr. A, Cl. 3; 5.4 kJ/mm; as-welded.

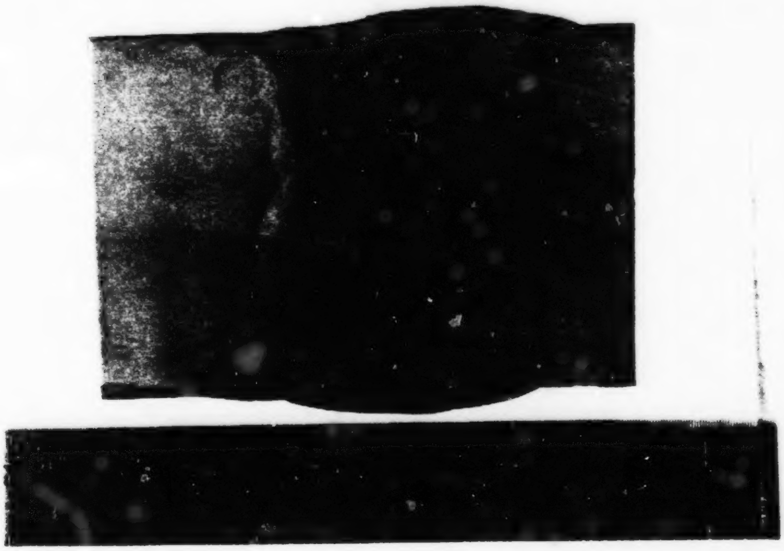

FIGURE B8: K-joint macrosection for Condition 3S - A710 Gr. A, Cl. 3; 5.4 kJ/mm; stress-relieved.

FIGURE B9: K-joint macrosection for Condition 4A - A710, Gr. A, Cl. 3; 3.5 kJ/mm; as-welded.

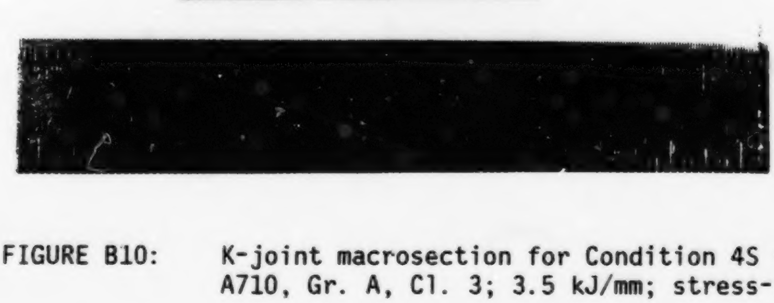

FIGURE B10: K-joint macrosection for Condition 4S - A710, Gr. A, Cl. 3; 3.5 kJ/mm; stress-relieved.

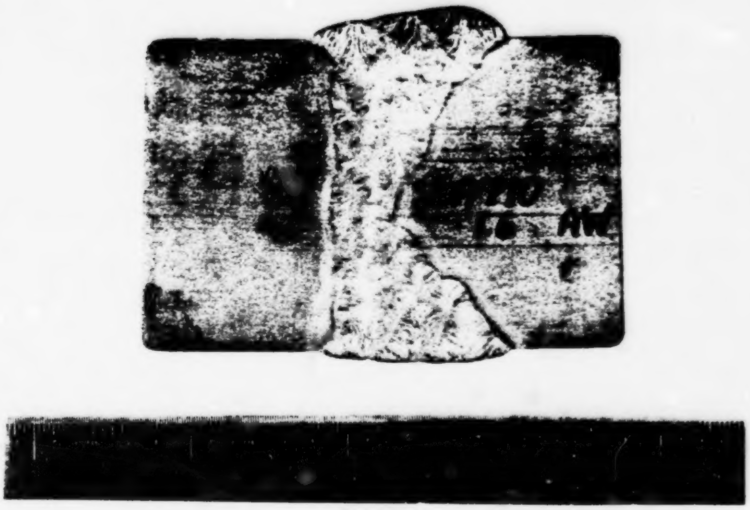

FIGURE B11: K-joint macrosection for Condition 5A - A710, Gr. A, Cl. 3; 1.6 kJ/mm; as-welded.

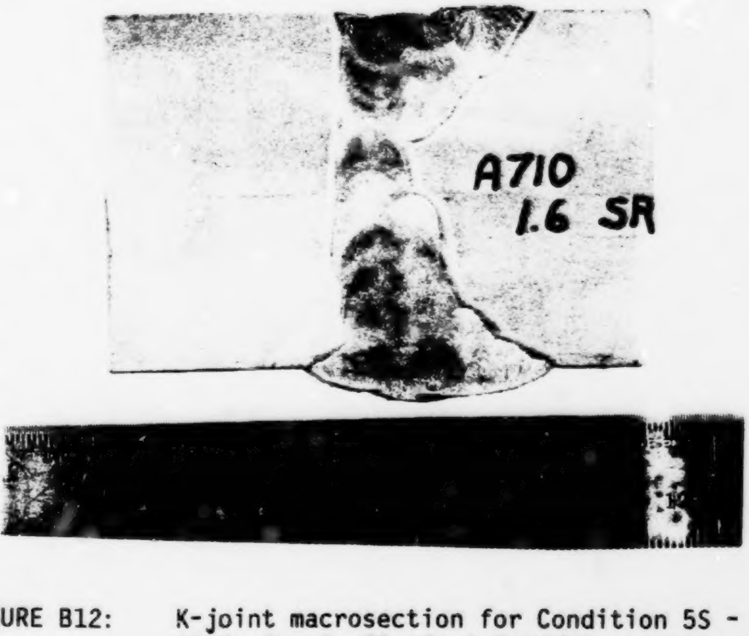

FIGURE B12: K-joint macrosection for Condition 5S - A710, Gr. A, Cl. 3; 1.6 kJ/mm; stress-relieved.

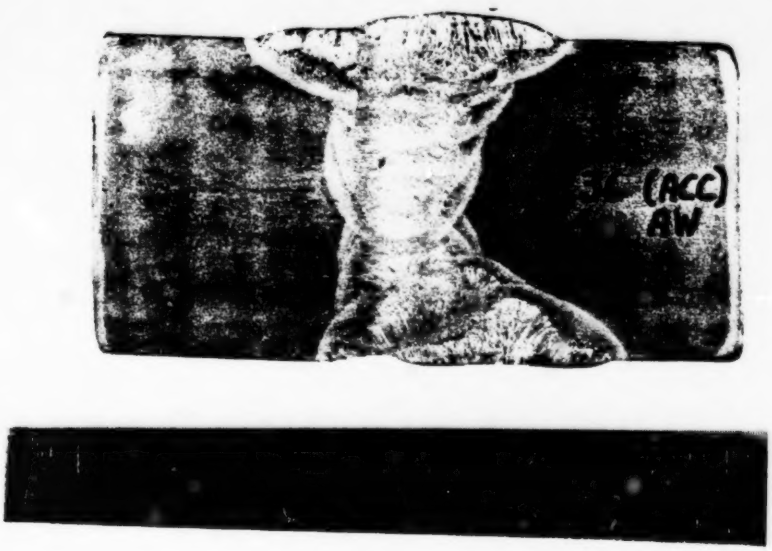

FIGURE B13: K-joint macrosection for Condition 6A - EH 36 (ACC); 5.4 kJ/mm; as-welded.

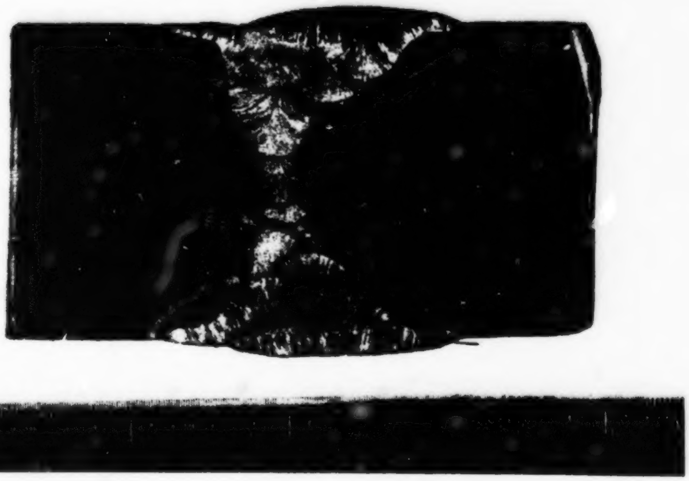

FIGURE B14: K-joint macrosection for Condition 6S - MACS (DQT), 5.4 kJ/mm; stress-relieved.

APPENDIX "C"

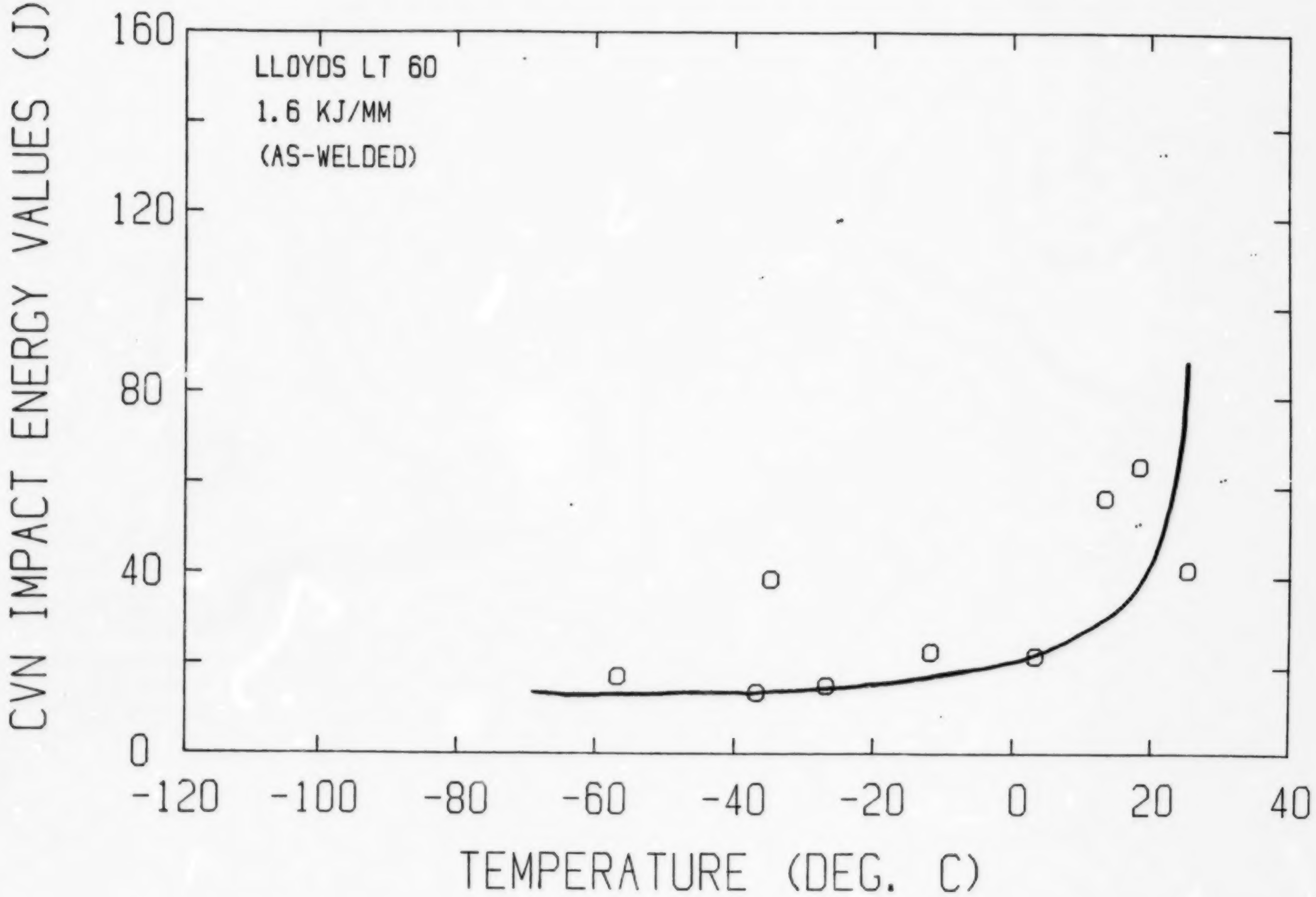

FIGURE C1: CVN transition curve for Lloyds LT 60, Gleeble cycled to simulate 1.6 kJ/mm in the "as-welded" conditon.

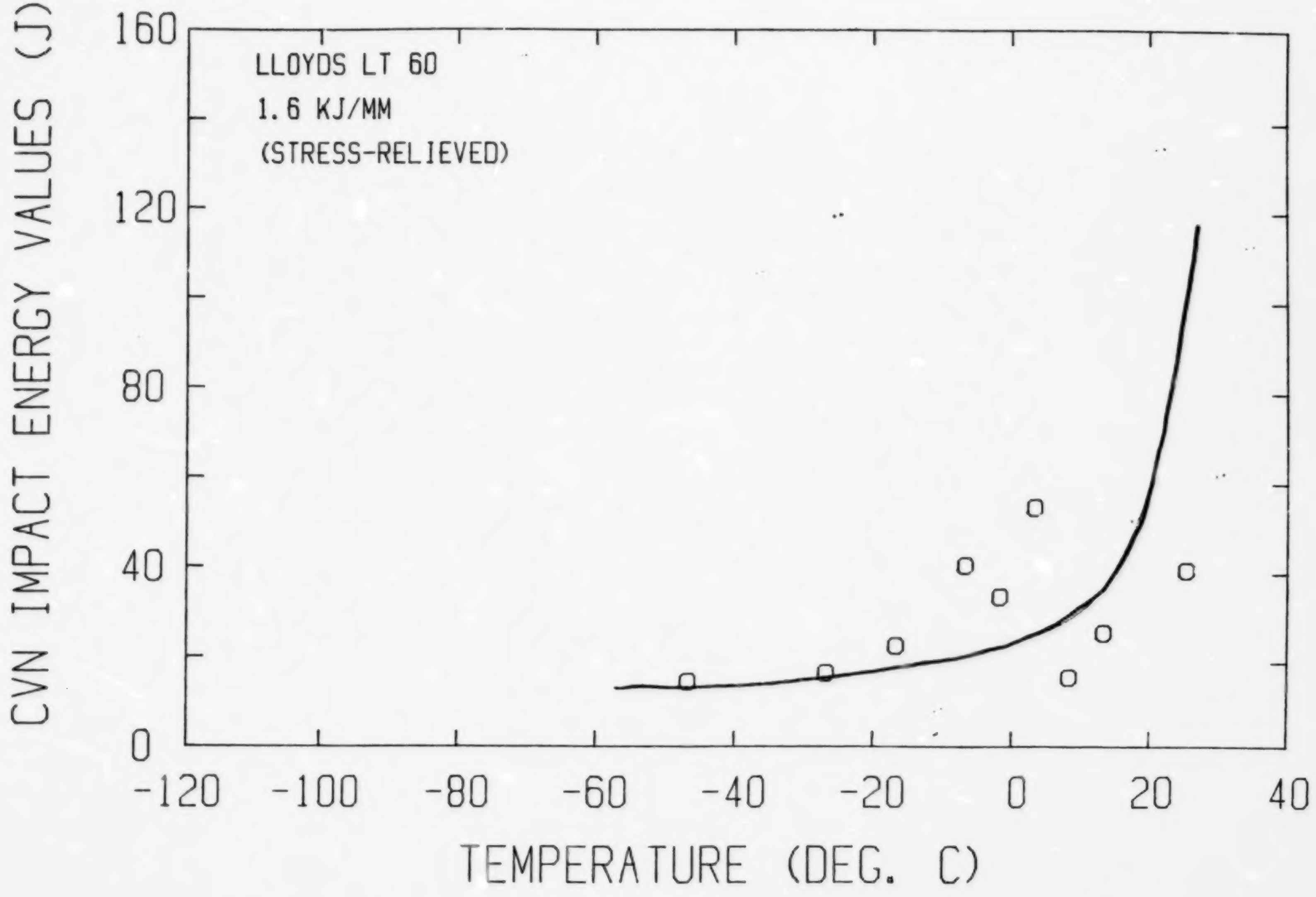

FIGURE C2: CVN transition curve for Lloyds LT 60, Gleeble cycled to simulate 1.6 kJ/mm in the "stress-relieved" condition.

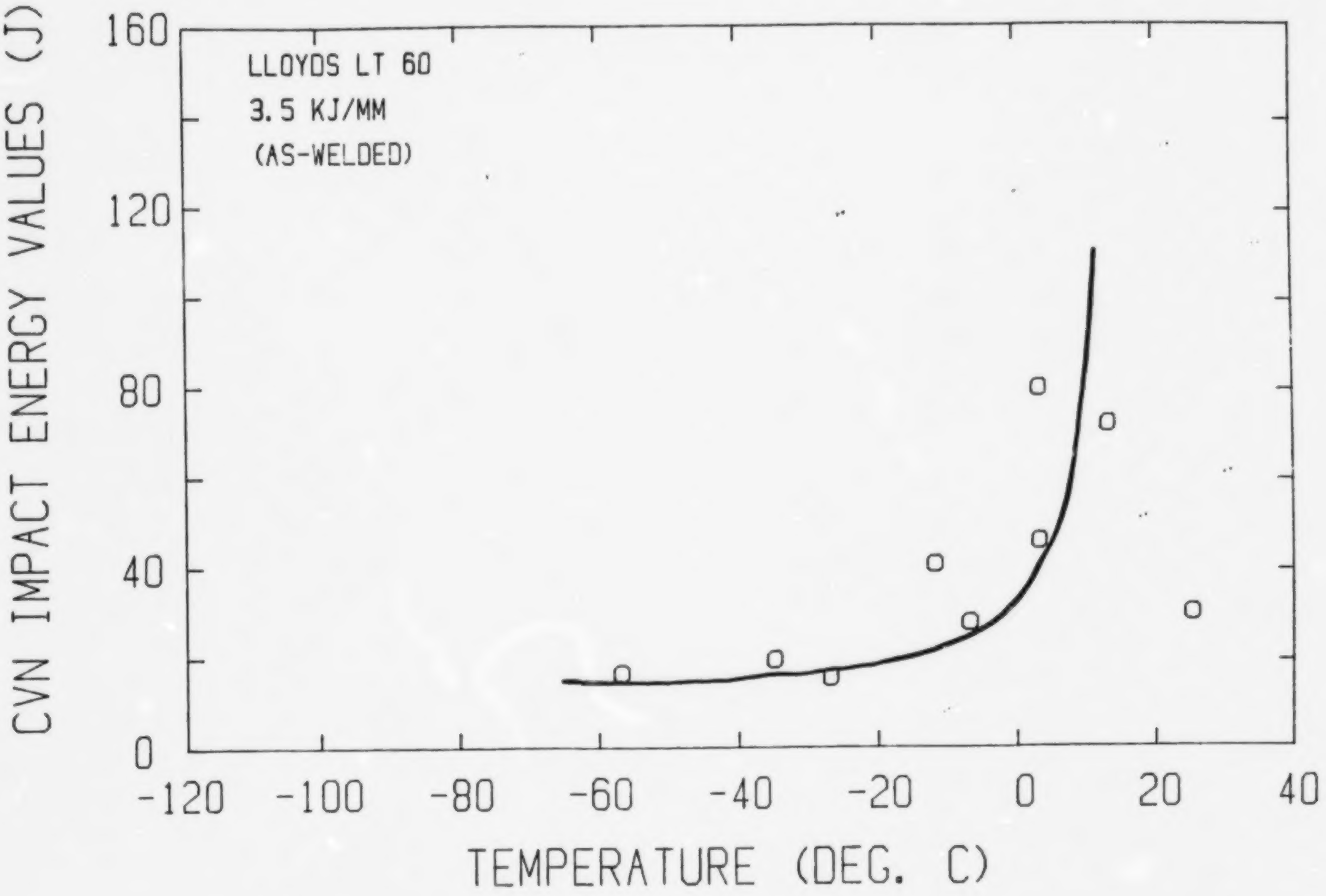

FIGURE C3: CVN transition curve for Lloyds LT 60, Gleeble cycled to simulate 3.5 kJ/mm in the "as-welded" condition.

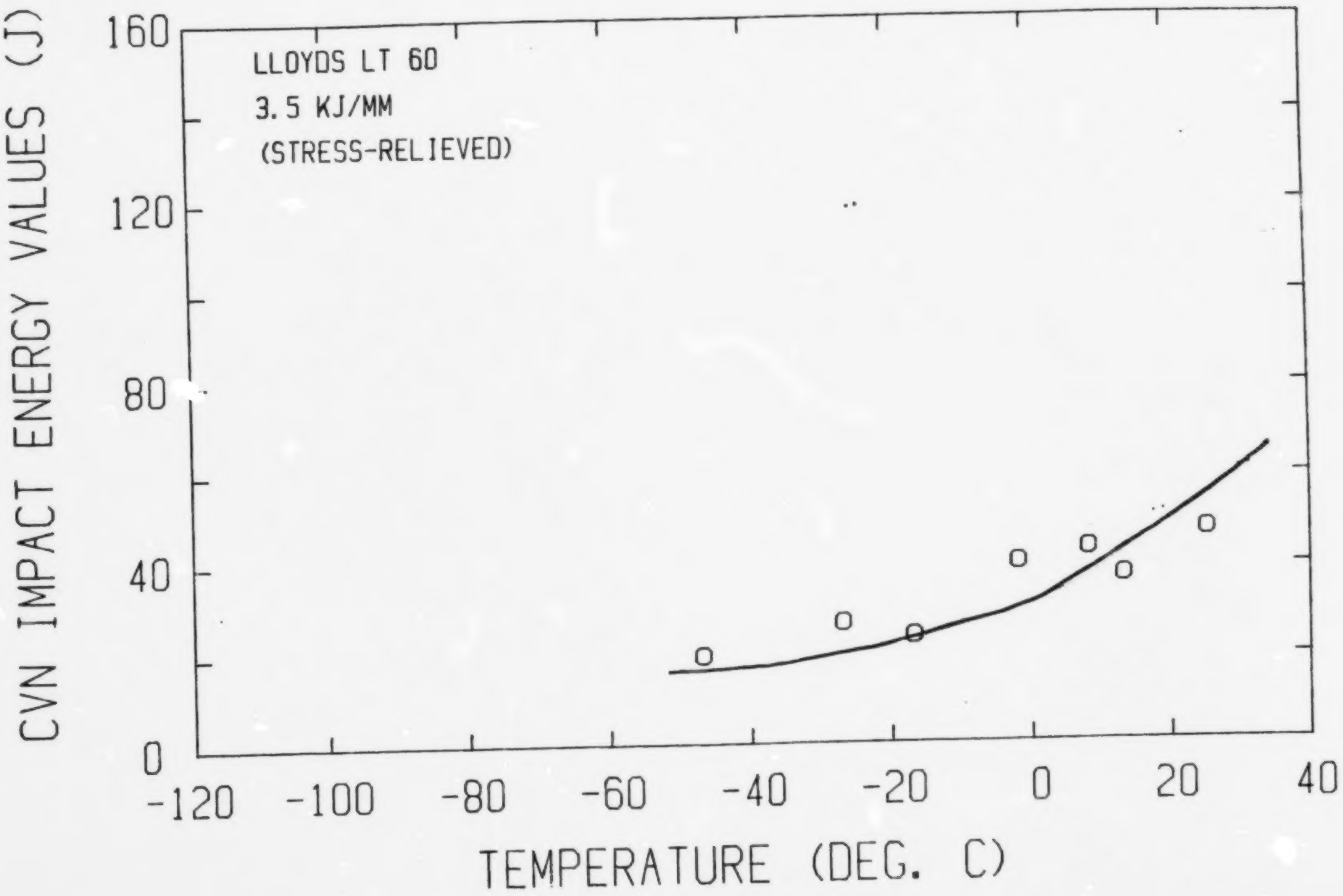

FIGURE C4: CVN transition curve for Lloyds LT 60, Gleeble cycled to simulate 3.5 kJ/mm in the "stress-relieved" condition.

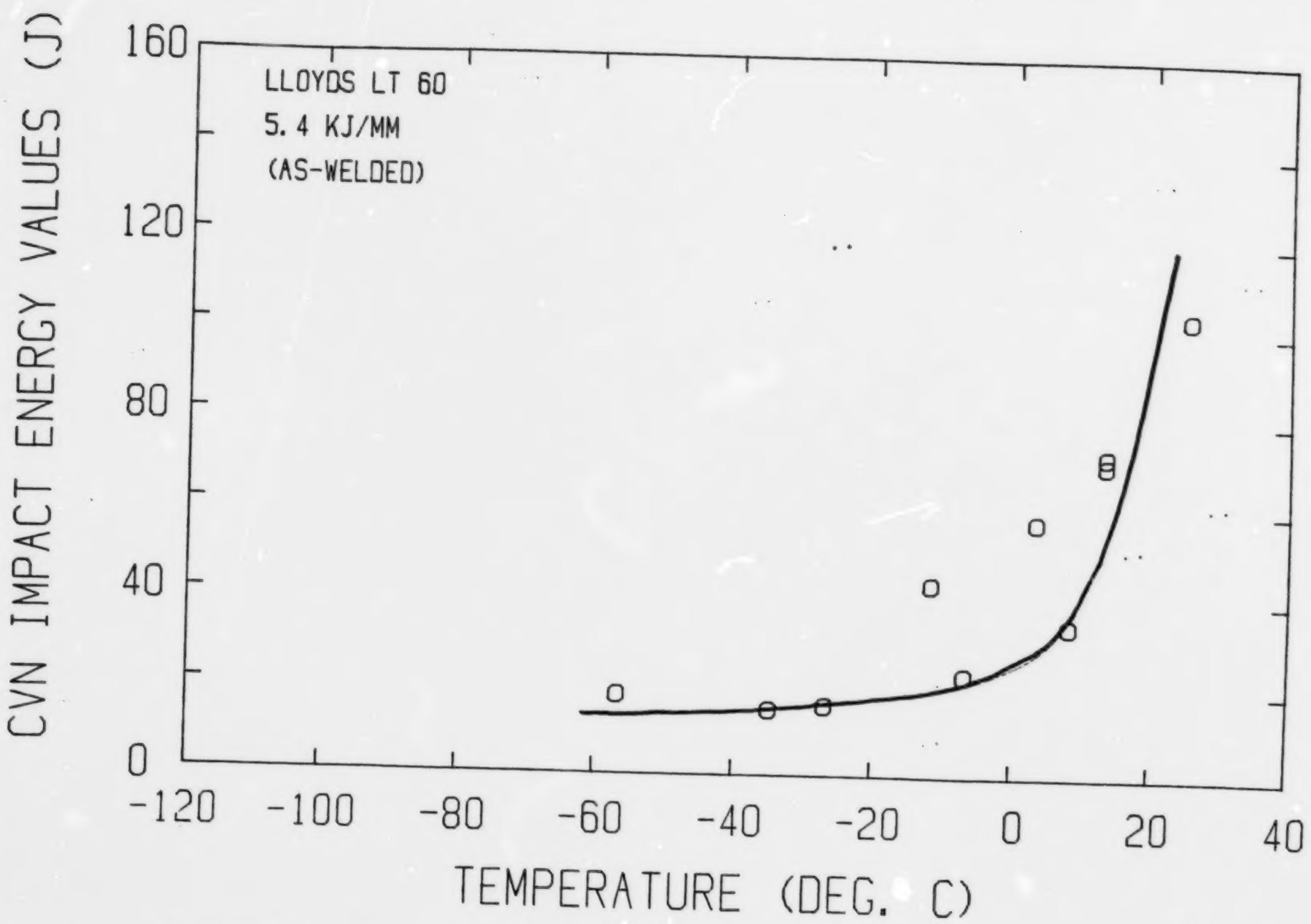

FIGURE C5: CVN transition curve for Lloyds LT 60, Gleeble cycled to simulate 5.4 kJ/mm in the "as-welded" condition.

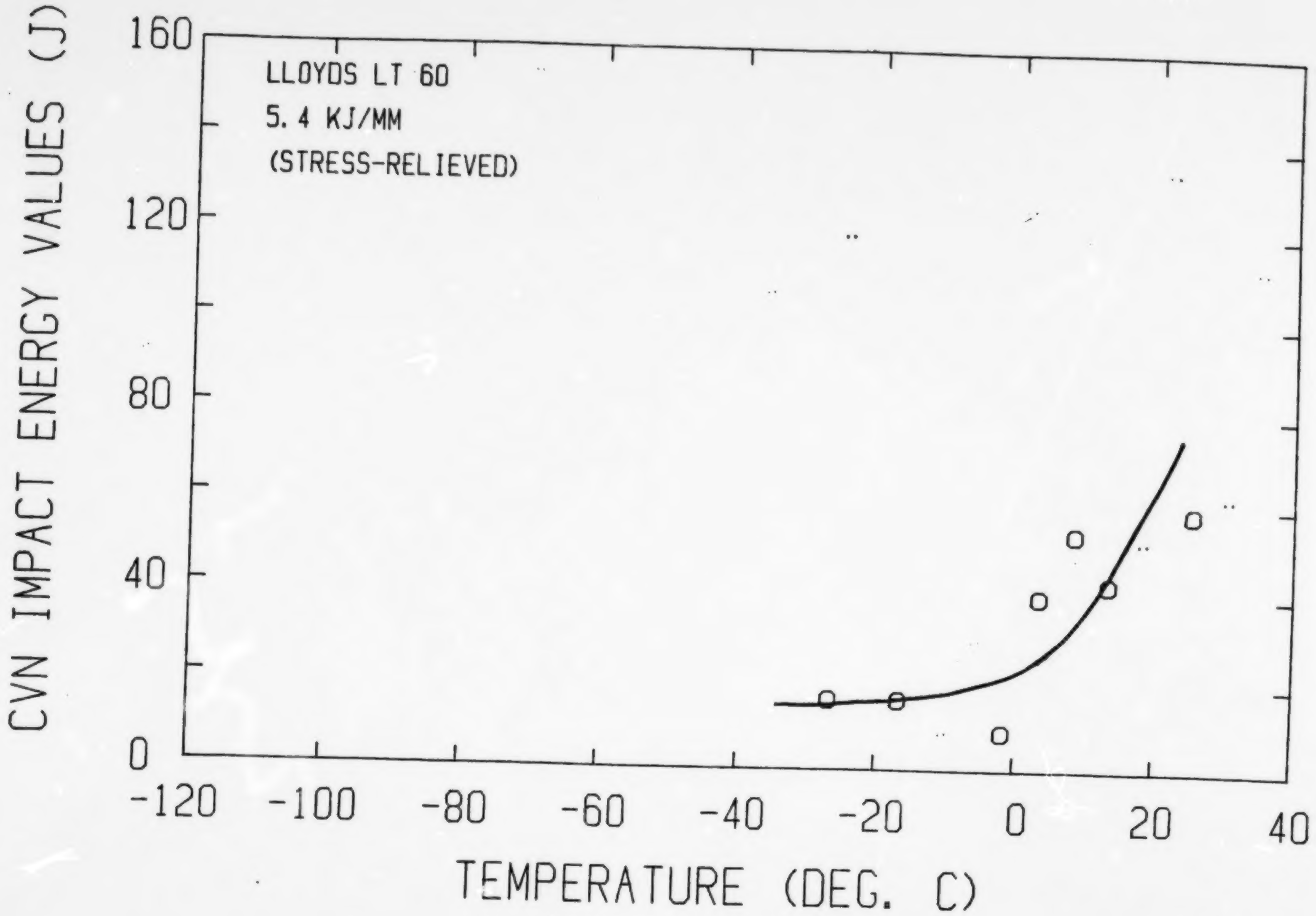

FIGURE C6: CVN transition curve for Lloyds LT 60, Gleeble cycled to simulate 5.4 kJ/mm in the "stress-relieved" condition.

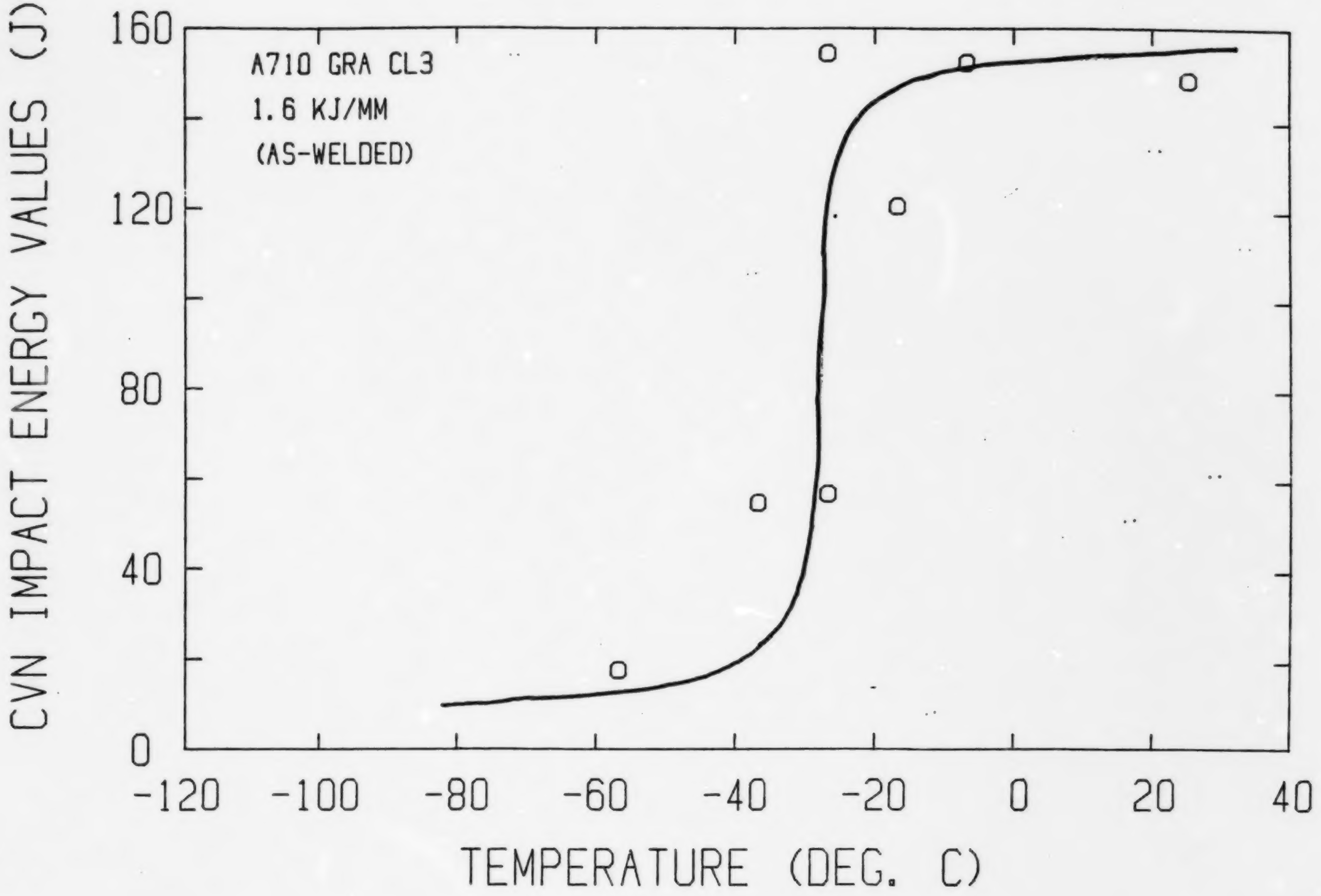

FIGURE C7: CVN transition curve for A710, Gr. A, Cl. 3, Gleeble cycled to simulat 1.6 kJ/mm in the "as-welded" condition.

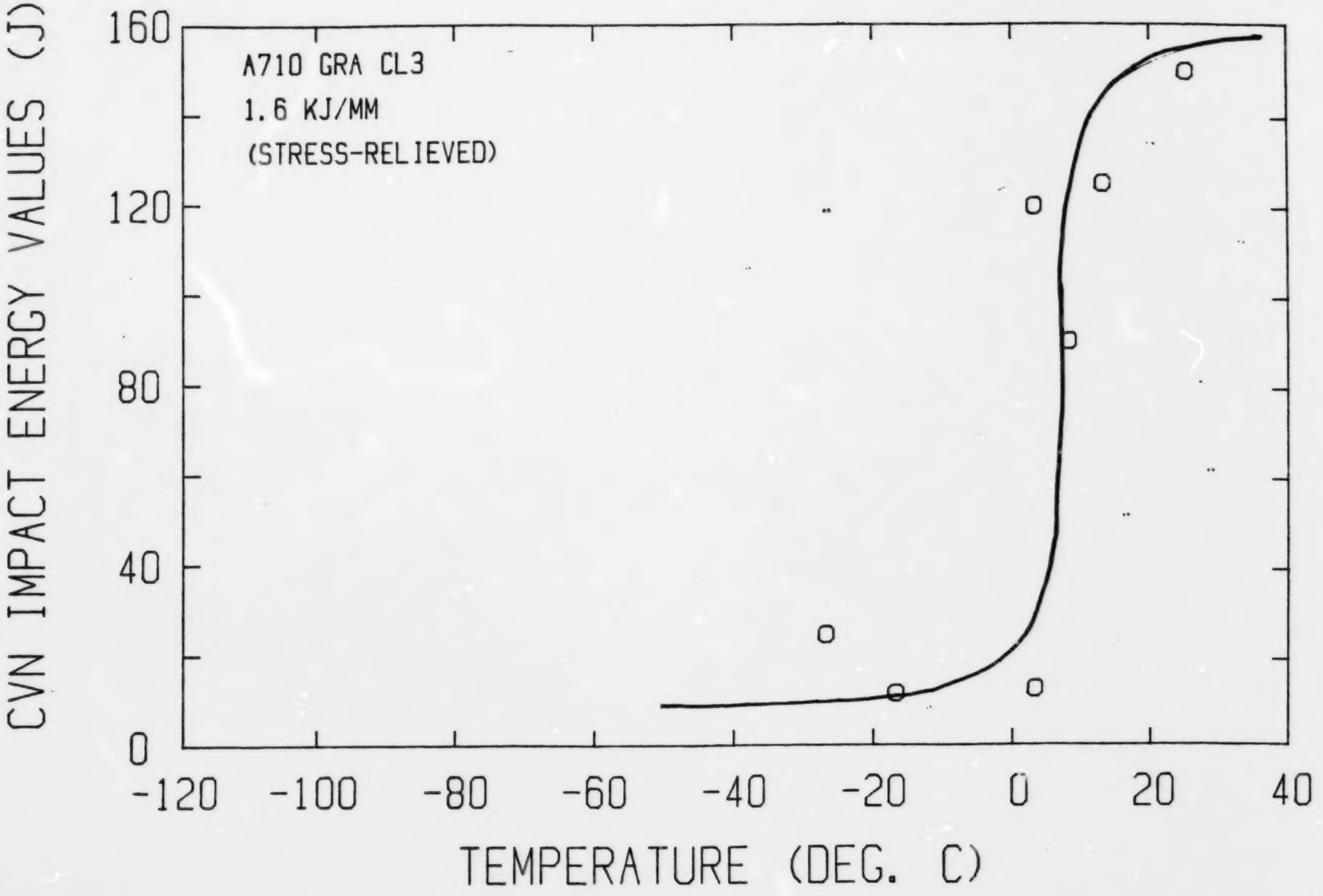

FIGURE C8: CVN transition curve for A710, Gr. A, Cl. 3, Gleeble cycled to simulate 1.6 kJ/mm in the "stress-relieved" condition.

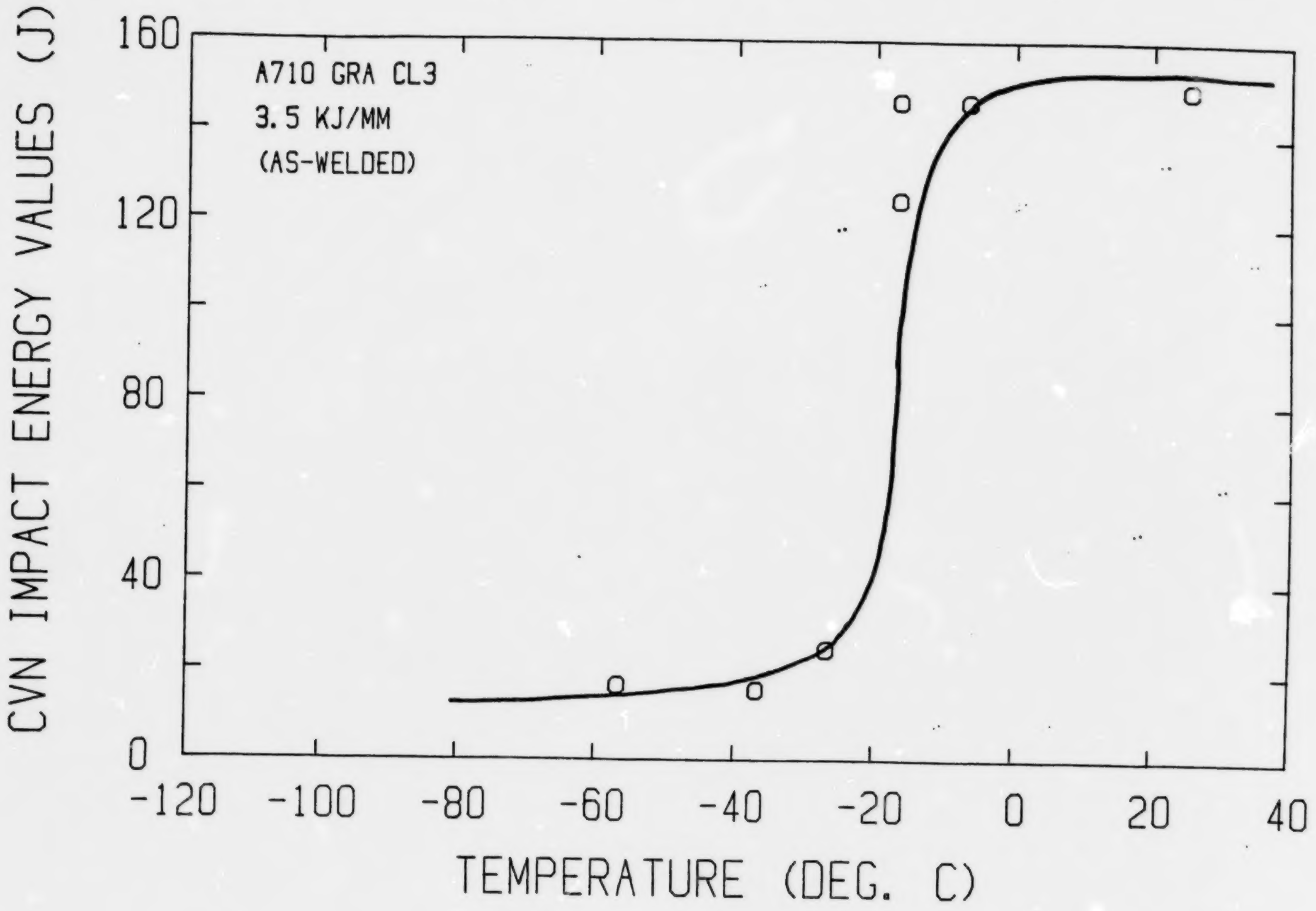

FIGURE C9: CVN transition curve for A710, Gr. A, Cl. 3, Gleeble cycled to simulate 3.5 kJ/mm in the "as-welded" condition.

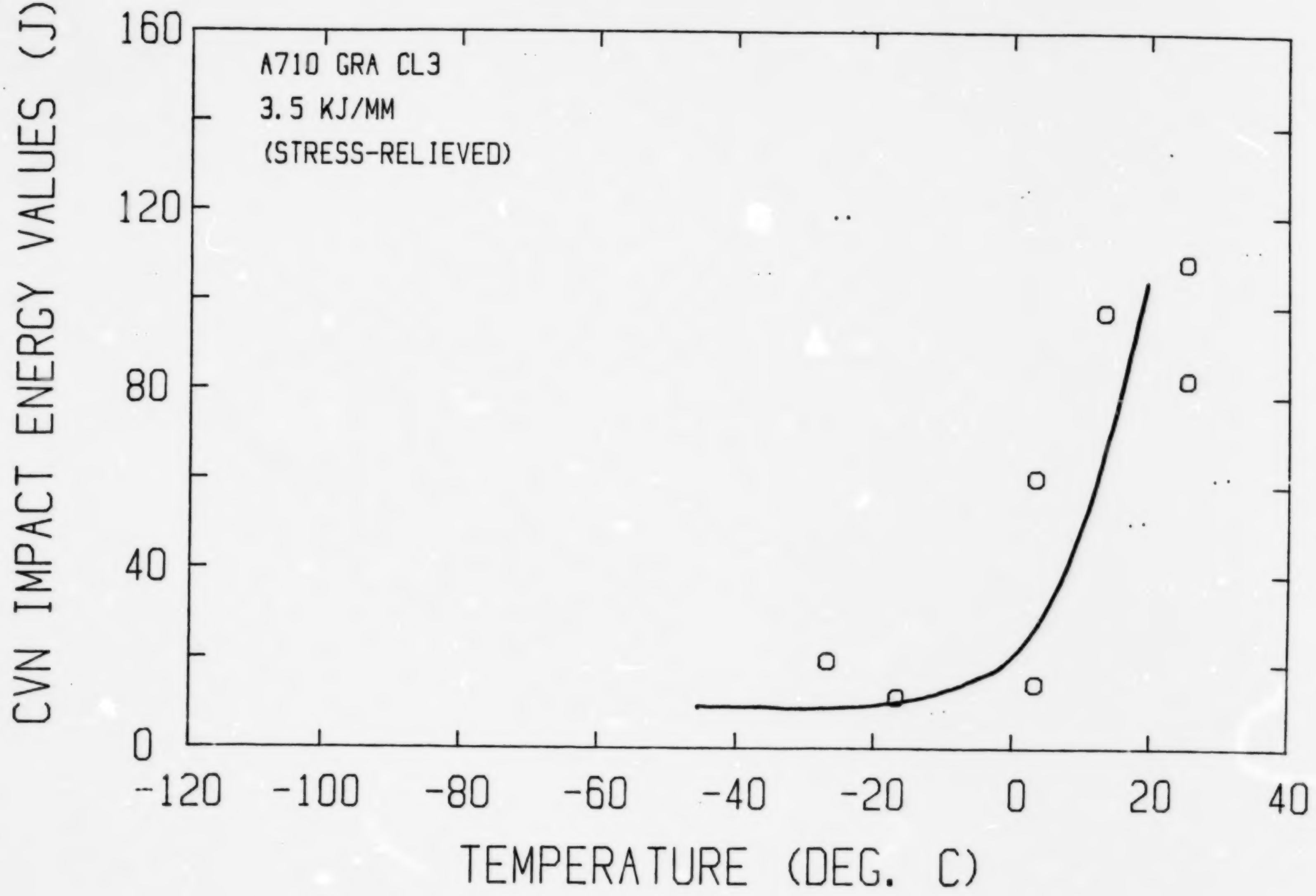

FIGURE C10: CVN transition curve for A710, Gr. A, Cl. 3, Gleeble cycled to simulate 3.5 kJ/mm in the "stress-relieved" condition.

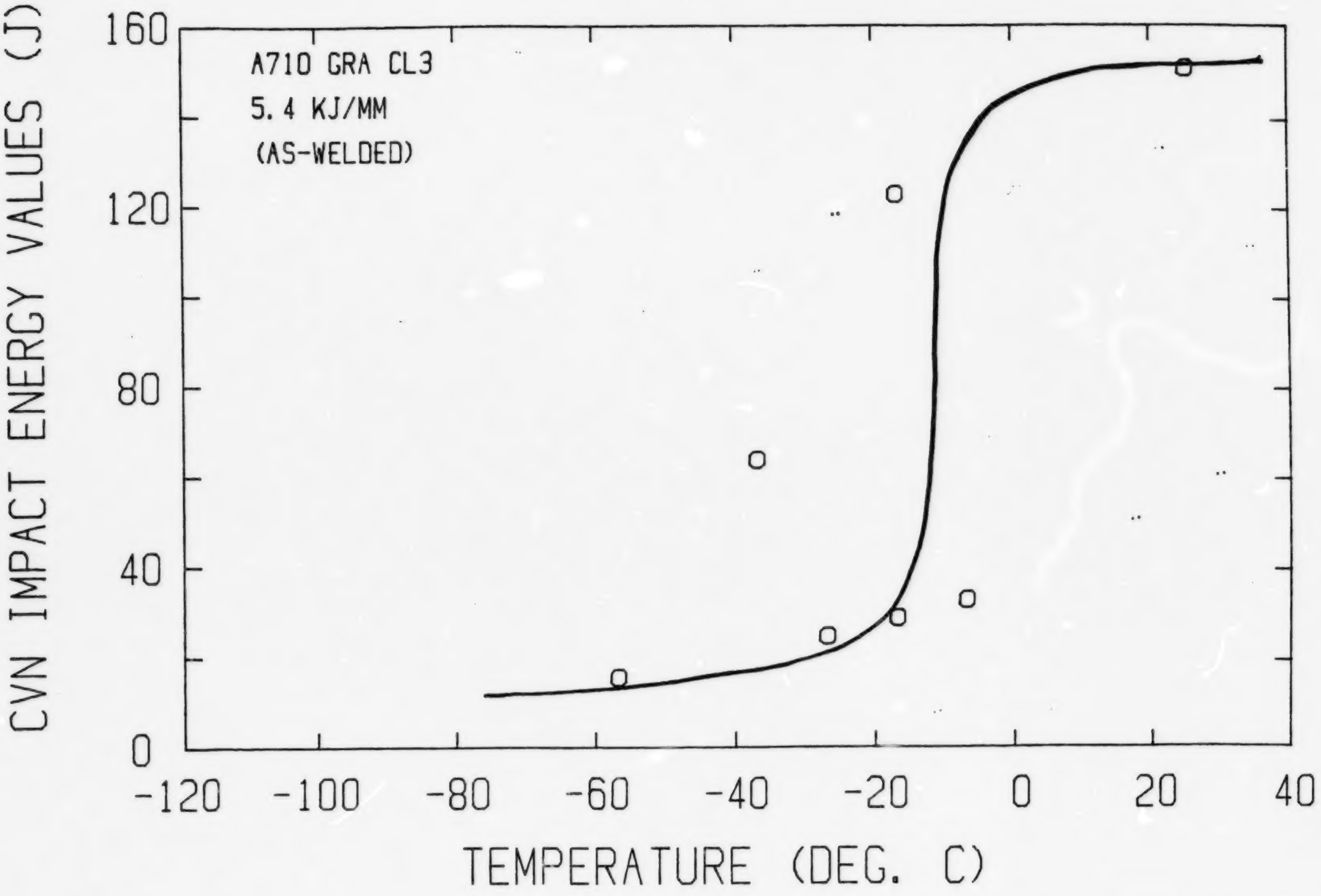

FIGURE C11: CVN transition curve for A710, Gr. A, Cl. 3, Gleeble cycled to simulate 5.4 kJ/mm in the "as-welded" condition.

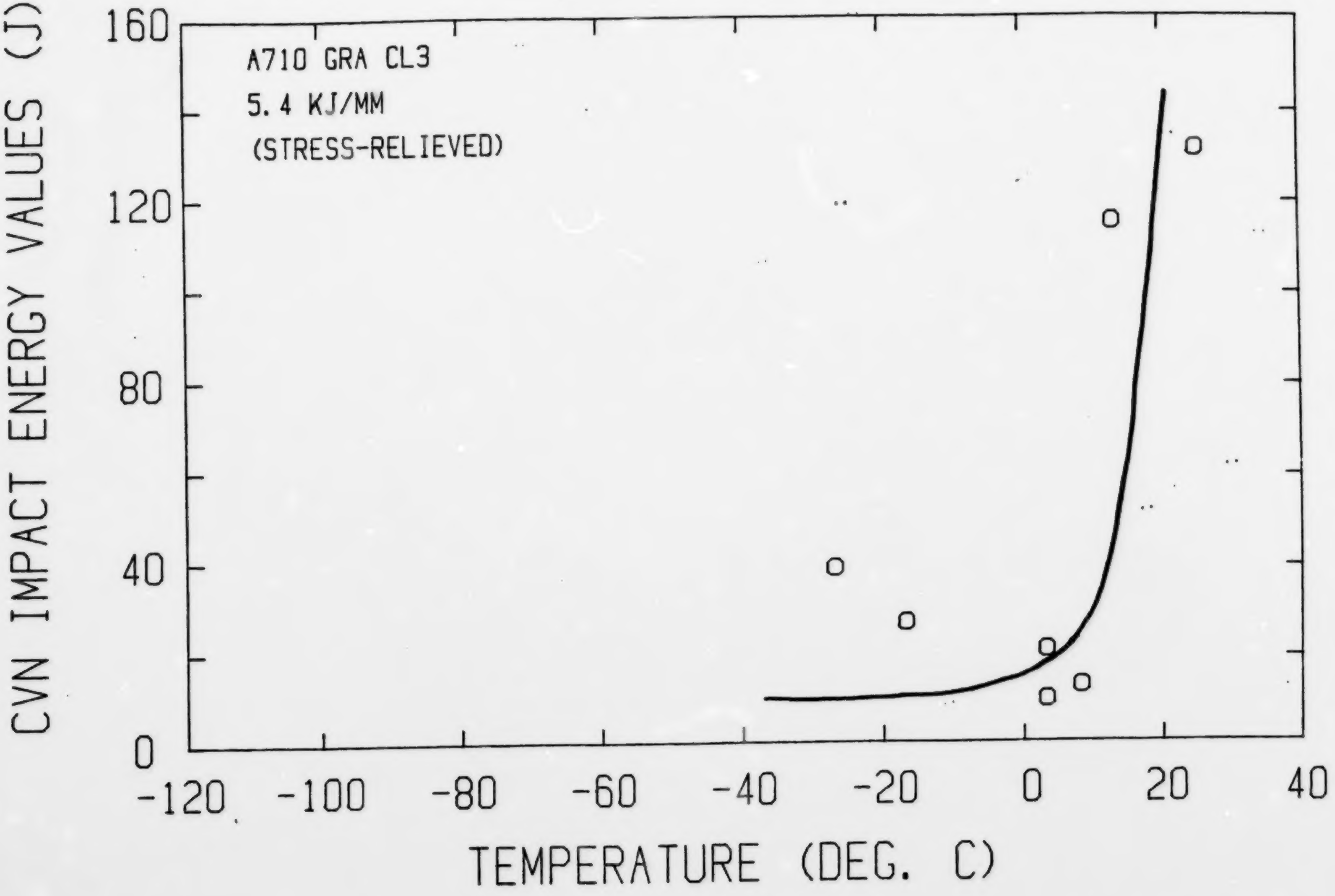

FIGURE C12: CVN transition curve for A710, Gr. A, Cl. 3, Gleeble cycled to simulate 5.4 kJ/mm in the "stress-relieved" condition.

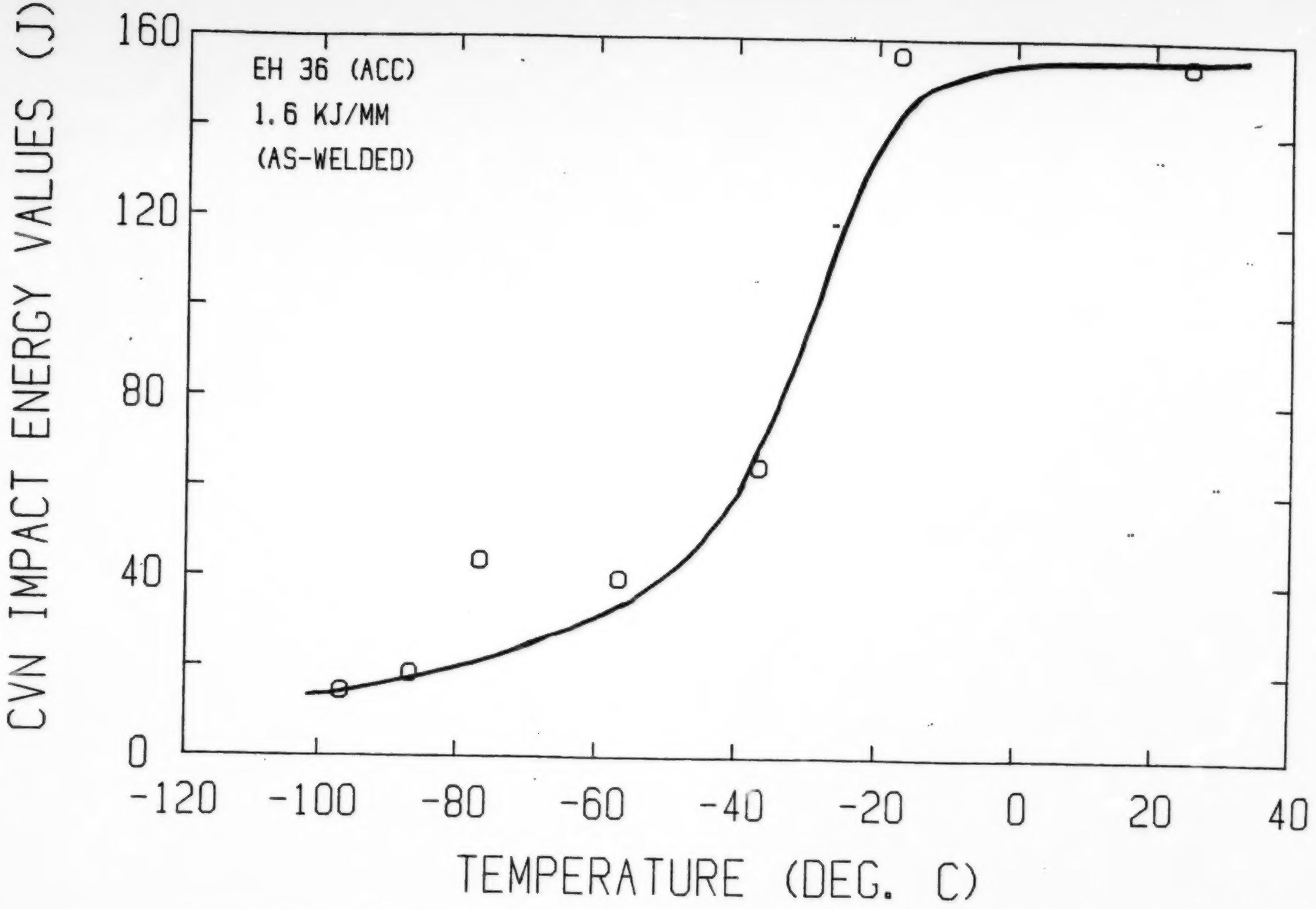

FIGURE C13: CVN transition curve for MACS (ACC), Gleeble cycled to simulate 1.6 kJ/mm in the "as-welded" condition.

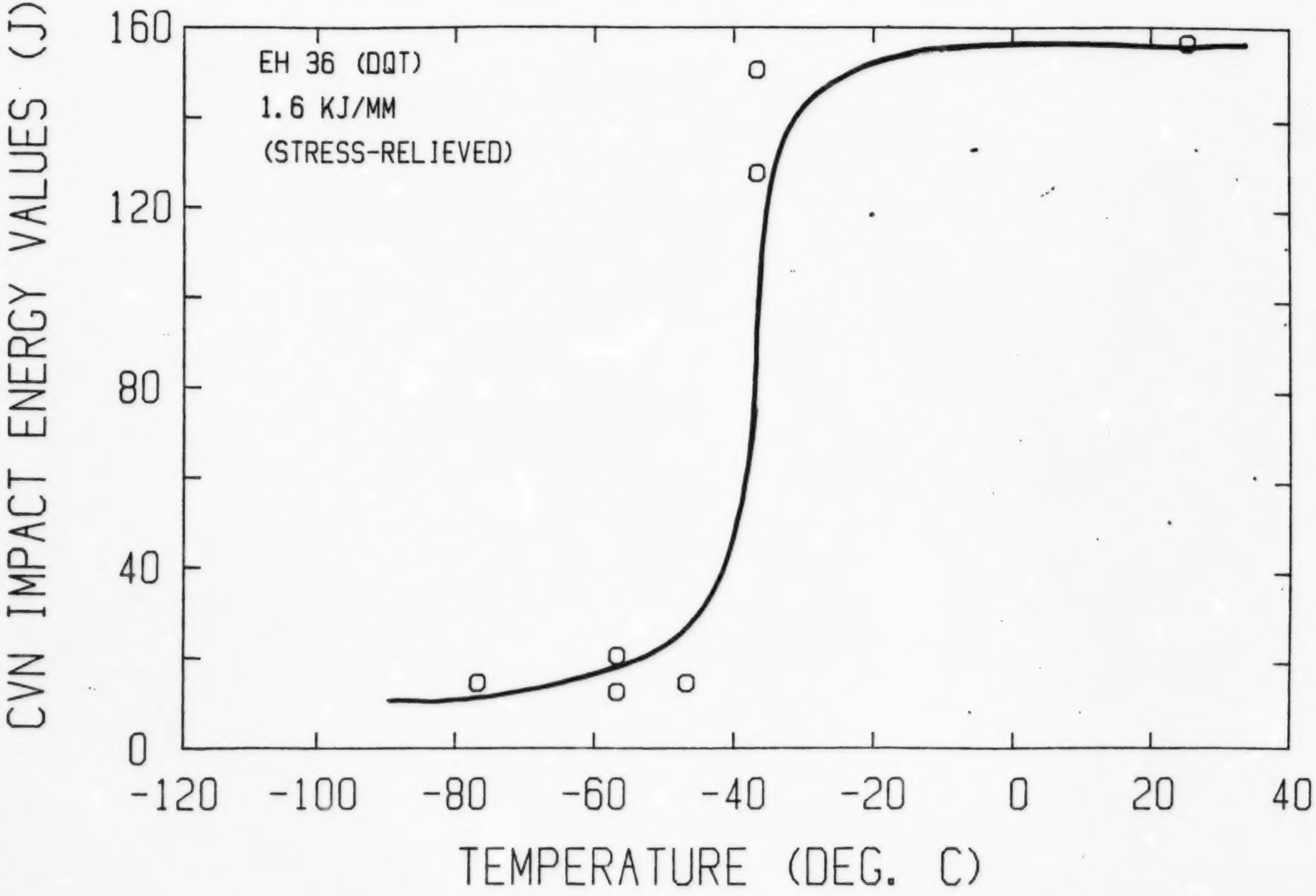

FIGURE C14: CVN transition curve for MACS (DQT), Gleeble cycled to simulate 1.6 kJ/mm in the "stress-relieved" condition.

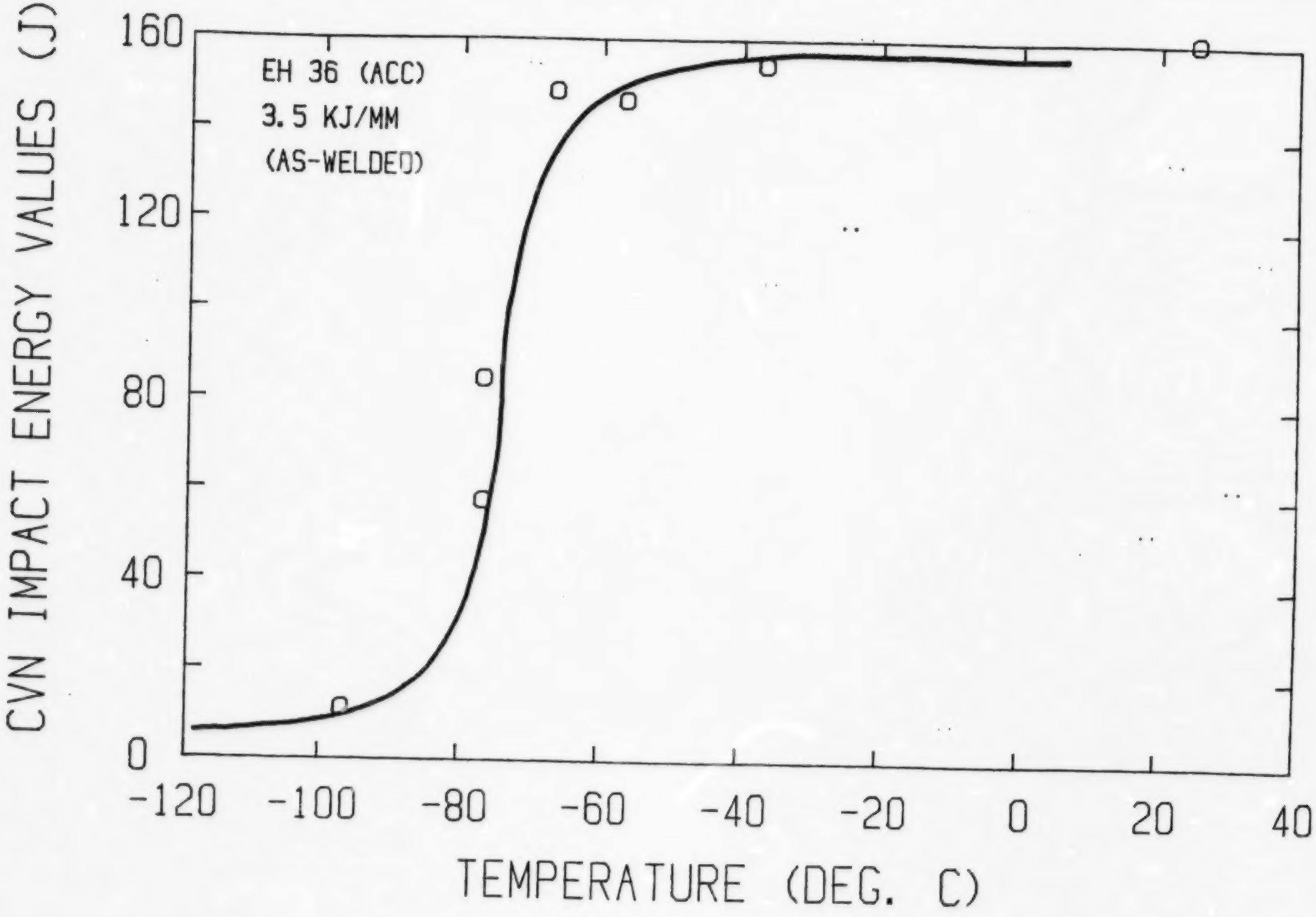

FIGURE C15: CVN transition curve for MACS (ACC), Gleeble cycled to simulate 3.5 kJ/mm in the "as-welded" condition.

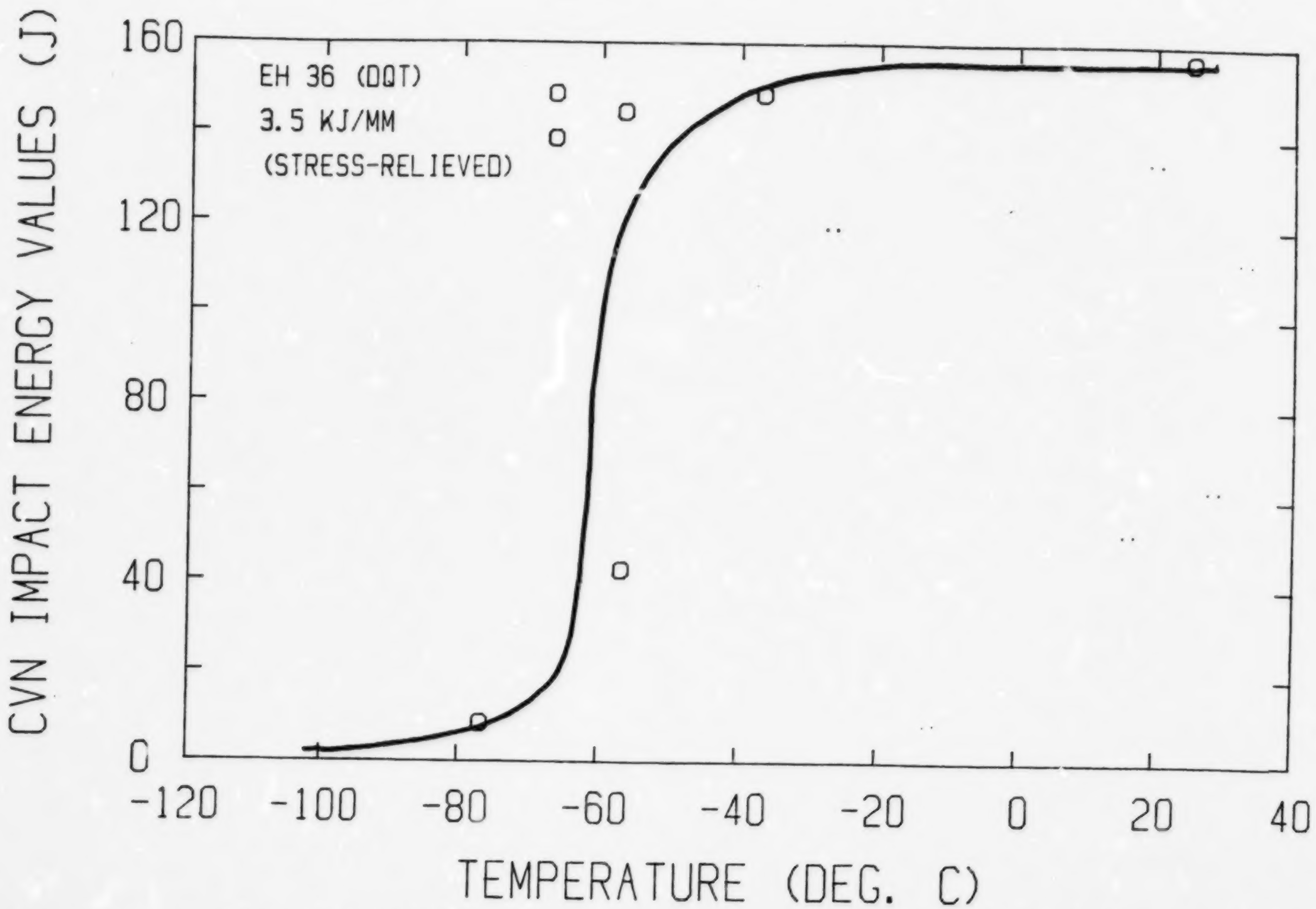

FIGURE C16: CVN transition curve for MACS (DQT), Gleeble cycled to simulate 3.5 kJ/mm in the "stress-relieved" condition.

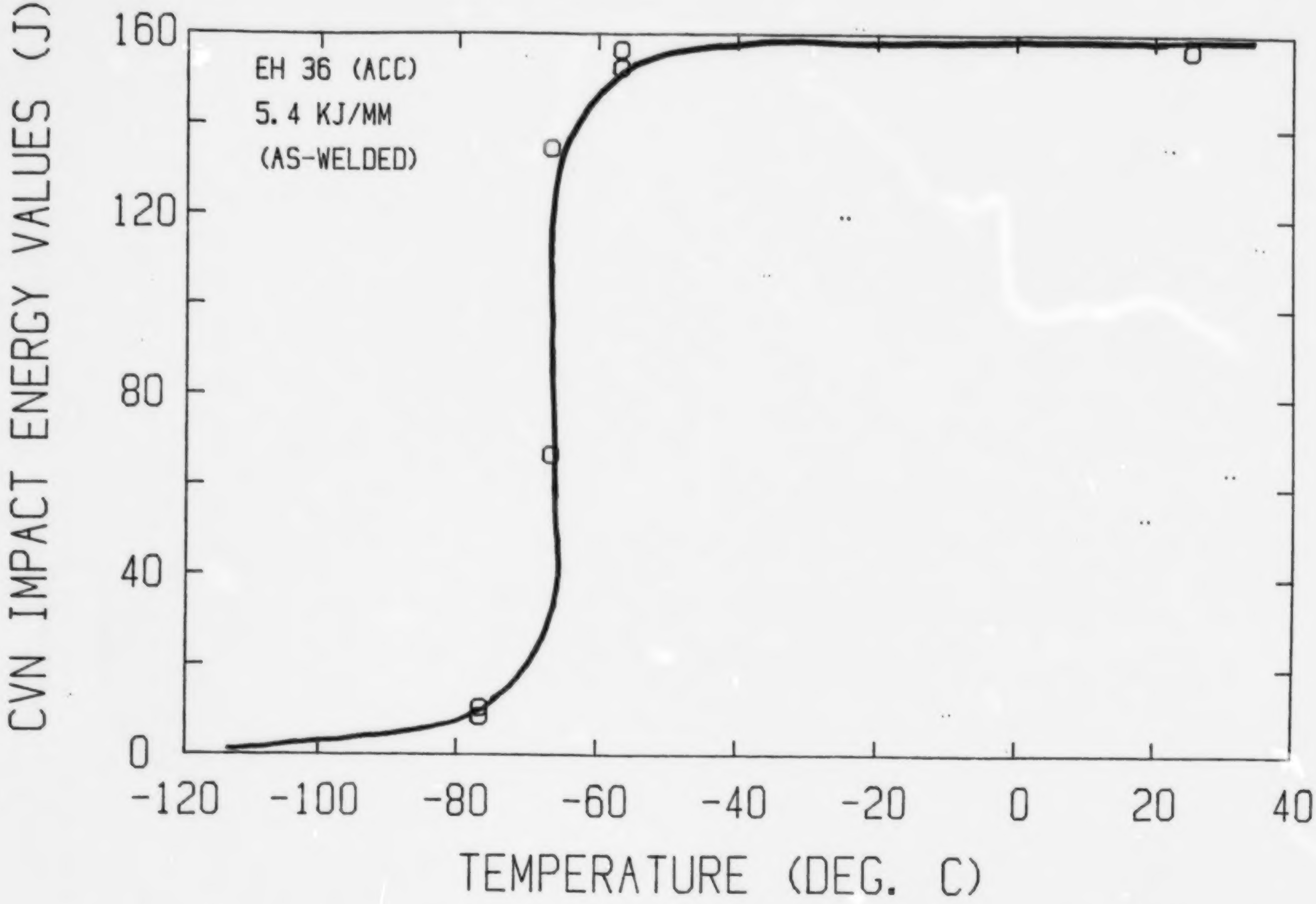

FIGURE C17: CVN transition curve for MACS (ACC), Gleeble cycled to simulate 5.4 kJ/mm in the "as-welded" condition.

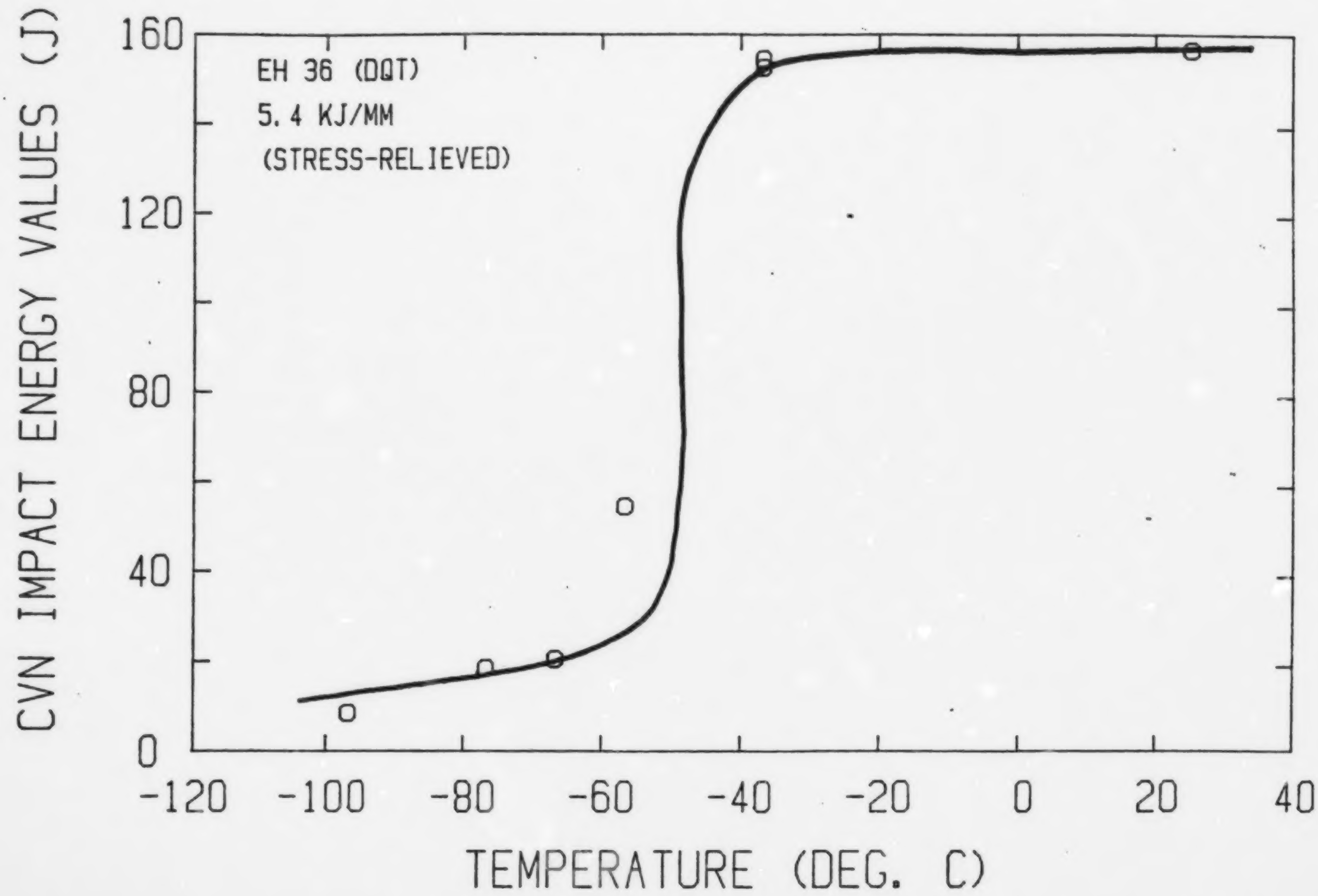

FIGURE C18: CVN Transition curve for MACS (DQT), Gleeble cycled to simulate 5.4 kJ/mm in the "stress-relieved" condition.

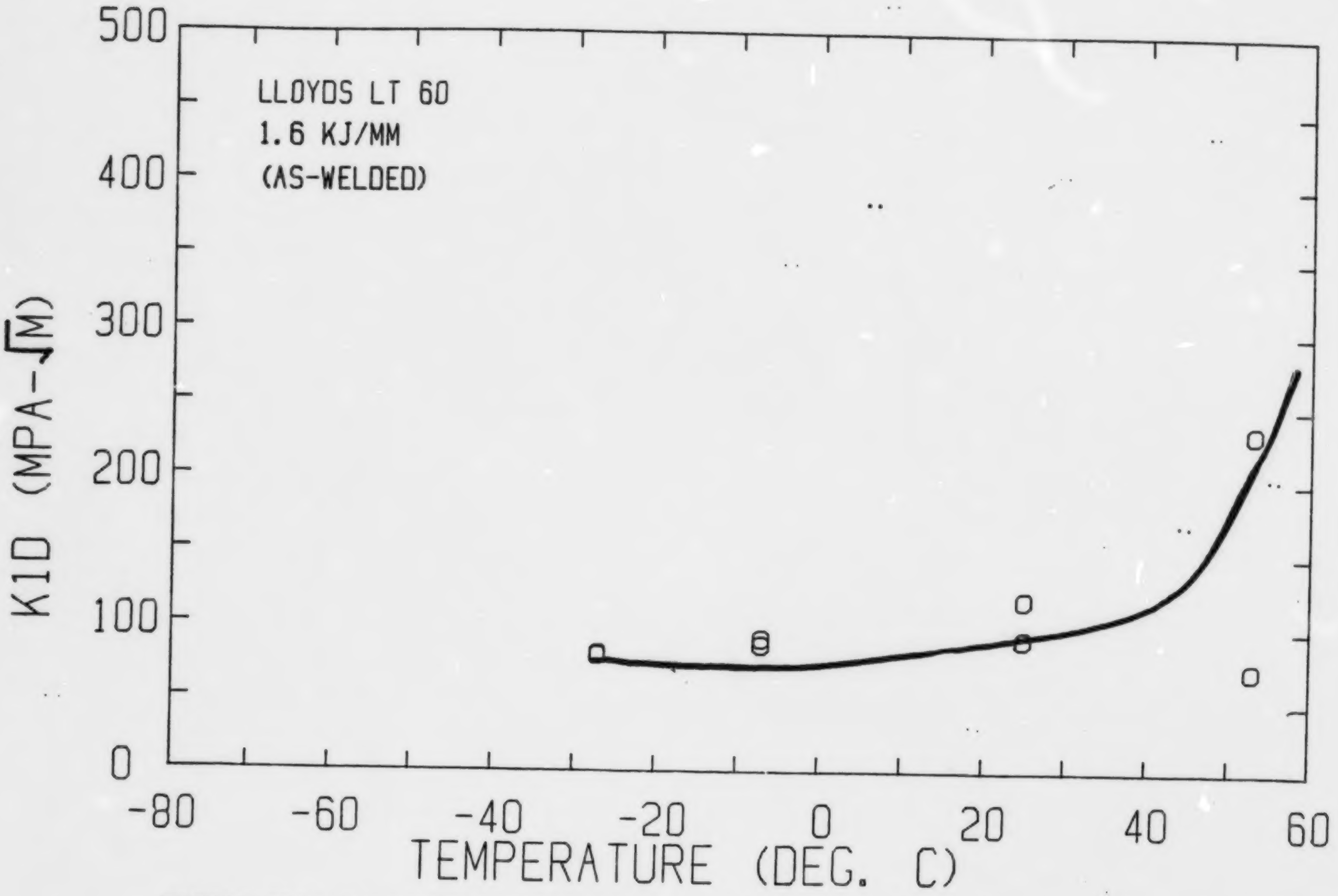

FIGURE C19: Fracture toughness parameter K_{1d} plotted with respect to temperature for Lloyds LT 60, Gleeble cycled to simulate 1.6 kJ/mm in the "as-welded" condition.

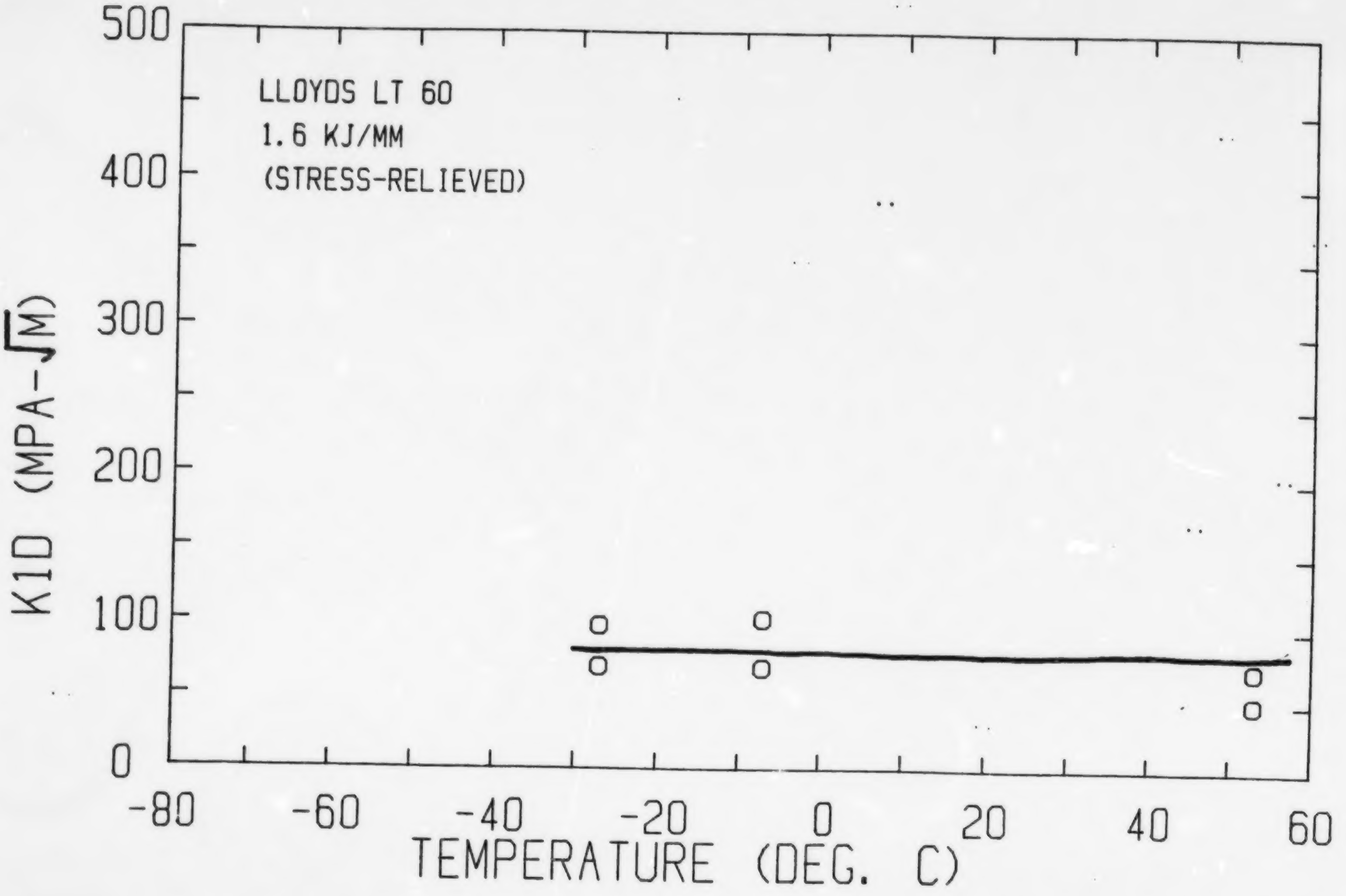

FIGURE C20: Fracture toughness parameter K_{1d} plotted with respect to temperature for Lloyds LT 60, Gleeble cycled to simulate 1.6 kJ/mm in the "stress-relieved" condition.

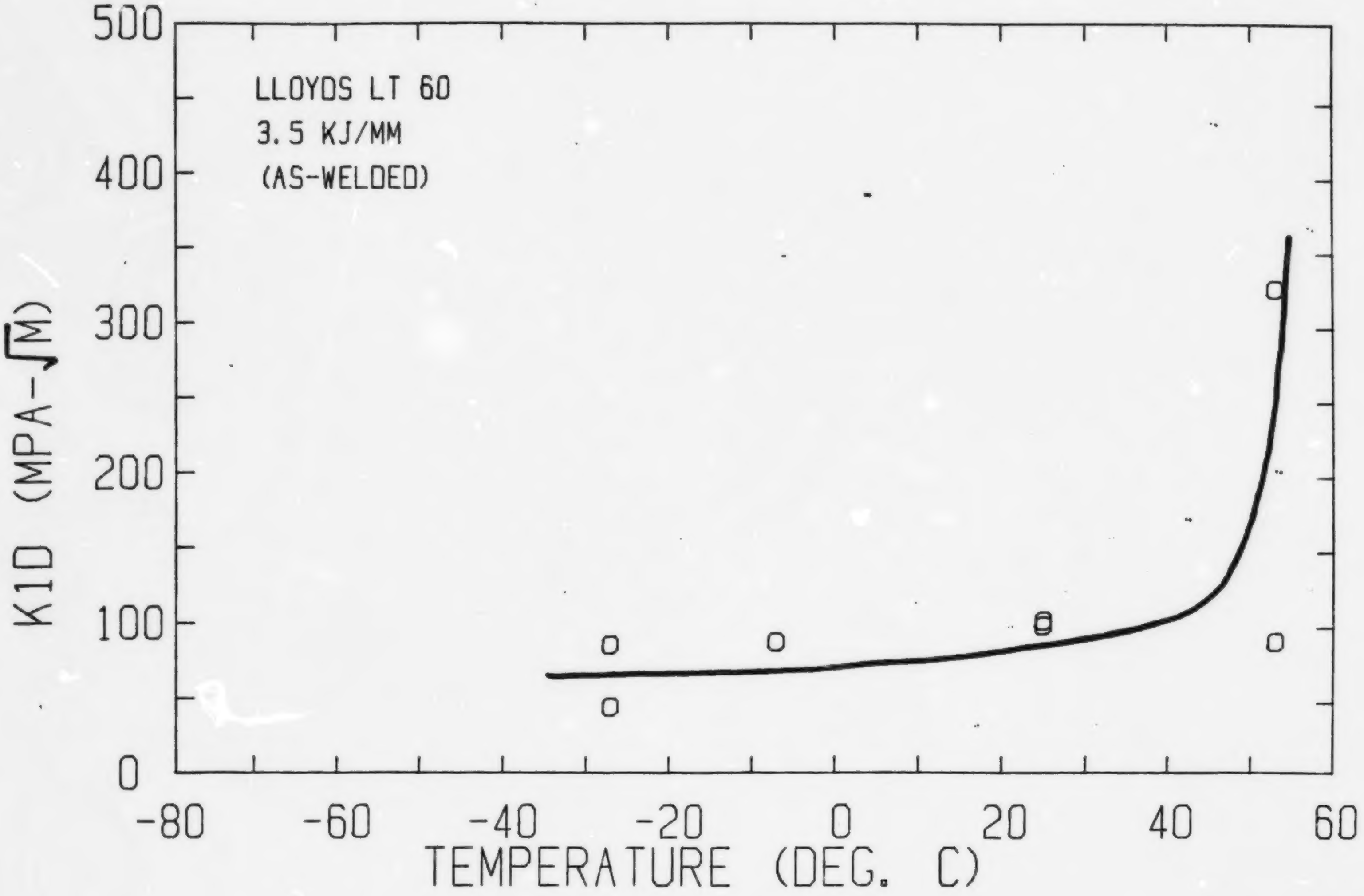

FIGURE C21: Fracture toughness parameter K_{1d} plotted with respect to temperature for Lloyds LT 60, Gleeble cycled to simulate 3.5 KJ/mm in the "as-welded" condition.

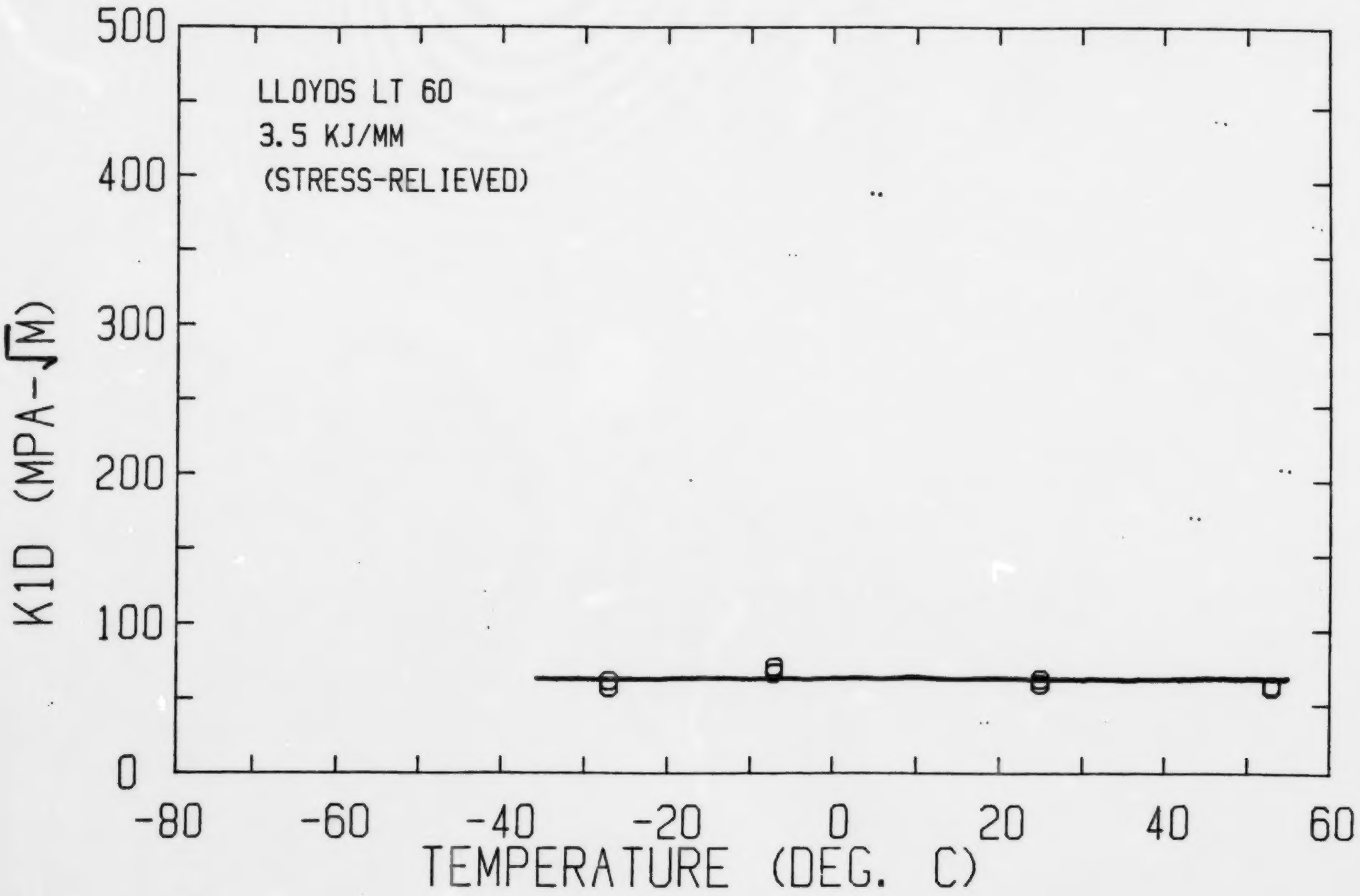

FIGURE C22: Fracture toughness parameter K_{1d} plotted with respect to temperature for Lloyds LT 60, Gleeble cycled to simulate 3.5 kJ/mm in the "stress-relieved" condition.

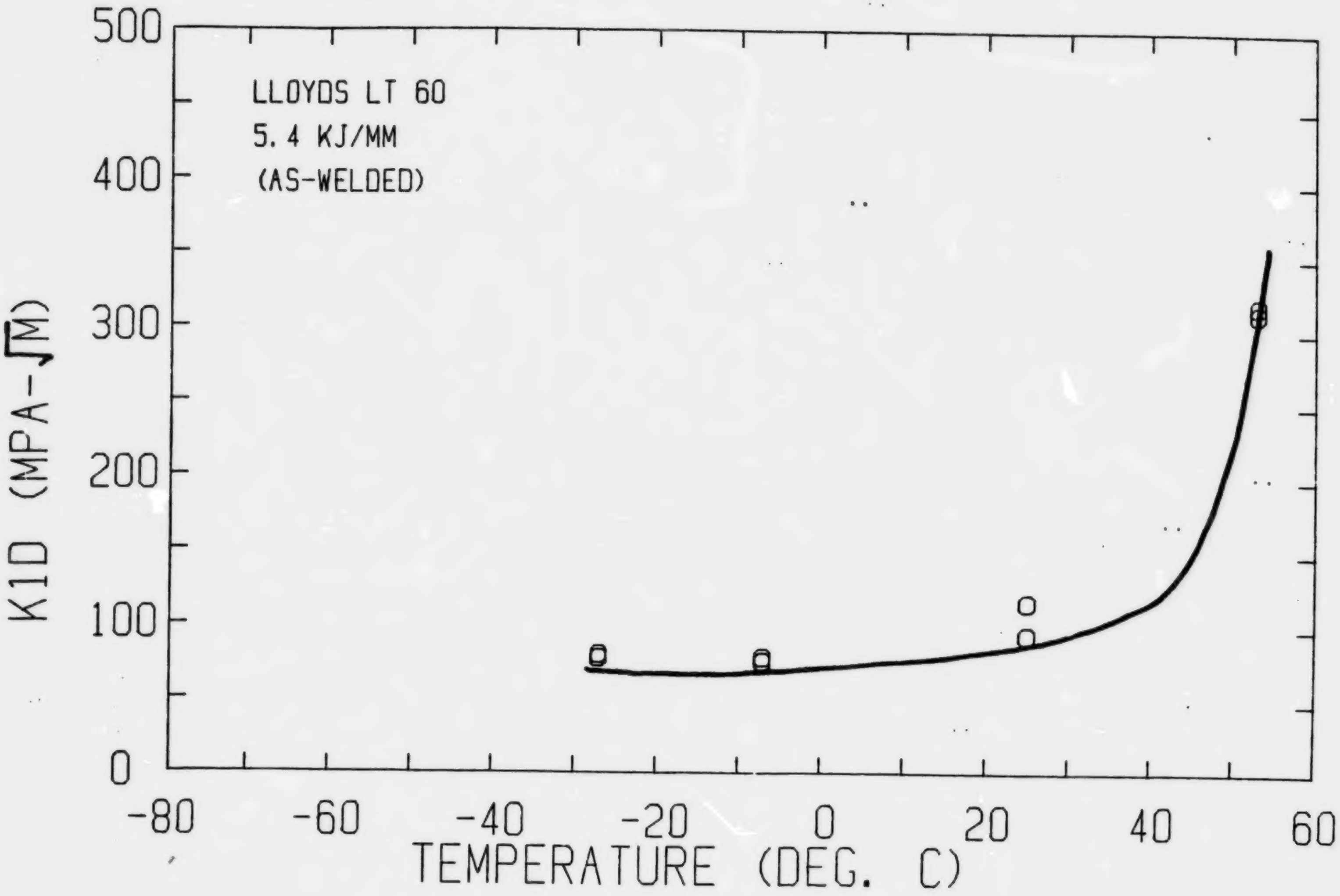

FIGURE C23: Fracture toughness parameter K_{1d} plotted with respect to temperature for Lloyds LT 60, Gleeble cycled to simulate 5.4 kJ/mm in the "as-welded" condition.

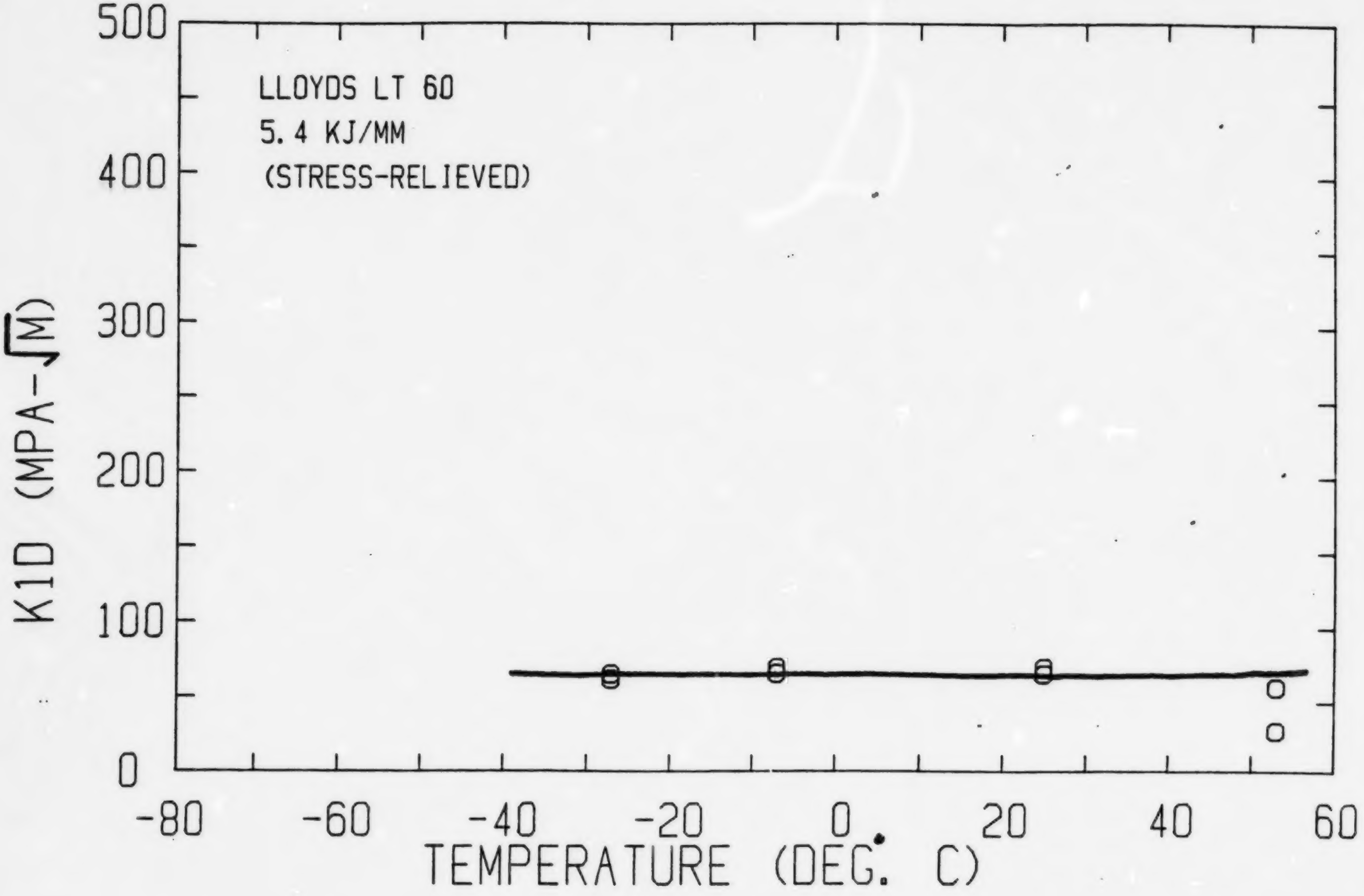

FIGURE C24: Fracture toughness parameter K_{1d} plotted with repsect to temperature for Lloyds LT 60, Gleeble cycled to simulate 5.4 kJ/mm in the "stress-relieved" condition.

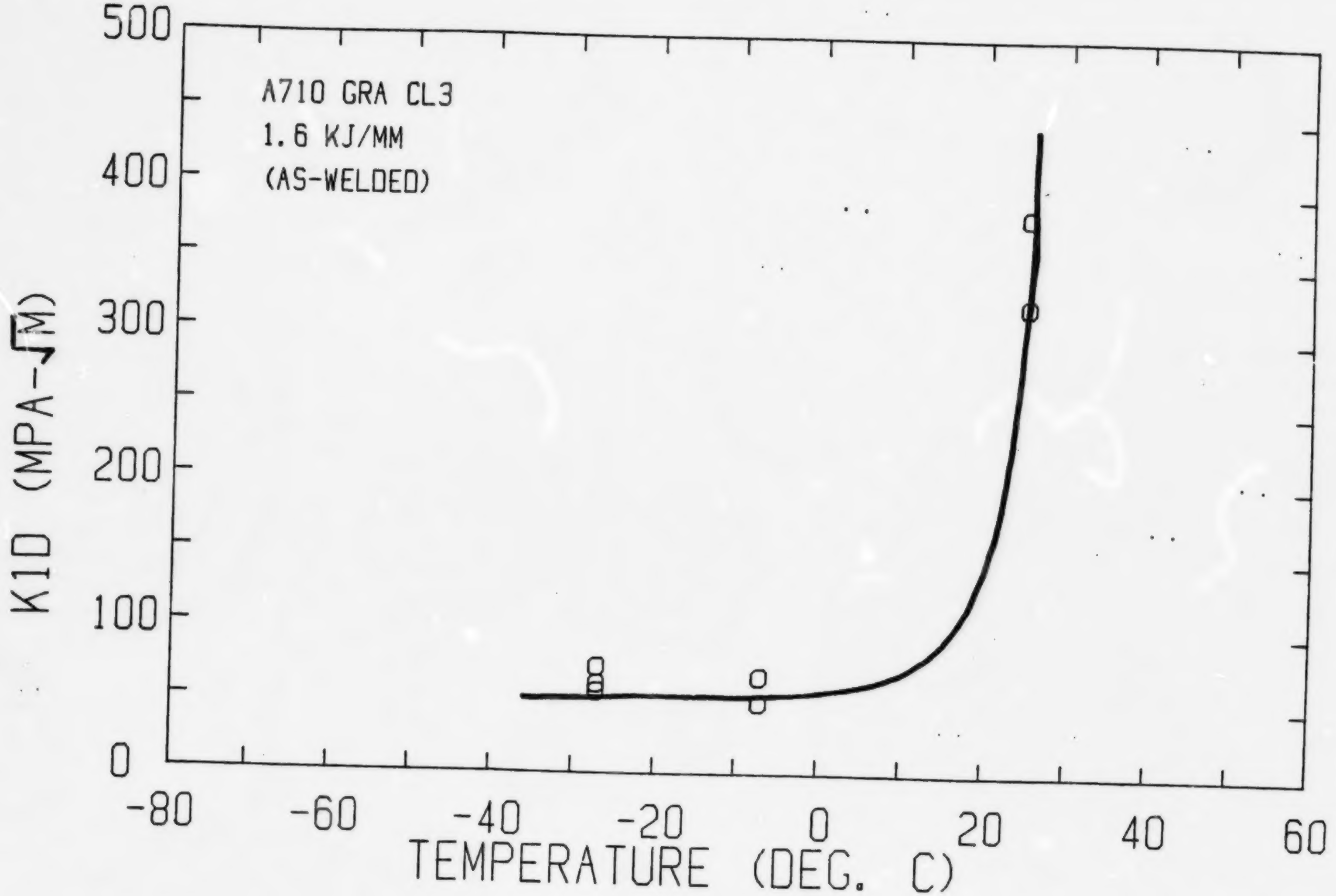

FIGURE C25:Fracture toughness parameter K_{1d} plotted with respect to temperature for A710, Gr. A, Cl. 3, Gleeble cycled to simulate 1.6 kJ/mm in the "as-welded" condition.

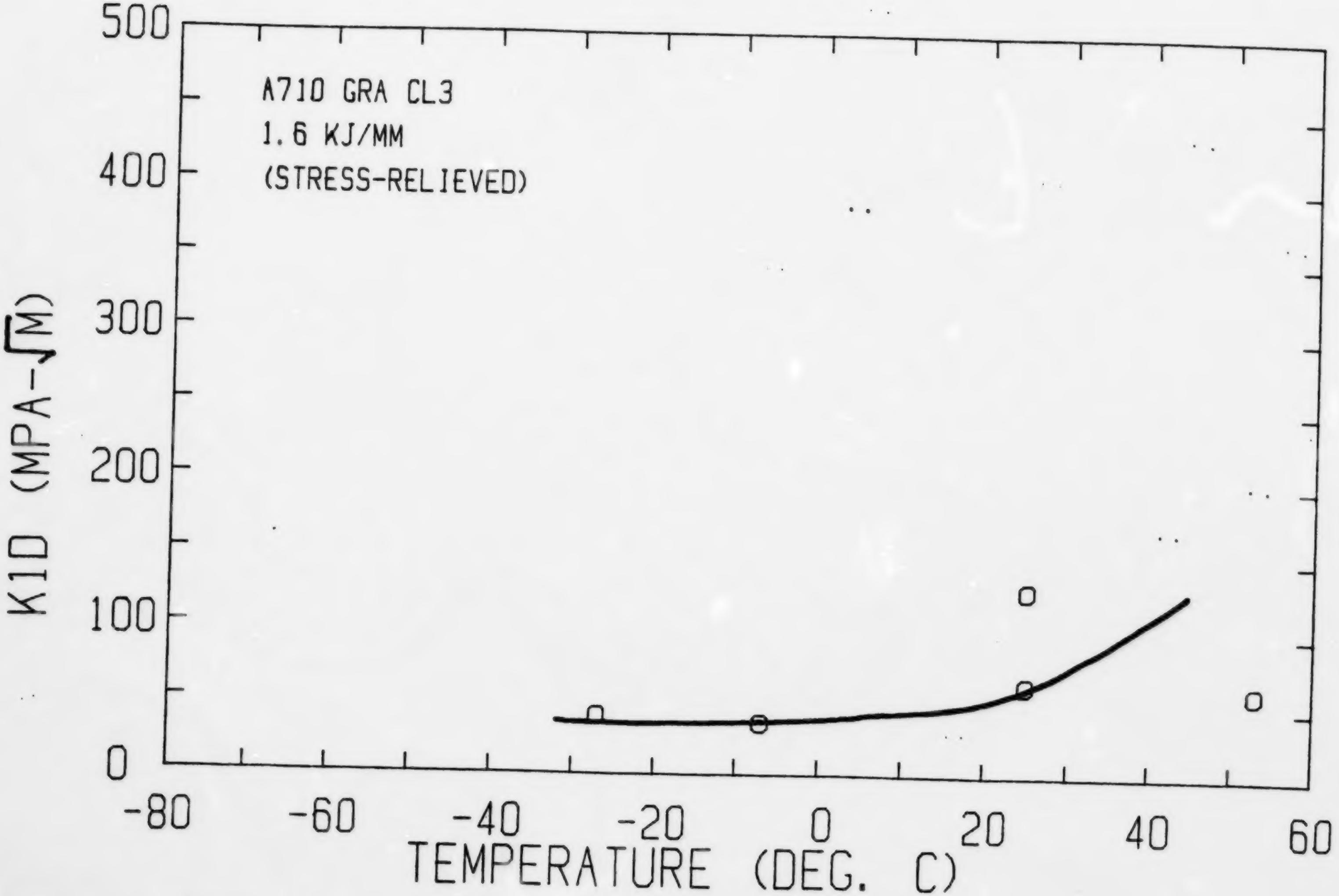

FIGURE C26: Fracture toughness parameter K_{1d} plotted with respect to temperature for A710, Gr. A, Cl. 3, Gleeble cycled to simulate 1.6 kJ/mm in the "stress-relieved" condition.

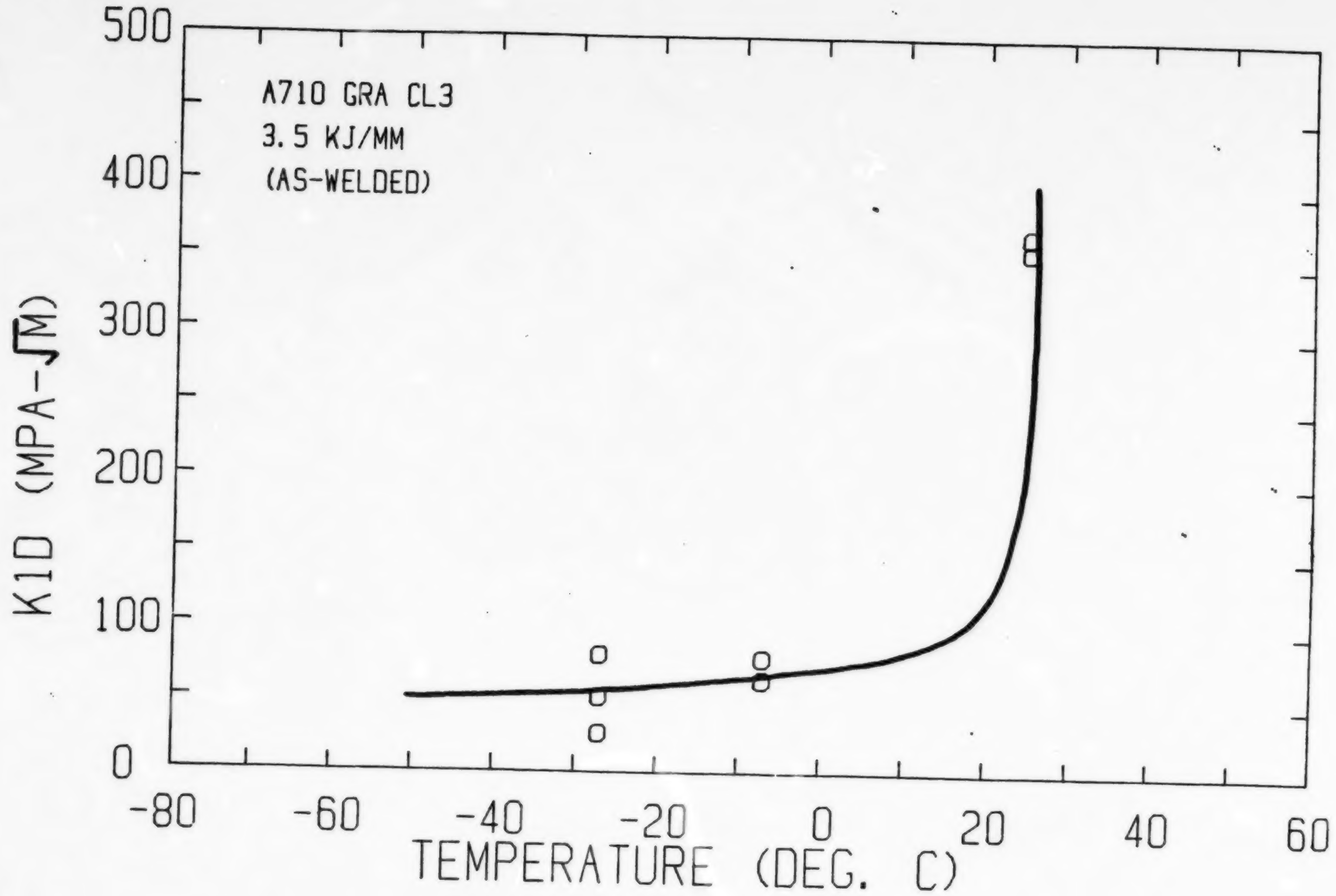

FIGURE C27: Fracture toughness parameter K_{1d} plotted with respect to temperature for A710, Gr.A, Cl3, Gleeble cycled to simulate 3.5 kJ/mm in the "as-welded" condition.

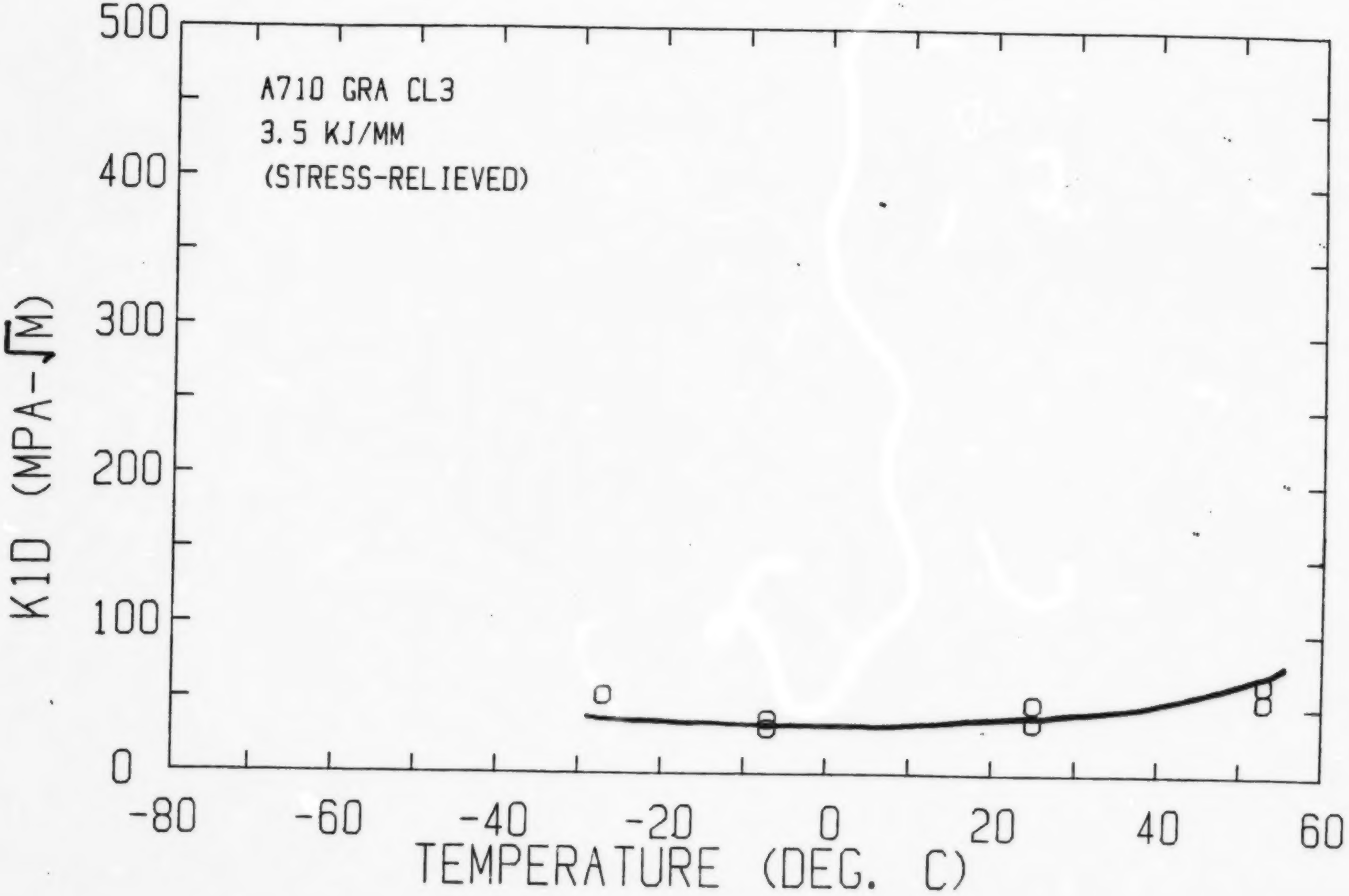

FIGURE C28: Fracture toughness parameter K_{1d} plotted with respect to temperature for A710, Gr. A, Cl. 3, Gleeble cycled to simulate 3.5 kJ/mm in the "stress-relieved" condition.

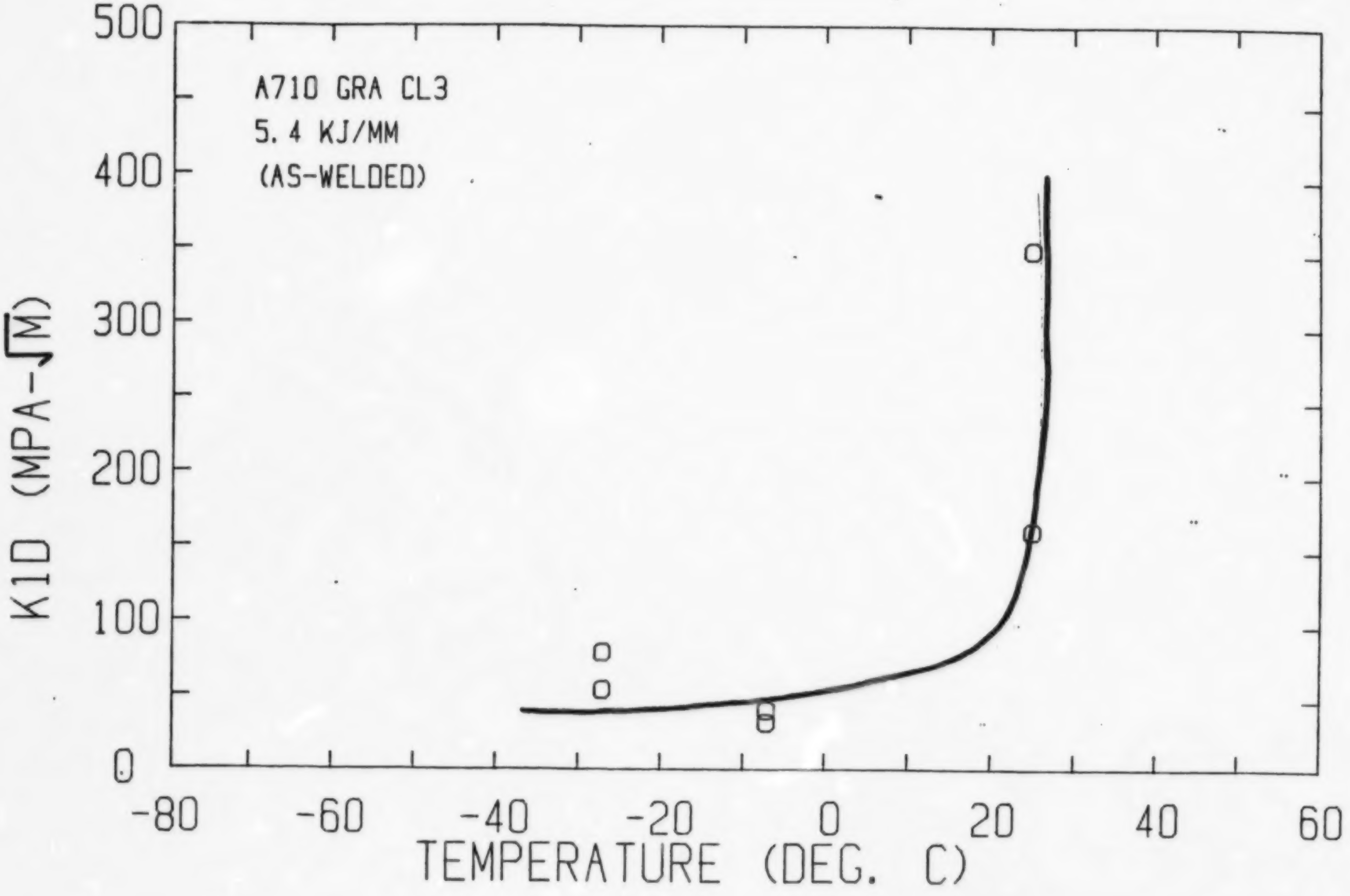

FIGURE C29: Fracture toughness parameter K_{1d} plotted with respect to temperature for A710. Gr. A, Cl. 3, Gleeble cycled to simulate 5.4 kJ/mm in the "as-welded" condition.

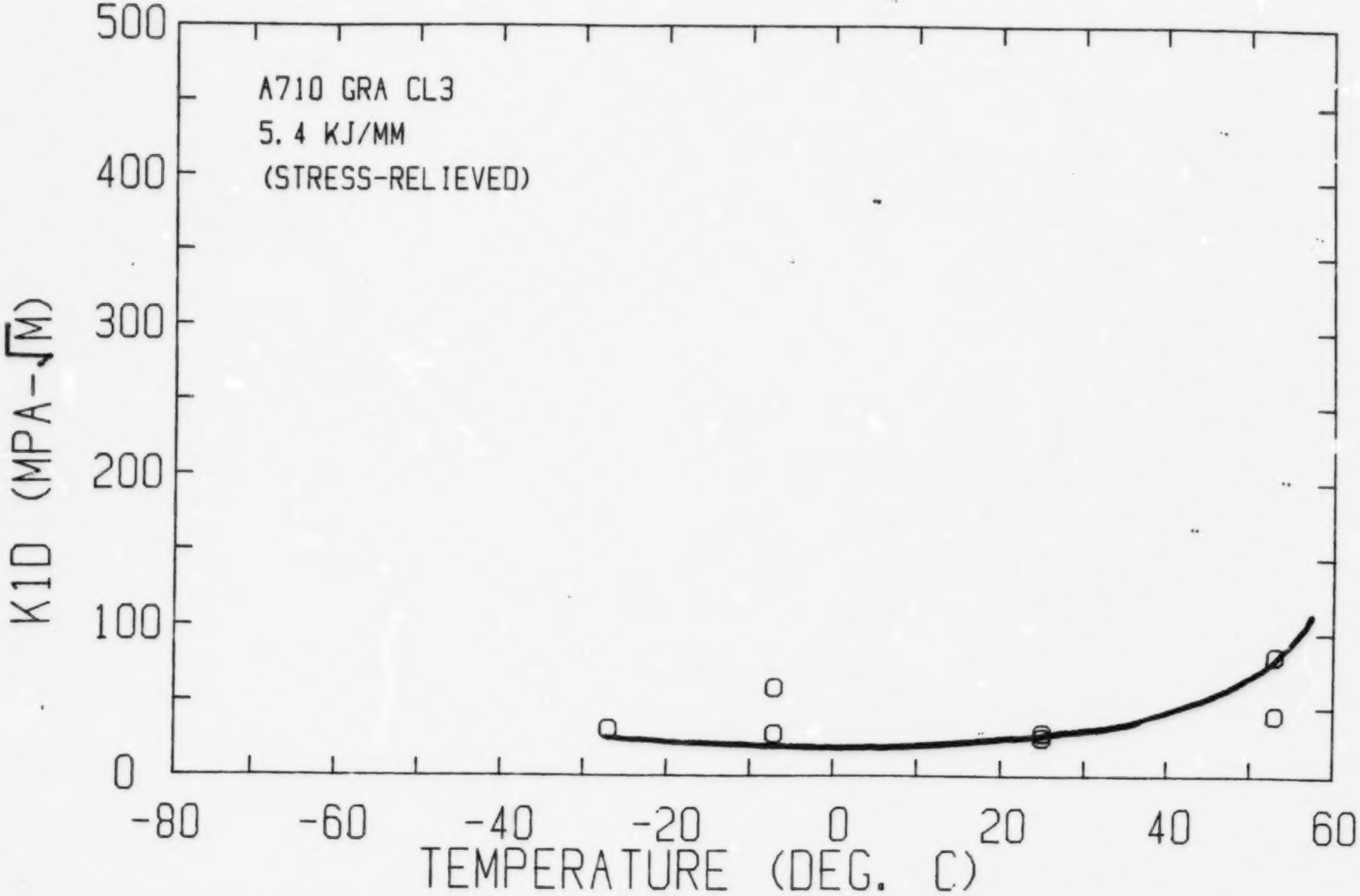

FIGURE C30: Fracture toughness parameter K_{1d} plotted with respect to temperature for A710, Gr. A, Cl 3, Gleeble cycled to simulate 5.4 kJ/mm in the "stress-relieved" condition.

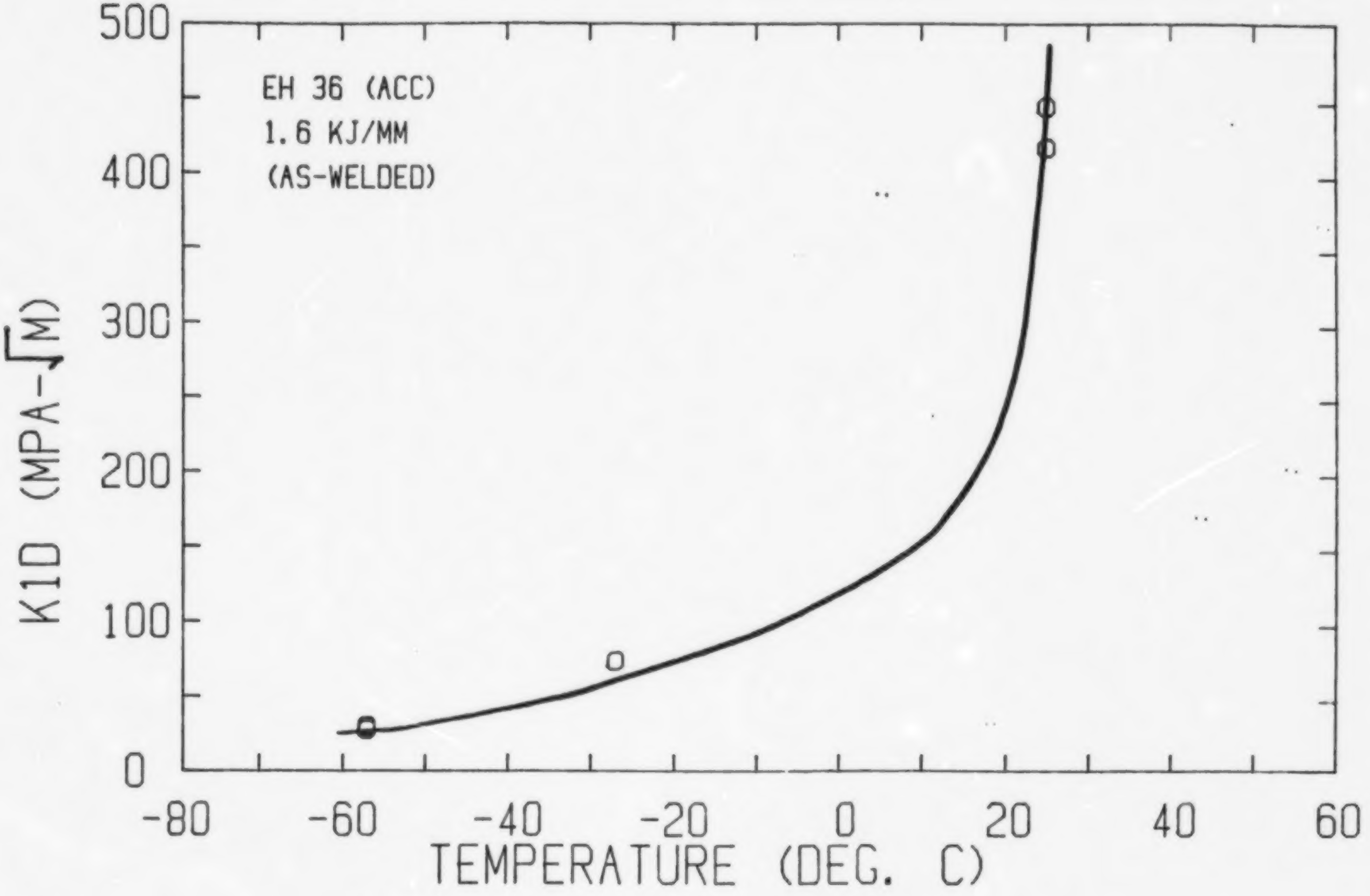

FIGURE C31: Fracture toughness parameter K_{1d} plotted with respect to temperature for EH 36 (ACC), Gleeble cycled to simulate 1.6 kJ/mm in the "as-welded" condition.

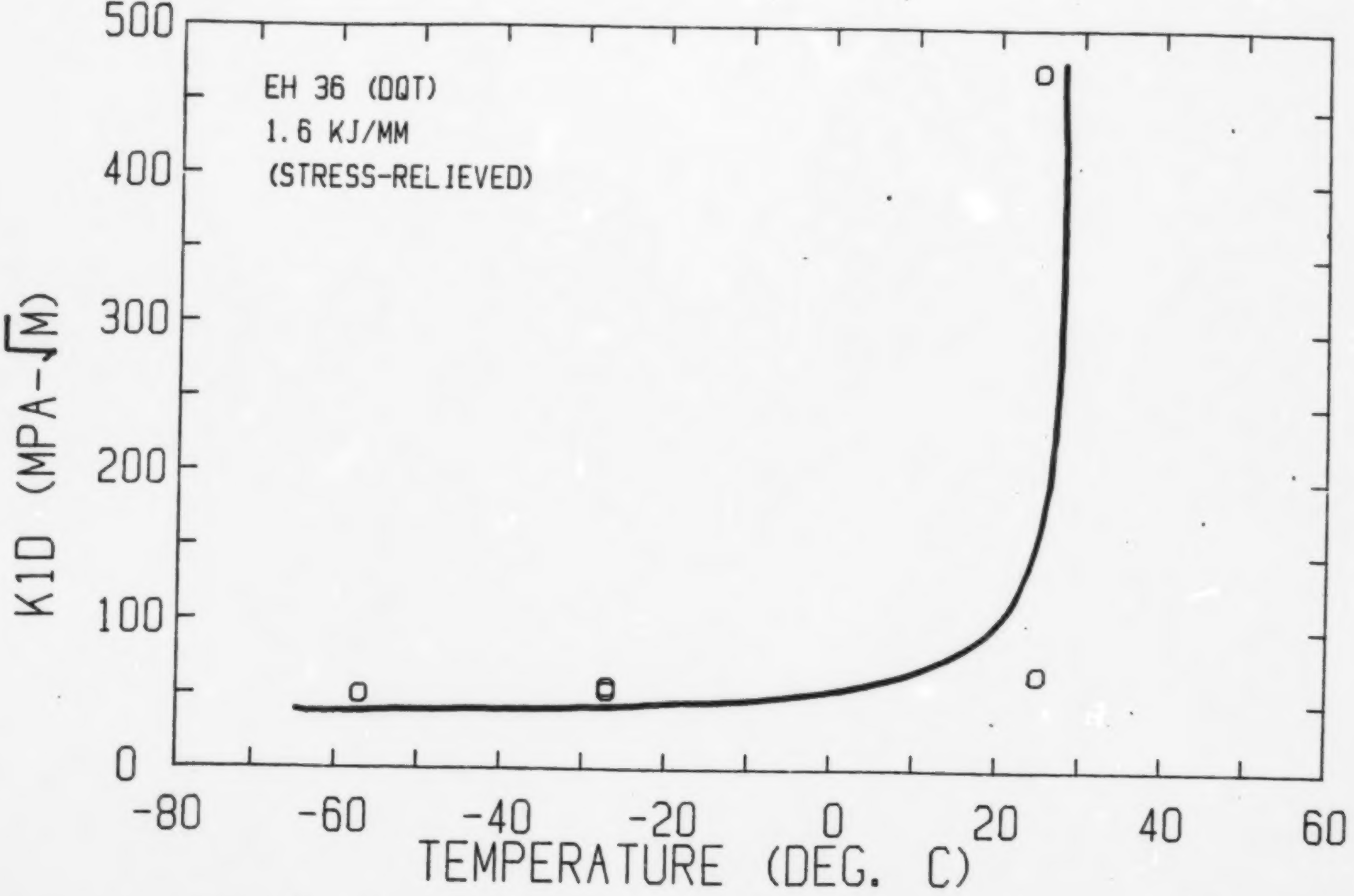

FIGURE C32: Fracture toughness parameter K_{Id} plotted with respect to temperature for EH 36 (DQT), Gleeble cycled to simulate 1.6 kJ/mm in the "stress-relieved" condition.

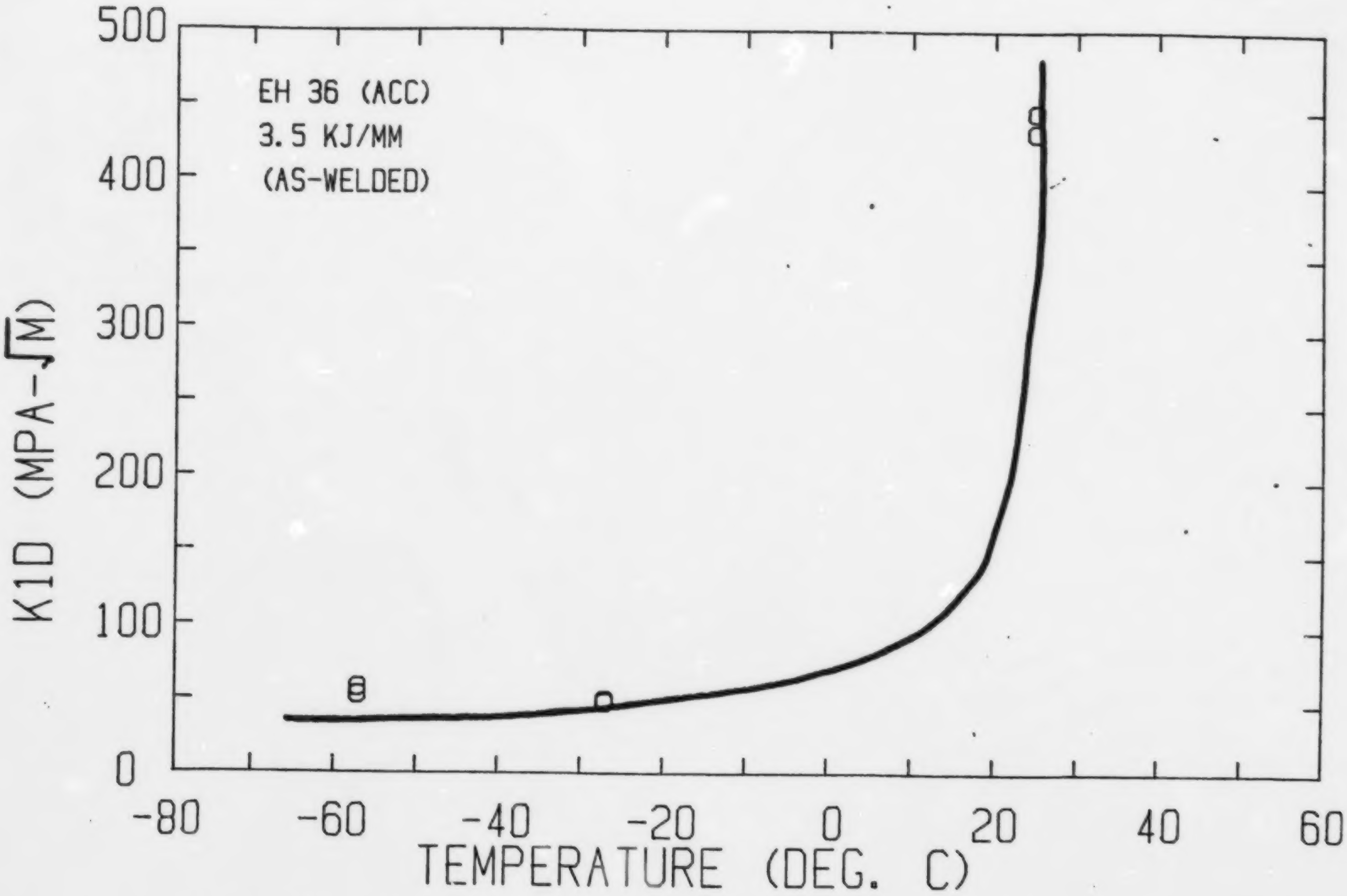

FIGURE C33: Fracture toughness parameter K_{1d} plotted with respect to temperature for MACS (ACC), Gleeble cycled to simulate 3.5 kJ/mm in the "as-welded" condition.

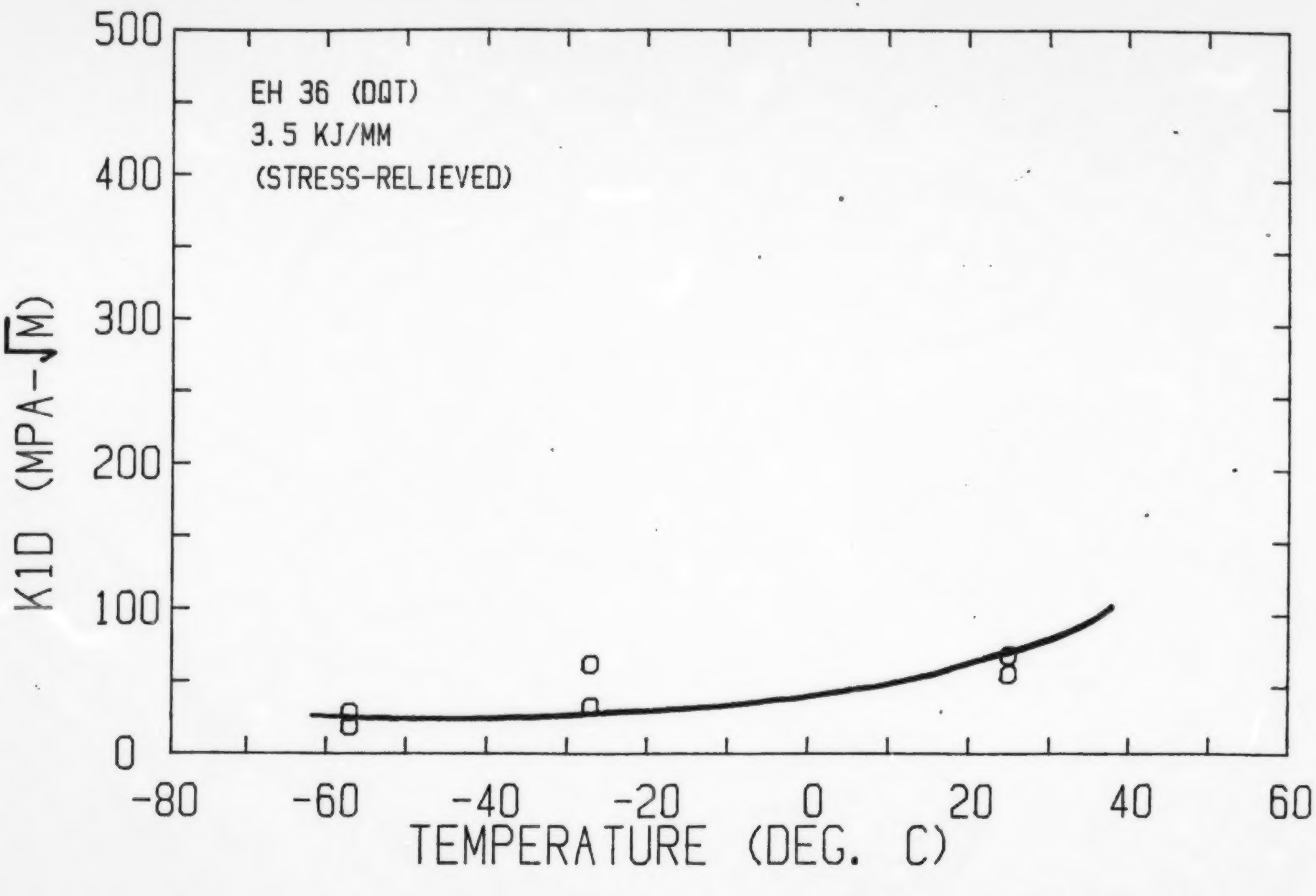

FIGURE C34: Fracture toughness parameter K_{1d} plotted with respect to temperature for MACS (DQT), Gleeble cycled to simulate 3.5 kJ/mm in the "stress-relieved" condition.

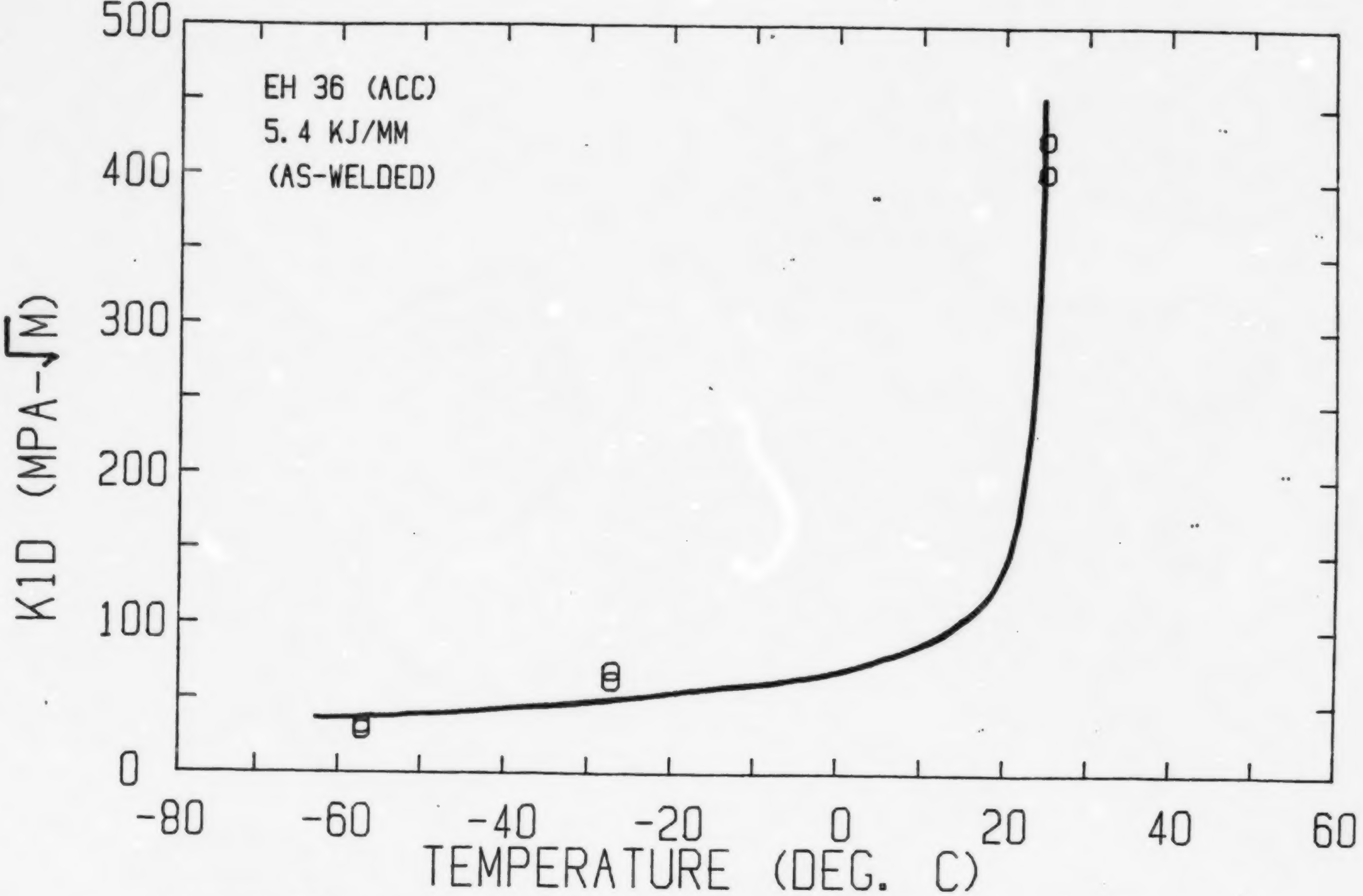

FIGURE C35: Fracture toughness parameter K1d plotted with respect to temperature for MACS (ACC), Gleeble cycled to simulate 5.4 kJ/mm in the "as-welded" condition.

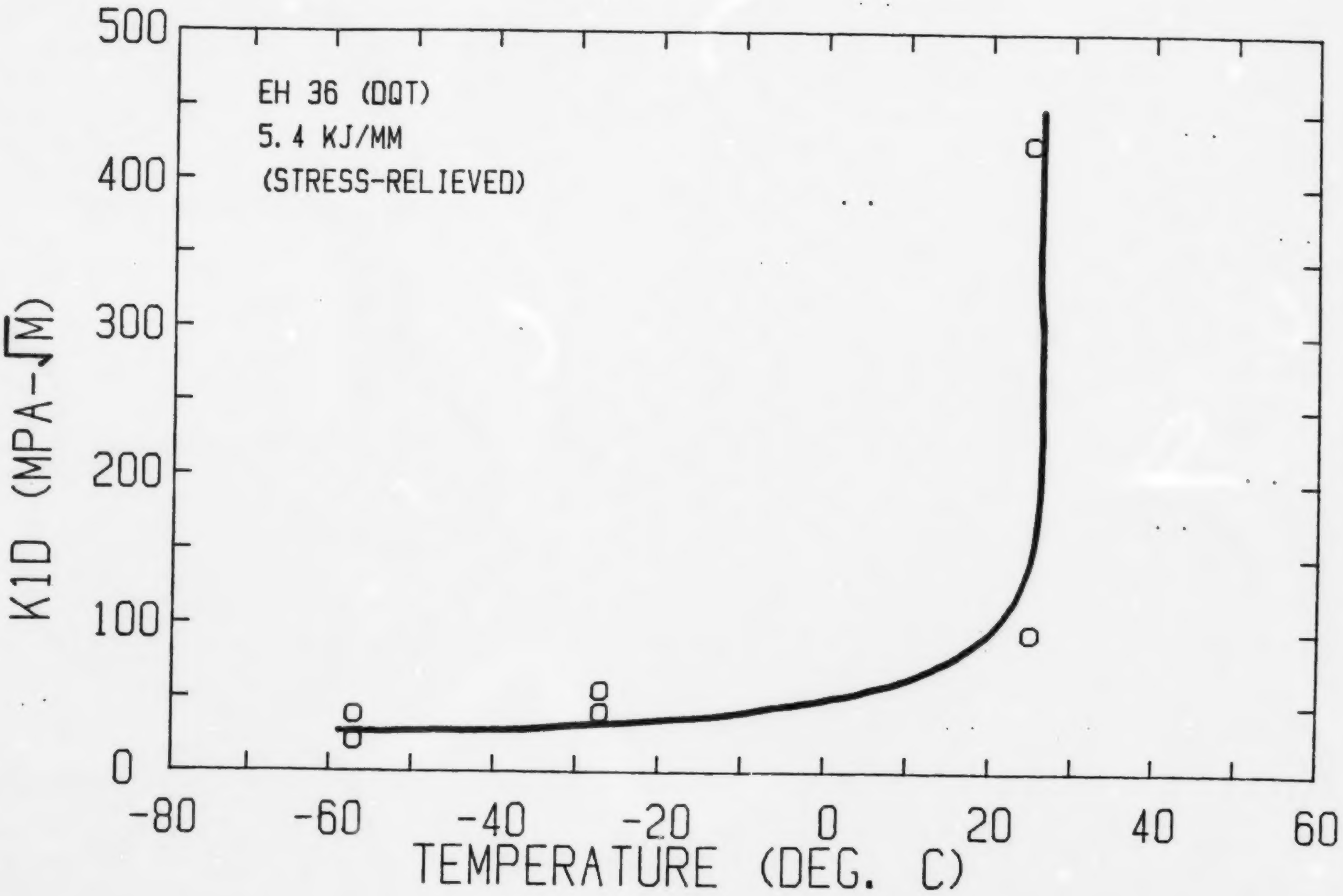

FIGURE C36: Fracture toughness parameter K_{1d} plotted with respect to temperature for MACS (DQT), Gleeble cyclted to simulate 5.4 kJ/mm in the "stress-relieved" condition.

Table C1: CVN Impact Test Data for the CG HAZ, obtained using 3.5 kJ/mm heat input, in LT60 Steel. (1AS = as-welded subsurface; 1AR = as-welded root; 1SS = stress-relieved subsurface; and 1SR = stress-relieved root).

1AS				1AR				1SS (II)				1SR			
Temp. °C	E J	L.E. mm	Shear %	Temp. °C	E J	L.E. mm	Shear %	Temp. °C	E J	L.E. mm	Shear %	Temp. °C	E J	L.E. mm	Shear %
24	148	2.24	NB	24	146	2.16	NB	24	145	2.06	NB	24	148	2.31	NB
24	148	2.36	NB	24	122	1.37	40	0	133	1.57	40				
0	145	1.85	NB	0	96	1.17	20	-10	134	1.52	40	0	152	2.11	80
-10	151	2.16	NB	-10	151	2.06	NB	-20	15	0.46	10	-10	148	1.98	NB
-10	148	2.18	NB	-10	66	0.86	30	-30	148	2.06	NB	-10	145	2.13	NB
-20	149	2.16	NB	-18	127	1.40	30	-40	46	0.58	10	-20	62	0.99	40
-30	146	2.18	NB	-30	54	0.74	10	-50	133	1.65	50	-30	12	0.18	5
-40	145	2.16	NB	-40	71	1.04	20	-60	20	0.33	5	-40	90	1.32	40
-50	27	0.46	20	-50	48	0.66	10	-80	12	0.25	0				
-60	52	0.66	10	-60	16	0.23	5	0	155	2.03	NB	-60	14	0.23	0
-40	151	2.11	NB					-10	152	2.23	NB	-50	11	0.28	0
-60	90	1.14	20	-50	5	0.13	0	-20	145	2.03	NB				
-70	30	0.41	10	-20	46	0.58	10	-30	118	1.48	30	-70	4	0.10	0
-80	29	0.46	10					-30	42	0.53	10				
-70	12	0.18	0					-30	107	1.48	20	-30	87	1.27	20
-80	20	0.25	5					-40	121	1.60	40				
								-40	134	1.88	50				
								-50	16	0.30	10				
								-50	45	0.84	10				

Table C2: CVN Impact Test Data for the CG HAZ, obtained using 5.4 kJ/mm heat input, in LT60 Steel. (2AS = as-welded subsurface; 2AR = as-welded root; 2SS = stress-relieved subsurface; and 2SR = stress-relieved root).

2AS				2AR				2SS				2SR			
Temp. °C	E J	L.E. mm	Shear %	Temp. °C	E J	L.E. mm	Shear %	Temp. °C	E J	L.E. mm	Shear %	Temp. °C	E J	L.E. mm	Shear %
25	142	1.62	50	25	144	2.06	NB	25	148	2.49	NB	25	138	2.34	NB
0	145	2.29	NB	0	133	1.63	30	0	148	2.41	NB	0	151	2.26	NB
-20	31	0.53	10	-20	96	1.30	10	-20	149	2.06	90	-20	132	1.78	70
-30	94	1.25	20	-30	46	0.64	10	-30	137	2.39	NB	-40	123	1.80	70
-40	130	1.75	40	-40	58	0.76	5	-40	29	0.58	30	-60	76	1.19	10
-40	85	1.14	20	-40	37	0.48	0	-40	133	2.11	90	-60	66	1.02	10
-50	18	0.30	0	-50	57	0.74	10	-50	140	2.06	90	-80	77	1.17	10
-60	65	0.91	10	-60	92	1.25	10	-60	41	0.64	5	-60	39	0.66	0
-60	16	0.28	5	-60	20	0.28	0	-60	117	1.91	40	-80	8	0.18	0
-80	16	0.23	0	-80	12	0.15	0	-80	7	0.07	0	-40	92	1.40	40
-40	90	1.14	20	-50	45	0.58	0	-60	18	0.36	0	-20	150	2.24	60
-30	31	0.51	20	-30	22	0.33	5	-50	119	1.91	30	-30	130	1.75	70
0	127	1.42	30	-10	52	0.71	10	-40	19	0.38	10				
-10	129	2.11	NB	-20	100	1.32	20	-30	48	0.79	20				
-10	132	2.21	NB	-20	108	1.37	30	-20	150	2.41	NB				
-20	27	0.46	10					-20	132	1.88	70				
-40	48	0.74	5												

Table C3: CVN Impact Test Data for the CG HAZ, obtained using 5.4 kJ/mm heat input, in A710 Gr. A Cl. 3 Steel. (3AS = as-welded subsurface; 3AR = as-welded root; 3SS = stress-relieved subsurface; and 3SR = stress-relieved root).

3AS				3AR				3SS				3SR			
Temp. °C	E J	L.E. mm	Shear %	Temp. °C	E J	L.E. mm	Shear %	Temp. °C	E J	L.E. mm	Shear %	Temp. °C	E J	L.E. mm	Shear %
25	148	2.34	NB	25	152	2.16	90	25	146	2.46	NB	25	148	2.44	NB
0	148	2.46	NB	0	148	2.29	NB	0	148	2.31	NB	0	145	2.18	NB
0	145	2.44	NB	0	129	1.65	30	-20	148	2.44	NB	-20	87	1.17	30
-20	148	2.41	NB	-20	104	1.40	20	-30	148	2.44	NB	-30	152	2.06	NB
-30	151	2.54	NB	-30	108 41	1.40 0.74	20 10	-40	145	2.34	NB	-40	149	2.31	NB
-30	148	2.08	NB	-30	37	0.64	10	-50	148	2.59	NB	-50	149	2.44	NB
-40	144	2.36	NB	-40	20 146	0.51 2.18	10 NB	-60	148	2.24	NB	-60	149	2.29	NB
-50	146	1.98	50	-50	42 103	0.64 1.35	10 20	-80	39 146	0.66 2.29	10 NB	-80	149 138	2.08 1.91	40 40
-50	149	2.24	NB	-50	20	0.36	10	-100	11 4	0.13 0.13	0 0	-100	10 10	0.28 0.20	0 0
-60	146 149 5	2.46 2.36 0.23	NB NB 10	-60	18 26	0.36 0.51	10 10	-90	42	0.69	0	-90	23	0.41	0
-80	142 94	1.98 1.45	40 20	-80	20	0.38	0								
-100	12	0.25	0	-80	23	0.51	10								
-110	8	0.15	0	-90	84 37	1.27 0.69	20 70								
-70	145	2.29	NB	-100	7 10	0.17 0.18	0 0								
-90	12 39	0.28 0.91	0 0												
-100	20	0.38	0												

Table C4: CVN Impact Test Data for the CG HAZ, obtained using 3.5 kJ/mm heat input, in A710 Gr. A Cl. 3 Steel. (4AS = as-welded subsurface; 4AR = as-welded root; 4SS = stress-relieved subsurface; and 4SR = stress-relieved root).

4AS				4AR				4SS				4SR			
Temp. °C	E J	L.E. mm	Shear %	Temp. °C	E J	L.E. mm	Shear %	Temp. °C	E J	L.E. mm	Shear %	Temp. °C	E J	L.E. mm	Shear %
25	152	2.11	80	25	149	2.46	NB	25	145	2.26	80	25	100	1.45	NB
0	146	2.31	NB	0	149	2.13	NB	0	151	2.13	NB	0	145 22	2.31 0.33	NB NB
0	148	2.26	NB	0	149	2.34	NB	0	151	1.85	NB	0	145	2.29	NB
-20	146	2.24	NB	-20	146	2.54	NB	-20	152	2.16	NB	-20	5 148	0.13 2.39	0 NB
-30	152 92 152	2.31 1.32 2.13	NB 30 NB	-30	77 85	1.14 1.32	20 20	-30	152 114	2.26 1.73	NB 30	-30	46	0.76	20
-30	149	2.49	NB	-30	144	2.36	NB	-30	19	0.38	NB	-30	141	2.08	NB
-40	150	2.24	NB	-40	145	2.29	NB	-40	168 16	2.23 0.30	NB NB	-40	148 31	1.88 0.56	NB NB
-50	152	1.91	80	-50	152	2.11	NB	-50	132	2.16	80	-50	144	2.29	NB
-50	145	2.11	NB	-50	125	1.96	50	-50	79 12	1.14 0.25	10 NB	-50	149	2.29	50
-60	130 148	1.55 1.93	NB 40	-60	81 142	1.30 2.44	20 NB	-60	11 149	0.33 2.29	10 40	-60	81 144	1.14 2.24	20 NB
-80	14 129	0.33 1.71	0 30	-80	50 60	0.86 0.91	20 10	-80	19 152	0.41 1.98	10 30	-80	4 14	0.28 0.28	0 10
-100	37 22	0.64 0.36	0 0	-100	73 8	1.07 0.20	20 0	-100	8 12	0.23 0.25	0 0	-80	10 12	0.41 0.20	0 0
-110	7	0.20	0	-110	7	0.30	0	-110	5	0.13	0	-90	5	0.15	0
-90	22	0.43	0	-70	107	1.52	20	-90	5	0.25	0	-70	4	0.18	0
				-90	7 14	0.33 0.30	0 10								

Table C5: CVN Impact Test Data for the CG HAZ, obtained using 1.6 kJ/mm heat input, in A 710 Gr. A Cl. 3 Steel. (5AS = as-welded subsurface; 5AR = as-welded root; 5SS = stress-relieved subsurface; and 5SR = stress-relieved root).

5AS				5AR				5SS				5SR			
Temp. °C	E J	L.E. mm	Shear %	Temp. °C	E J	L.E. mm	Shear %	Temp. °C	E J	L.E. mm	Shear %	Temp. °C	E J	L.E. mm	Shear %
25	149	2.39	NB	25	145	1.96	40	25				25			
0	148	1.93	80	0	155	2.01	NB	0	145	2.31	NB	0	146	2.39	NB
-20	133	1.88	30	-20	151	2.29	40	-20	65	1.14	80	-20	133	2.34	NB
	96	1.45	50		148	1.98	90		153	2.34	NB				
-30	149	2.39	NB	-30	99	1.42	NB	-30	58	1.24	20	-30	146	2.31	NB
	148	2.49	NB		152	2.03	NB		149	1.80	40		148	2.31	NB
-30				-30	151	2.03	40	-30				-30			
-40	145	2.36	NB	-40	132	1.88	30	-40	144	2.31	NB	-40	144	1.96	40
	102	1.40	20		145	1.80	40								
-50	145	2.36	NB	-50	148	1.96	30	-50	71	1.14	20	-50	144	2.36	NB
	104	1.45	30		151	2.16	NB		41	0.76	20		152	2.26	NB
-50	83	1.27	20	-50				-50	30	0.56	10	-50			
-60	148	2.39	NB	-60	151	2.24	NB	-60	114	1.63	20	-60	7	0.33	10
	161	2.46	NB		149	1.37	40		15	0.46	10		56	1.02	10
	18	0.36	10												
-80	14	0.33	10	-80	60	1.04	30	-60	152	2.23	NB	-80	30	0.53	0
	39	0.64	10		95	1.32	30								
-90	29	0.53	10	-90	43	0.84	20	-80	50	0.81	20	-60	149	2.29	NB
	8	0.28	0		34	0.56	10								
-100	14	0.30	10	-100	103	1.50	40	-90	38	0.69	0	-70	80	1.30	20
	29	0.48	10		27	0.46	10						16	0.30	10
					98	1.45	20								
-110	11	0.30	0	-110	19	0.38	20	-100	14	0.36	10	-100	18	0.33	0
					24	0.51	0		8	0.23	0				
-120	41	0.30	10	-120	10	0.23	0					-110	11	0.23	0
					34	0.64	20								
-70	22	0.43	10									-120	10	0.61	0
	50	0.84	20												

Table C6: CVN Impact Test Data for the CG HAZ, obtained using 5.4 kJ/mm heat input, in MACS (ACC) Steel (6AS = as-welded subsurface; 6AR = as-welded root) and MACS (DQT) Steels (6SS = stress-relieved subsurface; and 6SR = stress-relieved root).

6AS				6AR				6SS				6SR			
Temp. °C	E J	L.E. mm	Shear %	Temp. °C	E J	L.E. mm	Shear %	Temp. °C	E J	L.E. mm	Shear %	Temp. °C	E J	L.E. mm	Shear %
25	144	2.64	NB	25	160	2.57	NB	25	148	2.62	NB	25	136	2.54	NB
0	137	2.67	NB	0	151	2.67	NB	0	146	2.59	NB	0	146	2.59	NB
	148	2.49	NB		146	2.64	NB	-20	99	1.40	20	-20	146	2.54	NB
-20	146	2.62	NB	-20	146	2.62	NB		148	2.54	NB		142	2.51	NB
-30	144	2.54	NB		146	2.54	NB	-30	144	2.59	NB	-30	84	1.55	20
	145	2.52	NB	-30	153	2.67	NB	-30	146	2.57	NB		148	2.59	NB
-30					152	2.54	NB	-40	149	2.59	NB	-30	146	2.49	NB
-40	152	2.59	NB	-30					152	2.26	NB	-40	149	2.59	NB
	145	2.44	NB	-40	149	2.46	NB	-50	148	2.54	NB		146	2.49	NB
-50	152	2.64	NB		145	2.57	NB		152	2.64	NB	-50	140	2.59	NB
	151	2.54	NB	-50	14	0.33	10	-60	146	2.56	NB		145	2.49	NB
-60	149	2.62	NB		76	1.22	20	-60	152	2.59	NB	-60	149	2.36	NB
	153	2.87	NB	-60	7	0.25	10	-80	149	2.56	NB	-60	152	2.49	NB
-60					14	0.28	10		140	2.57	NB	-80	145	2.49	NB
-80	149	2.49	NB	-60	14	0.28	10	-90	144	2.49	40		20	0.48	10
	141	2.54	NB	-80	5	0.13	0		148	2.31	40		20	0.43	10
-90	10	0.25	10		5	0.15	0	-100	19	0.41	0	-90	46	0.84	10
	14	0.30	10	-50	149	2.69	NB		10	0.23	0		24	0.58	0
-100	7	0.15	0	-90	4	0.28	0		58	1.02	10	-100	24	0.48	10
	10	0.33	10		10	0.23	0	-20	146	2.62	NB		10	0.36	0
				-70	111	1.93	30	-110	26	0.48	10	-70	138	2.57	NB
					11	0.33	0		18	0.33	0		54	0.99	10
								-120	4	0.23	0	-110	8	0.30	0
									5	0.18	0		5	0.18	0

Table C7: CVN Impact Test Data for the subsurface CG HAZ (IASI), weld metal (IAW) and the intercritical region of HAZ (IAI II), obtained using 3.5 kJ/mm heat input, in LT 60 steel (as-welded condition).

IAS (II)				IAW Subsurface				IAI (II) Subsurface							
Temp. °C	E J	L.E. mm	Shear %	Temp. °C	E J	L.E. mm	Shear %	Temp. °C	E J	L.E. mm	Shear %	Temp. °C	E J	L.E. mm	Shear %
25	159	2.13	NB	0	156	2.06	NB	0	156	1.96	70				
0	153	2.13	NB	-20	153	2.06	85	-20	155	2.11	50				
-20	152	1.98	NB	-40	137	1.91	50	-40	126	1.63	20				
-20	146	1.63	70	-60	111	1.50	35	-60	103	1.57	15				
-40	41	0.41	30	-80	30	0.38	10	-80	99	1.45	30				
-40	151	2.08	NB												
-60	153	1.68	NB												
-60	84	1.09	30												
-60	91	1.27	40												
-80	14	0.23	5												
-80	18	0.33	15												

TABLE C8: INSTRUMENTED IMPACT RESULTS

Identification		Test Temp. (0°C)	Dial Energy (J)	Integrative Energy (J)			KId Fracture Toughness (MPa $\sqrt{m}$)
				Initiation	Propagation	Total	
Lloyds LT60							
1.6AW	10A	RT	15	.39	14.93	15.32	75.8
	11A	RT	11	1.11	9.53	10.64	102.4
	12A	-10				5.95	75.7
	13A	-10				4.41	71.5
	14A	-30	3	.43	2.89	3.32	65.3
	15A	-30	5	.44	4.24	4.68	64.3
	47A	+50		.16	36.88	37.04	216.0
	46A	+50		1.23	30.08	31.31	55.5
3.5AW	25A	RT	15	1.00	13.91	14.91	86.7
	26A	RT	15	.42	13.76	14.18	83.5
	27A	-10				7.05	72.7
	29A	-30	3	.15	2.98	3.13	29.6
	30A	-30	2	.47	1.50	1.97	70.8
	48A	+50		1.06	21.73	22.79	72.5
	49A	+50		1.86	25.42	27.28	308.4
5.4AW	41A	RT		1.13	16.01	17.14	100.2
	42A	RT		.37	15.48	15.85	78.5
	43A	-10		7.1	.66	7.76	60.5
	44A	-10		.65	4.24	4.89	63.3
	45A	-30	3	.45	2.87	3.32	62.9
	46A	-30	3	.38	2.14	2.52	65.3
	50A	+50		.63	34.28	34.91	300.9
	51A	+50		.59	23.22	23.81	295.8
1.6SR	10S	RT		.35	.98	1.33	
	11S	RT		.25	.98	1.23	
	12S	-10				1.75	54.5
	13S	-10		.92	.31	1.23	87.5
	14S	-30		.89	.34	1.23	82.7
	15S	-30		.39	.30	.69	55.0
	46S	+50		.63	9.89	10.52	32.6
	47S	+50		.59	9.75	10.34	55.4
3.5SR	24S	RT		.33	3.48	3.81	48.8
	25S	RT		.36	4.28	4.64	45.8
	26S	-10				1.33	56.8
	27S	-10		.89	.37	1.26	52.8
	28S	-30		.15	.53	.68	47.4
	29S	-30		.09	.56	.65	43.0
	48S	+50		.61	9.32	9.93	43.5
	49S	+50		.12	8.60	8.72	45.0

INSTRUMENTED IMPACT RESULTS

(Table C8 Cont'd)

Identification	Test Temp. (0°C)	Dial Energy (J)	Integrative Energy (J) Initiation	Integrative Energy (J) Propagation	Integrative Energy (J) Total	Kld Fracture Toughness (MPa $\sqrt{m}$)
Lloyds LT60						
5.4SR 37S	RT		.43	3.90	4.33	
38S	RT		.35	5.10	5.45	
39S	RT		.37	3.29	3.66	51.1
40S	RT		.36	5.14	5.50	55.4
41S	-10				1.79	51.0
42S	-10		.37	.95	1.32	54.9
43S	-30		.10	.61	.71	47.0
44S	-30		.10	.52	.62	50.6
50S	+50		.63	13.08	13.71	13.1
51S	+50		.56	8.88	9.44	42.4
A710 GRA C13						
1.6AW 10A7	RT		14.25	37.25	51.50	365.0
11A7	RT	54	9.1	49.99	51.09	304.1
12A7	-30		.59	7.29	7.88	45.9
13A7	-30	7	.77	5.96	6.73	40.9
14A7	-30	10	.41	9.29	9.70	57.6
15A7	-10	13	.48	12.79	13.27	33.7
16A7	-10	18	.41	16.04	16.45	51.3
3.5AW 26A7	RT	62	14.54	45.82	60.36	351.0
27A7	RT	63	1.37	62.68	64.05	340.7
28A7	-30	8	.47	6.04	6.51	64.9
29A7	-30	5	.71	4.49	5.20	11.9
30A7	-10	10	.79	10.38	11.17	48.4
31A7	-10	26	.43	25.07	25.50	63.2
32A7	-30		.66	6.85	7.51	36.5
5.4AW 42A7	RT	34	1.09	32.41	33.50	334.9
43A7	RT	32	1.11	31.41	32.52	145.5
44A7	-30	5	.44	4.37	4.81	
45A7	-30	6	.65	3.09	3.74	64.1
46A7	-30	19	.48	5.47	5.95	39.2
47A7	-10	19	.60	17.60	18.20	17.3
48A7	-10	9	.41	7.84	8.25	25.8
1.6SR 11S7	RT	8	.59	7.71	8.30	47.7
12S7	RT	15	1.06	12.77	13.83	111.4
13S7	-30	2	.47	.89	1.4	25.1
14S7	RT	8	.95	.34	1.29	
15S7	+50	12	.18	11.30	11.48	44.1
16S7	-10	4	.37	3.87	4.24	20.7

INSTRUMENTED IMPACT RESULTS

(Table C8 Cont'd)

Identification		Test Temp. (0°C)	Dial Energy (J)	Integrative Energy (J)			Kld Fracture Toughness (MPa m)
				Initiation	Propagation	Total	
A710 Gr A, C13							
3.5SR	26S7	RT	6	.65	4.88	5.53	33.2
	27S7	RT	8	.30	7.37	7.67	20.7
	28S7	-30	3	.38	.60	.98	38.0
	29S7	+50	8	.11	6.25	6.36	36.2
	30S7	+50	11	.15	9.98	10.13	47.8
	31S7	-10	4	.43	1.66	2.09	16.1
	32S7	-10	2	.38	1.77	2.15	22.3
5.4SR	42S7	-10	3	.35	2.25	2.60	44.2
	43S7	-10	2	.41	.92	1.33	13.6
	44S7	+50	14	.95	9.94	10.89	66.7
	45S7	-30	2	.40	.63	1.03	16.9
	46S7	+50	16	.14	13.64	13.78	27.1
	47S7	RT	9	.58	7.56	8.14	14.5
	48S7	RT	10			7.95	11.4
MACS (ACC)							
1.6AW	10AJ	RT	66	.57	61.15	61.72	
	11AJ	RT	110	16	90.68	106.68	430.1
	12AJ	RT	122	1.19	117.20	118.29	402.6
	13AJ	-60	7	.51	4.81	5.32	13.3
	14AJ	-60	4	.82	3.17	3.99	15.7
	15AJ	-30	9	1.33	.61	1.94	59.3
3.5AW	25AJ	-30	20	.64	17.61	18.25	33.3
	26AJ	RT	120	21.38	93.46	114.84	417.3
	27AJ	RT	117	18.95	93.64	112.59	431.0
	28AJ	-60	4	.45	3.05	3.50	43.0
	29AJ	-60		.39	3.04	3.43	38.1
	30AJ	-30		.82	8.82	9.64	35.0
5.4AW	40AJ	RT	12	15.96	92.08	108.04	387.8
	41AJ	RT	114	18.07	91.26	109.33	409.9
	42AJ	-60	3	.38	2.67	3.05	17.7
	43AJ	-60	3	.46	1.44	1.90	14.3
	44AJ	-30		.57	17.94	18.51	54.0
	45AJ	-30	10	.79	8.82	9.61	47.2
MACS (DQT)							
1.6SR	7SJ	RT	47	1.16	41.91	43.07	50.7
	10SJ	RT	14	113.50	88.30	110.72	456.9
	11SJ	-60	2	.44	1.11	1.55	
	12SJ	-60	4	.40	3.30	3.70	35.5
	13SJ	-30	12	.54	9.85	10.39	40.9
	14SJ	-30	9	.22	7.68	7.90	38.1

(Table C8 Cont'd)

INSTRUMENTED IMPACT RESULTS

Identification		Test Temp. (0°C)	Dial Energy (J)	Integrative Energy (J)			K1d Fracture Toughness (MPa m)
				Initiation	Propagation	Total	
3.5SR	22SJ	RT	44	.59	38.22	38.81	40.6
	25SJ	RT	36	.99	30.98	31.97	53.6
	26SJ	-60	3	.36	.47	.83	14.2
	27SJ	-30	13	.38	10.34	10.72	47.4
	28SJ	-60	3	.41	1.14	1.55	4.2
	29SJ	-30	9	.48	6.57	7.05	18.3
5.4SR	37SJ	RT	59	.99	54.90	55.89	80.0
	40SJ	RT	48	1.46	45.02	46.48	410.4
	41SJ	-60	3	.31	.90	1.21	24.0
	42SJ	-60	2	.31	1.95	2.26	6.3
	43SJ	-30	6	.44	4.75	5.19	40.5
	44SJ	-30	19	.38	9.52	9.90	25.9

Research & Technology Centre

[redacted]

REPORT NO.: 7-184-071-099/F CLASS 4

TITLE: Evaluation of Heat Affected Zone and Weld Metal Toughness in Selected Steels - Phase 1 (Volume 2 of 2)

CLIENT: Department of Supply and Services

Final Report Submitted to the Department of Supply and Services on completion of the 50/50 Cost Shared Program.

D.S.S. File No.: 23SQ.23440-4-9056
Serial No.: 0SQ84-00032

MICROMEDIA

AMCA INTERNATIONAL LIMITED
Research and Technology Centre
August 1986

29pp

WELDING INSTITUTE OF CANADA
INSTITUT DE SOUDAGE DU CANADA
HEAD OFFICE: 391 Burnhamthorpe Road East, Oakville, Ont. L6J 6C9 - Ph:(416) 845-9881

WIDE PLATE TESTING OF THE HEAT AFFECTED ZONE OF LT60 AND A710 PLATE MATERIAL

Report to:
AMCA International
By:
Welding Institute of Canada Report
RC265/86

Approved by:

Dr. A. G. Glover,
Director of Technology

September 1986

TABLE OF CONTENTS

Page

1.0 Introduction 1
2.0 Background 1
3.0 Background of Wide Plate Tests 3
4.0 Experimental Program 5
5.0 Wide Plate Tests 6
  5.1 Test 1 7
  5.2 Test 2 8
  5.3 Test 3 8
  5.4 Test 4 9
6.0 Analysis 9
7.0 Summary 10
8.0 References 11
9.0 Acknowledgements 12

LIST OF TABLES

1. Properties of Algoma LT60 Steel 13
2. Properties of ASTM A710 GrA Cl 2 Steel 14
3. Defect Lengths for Test Program 15
4. Temperature Distribution 15
5. Analysis of Results 16

LIST OF ILLUSTRATIONS

Page

1. Wide Plate Test Facility. 17

2. Etched end of test plate W1 and proposed location of HAZ defect. 18

3. Etched end of test plate W2 and proposed location of HAZ defect. 18

4. Etched end of test plate W3 and proposed location of HAZ defect. 19

5. Etched end of test plate W4 and proposed location of HAZ defect. 19

6. Through-thickness defect inserted in test plate W1. 20

7. Line-up frame being used in electroslag welding test plate into end lugs. 20

8. Typical instrumentation on one side of the plate. 21

9. Cool box in place prior to final location of the test pistons. 21

10. Comparison of the strain developing in the weld and the HAZ for test 1, plate W3, stress relieved A710. 22

11. CMOD output of test 2, plate W4, A710 as welded, showing onset of tearing. 23

12. Section through crack tip of test 2, plate W4, showing void formation and initiation of tearing on 45° shear plane. 23

13. Strain build up in the HAZ ahead of the crack tip for test 3, plate W1 LT60, stress relieved. 24

14. Linear strain relationship with loading in the base plate, test 3, plate W1 LT60 stress relieved. 24

15. Strain developed in the HAZ of test 4, plate W2, LT 60 as welded. 25

WIDE PLATE TESTING OF THE HEAT AFFECTED ZONE OF LT60 AND A710 PLATE MATERIAL

Report to:
AMCA International
By
Welding Institute of Canada RC265/86

1.0 Introduction

As part of the energy cost shared program for DSS/PMRL, AMCA International have been evaluating the heat affected zone toughness of two steels as a function of weld heat input and post weld heat treatment. The majority of this work had been to evaluate small scale CTOD toughness, however the last phase involved testing of four wide plate specimens. This latter part of the program was subcontracted to the Welding Institute of Canada and this report analyzes the results obtained from the four tests.

2.0 Background

The need to assess the risk of fracture at low temperatures is essential in view of forthcoming requirements for Canadian frontier oil and gas development. In these regions the severe environmental conditions will necessitate thick section weldments in a range of structures and support vessels. For such components, it will be necessary to review those aspects which determine the fracture risk, i.e. material properties and toughness, stress levels and defect sizes, and the relation of these to codes and standards. The structures and vessels to which the wide plate test results will apply are subjected to both static, intermediate and dynamic loading. Potentially a large number of service fractures could result from static loading and hence the slow strain rate capabilities of the wide plate test will permit investigation of this failure mode.

Traditionally, workmanship standards relating to the defect acceptance levels in welds used in fabrication, are not based on the engineering significance of defects, but rather are historical and simply reflect what is reasonably achievable with the welding process used. Tests such as the Charpy V-notch and drop weight tests have been used for many years as a measure of toughness acceptance criteria. However these do not adequately include actual stress distributions around the defect and the effect of local brittle zones in weldments. Although the acceptance levels derived from these tests provide a given standard of quality, they do not provide any quantitative information on the actual failure risk. In the event that the workmanship standards are not achieved or where there is damage during service or the growth of weld defects due to corrosion or fatigue, decisions to repair, or not, must be based on an engineering assessment of the significance of the damage or weld defect. The study of fracture mechanics has allowed a methodology for this assessment to be developed in the United Kingdom which has been formally documented. The fracture mechanics tests used in the assessment have been indexed to full scale tests on welded plates and the design curve used is considered to be conservative [1].

A similar approach has been taken in Canada for the evaluation of defects in pipeline girth welds. CSA Standards have recently been amended to allow the use of an engineering critical assessment for defects that exceed workmanship standards, and to consider it as a design approach. As part of this work the Welding Institute of Canada undertook full scale tests on large diameter pipes in which girth welds containing known defects were subjected to stress by bending of a 12.2 m length of pipe. The results were compared with small laboratory fracture mechanics tests on various regions of the weld to establish the degree of conservatism in the existing proposed design curves, to determine how residual stress might be included and to determine the effects of the shape of the defect. In some cases it was found that the design curve was overly conservative and it is believed that modification of the proposed methodology is warranted, [2, 3, and 4].

To date, no full scale tests on welded plates of the type considered for marine vessel or fixed structures application in the Arctic have been carried out in Canada. It is considered that such tests are essential to provide a proper data base for the development of fabrication standards, weldment material toughness requirements and of particular importance is the defect tolerance in welded plates in the thickness range 50-75 mm. In marine vessel construction such welds would not be stress relieved whereas in pressure vessel applications plates of such thickness would normally be stress relieved. It is known that thermal stress relief has a significant effect on the risk of fracture both by changes in weldment properties and by lowering residual stresses [5]. In many other critical structures, (e.g. North Sea structures) plates thicker than about 40 mm are often required to be thermally stress relieved. An Arctic vessel, therefore, with thicker section welded plates in the as welded condition, represents a unique situation.

One approach to the study of fracture behaviour of heavy section plate weldments for offshore applications is to carry out wide plate tests. While development and experience elsewhere in the world, ie. the North Sea, have provided a good basis for design and construction the particular features of the Canadian offshore, lower temperatures, ice loads, icebergs and storm frequencies need special attention. The results of wide plate testing of Arctic grade steels will be compared to small scale fracture mechanics tests (such as CTOD tests) as in previous work with a view to obtaining empirical relationships [6]. These test results will be invaluable in the ongoing development of fracture control plans for the Canadian offshore platforms, icebreaking LNG and crude carriers.

3.0 Background of Wide Plate Tests

The concept of wide plate tests has been in existence for some 30 years and evolved principally as a result of ship fracture problems in World War II. However, due to the expense and time required to conduct such studies the number of investigations pursued was relatively small and hence limited data is available. Small scale fracture tests have enabled a more convenient study of fracture initiation, propagation, and arrest, but they are limited in their ability to study the effects of residual strain fields. Previous studies of brittle fracture propagation in wide plates tests using pre-strained plates 610 mm wide indicated that an induced residual strain field had a marked effect on the propagation characteristics of a fracture, [7] and are therefore necessary to confirm full scale behaviour. However, the magnitude and the extent of the strain field was necessarily limited by the size of specimen and it was not always possible to easily separate the effects of the properties, size and residual strain on fracture. Hence further studies have used plate widths ranging from 914 mm to 1830 mm to facilitate a study of the factors influencing fracture propagation through a residual strain field and to quantify the effects of the material behaviour and residual strain. The primary purpose of such investigations were to study the propagation characteristics of a brittle fracture by examining the fracture speed and the strain field associated with the tip of the propagating crack [8].

Various test piece designs have been utilized in wide plate tests, notably the David Taylor Model Basic (DTMB), Standard Oil Development Company (SOD), Robertson, Wells and Japanese double tension test in order to investigate different fracture phenomena and concepts such as initiation, propagation and arrest [9]. Results from the Wells wide plate tests [11, 12, 12], which were established on a rigid type of machine, were used to establish toughness criteria for pressure vessels and were, and still are, incorporated in British Standard BS5300. Data from these previous tests is only available for basic C-Mn steels and not the grain refined micro-alloyed steels now available for structural marine applications. These results were utilized primarily for an initiation approach to fracture.

With regard to the concept of crack arrest, a simple fracture mechanics approach has been successfully applied to the analysis of the experimental results of several conditions of brittle crack arrest using medium-sized wide plate specimens [13]. This analysis is based on the arrest toughness concept and the consideration that the dynamic aspect of the stress intensity factor or strain energy release rate can be taken into account. In this case, the crack length is relatively small, and can be analyzed as equivalent to an arresting crack or a crack running at a speed near to the lower critical velocity of a brittle crack [13]. Previous work on wide plate tests 900 mm wide has indicated that crack arrests were only produced under isothermal conditions when the tensile residual stress field arising from the weld is allowed to remain, that is, the specimens are not given a mechanical or thermal stress-relief treatment. The arresting conditions are apparently produced by a downward gradient of crack extension force along the crack path from the weld at the center of the plate. Wells [10] found that crack arrest occurred only with spontaneous initiation (cooling without external loads) or with external loads giving rise to average stresses less than about one third of the yield. While it is possible to investigate brittle fracture arrest characteristics for short arrested cracks with plates of this size, it has been shown [9] that in order to study the arrest of long cracks, plates of at least 2500 mm wide would have to be considered, thus requiring a test rig with at least a 9000 metric ton capacity. The present study was therefore limited to evaluate initiation behaviour of two potential Arctic grade materials.

4.0 Experimental Program

Four wide plate tests were to be carried out on the Arctic grade materials. The materials are Algoma LT60 and an ASTM A710 Gr. A. Class 3. The LT60 had a nominal yield strength of 350 MPa and was supplied in 63.5 mm thickness. The A710 had a nominal yield strength of 580 MPa and was supplied in 51.0 mm thickness. All the welds were fabricated by AMCA International using a K preparation and submerged arc welding at a fixed heat input of 5.5 kJ/mm. AMCA International also performed a range of small scale tests on the weldments and the results for the LT60 weldment are summarized in Table 1 and for the A710 weldment in Table 2.

Four plates were supplied identified as follows:

W1;	Algoma LT60
W2;	Algoma LT60
W3;	A710 Grade A Cl 3
W4;	A710 Grade A Cl 3

All welds were supplied in the as-welded condition and plates W1 and W3 were subsequently sent out and stress relieved at 620°C for two hours, at heating and cooling rates according to ASME.

The wide plate tests were performed on the test rig shown in Figure 1 which has a load capacity of 4000 tons. Each test was to be carried out at -30°C with the defect located in the coarse grained heat affected zone. Prior to notching each end of the plate was ground and etched to reveal the weldment and to determine the location of the HAZ. The details of the weld and the location of the proposed HAZ defect are shown in Figures 2, 3, 4 and 5. The defects to be produced were located in the centre of the plate and hence this was determined by joining the lines at the top and bottom of the plate based on the etched ends. All the defects were through-thickness, produced by making a central hole and extending this to the proposed length by a saw cut, with a final notch tip produced by a 0.005" saw. A typical example from one of the latter tests is shown in Figure 6.

The test plates were electroslag welded into the test frame using a custom built line-up frame to ensure linearity of the test plates (Figure 7). In order to facilitate the welding operations tests on the 51.00 mm A710 plates were carried out first using a 75 mm to 51 mm tapered insert. The tests on the 63.5 mm plate were carried out using a tapered weld from the 75 mm end plate. All electroslag welds were ultrasonically inspected and blended to the test plate prior to the actual test.

Prior to testing the test plates are fully instrumented with strain gauges and thermocouples (Figure 8). After instrumentation potential drop attachments are made to the plate at one end of the defect tip and the cold box attached (Figure 9). Cooling is performed by pre-cooling the plate with dry ice and then circulating liquid nitrogen vapour around the plate. Once the plate is at the test temperature, the clip gauge is attached across the defect through an insert in the cooling box. Following calibration of all the test equipment, pressure transducers and computer controlled data acquisition system the test is carried out to failure. At the completion of the test the actual defect size is measured, sections are taken through the defect tip to identify the actual region that contains the notch tip and a complete analysis carried out.

5.0 Wide Plate Tests

The defect sizes chosen for the test program were based on the small scale

CTOD test results and the requirement to achieve failure at or below the yield strain. The pre-analysis was based on the following equation:

$$\varepsilon_t = \frac{\delta}{2\pi\bar{a}} + 0.25\varepsilon_y$$

where ε_t = tolerable failure strain
δ = CTOD value
$\bar{a}$ = effective defect parameter
ε_y = yield strain

In the case of a through wall defect $\bar{a}$ is half the defect length. This analysis, based on the original COD design curve, assumes a safety factor of at least two on failure strain.

The actual defect lengths chosen for this test program are given in Table 3.

5.1 Test 1

This test was carried out on the A710 material, plate W3, in the stress relieved condition. A relatively short defect was chosen based on the low CTOD value of 0.034 mm reported from the small scale tests. The temperature distribution at the start of the test is given in Table 4, showing that a good distribution was achieved. The test was stopped at a jack pressure of 138 MPa (20,000 psi) when excessive yielding of submerged-arc test weld was occuring, and the strain in the HAZ was dropping. A comparison of the strain output in the weld and HAZ is shown in Figure 10. In this particular test the stress relieved weld metal yield strength is estimated to be 448 MPa, whereas the HAZ yield strength is in excess of 600 MPa. Hence once net section yielding of the weld metal occurs at about 120 MPa (17,500 psi) jack pressure the strain in the HAZ drops and the defect does not continue to be loaded, (Figure 10). The average strains in the various regions at the time of unloading were,

weld metal	6176 microstrain
HAZ	2732 microstrain
Base Plate	2689 microstrain

Subsequent metallographic examination revealed that the defect was located in the coarse grain HAZ except at either edge and that no growth had occurred.

5.2 Test 2

This test was carried out on the A710 material, plate W4 in the as-welded condition. Based on the stress relieved results and the CTOD value of 0.07 mm in the as-welded condition a defect length of 150 mm was chosen. The temperature distribution of the plate prior to the test is given in Table 4. Once again the strain in the weld metal exceeded yield prior to obtaining net section yield in the plate. The test was stopped at a jack pressure of 125 MPa (18,000 psi), at which point the CMOD and potential drop were indicating some tearing (Figure 11). The average strain in the weld metal at this point was 7000 microstrain and in the HAZ and base plate was 2848 and 2780 micro strain respectively. As the load was beginning to off load in the HAZ and only tearing was progressing it was decided that a valid test point had been reached. Following testing the notch tip was sectioned and examined for actual location. 50% of the notch tip was in the HAZ and the remainder in the weld metal. Evidence of tearing at the crack tip was apparent and the formation of voids and tearing at 45° shear planes is shown in Figure 12.

5.3 Test 3

This test was carried out on the LT60 material, plate W1, in the stress relieved condition. Based on the lower yield strength of this material and a CTOD of 0.2 mm a defect length of 200 mm was chosen. the temperature distribution at the start of testing is given in Table 4. The test failed at 100 MPa (14,500 psi) jack pressure by sudden brittle fracture through the plate. This time because the weld metal strength exceeds the base plate strength no offloading of strain occurs and rapid strain build up occurs in the HAZ ahead of the crack tip (Figure 13). The strain in the plate remains linear (Figure 14) and failure occurs just prior to yield in the plate. The CMOD and potential drop revealed no growth before failure. Sectioning after the test revealed that the failure had initiated in the HAZ and that no ductile tearing preceeded brittle fracture.

5.4 Test 4

This test was carried out on the LT60 material plate W2 in the as-welded condition. There was considerable scatter in the small scale CTOD results and some very low values. Based on the experience from Test 3 and the results of Test 2 which had some relatively low CTOD values a defect length of 125 mm was chosen for this test. The temperature distribution at the start of the test is given in Table 4. The test failed at 93 MPa (13,500 psi) jack pressure by sudden brittle fracture through the plate. Analysis of the strain results shows the HAZ to be approaching ligament yielding at the plate surface when the failure took place. The average strain in the base plate was 1400 microstrain at failure, below yield. No off loading of the HAZ occurred as the local strain developed, (Figure 15). Sectioning of the defect after failure showed that no crack growth had occurred prior to failure and that the crack tip was located 50% in the HAZ and 50% in the weld metal.

6.0 Analysis

The behaviour of the tests have been analyzed using the approach of PD6493 and the equation given in section 5. Initially the results were analyzed in terms of the tolerable failure strain and actual failure strain, given in Table 5. The results of tests 1 and 2 show that for matching strength level, normally a failure would have resulted at the nominal applied strain levels reached in these tests. However because the base plate and especially the HAZ overmatched the weld metal strength yielding was confined to the weld metal. Under these circumstances the weld metal begins to behave under plane strain conditions because necking is restricted and Von Mises conditions do not apply. Hence the weld, because it has a low width to depth ratio, will approach the theoretical strength of the base metal, and strain is offloaded from the HAZ into the weld metal. The defect in the HAZ is therefore not fully loaded and no failure results.

Tests 3 and 4 have initially been analyzed without including any allowance for residual strain in Test 4. The safety factor on strain in terms of failure strain divided by tolerable strain exceeds 2 in both cases. This is consistent with the COD design analysis on which PD6493 is based in that a factor of two was included in the original wide plate analysis. It is clear that adding a residual strain level to the failure strain of Test 4 would make it overly conservative and in fact would predict that the test should fail on cool down with no applied load. The effect of residual strain on fracture of pipelines has been studied by Glover et al (3, 4) and shown that residual strain can be ignored for engineering assessments and still achieve safety levels greater than two.

Another approach that can be taken is to assess the level of CTOD required to achieve a safety factor of two using the actual failure strain as the criteria. This has been analyzed for in the cases of Tests 3 and 4 only, and the results given in Table 5. In the case of the stress relieved welds the predicted CTOD value is experimentally close to the measured values. The as-welded, situation, gives a much larger CTOD than the lower bound results and possibly illustrates the effect of local low toughness region on overall fracture behaviour. This factor is an extremely important one and needs further test evaluation than the limited program presently undertaken. Similarly the effect of the defect in the high strength material is marked by the effect of the lower strength weld metal, and may be significantly changed when matching strength weld metals are utilized. Further tests are required to evaluate this behaviour.

7.0 Summary

Four wide plate tests have been carried out on materials that could be used for Arctic applications. The tests evaluated the heat affected zone behaviour of a high (A710) and a medium strength (LT60) steel. The tests were carried out on defects inserted in the heat affected zone designed to give cleavage failures at -30°C. The tests were carried out in the as-welded and stress relieved condition. The two tests on the high strength material did not produce failures as the strain was limited in the HAZ because of the very much undermatched weld metal strength. In this case all the deformation was occuring in the weld metal and only limited amount of ductile tearing took place at the tip of the HAZ defect.

In the case of the LT60 material cleavage failures occurred and the behaviour could be described in terms of the COD design curve. In both cases the safety factor in terms of strain exceeded two. These analyses were carried out without including residual strain and the present tests would indicate that the inclusion of residual strain would be overly conservative. Further investigation of this factor is warranted because of the limited number of tests and the method of crack insertion. Similarly an analysis based on CTOD safety factors showed that although the HAZ had low toughness in the as-welded condition the full scale tests behaved at a much higher CTOD value. This factor also needs further investigation than the limited results from these present tests.

8.0 References

1. British Standard Publication PD6493-1980, Guidance on Some Methods for Derivation of Acceptance Levels for Defects in Fusion Welded Joints.
2. Welding Institute of Canada Report: RC75/2/83, May 1983.
3. Glover, A.G., Coote, R.I. and Pick, R.J., "Engineering Critical Assessment of Pipeline Girthwelds", Fitness for Purpose Validation of Welded Construction, Welding Institute UK, London, 1981.
4. Glover, A.G. and Coote, R.I., "Full Scale Fracture Tests of Pipeline Girth Welds", Conference ASME, Circumferential Cracks in Pressure Vessels and Piping, Portland, June 1983.
5. Soete, W., "The Wide Plate Test", Metal Construction, February 1980.
6. Marique, C. and Bragard, A., "Weldability of Structural Steels - Assessment by Wide Plate and COD Tests", Metal Construction, June 1979.
7. Rolfe, S.T. and Hall, W. J., "Brittle Fracture Tests of Two Feet Wide Steel Plates Containing Residual Compressive Strain", Welding Research Supplement, Welding Journal, April 1959.
8. Barron, R. W. and Hall, W.J., "Brittle Fracture Tests of Six Foot Wide Prestressed Steel Plates", Welding Research Supplement, Welding Journal, Sept. 1960.
9. Kihara, H., Hall, W.J., Soete, W. and Wells, A.A., "Brittle Fracture of Welded Plate", Prentice-Hall publication, 1967.

10. Wells, A.A., "Brittle Fracture Strength of Welded Steel Plates", British Welding Journal, May 1961.

11. Wells, A.A., "Testing Thick Plates for Brittle Fracture", Nuclear Engineering 69:7, 1962.

12. Rosenstein, A.M. and Labahn, J.D., "Brittle Fracture of Welded Steel Plates", Welding Research Supplement, Welding Journal, Nov. 1967.

13. Hahn, G.T. and Kanninen, M.F., ASTM Special Technical Publication 627, "Fast Fracture and Crack Arrest", 1977.

9.0 Acknowledgements

This work was sponsored by AMCA International as part of their 50/50 CANMET/DSS program. The author would like to thank Dirk Varo, Neil Sweetman, Paul Koornneef and Azael Aguire who carried out the experimental program.

TABLE 1

Properties of Algoma LT60 Steel

(As supplied by AMCA International)

Base Plate

	Normalized	Stress Relieved
Yield Strength MPa	386	350
Ultimate Strength MPa	516	496
Elongation %	30	35.6
CVN (L) at -30°C(J)	207	204
CVN (L) at -60°C(J)	211	192

HAZ Properties (5.5 kJ/mm)

Coarse Grain Hardness (HV10)	265 (as-welded)
	220 (stress relieved)

CTOD Values at -30°C

	As Welded (mm)	Stress Relieved (mm)
1	0.082	0.24
2	0.271	0.251
3	0.286	0.848
4	0.043	0.250
5	0.033	0.181
6	0.158	

TABLE 2

Properties of ASTM A710 GrA Cl 3 Steel

(As supplied by AMCA International)

Base Plate

	As Received	Stress Relieved
Yield Strength MPa	581	N/A
Ultimate Strength MPa	669	N/A
Elongation %	29	N/A
CVN (L) at -60°C(J)	182	N/A

HAZ Properties (5.5 kJ/mm)

Coarse Grain Hardness (HV10)	270 (as-welded) 290 (stress relieved)

CTOD Values at -30°C

	As Welded (mm)	Stress Relieved (mm)
1	0.151	0.596
2	0.209	0.238
3	0.109	0.168
4	0.07	0.062
5	0.144	0.034
6	0.600	1.029

TABLE 3

Defect Lengths for Test Program

Test Number	Plate Identification	Condition	Defect Length mm	$\bar{a}$ mm
1	W3	Stress Relieved	60	30
2	W4	As Welded	150	75
3	W1	Stress Relieved	200	100
4	W2	As Welded	125	62.5

TABLE 4

Temperature Distribution

Test Number	Temperature °C (Location)					
	Crack				Plate	
	Top		Bottom		Top	Bottom
	1	2	1	2		
1	-31	-29	-30	-30	-36	-36
2	-33	-31	-34	-33	-37	-32
3	-31	-31	-30	-32	-30	-30
4	-30	-29	-33	-29	-29	-32

TABLE 5

Analysis of Results

Test	Failure Strain %	Tolerable + Strain %	Safety Factor on Strain	CTOD to Achieve a Factor of Two (mm)
1	>0.27*	0.090	>3	-
2	>0.28*	0.085	>3	-
3	0.17	0.07	2.42	0.27
4	0.14	0.055	2.54	0.11

+ based on lower bound
CTOD in HAZ

* test stopped

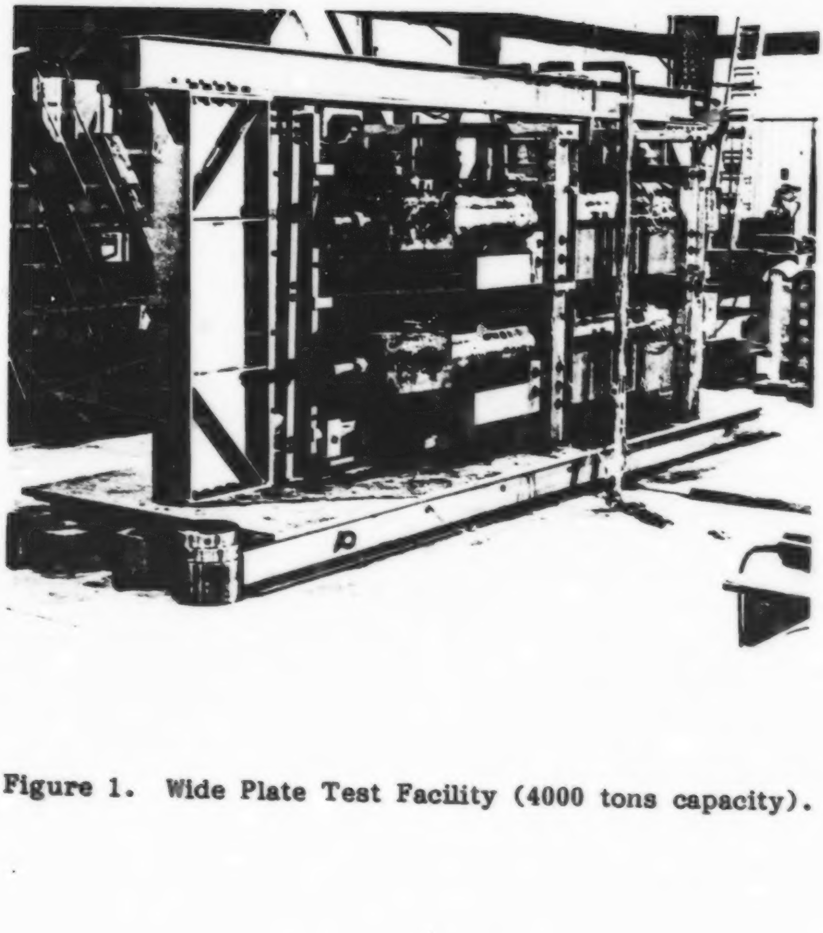

Figure 1. Wide Plate Test Facility (4000 tons capacity).

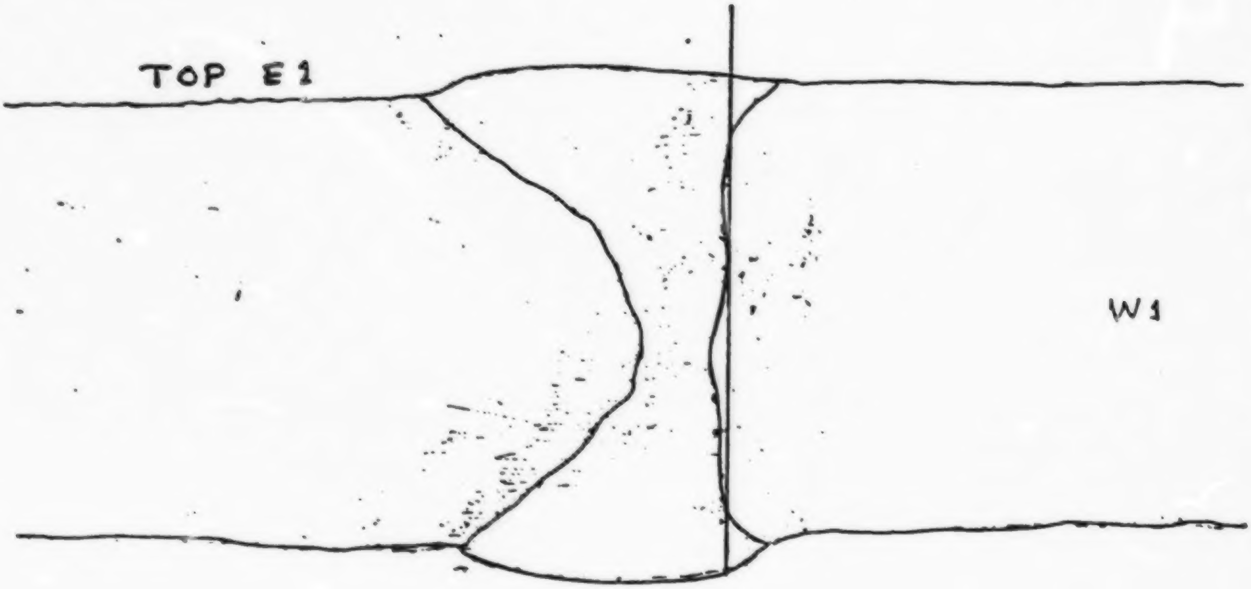

Figure 2. Etched end of test plate W1 and proposed location of HAZ defect.

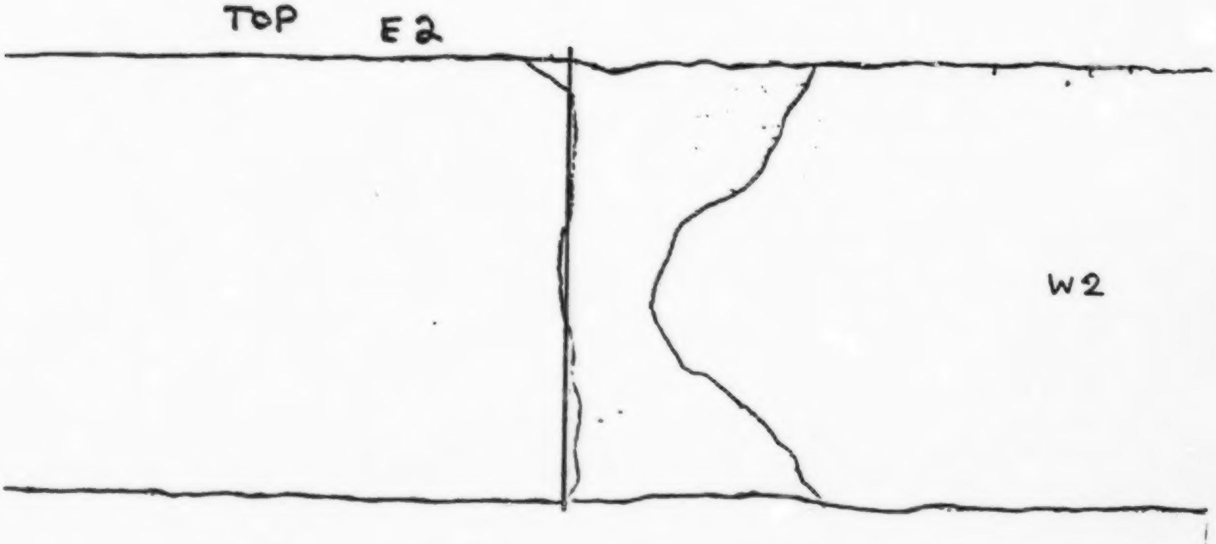

Figure 3. Etched end of test plate W2 and proposed location of HAZ defect.

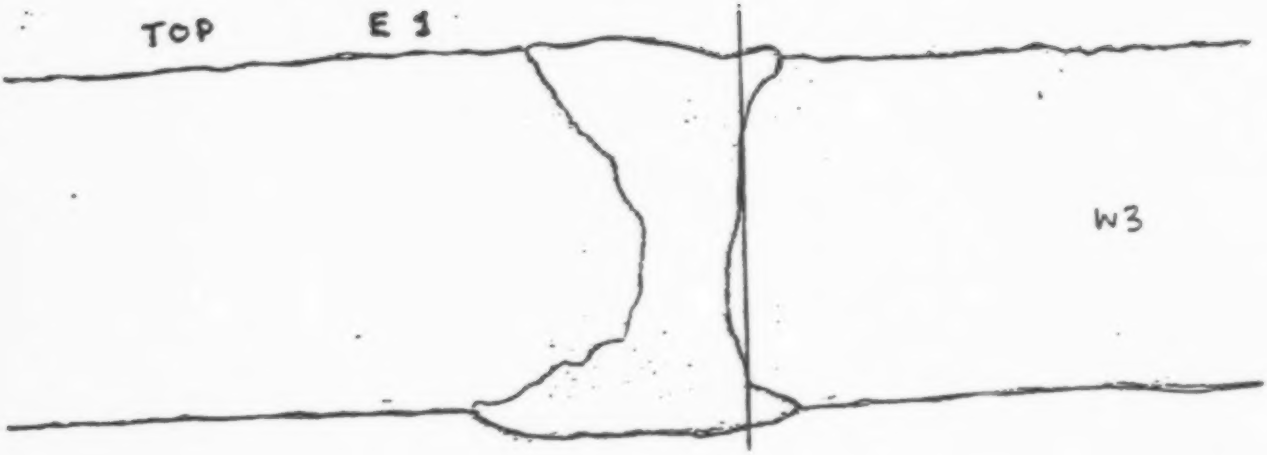

Figure 3. Etched end of test plate W3 and proposed location of HAZ defect.

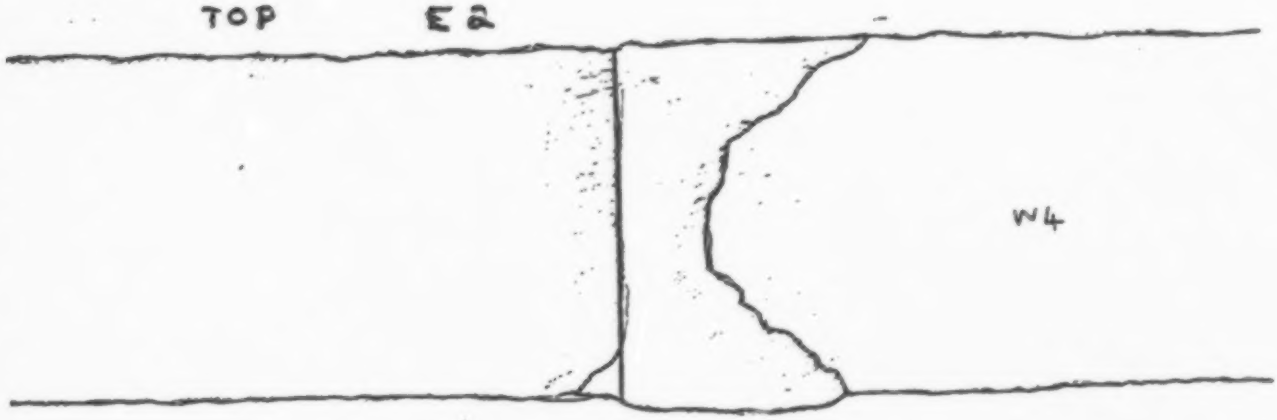

Figure 4. Etched end of test plate W4 and proposed location of HAZ defect.

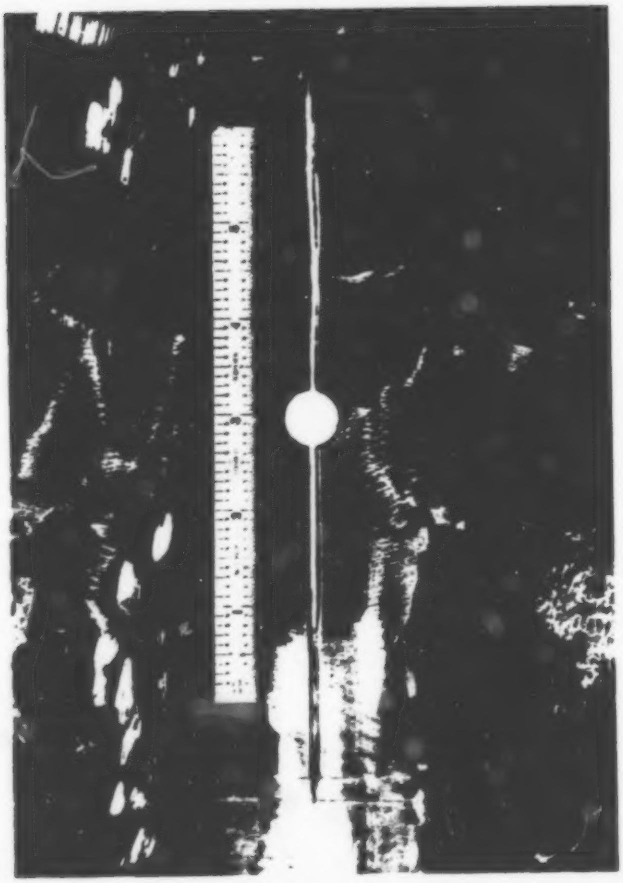

Figure 6. Through-thickness defect inserted in test plate W1.

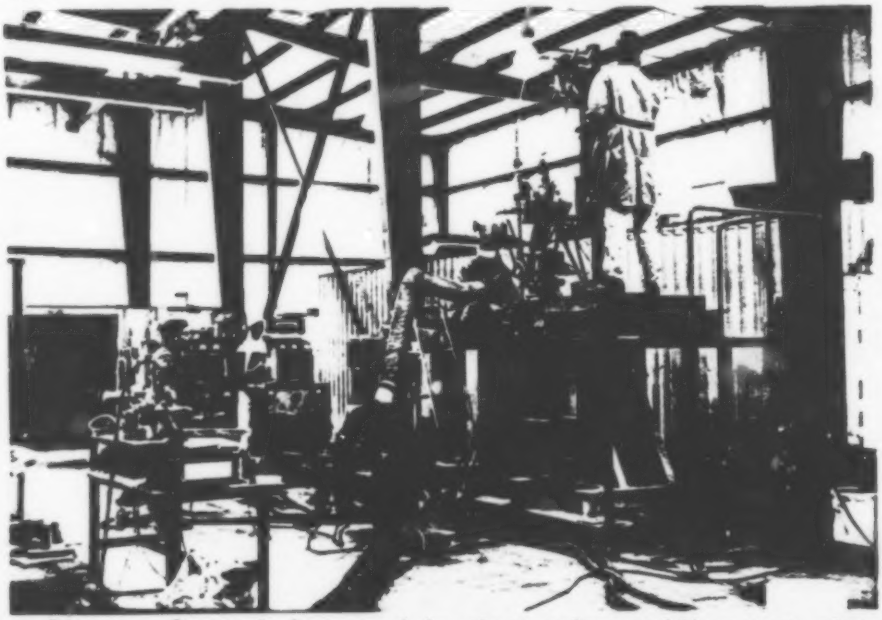

Figure 7. Line-up frame being used in electroslag welding test plate into end lugs.

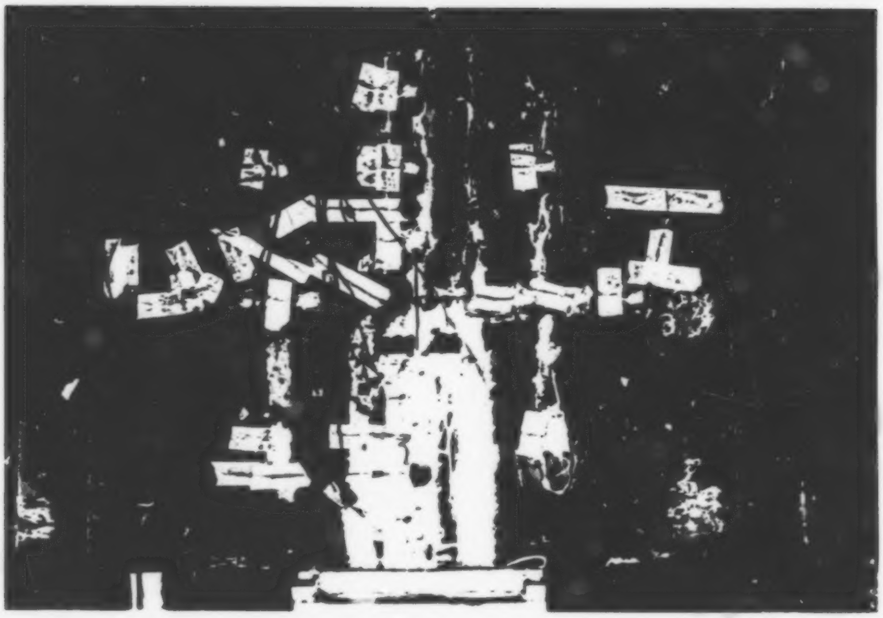

Figure 8. Typical instrumentation on one side of the plate (equally matched on other side).

Figure 9. Cool box in place prior to final location of the test pistons.

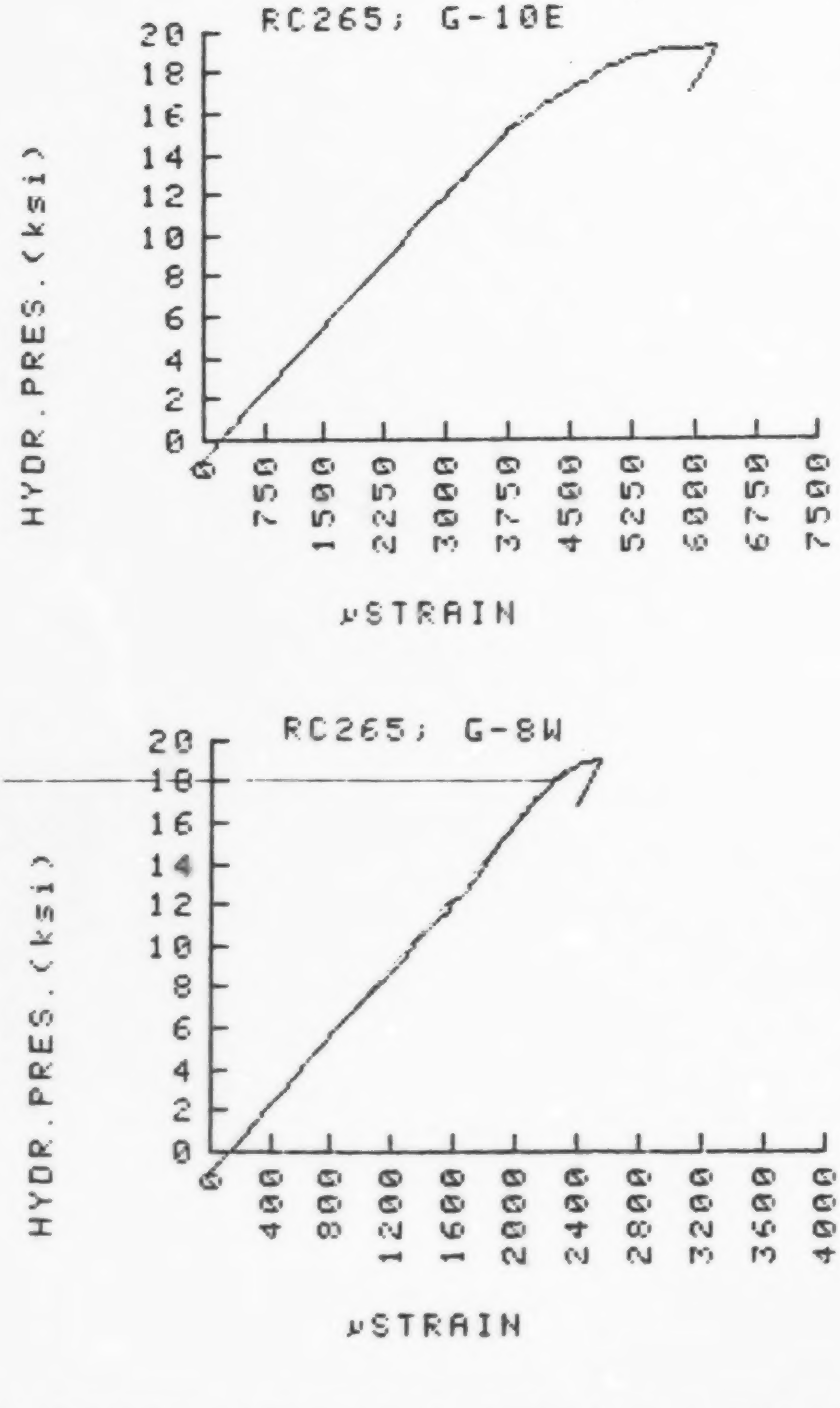

Figure 10. Comparison of the strain developing in the weld (top) and the HAZ (bottom) for test 1, plate W3, stress relieved A710.

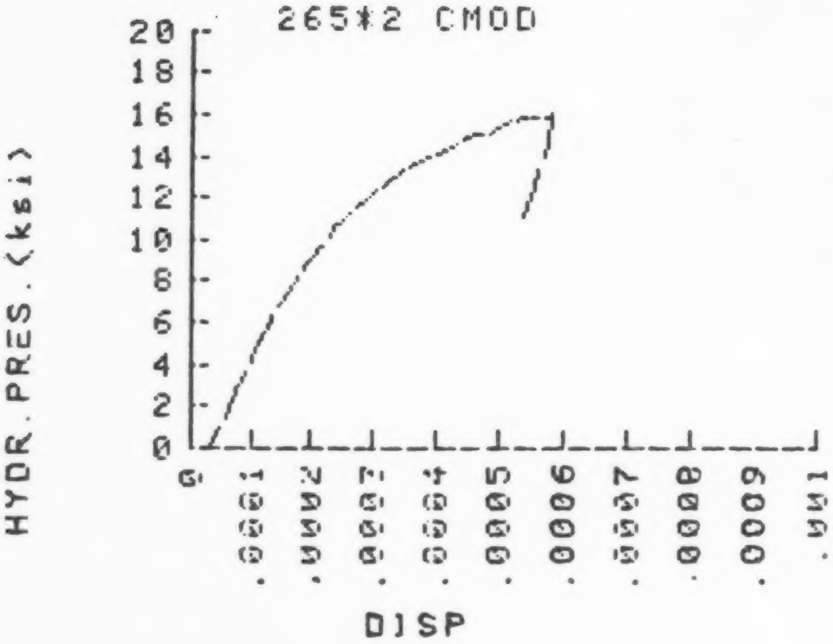

Figure 11. CMOD output of test 2, plate W4, A710 as welded, showing onset of tearing.

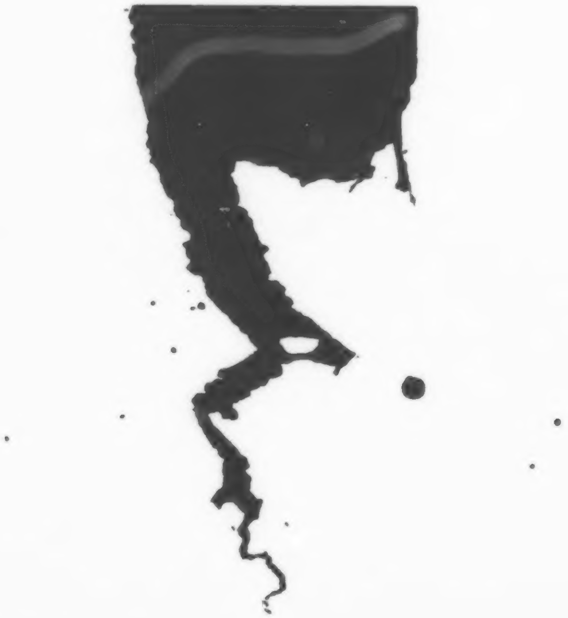

Figure 12. Section through crack tip of test 2, plate W4, showing void formation and initiation of tearing on 45° shear plane. Mag X100.

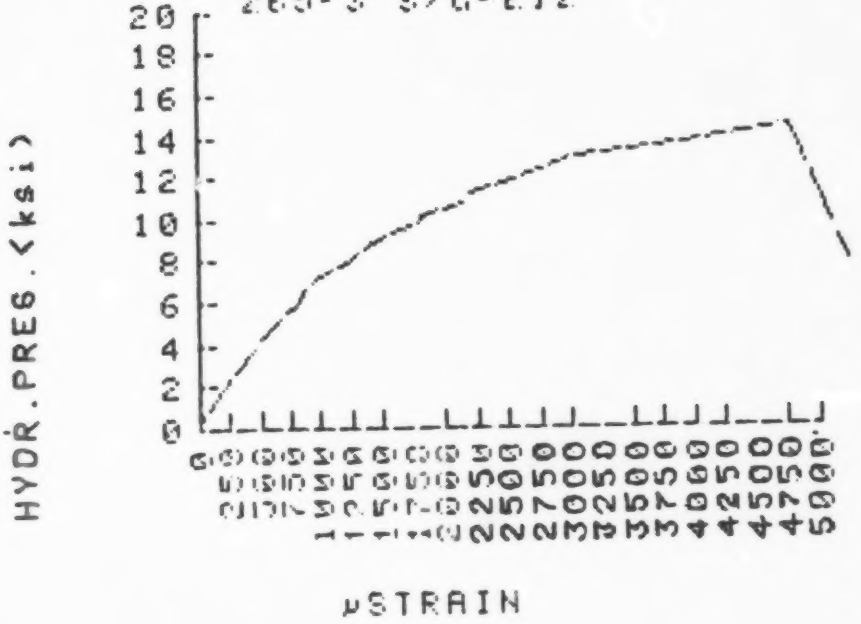

Figure 13. Strain build up in the HAZ ahead of the crack tip for test 3, plate W1 LT60, stress relieved.

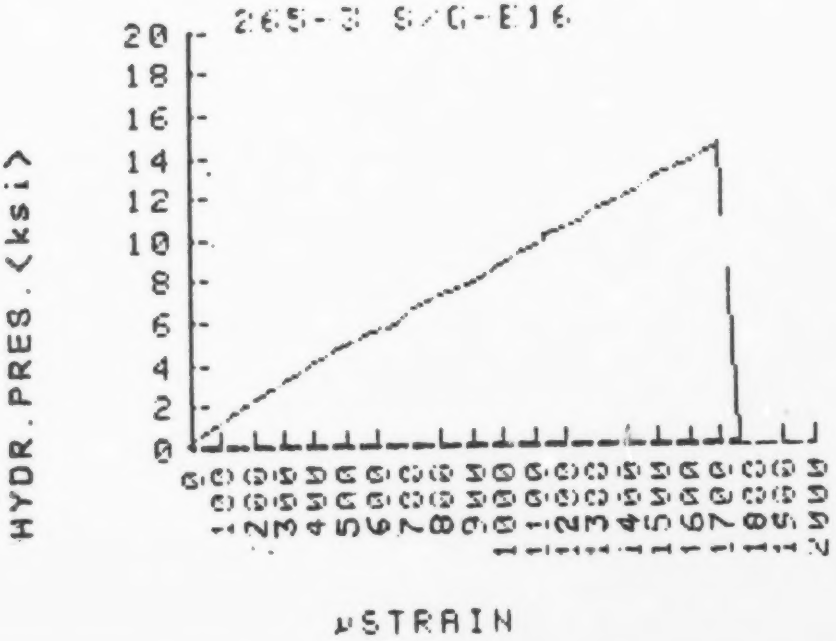

Figure 14. Linear strain relationship with loading in the base plate, test 3, plate W1 LT60 stress relieved.

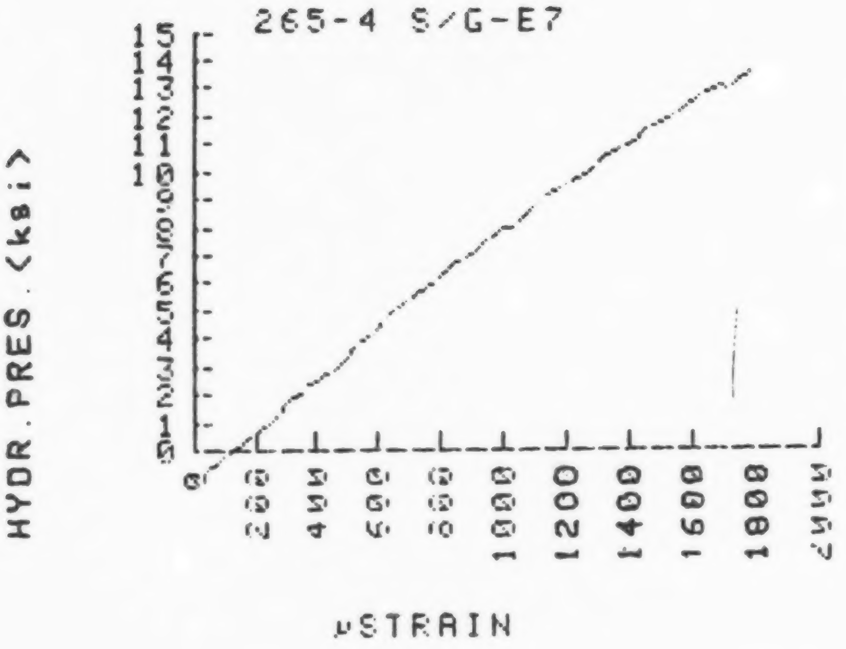

Figure 15. Strain developed in the HAZ of test 4, plate W2, LT60 as welded.